SCHOLARLY PUBLICATIONS

A CURRENT AWARENESS BULLETIN
OF RESEARCH OUTPUT

@DTU

(66th Edition)

JUNE, 2018

BY: CENTRAL LIBRARY

DELHI TECHNOLOGICAL UNIVERSITY
(FORMERLY *DELHI COLLEGE OF ENGINEERING)*
GOVT. OF N.C.T. OF DELHI
SHAHBAD DAULATPUR, MAIN BAWANA ROAD
DELHI 110042

PREFACE

This is the **Sixty Sixth** Issue of Current Awareness Bulletin started by Delhi Technological University, Central Library. The aim of the bulletin is to compile, preserve and disseminate information published by the faculty, students and alumni for mutual benefits. The bulletin also aims to propagate the intellectual contribution of Delhi Technological University (DTU) as a whole to the academia.

The bulletin contains information resources available in the internet in the form of articles, reports, presentations published in international journals, websites, etc. by the faculty and students of DTU. The publications of faculty and student which are not covered in this bulletin may be because of the reason that the full text either was not accessible or could not be searched by the search engine used by the library for this purpose.

The learned faculty and students are requested to provide their uncovered publications to the library either through email or in CD, etc. to make the bulletin more comprehensive.

This issue contains the information published during **June, 2018**. The arrangement of the contents is alphabetical. The full text of the article which is either subscribed by the university or available in the web is provided in this bulletin.

Central Library

CONTENTS

1. Alfven Wave Instability with Streaming Electrons in Magnetized Dusty Plasma, Ved Prakash, Ruby Gupta and ***3.S. C. Sharma***, Applied Physics, DTU

2. Work function and electrical properties of individual multiwalled carbon nanotube: influenced by nature of catalyst and substrate, ***6.Reetu Kumari***, ***3.Pawan K. Tyagi*** and ***3.Nitin K. Puri***, Applied Physics, DTU

3. Chance Constraints Integrated MPC Navigation in Uncertainty amongst Dynamic Obstacles: An overlap of Gaussians approach, Dhaivat Bhatt, ***6.Akash Garg***, Bharath Gopalakrishnan and K. Madhava Krishna, DTU

4. Coefficient of friction and microhardness analysis of CrC coating, ***6.Shailesh Mani Pandey***, Mechanical, DTU

5. Corroborating the Spin Gapless Character of Ti2Mnal Inverse Heusler Alloy: A study of Strains Effect, ***3.Mukhtiyar Singh***, Manish K. Kashyap and Hardev S. Saini, Applied Physics, DTU

6. DermaGene and VitmiRS: a comprehensive systems analysis of genetic dermatological disorders, ***7.Razia Rahman***, ***6.Isha Sharma***, ***6.Lokesh K. Gahlot*** and ***3.Yasha Hasija***, Biotechnology, DTU

7. Dielectric and absorption properties of as-grown Bilayer and Single layer graphene at the microwave frequencies, ***6.Kamlesh Patel*** and ***3.Pawan K. Tyagi,*** A Physics, DTU

8. Direct Power Neuro-Fuzzy Controller Scheme of Three-Phase PWM Rectifiers for Power Quality Improvement, Mustapha Jamma, ***3.Dheeraj Joshi***, Mohammed Akherraz and Abderrahim Bennassar, Electrical, DTU

9. Editorial Preface on the Proceedings of INN International Conference/Workshop on Nanotechnology and Nanomedicine (NTNM2017), ***6.Masoud Mozafari***, Biotechnology, DTU

10. Effect of Drive Side Pressure Angle on Load Carrying Capacity of Asymmetric Involute Helical Gear, ***8.Jairaj Gambhir***, ***3.Paras Kumar***, ***6.Bhuvan Aggarwal*** and ***6.Harshit Arya***, Mechanical, DTU

11. Enhanced red down-conversion luminescence and high color purity from flux assisted Eu3+ doped calcium aluminozincate phosphor, Sumandeep Kaur, ***3.A.S.Rao*** and ***3.M.Jayasimhadri***, Physics, DTU

12. Formulation of cereal based spread using oats fermented with Baker's Yeast, Sukirti Tiwari, Abha Sharma and ***6.Rajinder Kumar Gupta***, Biotechnology, DTU

13. Krill Herd based Optimization for Job Shop Scheduling Problems (JSSP) to Minimize Make Span Time, Vineet Kumar, Om Pal Singh and ***3.Radhey Shyam Mishra***, Mechanical, DTU

14. Modeling of a neural network based controller for vibration suppression of a building structure, ***3.Nilam Rathi***, Harendra Pal Singh and Surendra Kumar, Applied Mathematics, DTU

15. Nature Inspired Power Optimization in Smartphones, ***6.Nirmal Pandey***, ***3.O.P. Verma***, ***6.Amioy Kumar***, Electronics & Communication, DTU

16. New realization of third order sinusoidal oscillator using single OTRA, Gurumurthy Komanapalli, ***3.Neeta Pandey*** and ***3.Rajeshwari Pandey***, ECE, DTU

17. Performance Review of Fuzzy Logic Based Controllers Employed in Brushless DC Motor, ***6.Rakesh Goswami*** and ***3.Dheeraj Joshi***, Electrical, DTU

18. Potential application of multi-walled carbon nanotubes/activated carbon/bamboo charcoal for efficient alcohol sensing, ***6.Vinay Kumar*** and ***3.Pawan K. Tyagi***, Applied Physics, DTU

19. Realization of class – A chopper using dSPACE, ***6.Akshat Jain*** and ***3.Dheeraj Joshi***, Electrical, DTU

20. Realization of Recursive Algorithm for One-Dimensional Discrete Cosine Transform and Its Inverse, Pragati Dahiya and ***3.Priyanka Jain***, DTU

21. Recognition of Multiple PQ Issues using Modified EMD and Neural Network Classifier, ***6.1.M. K. Saini*** and R. K. Beniwal, Electronics and Communication, DTU

22. Review on Different Types of 3D Watermarking, ***6.Akshay Mool***, ***8.Pran Swarup Borah***, ***7.Ramjan Ali*** and ***3.Dr. Jeebananda Panda***, Information Technology and ECE, DTU

23. Robust Object Tracking with Crow Search Optimized Multi-cue Particle Filter, ***3.Kapil Sharma***, Gurjit Singh Walia, ***8.1.Ashish Kumar***, Astitwa Saxena and Kuldeep Singh, IT, DTU

24. Role of Different Etchants on the Growth of Catalyst Nanoparticles During the Plasma Processing of Metal Catalyst Thin Film, ***6.Ravi Gupta***, ***3.Suresh C. Sharma*** and ***6.Neha Gupta***, Applied Physics, DTU

25. Role of Dust Grains in Beam-Driven Instabilities ***3.S. C. Sharma***, Ved Prakash and Ruby Gupta, Applied Physics, DTU

26. Solid Flavinium perchlorate salt as catalyst for Bayer-Villiger Oxidation: Effect of N10 chain length, ***3.Ram Singh***, ***6.Deepshikha Rathore***, Geetanjali and ***3.Richa Srivastava***, Applied Chemistry,DTU

27. Synthesis and enhancement of photoluminescent properties in spherical shaped Sm3+/Eu3+ co-doped NaCaPO4 phosphor particles for w-LEDs, ***6.Mukesh K. Sahu***, ***3.M. Jayasimhadri***, ***6.Kaushal Jha***, ***6.B. Sivaiah***, ***3.A.S. Rao***, D. Haranath, Applied Physics, DTU

28. Terahertz radiation emission using plasma-filled dielectric liner with the effects of pre-modulated relativistic electron beam, ***6.Jyotsna Panwar*** and ***3.Suresh C. Sharma***, Applied Physics, DTU

29. Wind Energy in India: Current Status and Potential, ***3.Prem Prakash***, Electrical, DTU

1. *Chancellor*
2. *Pro Vice Chancellor* — ***2.1.*** *Ex Pro Vice Chancellor*
3. *Faculty* — ***3.1.*** *Ex Faculty*
4. *Teaching-cum-Research Fellow* — ***4.1.****Asst. Librarian*
5. *Alumni*
6. *Research Scholar* — ***6.1.*** *Ex Research Scholar*
7. *PG Scholar* — ***7.1.*** *Ex PG Scholar*
8. *Undergraduate Student* — ***8.1.*** *Ex Undergraduate Student*

Available online at www.sciencedirect.com

ScienceDirect

Materials Today: Proceedings 5 (2018) 15366–15370

materialstoday: PROCEEDINGS

www.materialstoday.com/proceedings

ISCAS 2017

Alfven Wave Instability with Streaming Electrons in Magnetized Dusty Plasma

Ved Prakash[1], Ruby Gupta[2*] and S. C. Sharma[3]

[1]India Meteorological Department, Ministry of Earth Sciences, Lodi Road, New Delhi-110 003, India
[2]Department of Physics, Swami Shraddhanand College, University of Delhi, Alipur, Delhi-110 036, India
[3]Department of Applied Physics, Delhi Technological University, Shahbad Daulatpur, Bawana Road, Delhi-110 042, India

Abstract

Alfven waves are observed in the solar wind and may be responsible for generation of the parallel electric fields in the aurora. In the present work, we investigate the electromagnetic Alfven waves in three component dusty plasmas. The negative ions streaming through magnetized dusty plasma drive Alfven waves to instability via Cerenkov interaction. The presence of charged dust grains and streaming electrons modify the dispersion relation of low frequency Alfven waves. The charge and number density of dust grains and external magnetic field significantly modify the dispersion properties of these waves. The impact of the electron streaming velocity and the thermal electron speed on the growth of the instability is studied analytically. The Alfven modes with phase velocity comparable to the electron streaming velocity possess a large growth rate. The maximum value of growth rate increases with an increase in thermal electron speed or electron temperature. However, the maximum value of growth rate decreases with an increase in dust grain number density. Numerical calculations are done using the plasma parameters suitable for the earth's magnetosphere. The results of the proposed theory are applied to understand some of the experimental observations.

© 2018 Elsevier Ltd. All rights reserved.
Selection and Peer-review under responsibility of 10th NATIONAL CONFERENCE ON SOLID STATE CHEMISTRY AND ALLIED AREAS (ISCAS - 2017).

Keywords: Dispersion, Growth rate, Cerenkov, Ion speed

*Email address: *rubyssndu@gmail.com*

2214-7853 © 2018 Elsevier Ltd. All rights reserved.
Selection and Peer-review under responsibility of 10th NATIONAL CONFERENCE ON SOLID STATE CHEMISTRY AND ALLIED AREAS (ISCAS - 2017).

1 Introduction

Alfven waves were identified in the solar wind environment by the Mariner V spacecraft near the Earth because of the high correlation observed between the magnetic and velocity fields. Several theoretical models have been proposed Alfven waves as a possible accelerating mechanism for solar and stellar winds [1-4]. The Alfven wave is the dominant low frequency transverse mode of magnetized plasma. The wave propagates along the magnetic field and displays a continuous spectrum even in a bounded plasma. Plasma instabilities driven by the perpendicular or cross-field currents due to relative motion of plasma constituents have received a lot of attention. The particle drifts provide free source of energy in space and astrophysical environments. The electron-inertia or pressure leads to localized parallel electric fields of the Alfven wave and cross-field propagation, considered to be driving sources of accelerated electron fluxes in space. The generation of kinetic Alfven waves by ion-ion streaming along the magnetic field at relatively low Alfven speed and low plasma beta have been investigated [5] and it is found that when the ratio of the Alfven speed to the electron thermal speed is large enough, the interaction of waves with the electrons produces strong parallel heating.

Most of the space plasmas are dusty and they contain charged grains and coupling of the grains to the magnetic field determined the wave propagation in the planetary and interstellar medium. Alfven waves propagating at frequencies above the dust-cyclotron frequency and below the ion-cyclotron frequency in a dusty plasma are strongly modified when a fraction of negative charge settles down on the dust grain surface. The presence of dust particles significantly modifies the electrostatic and electromagnetic modes in plasma [6-10].

In this paper, we study the electromagnetic Alfven waves in three component dusty plasmas with streaming electrons. In Sec. 2, we carry out the instability analysis and find the expression for growth rate using first order perturbation technique. Results and discussions are given in Sec. 3. And the conclusion part is given in Sec. 4.

2 Instability Analysis

We consider a collisionless and uniformly magnetized dusty plasma whose constituents are electrons, ions and negatively charged dust grains, in which the electrons are streaming across the magnetic field direction with a constant electron drift velocity $v_{eo}\,\hat{x}$. At equilibrium, the plasma system is quasineutral, i.e., $n_{io}= n_{eo}+ Z_d n_{do}$, where $n_{io,}\, n_{eo},\, n_{do}$ are the number densities of ions, electrons and dust grains, respectively, Z_d (= Q_{do}/e) is the number of electrons residing on the surface of negatively charged dust grains; Q_{do} being the equilibrium dust grain charge and e is the magnitude of the electronic charge. Let us consider an electromagnetic wave, such as Alfven mode, propagating parallel to the external static magnetic field ($\mathbf{B_0} \,//\, \hat{z}$) with propagation wave vector $\vec{\mathbf{k}}$. We assume the t, z variations of Alfven fields as $\mathbf{E}, \mathbf{B} \sim \exp[-i(\omega t - k_z z)]$ and consider plane polarization i.e.

$\mathbf{k} \,//\, \mathbf{B_0}$, $\mathbf{k} = (0,0,k_z)$ and $\mathbf{E} = (E_x,0,0)$

The perturbed magnetic field of the wave is $\mathbf{B} = \frac{c}{\omega}\mathbf{k}\times\mathbf{E}$.

The equation of motion for the perturbed plasma electrons is

$$\frac{\partial \mathbf{v}}{\partial t} + \mathbf{v}\cdot\nabla(\mathbf{v}) = -\frac{e}{m}\left(\mathbf{E} + \frac{1}{c}\mathbf{v}\times\mathbf{B}_0\right) - \frac{1}{mn}\nabla(n\mathbf{T}_e)\cdot \tag{1}$$

where $\mathbf{v} = v_{e0}\hat{x} + \mathbf{v}_{e1}$, $\mathbf{v}_{e1}$ refers to perturbed electron velocity.

On linearizing Eq. (1), we obtain the perturbed electron velocities. Using them in the equation of continuity, we obtain the perturbed electron density as

$$n_{e1} = \frac{e n_{eo} v_{e0} k_z^2 E_x}{i m_e \omega \bar{\omega}^2}\left(1 - \frac{k_z v_{te}^2}{\bar{\omega}^2}\right)^{-1}, \tag{2}$$

where $\bar{\omega} = \omega - k_z v_{eo}$, $v_{te}^2 = \frac{T_e}{m_e}$ and m_e is the mass of electron.

The response of the plasma ions and dust grains can be obtained from Eq. (2) by replacing e, $m_{e,}$ ω_{ce}, n_{e0} by -e, m_i, -ω_{ci}, n_{i0} for ions and by Q_{d0}, m_d, 0 and n_{d0} for dust grains. The dust response is taken as unmagnetized as

$\omega_{cd} << \omega << \omega_{ci} << \omega_{ce}$; ω_{cd}, ω_{ci} and ω_{ce} are the dust, ion and electron cyclotron frequencies respectively.

The perturbed current density along x-direction is given as:

$$J_{1x} = -e\,n_{e0}v_{e1x} + e\,n_{i0}v_{i1x} - e\,n_{e1}v_{e0} + Q_{d0}n_{d0}v_{d1x}. \quad (3)$$

Using the values of perturbed velocities and number densities of various constituents of plasma in Eq. (3), we obtain

$$J_{1x} = -\frac{i\,e^2 n_{eo}}{m_e\omega}\frac{\bar{\omega}^2}{\omega_{ce}^2}E_x - \frac{i\,e^2 n_{io}}{m_i\omega}\frac{\bar{\omega}^2}{\omega_{ci}^2}E_x + \frac{ie^2k_z^2 n_{eo}v_{e0}^2}{m_i\omega\bar{\omega}^2}\left(\frac{\bar{\omega}^2}{\bar{\omega}^2 - k_z^2v_{te}^2}\right)E_x + \frac{i\,Q_{d0}^2 n_{do}}{m_d\omega}E_x \quad (4)$$

where $\omega_{ci} = \frac{eB_0}{m_ic}$ and $\omega_{ce} = \frac{eB_0}{m_ec}$.

The wave equation which governs the mode structure of low frequency Alfven waves is given as

$$\frac{\partial^2 E_x}{\partial z^2} = \frac{4\pi}{c^2}\frac{\partial J_{1x}}{\partial t} + \frac{1}{c^2}\frac{\partial^2 E_x}{\partial t^2}. \quad (5)$$

Substituting Eq. (4) in Eq. (5), we get

$$\alpha\omega^2 - \left(k_z^2c^2 + \omega_{pd}^2 + \frac{\omega_{pi}^2k_z^2v_{e0}^2}{\omega^2 - k_z^2v_{te}^2}\right) = 0\ , \quad (6)$$

where $\alpha = 1 + \frac{\omega_{pi}^2}{\omega_{ci}^2}\left(1 + \frac{n_{eo}m_e}{n_{io}m_i}\right)$, $\omega_{pe}^2 = \frac{4\pi\,n_{eo}\,e^2}{m_e}$, $\omega_{pi}^2 = \frac{4\pi\,n_{io}\,e^2}{m_i}$ and $\omega_{pd}^2 = \frac{4\pi\,n_{do}\,Q_{do}^2}{m_d}$.

$$\text{or } \left(\omega^2 - \omega_1^2\right)\left(\omega^2 - k_z^2v_{te}^2\right) = \frac{1}{\alpha}\omega_{pi}^2k_z^2v_{e0}^2. \quad (7)$$

A perturbative solution of Eq. (7), i.e. $\omega = \omega_1 + \Delta$ and $\omega = k_zv_{te} + \Delta$, where Δ is the small frequency mismatch, we obtain a growth rate $\gamma = \mathrm{Im}(\Delta)$

$$\text{or } \gamma = \frac{\omega_{pi}^2k_z^2v_{e0}^2}{2\omega\left(\omega^2 - k_z^2v_{te}^2\right)}\left[1 + \frac{\omega_{pi}^2}{\omega_{ci}^2}\left(1 + \frac{n_{eo}m_e}{n_{io}m_i}\right)\right]^{-1}. \quad (8)$$

In the absence of dust grains and electron streaming, Eq. (7) yields

$$\omega_1^2 = k_z^2c^2\left[1 + \frac{\omega_{pi}^2}{\omega_{ci}^2}\left(1 + \frac{n_{eo}m_e}{n_{io}m_i}\right)\right]^{-1} \approx V_A^2k_z^2, \quad (9)$$

where $V_A = \frac{c\omega_{ci}}{\omega_{pi}}$ is the Alfven speed.

3 Results and Discussion

The parameters used in the present calculations are: ion plasma density $n_{i0} = 10^3$ cm^{-3}, magnetic field $B_0 = 0.043$ G, mass of ion m_i, mass of dust grain $m_d = 10^{-15}$ kg, electron streaming velocity $v_{e0} = 20$ cm/s. The dust grain number density of negatively charged dust grains n_{d0} has been varied from 0.1×10^{-5} cm^{-3} to 100×10^{-5} cm^{-3}, and the electron thermal velocity has been varied from 0.5×10^4 cm/s to 5×10^4 cm/s.

In Fig. 1, we have plotted the dispersion curves of Alfven waves in magnetized dusty plasma, for different values of dust grain number density n_{d0}. The unstable frequencies of the Alfven waves in presence of dust grains increase with increase in number density of negatively charged dust grains. The phase velocity of the wave increases but the group velocity decreases with an increase in the concentration of dust grains. It is also observed that the effect of dust grain concentration on the wave frequency decreases for higher values of k_z.

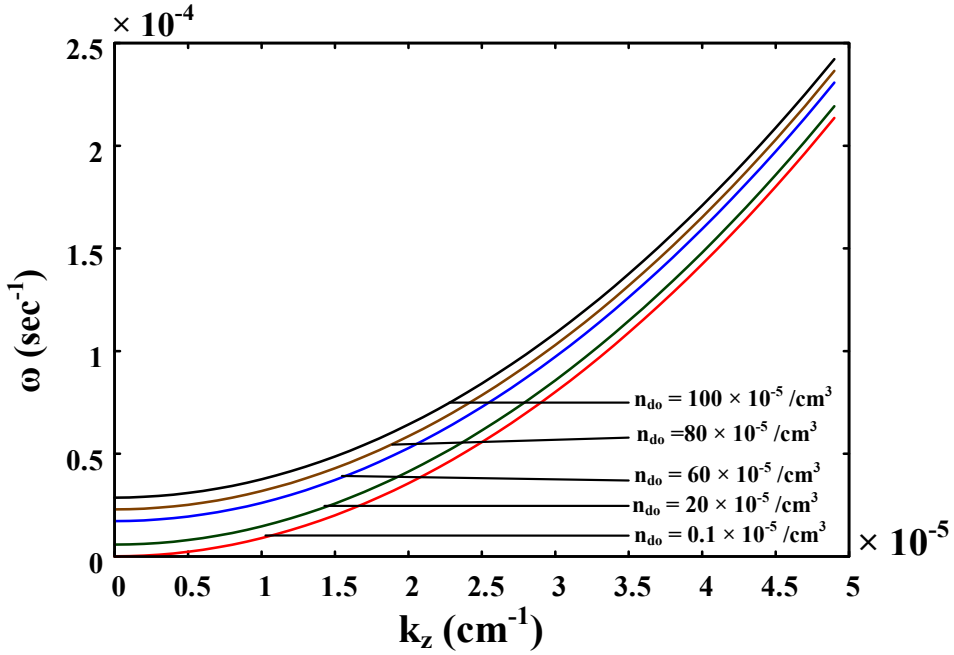


Fig. 1. Dispersion curves of Alfven waves over a magnetized dusty plasma for different values of dust grain number density.

Fig. 2 shows the variation of growth/damping rate γ (rad/s) of Alfven wave instability as a function of unstable wave number k_z for different values of dust grain concentration. It is noticed that the streaming electrons enhance the growth/damping rate of the wave. At lower k_z the growth rate and damping rates are increased which are decreased at the higher k_z. The growth rate curves show a maxima and the maximum value of growth rate decreases with an increase in dust number density. The existence of streaming thermal electrons is necessary to influence the wave, as is evident from Eq. (8). The streaming speed has a significant impact on the growth rates. By increasing the dust grain number density, the magnitude of the growth rate decreases drastically as shown in Fig. 2. It is seen that the unstable region becomes narrow and shifts towards small wavenumbers with an increase in dust grain number density. When a large number of dust grains are settled down in plasma, the dust grains together have a large apetite for the electrons but the number of available electrons per dust grain decreases. This reduces the average dust grain charge Q_{d0}, and thus leads to a decrease in growth rate.

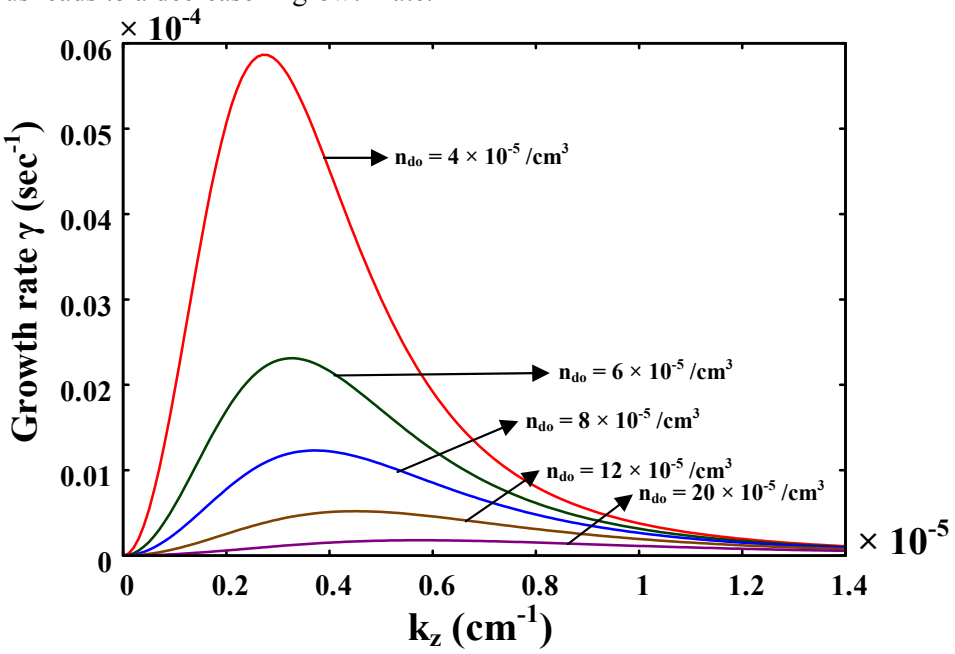


Fig. 2. Growth rate of the Alfven wave instability as a function of unstable wavenumber k_z for different values of dust grain number density.

Fig. 3 shows the variation of growth rate as a function of parallel wave number k_z, for different values of thermal electron speed. The growth/damping rate increases with an increase in thermal electron speed. The higher thermal velocity may provide energy to the wave hence the growth rate increases due to inverse Landau damping through the wave particle energy exchange. The growth rates are not stabilized when the relative superthermal electron speed is much larger than the Alfven speed [cf. Eq. (8)].

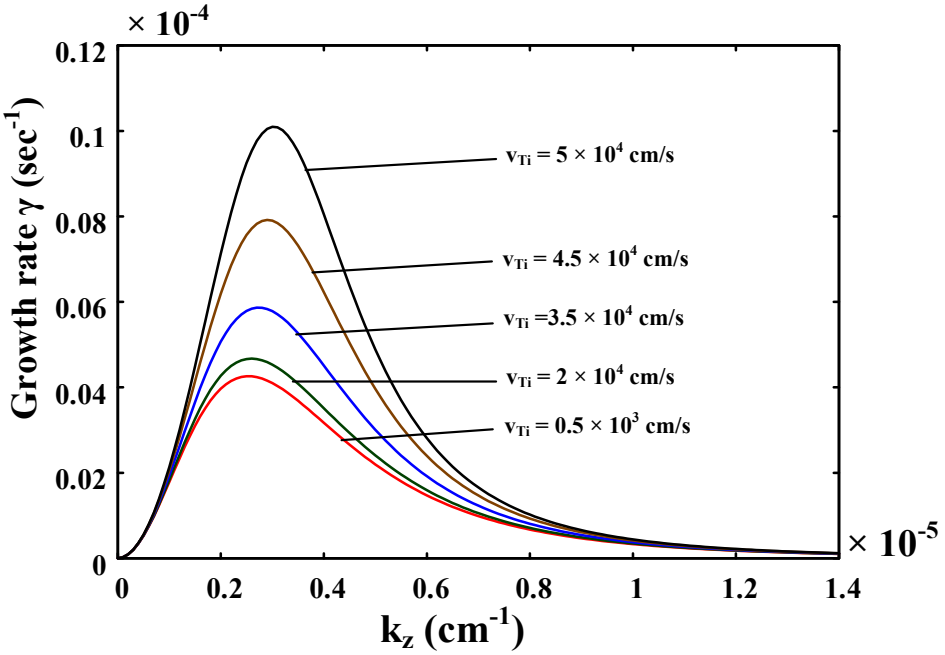


Fig. 3. Growth rate of the Alfven wave instability as a function of unstable wavenumber k_z for different values of thermal electron speed.

4 Conclusion

The excitation of Alfven waves by streaming electrons in a magnetized dusty plasma has been studied. The electromagnetic Alfven waves were driven to instability by the thermal streaming electrons. It was found that the instability had the largest growth rate when the thermal velocity of electrons was comparable to the Alfven speed. The frequency of the Alfven mode increases with an increase in the number density of dust grains. An increase in the dust population enhances the growth rate of the Alfven waves through the effect of capturing electrons, modifying the dispersion properties of Alfven waves in plasmas. As the number density of dust grains n_{d0}increases, the electron plasma density n_{e0} decreases with respect to ion plasma density n_{i0}. Thus, the ions have an effective mass that is less than m_i and their greater mobility leads to increased wave generation.

The maximum growth rate increases with an increase in the thermal speed of electrons across the magnetic field Since the growth rate is maximum when the parallel wave phase velocity of the Alfven waves is approximately of the order of the electron thermal speed, we expect efficient energy transport from the wave to the bulk of the electrons via Landau damping, accelerating the electrons or heating them. The maximum growth rate also increases with a decrease in the dust grain number density. It may be attributed to the fact that the presence of negatively charged dust grains reduces the critical electron drift [11] and hence decreases the growth rate.

References

[1]. G. Alazraki and P. Couturie, Astron. Astrophys., 13(3) (1971) 380-389.
[2]. V. Jatenco-Pereira, R. Opher and L. C. Yamamoto, Astrophys. J., 432(1) (1994) 409-416.
[3]. D. Falceta-Goncalves and V. Jatenco-Pereira, Astrophys. J., 576(2) (2002) 976-981.
[4]. J. Hollweg, J. Astrophy. Astron., 29(1) (2008) 217-237.
[5]. L. Yin, D. Winske, W. Daughton and K. J. Bowers, Phys. Plasmas, 14 (2007) 062104(1)-062104(12)
[6]. V. Prakash and S.C. Sharma, Phys. Plasmas, 16 (2009) 093703(1)-093703(9).
[8] V. Prakash, S.C. Sharma, Vijayshri and R. Gupta, Laser Part. Beams, 31 (2013) 411-419.
[7] V. Prakash, S.C. Sharma, Vijayshri and R. Gupta, Phys. Plasmas, 21 (2014) 033701(1)-033701(7).
[9] R. Gupta, V. Prakash, S.C. Sharma, Vijayshri and D. N. Gupta, J. At. Mol. Con. Phys., 3(1) (2016) 45-53.
[10] R. Gupta, S.C. Sharma and V. Prakash, Phys. Plasmas, 18 (2011) 053701(1)-053704(6).
[11] V. W. Chow and M. Rosenberg, Planet. Space Sci. 44 (1996) 465-467.

Applied Physics A (2018) 124:466
https://doi.org/10.1007/s00339-018-1850-8

Applied Physics A
Materials Science & Processing

Work function and electrical properties of individual multiwalled carbon nanotube: influenced by nature of catalyst and substrate

Reetu Kumari[1] · Pawan K. Tyagi[1] · Nitin K. Puri[1]

Received: 18 December 2017 / Accepted: 11 May 2018
© Springer-Verlag GmbH Germany, part of Springer Nature 2018

Abstract
To employ the multiwalled carbon nanotubes (MWCNTs) in electronic devices, their growth on conductive substrates is a prerequisite. Since electronic properties of MWCNT might be influenced by catalyst and substrate, therefore, to understand their influence on the work function and electrical resistance, individual MWCNT needs to be studied. In this report, we have demonstrated the growth of MWCNTs on conducting substrates such as copper, stainless steel, and insulating SiO_2 using thermal CVD technique. First, as-grown MWCNTs on different substrates have been characterized with scanning electron microscopy and Raman spectroscopy. Furthermore, electrical measurements on as-grown individual MWCNT has been performed using electrostatic force microscopy and conductive atomic force microscopy. Performed measurements reveal that work function and electrical resistance of MWCNT vary from 4.32 to 5.32 eV and 4–498 kΩ, respectively, depending on the nature of catalyst as well as substrates. We envision that performed study might boost the on-going research activity in the area of MWCNT-based nanoelectronic devices.

1 Introduction

MWCNTs grown on a conducting substrate are technologically essential to exploit their outstanding electronic properties for potential applications such as sensors [1], field emission [2], supercapacitors [3], and nanoelectronic devices [4, 5]. Recently, Vyas et al. [6] reported that MWCNTs can be used as interconnects. They found that top-contact metallized MWCNT vias have current-carrying capacities two orders of magnitude higher than their Cu and W counterparts and can be further enhanced by reduced via resistance due to contact engineering. Van der Veen et al. [7] demonstrated the integration of MWCNT taking Cu as top contact using mask-set compatible with 130 nm device technologies on 200 mm wafers, where a single MWCNT–Cu contact hole resistance of 3.4 k Ω was found. Recently, few efforts have been made to grow MWCNTs on conducting substrates such as inconal, TiN, stainless steel (SS), Cu, etc. using CVD technique [3, 8–11]. However, MWCNTs grown on conducting substrates exhibit poor quality as compared to those grown on insulating substrates [12]. Therefore, the growth of MWCNT on conducting substrates having good structural quality has been proven to be a challenging task. Apart from structural quality, the electronic properties such as resistance as well as work function which might be influenced by substrate nature need to be controlled for efficient electronic applications. Mostly, thermal CVD technique is used to grow the MWCNTs and many research groups have reported the growth of vertical-aligned MWCNTs on SiO_2/Si substrates. Zhang et al. have reported the site-specific growth of aligned MWCNTs on the substrate Si/SiO_2 without pre-patterning of catalyst particles [13]. Furthermore, selective growth of organized vertical-aligned MWCNT on patterned Si/SiO_2 substrate and its mechanism have also been reported [14, 15]. Chakraborty et al. [16] have reported the growth of MWCNTs on Si substrates using ethylene as carbon precursor and an iron as catalyst. They have suggested that MWCNT yield initially increases and then declines at high temperature due to loss of the catalyst through subsurface diffusion in substrate. Apart from the thermal CVD techniques, other techniques such as DC and microwave PECVD process have been popular to grow vertical-aligned MWCNTs. Meyyappan et al. have

Electronic supplementary material The online version of this article (https://doi.org/10.1007/s00339-018-1850-8) contains supplementary material, which is available to authorized users.

✉ Pawan K. Tyagi
pawantyagi@dtu.ac.in; pawankumartyagi@gmail.com

[1] Department of Applied Physics, Delhi Technological University, Delhi, India

Published online: 01 June 2018

presented a review on MWCNT growth using PECVD system and discussed the various plasma sources [17]. Various plasma sources such as dc [18, 19], hot-filament aided with dc [20, 21], rf [22], microwave [23, 24], and inductively coupled plasma reactors [25] have used by the researchers for MWCNT growth. Unlike SiO_2/Si substrates very few reports are available proposing the growth of MWCNTs on conducting substrates [26–28]. Chandra Kishore et al. demonstrated the growth of MWCNTs on SS using pre-deposited Co, Ni, and Fe catalyst [29]. However, it was reported that MWCNTs can grow on bare SS substrates, because it contains Fe as a constituent which is reported as good catalyst for MWCNT growth [29, 30]. However, due to the formation of large sized grains, quality of MWCNT was not found to be as good as it was in MWCNTs grown using pre-deposited catalyst. Furthermore, to improve the field emission properties, the growth of MWCNT has been reported on patterned conducting layer of TiN deposited on SiO_2 [8]. Since it is desirable that MWCNT should be in contact with conductive substrate for any promising application, to fulfil this requirement few groups have reported the growth of MWCNT on Cu using thermal CVD and MPCVD techniques [31–34]. They all have used pre-deposited catalyst layer on Cu substrate either using e-beam evaporation technique [33], sputtering process [34] or electroplating [35]. Recently, Ahmad et al. measured the resistance of single MWCNT and found it to be 250 kΩ, comparable with previously reported values [8]. It has been observed that contact of MWCNT with substrate can influence contact resistance as well as work function, which are important parameters for many envisioned applications in nanoelectronic devices. Therefore, in recent reports electrical measurements have been performed to determine their work function [36, 37]. Gao et al. measured the work function of individual MWCNT and found the values in the range 4.6–4.8 eV [38]. Work function on the side wall of MWCNT was also measured by Liu et al. and found to be around 4.9 eV [39]. They have also reported that the diameter and the number of walls did not influence the work functions and work function of side wall is always higher than tip.

The performance of MWCNTs in application mainly as field emitters depend on the crystallinity, number of defects, work function, contact resistance between MWCNTs and substrate and resistance of MWCNTs. To boost the applications of MWCNTs as field emitter, the present study will be valuable. In the present study, first, we have demonstrated the growth of MWCNTs on insulating substrates such as quartz and SiO_2/Si to optimize the processes parameters such as flow of carrier gas, growth temperature, volume of benzene and dissociation temperature of metallocene and benzene. After optimizing this process parameter, MWCNTs were grown on conducting substrates. This is achieved by growing them on bare metal substrates without using any pre-deposited catalyst layer. Afterwards, detailed electrical measurements were performed to understand the influence of substrate and catalyst on the resistance which includes MWCNT resistance as well as contact resistance and work function. These measurements were performed using electrostatic force microscopy (EFM) and conductive atomic force microscopy (c-AFM). Growth of CNTs on conducting substrate like Cu by adopting conventional techniques and parameters similar to Si/SiO_2 is a major achievement of this work. The whole study was extended to semiconducting Si with thin coating of insulator SiO_2 as well as less conducting SS. It is well known that lower value of resistance in conducting substrates makes them expedient in device applications. However, in the present work, the observations reveal that the conduction across the CNT/substrate proficiently depends on structure of CNT as well. Interestingly, it was found that the total electrical resistance of CNT/substrate could be lower for SiO_2 than Cu. The analysis also shows that the optimum morphological structure, graphitic nature as well as orientation of CNT are required for optimum benefits of CNT grown on conducting substrates. Optimization of CNT growth on Cu substrate needs to be studied further in detail.

2 Experimental details

MWCNTs growth on conducting substrates was carried out in thermal chemical vapor deposition (thermal CVD) technique using metallocene as catalyst precursor. SiO_2-coated Si as well as Cu and SS substrates have been procured. Schematic of various stages of the growth process is demonstrated in Fig. 1a. In this process, firstly, substrates were cut in the size of ~ 1×1 cm^2 and then kept in HNO_3 to remove the oxidized surface layer and then washed with DI before placing in the middle of the rector. In our procedure, 0.15 g of either ferrocene, cobaltocene or nickelocene, as required, were kept in a quartz boat to act as catalyst precursor and 10 ml of benzene was used as a carbon precursor. During heating to a desired set point (850 °C), the quartz reactor was placed in such a manner that quartz boat which was containing metallocene remains at room temperature. Once desired temperature is achieved, tube was dragged inside the hot zone in such a manner that the substrates remain at 850 °C and boat at 400–550 °C. Benzene was then inserted at a flow rate of 0.05 ml/min and its vapors were carried towards the hot zone by argon/hydrogen gas mixture in the ratio of 2:1 with total flow rate of 150 sccm. At this set temperature, metallocene starts to decompose, and as a result, metal atoms get released. These free metal atoms diffuse and make clusters on the substrates which were kept a few centimeters away from metallocene source. These clusters facilitate the nucleation

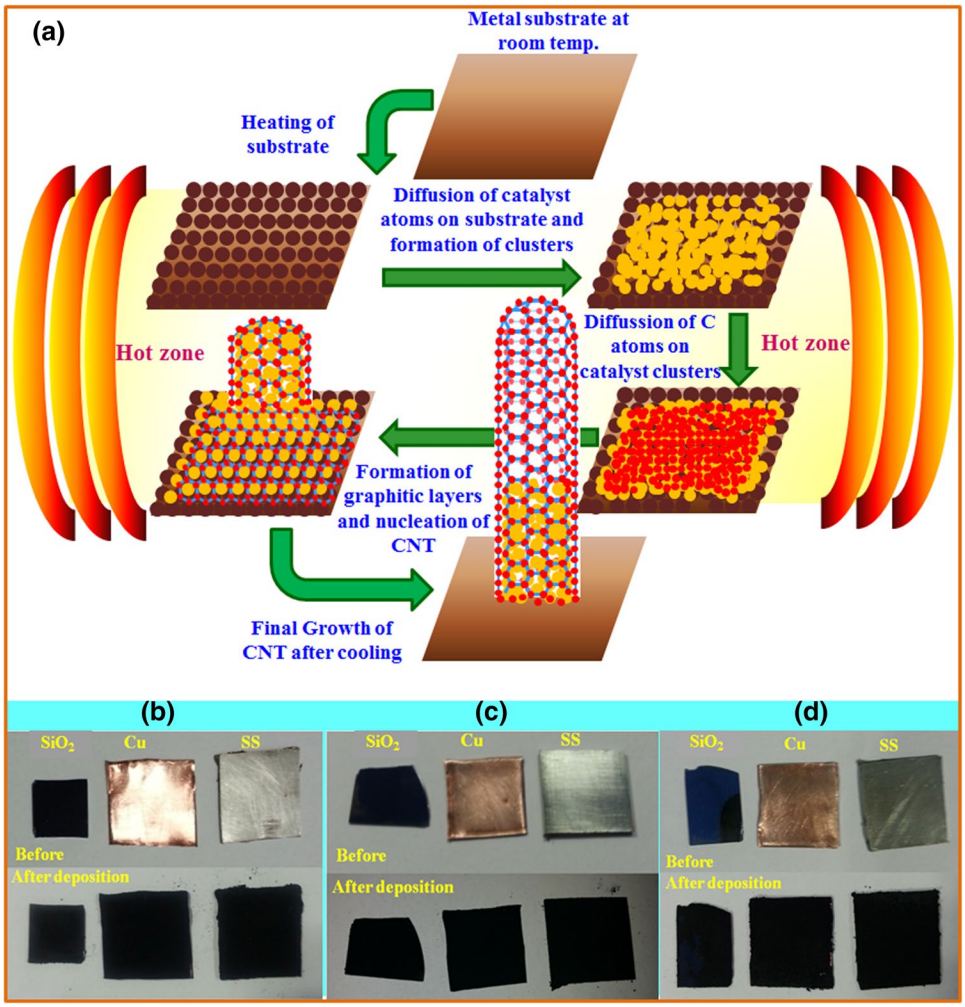


Fig. 1 **a** Schematic presentation of MWCNT growth steps on substrate, **b–d** top view of Si, Cu and SS substrates before and after growth of MWCNT using Fe, Co and Ni as catalyst, respectively

of graphitic layer on their surface and this layer lifts off from the surface to grow the MWCNT walls. The details of the mechanism involved in the growth process have been discussed in terms of diffusion and their energy barrier elsewhere [40, 41]. After completion of the synthesis process, we found black powder deposited on the wall of quartz reactor and film of MWCNTs on substrates. The substrates were uniformly covered with a thick layer of MWCNT, as shown in Fig. 1b–d.

As-grown MWCNTs were characterized using SEM (Hitachi S3100) and Micro-Raman (Horiba HR Evolution confocal micro-Raman spectrometer), with an excitation wavelength of 532 nm Ar^+ laser. EFM probing was performed using scanning probe microscopy (SPM) system (Park system XE-100) with gold-coated Si tip (NCSTAu), where the set point and resonance frequency of the tip were taken as 21.04 nm and 138 kHz, respectively. Platinum coated Si tip (CONTSCP) has been used for c-AFM measurements. Herein, we are referring MWCNTs grown using Fe, Co and Ni as Fe–MWCNT, Co–MWCNT and Ni–MWCNT, respectively.

3 Results and discussion

SEM micrographs of as-grown MWCNTs using Fe, Co and Ni on different substrates are shown in Fig. 2. Detailed SEM analysis of as-grown MWCNTs on Cu substrate reveals that Fe–MWCNTs@Cu was long and straight, whereas Co–MWCNTs@Cu were observed to be twisted having almost uniform diameter. Ni–MWCNTs@Cu which were curly in nature with non-uniform diameter, did not exhibit good quality. As shown in Fig. 2, Fe–MWCNT and Co–MWCNTs grown on SS substrates were found to be straight and aligned. The Ni–MWCNTs@SS was seen to be tangled, with uniform diameter distribution and less curly as compared to those grown on Cu. In case of SiO_2 substrate, both Fe–MWCNTs and Co–MWCNTs were found to be vertically aligned; however, alignment was not observed in Ni–MWCNTs. The morphology of Ni–MWCNTs grown on SiO_2 substrate was almost similar to those grown on SS. The TEM analysis of MWCNTs grown on SiO_2 reveals that Ni–MWCNTs are thin and twisted. More SEM images revealing the alignment and orientation are shown in Figs.

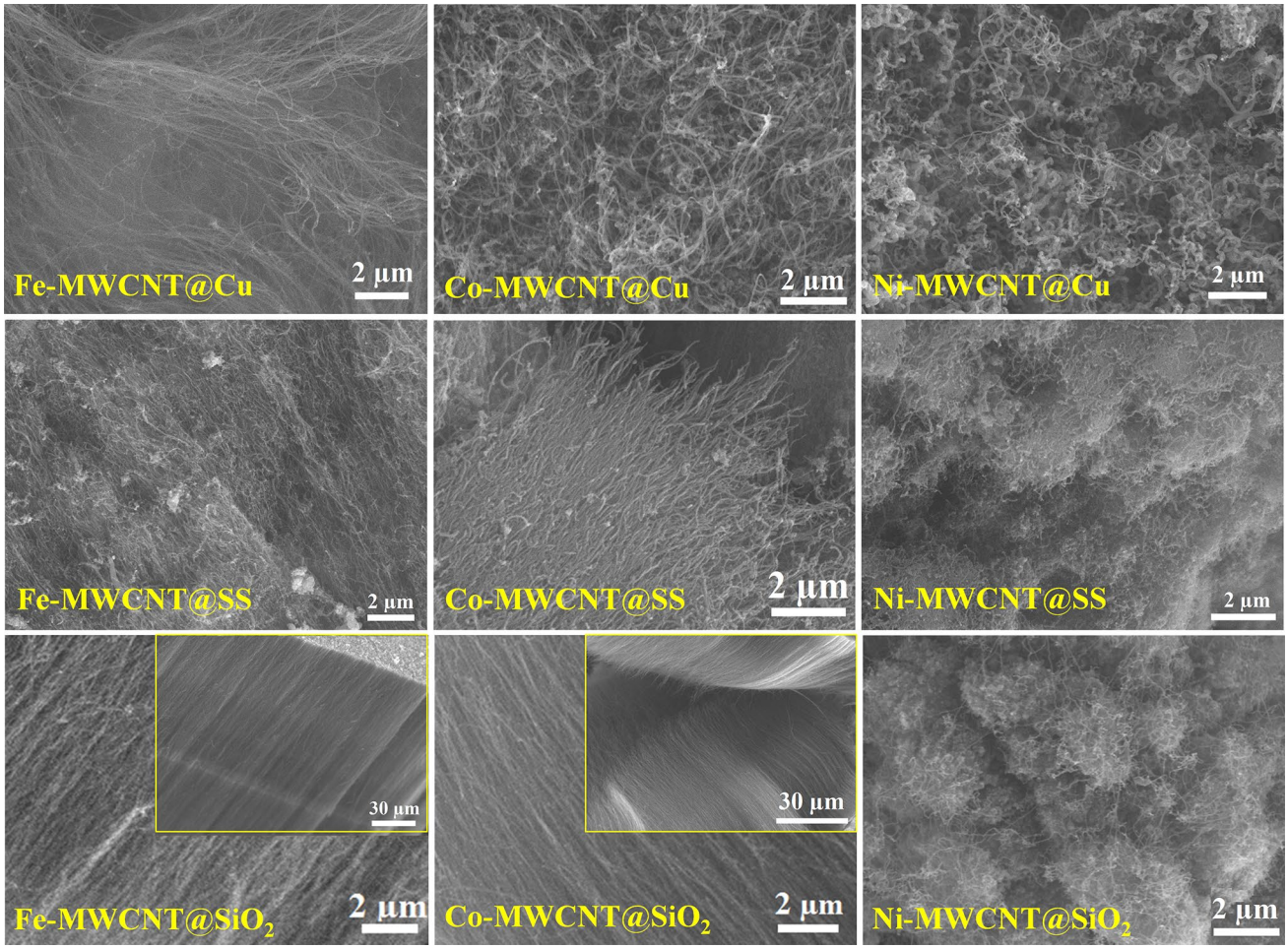


Fig. 2 SEM micrographs of as-grown MWCNTs on Cu, SS and SiO_2 and substrates (from top to bottom). The types of CNTs are marked in the respective image. The low magnification images of Fe–MWCNTs and Co–MWCNTs on SiO_2 substrate have been represented in the corresponding images

S4–7 in supplementary information. The outer diameters of Fe–MWCNTs, Co–MWCNTs and Ni–MWCNTs were found to be in range of 38–48, 23–37 and 10–20 nm, respectively, as shown in Fig. S2. These results are supported by analysis of Raman spectra.

A series of Raman spectra recorded on as-grown samples with 532 nm laser wavelength is shown in Fig. 3. In all spectra, two major peaks located at ~ 1342 and 1572 cm^{-1}, have been observed which are attributed to well known D-band and G-band. These spectra were further deconvoluted by adopting Lorentzian fitting and represented by different colors and their possible identities have been mentioned in the figure. Peak observed in range of 1602–1608 cm^{-1} was identified as D′ band, another weak disorder-induced feature observed in most of the spectra of graphitic carbon. In some samples, two weak bands at 1490 and 1270 cm^{-1} were observed which are known to be associated with M and K points in disordered graphite [42, 43]. I_D/I_G ratio, band position has been mentioned in panels and summarized in Table 1. To have better representation of I_D/I_G ratio, variation in intensities of all D peaks which are normalized with respect to $I_{G,}$ is represented in Figure S1 (Supporting information). Now, taking into account both Raman analysis and SEM morphologies of as-grown MWCNTs, it was observed that Fe–MWCNTs@SiO_2 is vertically aligned, longer and denser possessing highest I_G/I_D ratio. This ratio was found to be in order as: Fe–MWCNTs > Co–MWCNTs > Ni–MWCNTs and reveals that Ni–MWCNTs have least graphitic quality. The same trend regarding growth quality was followed in case of Cu substrate, where quality of MWCNT was found to be best in case of Fe, then Co and Ni. Interestingly, on SS substrate, we found Co as the best catalyst for growth of MWCNT in comparison to Fe and Ni.

Before we proceed for electrical characterization, we made an effort to estimate areal density of vertical-aligned MWCNT. The topographical image of a flake of Co–MWCNTs sample consisting vertical-aligned tubes has been taken with the SPM tip (see supporting information Fig. S3). The

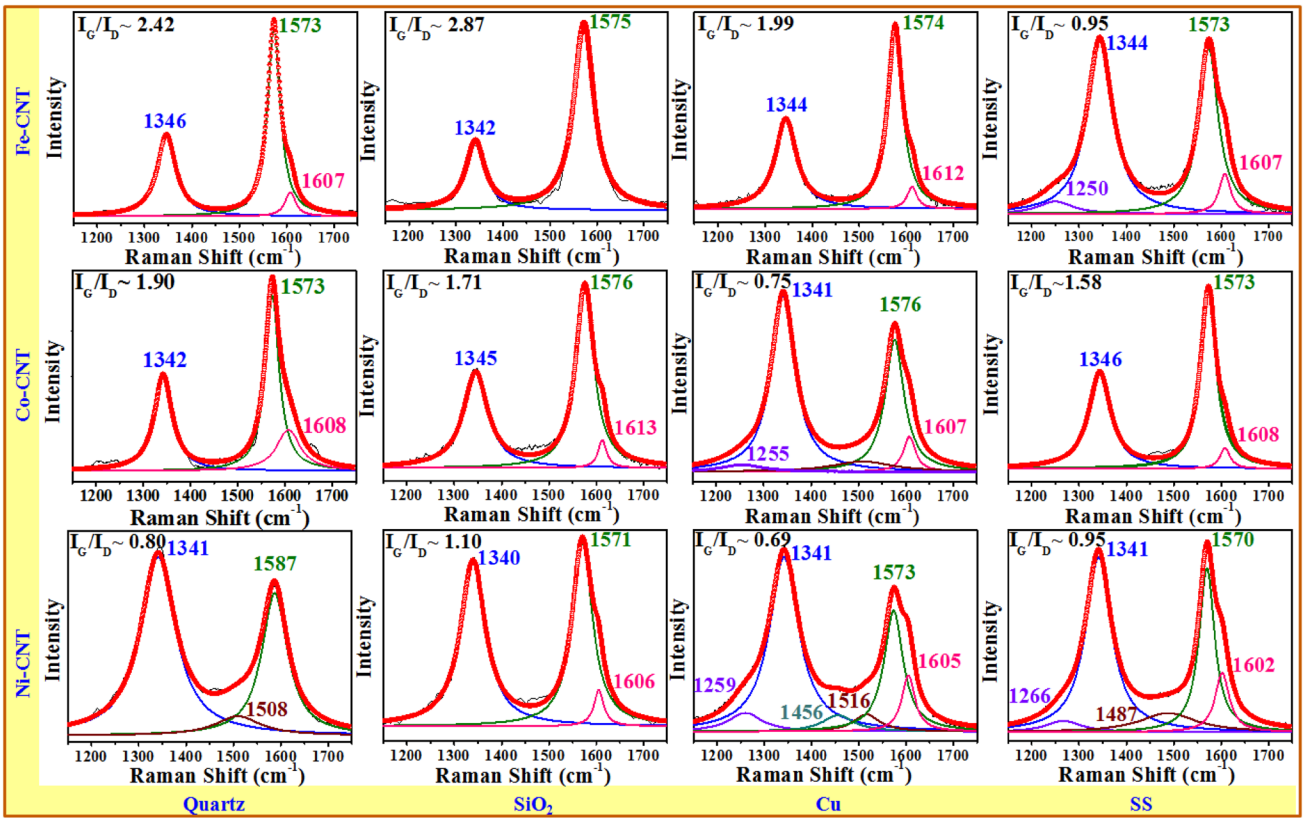


Fig. 3 Detailed visible Raman spectra of all types of as-grown samples

Table 1 Surface contact potential difference (CPD) and work function of MWCNTs grown on Cu, SS and SiO_2 using Fe, Co and Ni as catalyst

Outputs	Samples details											
	Cu	SS	SiO_2	Fe–MWCNT			Co–MWCNT			Ni–MWCNT		
				Cu	SS	SiO_2	Cu	SS	SiO_2	Cu	SS	SiO_2
CPD (V)	0.3	−0.1	−0.2	0.3	0.1	0.3	−0.5	0.1	0.5	−0.1	−0.2	−0.2
W.F. (eV)	4.52	4.92	5.02	4.52	4.72	4.52	5.32	4.72	4.32	4.92	5.02	5.02
D-band position (cm^{-1})				1344	1344	1342	1341	1346	1345	1341	1341	1340
G-band position (cm^{-1})				1574	1573	1575	1576	1573	1576	1573	1570	1571
I_G/I_D ratio				1.99	0.95	2.78	0.75	1.58	1.71	0.69	0.95	1.10
Total resistance (KΩ)	965	1722	–	11	54	64	103	4	17	312	175	498

image exhibit high spatial resolution and reveal resistive regions (dark spots). The bright region corresponds to the MWCNTs and the darker region corresponds to the void between the MWCNTs, as shown in Figure S3. The average diameter of the MWCNT was observed to be 35 nm which is in good agreement with transmission electron microscopy (TEM) analysis of this sample (Figure S2). Therefore, the areal density of MWCNTs can be calculated. On performing this statistical analysis, we have found the areal density is in the range of 10^{10} MWCNTs/cm^2.

To estimate the work function of individual MWCNTs, EFM measurements were performed. In EFM mode, surface contact potential was obtained by minimizing electrostatic interaction generated between tip and the sample through applying dc-tip bias. In this process, initially the image was taken with grounded tip in the contact mode and then tip was lifted up to the height of 50 nm and dc-bias voltage was applied to the tip. Afterwards, force, amplitude and phase image were recorded at different tip–bias voltage (V_{EFM}) in the range 3 to −3 V. Schematic diagram of EFM setup and topography image of MWCNTs is shown in Fig. 4a, b, respectively. Topographical images of these samples are not sufficiently distinguishing that they can provide any remarkable information and they look almost alike. Therefore, only

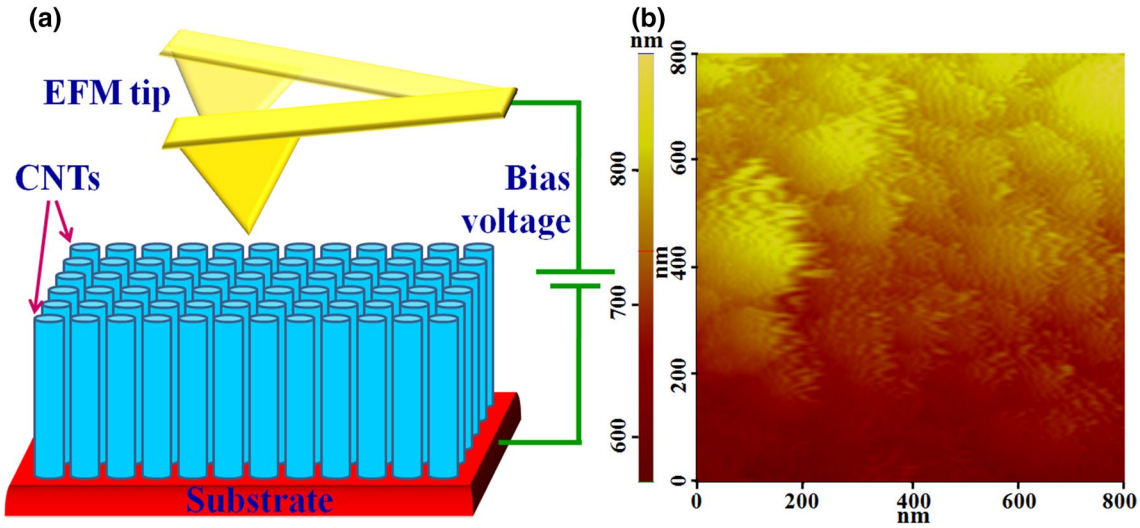


Fig. 4 **a** Schematic presentation of interaction between tip and MWCNT grown on substrates, **b** topographical image of sample scanned with EFM tip

one topographical image is demonstrated here which is for sample Fe–MWCNT@SiO_2 (Fig. 4b).

Electrostatic force experienced between tip and MWCNT at different tip bias has been plotted in Fig. 5. This force gets minimized when V_{tip} is equivalent to surface contact potential (CPD) as shown in Fig. 5. The outcomes of the performed measurements are tabulated in Table 1. After estimating surface contact potential difference (CPD), work functions were determined using the relation $\Delta V_{CPD} = \frac{\phi_{tip} - \phi_{MWCNT}}{e}$, where ϕ_{MWCNT} and ϕ_{tip} are the work function of MWCNT and tip, respectively. By taking the reported value of work function for gold-coated tip 4.82 ± 0.08 eV [44], work functions of all type MWCNT were determined and summarized in the Table 1.

Work functions of as-grown MWCNT on different substrates were found in the range 4.32–5.32 eV. The lowest work function obtained was 4.32 eV for Co–MWCNT@SiO_2, whereas highest 5.32 eV for Co–MWCNT@Cu. Interestingly, Fe–MWCNT@SS and Co–MWCNT@SS exhibited similar work function (4.72 eV). Afterwards, I-AFM measurements were performed to probe the electrical resistance which include quantum and scattering resistance of MWCNT, substrate, contact resistance of MWCNT/substrate interface and MWCNT/tip. All measurements were

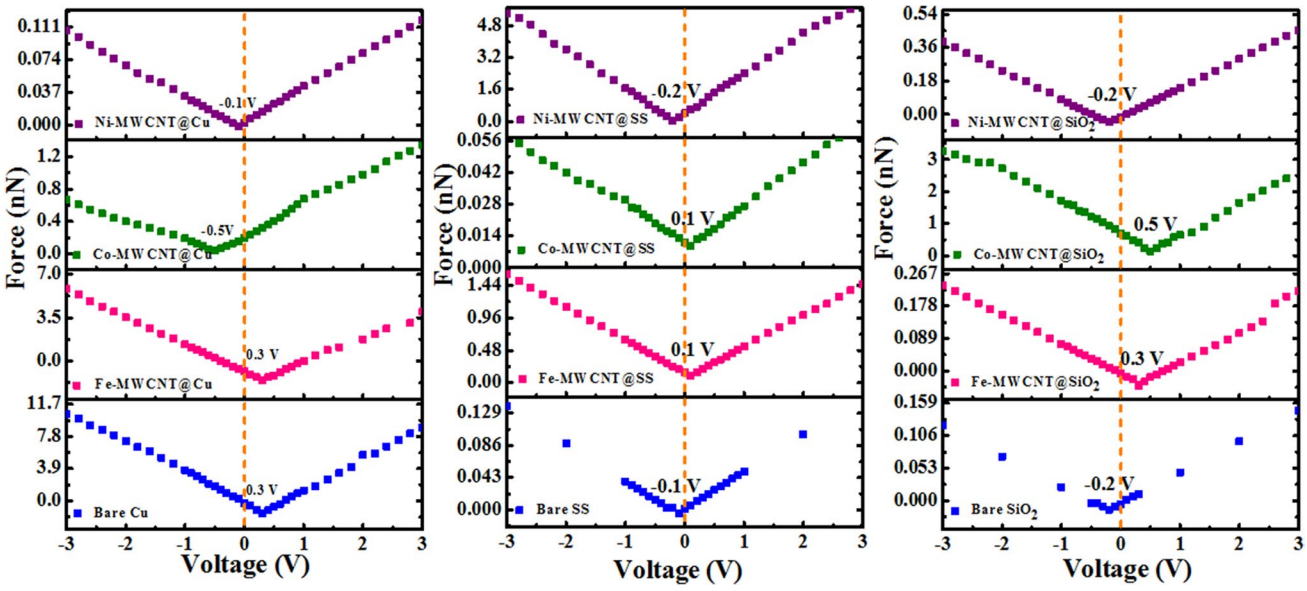


Fig. 5 Substrate and catalyst dependent variation in force with applied voltage in the range − 3 to 3 V

performed using c-AFM probe (tip radius < 40 nm) with a spring constant of ~ 0.12 N/m and schematic is shown in Fig. 6a. To have accuracy, the *I–V* characteristics were mapped in the matrix of 4 × 4, i.e., 16 points for each sample. The total points, where tip–MWCNT interaction was made, are represented by square blocks in green colour in topographical image, as shown in Fig. 6b. Therefore, mapping was performed on total 16 points to obtain *I–V* characteristic and similar results have been obtained for all measurements. averaged total resistance values of all 16 measured points. The average values of total resistance of all 16 measured points are shown in Table 1.

As-mentioned above, since tip radius is < 40 nm which is comparable to the MWCNT diameter, it can be presumed that single MWCNTs were probed during *I–V* measurement taken at one point. To validate this, TEM measurements were performed for MWCNTs grown using Fe, Co and Ni catalyst (as shown in supporting information Fig. S2). TEM results corroborate that individual MWCNT being probed. It should be noted that in general, electrical resistance of Cu is in the range of Ohms. However, in the present case, resistance of bare Cu substrate was found to be 965 KΩ which is probably due to the formation of oxide layer on the substrate. As shown in Fig. 7, *I–V* plots clearly indicate that Fe–MWCNT and Co–MWCNT exhibit ohmic behaviour, whereas it was Schottky for those Ni–MWCNT grown on SiO_2 and Cu. Total resistance was obtained in wide range 4–498 kΩ, where it was highest and lowest was for Ni–MWCNT@SiO_2 and Co–MWCNTs@SS, respectively. The obtained values for all samples are also summarized in Table 1.

To understand the influence of catalyst as well as substrates on the electronic/electrical properties of MWCNT, an explicit interpretation of growth process is important. In our process, benzene was used as carbon precursor and metallocene as catalyst. It is reported that apart from being a carbon precursor, benzene also favours the polymerization-based growth of MWCNTs [45]. This happens due to preferable dissociation of C–H bonds over C–C bonds that can directly integrate the six membered rings to precede further growth and results in dense growth [45]. In addition, the ability of transition metals to make the bond with carbon

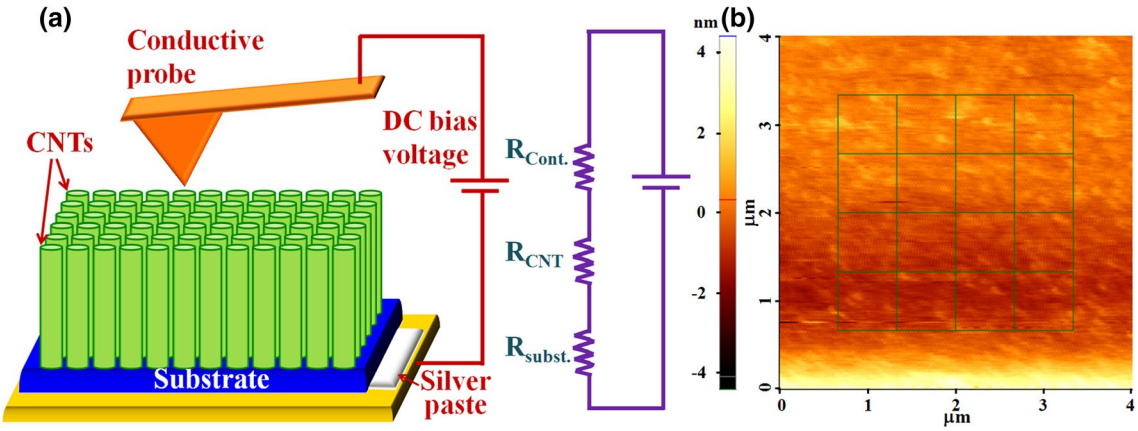


Fig. 6 **a** Schematic representing interaction generated between conductive tip and MWCNT grown on substrates, **b** topography of sample scanned with c-AFM tip

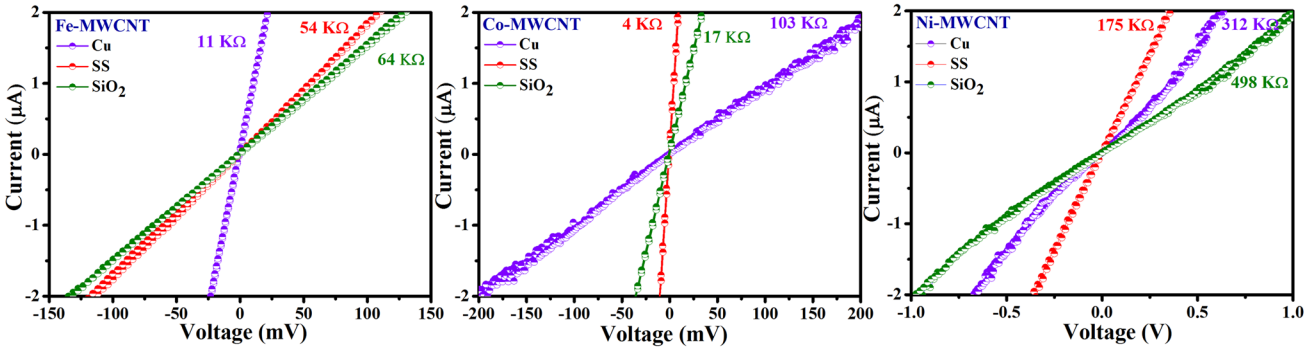


Fig. 7 Current–voltage (*I–V*) characteristics of MWCNTs grown on Cu, SS and SiO_2 substrates. **a** Fe–MWCNT, **b** Co–MWCNT, **c** NI–MWCNT. Total electrical resistance are mentioned in the individual plots

is assumed to increase as number of unfilled *d*-orbitals increases. Metals without unfilled *d*-orbital, display a negligible affinity to carbon such as Au and Cu, whereas metals with unfilled *d*-orbital such as Ni, Fe, and Co exhibit finite carbon solubility. Among three transition metals, the solubility for carbon was reported to be 0.3–0.5% in Ni, 1.2% in Co at 800 °C and 4% in Fe at 800 °C [46]. The solubility of carbon in metals generally increases with temperature as well as with reduction in size of nanoparticles [47]. This happens due to closure of large fraction of carbon atoms on subsurface of catalyst. These factors significantly influence the structural properties of as-grown MWCNTs and are evident from structural characterization performed in this study. In the present case, all samples were synthesized under the same experimental conditions and clusters of Fe/Co/Ni atoms were formed in situ after the dissociation of corresponding metallocene. It can be said that after dissociation, the vapors of these atoms were carried to surface of the substrates by carrier gas and then these metal atoms easily diffused on the substrates and formed clusters. These clusters might have served as nucleation sites, as demonstrated in Fig. 1. Therefore, morphology of as-grown MWCNTs mainly depends on cluster size of catalysts which is reported to be influenced by surface diffusion of metal atoms on the substrates as well as diffusion and solubility of carbon atoms in the cluster. For example, in case of Cu substrate, it was reported that the surface diffusion of Fe atoms is higher on Cu as compared to that of other two. Surface diffusion rate of Fe, Co and Ni atoms on Cu is 7.8×10^{-11}, 5.09×10^{-11} and 2.61×10^{-11} cm^2/s, respectively, in temperature range of 830 to 850 °C [48]. High diffusion rate of Fe atoms not only leads to the formation of larger size cluster but also provide more nucleation sites than that of Co and Ni and favours dense growth. Cluster size is very crucial in CVD process as the diameter of the nanotubes is usually controlled by the size of the catalyst particles. Consequently, Fe–MWCNT have larger diameter than Co and Ni–MWCNTs which is evident by TEM observations (Fig. S2). This observation supports the results by Lee et al [49], where they have reported that in thermal CVD process, the diameters of catalyst particles were as follows Fe > Co > Ni. Furthermore, temperature also has a significant impact on the morphology of MWCNTs. As-mentioned above, to have comparative analysis, the same temperature was selected for all samples which can be considered to be high for Ni clusters as growth of MWCNTs using Ni as catalyst require less temperature as compared to Fe and Co [50]. Thus, high temperature may further reduce the density of clusters and favours agglomeration of the small sized Ni clusters as compared to Fe or Co. This may result in uneven size distribution of clusters. Therefore, such a high-temperature growth leads to wide distribution of diameter of Ni–MWCNT and causes more defects with curly structure.

Furthermore, the previous studies have shown that along with above-discussed factors, catalyst–substrate interaction also plays a vital role in MWCNT growth. Apart from different surface diffusion rates of the catalyst particles on different substrate surfaces, the difference in alignment could be related to the different adhesion of the catalysts on substrate surfaces [51]. Generally, a strong substrate–catalyst interaction restrains the growth of MWCNTs [52]. Moreover, minimal surface diffusion and dense cluster formation of catalyst on the substrate is another important criterion for providing the nucleation sites to grow vertical-aligned MWCNT. Since, among all used substrates, SiO_2 is highly smooth and favours the growth of vertical-aligned MWCNTs, we presumed that above-discussed factors optimally get balanced on SiO_2 substrate and facilitates the formation of stable catalyst particles of Fe and Co. As compared to Fe and Co, Ni exhibits poorer wettability on SiO_2 surfaces and can get ripened off during growth. Eventually, this loss of catalyst results in random growth, whereas appropriate catalyst supports surface diffusion which can sustain the high-density catalytic nanoparticles and lead to the growth of highly aligned dense MWCNT forests.

In contrast, it is interesting to note that MWCNTs grown on SS substrates exhibit poor graphitization as evident by Raman analysis compared to those grown using Co as catalyst. This might be due to formation of optimum nucleation sites by Co nanoparticles. Although iron species are well known catalyst for MWCNTs growth but they diffuse quickly on SS resulting in increase of grain size and growth of large diameter MWCNTs. In case of nickel, MWCNTs grown on SS are thin and have curly structure. Therefore, we suggest that due to large curvature size they possess more defects which might influence their electronic state.

As described hereafter, the catalyst–substrate interaction strongly influences their electrical properties. As evident from the EFM observations, CPD of Ni–MWCNTs is always negative for all the substrates, whereas it is positive for Fe–MWCNT. For Co–MWCNT it is positive except for Cu substrate which may also be associated with the twisted structure as observed in SEM. Since, twisted and coiled structure cause strain in the MWCNT walls, it might influence the band structure, Fermi levels and work function. Previously, it was reported that due the strain which was generated due the presence of non-hexagonal ring in MWCNT tip, it possesses lower work function than that of the sidewalls [38]. This difference may originate due to their unlike electronic structures as well as atomic and geometric structures. Furthermore, an explicit interpretation for finding of wide range of resistance of MWCNTs grown on different substrates can be explained in terms of substrate and catalyst nature as main influencing factors. Due to insulating nature of SiO_2, we were unable to measure the electrical resistance of bare SiO_2/Si substrates but after MWCNTs growth, we

succeeded to measure the electrical resistance. The reason is that during the growth process as explained above Fe/Co/Ni atoms diffuse in/on SiO_2 surface. Since growth of MWCNTs was accomplished at high temperature, there is as possibility that these metal atoms get diffused in to SiO_2 layer [16, 53]. Yao et al. have reported the high-temperature annealing in presence of hydrogen cause diffusion of Fe inside SiO_2 layer and formation of other compounds [53]. Thus, due to diffusion of metal impurities, conduction path might be formed through SiO_2 layer. MWCNT grown on SiO_2 has higher electrical resistance as compared to Cu and SS if they have similar morphology and orientation (Ni–MWCNT). This can be understood as follows: at the MWCNT/SiO_2 interface redistribution of charge occurs locally within the first few atomic layers [54]. Due to this distribution, electrons get strongly localized. In contrast, in the case of conducting substrates charge redistribution is long ranged and influenced by the Fermi energies, as consequence electrons will be delocalized. However, Co–MWCNTs grown on SiO_2 exhibit lower resistance as compared to that grown on Cu which is due to the vertical alignment of MWCNTs on SiO_2. Co–MWCNTs grown on Cu are randomly oriented and have twisted structure, whereas MWCNTs on SiO_2 are vertically aligned and straight. This results in the direct transport of electron leading overall high conduction in spite of very small conduction through SiO_2. Fe–MWCNTs grown on SiO_2 also possess such orientation and longer than Co–MWCNTs and exhibit high value of resistance than that of Co–MWCNTs@SiO_2. In the present case, wide range of resistance from 4 to 498 kΩ is obtained which is in the range of previously reported values for MWCNTs (10^3–10^6 Ω) [5, 55, 56]. It has been reported that in MWCNT, each graphitic wall with in the MWCNT can have either a metallic or semiconducting nature depending on its diameter and chirality. Due to this variation among walls, the net electrical behaviour of a MWCNT will be typically metallic and exhibits Ohmic transport [57]. However, Ni–MWCNTs are showing slight shift from ohmic-behaviour tending towards non-ohmic behaviour. Recently, Souier et al. [58] have also reported both ohmic and non-ohmic *I–V* curves in MWCNTs coexist. They reported that Schottky barrier between the Pt-tip (work function of 6 eV) and the semiconducting shells of MWCNT (work function of 4.5−6 eV) formed. If a MWCNT is not in direct contact with the substrate then electrons need to transport through alternative paths which includes jumping from the tip contacted MWCNT to nearby MWCNTs that are in contact with the back and, thus, going through MWCNT-to-MWCNT junctions. However, they have also stated that if applied bias is 1–2 V used during probing, the conductance of the semiconducting walls reaches comparable to the conductance of metallic walls. In the present case, this mechanism mainly occurs in randomly oriented MWCNTs, where cross-plane conductivity and as well as in-plane conductivity of MWCNTs contribute to enhance the resistance. The electron tunnelling through these junctions may be the key element in justifying the higher measured resistance values as observed in Ni–MWCNTs. Furthermore, to understand the influence of substrates and MWCNTs morphology as well as their orientation, bare substrates were probed to measure their contact resistance. Surprisingly, it was found that resistance of bare substrates were considerably higher than after MWCNTs deposition. From this observation it can be concluded that the resistance might be reduced due to adhering of MWCNTs on the substrates. As discussed above, the resistance reduction is observed for all types of MWCNTs grown on all used substrates. This reduction may depend on substrate, MWCNT/substrate interface, structure/orientation of MWCNTs and contact resistance between tip and MWCNT. From the above-mentioned factors, it can be concluded that the structure and orientation may be dominating factors influencing the nature of contact made between substrate and MWCNT tip. Furthermore, length, work function and wettability of MWCNTs to the substrates might be other influencing factors in the present case which affect the overall electrical resistance. The total electrical resistance of MWCNT includes contact resistance along with resistance of MWCNTs and substrates. Recently, it has been reported that contact resistance depends on work function or wettability of CNTs with substrates [59, 60]. Lim et al. have reported that in case of strong wettability, contact resistance does not depend on work function, whereas in case of poor wettability, resistance depends on work function difference of substrate and grown CNTs [59]. In case of metal substrates with good wettability, contact between metal and CNTs is Ohmic contact by Fermi level matching resulting in smaller resistance, whereas in case of poor wettability resistance increases with increase in work function difference. It has been shown that Fe and Cu have strong wettability with CNTs and oxides have less. Considering these facts, in the present case, SS (major content is Fe) and Cu show strong wettability and in such a case contact resistance should depend on wettability instead of work function difference. However, to study the influence of wettability on contact resistance, MWCNTs should grow vertically aligned which possess direct contact with substrate. Hence, the contact resistance of Ni–MWCNTs grown on all substrates cannot be discussed in this perspective. Similarly, all types of CNT grown on Cu substrate could not be taken in to account in such a viewpoint despite having strong wettability towards MWCNT as they have random orientation. Therefore, to have a comparative influence on their contact resistance, only vertically grown MWCNTs (Fe–MWCNTs and Co–MWCNTs on SS and SiO_2) can be discussed in terms of wettability. Since SS has strong wettability as compared to SiO_2, in such a case, the contact resistance should also be less apart from resistance of MWCNT which depend on other factors. Eventually, in the present

case, the overall resistance for both types of MWCNTs on SS is also less for SS as compared to those in SiO_2 clear from Fig. 7. On the same substrates, both types of MWCNTs have difference in their total electrical resistance due to their structure and morphologies which has been discussed above.

As mentioned above, Ni–MWCNTs are always grown randomly and have twisted structure. In such a case, contact area gets reduced, because tip makes contact on the side wall of MWCNT by either lying on other MWCNTs or on the substrates. Since contact is made on side walls of MWCNT, effective contact area of tip as well as substrate with MWCNT decreases with a decrease in diameter of MWCNT, which happens probably due to large curvature size of thin MWCNT. Park et al. have probed Ni–MWCNT randomly grown on Cu and found that its resistance of Cu significantly decreased after MWCNT deposition [57]. They proposed that this reduction is caused due to multiple electrical junctions made in MWCNTs network. In case of vertically aligned MWCNTs, parallel electrical network made by adjacent MWCNTs lowers the total resistance. In addition, effective contact area between MWCNTs and tip increases; therefore, effective electrical resistance will be minimum as observed in vertical-aligned Fe–MWCNT and Co–MWCNT grown on SiO_2 and SS. When we discuss MWCNTs grown on Cu substrate, which are randomly oriented, as shown in Fig. 2, similar interpretation can be given as in case of randomly oriented Ni–MWCNTs taking structure and orientation into account. Since Fe–MWCNTs are straighter and longer as compared to Co–MWCNTs, they exhibit lower resistance as compared to that of other one. Above observations suggest that contact resistance of substrate as well as structure and orientation (vertical or random) of MWCNTs has strong influence on total electrical resistance. Despite having perfect vertical alignment Co and Fe–MWCNT grown on SiO_2, exhibit higher resistance as compared to less-aligned Co–MWCNTs@SS which might be due to high contact resistance of MWCNT/SiO_2 interface. On the other hand, in case of SS and Cu, even SS has low conductivity as compared to Cu but Co–MWCNTs@SS exhibit low resistance, while reverse was found for Fe–MWCNT@Cu, which can be associated with their vertical and random/twisted growth. Therefore, to achieve minimum electrical resistance of MWCNT/substrate interface, vertically aligned growth on highly conducting substrate could be most appropriate.

4 Conclusion

The growth of MWCNTs on conducting as well as insulating substrates has been demonstrated. Electrical and electronic properties were investigated and found to be dependent on catalyst and substrate interaction. Performed measurements reveal that work function and electrical resistance of MWCNTs vary from 4.32 to 5.32 eV and 4–498 kΩ, respectively, depending on nature of catalyst and substrates. We envision that performed study might be helpful in various on-going research attempts to develop the real world electronic applications of MWCNTs.

References

1. L. Valentini, I. Armentano, J.M. Kenny, C. Cantalini, L. Lozzi, S. Santucci, Sensors for sub-ppm gas detection based on carbon nanotube thin films. Appl. Phys. Lett. **82**, 961–963 (2003)
2. D.P. Jenicek, A. McCarthy, J.G. Kassakian, Modifying the characteristics of carbon nanotubes grown on metallic substrates for ultracapacitor applications. J. Appl. Phys. **115**, 204309 (2014)
3. S. Talapatra, S. Kar, S. Pal, R. Vajtai, P. Ajayan, Carbon nanotube growth on metallic substrate using vapor phase catalyst delivery. US patent 8207658 B2 (2012)
4. M.S. Bakir, J.D. Meindl, Integrated interconnect technologies for 3D nanoelectronic systems (Artech House, London, 2009)
5. H. Ryu, D. Kälblein, O.G. Schmidt, H. Klauk, Unipolar sequential circuits based on individual-carbon-nanotube transistors and thin-film carbon resistors. ACS Nano **9**, 7525–7531 (2011)
6. A.A. Vyas, C. Zhou, Y. Chai, P. Wang, C.Y. Yang, Effect of improved contact on reliability of sub-60 nm carbon nanotube vias. Nanotechnology **27**, 375202 (2016)
7. M.H. Van der Veen, B. Vereecke, C. Huyghebaert, D.J. Cott, M. Sugiura, Y. Kashiwagi, L. Teugels, R. Caluwaerts, N. Chiodarelli, P.M. Vereecken, G.P. Beyer, M.M. Heyns, S.D. Gendt, Z. Tökei, Electrical characterization of CNT contacts with Cu damascene top contact. Microelectron. Eng. **106**, 106 (2013)
8. M. Ahmad, J.V. Anguita, V. Stolojan, T. Corless, J.S. Chen, J.D. Carey, S. Ravi, P. Silva, High quality carbon nanotubes on conductive substrates grown at low temperatures. Adv. Funct. Mater. **25**, 4419–4429 (2015)
9. C.E. Baddour, F. Fadlallah, D. Nasuhoglu, R. Mitra, L. Vandsburger, J.L. Meunier, A simple thermal CVD method for carbon nanotubesynthesis on stainless steel 304 without the addition of an external catalyst. Carbon **47**, 313–347 (2008)
10. C. Masarapu, B. Wei, Direct growth of aligned multiwalled carbon nanotubes on treated stainless steel substrates. Langmuir **23**, 9046–9049 (2007)
11. V. Pushparaj, G. Maramag, Carbon nanotube growth on copper. US patent (2014)
12. G. Li, S. Chakrabarti, Growth of aligned multiwalled carbon nanotubes on bulk copper substrates by chemical vapor deposition. J. Mater. Res. **24**, 2813–2820 (2009)
13. Z. Zhang, B.Q. Wei, G. Ramanath, P.M. Ajayan, Substrate-site selective growth of aligned carbon nanotubes. Appl. Phys. Lett. **77**, 23 (2000)
14. B.Q. Wei, R. Vajtai, Y. Jung, J. Ward, R. Zhang, G. Ramanath, P.M. Ajayan, Organized assembly of carbon nanotubes. Nature **416**, 495 (2002)
15. Y.J. Jung, B. Wei, R. Vajtai, P.M. Ajayan, Mechanism of selective growth of carbon nanotubes on SiO_2/Si patterns. Nano Lett. **3**, 561 (2003)
16. A.K. Chakraborty, J. Jacobs, C. Anderson, C.J. Roberts, M.R.C. Hunt, Chemical vapor deposition growth of carbon nanotubes on Si substrates using Fe catalyst: what happens at the nanotube Fe/Si interface. J. Appl. Phys. **100**, 08432 (2006)
17. M. Meyyappan, L. Delzeit, A. Cassell, D. Hash, Carbon nanotube growth by PECVD: a review. Plasma Sour. Sci. Technol. **12**, 205 (2003)

18. Y.Y. Wei, G. Eres, V.I. Merkulov, D.H. Lowndes, Effect of catalyst film thickness on carbon nanotube growth by selective area chemical vapor deposition. Appl. Phys. Lett. **78**, 1394 (2001)
19. K.B.K. Teo, M. Chhowalla, G.A.J. Amaratunga, W.I. Milne, D.G. Hasko, G. Pirio, P. Legagneux, F. Wyczisk, D. Pribat, Uniform patterned growth of carbon nanotubes without surface carbon. Appl. Phys. Lett. **79**, 1534 (2001)
20. Y. Chen, Z.L. Wang, J.S. Yin, D.J. Johnson, R.H. Prince, Well-aligned graphitic nanofibers synthesized by plasma-assisted chemical vapor deposition. Chem. Phys. Lett. **272**, 178 (1997)
21. Z.F. Ren, Z.P. Huang, J.W. Xu, J.H. Wang, P. Bush, M.P. Siegel, P.N. Provencio, Synthesis of large arrays of well-aligned carbon nanotubes on glass. Science **282**, 1105 (1998)
22. G.W. Ho, A.T.S. Wee, J. Lin, W.C. Tjiu, Synthesis of well-aligned multiwalled carbon nanotubes on Ni catalyst using radio frequency plasma-enhanced chemical vapor deposition. Thin Solid Films **388**, 73 (2001)
23. L.C. Qin, D. Zhou, A.R. Krauss, D.M. Gruen, Growing carbon nanotubes by microwave plasma-enhanced chemical vapor deposition. Appl. Phys. Lett. **72**, 3437 (1998)
24. Y.C. Choi, Y.M. Shin, S.C. Lim, D.J. Bae, Y.H. Lee, B.S. Lee, D. Chung, Effect of surface morphology of Ni thin film on the growth of aligned carbon nanotubes by microwave plasma-enhanced chemical vapor deposition. J. Appl. Phys. **88**, 4898 (2000)
25. L. Delzeit, I. Mc Aninch, B.A. Cruden, D. Hash, B. Chen, J. Han, M. Meyyappan, Growth of multiwall carbon nanotubes in an inductively coupled plasma reactor. J. Appl. Phys. **91**, 6027 (2002)
26. Z. Gao, X. Zhang, K. Zhang, M.M.F. Yuen, Growth of vertically aligned carbon nanotube arrays on al substrates through controlled diffusion of catalyst. J. Phys. Chem. C **119**(27), 15636–15642 (2015)
27. K.D. Matthews, M.G. Lemaitre, T. Kim, H. Chen, M. Shim, J.-M. Zuo, Growth modes of carbon nanotubes on metal substrates. J. Appl. Phys. **100**, 044309 (2006)
28. Fei-Lung Lu, J.-M. Ting, Very rapid growth of aligned carbon nanotubes on metallic substrates. Acta Mater. **61**(6), 2148–2153 (2013)
29. S. Chandrashekhar, A. Pandurangan, Electrophoretic deposition of cobalt catalyst layer over stainless steel for the high yield synthesis of carbon nanotubes. Appl. Surf. Sci. **258**, 7936–7942 (2012)
30. C.E. Baddour, F. Fadlallah, D. Nasuhoglu, R. Mitra, L. Vandsburger, J.-L. Meunier, A simple thermal CVD method for carbon nanotube, synthesis on stainless steel 304 without the addition of an external catalyst. Carbon **47**, 313 (2008)
31. X. Yin, Q. Wang, C. Lou, X. Zhang, W. Lei, Growth of multi-walled MWCNTs emitters on an oxygen-free copper substrate by chemical-vapor deposition. Appl. Surf. Sci. **254**, 6633–6636 (2008)
32. G. Atthipalli, R. Epur, P.N. Kumta, B.L. Allen, Y. Tang, A. Star, J.L. Gray, The effect of temperature on the growth of carbon nanotubes on copper foil using a nickel thin film as catalyst. Thin Solid Films **519**, 5371 (2011)
33. S. Sepahvand, P. Safaei, Z. Sanaee, Growth of carbon nano tubes on copper substrate suitable for lithium ion battery anode. Proc. Mater. Sci. **11**, 634–638 (2015)
34. P.K. Tyagi, M.K. Singh, A. Misra, U. Palnitkar, D.S. Misra, E. Titus, N. Ali, G. Cabral, J. Gracio, M. Roy, S.K. Kulshreshtha, Preparation of Ni-filled carbon nanotubes for key potential applications in nanotechnology. Thin Solid Films **469**, 127–130 (2004)
35. G. Atthipalli, R. Epur, P.N. Kumta, M. Yang, Jung-K. Lee, J.L. Gray, Nickel catalyst-assisted vertical growth of dense carbon nanotube forests on bulk copper. J. Phys. Chem. C **115**, 3534–3538 (2011)
36. S.C. Lim, H.J. Jeong, K.S. Kim, I.B. Lee, D.J. Bae, Y.H. Lee, Extracting independently the work function and field enhancement factor from thermal-field emission of multi-walled carbon nanotube tips. Carbon **43**, 2801–2807 (2005)
37. W.S. Su, T.C. Leung, C.T. Chan, Work function of single-walled and multiwalled carbon nanotubes: First-principles study. Phys. Rev. B **76**, 235413 (2007)
38. R. Gao, Z. Pan, Z.L. Wang, Work function at the tips of multiwalled carbon nanotubes. Appl. Phys. Lett. **78**, 1757–1759 (2001)
39. P. Liu, Q. Sun, F. Zhu, K. Liu, K. Jiang, L. Liu, Q. Li, Q. Fan, Measuring the work function of carbon nanotubes with thermionic method. Nano Lett. **8**, 647–651 (2008)
40. R. Kumari, L. Krishnia, V. Kumar, S. Singh, H.K. Singh, R.K. Kotnala, R.R. Juluri, U.M. Bhatta, P.V. Satyam, B.S. Yadav, Z. Naqvi, P.K. Tyagi, Fe_3 C-filled carbon nanotubes: permanent cylindrical nanomagnets possessing exotic magnetic properties. Nanoscale **8**, 4299 (2016)
41. R. Kumari, A. Singh, B.S. Yadav, D.R. Mohapatra, A. Ghosh, P. Guha, P.V. Satyam, M.K. Singh, P.K. Tyagi, Filled-carbon nanotubes: 1D nanomagnets possessing uniaxial magnetization axis and reversal magnetization switching. Carbon **119**, 464 (2017)
42. C. Thomsen, S. Reich, Double resonant Raman scattering in graphite. Phys. Rev. Lett. **80**, 5214–5217 (2000)
43. S. Vollebregt, R. Ishihara, F.D. Tichelaar, Y. Hou, C.I.M. Beenakker, Influence of the growth temperature on the first and second order Raman band ratios and widths of carbon nanotubes and fibers. Carbon **50**, 3542 (2012)
44. Y.-J. Yu, Y. Zhao, S. Ryu, L.E. Brus, K.S. Kim, P. Kim, Tuning the graphene work function by electric field effect. Nano Lett. **9**, 3430 (2009)
45. Y. Tian, Z. Hu, Y. Yang, X. Wang, X. Chen, H. Xu, Q. Wu, W. Ji, Y. Chen, In situ TA-MS study of the six membered-ring-based growth of carbon nanotubes with benzene precursor. J. Am. Chem. Soc. **126**, 1180–1183 (2003)
46. V. Jourdain, C. Bichara, Current understanding of the growth of carbon nanotubes in catalytic chemical vapour deposition. Carbon **58**, 2–39 (2013)
47. A. Moisala, A.G. Nasibulin, E.I. Kauppinen, The role of metal nanoparticles in the catalytic production of single-walled carbon nanotubes—a review. J. Phys. Condens. Matter **14**, S3011-S3035 (2003)
48. C.A. Mackliet, Diffusion of iron, cobalt and nickel in single crystals of pure copper. Phys. Rev. B. **109**, 1964–1970 (1958)
49. C.J. Lee, J. Park, J.A. Yu, Catalyst effect on carbon nanotubes synthesized by thermal chemical vapor deposition. Chem. Phys. Lett. **360**, 250–255 (2002)
50. R. Seidel, G.S. Duesberg, E. Unger, A.P. Graham, M. Liebau, F. Kreupl, Chemical vapor deposition growth of single-walled carbon nanotubes at 600 °C and a simple growth model. J. Phys. Chem. B **108**, 1888 (2004)
51. Z.J. Zhang, B.Q. Wei, G. Ramnath, P.M. Ajayan, Substrate-site selective growth of aligned carbon nanotubes. Appl. Phys. Lett. **77**, 3764 (2000)
52. S. Talapatra, S. Kar, S.K. Pal, R. Vajtai, L. Ci, P. Victor, M.M. Shaijumon, S. Kaur, O. Nalamasu, P.M. Ajayan, Direct growth of aligned carbon nanotubes on bulk metals. Nat. Nanotechnol. **1**, 112–116 (2006)
53. B.R. Yao, V. Petrova, R.R. Vanfleet, K.R. Coffey, Compositional stability of FePt nanoparticles on SiO/Si during annealing. J. Appl. Phys. **99**, 08E913 (2006)
54. Q. Fu, T. Wagner, Interaction of nanostructured metal overlayers with oxide surfaces. Surf. Sci. Rep. **62**, 431–498 (2007)
55. H. Fiedler, M. Toader, S. Hermann, R.D. Rodriguez, E. Sheremet, M. Rennau, S. Schulze, T. Waechtler, M. Hietschold, D.R.T. Zahn, S.E. Schulz, T. Gessner, Carbon nanotube based via interconnects: performance estimation based on the resistance of individual carbon nanotubes. Microelectron. Eng. **120**, 210–215 (2014)

56. T.T. Vo, C. Poulain, J. Dijon, A. Fournier, N. Chevalier, D. Mariolle, An experimental method to determine the resistance of a vertically aligned carbon nanotube forest in contact with a conductive layer. J. Appl. Phys. **112**, 044901-1-8 (2012)
57. M. Park, B.A. Cola, T. Siegmund, J. Xu, M.R. Maschmann, T.S. Fisher, H. Kim, Effects of a carbon nanotube layer on electrical contact resistance between copper substrates. Nanotechnology **17**, 2294–2303 (2006)
58. T. Souier, C. Maragliano, M. Stefancich, M. Chiesa, How to achieve high electrical conductivity in aligned carbon nanotube polymer composites. Carbon **64**, 150 (2013)
59. S.C. Lim, J.H. Jang, D.J. Bae, G.H. Han, S. Lee, I.S. Yeo, Y.H. Lee, Contact resistance between metal and carbon nanotube interconnects: effect of work function and wettability. Appl. Phys. Lett. **95**, 264103-1-4 (2009)
60. M.H. Yang, K.B. Teo, W.I. Milne, D.G. Hasko, Carbon nanotube Schottky diode and directionally dependent field-effect transistor using asymmetrical contacts. Appl. Phys. Lett. **87**, 253116-1-3 (2005)

arXiv:1806.09929v1 [math.OC] 26 Jun 2018

Chance Constraints Integrated MPC Navigation in Uncertainty amongst Dynamic Obstacles: An overlap of Gaussians approach

Dhaivat Bhatt[1] Akash Garg[2] Bharath Gopalakrishnan[1] K. Madhava Krishna[1]

***Abstract*— In this paper, we formulate a novel trajectory optimization scheme that takes into consideration the state uncertainty of the robot and obstacle into its collision avoidance routine. The collision avoidance under uncertainty is modeled here as an overlap between two distributions that represent the state of the robot and obstacle respectively. We adopt the minmax procedure to characterize the area of overlap between two Gaussian distributions, and compare it with the method of Bhattacharyya distance. We provide closed form expressions that can characterize the overlap as a function of control. Our proposed algorithm can avoid overlapping uncertainty distributions in two possible ways. Firstly when a prescribed overlapping area that needs to be avoided is posed as a confidence contour lower bound, control commands are accordingly realized through a MPC framework such that these bounds are respected. Secondly in tight spaces control commands are computed such that the overlapping distribution respects a prescribed range of overlap characterized by lower and upper bounds of the confidence contours. We test our proposal with extensive set of simulations carried out under various constrained environmental configurations. We show usefulness of proposal under tight spaces where finding control maneuvers with minimal risk behavior becomes an inevitable task.**

I. INTRODUCTION

Quadcopter MAVs (Micro Aerial Vehicle) are an ideal choice for autonomous reconnaissance and surveillance because of their small size, high maneuverability, and ability to fly in very challenging environments. To perform these tasks effectively, the quad-copter MAV must be able to precisely avoid obstacles while navigating from one point to another. The obstacles include static and dynamic objects as well as other quad-copters operating in the surrounding environment. The field of obstacle avoidance for quad-copters has been explored for quite a long time. Many algorithms proposed in past fails to produce desired result because of the uncertainty involved in belief of the MAV/obstacle. A deterministic obstacle avoidance algorithm is not an appropriate in unstructured and uncertain environments. This can lead to substantial degradation in the desired result and can even make the source robot to collide into the obstacle, in the worst case.

In order to deal with the challenges mentioned, we propose a probabilistic Model Predictive Control framework for trajectory optimization of quad-copters. MPC is proven to be an efficient framework due to its receding horizon planning capability. It is an optimization based approach to handle arbitrary number of constraints on state and control. The framework optimizes the given cost function which takes maneuverability and actuation limitations of the source robot into consideration. In the paper presented, a quadratic goal reaching objective is provided as cost in addition with a jerk cost to obtain a smooth trajectory. We also incorporate actuation constraints to ensure kinematic feasibility of optimal trajectory. This paper has several novel findings and contributes in following ways,

[1]Affiliated with KCIS, Robotics Research Center, IIIT Hyderabad
[2]Affiliated with Delhi Technological University

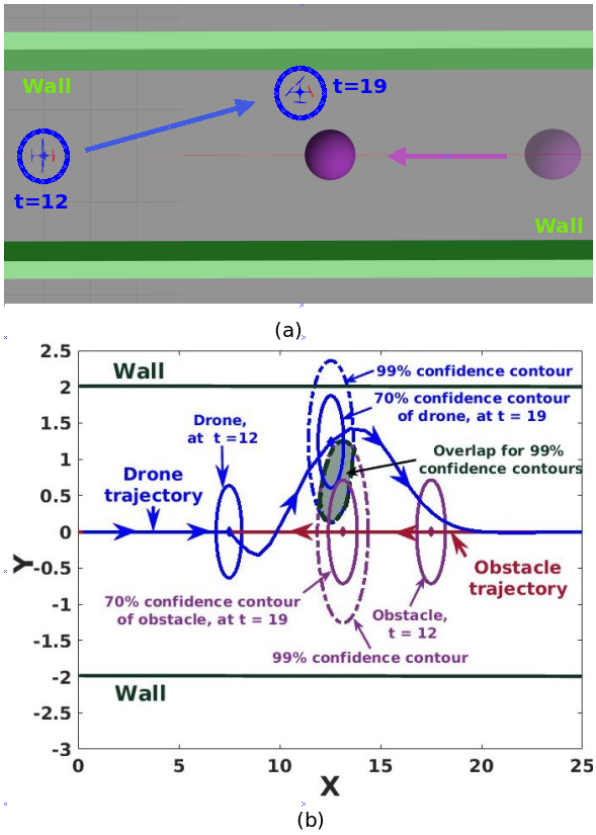


Fig. 1. We show result of our probabilistic obstacle avoidance algorithm in constrained corridor when an obstacle is approaching in antipodal configuration. Figure 1(a) shows gazebo snapshot of drone positions for two diffrent time instances. In figure 1(b). For example, at time t=19, we can see clear overlap between $\mathbf{99}\%$ confidence contours of the drone, however, $\mathbf{70}\%$ confidence contours, which correspond to lower bound are able to avoid penetration.

- This is first such formulation, conditioned on MAV and obstacle uncertainty into an MPC framework through theory of overlapping Gaussians.
- We demonstrate why our modeling is more consistent and appropriate compared to entropic distances between probability distributions
- We further introduce this particular uncertainty modeling into an optimal control framework, and jointly optimize in both, the control and overlap parameter space.
- We show effective results in various simulation settings that showcase versatility of the method. Specifically we show where the distributions are non isotropic, which is closer to real setting.

The remainder of this paper is organized as follows. Section II discusses earlier line of work. Section III outlines deterministic tra-

jectory optimization framework. Section IV talks about formulating collision avoidance under uncertainty. It also outlines methods to quantify overlap between two Gaussians through various methods. Section V talks about modeling probabilistic collision avoidance using theory built in IV-C. In section V-A, we talk about formulating trajectory optimization algorithm under chance constraints. We show evaluation of trajectory optimization algorithm for a simple case in section V-B. In section VI, we evaluate proposed formulation into an MPC framework for two scenarios. In section VI-A, we show results for antipodal configuration and in section VI-B we show results for tightly bounded constrained corridor setting. In last section, we conclude the paper and discuss future scope of improvement.

II. Related work

This section review the recent advances in MPC for autonomous navigation. The evident advantage of using MPC in motion planning and autonomous navigation has been well demonstrated in ([1],[2], [3], [4]) among many. Formulations along the lines of [1], [2] do a great job in achieving performance in terms of quality of trajectory, computation time and novelty of approach. However, they have been developed for a deterministic setting and hence do not take into consideration the uncertainty in state of the robot and obstacle into their collision avoidance routine. While MPC formulations along the lines of [4] does take into consideration the state uncertainty and demonstrate interesting maneuvers in complex driving scenarios, [4] considers uncertainty only in the state of the obstacle, and the collision avoidance is modeled through a Minkowski sum approach. Considering robot's uncertainty into Minkowski sum formulation would be very cumbersome as Minkowski sum between two ellipses is very complex. [5] takes into consideration the uncertainty of the drone and assumes the obstacle to be static and determinstic, it models collision as a measure of entropic distance(Similar to Mahalanobis distance[6]). It is shown in the later section of this paper that formulating probabilistic collision avoidance as an entropic distance may not be the most appropriate approach when uncertainty in the robot and obstacle is considered. [7] attempts to solve for collision avoidance in a multiagent scenario under uncertainty. It achieves it through an RRT framework and a sampling strategy to choose a path corresponding to a desired level of safety confidence. Formulating collision avoidance as a chance constraint is well explored in [8],[9] among the many. [9] demonstrates an efficient way of solving an intractable chance constraint through a series of reformulations. These were built on time scale velocity obstacle concepts [10]. In this work, we look at an alternative take on modeling probabilistic collision avoidance as a chance constraint that could seamlessly integrate itself into an MPC framework. We accomplish thus by reformulating collision avoidance as a measure of overlap between two Gaussians(representing state uncertainties of the robot and obstacle). By such a reformulation, we easily avoid the complexity of considering Minkowski sums between two ellipses and other approaches that model probabilistic collision avoidance through entropic distances.

A. Symbols and notations:

There are several variables of interest to us. We will follow a generic notation scheme. A variable of interest for drone at some time instance $\mathbf{t_i}$ will be expressed in form of $\xi^{\mathbf{d}}_{\mathbf{t_i}}$. For example, uncertainty of drone at time $\mathbf{t_i}$ is denoted by $\mathbf{\Sigma}^{\mathbf{d}}_{\mathbf{t_i}}$. A variable of interest for obstacle j at time instance $\mathbf{t_i}$ will be expressed in form of $\xi^{\mathbf{o_j}}_{\mathbf{t_i}}$. For example, uncertainty of obstacle j at $\mathbf{t_i}$ is expressed as $\mathbf{\Sigma}^{\mathbf{o_j}}_{\mathbf{t_i}}$. A variable of mutual interest of obstacle j and drone at time $\mathbf{t_i}$ will be expressed in form of $\xi^{\mathbf{j}}_{\mathbf{t_i}}$. For example, overlap between Gaussian populations of obstacle j and drone at time $\mathbf{t_i}$ is defined as $\mathbf{\Upsilon}^{\mathbf{j}}_{\mathbf{t_i}}$ in section V-A.

III. Prerequisite

This section describes a deterministic MPC framework, formulated along the lines of [1]. The motion model considered here is of a holonomic bot, and obstacle avoidance is added as an affine constraint. The entire framework is solved as a sequential convex programming(SCP) routine[11].

A. Trajectory optimization in a deterministic setting

In deterministic trajectory optimization setting, our objective is to reach the goal in a given amount of time while ensuring a collision-free trajectory. The problem is modeled by considering a set of cost functions and constraints.

Let the start position of the drone be $\mathbf{X_0} = (\mathbf{x_0}, \mathbf{y_0}, \mathbf{z_0})$. Our objective is to reach the goal position $\mathbf{G_f} = (\mathbf{G^x_f}, \mathbf{G^y_f}, \mathbf{G^z_f})$ in $\mathbf{N}$ time-steps, each time-step of duration τ. The state of the drone at any time instant $\mathbf{t_i}$ is $\mathbf{X_{t_i}} = (\mathbf{x_{t_i}}, \mathbf{y_{t_i}}, \mathbf{z_{t_i}}, \mathbf{v^x_{t_i}}, \mathbf{v^y_{t_i}}, \mathbf{v^z_{t_i}})$. Where $\mathbf{V_{t_i}} = (\mathbf{v^x_{t_i}}, \mathbf{v^y_{t_i}}, \mathbf{v^z_{t_i}})$ is the velocity of the drone at time instant $\mathbf{t_i}$. We have P obstacles in the environment. Their position at time $\mathbf{t_i}$ is defined as $\mathbf{O^j_{t_i}} = (\mathbf{o^{xj}_{t_i}}, \mathbf{o^{yj}_{t_i}}, \mathbf{o^{zj}_{t_i}})$, for $\forall\ j = \{1, 2, 3, \dots P\}$. For static obstacles, the obstacle locations will be independent of $\mathbf{t_i}$. The drone and obstacles are approximated as circular objects with radius of the drone being $\mathbf{R_{drone}}$ and radius of obstacle $\mathbf{j}$ is $\mathbf{R_j}$, $\forall\ j = \{1, 2, 3, \dots P\}$.

$$\underset{\mathbf{V_{t_i}}}{\operatorname{argmin}} \quad \mathbf{J} = \mathbf{J_{terminal}} + \mathbf{J_{smooth}} \tag{1a}$$

$$\mathbf{X_{t_i+1}} = f(\mathbf{X_{t_i}}, \mathbf{V_{t_i}}) \tag{1b}$$

$$\mathbf{V_{min}} \leq \mathbf{V_{t_i}} \leq \mathbf{V_{max}} \tag{1c}$$

$$\mathbf{a_{min}} \leq \frac{\mathbf{V_{t_i+1}} - \mathbf{V_{t_i}}}{\tau} \leq \mathbf{a_{max}} \tag{1d}$$

$$\mathbf{C}_{obs_j}(\mathbf{x_{t_i}}, \mathbf{y_{t_i}}, \mathbf{z_{t_i}}, \mathbf{o^{xj}_{t_i}}, \mathbf{o^{yj}_{t_i}}, \mathbf{o^{zj}_{t_i}}, \mathbf{R_{drone}}, \mathbf{R_j}) \leq \mathbf{0} \tag{1e}$$

The above set of equations defines the cost function as well as constraints. The objective function as described in equation 1a.

$$\mathbf{J_{terminal}} = (\mathbf{x_{t_N}} - \mathbf{G_x})^2 + (\mathbf{y_{t_N}} - \mathbf{G_y})^2 + (\mathbf{z_{t_N}} - \mathbf{G_z})^2 \tag{2}$$

The terminal cost forces our system to achieve goal-state($\mathbf{G_f}$) at the end of the trajectory.

$$\mathbf{J_{smooth}} = \sum_{i=2}^{\mathbf{N-1}} \left(\frac{(\mathbf{V_{t_i+1}} + \mathbf{V_{t_i-1}} - \mathbf{2V_{t_i}})}{\tau^{\mathbf{2}}}\right)^2 \tag{3}$$

The smoothness cost as described above ensures smooth trajectory with minimal jerk. It minimizes the jerk which is modeled as second order finite difference between subsequent linear velocities. This term penalizes sudden deviations in the acceleration profile and ensures smooth velocity transitions.

Equation 1b is the process model of the vehicle. These equations ensure that control variables and states are adhering the motion model of the drone. The motion model for holonomic bot can be described as following,

$$\mathbf{x_{t_i}} = f(\mathbf{x_0}, \mathbf{v^x_{t_1}}, \mathbf{v^x_{t_2}}, \dots \mathbf{v^x_{t_i}}, \tau) = \mathbf{x_0} + \sum_{\mathbf{k=1}}^{\mathbf{i}} \mathbf{v^x_{t_k}} \tau \tag{4a}$$

$$\mathbf{y_{t_i}} = f(\mathbf{y_0}, \mathbf{v^y_{t_1}}, \mathbf{v^y_{t_2}}, \dots \mathbf{v^y_{t_i}}, \tau) = \mathbf{y_0} + \sum_{\mathbf{k=1}}^{\mathbf{i}} \mathbf{v^y_{t_k}} \tau \tag{4b}$$

$$\mathbf{z_{t_i}} = f(\mathbf{z_0}, \mathbf{v^z_{t_1}}, \mathbf{v^z_{t_2}}, \dots \mathbf{v^z_{t_i}}, \tau) = \mathbf{z_0} + \sum_{\mathbf{k=1}}^{\mathbf{i}} \mathbf{v^z_{t_k}} \tau \tag{4c}$$

Equations 1c-1d, represents constraints to model actuation limitations of the drone. The bounds on linear acceleration and velocity ensures that the actuation capabilities of the drone are not violated.

Equation 1e models collision avoidance constraint between obstacle $\mathbf{j}$ and drone. For a deterministic setting, this will be a simple euclidean distance constraint as below.

$$\begin{aligned}\mathbf{C}_{obs_j}(.) = -(\mathbf{x_{t_i}} - \mathbf{o^{xj}_{t_i}})^2 - (\mathbf{y_{t_i}} - \mathbf{o^{yj}_{t_i}})^2 \\ -(\mathbf{z_{t_i}} - \mathbf{o^{zj}_{t_i}})^2 + (\mathbf{R_j} + \mathbf{R_{drone}})^2 \leq \mathbf{0}.\end{aligned} \tag{5}$$

Above constraint is purely non-linear in nature for drone position variable ($\mathbf{x_{t_i}}$, $\mathbf{y_{t_i}}$, $\mathbf{z_{t_i}}$). We linearize it along the lines of [1] and solve the proposed routine using sequential convex programming. The trajectory optimization routine is then integrated into a model predictive control framework.

IV. Collision Avoidance Under Uncertainty

Robot motions are generally erroneous in nature. There is always some uncertainty associated with the location of the drone. Apart from that, the sensing module also gives inaccurate estimate of the state of the obstacle. Uncertain position estimate of the obstacle leads to erroneous trajectory estimation. In such cases, the constraint in equation 1e takes the form of 6

$$\begin{aligned}\Pr_j(\mathbf{C}_{obs_j}(\mathbf{x_{t_i}}, \mathbf{y_{t_i}}, \mathbf{z_{t_i}}, \mathbf{o^{xj}_{t_i}}, \mathbf{o^{yj}_{t_i}}, \mathbf{o^{zj}_{t_i}}, \mathbf{R_{drone}}, \mathbf{R_j}) \leq \mathbf{0}) \\ \forall\ j \in \{1, 2, 3, \ldots P\}\end{aligned} \tag{6}$$

Constraints of the form 6, are generally known as chance constraints, and in most cases may not have a distribution that can be computed in closed form. The nature of these chance constraints also depends on the form of the deterministic constraints that they are built on. For example chance constraint 6 arising out of 5 can be expressed as an entropic distance. The following three sections provide a detailed discussion on three important ways to formulate a chance constraint.

A. Theoretical characterization of chance constraint

The chance constraint in 6 can take the form of a transformed distribution of 5 as shown in Equation 5,

$$\int \cdots \int_{V_j} \Pr(\mathbf{D_{t_i}}, \mathbf{O^j_{t_i}}) d\mathbf{D_{t_i}} d\mathbf{O^j_{t_i}} \tag{7}$$

Where, $\mathbf{D_{t_i}} = (\mathbf{x_{t_i}}, \mathbf{y_{t_i}}, \mathbf{z_{t_i}})$, position of the drone at time $\mathbf{t_i}$. Under state uncertainty, let $\mathbf{D_{t_i}} \sim \mathcal{N}(\hat{\mathbf{D}}_{\mathbf{t_i}}, \mathbf{\Sigma^d_{t_i}})$ and $\mathbf{O^j_{t_i}} \sim \mathcal{N}(\hat{\mathbf{O}}^{\mathbf{j}}_{\mathbf{t_i}}, \mathbf{\Sigma^{o_j}_{t_i}})$ be the Gaussian parameterization of the drone and obstacle $\mathbf{j}$ positions at time $\mathbf{t_i}$. Then, $\Pr(\mathbf{D_{t_i}}, \mathbf{O^j_{t_i}})$ takes the following form,

$$\Pr(\mathbf{D_{t_i}}, \mathbf{O^j_{t_i}}) \sim \mathcal{N}\left(\begin{pmatrix}\hat{\mathbf{D}}_{\mathbf{t_i}} \\ \hat{\mathbf{O}}^{\mathbf{j}}_{\mathbf{t_i}}\end{pmatrix}, \begin{pmatrix}\Sigma^d_{t_i} & 0 \\ 0 & \Sigma^{o_j}_{t_i}\end{pmatrix}\right) \tag{8}$$

When we substitute equation 8 in equation 7, equation 7 becomes analytically intractable. The closed form solution of equation 7 doesn't exist. Authors in [7] attempted to tackle problem of multi-robot motion planning for differential drive robots, where the authors numerically evaluate equation 7 over the region of interest. The region of interest here would be set of positions of the drone and obstacles for which collision occurs. Our objective would be to minimize the value of 7, which means we want to maximize the probability collison of avoidance. However, one drawback of this procedure is that characterization of such a region($\mathbf{V_j}$) is generally tough.

Uncertainty matrices($\mathbf{\Sigma^d_{t_i}}, \mathbf{\Sigma^{o_j}_{t_i}}$) have been scaled up to accommodate radius values $\mathbf{R_{drone}}$ and $\mathbf{R_j}$.

There has been a lot of work to characterize the entropic distance between two distributions. One of the commonly used techniques for entropic distances are chi-square distances, Bhattacharyya distances among the many. We describe case of Bhattacharyya distances which is an extension to Mahalanobis distance[6].

B. Bhattacharyya distance

Bhattacharyya distance gives measure of similarity between two continuous/discrete probability distributions. It attempts to quantify the overlap between two distributions. For Gaussian distributions, Bhattacharyya distance has well-defined analytical formula to capture the overlap. For two multivariate normal distributions, $\mathbf{p_i} = \mathcal{N}(\mu_\mathbf{i}, \mathbf{\Sigma_i})$ with $\mathbf{i} = \{1,2\}$, the Bhattacharyya distance metric is defined as following,

$$\begin{aligned}\mathcal{BC}(\mathbf{p_1}, \mathbf{p_2}) = \frac{1}{8}(\mu_\mathbf{1} - \mu_\mathbf{2})^\mathbf{T}\mathbf{\Sigma}^{-\mathbf{1}}(\mu_\mathbf{1} - \mu_\mathbf{2}) + \\ \frac{1}{2}\ln\frac{det(\mathbf{\Sigma})}{\sqrt{det(\mathbf{\Sigma_1})det(\mathbf{\Sigma_2})}}\end{aligned} \tag{9}$$

Where, $\mathbf{\Sigma} = (\mathbf{\Sigma_1} + \mathbf{\Sigma_2})/2$. This is an extension of Mahalanobis distance. However, equation 6 can not be completely characterized through similarity/dissimilarity given by such entropic measure. Because the notion of probability is not complete in Bhattacharyya metric and particular distance doesn't map to a certain value in probability space. In figure 2, we demonstrate that for different Gaussian distributions with same overlap have different Bhattacharyya distances. Due to this limitation, entropic distance can't be used to model chance constraint.

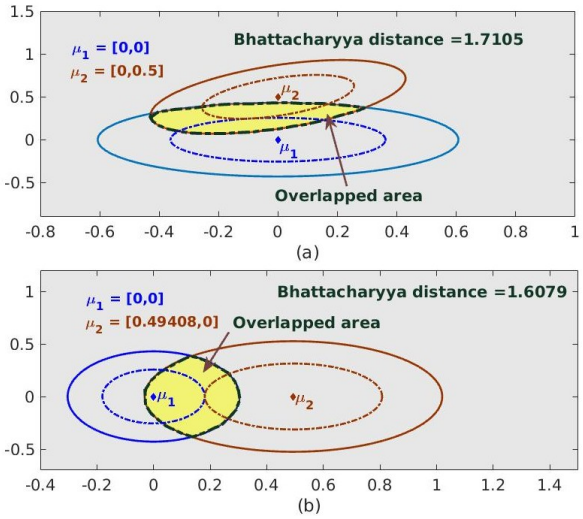


Fig. 2. Diagrammatic explanation of why Bhattacharyya distance is not a perfect metric to model chance constraint problem. In the figure, we have taken **2** sets of Gaussian distribution pairs which are touching at same confidence contour of $\mathbf{80.51}\%$. Meaning, area of overlap between two Gaussians shaded in yellow is same for both sets of Gaussian distributions. For figure 2(a), $\mathbf{\Sigma_1} = \left(\begin{smallmatrix}0.04 & 0 \\ 0 & 0.02\end{smallmatrix}\right)$, $\mathbf{\Sigma_2} = \left(\begin{smallmatrix}0.02 & 0.01 \\ 0.01 & 0.02\end{smallmatrix}\right)$. Bhattacharyya distance evaluated using equation 9 for this set of covariances turns out to be $\mathbf{1.7105}$. While, for figure 2(b), $\mathbf{\Sigma_1} = \left(\begin{smallmatrix}0.01 & 0 \\ 0 & 0.02\end{smallmatrix}\right)$, $\mathbf{\Sigma_2} = \left(\begin{smallmatrix}0.03 & 0 \\ 0 & 0.03\end{smallmatrix}\right)$. Value of Bhattacharyya distance for figure 2(b) is $\mathbf{1.6079}$. Hence, for same amount of overlap between two sets of Gaussian distributions, Bhattacharyya distances are turning out to be different. Areas shaded with yellow in figure indicate amount of overlap.

C. Theory of overlapping of Gaussians

The theory of overlap between two Gaussians has widely been studied in [12], which is built upon [13]. The authors in [13] attempts to get an optimal linear separator which minimizes the misclassification error when the objective is to classify the sample as coming from one of the several populations. We briefly state the theory to get approximate estimate of component of overlap between two Gaussians. The linear separator proposed in[13] works for two Gaussians of dimension $\mathbf{d} \geq \mathbf{1}$.

Let the linear separator(a hyperplane in $\mathbf{d}$ dimensional space) be $\alpha^{\mathbf{T}}\mathbf{x} = \beta$ where $\alpha, \mathbf{x} \in \mathbb{R}^{\mathbf{d}}$ and $\beta \in \mathbb{R}$. $\alpha^{\mathbf{T}}\mathbf{x} \leq \beta$ classifies $\mathbf{x}$ into a first cluster and $\alpha^{\mathbf{T}}\mathbf{x} > \beta$ classifies $\mathbf{x}$ into second cluster. We will briefly explain the procedure to obtain α, β and estimate the area of overlap($\boldsymbol{\Upsilon}$) between two Gaussian distributions $\mathcal{N}(\mu_{\mathbf{i}}, \boldsymbol{\Sigma}_{\mathbf{i}})$ with $\mathbf{i}$ = {1,2}. $\mathbf{x}$ is coming from one of the above two Gaussian distributions. $\alpha^{\mathbf{T}}\mathbf{x}$ is a transformation which transforms the original distribution into univariate normal distribution. The probability of misclassification when $\mathbf{x}$ is coming from first distribution is,

$$\mathbb{P}_1(\alpha^{\mathbf{T}}\mathbf{x} > \beta) = \mathbb{P}_1(\frac{\alpha^{\mathbf{T}}\mathbf{x} - \alpha^{\mathbf{T}}\mu_{\mathbf{1}}}{\sqrt{\alpha^T\Sigma_1\alpha}} > \frac{\beta - \alpha^{\mathbf{T}}\mu_{\mathbf{1}}}{\sqrt{\alpha^T\Sigma_1\alpha}})$$
$$\mathbb{P}_1(\alpha^{\mathbf{T}}\mathbf{x} > \beta) = 1 - \boldsymbol{\Phi}(\frac{\beta - \alpha^{\mathbf{T}}\mu_{\mathbf{1}}}{\sqrt{\alpha^T\Sigma_1\alpha}}) = 1 - \boldsymbol{\Phi}(\eta_1) = \mathbb{P}_1(\eta_1) \tag{10}$$

Similarly, probability of misclassification when sample $\mathbf{x}$ belongs to population $\mathbf{2}$ equals,

$$\mathbb{P}_2(\alpha^{\mathbf{T}}\mathbf{x} \leq \beta) = \mathbb{P}_2(\frac{\alpha^{\mathbf{T}}\mathbf{x} - \alpha^{\mathbf{T}}\mu_{\mathbf{2}}}{\sqrt{\alpha^T\Sigma_2\alpha}} \leq \frac{\beta - \alpha^{\mathbf{T}}\mu_{\mathbf{2}}}{\sqrt{\alpha^T\Sigma_2\alpha}})$$
$$\mathbb{P}_2(\alpha^{\mathbf{T}}\mathbf{x} \leq \beta) = 1 - \boldsymbol{\Phi}(\frac{\alpha^{\mathbf{T}}\mu_{\mathbf{2}} - \beta}{\sqrt{\alpha^T\Sigma_2\alpha}}) = 1 - \boldsymbol{\Phi}(\eta_2) = \mathbb{P}_2(\eta_2) \tag{11}$$

Where, $\eta_{\mathbf{1}} = \frac{\beta - \alpha^{\mathbf{T}}\mu_{\mathbf{1}}}{\sqrt{\alpha^{\mathbf{T}}\boldsymbol{\Sigma}_{\mathbf{1}}\alpha}}$ and $\eta_{\mathbf{2}} = \frac{\alpha^{\mathbf{T}}\mu_{\mathbf{2}} - \beta}{\sqrt{\alpha^{\mathbf{T}}\boldsymbol{\Sigma}_{\mathbf{2}}\alpha}}$ are two random variables with univariate standard normal distribution. $\boldsymbol{\Phi}$ in equations 10-11 denotes a cumulative distribution function for a univariate standard normal distribution. $\boldsymbol{\Phi}$ is a monotonically increasing function. Our objective is following,

$$max(\mathbb{P}_1(\eta_1), \mathbb{P}_2(\eta_2)) \rightarrow \min_{\alpha \in \mathbb{R}^{\mathbf{d}} \beta \in \mathbb{R}} \tag{12a}$$
$$min(\eta_1, \eta_2) \rightarrow \max_{\alpha \in \mathbb{R}^{\mathbf{d}} \beta \in \mathbb{R}} \tag{12b}$$

Equations 12a-12b are equivalent due to monotonic nature of the $\boldsymbol{\Phi}$. The objective is to maximize the minimum of (η_1, η_2). The objective is to find α, β, which will minimize the maximum probability of misclassification. Analytical characterization of α, β in terms of $\mu_{\mathbf{1}}, \boldsymbol{\Sigma}_{\mathbf{1}}, \mu_{\mathbf{2}}, \boldsymbol{\Sigma}_{\mathbf{2}}$ can be expressed as following,

$$\alpha = (\lambda_1\boldsymbol{\Sigma}_{\mathbf{1}} + \lambda_2\boldsymbol{\Sigma}_{\mathbf{2}})^{-1}(\mu_{\mathbf{2}} - \mu_{\mathbf{1}}) \tag{13a}$$
$$\beta = \alpha^T\mu_{\mathbf{1}} + \lambda_1\alpha^T\boldsymbol{\Sigma}_{\mathbf{1}}\alpha = \alpha^T\mu_{\mathbf{2}} - \lambda_2\alpha^T\boldsymbol{\Sigma}_{\mathbf{2}}\alpha \tag{13b}$$

Here, λ_1 and λ_2 are two scalars and resulting procedure to estimate these parameters is referred to as **minmax procedure**. The minmax procedure is an admissible procedure[13] when η_1 = η_2. For admissible procedure, λ = λ_1 = 1 - λ_2. If we substitute analytical characterization of α, β in η_1, η_2, the following equality must hold for admissible procedure.

$$\eta_1^2 - \eta_2^2 = \alpha^T[\lambda^2\boldsymbol{\Sigma}_{\mathbf{1}} - (1-\lambda)^2\boldsymbol{\Sigma}_{\mathbf{2}}]\alpha = \mathbf{0} \tag{14}$$

The above criterion is a necessary condition to get the best approximation of the amount of overlap. We will call λ *overlap parameter* as it is a deciding factor which completely characterizes the overlap for a given first and second order Gaussian moments.

Here, the value of overlap parameter λ is determined heuristically using equation 14 as a base condition. Algorithm to determine λ is outlined in [12]. The overlap parameter λ completely dictates the linear separator parameters α and β. Once we get optimal value of λ, we can estimate linear separator parameters α, β. Since the procedure is admissible, we can compute $\mathbb{P}_1(\eta_1)$ = $\mathbb{P}_2(\eta_2)$ = $\mathbb{P}_{minmax}$. The amount of overlap($\boldsymbol{\Upsilon}$) can be computed as below,

$$\eta_{\mathbf{1}} = f(\alpha, \beta), \quad \alpha = f(\lambda), \quad \beta = f(\lambda)$$
$$\boldsymbol{\Upsilon} = \mathbb{P}_1(\eta_1) + \mathbb{P}_2(\eta_2) = \mathbf{2}\mathbb{P}_{minmax} = h(\mu_{\mathbf{1}}, \mu_{\mathbf{2}}, \boldsymbol{\Sigma}_{\mathbf{1}}, \boldsymbol{\Sigma}_{\mathbf{2}}, \lambda) \tag{15}$$

Here, we can notice that component of overlap($\boldsymbol{\Upsilon}$) is parameterized by linear separator parameters α and β. Overlap λ is completely dictating α and β. Hence, λ dictates the amount of overlap $\boldsymbol{\Upsilon}$. Here, λ is determined through an iterative procedure. As seen in figure 3, the overlap is determined by substituting for different values of λ in 15, a typical iterative routine settles for some value of λ, when the overlap is correctly determined, this can be noticed in Fig 3(d)-3(f).

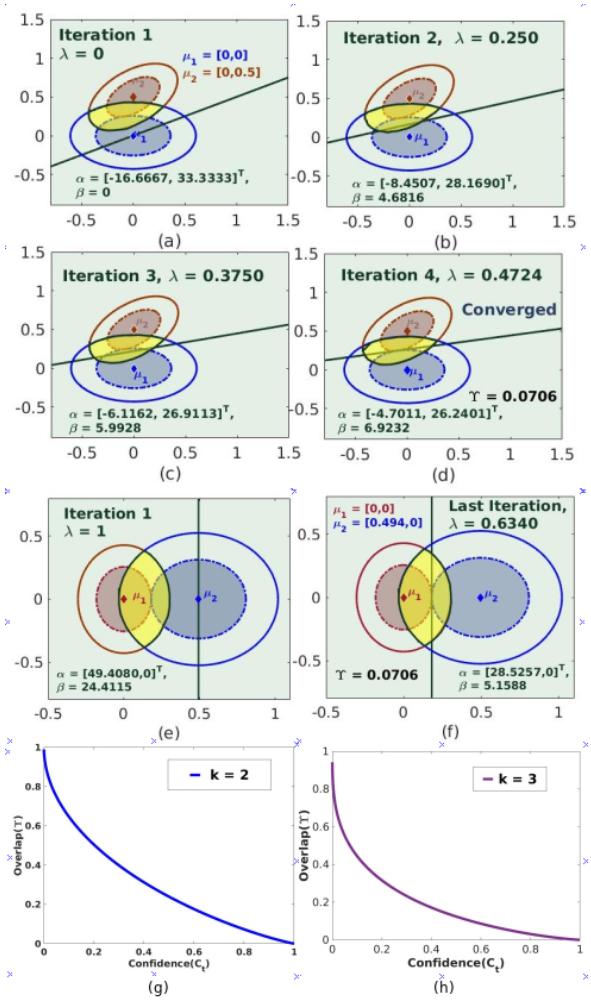
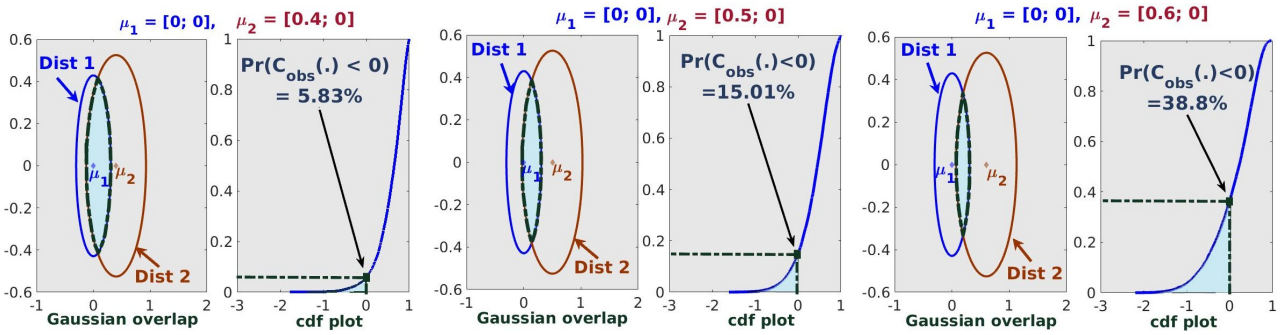


Fig. 3. This figure demonstrates how the values of overlap parameter λ evolves as algorithm outlined in [12] executes. It starts with initialized value of λ and ultimately converges to the value where the linear separator divides the two Gaussian distributions at the same confidence interval. From figure 3(a) -3(d), the Gaussian configuration considered is same as that of figure 2(a). Both the Gaussian distributions are touching at confidence contour corresponding to $\mathbf{80.51}\%$. Equality constraint of equation 14 ensures that both the Gaussians are touching at the same confidence interval. The line drawn in the figure is $\alpha^{\mathbf{T}}\mathbf{x} = \beta$. We can see orientation and position of the line evolving as overlap parameter λ converges. For converged value of λ, we can see that the optimal linear separator passes through the point of touch of the two Gaussian distributions. Figure 3(e) -3(f) shows λ converging for Gaussian configuration considered in figure 2(b). We can see value of overlap turning out to be same for both sets as shown in figure 3(d)-3(f).



(a) (b) (c)

Fig. 4. We establish an analogy between minimization of overlap between Gaussians as maximization of probability of collision avoidance modeled according to equation 6. Through an illustration, we demonstrate that as the amount of overlap between two distributions decreases, probability of collision avoidance increases. This is aptly conveyed through figure 4(a)-4(b)-4(c). For example, in figure 4(a), for a significant amount of overlap, the area below $\mathbf{0}$ in the cdf plot is very less. However, in figure 4(b) and 4(c), as the overlap decreases(achieved through incrementally separating μ_2 from μ_1), the corresponding area below $\mathbf{0}$ observed in the cdf plots significantly increases. Thus, it is clear that as the overlap between these two distributions decreases, the probability of collision avoidance[6](conveyed through cdfs) increases. The cdf plots of equation 6 were generated through *ecdf()* function of Matlab. The covariances considered for this demonstration are, $\mathbf{\Sigma_1} = \begin{pmatrix} 0.01 & 0 \\ 0 & 0.02 \end{pmatrix}$ and $\mathbf{\Sigma_2} = \begin{pmatrix} 0.03 & 0 \\ 0 & 0.03 \end{pmatrix}$.

When we estimate area of overlap for the two sets of Gaussian distributions in figure 2 using algorithm outlined in [12], the area of overlap turns out to be $\mathbf{\Upsilon}$ = 0.0706, which is same for both sets of Gaussian distributions shown in figures 2(a) and 2(b). This leads to the fact that for any two 2D Gaussian distributions touching at the confidence interval of $\mathbf{80.51}\%$, their area of overlap will always be equal to 0.0706. In other words, there is a unique mapping between area of overlap of two $\mathbf{k}$ variate Gaussians and confidence contours $\mathbf{c_t}$(where they are touching each other). The current scope of this paper explores this concept for $\mathbf{k = 2, 3}$. We create a table that would give us unique value of overlap for a given value of $\mathbf{c_t}$. We show relation between contour of touch($\mathbf{c_t}$) and area of overlap($\mathbf{\Upsilon}$), in the figure 3(g)-3(h).

V. Probabilistic Collision Avoidance as Overlap between Two Gaussians

Equation 7 represents analytical expression of chance constraint defined in section IV. Our objective is to maximize the probability of collision avoidance. Here, we propose a novel formulation by posing chance constraint problem as minimization of overlap between component of two Gaussian distributions. We demonstrate in figure 4 that minimization of overlap between two Gaussians is analogous to maximization of probability of collision avoidance.

A. Trajectory optimization with chance constraints

In section III, we discussed deterministic trajectory optimization routine. In this section, we reformulate this routine to accommodate state uncertainty. We express collision avoidance constraint as desired measure of overlap between Gaussian populations of drone and obstacle. The remodeling will use theory of overlapping of Gaussians described in section IV-C. Since there is an uncertainty in drone's position, we will redefine $\mathbf{J_{terminal}}$ as below,

$$\mathbf{J_{terminal}} = (\mathbf{D_{t_N}} - \mathbf{G_f})(\mathbf{\Sigma^d_{t_N}})^{-1}(\mathbf{D_{t_N}} - \mathbf{G_f})^{\mathbf{T}} \tag{16}$$

Equation 16 is mahalanobis distance[6], which characterizes the number of standard deviations a point is away from mean of a distribution. Equation 16 will minimize number of standard deviations goal point is away from the mean position of the drone at the end of the trajectory.

Here, we are assuming no uncertainty in the actuation. Further, we assume that belief propagation for drone and obstacles for a given time-horizon is known. Hence, minimization of overlap between drone and obstacle populations can be thought of as minimum number of standard deviations($\mathbf{c_{min}}$) a drone should deviate from its path to ensure collision free trajectory. Let that number be denoted by $\mathbf{c_{t_i}}$ at time instance $\mathbf{t_i}$. While planning the trajectory, our constraint is to ensure that the minimum value of $\mathbf{c_{t_i}}$ for $\mathbf{i} \in \{\mathbf{1}, \mathbf{2}..., \mathbf{N}\}$ is larger than certain threshold $\mathbf{c_{min}}$. Which is analogous to saying that the overlap between drone and obstacle at any time instant should not be greater than overlap threshold $\mathbf{\Upsilon_{max}}$.

1) Reformulation of collision avoidance constraint: Our goal is to reach $\mathbf{G_f}$ from the start position $\mathbf{X_0}$ in $\mathbf{N}$ time-steps, each time-step of duration τ. Here, our objective is to find optimal set of velocity commands $\mathbf{V_{t_i}} = (\mathbf{v^x_{t_i}}, \mathbf{v^y_{t_i}}, \mathbf{v^z_{t_i}})$ which would satisfy our constraints as well as minimize the cost. We will be using the process model of the drone explained in section III.

Let the overlap between drone and obstacle $\mathbf{j}$ at time instance $\mathbf{t_i}$ be $\mathbf{\Upsilon^j_{t_i}}$, which is dictated by overlap parameter $\lambda^{\mathbf{j}}_{\mathbf{t_i}}$. then,

$$\mathbf{D_{t_i}} = f(\mathbf{V_{t_1}}, \mathbf{V_{t_2}}, \mathbf{V_{t_3}}....\mathbf{V_{t_i}}) \tag{17a}$$

$$\mathbf{\Upsilon^j_{t_i}} = g_1(\mathbf{D_{t_i}}, \mathbf{\Sigma^d_{t_i}}, \mathbf{\hat{O}^j_{t_i}}, \mathbf{\Sigma^{o_j}_{t_i}}, \lambda^{\mathbf{j}}_{\mathbf{t_i}}) \tag{17b}$$

In equation 17b, overlap is expressed in terms of drone/obstacle positions and their corresponding uncertainties. Drone position is expressed in terms of control commands($\mathbf{V_{t_1}}, \mathbf{V_{t_2}}, ...\mathbf{V_{t_i}}$) as explained in motion model(equation 4). Hence, equation 17b is completely parameterized by control commands($\mathbf{V_{t_1}}, \mathbf{V_{t_2}}, ...\mathbf{V_{t_i}}$) and overlap parameter($\lambda^{\mathbf{j}}_{\mathbf{t_j}}$). We can express condition to admissible procedure(equation 18a) in terms of control and overlap parameter,

$$\left.\begin{aligned} (\eta^{\mathbf{d}}_{\mathbf{t_i}})^2 - (\eta^{\mathbf{o_j}}_{\mathbf{t_i}})^2 &= g_2(\mathbf{D_{t_i}}, \mathbf{\Sigma^d_{t_i}}, \mathbf{\hat{O}^j_{t_i}}, \mathbf{\Sigma^{o_j}_{t_i}}, \lambda^{\mathbf{j}}_{\mathbf{t_i}}) \\ (\eta^{\mathbf{d}}_{\mathbf{t_i}})^2 - (\eta^{\mathbf{o_j}}_{\mathbf{t_i}})^2 &= f_2(\lambda^j_{t_i}, \mathbf{V_{t_1}}, \mathbf{V_{t_2}}, \mathbf{V_{t_3}}...\mathbf{V_{t_i}}) \end{aligned}\right\} \tag{18a}$$

$$\mathbf{\Upsilon^j_{t_i}} = 2\mathbb{P}^d_{t_i}(\eta^{\mathbf{d}}_{\mathbf{t_i}}) = 2\mathbb{P}^{o_j}_{t_i}(\eta^{\mathbf{o_j}}_{\mathbf{t_i}}) = f_1(\lambda^j_{t_i}, \mathbf{V_{t_1}}, \mathbf{V_{t_2}}, \mathbf{V_{t_3}}...\mathbf{V_{t_i}}) \tag{18b}$$

Equation 18a-18b are in accordance with equation 14-15, equation 18a models necessary condition for the procedure to be admissible in nature.

The maximum allowed overlap $\mathbf{\Upsilon_{max}}$ is uniquely related to minimum number of standard deviations($\mathbf{c_{min}}$) a drone should deviate in order to avoid obstacle with certain minimum confidence. $\mathbf{c_{min}}$ is expressed in terms of confidence intervals directly. So for a particular confidence interval, $\mathbf{c_{min}}$ will have a unique scalar value. Hence, a unique $\mathbf{\Upsilon_{max}}$ value as explained in section IV-C. So, a

chance constraint in terms of overlap between two Gaussians can be expressed as below.

$$C_{obs_j}(.) = \begin{cases} \mathbf{\Upsilon^j_{t_i}} = f_1^{lin}(\lambda^{\mathbf{j}}_{\mathbf{t_i}}, \mathbf{V_{t_i}}) \leq \mathbf{\Upsilon_{max}} \\ (\eta^{\mathbf{d}}_{\mathbf{t_i}})^2 - (\eta^{\mathbf{o_j}}_{\mathbf{t_i}})^2 = f_2^{lin}(\lambda^j_{t_i}, \mathbf{V_{t_i}}) = \mathbf{0} \end{cases} \quad (19)$$

Both sub-constraints of collision avoidance constraint(equation 19) are parameterized by velocity controls($\mathbf{V_{t_1}}, \mathbf{V_{t_2}}, ...\mathbf{V_{t_i}}$) and overlap parameter($\lambda^{\mathbf{j}}_{\mathbf{t_i}}$). $\mathbf{\Upsilon^j_{t_i}} \leq \mathbf{\Upsilon_{max}}$ ensures that the drone is avoiding the obstacle with certain minimum confidence. $(\eta^{\mathbf{d}}_{\mathbf{t_i}})^2 - (\eta^{\mathbf{o_j}}_{\mathbf{t_i}})^2 = 0$ ensures that the overlap parameter($\lambda^{\mathbf{j}}_{\mathbf{t_i}}$) we get through SCP routine is optimal and satisfies condition to admissible procedure. Closed form expressions for $f_1(.)$ and $f_2(.)$ are functions of optimization variables($\mathbf{V_{t_i}}$, $\lambda^{\mathbf{j}}_{\mathbf{t_i}}$) which are computed using mathematica[14]. They are non-linear in our variables of interest. We linearize them as shown below,

$$f_1^{lin}() = \bar{f}_1() + \sum_{k=1}^{i} \nabla_{\mathbf{V_{t_k}}}(\mathbf{V_{t_k}} - \bar{\mathbf{V}}_{\mathbf{t_k}}) + \nabla_{\lambda^{\mathbf{j}}_{\mathbf{t_i}}}(\lambda^{\mathbf{j}}_{\mathbf{t_i}} - \bar{\lambda}^{\mathbf{j}}_{\mathbf{t_i}}) \quad (20)$$

$$f_2^{lin}() = \bar{f}_2() + \sum_{k=1}^{i} \nabla_{\mathbf{V_{t_k}}}(\mathbf{V_{t_k}} - \bar{\mathbf{V}}_{\mathbf{t_k}}) + \nabla_{\lambda^{\mathbf{j}}_{\mathbf{t_i}}}(\lambda^{\mathbf{j}}_{\mathbf{t_i}} - \bar{\lambda}^{\mathbf{j}}_{\mathbf{t_i}}) \quad (21)$$

$f_1^{lin}(.)$ and $f_2^{lin}(.)$ are affine approximations of $f_1(.)$ and $f_2(.)$. $\nabla_{\mathbf{V_{t_k}}}$ and $\nabla_{\lambda^{\mathbf{j}}_{\mathbf{t_i}}}$ are partial derivatives with respect to $\mathbf{V_{t_k}}$ and $\lambda^{\mathbf{j}}_{\mathbf{t_i}}$ respectively.

2) Trajectory optimization algorithm: We outline complete trajectory optimization algorithm built on above scheme. Let the trajectory of obstacle $\mathbf{j}$ be denoted by $\Omega_j = \{\mathbf{O^j_{t_1}}, \mathbf{O^j_{t_2}}, \mathbf{O^j_{t_3}}, ...\mathbf{O^j_{t_N}}\}$ and trajectory of all $\mathbf{P}$ obstacles be $\mathbf{\Pi_P} = \{\Omega_1, \Omega_2, \Omega_3, ...\Omega_P\}$. Let overlap parameters between obstacle $\mathbf{j}$ and drone for $\mathbf{N}$ timesteps be $\mathbf{\Lambda_j} = \{\lambda^{\mathbf{j}}_{\mathbf{t_1}}, \lambda^{\mathbf{j}}_{\mathbf{t_2}}...\lambda^{\mathbf{j}}_{\mathbf{t_N}}\}$. Algorithm $\mathbf{1}$ outlines proposed SCP routine where we jointly optimize over control($\mathbf{V_{t_i}}$) and overlap parameter($\lambda^{\mathbf{j}}_{\mathbf{t_i}}$) space.

Algorithm 1 ProbabilisticTrajOpt($\mathbf{\Upsilon_{max}}$, $\mathbf{\Pi_P}$, $\mathbf{\Sigma_{drone}}$, $\mathbf{\Sigma_{obstacle}}$)

1: **Initialization:** Guess for $\bar{\mathbf{\Lambda}}^{\mathbf{k}}_{\mathbf{j}}(\mathbf{t})$, $\bar{\mathbf{V}}^{\mathbf{k}}(\mathbf{t})$, iteration counter $k = 0$
2: $\bar{\mathbf{D}}^k(\mathbf{t}) = \mathit{InitializeTrajectory}(\bar{\mathbf{V}}^k(\mathbf{t}))$
3: **while** $\mid \mathbf{J}_{k+1} - \mathbf{J}_k \mid \geq \delta$ **do**

$$\mathbf{V}^k(\mathbf{t}), \mathbf{\Lambda}^k_{\mathbf{j}}(\mathbf{t}) = \text{argmin} \quad \mathbf{J}_k$$

subject to

$$\mathbf{X_{t_i+1}} = f(\mathbf{X_{t_i}}, \mathbf{V_{t_i}})$$
$$\mathbf{V_{min}} \leq \mathbf{V_{t_i}} \leq \mathbf{V_{max}}$$
$$\mathbf{a_{min}} \leq (\frac{\mathbf{V_{t_i+1}} - \mathbf{V_{t_i}}}{\tau}) \leq \mathbf{a_{max}}$$
$$C_{obs_j}(\bar{\mathbf{\Lambda}}^k_{\mathbf{j}}(\mathbf{t}), \bar{\mathbf{V}}^k(\mathbf{t})) \leq \mathbf{0}, \ \forall\ j = \{1, 2, 3, ... P\}$$

4: $\bar{\mathbf{\Lambda}}^k_{\mathbf{j}}(\mathbf{t}) \leftarrow \mathbf{\Lambda}^k_{\mathbf{j}}(\mathbf{t})$
5: $\bar{\mathbf{V}}^k(\mathbf{t}) \leftarrow \mathbf{V}^k(\mathbf{t})$
6: $k \leftarrow k + 1$
7: **end while**

B. Evaluation of trajectory optimization

In this section, we evaluate proposed trajectory optimization routine for single obstacle-drone configuration. The start position of the drone is $\mathbf{X_0} = [\mathbf{0}, \mathbf{0}, \mathbf{0}]$ and it has to reach destination $\mathbf{G_f} = [\mathbf{10}, \mathbf{0}, \mathbf{0}]$ in $\mathbf{N} = \mathbf{20}$ timesteps of duration $\tau = \mathbf{1.0}$ seconds. Obstacle starts from $\mathbf{O^1_{t_1}} = [\mathbf{10}, \mathbf{0}, \mathbf{0}]$ to reach $\mathbf{O^1_{t_N}} = [\mathbf{0}, \mathbf{0}, \mathbf{0}]$. Our objective is to find an optimal trajectory where $\mathbf{c_{min}} = \mathbf{60}\%$ confidence contour of the drone avoids $\mathbf{60}\%$ confidence contour of the obstacle. Meaning, during the entire trajectory, $\mathbf{60}\%$ confidence contour of drone should not penetrate $\mathbf{60}\%$ confidence contour of obstacle. When two $\mathbf{3}$ dimension Gaussians touch each other at $\mathbf{60}\%$ confidence contours, the area of overlap is $\mathbf{0.0861}$. Overlap between drone and obstacle populations at any point of time during the trajectory can not be more than $\mathbf{\Upsilon_{max}} = \mathbf{0.0861}$. We use algorithm $\mathbf{1}$ to get optimal trajectory satisfying the constraints.

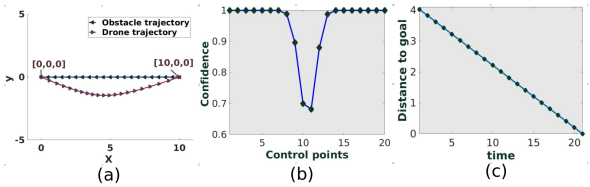


Fig. 5. In this figure, we show evaluation of trajectory optimization routine proposed in Algorithm $\mathbf{1}$. In figure 5(a), we see trajectory of drone and obstacle for a simple scenario. Figure 5(b) shows confidence contour avoidance profile for this case. We see that as drone and Obstacle keep coming closer, their confidence contours corresponding to confidence = $\mathbf{60}\%$ avoid each-other. 5(c) shows how Mahalanobis distance[6] between goal point and drone reduces over time.

VI. Results and Discussions

We construct a model predictive control framework by using proposed probabilistic trajectory optimization routine as a base. Our proposal has been extensively evaluated for wide range of safety critical configurations. We show two such challenging situations to evaluate our proposal. We use Matlab based CVX[15] to prototype many of these scenarios. For a faster implementation, we use python based CVXOPT[16]. The simulations are carried out using Rotors[17], which is a micro aerial vehicle simulation framework built in gazebo[18]. The proposed approach is implemented in a model predictive control framework(MPC) along the lines of [19], [19] uses the idea of a receding horizon as the basis for building an MPC. We plan for a finite horizon and upto some intermediate way-point along the original trajectory. Intermediate way-points are placed at regular intervals to avoid extreme deviations in drone trajectory. In this section, we show results for two interesting applications. The detailed video of simulations under various safety critical situations is provided at http://robotics.iiit.ac.in/people/dhaivat.bhatt/CDC_video/index.html

A. Antipodal configuration

In this experiment, we show 3 obstacles attacking drone in an antipodal configuration. The drone detects obstacles at sensing range of $\mathbf{S_r} = \mathbf{10}$ meters. The acceleration bounds $\mathbf{a_{min}}, \mathbf{a_{max}}$ are $-\mathbf{0.5}\ m/s^2$, $\mathbf{0.5}\ m/s^2$ respectively. Value of $\mathbf{V_{min}}$ and $\mathbf{V_{max}}$ are $\mathbf{0}\ m/s$, $\mathbf{3.0}\ m/s$ respectively. We keep a planning horizon of $\mathbf{28}$ steps, each of duration $\tau = \mathbf{0.3}$ seconds. We keep re-planning at every $\mathbf{0.3}$ seconds. Radius of drone/obstacles is taken as $\mathbf{0.5}$ meters. For this configuration, we consider $\mathbf{c_{min}} = \mathbf{90}\%$. In other words, our objective is to ensure that at least $\mathbf{90}\%$ confidence contours of drone and obstacles do not penetrate each other during entire journey of the drone. As soon as it detects the obstacles, it starts deviating from its trajectory and $\mathbf{90}\%$ confidence contour of the drone avoids $\mathbf{90}\%$ confidence contours of all 3 obstacles. The position uncertainties considered are $\mathbf{\Sigma_{drone}} = \mathbf{\Sigma_{obs1}} = \mathbf{\Sigma_{obs2}} = \mathbf{\Sigma_{obs3}} = \begin{pmatrix} 0.02 & 0 & 0 \\ 0 & 0.02 & 0 \\ 0 & 0 & 0.02 \end{pmatrix}$. With this configuration, we show comprehensive results in figure 6. Sequence of images in figure 6 shows some snaps during obstacle avoidance maneuver, the navigation was successful and the lower bound was respected throughout the trajectory. As shown in confidence plots in figure 6(d)-6(e)-6(f), the maximum penetration for violet and dark green obstacles was at $\mathbf{5}\%$, while for blue obstacle, it was $\mathbf{2}\%$.

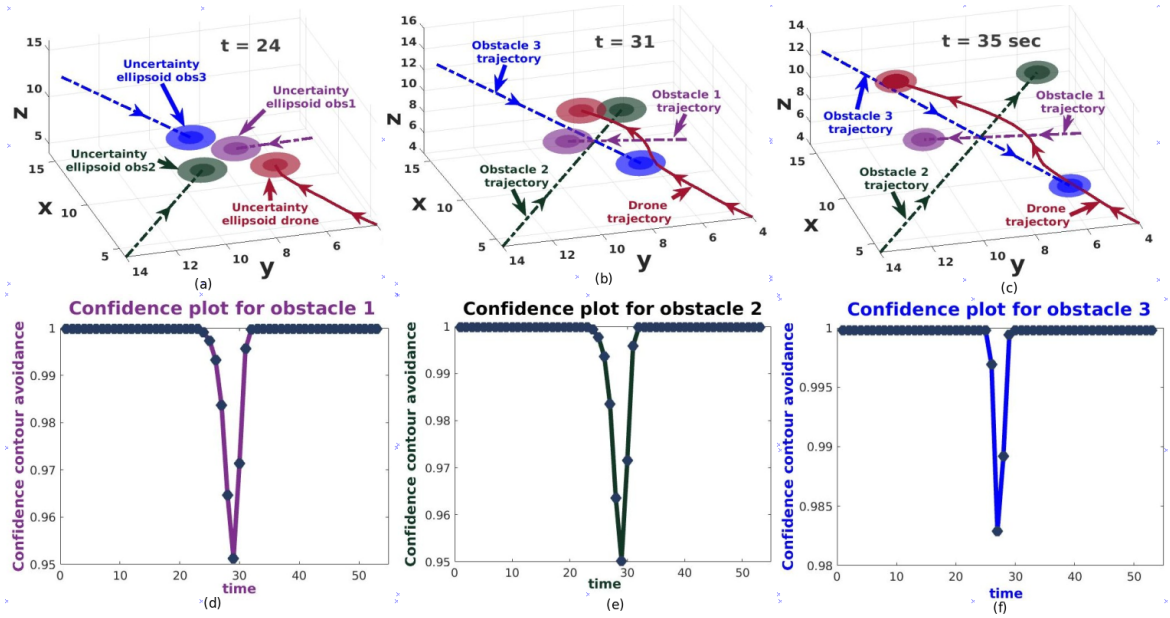


Fig. 6. Antipodal setting: The drone adopts a maneuver relating to a particular confidence of safety when it encounters obstacles in its sensing range. This is clearly shown in figure 6(a)-6(c). Figure 6(a), shows the situation, where the drone encounters obstacles, withing its sensor range and starts taking appropriate control actions.Figure 6(b), highlights the resultant maneuver, that the drone adopts to achieve a targeted level of safety. Figure 6(c) shows the goal reaching ability of the drone, after avoiding obstacles. The lighter ellipsoidal shades in these figures represent the uncertainty region encompassing the mean positions of the drone and obstacles(filled with darker shades). Figures 6(d)-6(e)-6(f), shows the plots of confidence intervals for the collision avoidance maneuvers the that drone adopted in figures 6(a)-6(c). Our constraint was to ensure that $\mathbf{90}\%$ confidence contours of drone avoids at least $\mathbf{90}\%$ confidence contours of all obstacles. From figures 6(d)-6(e)-6(f), we can observe that maximum overlap between the drone and any obstacle is $\mathbf{5}\%$,, i.e. only the $\mathbf{95}\%$ confidence contours grace each-other.

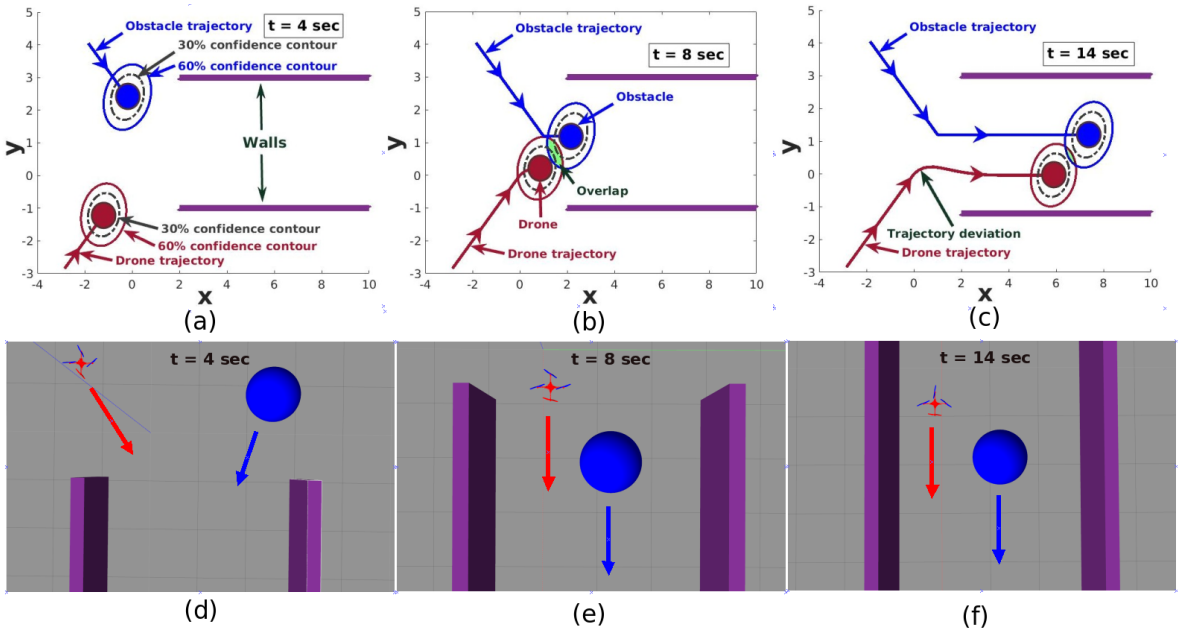


Fig. 7. Constrained corridor setting: In figure 7(a), confidence contour for 30% and 60% are shown for both, drone and obstacle. Drone senses presence of obstacle at time $\mathbf{t = 4sec}$. As drone enters in corridor, lower and upper bound constraints are enforced. Which ensures minimum risk behavior. For example, in figure 7(b)- 7(c), we can see overlap between drone and obstacle shaded in green for 60% confidence contours. While, 30% confidence contours which correspond to lower bound never penetrate each other as visible in figure 7(b)-7(c). Figure 7(e) shows top view of figure 7(b) in gazebo. Under such tightly bounded spaces, we observe that drone is able to safely maneuver constraints without crashing into walls. Trajectory deviation shown in 7(c) depicts that drone can maneuver in a way that would stay reasonably behind the obstacles while satisfying both lower and upper bound constraints. Figures 7(d)-7(e)-7(f) are gazebo results of figures 7(a)-7(b)-7(c) in bird's eye view.

B. Obstacle avoidance in constrained corridor

We show another interesting application of our proposal. If drone and obstacle are entering in a constrained corridor, apart from putting lower bound $\mathbf{c_{min}}$, we can also put upper bound($\mathbf{c_{max}}$) in such tight spaces. Putting upper bound will ensure that drone is not slowing down too much. Sub-constraint 1 of equation 19 will take a form like $\boldsymbol{\Upsilon}_{\mathbf{min}} \leq \boldsymbol{\Upsilon}^{\mathbf{j}}_{\mathbf{t_i}} \leq \boldsymbol{\Upsilon}_{\mathbf{max}}$. Through demonstration, we advocate the usage of upper bound constraint in tight spaces. Upper bound ensures that drone is within certain range of obstacle, which will reduce deviation in drone trajectory, thus ensuring no collision with surrounding walls. We consider a case where drone and obstacle are entering in a constrained corridor at same time. In this case, we take $\mathbf{c_{min}} = \mathbf{30}\%$ and $\mathbf{c_{max}} = \mathbf{60}\%$. In other words at least $\mathbf{30}\%$ confidence contours of drone and obstacle can not penetrate into each other, while $\mathbf{60}\%$ confidence contours can't have $\mathbf{0}$ overlap at any time instant during the trajectory. Our planning horizon is of $\mathbf{40}$ timesteps, each of duration $\tau = \mathbf{0.3}$ seconds. In this case, we take $\boldsymbol{\Sigma}_{\mathbf{drone}} = \begin{pmatrix} 0.02 & 0.01 & 0 \\ 0.01 & 0.02 & 0 \\ 0 & 0 & 0.02 \end{pmatrix}$ and $\boldsymbol{\Sigma}_{\mathbf{obs}} = \begin{pmatrix} 0.03 & 0.02 & 0 \\ 0.02 & 0.03 & 0 \\ 0 & 0 & 0.02 \end{pmatrix}$. Before solving an MPC, these matrices are scaled up to incorporate radius of drone and obstacle. We consider non-isotropic uncertainty for this demonstration and show efficacy of our algorithm under tight spaces. In figure 7, We show snippets of various time-instances. The walls are modeled as stationary obstacles. For example, in figure 7(a), drone and obstacle are entering in the corridor. Both upper bound and lower bound constraints are enforced and we can see that drone is able to maintain sufficient distance from the wall as well as the obstacle while respecting the constraints. An absence of upper-bound constraint results in slowing down of the drone and we encounter a longer time for flight completion. Having upper bound favorably changes the velocity profile to complete trajectory in faster time. This shows usefulness of our proposal in tightly bounded spaces. We can use such modeling in object tracking/following. In figure 8, we show confidence plot for entire trajectory.

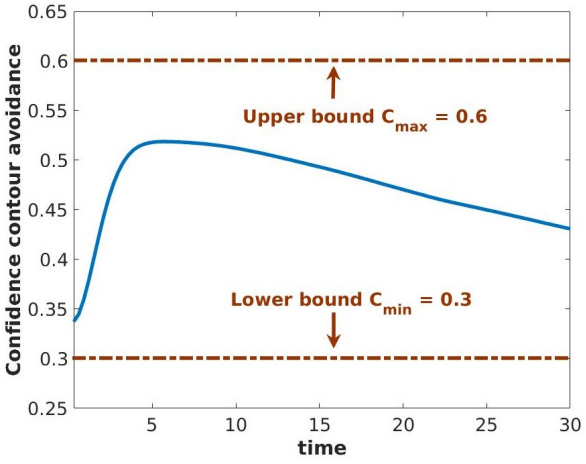


Fig. 8. This figure shows how confidence contour of touch($\mathbf{c_{t_i}}$) is changing over time for setting considered in VI-B. Throughout the trajectory, our drone is able to satisfy both, lower and upper-bound constraints. Initial rise in plot suggests that drone was slowing down first, and then it gradually accelerated to satisfy upper-bound constraint.

VII. Conclusion and Future Work

In this paper, a novel approach to dynamic collision avoidance under uncertainty in state of robot and obstacles, modeled using Gaussian distribution, has been proposed. It has been derived by using area of overlap of the Gaussian distributions, which has unique characterization for a given confidence contour. The proposed algorithm, integrated with Linear MPC, optimizes over velocity profile and overlap parameter space to generate a navigation path in constrained dynamic environment. The paper puts forward results for two safety critical configurations: Antipodal configuration and Constrained Corridor setting. The findings of this study have been validated for various other possible scenarios using numerical simulations. In future, we intend to model actuation dynamics into overlap of Gaussian framework and attempt to solve for challenging scenarios with unbounded covariances.

References

[1] M. Babu, R. R. Theerthala, A. K. Singh, B. Gopalakrishnan, and K. M. Kirshna, "Model predictive control for autonomous driving considering actuator dynamics," 2018.

[2] D. Kim, J. Kang, and K. Yi, "Control strategy for high-speed autonomous driving in structured road," in *Intelligent Transportation Systems (ITSC), 2011 14th International IEEE Conference on*. IEEE, 2011, pp. 186–191.

[3] C. Katrakazas, M. Quddus, W.-H. Chen, and L. Deka, "Real-time motion planning methods for autonomous on-road driving: State-of-the-art and future research directions," *Transportation Research Part C: Emerging Technologies*, vol. 60, pp. 416–442, 2015.

[4] W. Schwarting, J. Alonso-Mora, L. Pauli, S. Karaman, and D. Rus, "Parallel autonomy in automated vehicles: Safe motion generation with minimal intervention," in *Robotics and Automation (ICRA), 2017 IEEE International Conference on*. IEEE, 2017, pp. 1928–1935.

[5] G. Garimella, M. Sheckells, and M. Kobilarov, "Robust obstacle avoidance for aerial platforms using adaptive model predictive control," in *Robotics and Automation (ICRA), 2017 IEEE International Conference on*. IEEE, 2017, pp. 5876–5882.

[6] Wikipedia, "Mahalanobis distance — Wikipedia, the free encyclopedia," https://en.wikipedia.org/wiki/Mahalanobis_distance.

[7] J. Van Den Berg, P. Abbeel, and K. Goldberg, "Lqg-mp: Optimized path planning for robots with motion uncertainty and imperfect state information," *The International Journal of Robotics Research*, vol. 30, no. 7, pp. 895–913, 2011.

[8] B. Gopalakrishnan, A. K. Singh, M. Kaushik, K. M. Krishna, and D. Manocha, "Prvo: Probabilistic reciprocal velocity obstacle for multi robot navigation under uncertainty," 2017.

[9] B. Gopalakrishnan, A. K. Singh, and K. M. Krishna, "Closed form characterization of collision free velocities and confidence bounds for non-holonomic robots in uncertain dynamic environments," in *Intelligent Robots and Systems (IROS), 2015 IEEE/RSJ International Conference on*. IEEE, 2015, pp. 4961–4968.

[10] A. K. Singh and K. M. Krishna, "Reactive collision avoidance for multiple robots by non linear time scaling," in *Decision and Control (CDC), 2013 IEEE 52nd Annual Conference on*. IEEE, 2013, pp. 952–958.

[11] S.Boyd, "sequential convex programming," https://web.stanford.edu/class/ee364b/lectures/seq_slides.pdf, 2008.

[12] E. Nowakowska, J. Koronacki, and S. Lipovetsky, "Tractable measure of component overlap for gaussian mixture models," *arXiv preprint arXiv:1407.7172*, 2014.

[13] T. W. Anderson, R. R. Bahadur, *et al.*, "Classification into two multivariate normal distributions with different covariance matrices," *The annals of mathematical statistics*, vol. 33, no. 2, pp. 420–431, 1962.

[14] W. R. Inc., "Mathematica, Version 11.0," champaign, IL, 2016.

[15] M. Grant and S. Boyd, "CVX: Matlab software for disciplined convex programming, version 2.1," http://cvxr.com/cvx, Mar. 2014.

[16] M. Andersen and L. Vandenberghe, "CVXOPT: A python package for convex optimization, version 1.1.9," http://cvxopt.org/index.html, 2016.

[17] F. Furrer, M. Burri, M. Achtelik, and R. Siegwart, "Rotorsa modular gazebo mav simulator framework," in *Robot Operating System (ROS)*. Springer, 2016, pp. 595–625.

[18] N. Koenig and A. Howard, "Design and use paradigms for gazebo, an open-source multi-robot simulator," in *Intelligent Robots and Systems, 2004.(IROS 2004). Proceedings. 2004 IEEE/RSJ International Conference on*, vol. 3. IEEE, 2004, pp. 2149–2154.

[19] A. Raemaekers, "Design of a model predictive controller to control uavs."

Available online at www.ijapie.org

International Journal of Advanced
Production and Industrial Engineering

IJAPIE-SI-IDCM 611 (2018) 54–56

Special Issue on

INNOVATIVE DESIGN
&
COMPUTATIONAL
MODELLING

Coefficient of friction and microhardness analysis of CrC coating

Shailesh Mani Pandey
[1]*(Department of Mechanical Engineering, Delhi Technological University, India)*
Email: shaileshmanipandey@dce.ac.in

Abstract : Efficiency and performance are two critical characteristics of the internal combustion engine. The power generating component is required to be efficient so as to increase the overall performance of the vehicle and to make maximum use of the energy. The present study mainly focused upon development of CrC coating on cast iron substrate. The study shows that CrC coating enhanced tribological properties. Microhardness of developed coating as well as coefficient of friction is analyzed in this research

Keywords: Coefficient of friction, microhardness, CrC coating, PVD technique.

I. INTRODUCTION

An efficient power generating component (engine) of a vehicle (automobile) improves the overall performance of the automobile. Also, it plays an important role in utilizing the maximum use of the internal energy generated by the combustion of working fluid. And because of these reasons a lot of research is going on in this sector to increase and maintain the performance of the engine [1].

Many researchers have investigated the mechanisms of damage to piston, which mainly involved wear, temperature, and fatigue [2–5]. Since internal combustion engine with high efficiency has a tendency to operate at higher temperatures, the heat resisting properties of piston rings have become a major issue. And hence, the demand for better piston rings for internal combustion (IC) engine increases particularly in diesel engine pistons rings for higher heat resistance.

The tribological behavior of piston rings has been recognized as an important influence on the performance of internal combustion engines regarding power loss, fuel consumption, oil consumption, and harmful exhaust emissions. Therefore, the piston ring is one of the largest sources of friction in the internal combustion engine over the standard range of engine speeds and loads encountered in service [4, 5]. In practice, the damage in piston rings is attributed first to wear (as there are parts in contact and relative motion), then to lubrication and fatigue. Also, piston assembly accounts for approximately 35–45% of all the internal combustion engine frictional losses [6,7]. In spite of continuous evolution and research on piston rings, its failure is still a common phenomenon. It is the only component of the engine that encounters failure from different origins such as thermo-mechanical stresses, wear, fatigue, extreme temperatures, oxidations, etc.

The failures also occur due to the engine working conditions like advanced ignition timing, lean carburetor jetting, foreign material trapped inside, inappropriate piston-to-cylinder clearance, low octane fuel, loss of lubrication, high compression ratio and soon. [8,9]. Different types of coatings are used on piston rings to improve their characteristics. The coating can increase the hardness along with excellent surface finishing, thus reducing the friction and wear rate.

Various conventional techniques are being used for a long time [10]. Thermal spray coatings such as wire spray, high oxy fuel velocity spray, plasma spray Coatings are used act as an effective barrier to tribological failure [11]. As thermal spray processes advantage is that the large variety of single material or composite materials use to coat the substrate without significantly heating it [12–14].

The present study study mainly focused upon development of CrC coating on cast iron substrate and find out the effect of developed coating on the tribological properties such as wear behavior.

II. EXPERIMENTAL PROCEDURE

In this investigation, a four-stroke, single barrel and direct infusion diesel motor has been used. Table 1 shows deposition condition of CrC coating using PVD (physical vapor deposition) on cast iron substrate materials. PVD coating technique is used to develop coating and enhanced tribological properties. The multilayer coatings were prepared to utilize a PVD. Initiallya Cr target was controlled by a DC control power for the deposition of the Cr–C coating. Both the Ar and N_2were supplied continuously to prevent coating from contamination.

Additive layer of Si was deposited on the substrate material for improving adhesive strength of substrate material. Test

examples were cleaned in a ultrasonic cleaner with surfactant for 15 min took after by de-ionized water for 10 min and after that dried at 100 °C for 15 min before the covering statement. Prior to deposition, the coating chamber was pumped down to 2.6×10^{-3} Pa. The CrC coating was successfully developed on CI substrate having variable film thickness ranging from 100-200 microns

Table 1 Deposition conditions of CrC Coating

Coating temperature (C)	250
Deposition time per run (min)	50
Cathode current (A)	135
Bias voltage (V)	110
Coating pressure (Pa)	4 *10

III. RESULTS

The wear measured on the cylinder liner surface is small (wear depth of sample 2 is<100nm), both in comparison to real wear and comparison to the total surface amplitude. The results reveals that coefficient of friction is minimum at coated sample 4 having film thickness 200 microns and maximum at coated sample 1 having film thickness of 100 microns as shown in figure 1.

Figure 2 reveals the result of micro hardness of CrC coating on cast iron substrate. Microhardness of CrC coating minimum at coated sample 1 having film thickness 100 microns and maximum at coated sample 4 having film thickness of 200 microns.

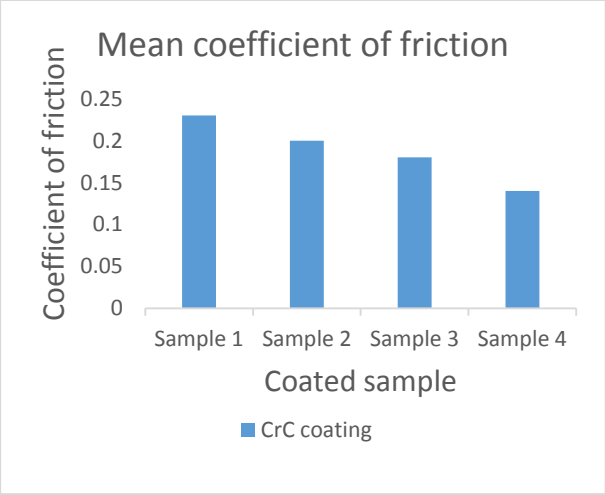


Fig. Shows variation of coefficient of friction of CrC coating

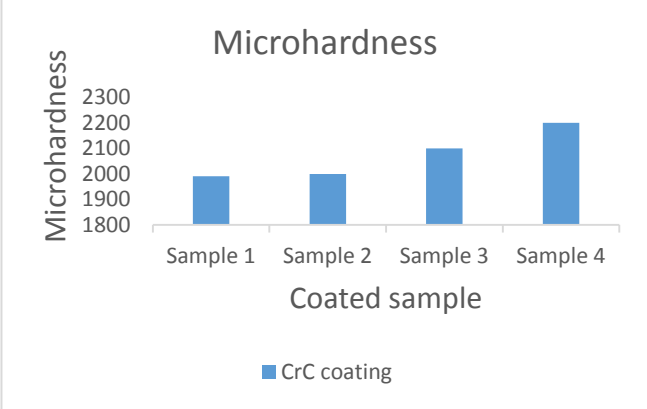


Fig. 2 Shows variation of microhardness of CrC coating

IV. CONCLUSION

The CrC coating on CI substrate was successfully developed using PVD coating. The experimental results of coating sample 4 having film thickness of 200 microns shows excellent tribological behavior and high hardness value.

REFERENCES

[1] Skopp A, Kelling N, Woydt M, et al. *Thermally sprayed titanium suboxide coatings for piston ring/cylinder liners under mixed lubrication and dry-running conditions. Wear 2007;262(9):1061–1070.*
[2] Liu Q, Song Y, Xu G, et al. *On the laser quenching of the groove of the piston head in large diesel engines. J Mater Eng Perform. 1998;7:402–406.*
[3] Silva FS. *Fatigue on engine pistons – a compendium of case studies. Eng Fail Anal. 2006;13:480–492.*
[4] Monaghan ML. Putting friction in its place, *2nd Int. Conf.: combustion engines – reduction offriction and wear. InstMechEng Conf. Pub. 1989-9, Paper C375rKN1. 1989. p. 1–5.*
[5] Parker DA, Adams DR. *Friction losses in the reciprocating internal Combustion engine, tribology – key to the Efficient Engine. InstMechEng Conf. Pub. 1982-1, Paper C5r82. 1982.p. 31–39.*
[6] Shahmohamadi H, Mohammadpour M, Rahmani R, et al. *On the boundary conditions in multiphaseflow through the piston ring-cylinder liner conjunction. Tribol Int. 2015;90:164–174.*
[7] Pandey S, Murtaza Q, Gupta K. *Friction and sliding wear characterization of ion chrome coating.SAE Technical Paper 2014-01-0946. 2014. doi:10.4271/2014-01-0946.*
[8] Offner G, Lorenz N, Knaus O. *Piston clearance optimization using thermo-elasto hydrodynamicsimulation to reduce piston slap excitation and friction loss. SAE Technical Paper No. 2012-01-1530. 2012. doi:10.4271/2014-01-0946.*
[9] Li CH. Piston thermal deformation and friction considerations. SAE Technical Paper (No. 820086). 1982.
[10] Chen J, Wang Y, Li H, et al. *Microstructure, morphology, and properties of titanium containing graphite-like carbon films deposited by unbalanced magnetron sputtering.TribolLett. 2013;49(1):47–59.*

[11] Wood RJ. *Tribo-corrosion of coatings: a review. J Phys D Appl Phys. 2007;40(18):5502–5521.*
[12] Murtaza Q. *A critical investigation into the spray-drying of hydroxyapatite powder for thermalspray applications [Ph.D. Thesis]. Ireland: Dublin City University, Dublin; 2006.*
[13] Murtaza Q, Pandey SM, Niranjan MS. *A novel manufacturing route for automobile parts throughtwo-wire-arc thermal spray process. Mater Manuf Proc. 2016;31(11):1424–1432.*
[13] Kumar D, Murtaza Q, Singh RC. *Sliding wear behavior of aluminum alloy coating prepared bytwo-wire electric arc spray process. Int J AdvManuf Technol. 2016;85(1–4):237–252.*
[14] Berger L-M. *Application of hardmetals as thermal spray coatings. Int J Refract Metals HardMater. 2015;49:350–364.*

Available online at www.sciencedirect.com

ScienceDirect

Materials Today: Proceedings 5 (2018) 15421–15425

materialstoday: PROCEEDINGS

www.materialstoday.com/proceedings

ISCAS 2017

Corroborating the Spin Gapless Character of Ti_2MnAl Inverse Heusler Alloy: A study of Strains Effect

Mukhtiyar Singh[1*], Manish K. Kashyap[2] and Hardev S. Saini[3]

1 Department of Applied Physics, Delhi Technological University, Delhi, India

2 Department of Physics, Kurukshetra University, Kurukshetra, Haryana, India

3 Department of Physics, Guru Jambheshwar University of. Science & Technology, Hisar, Haryana, India

Abstract

Nowadays, In the present study, inverse Heusler alloy based spin-gapless semiconductor (SGS), Ti2MnAl is investigated using full potential linearized augmented plane wave (FPLAPW) method implemented in WIEN2k crystal programme. Our investigation reveals that this alloy behaves as SGS, with zero total magnetic moment, for equilibrium lattice constant (6.23 Å). Further, it keeps its spin gapless state within -15% to 10% uniform strain. On the other hand, for -5% of tetragonal strain, the system behaves as SGS whereas the positive 5% tetragonal strain completely destroys the spin-gapless character of Ti2MnAl Heusler alloy. The up-spin band gap for Ti2MnAl is 0.55 eV and 0 eV for spin down channel for equilibrium lattice constant. It varies up to a maximum value of 0.31 eV and 0.36 eV for positive and negative uniform strain, respectively. The value of this gap for -5% and 5% of tetragonal strain is 0.51 eV and 0.46 eV, respectively. Our calculations provide an exhaustive data to be compared with future experiments and advocate the future applications of this alloy in spintronic applications.

© 2018 Elsevier Ltd. All rights reserved.

Selection and Peer-review under responsibility of 10th NATIONAL CONFERENCE ON SOLID STATE CHEMISTRY AND ALLIED AREAS (ISCAS - 2017).

Keywords: Heusler Alloys, Spin-Gapless Semiconductors, FPLAPW Method

*Email address: mukhtiyarsingh@dtu.ac.in, msphysik09@gmail.com

2214-7853 © 2018 Elsevier Ltd. All rights reserved.

Selection and Peer-review under responsibility of 10th NATIONAL CONFERENCE ON SOLID STATE CHEMISTRY AND ALLIED AREAS (ISCAS - 2017).

1 Introduction

The development of high performance computing during last decades along with the amazing predictive power of material modeling methods with consistent accuracy enable material scientists to discover new novel materials and motivates experimentalists to fabricate these for technological advancement. Heusler alloys are one of such novel materials. Since the discovery of ternary Heusler alloy NiMnSb [1] as half-metal, a large amount of scientific endeavor has been devoted to this arena. Apart from the conventional ternary Heusler alloys with stoichiometric composition, $L2_1$- and $C1_b$-type structures, the new structural variant of Heusler structure i.e. inverse Heusler alloys (*X*-structure) have also potential in spintronics applications [2-4]. These alloys are known for high T_C and small magnetic moment [5] due to strong direct exchange interaction between like atoms.
Recently, Wang [6] suggested a new material terminology, namely, spin-gapless semiconductors (SGS) which is a class of materials bridging the gap between half-metals and magnetic semiconductors; where there is an almost vanishing zero-width energy gap at the Fermi level (E_F) in the one spin-direction and a usual energy gap in the other spin-direction. The SGS can be thought as a combination of gapless semiconductor and a half-metallic (HM) ferromagnet [7]. In the case of SGS, the picture of the either spin band is similar to the HM ferromagnet but in the other spin band the E_F falls within a zero-width gap.
It is observed that when any material is incorporated as a device, such as thin films, mechanical strains may arise either naturally or unintentionally. This induced strain may substantially alter the electronic and magnetic properties of the device [8]. Therefore, it is very important to study a system under the effect of strains. With this motivation, we have treated Ti_2MnAl SGS under volume conserving uniform and tetragonal strains.

2 Theoretical approach

The density functional theory (DFT) based all-electron full potential linearized augmented plane wave (FPLAPW) method, as implemented in WIEN2k code [9], has been used to perform the electronic structure calculations of SGS Ti_2MnAl. In this method, the core states are treated fully relativistically whereas the valence states as semirelativistically. The exchange and correlation (XC) effects were taken in to account by GGA (Generalized Gradient Approximation) formalism under parameterization of Perdew-Burke-Ernzerhof (PBE) [10]. The non-overlapping muffin-tin radii (R_{MT}) of Ti, Mn and Al were chosen as large as possible so as to obtain nearly touching spheres and to ensure minimum charge leakage. The energy convergence criterion was set to 10^{-4} Ry and the charge convergences were also monitored along with it.

3 Result and Discussion

The equilibrium lattice constants of unstrained Ti_2MnAl inverse Heusler alloy were estimated for both *X*- and $L2_1$-structures by fitting the semi-empirical Murnaghan equation of state [11]. It is observed that this alloy is stable in *X*-structure and the corresponding optimized lattice constant is found to be 6.23 Å which is in a close agreement with 6.24 Å, as calculated by Skaftouros et al. [12]. Our investigation reveals that this alloy behaves as SGS, with zero total magnetic moment, for equilibrium lattice constant.
Since the spin-gapless property is very delicative and often attributed to unstrained structure, it is very important to analyse, for realistic application, whether the spin-gapless character of Ti_2MnAl inverse Heusler alloy retains or not with the strains. We have treated this system with uniform and tetragonal strains. The total density of states (DOS) for various values of uniform and tetragonal strains are represented in Fig.1(a) and 1(b), respectively.
Ti_2MnAl Heusler alloy retains its spin-gapless state from -15% to 10% of uniform strain. On the other hand, for negative 5% of tetragonal strain the system behaves as SGS whereas the positive 5% tetragonal strain completely destroys the spin-gapless character of Ti_2MnAl Heusler alloy.

We have also studied the effect of both types of strains on magnetic moment of Ti_2MnAl. The total magnetic moment for unstrained Ti_2MnAl and for all studied strain values remains zero. This makes Ti_2MnAl of special interest for spintronics application since it creates no external stray fields and thus exhibiting minimum energy loses. The magnetic moment at Mn site positive and of the order of 2.2 μ_B but magnetic moment at two Ti sites alling antiferromagnetically to the Mn atom, which fully compensate the total magnetic moment to zero.

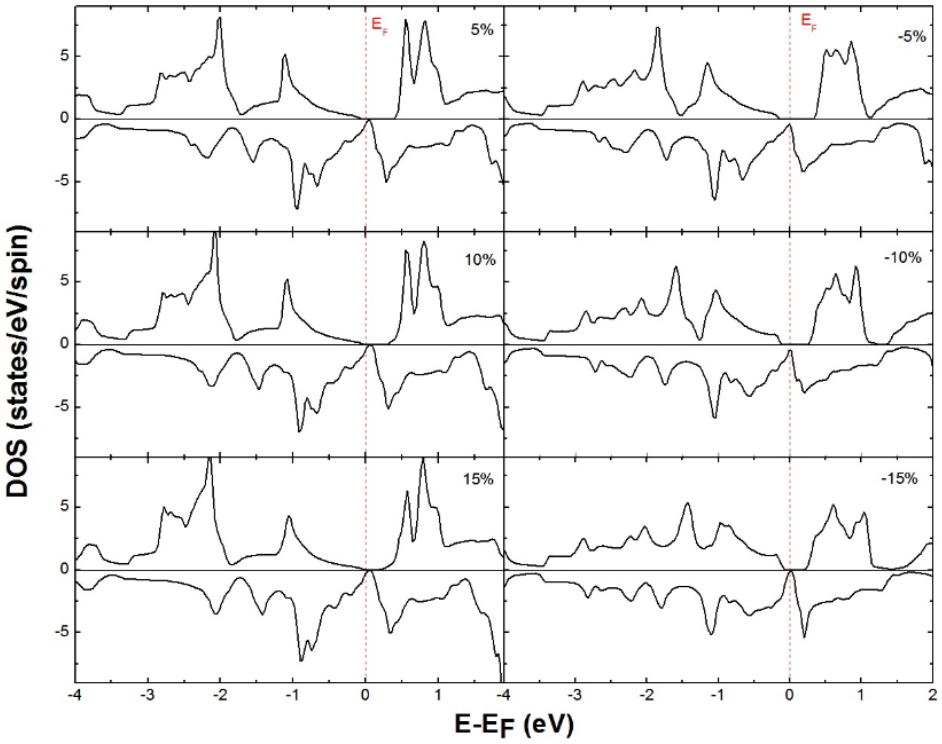


Fig. 1(a): Calculated total DOS of Ti_2MnAl under uniform strain.

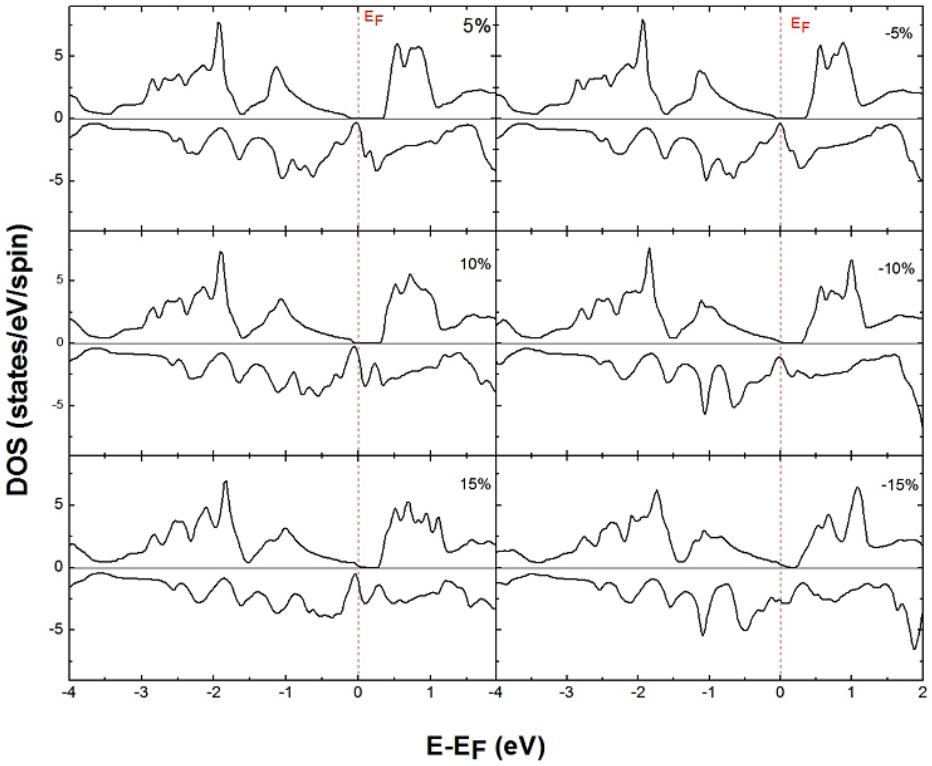


Fig. 1(b): Calculated total DOS of Ti_2MnAl under tetragonal strain.

The origin of band gap in upper spin channel in this SGS is same as in other inverse Heusler alloys. It mainly *d-d*-hybridizations between transtiom metal atoms which lead to the band formation in the particular spin channel. The *sp*-element (Al) does not affect the band-gap, its interaction with transition metal atoms i.e. *p-d* hybriizations only covers up the effect of lattice constant. This is due to the fact that expansion or contraction of lattice parameter only affect the delocalized *p* electrons not the well localized transition metal *d* electrons [13]. The value of band gap in up spin channel for equilibrium lattice constant is 0.55 eV and 0 eV for down spin channel. It varies up to 0.31 eV and 0.36 eV for 10% of positive and 15% of negative uniform strain, respectively as shown in Fig. 2. The value of this gap for -5% and 5% of tetragonal strain is 0.51 eV and 0.46 eV, respectively. Thus, an appreciable magnetic moment and SGS character makes Ti_2MnAl makes the an important material for magnetic storage devices also.

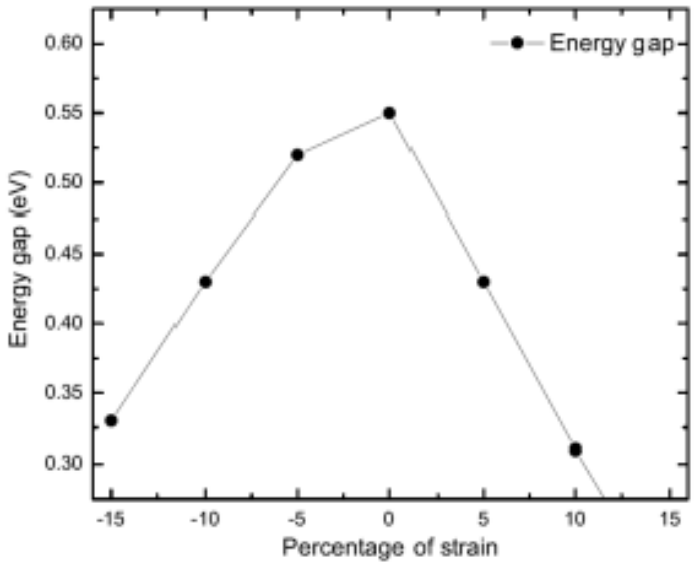


Fig. 2: Variation of energy band gap in up spin channel vs uniform strain.

4 Conclusions

we have focused on the investigating the effect of volume conserving uniform and tetragonal strains on the spin gapless character of Ti_2MnAl inverse Heusler alloy. We carried out this work using DFT based FPLAPW method. Ti_2MnAl is a perfect spin-gapless semiconductor at equilibrium lattice constant. The spin-gapless character of this alloy analyzed under uniform and tetragonal strains keeping the volume of unit cell constant and it is found that the spin-gapless character is robust against the uniform strain from -15% to 10% whereas it retains for -5% of tetragonal strain. However, the value of tetragonal strain equal to or more than 5% completely destroy the spin-gapless character of Ti_2MnAl. Its total spin magnetic moment is found to be 0.0 μ_B and not affected by any type of strains. The energy band gap in up spin channel varies up to 0.31 eV and 0.36 eV for maximum values of positive and negative uniform strain, respectively.. The value of this gap for -5% and 5% of tetragonal strain is 0.51 eV and 0.46 eV, respectively. The present theoretical data could play a key role for the possible future experiment on this type of spin-gapless semiconductor.

References

[1]. R. A. de Groot, F. M. Mueller, P. G. van Engen and K. H. J. Buschow, Phys. Rev. Lett. 50 (1983) 2024-2027.
[2]. X. Dai, G. Liu, G. H. Fecher, C. Felser and Y. Li, J. Appl. Phys. 105 (2009) 07E901-3.
[3]. I. Galanakis, K. Ozdogan, E. Sasioglu and B. Aktas, Phys. Rev. B 75 (2007) 172405-4.
[4]. M. Meinert, J.-M. Schmalhorst, C. Klewe, G. Reiss, E. Arenholz, T. Böhne and K. Nielsch, Phys. Rev. B 84 (2011) 132405-4.
[5]. M. Meinert, J.-M. Schmalhorst and G. Reiss, J. Phys.: Condens. Matter 23 (2011) 116005-7.
[6]. X. L. Wang, Phys. Rev. Lett. 100 (2008) 156404-4.
[7]. G. Z. Xu, E. K. Liu, Y. Du, G. J. Li, G. D. Liu, W. H. Wang and G. H. Wu, Euro. Phys. Lett. 102 (2013) 17007-6.
[8]. M. J. Carey, T. Block and B. A. Gurney, Appl. Phys. Lett. 85 (2004) 4442-4444.

[9]. P. Blaha, K. Schwarz, G.K.H. Madsen, D. Kvasnicka and J. Luitz, WIEN2k, An augmented plane wave + Local Orbitals Program for calculating Crystal Properties, Karlheinz Schwarz, Techn. Universitat Wien, Wien, Austria, 2001, ISBN 3-9501031-1-2.P.
[10]. Perdew, S. Burke and M. Ernzerhof, Phys. Rev. Lett. 77 (1996) 3865-3868.
[11]. F. D. Murnaghan, Proc. Natl. Acad. Sci. USA 30 (1944) 244-247.
[12]. S. Skaftouros, K. Özdoğan, E. Şaşıoğlu and I. Galanakis, Appl. Phys. Lett. 102 (2013) 022402-022404.
[13]. G. D. Liu, X. F. Dai, H. Y. Liu, J. L. Chen, Y. X. Li, G. Xiao and G. H. Wu, Phys. Rev. B 77 (2008) 014424-12.

Rahman et al. Biomedical Dermatology (2018) 2:18
https://doi.org/10.1186/s41702-018-0028-5

Biomedical Dermatology

RESEARCH Open Access

DermaGene and VitmiRS: a comprehensive systems analysis of genetic dermatological disorders

Razia Rahman†, Isha Sharma†, Lokesh K. Gahlot and Yasha Hasija*

Abstract

Background: The interaction of genetic variants and their distribution in the genome is firmly believed to contribute to genetic dermatological disorders. For the convenience of clinicians and researchers to explore such genetic variants, we identified and validated the genetic association of human SNPs with dermatological disorders through manual curation and computational analysis.

Methods: Multiple online resources were investigated for creating a comprehensive list of dermatological disorders followed by identification and manual curation of data description of the SNP–disease relationship. The process for database creation involved extensive review of published literature and relevant articles that probed association of miRNAs and SNPs with vitiligo. Furthermore, computational analysis for deleterious SNPs and polypharmacological studies was performed with an effort to provide potential novel drug candidates for optimal therapeutic interventions.

Results: We established a dedicated database on dermatological disorders, DermaGene, which proffers a user-friendly interface to enable systematic querying and analysis of SNPs associated with dermatological disorders. Based on our disease network analysis, we further extended our present work to construct another comprehensive database, VitmiRS (Vitiligo associated miRNAs and SNPs), which furnishes detailed information on each miRNA and SNP association that renders susceptibility to vitiligo. Also, our systems analysis approach unraveled potential molecular determinants that may pose as novel drug candidates and can be targeted for efficient therapeutic approaches in vitiligo treatment.

Conclusions: Both the databases are freely accessible and will serve as a significant resource providing insights into previously undiscovered disease–gene and disease–SNP relationships. Our analysis unveiled significant findings that we believe may furnish a comprehensive understanding of the biological mechanisms that mediate vitiligo disease pathogenesis, thereby, driving the way towards better therapeutic interventions for disease management.

Keywords: miRNAs, SNPs, Dermatological disorders, Vitiligo

Background

The importance of systems and personalized medicine in the field of healthcare has grown vastly, especially in the last decade. Recent research has growingly demonstrated that many of the seemingly disparate diseases have a common molecular mechanism and strong association among them. This signifies the deeper interplay of genes, in contrast to one gene-one disease commonality well indicating towards the possibility of the related diseases to occur together in an individual (Yu et al. 2015). The exhibition of comorbidity association suggests that the occurrence of one disease will increase the likelihood of the other thereby contributing to compounded healthcare costs and multiplex clinical management. Also, a higher degree of interaction between many diseases indicates a greater prevalence and mortality rate associated with it. Due to the contribution of disease comorbidities as a burden on societies at large, it becomes

* Correspondence: yashahasija06@gmail.com
†Equal contributors
Department of Biotechnology, Delhi Technological University, Shahbad Daulatpur, Main Bawana Road, Delhi 110042, India

© The Author(s). 2018 **Open Access** This article is distributed under the terms of the Creative Commons Attribution 4.0 International License (http://creativecommons.org/licenses/by/4.0/), which permits unrestricted use, distribution, and reproduction in any medium, provided you give appropriate credit to the original author(s) and the source, provide a link to the Creative Commons license, and indicate if changes were made. The Creative Commons Public Domain Dedication waiver (http://creativecommons.org/publicdomain/zero/1.0/) applies to the data made available in this article, unless otherwise stated.

crucial for risk stratification and charting treatment course. One of the most powerful approaches in the present times, the Genome-Wide Association Studies (GWAS), serves as the primary pipeline for identifying disease variants and researching association of diseases and their phenotypes (Lewis et al. 2011). The complete sequen

The advent of SNP genotyping of dermatological disorders has revolutionized our understanding of the genetics of such disorders (Maruthappu et al. 2014). Relevant information from several published literature concerning the disease–SNP association in dermatological disorders are interspersed which impels the need for a repository that stores SNPs having prime roles in the initiation of dermatological disorders. Such a resource would be valuable for clinicians and researchers making it convenient for them to study the regulatory mechanisms of SNPs that underpin disease pathogenesis and translate their discoveries into clinical practice. We, therefore, aimed to fulfill this void concerning a dedicated genetic dermatological disorder database. DermaGene is the first attempt at providing information pertaining to human genetic dermatological disorders establishing itself as the primary pipeline for identifying disease variants and researching association of dermatological diseases and their phenotypes. The database as of now stores 114 unique diseases, as described by 244 different genes along with 871 associated SNPs and have been made freely accessible online. The present work not only provides information on experimentally validated dermatological disorders associated SNPs curated from a large scale of literature but also offers computationally predicted insights into previously undiscovered disease–gene and disease–SNP relationships.

Our disease association network analysis highlighted vitiligo to exhibit maximum interactions with different genes from our database. Vitiligo is a chronic, acquired depigmentation disorder of the skin resulting in an episodically progressive loss of functional melanocytes causing pigment dilution in the affected areas of the skin (Picardo et al. 2015). Affecting 0.5–1% of the world population (Boisseau-Garsaud et al. 2000; tHowitz et al. 1977) and with a prevalence rate of 0.5–2.5% in India (Handa and Kaur 1999), vitiligo can develop at any age irrespective of the type of skin, gender, race, or geographical location underlying both genetic and non-genetic factors in a complex interactive manner. We, therefore, investigated the role of specific miRNAs and SNPs reported to be associated with vitiligo in the human genome to identify their plausible effect on vitiligo susceptibility using computational platforms. The cataloging of susceptible miRNAs and SNPs is essential for narrowing down the plausible concomitant genetic determinants of vitiligo. Protein–protein interactions are virtually intrinsic for every cellular and regulatory process, and a damaging alteration in such interactions have been deduced to cause and sometimes even accelerate human diseases. The regulation or impediment of a known detrimental protein–protein interaction delineates a principal target for drug discovery. Hence, a systems biology approach was implemented that unveiled significant interconnections and revealed intricate patterns of disease association. Such a network analysis is helpful in studying the gene expressions and analyzing a large set of disease-associated proteins (Barabasi and Oltvai 2004). Furthermore, we prioritized a few proteins in our protein–protein interaction network as pertinent hub proteins which may be targeted for treating vitiligo. We performed computational analysis for harmful SNPs and scrutinized drug–target and drug–similarity interactions with an effort to provide potential novel drug candidates for optimal therapeutic interventions. Subsequently, we manually curated all miRNAs and SNPs and established a vitiligo specific database, VitmiRS (Vitiligo associated miRNAs and SNPs), to provide a comprehensive, user-friendly interface to detailed information on each miRNA and SNP association that renders susceptibility to vitiligo supported with pertinent data. VitmiRS currently houses 41 miRNAs and 134 associated SNPs for 84 genes which have been made online allowing easy retrieval of data. Till date, no systematic efforts have been made for the compilation of such data in a single platform that is specifically designed for dermatological disorders thereby contributing to the uniqueness of both the databases. A comprehensive view of the databases is shown in Fig. 1. We hope they serve as a significant resource that would benefit the scientific community. The present polypharmacogenomic network integration approach in vitiligo disease module is novel to the best of our knowledge that attempts to furnish a comprehensive understanding of the biological mechanisms that mediate vitiligo disease pathogenesis and offering novel interventional drug targets for efficient therapeutic interventions for genetically susceptible individuals. The graphical representation of the workflow is shown in Fig. 2.

Methods

Construction of DermaGene: data sourcing, curation, and reassessment

We initiated by creating a comprehensive list of dermatological disorders by referring to various online and offline resource databases followed by identification and mining of data to make every entry in our database descriptive of the SNP–disease relationship. The three top databases that we referred to included UniProt, DisGeNET (Pinero et al. 2015), and OMIM.

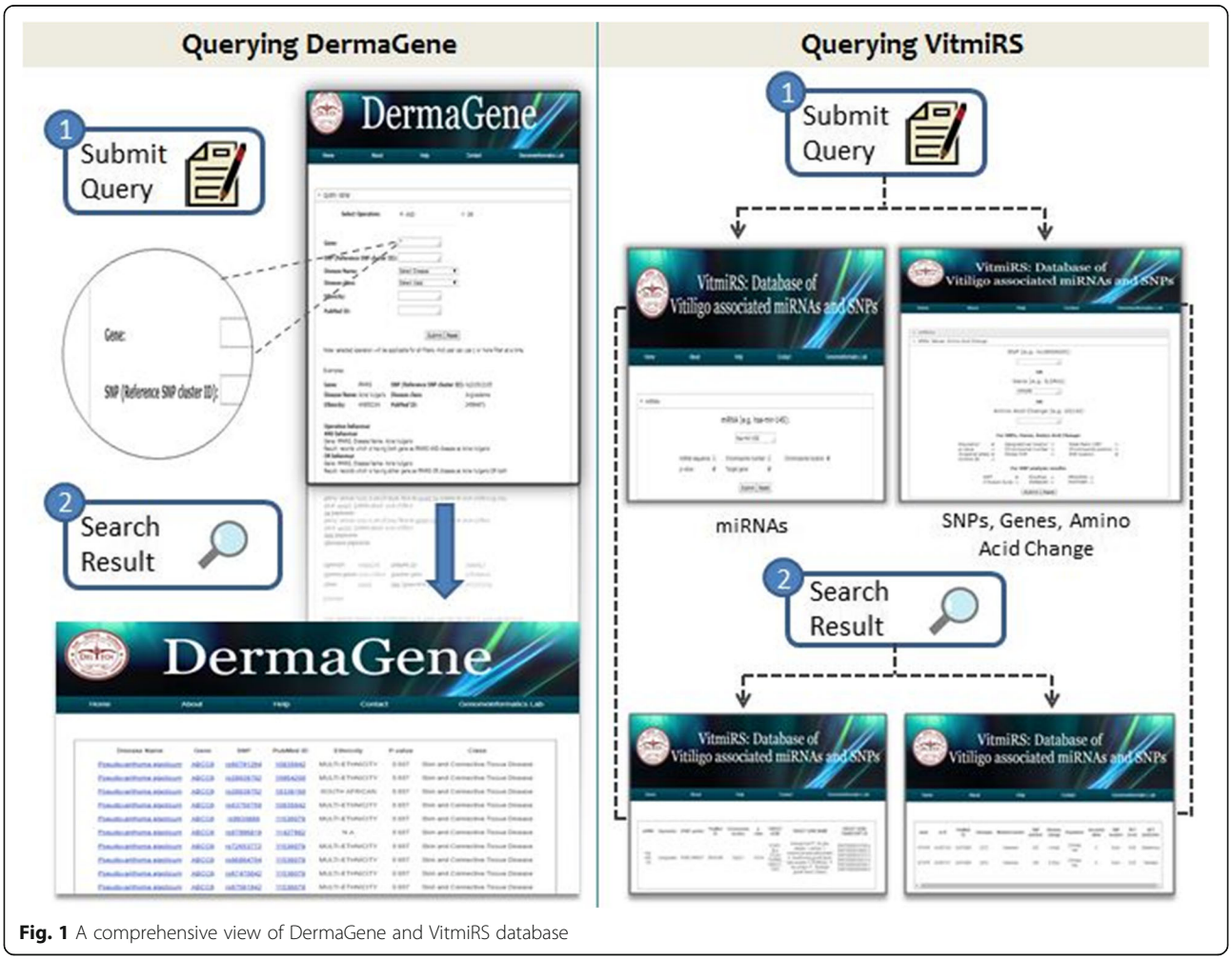


Fig. 1 A comprehensive view of DermaGene and VitmiRS database

Database creation was initiated by procuring the entire UniProt database, followed by converting the data obtained into the suitable and workable MS Excel format. A significant volume of data downloaded was delimited which required to be segregated into distinct columns, and we applied text to column—delimited to get a succinct view. This first stage download of database was subjected to filters from where we manually selected every possible dermatological disorder from the pool of 74,177 entries. This was achieved by referring to our previously generated comprehensive list of dermatological disorders. At this stage, we had the Gene name and rs ID indicating the SNP and the corresponding disease name. We thus reduced our database to 5000 entries, followed by removal of incomplete or duplicate entries thereby condensing it further to 2800 entries described by three attributes.

As the next step, we utilized disGeNET, to individually query every single gene (obtained from the UniProt database) to identify the *p* value and the PubMed ID. This was achieved by manually matching the results obtained with their corresponding rs IDs. Additionally, we populated the database with corresponding PubMed ID, *p* value, and disease class. Further, OMIM was put to use to support filling of gaps in the database. Extensive research helped us identify the missing values, which we were required to eliminate owing to insufficient data, thus reducing the database to 1116 entries.

Once we were finished with supplementing the database in its creation stage with requisite data, we proceeded to utilize PubMed as our primary source and to access all the research papers linked through their PubMed ID with our database. The work culminated into exhaustive reading of research papers to discern the ethnicities associated with the research conducted. Exhaustive study of research papers enabled us to determine ethnicities and to subsequently complete the database. Once the database was generated, the data was carefully re-assessed to ensure authenticity, through manual analysis of input data with the intention to establish the veracity of information as sourced from the specified databases. Besides, identification of alternative names for the specific diseases allowed for scope expansion of the database.

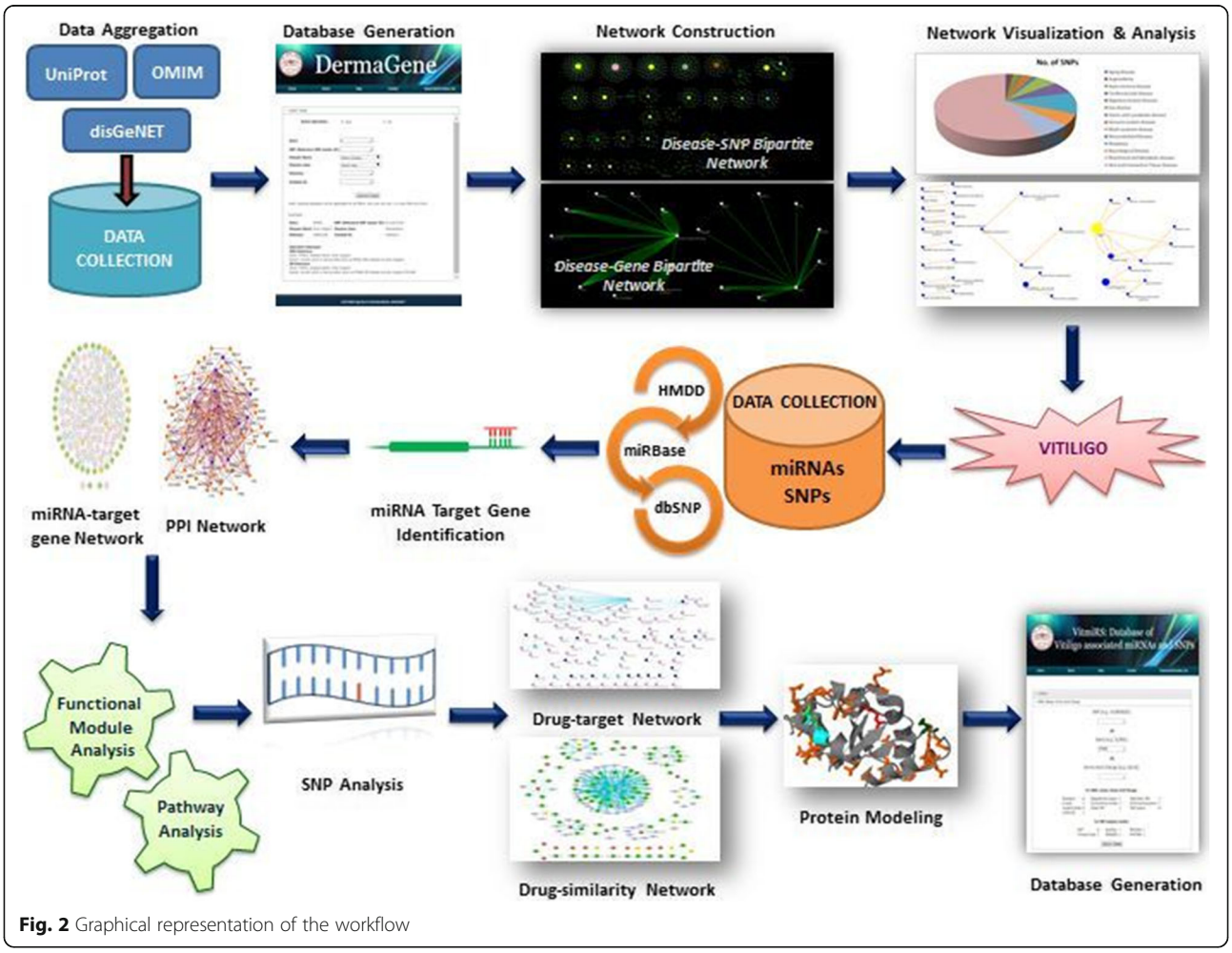


Fig. 2 Graphical representation of the workflow

Each entry in this database therefore describes the genes, the SNPs associated with diseases, the PubMed IDs of texts referred, and the frequency of disease occurrence along with the population ethnicity where it exists. Also, we have taken into consideration the ethnicity of the genotypic variation to identify disease susceptibility in specific populations, the *p* value for the occurrence of genetic dermatological disorders which enables recognition of how strongly a particular gene influences the mentioned diseases. We thus have included six fields, and the data obtained was subsequently used to chart patterns within multiple genes and diseases. The information sourced aims to provide in-depth knowledge on common dermatological disorders, subsequently provisioning us to analyze the risk of genetic variants on their contribution to disease susceptibility.

Disease classification and network analysis of DermaGene data

Network theory involves the analysis of complex systems and serves as a potent biological tool, thereby, facilitating a better understanding of gene interactions and their role in causing diseases. To perform disease association network analysis, we constructed disease–gene bipartite network (DGN) and disease–SNP bipartite network (DSN) using Cytoscape (Shannon et al. 2003) with each network comprising a pair of disjoint set of nodes. The two sets of nodes are chosen such that there is no intra-connection but capable of exhibiting inter-connection. The nodes communicate with each other via edges, where the edges are the representatives of the nature of the interaction between the pair of nodes. In DGN, all the genes present in our database formed one set of nodes and the other set of nodes were reflected by all the known dermatological disorders in DermaGene. An edge connected the two sets of nodes if a disease–gene association was found. Whereas in DSN, all the diseases in our database formed one set of nodes and the other set of nodes comprised of the associated SNPs. The diseases were linked only if they showed common genetic variants. We also illustrated the correlation between the diseases as a result of a shared gene between the two. The diseases were selected as nodes while the edge attributes represented the genes common between them.

Data collection for vitiligo disease module analysis

To analyze the role of miRNAs associated with vitiligo, the miRNA information was obtained from published literatures available in NCBI PubMed server (https://www.ncbi.nlm.nih.gov/pubmed/) and mined publicly available online databases, namely, HMDD v2.0 (the Human microRNA Disease Database) (Li et al. 2014), Entrez GENE database of NCBI, and miRBase (Griffiths-Jones 2006) for relevant entries. A total of 41 types of miRNAs were found to be associated with vitiligo.

On the other hand, we extracted the information of genes associated with vitiligo and its SNPs from the GENE database and dbSNP of NCBI. The build 141 of NCBI dbSNP database is the latest release containing nearly 44 million validated human SNPs (Sherry et al. 2001). A total of 186 genes were reported to be associated with the disease among which 134 polymorphisms for 84 genes were reported to be positively associated. UniProt IDs of the proteins were also noted.

Identification of miRNA target genes and construction of miRNA–target gene network

The miRNAs identified to be associated with vitiligo were used to find their respective target genes. TargetScanHuman 7.1 (Agarwal et al. 2015) was used to detect targets in the 3′UTR of the protein-coding transcripts by base-pairing rules where predictions with both broadly conserved and poorly conserved sites are provided. These target sites are the conserved sites that match or are complementary to the seed region of the miRNA that ultimately facilitates the binding of miRNA with the mRNA to functionally degrade the mRNA thereby resulting in gene silencing.

A structured network layout explaining network integrity is the core requirement to justify the interaction between miRNA and disease. A miRNA–target gene interaction network was therefore constructed and analyzed to understand the miRNA–target gene relationship and validate the miRNA–disease association. The miRNA–target gene bipartite network consists of two sets of nodes—one set represents the miRNAs, and the other set represents the target genes. Nodes from the two sets were connected if a particular miRNA is associated with a particular target gene. The datasheet prepared which included all the miRNAs associated with vitiligo along with their target genes was used to generate the network in Cytoscape (Shannon et al. 2003).

Construction of vitiligo-associated protein–protein interaction network

Interactions between genes whose expression profiles are correlated with disease pathogenesis may contribute to the progression of the disease (Srivastava et al. 2017). To identify such interactions, we constructed the protein–protein interaction network using STRING (The Search Tool for the Retrieval of Interacting Genes) (Von Mering et al. 2005). It is a comprehensive database capable of providing an overall view of all the known and predicted protein–protein interactions of physical and functional associations. The PPI network generated based on STRING online database was then visualized in Cytoscape whose common feature lies in combing biological interaction networks with relevant large databases into a unified framework.

Functional module and enrichment analysis

Considering the connectivity properties of a network, we resolved to identify the significant clusters or modules enriched in biological processes from the complex bipartite network to extract biologically meaningful interactions. The modular analysis can provide a better insight into the relationship of the interconnected proteins assuming that the highly connected nodes in a network could form a cluster. As we know, cellular processes and functions are modular; therefore, it is more feasible to predict the structural and functional behavior of a particular module than that of an individual gene. Such module analysis has played a significant role in the past in determining disease mechanisms (Mitra et al. 2013). We used Markov Clustering Algorithm (MCL) method among the other clustering algorithms as it is the most widely used unsupervised clustering algorithms for functional module analysis and assigns a fast and reliable scalable method for finding functionally enriched clusters in complex networks. The granularity parameter for MCL clustering was kept at 1.8.

To interpret the biological impetus of the clusters in the network, we further performed functional enrichment analysis of the clustered gene groups using DAVID (The Database for Annotation, Visualization and Integrated Discovery) 6.8 (Huang et al. 2009). Functional enrichment analysis uses statistical approaches to identify the clusters of genes or proteins that are highly expressed or enriched in a large set of genes or proteins which may have an association with disease (Huang et al. 2008). All the genes were mapped into DAVID with the default settings selected as "*Homo sapiens*" in both the species background as well as the current background for the analysis.

Pathway analysis

To analyze the pathways in which these genes are involved, we conducted a pathway analysis using KEGG (Kyoto Encyclopedia of Genes and Genomes) pathways in DAVID 6.8. KEGG Pathway database is the most comprehensive and widely used database of annotation information. The pathway classification with $p \leq 0.001$ and Benjamini–Hochberg FDR ≤ 0.01 was considered to

have the most biological significance. Pathway analysis helps to interpret the data in the context of biological interactions and identify related proteins within a pathway.

A single protein may be involved in multiple pathways that are of importance to many biological processes. The biological cause of a disease can be explored by examining the changes in gene expression in a pathway. Also, the same pathway can be targeted for novel drug candidates (Wang et al. 2010). Deciphering the pathways which are explicitly targeted by the essential proteins may provide insight into their regulatory mechanisms. To better analyze the pathway analysis results, we constructed a protein pathway network to elucidate which pathways were eminently targeted by the proteins, specifically, the hub proteins. Such pathways, in turn, can be targeted for therapy and treatment approaches.

SNP analysis

The feasibility of the identification of the nsSNPs that vest susceptibility or resistance to human diseases has been improved with the use of in silico tools. To elucidate of the function of mutations in vitiligo-susceptible genes, we investigated the pathogenic effect of 134 SNPs which were reported to be associated with vitiligo. Among the 134 SNPs, the functional context of 36 nsSNPs was analyzed by employing various computational platforms. We used a combination of computational tools, namely, SIFT (Kumar et al. 2009), PolyPhen 2.0 (Adzhubei et al. 2010), PROVEAN (Choi et al. 2012), SNPs&GO (Magesh and Doss 2014), I-Mutant Suite 3.0 (Capriotti et al. 2008), and PANTHER Evolutionary Analysis of Coding SNP (Mi et al. 2005) to identify the nsSNPs that potentially affect the structure and function of proteins associated with vitiligo.

Additionally, MutPred 2 (Pejaver et al. 2017) was used to interpret the possible molecular cause of disease-inducing amino acid substitutions. Furthermore, NetSurfP (Petersen et al. 2009) was used to analyze the effect of such mutations in the stability of the protein by predicting the solvent accessibility of the substituted residue.

The information from different computational platforms was combined to prioritize the deleterious SNPs to increase the predictive power and accuracy of the results of the in silico techniques.

Construction of drug–target network and drug–similarity network

A single drug can target multiple proteins. To analyze this relationship between drug and protein targets (disease–gene products) and to understand how they intervene therapeutically in disease processes, we constructed a drug–target network (Yildirim et al. 2007). We extracted information about drugs with respect to our drug candidates from DrugBank (Knox et al. 2011), which is a chemo-informatics resource that is updated and maintained with the Food and Drug Administration (FDA) information. We used known FDA drugs (both approved and approved-investigational) concerning to the protein targets to generate the drug–target bipartite network.

To identify which drugs act similarly on the same target, we constructed a drug–similarity network to analyze the interactions of drugs and its action on protein targets. DrugBank provides clinically relevant drug interactions, and the information of the interacting drugs and its interacting mechanism with respect to a particular drug was taken from DrugBank. Such a network can provide insights on drug–drug interaction for a potential drug candidate where an interacting drug can act synergistically or antagonistically with another drug altering the benefit or effectiveness of the drug on disease conditions. An interacting drug of a particular drug can also pose as a potential drug for the protein targeted by that drug.

Protein modeling of TLR2

Finding the 3D structure of proteins is helpful in predicting the impact of SNPs on the structural level and in showing the degrees of alteration. To elucidate the molecular dynamic behavior of the SNP in TLR2 protein, we performed preliminary protein modeling by G23D (Genomic variant to 3D protein data) (Solomon et al. 2016) which is a tool for the conversion of human genomic coordinates to protein structures. G23D allows the mapping of evolutionary related as well as identical protein of genomic variants in a 3D model structure assisting in the feasibility of structural insight. Along with the mutated sites, it also displays the wild-type residue and other functional sites on the modeled 3D protein structure to facilitate better interpretation of the variant.

We further carried out TLR2 protein–protein interaction analysis to analyze its interaction with other proteins which might be influenced by the mutation in TLR2 protein.

Construction of VitmiRS

The primary data in VitmiRS constitutes the collection of miRNAs and SNPs that have been reported to be associated with vitiligo. The process for database creation relied on extensive review of high-quality published journals, relevant articles published in PubMed, and multiple online resources discussing the association of miRNAs and SNPs with vitiligo for the identification and the subsequent extrication of relevant mentions of the fields that we explored. Information from multiple comprehensive and relevant databases, namely, dbSNP (Sherry et al. 2001), UniProt, HMDD v2.0 (Li et al., 2014), miRBase (Griffiths-Jones 2006), and GENE database, was also taken into consideration. Every paper was read

manually to eliminate the errors that may arise from machine-generated information. The information included was filtered at the thresholds of p value ≤ 0.05 and carefully re-assessed through manual analysis to ensure authenticity. A user-friendly web interface was developed for the ease of data retrieval. Apache was used as the application server and PHP as the programming language. The presentation layer of VitmiRS was created using XHTML and CSS, while for the backend database, MySQL was used.

Results

DermaGene

We curated a total of 244 unique genes in our database, with each gene exhibiting multiple SNPs and describing 114 diseases. A total of 871 unique SNPs exist that exhibits both pleiotropy and epistasis over dermatological disorders. The present DermaGene version relies on the review of over thousand literature sources to generate a comprehensive source comprising of 1116 tuples described through six attributes. It provides a user-friendly interface for easy retrieval of data to query detailed information on each SNP–disease association and hopes to facilitate analysis of the comorbidity associations asserted between human variation and observed disease conditions.

Disease classification and network analysis of DermaGene data

Disease classification

Analysis of DermaGene database revealed the existence of maximum SNPs accounting for dermatological disorders to lie on chromosome 17. The distribution of SNPs was also analyzed to observe their association with the different disease classes included in our database. We identified that the primary disease class which exists in our database is skin and connective tissue diseases (632). This indicates that the maximum number of SNPs, as in our database accounts for the skin and connective tissue class of diseases, followed by neoplasia (116) and nutritional and metabolic diseases (78). The results are summarized in Fig. 3. Our database reveals the possibility for disease comorbidity existence. We have identified few diseases that share the SNP with other diseases, indicating association among them and the subsequent combinatorial occurrence of the diseases. This shows that in the presence of co-morbid associations, the incidence of one of them in an individual may elevate the possibility of another disease to occur. An additional file (see Additional files 1 and 2) lists the 12 incidences of disease comorbidity arising from shared SNPs and 22 disease–gene associations, identified from DermaGene respectively which may be responsible for comorbid associations.

Disease–gene bipartite network (DGN)

Our analysis of DGN (Fig. 4a) identified vitiligo from our database to be under the influence of a maximum number of different genes since it exhibited maximum disease correlations, therefore, indicating a probable multi-factorial genetic inheritance. From our database, various genes are showed a higher degree of influence compared to other genes which are defined by the number of diseases it influences (Fig. 4b). The genes that exhibit maximum association include IL2RA, PTPN22, and FGFR2 and are shown in Fig. 5. We observed that the gene IL2RA causes three distinct diseases—alopecia areata, urticaria pigmentosa, and vitiligo. At the same time, another gene PTPN22 accounts for alopecia areata, systemic lupus erythematosus, and vitiligo (Fig. 5a). The third gene IKZ4 also contributes to alopecia and vitiligo, which confronts us with possible idea of a genetic association between these diseases. The relationship between alopecia and vitiligo has been validated through previously conducted research studies (Huang et al. 2013; Krishnaram et al. 2013). Similarly, the gene FGFR2 contributes to Apert syndrome, Crouzon syndrome, and Beare–Stevenson cutis gyrata syndrome (Fig. 5b), in spite of the absence of definite literature, indicating epistasis, if at all. This means a probable novel finding which can be useful for doctors and researchers alike.

Disease–SNP bipartite network (DSN)

From our DSN (Fig. 6), we inferred that most SNPs are associated with single diseases, although we also report the occurrence of few SNPs that exhibit pleiotropic effect since they are linked to multiple diseases. We identified the SNPs rs28931615, rs121912737, rs2476601, rs121913478, rs28931594, rs11540654, rs1042522, rs59856285, and rs60723330 from our DermaGene database to reveal a probable pleiotropy effect defined through association with multiple diseases. Published studies explicitly authenticate our findings for the already existing relationship between acanthosis nigricans and Crouzon syndrome (Mir et al. 2013); acrokeratosis verruciformis and Darier disease (Harman et al. 2016); systemic lupus erythematosus and vitiligo (Nath and Kelly 2001); alopecia and vitiligo (Krishnaram et al. 2013); alopecia and systemic lupus erythematosus (Werth et al. 1992); ichthyosis hystrix with deafness and keratitis–ichthyosis–deafness syndrome (Dalamon et al. 2016); associations of ectodermal dysplasia (ED) and incontinentia pigmenti (IP) caused by IBKG gene, as resulting from complete loss of function in case of IP and X-linked recessive inheritance as in the case of ED (Zonana et al. 2000); Costello syndrome and seborrheic keratosis caused by germline mutation of Ras/MAPK signaling pathway (Hafner and Groesser 2013); and keratoderma palmoplantar which is often accompanied by

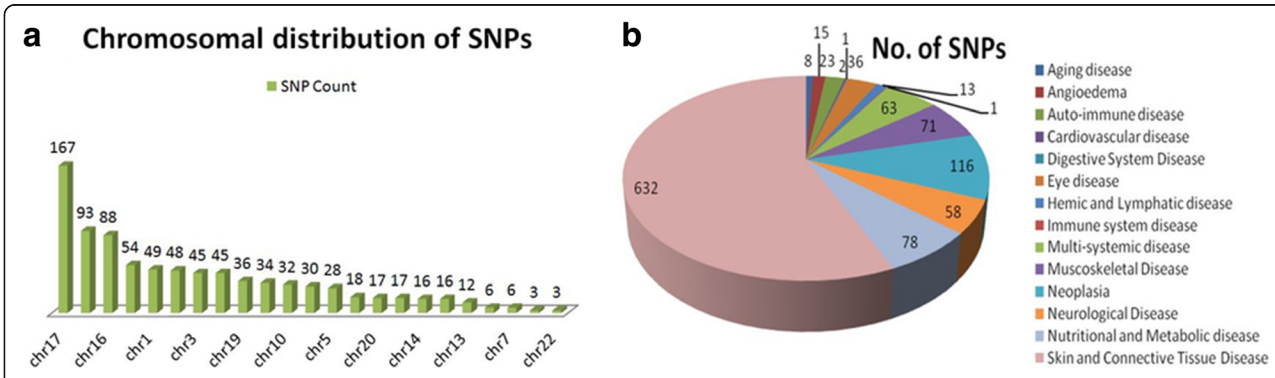


Fig. 3 SNP distribution and association in DermaGene database. **a** Chromosomal distribution of SNPs. **b** Pie chart depicting the distribution of disease class in DermaGene

pachyonychia congenita as described by Smith et al. (2000). There is thus a likelihood of epistatic effect and that the shared SNPs serve as an index of the biological relationship existing between them with subsequent co-manifestation of these diseases.

We also found that diseases xeroderma pigmentosum and keloid share two SNPs rs1042522 and rs11540654, which served as a revelation on the previously unidentified association between the two (Fig. 6a). Our database sheds light on the relationship between the diseases Beare–Stevenson cutis gyrata and Brooke–Spiegler syndrome as caused by the SNP rs121913478 which exhibits no prior known correlation (Fig. 6b).

We have identified various other genetic associations through network analysis as well, wherein we observe the role of a single gene in causing various dermatological disorders. Published evidence for a probable relationship between alopecia and Marie–Una syndrome can be inferred from a published study conducted on a seven generation British family, although the study is not directly indicative of the particular association as such (Marren et al. 1992). Xeroderma pigmentosum (XP) and Cockayne syndrome (CS), although phenotypically different, share genetic similarities, since the gene ERCC5 is responsible for both the cases and this is probably because the several mutations accounting for UV sensitivity may also account for somatic and brain growth failure, thus resulting in neurological problems. Additionally, an existence of literature for LMNA gene contributing to both Hutchinson–Gilford progeria syndrome and congenital muscular dystrophy establish the authenticity of our findings from the DermaGene database (Barateau et al. 2017). Also, we find that Menkes syndrome is a more severe variant of cutis laxa, the latter being initiated during early middle childhood. Both the diseases arising from a mutation in ATP2A2 gene exhibit loose skin as a phenotypic contribution to the affected individual. Lastly, previous reports show clear progression of chilblain lupus erythematosus to systemic lupus erythematosus (SLE) (Bansal and Goel 2014), with around 20% individuals developing SLE (Hedrich et al. 2008).

We also identified the gene ABCC6 located at chromosome 16 on short arm (p) at position 13.11, to have the maximum SNPs as shown in Fig. 7. This gene contributes to pseudoxanthoma elasticum and hence

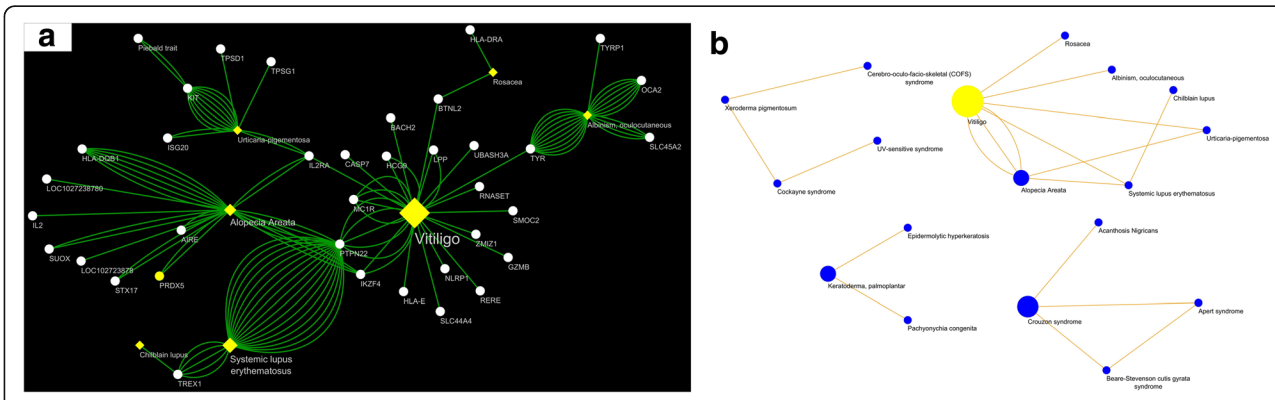


Fig. 4 Disease–gene bipartite network (DGN). **a** Vitiligo disease–gene bipartite network. The node size is indicative of the number of associations. **b** Disease–disease correlation network. The node size is indicative of the number of associations

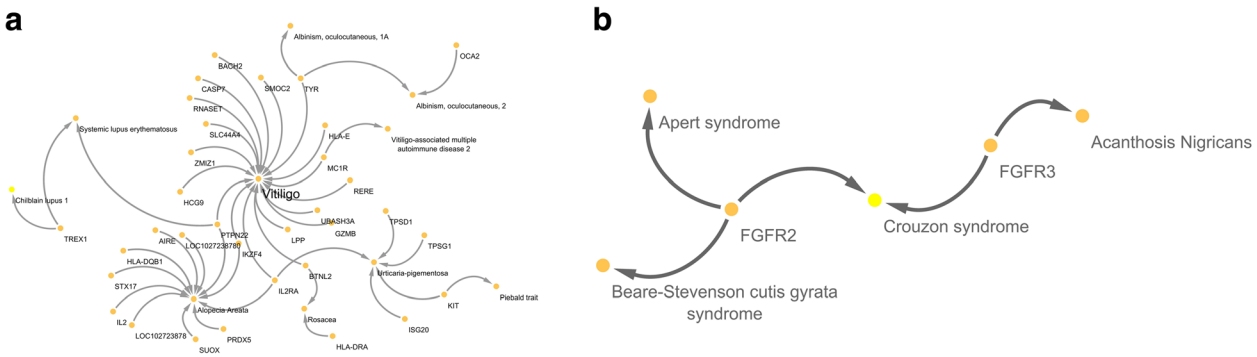


Fig. 5 Mapping disease comorbidity in disease–gene bipartite network (DGN). **a** Maximum association of the genes IL2RA and PTPN22 with multiple diseases. **b** Maximum association of the gene FGFR2 with multiple diseases

can play a key in disease prognosis. With a total of 91 SNPs within the gene, ABCC6 gene serves as a disease hotspot, with the existence of multiple SNPs contributing to the same disease. This reveals that ABCC6 gene is a relatively large gene, of size 74,766 bp to allow for a high number of SNPs.

Data collection for vitiligo analysis

We found 41 miRNAs to be associated with vitiligo with 34 upregulated and 7 downregulated in disease conditions. A total of 134 polymorphisms for 84 genes were found to be associated with vitiligo. Among the 134 SNPs, 36 are nsSNPs, 7 are coding synonymous SNPs, and 68 SNPs were found in the non-coding region.

Identification of miRNA target genes and construction of miRNA–target gene network

The respective target genes of the miRNAs were identified to explicate the biological targets of these miRNAs whereby they control gene expression and ultimately regulate the cellular and molecular responses during disease development and progression. The miRNA–target gene bipartite network represented a total of 41 miRNAs and 98 unique target genes consisting of 139 nodes and 220 edges (Fig. 8). The target genes are considered to be connected in the network if they share a common miRNA. To identify the hub miRNAs and target genes associated with vitiligo, among the number of methods available for hub identification, we chose maximum clique centrality (MCC) along with two other topological parameters, namely, betweenness centrality and bottleneck (Chin et al. 2014), and normalized the data to identify the top hubs in the network. In our analysis, we found seven hub miRNAs (hsa-miR-99b, hsa-miR-577, hsa-miR-9, hsa-miR-155, hsa-miR-211, hsa-miR-10a, and hsa-miR-145).

Protein–protein interaction network

Protein–protein interaction network of vitiligo-associated proteins exhibited significant interconnections between the proteins. It comprised of 71 nodes and 322 edges (Fig. 9). The proteins are considered to be connected in the network if they interact with each

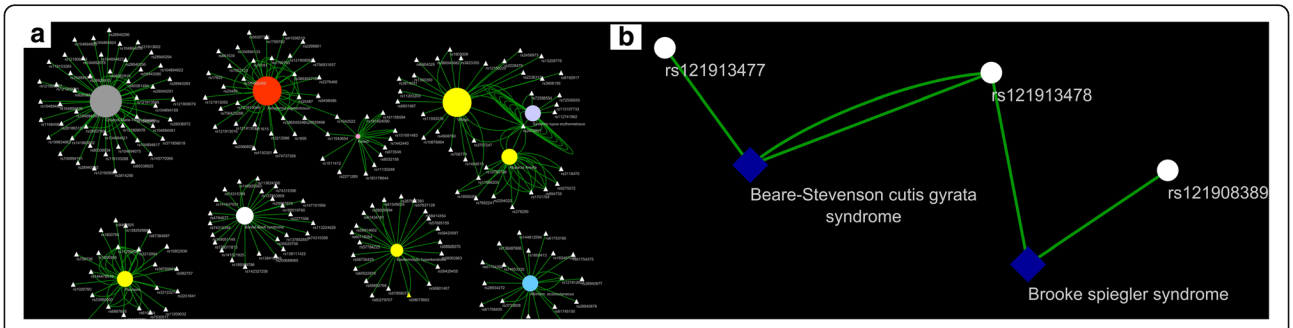


Fig. 6 Disease–SNP bipartite network (DSN). The triangular nodes represent the SNPs, and circular nodes indicate the disease. The size of circular nodes is proportional to the SNPs that the particular disease is associated with. **a** The diseases xeroderma pigmentosum and keloid share two SNPs rs1042522 and rs11540654. **b** Relationship between the diseases Beare–Stevenson cutis gyrata and Brooke–Spiegler syndrome as caused by the SNP rs121913478

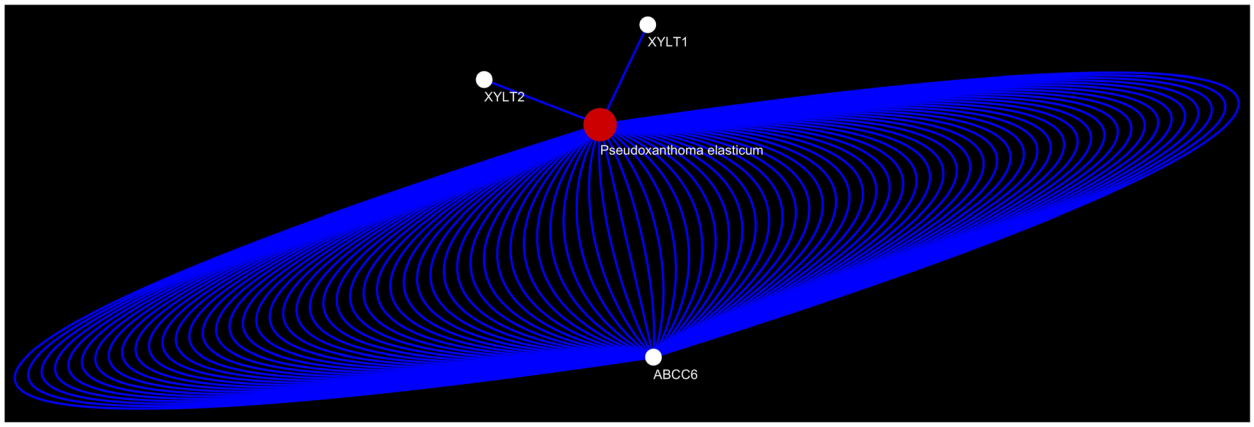


Fig. 7 Mapping ABCC6 gene to pseudoxanthoma elasticum. Multiple SNPs of ABCC6 gene are shown to be contributing to the same disease pseudoxanthoma elasticum

other. If each protein is not inclined to interact with another protein or specifically interacts with a single protein, then the bipartite network would be disconnected into many single nodes corresponding to specific or unique proteins with few or no edges between the nodes. Rather, the protein–protein interaction network generated displayed many interactions between the proteins. For prioritizing proteins as hubs, we chose MCC along with betweenness centrality and bottleneck as topological parameters (Chin et al. 2014) and normalized the data to identify the top 15 hubs in the network. These 15 essential (hub) proteins are IL10, IFNG, IL4, CD44, IL1B, CTLA4, GZMB, FOXP3, TNF, IL2RA, CAT, ESR1, TLR2, HLA-A, and GSTP1.

Functional module and enrichment analysis

The functional module analysis of vitiligo-associated proteins revealed four functional modules (Fig. 10). The average size of the clusters was 17.75, and they were ranked by their modularity score of 1. The majority of the proteins were found to form a single large cluster. This implies that these proteins have a biological similarity in their functions.

We performed functional enrichment analysis of the larger functional module consisting of 64 proteins using DAVID 6.8. Keeping the classification stringency at highest and considering the enrichment score value ≤ 1.3 to be significant, the given set of target genes was classified into nine functionally enriched clusters (see Additional file 3) that involved 15 genes from the given set of 64 genes. All the nine clusters were observed to be primarily associated with the immune system regulatory processes, such as MHC class I/II-like antigen recognition protein, conserved site of immunoglobulin/major histocompatibility complex, conserved site of interleukin-10, positive regulation of JAK-STAT cascade, apoptotic signaling, chemokines, and TNF.

Pathway analysis

According to the threshold of hypergeometric test $p \leq 0.001$ and Benjamini–Hochberg FDR ≤ 0.01, the mapped genes were found to be enriched in a total of 30 pathways, which involved a total of 40 genes from the given gene set. The most significant pathway was found to be the allograft rejection pathway with a p value of 5.70E−17 and FDR value of 1.51E−14 involving 13 genes. Among these 30 pathways, almost half of the pathways (15 pathways) were associated with immune system responses and related disorders, and autoimmunity, while 14 pathways were associated with infectious (viral, bacterial, and parasitic) disease pathways that have been reported to impair the proper regulation of the immune system.

In the protein–pathway network, a protein is connected to a pathway if the protein is known to be involved in that particular pathway. The network consisted of 71 nodes and 270 interactions representing 40 proteins and 30 pathways (Fig. 11).

Based on degree value, TNF showed maximum interaction in the network implying its participation in most of the pathways. Among the 30 pathways, TNF was found to be associated with 24 pathways. Similarly, IL1B, IFNG, IL10, and TLR2 were found to be involved in 19, 18, 15, and 14 pathways respectively. It was also observed that TLR2 was specifically associated with the infectious disease pathways that were responsible for deregulating the immune system processes as depicted in the results of KEGG pathway see analysis. An additional file (see Additional file 4) lists the pathways in which the hub proteins were found to be involved. Among the 15 hub proteins identified in the protein–protein interaction network, 11 were found in this network suggesting that these 11 essential proteins are involved in the filtered significant pathways.

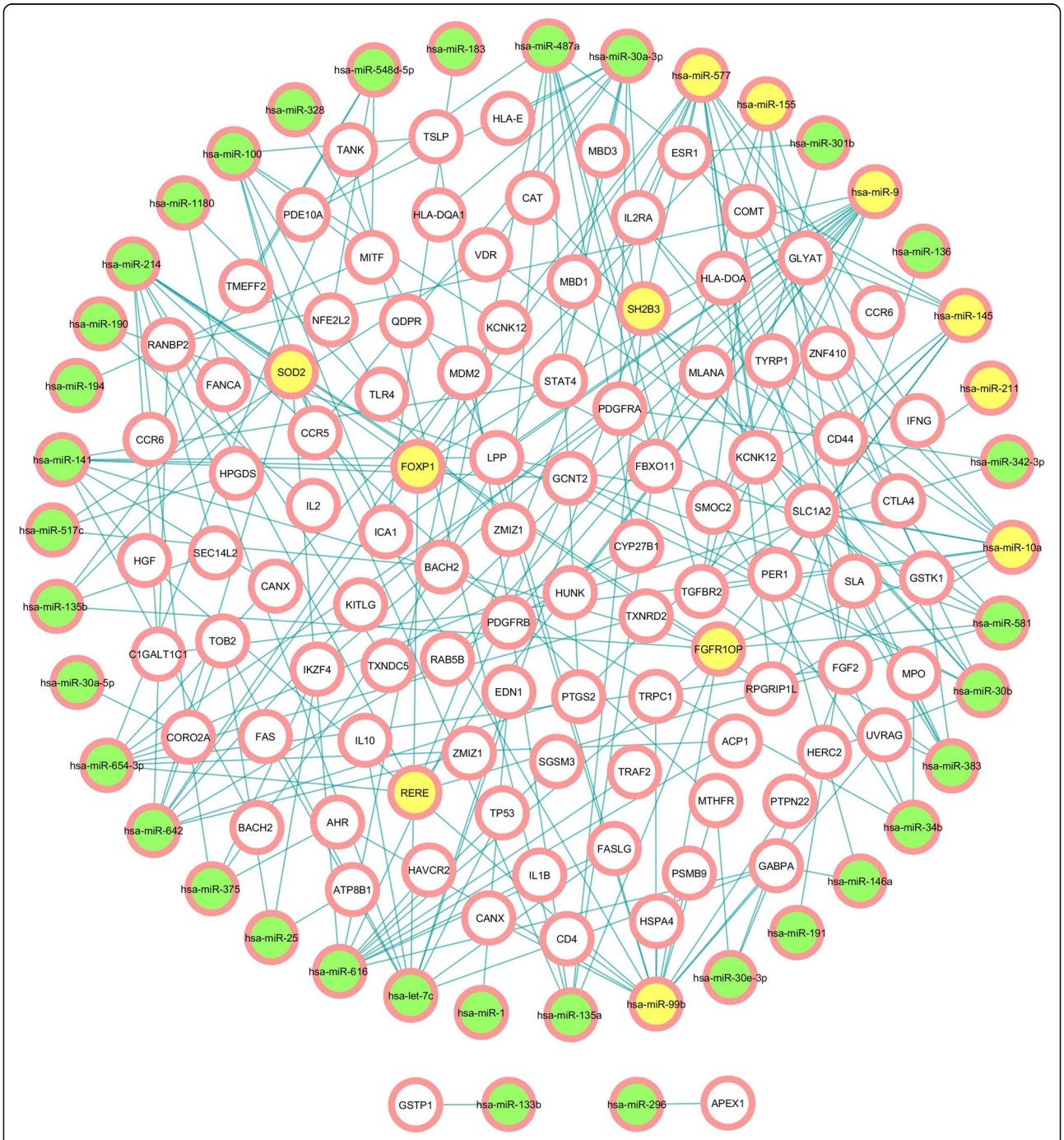


Fig. 8 miRNA–target gene interaction network. The green colored nodes represent the miRNAs, the white colored nodes represent the target genes, and yellow colored nodes represent the hub miRNAs along with the target genes of the highest degree in the network

SNP analysis

Among the 134 SNPs, 36 (26.9%) are nsSNPs and 7 (5.2%) are SNPs, while 68 (50.8%) SNPs were found in the non-coding region. SNPs in the non-coding region comprises of 44 (32.8%) SNPs in the intronic region, 19 (14.2%) in the near-gene region, and 5 (3. 8%) in the mRNA UTR region. The rest 23 (17.1%) among 134 SNPs are intergenic. The distribution of the SNPs is shown in Fig. 12a.

For our analysis, we selected the nsSNPs and UTR-region SNPs since UTRs are central for the post-transcriptional regulation of gene expression, and alterations in the functional UTR region can lead to severe pathology (Conne et al. 2000). The 36 nsSNPs

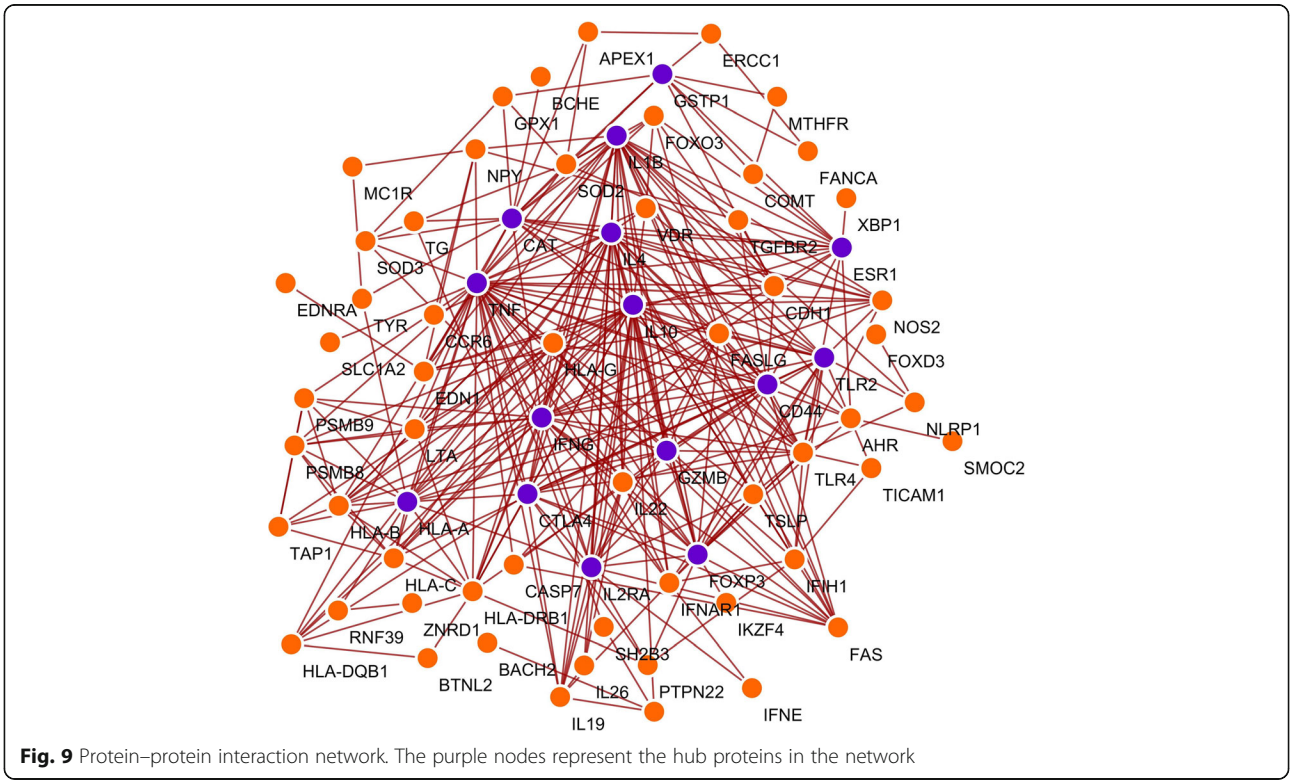


Fig. 9 Protein–protein interaction network. The purple nodes represent the hub proteins in the network

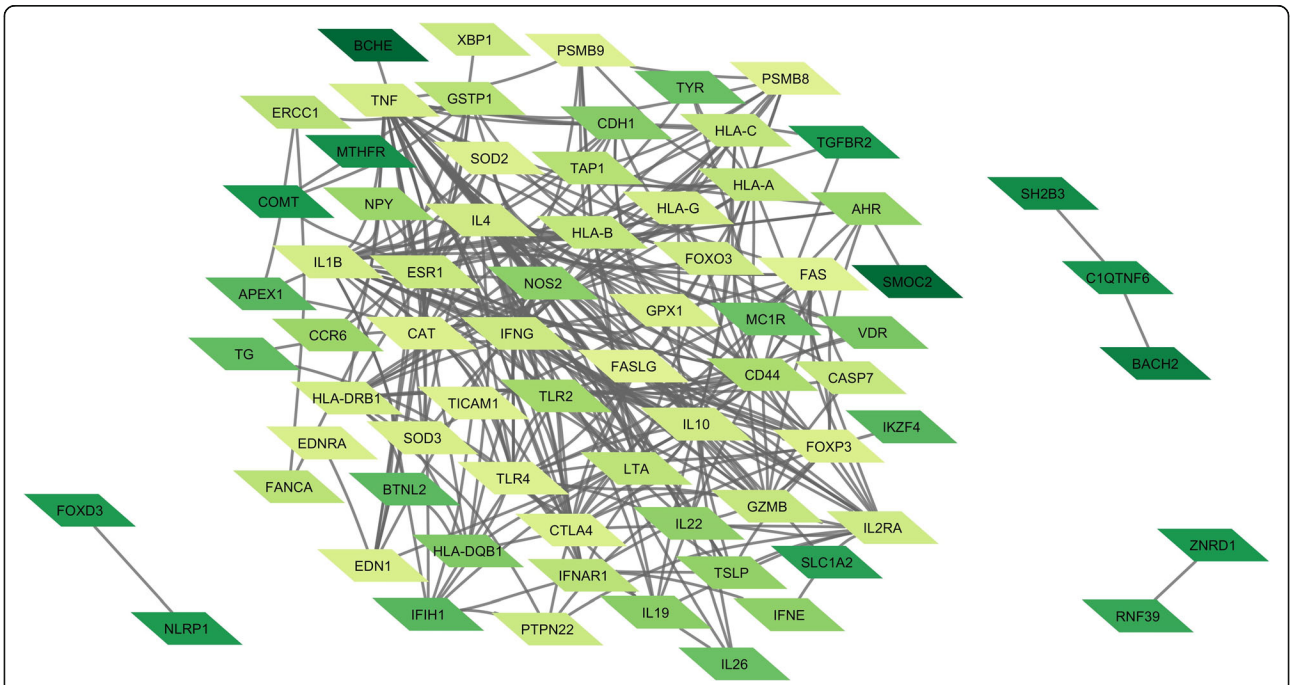


Fig. 10 Functional module (clusters) network. The shades of green color, from light to dark, represent the decrease in the number of interactions. The genes with the maximum number of interactions show lighter shades in the cluster

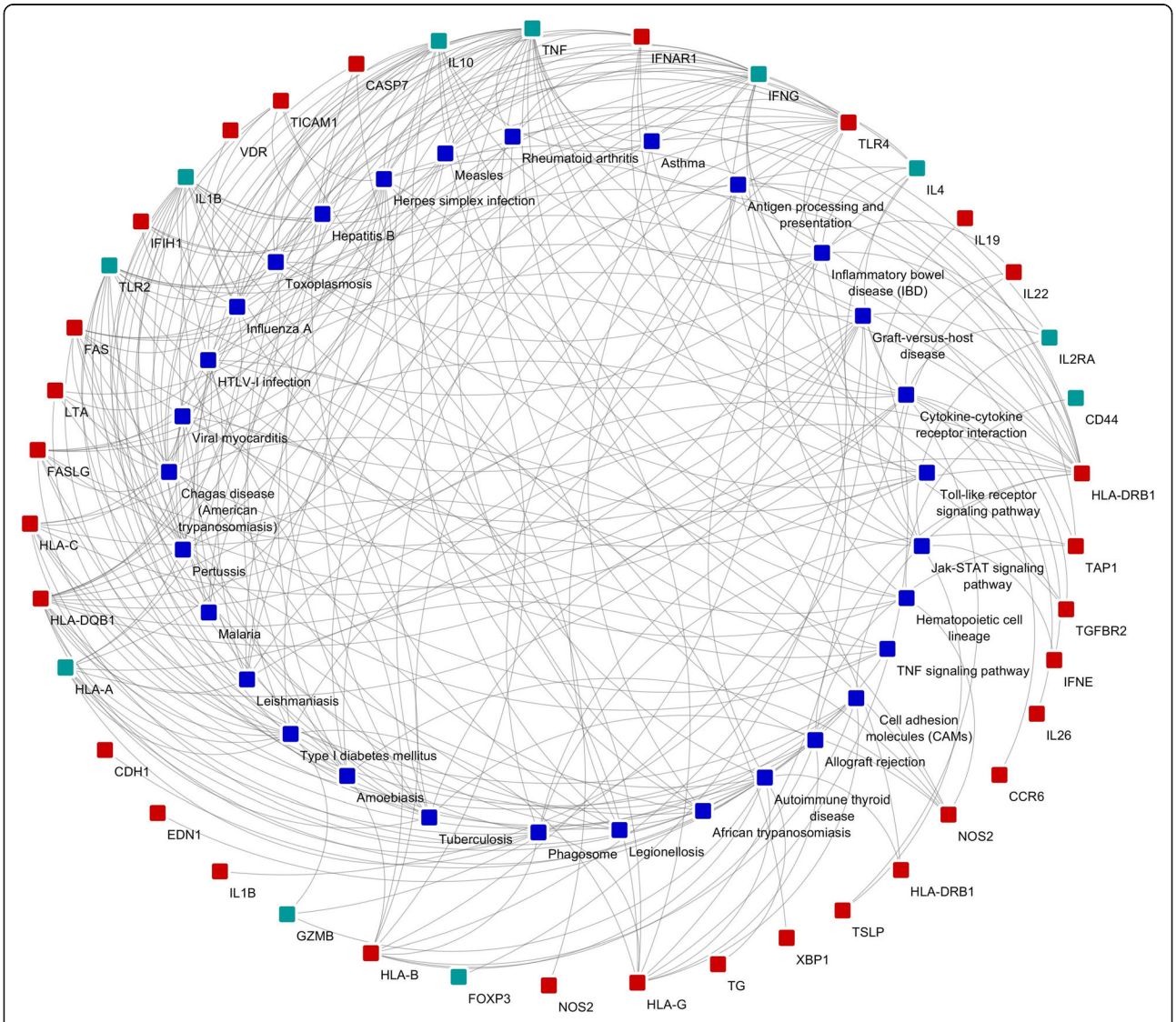


Fig. 11 Protein–pathway network. The red colored nodes represent the proteins, the dark blue colored nodes represent the pathways, and the light blue colored nodes represent the hub proteins

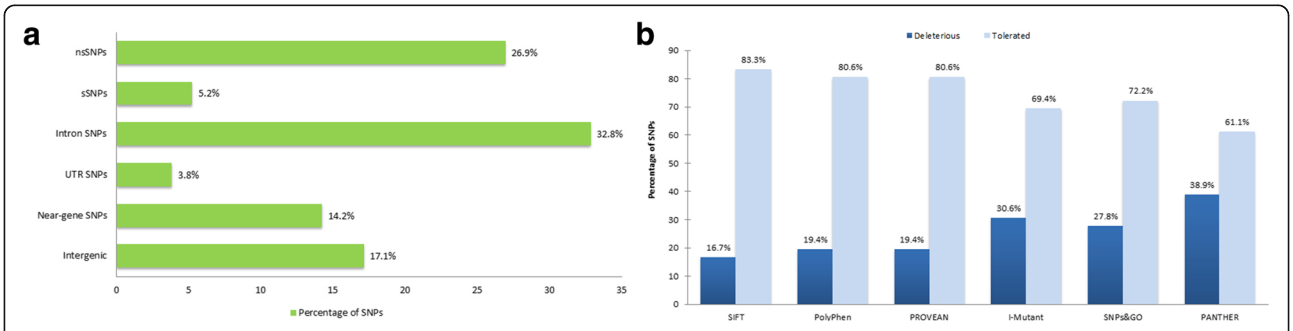


Fig. 12 Distribution of SNPs. **a** Graph of the distribution of SNPs. **b** Graph of the distribution of the deleterious and benign nsSNPs as predicted by SIFT, PolyPhen, PROVEAN, I-Mutant Suite, SNPs&GO, and PANTHER

were analyzed by using a combination of SIFT, PolyPhen, PROVEAN, SNPs&GO, I-Mutant Suite, and PANTHER Evolutionary Analysis of Coding SNP tools.

SIFT predicted six nsSNPs (16.7%) to be deleterious with a tolerance score cut off which is ≤ 0.05. Further analysis of the nsSNPs using PolyPhen predicted two nsSNPs to be "probably damaging" and five nsSNPs to be "possibly damaging" with a tolerance cut off score ≥ 0.5. Consequently, seven nsSNPs (19.4%) were characterized as damaging. Analysis using PROVEAN revealed a similar result as that of PolyPhen tool. Based on a tolerance cut off score value ≤ 0.05, it predicted seven nsSNPs (19.4%) to be damaging. Of these seven nsSNPs, one (rs5743708) was reported to be highly damaging with a tolerance score of 0.

To improve the prediction accuracy, we used I-Mutant Suite and SNPs&GO tools for further analysis. The output results in I-Mutant Suite predict the free energy change (DDG) and classifies it into any three of the mentioned classes, namely, largely unstable (DDG < − 0.5 kcal/mol), largely stable (DDG > 0.5 kcal/mol), or neutral (− 0.5 ≤ DDG ≤ 0.5 kcal/mol). The output result of a protein as largely unstable indicates the effect of a deleterious nsSNP. In our I-Mutant Suite results, we found that 11 nsSNPs (30.6%) exhibited a DDG value of less than − 0.5, which indicates that these are largely unstable resulting in disease-associated mutations. Whereas, SNPs&GO predicted 10 nsSNPs (27.8%) to be related to disease-associated mutations by using a tolerance cut off score ≥ 0.5.

A disease-causing mutation in the highly conserved regions of the genome may pose a high risk of that particular mutation to be damaging which is why we decided to carry out SNP conservation analysis. The probability of a mutation to cause a disease increases monotonically with the increase in the degree of site conservation (Vitkup et al. 2003). Conservation analysis by PANTHER Evolutionary Analysis of Coding SNP predicted 14 nsSNPs (38.9%) to be deleterious based on their preservation time. A longer preservation time implies a greater possibility of functional impact on a protein (Mi et al. 2005). Since different in silico tools have a diverse set of alignments and molecular characteristics, the results of the six tools were slightly different. Accordingly, we combined the results of SIFT, PolyPhen, PROVEAN, SNPs&GO, I-Mutant Suite, and PANTHER Evolutionary Analysis of Coding SNP (see Additional file 5) to predict the deleterious nsSNPs common in all the analysis.

Figure 12b shows the distribution of deleterious and benign nsSNPs obtained using SIFT, PolyPhen, PROVEAN, I-Mutant Suite, SNPs&GO and PANTHER.

Of all of the predictions, 16.7%, 19.4%, 19.4%, 30.6%, 27.8%, and 38.9% deleterious nsSNPs were specifically found by SIFT, PolyPhen, PROVEAN, SNPs&GO, I-Mutant Suite and PANTHER respectively. Combining the results of all the six tools, three nsSNPs, namely, rs1801133 (MTHFR), rs5743708 (TLR2), and rs11575993 (SOD2), were predicted to be functionally significant. Tables 1 and 2 presents the deleterious nsSNPs obtained through the SIFT, PolyPhen, PROVEAN, I-Mutant Suite, SNPs&GO, and PANTHER analysis of the vitiligo-associated nsSNPs.

MutPred predicted the molecular cause of the nsSNPs to become deleterious in MTHFR (rs1801133), TLR2 (rs5743708), and SOD2 (rs11575993). Analysis of the results showed an interrelation of the SNPs to be damaging with respect to the solvent accessibility of the protein. The type of mutated residue and its position in the sequence affect the stability of the protein which due to mutation decreases with the decrease in solvent accessibility of a residue (Vitkup et al. 2003).

NetSurfP predicted the surface solvent accessibility of amino acids by using the protein FASTA sequence as a query. The solvent accessibility is predicted to be buried or exposed, based on the accessibility of the amino acid residues to the solvent. The reliability of relative surface accessibility is verified in the form of *Z*-score which highlights the surface prediction reliability. As given in Table 3, the class assignment does not change for the three nsSNPs. Although there were very minimal changes in the relative surface accessibility (RSA) values for the three nsSNPs, a considerable drift in the *Z*-score was not observed between the wild-type and mutant-type proteins. A decrease in RSA value has been observed in the mutant types of MTHFR and SOD2 while there was an increase in the RSA value of the TLR2 mutant type.

Drug–target network and drug–similarity network

Drug–target network

The bipartite network of drug–protein target interaction consisted of 109 nodes and 84 interactions (Fig. 13a). A drug and protein are considered to be connected to each

Table 1 nsSNPs found to be deleterious using SIFT, PolyPhen, and PROVEAN

SNP	Genes	SIFT score	SIFT prediction	PolyPhen score	PolyPhen prediction	PROVEAN score	PROVEAN prediction
rs1801133	MTHFR	0.043	Deleterious	0.998	Probably damaging	0.002	Damaging
rs5743708	TLR2	0.016	Deleterious	1	Possibly damaging	0	Damaging
rs11575993	SOD2	0.014	Deleterious	1	Possibly damaging	0.001	Damaging

Table 2 nsSNPs found to be deleterious using I-Mutant Suite, SNPs&GO, and PANTHER

SNP	Genes	I-Mutant score	I-Mutant prediction	SNPs&GO score	SNPs&GO prediction	PANTHER prediction
rs1801133	MTHFR	− 0.78	Disease-related mutation	0.88	Disease-associated variation	Probably damaging
rs5743708	TLR2	− 2.78	Disease-related mutation	0.7	Disease-associated variation	Possibly damaging
rs11575993	SOD2	− 1.4	Disease-related mutation	0.66	Disease-associated variation	Probably damaging

other if the protein is a known target of the drug, giving rise to a drug–target network.

In our analysis, we found that the most of the drugs targeting a particular protein did not show any interaction with other protein targets in the network except for the two drugs, etanercept and carfilzomib. Etanercept targets both TNF and LTA while carfilzomib targets PSMB8 as well as PSMB9. Also, we found that out of the 15 hub proteins, only 9 protein targets were found to be present in this network. This illustrates the other 6 hub proteins (IL10, IL4, GZMB, FOXP3, TLR2, AND HLA-A) as potential drug candidates for which drug information is currently not available. Also, we found that 4 hub proteins, namely, CD44, CD152, CAT, and GSTP1, were targeted by a single drug. This highlights the imperative need to discover more effective drugs that target these proteins which may play a major role in therapeutics to alleviate disease conditions in patients.

Another notable finding in our analysis was that the drugs which showed a high degree in the network were mostly indicated for the treatment of autoimmune diseases and deregulated immune responses. One of them is etanercept that targets TNF, a major proinflammatory cytokine that affects various aspects of the immune response, and LTA as well. Etanercept is a genetically engineered decoy receptor that consists of the ligand-binding domain of TNFR2 and the Fc component of human IgG1. It competitively binds with high affinity to TNFR2 inhibiting the binding of both TNF-α and TNF-β to the cell surface receptors, consequently, inhibiting inflammation induced melanocyte death. It has been indicated to be clinically used for rheumatoid arthritis, psoriatic arthritis, ankylosing spondylitis, and Crohn's disease (Nanda and Bathon 2004). However, etanercept has been reported to be less efficient as a monotherapy in vitiligo patients requiring the need of a combinative therapy (Rigopoulos et al. 2007). LTA, on the other hand, is involved in the follicular dendritic cells development and has been observed to induce signals leading to lymphoid neo-organogenesis driving the inflammatory responses in autoimmune diseases like rheumatoid arthritis (Takemura et al. 2001). This suggests that etanercept may suppress lymphoid neo-organogenesis and reduce the proliferation of mature dendritic cells in vitiligo lesions (Wang et al. 2011). The other drug, carfilzomib, is a tetrapeptide epoxyketone-based proteasome inhibitor that targets PSMB9 and PSMB8. Peptides generated from ubiquitin-tagged cytosolic proteins are presented to CTLs by MHC class-I molecules which are degraded by multi-catalytic, cytosolic immune-proteasome complex called LMP2 and LMP7 encoded by PSMB9 and PSMB8 genes respectively (Cresswell et al. 2005). This intrinsic enzymatic activity of immune-proteasomes may be altered by genetic variations which reduce the expression of PSMB8 and PSMB9 in vitiligo PBMCs after IFNG stimulation. This leads to defective proteolytic degradation and accumulation of ubiquitinylated proteins in the epidermis of vitiligo patients leading to ROS production and auto-inflammatory immune responses which may be detrimental for the manifestation of vitiligo (Dani et al. 2017). Carfilzomib targets the catalytic activity of immune-proteasomes and irreversibly inactivates the proteasome, thereby inhibiting aberrant immune function (Miller et al. 2013).

Table 3 Solvent accessibility analysis of the mutated proteins by NetSurfP

Genes	Type	Class assignment	Relative surface accessibility (RSA)	*Z*-fit score for RSA prediction
MTHFR	Wild	B	0.027	0.737
	Mutant	B	0.026	0.781
TLR2	Wild	E	0.243	1.46
	Mutant	E	0.245	1.527
SOD2	Wild	B	0.2	− 0.736
	Mutant	B	0.166	− 0.705

Drug–similarity network

The drug similarity tripartite network of protein targets, drugs, and interacting drugs comprised of 178 nodes and 1331 interactions (Fig. 13b). A drug and its interacting drug are considered to be connected if they share a common protein target. Interacting drug partners of a particular drug may enhance the efficacy of the drug or may even target the same protein. Such interacting drugs may represent themselves as potential drug repositioning candidates. With this concept, we constructed the drug–similarity network that displayed interconnections between drugs and their interacting drug partners.

Apart from the drugs etanercept and carfilzomib targeting more than one protein as shown in the drug–target network, we found two other drugs showing interaction with another protein target in the network. Both diethylstilbestrol and conjugated equine estrogens

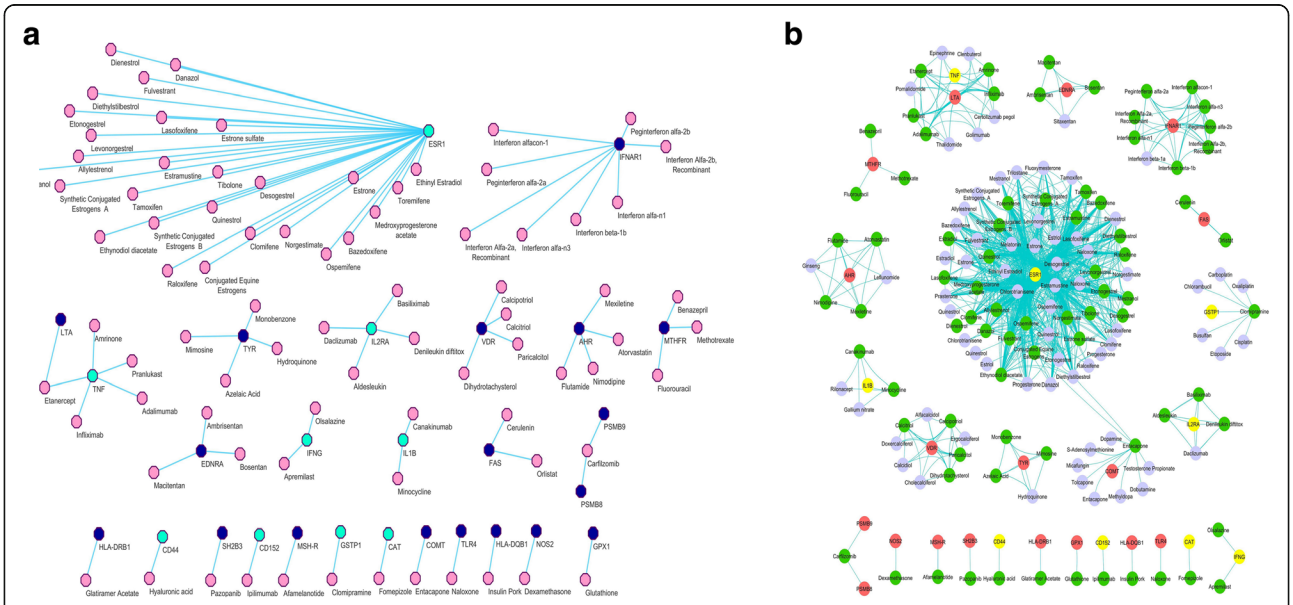


Fig. 13 Polypharmacological analysis. **a** Drug–target network. The light blue colored nodes represent the hub protein targets, the dark blue colored nodes represent the protein targets, and the pink colored nodes represent the drugs. **b** Drug–similarity network. The pink colored nodes represent the hub protein targets, the yellow colored nodes represent the protein targets, the green colored nodes represent the drugs, and the blue colored nodes represent the interacting drugs

targeting ESR1, which is one of the hub protein identified in the protein–protein interaction network analysis, were found to be interacting with the drug entacapone targeting COMT. This signifies that the two drugs interacting with entacapone might target COMT which is targeted by entacapone alone. Also, we found that there are no interacting drugs reported for etanercept targeting LTA and our drug similarity network analysis suggests that the interacting drugs for etanercept targeting TNF might as well target LTA. Etanercept has been less efficient as a monotherapy as mentioned earlier; therefore, the interacting drugs for etanercept as shown in the network might catalyze its efficiency when used in combination. Thus, further comprehensive study is required to validate the effectiveness of these drugs in combinative therapy. In addition, GSTP1, also a hub protein, was shown to be targeted by a single drug (clomipramine) in the drug–target network; however, seven interacting drugs were shown to be connected to this drug in this network. These interacting drugs can be further studied to investigate their potential as drug repositioning candidates for vitiligo treatment.

Protein modeling of TLR2

Among the three predicted functionally significant nsSNPs, we performed protein modeling of TLR2 since our drug–target network analysis showed TLR2 as a potential drug target for which drug information is currently not available. The G23D tool generated a full-length protein model for the TLR2 protein based on *E*-value which was 0.001 by default as generated from the PDB library and ModBase hits. Since we did not perform any molecular dynamics simulation studies for protein structure optimization, therefore, the 3D homology model generated by G23D is a preliminary model implicating the disruptive role of the SNP (rs5743708) on TLR2 protein.

Figure 14a shows the cartoon representation of the modeled protein structure including both the wild-type (green) and the mutant (light blue) amino acid. It also displayed the other variants as reported in ClinVar, COSMIC, and dbSNP for TLR2 which is colored as red, yellow, and dark green respectively in stick representation in the 3D structure.

An A/G mutation (rs5743708) caused the substitution of the amino acid from arginine into glutamine at position 753 (R753Q) of the protein. The mutation was identified to be located within the TIR domain as annotated in UniProt. Since it is a membrane protein, it is exposed on the surface which is in agreement with the previous NetSurfP results. Analysis of the 3D structure suggests that the residue glutamine in position 753 is located in the middle of a helix. There was a difference in the size observed in the wild-type and mutant amino acids with the mutant residue being smaller than the wild-type residue causing conformational changes on the DD loop which might lead to loss of interactions. Also, the wild-type residue is positively charged, but the amino acid substitution leads to a decrease in the positive charge that changes the interaction surface within

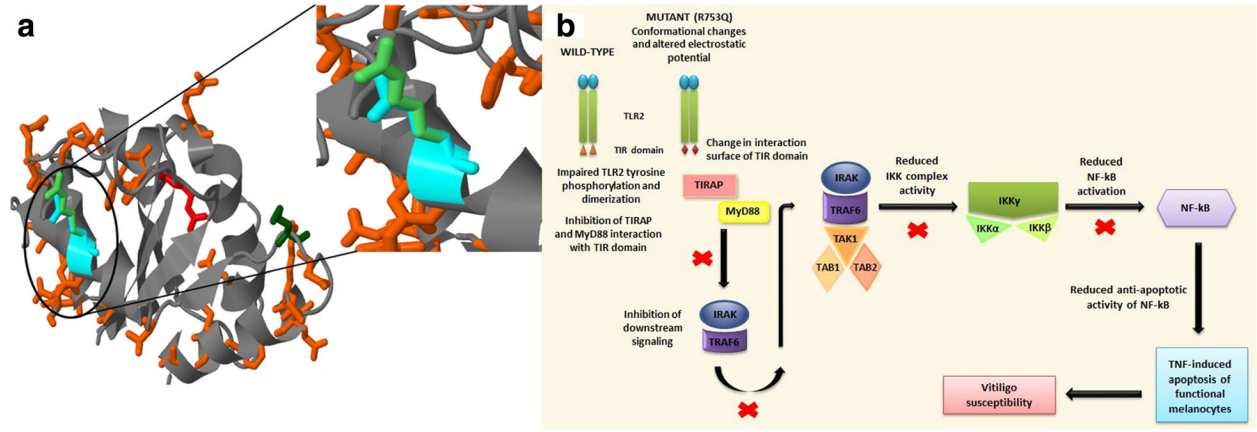


Fig. 14 Protein modeling. **a** 3D structure of modeled mutant (R753Q) TLR2 protein. The wild-type residue is represented in green color, and the mutant residue is colored light blue. Other variants are also displayed in this structure with the dbSNP variant colored dark green, COSMIC variant colored orange, and the ClinVar variant is represented in red color. The backbone of the protein is shown in gray color. **b** Disease mechanism influenced by R753Q TLR2 polymorphism

the TIR domain via altered electrostatic potential. These may affect TLR2 dimerization causing loss of interactions with other molecules or residues affecting the functional activity of the protein (Xiong et al. 2012). The R753Q polymorphism compromises the TLR2/1 or TLR2/6 assembly resulting in deficient tyrosine phosphorylation and impaired recruitment of MyD88. This reduces the phosphorylation of IRAK1 and diminishes the activation of MAPKs and NF-κB resulting in the deficient production of cytokines thus altering TLR2 signaling competence. Therefore, the compromised signaling is due to deficient tyrosine phosphorylation and not due to lower mutant receptor expression. The reduced activation of NF-κB signaling pathway results in melanocyte apoptosis suggesting their decisive role in the increased risk for the development of vitiligo (Karaca et al. 2013; Traks et al. 2015).

The protein–protein interaction analysis of TLR2 showed its interaction with TLR1, TLR6, LY96, MyD88, IRAK4, TRAF6, NFKB1, TIRAP, CD14, and HMGB1. All these proteins were found to have a fundamental role in regulating the innate immune responses. The amino acid substitution of arginine to glutamine at position 753 has been reported to be located in the TIR domain. TLR2 activates NF-κB in combination with either TLR1 or TLR6 by bringing together the TIR domains and triggering tyrosine phosphorylation. The TIR domain of TIRAP binds to the TIR domain of TLR2 which then extends a docking platform for MyD88 recruitment. MyD88 facilitates the recruitment of IRAK4 which activates TRAF6 leading to the translocation of activated NF-κB to the nucleus where it induces target gene expression generating inflammatory responses (Oliveira-Nascimento et al. 2012). Mutations in the TIR domain tend to have more severe impact on signaling than those affecting the extracellular domain (Karaca et al. 2013). Genetic alterations in TLR2 might affect its interaction with both TLR1 and TLR6 consequently affecting NF-κB activation (Brown et al. 2006). It was also found that this mutation significantly reduced NF-κB activation by about 50 and 75% (Merx et al. 2007; Ben-Ali et al. 2011). In the case of vitiligo, altered NF-kB signaling may result in impaired melanogenesis inciting human melanocytes susceptible to TNF induced apoptosis (Shang et al. 2002) (Fig. 14b).

This implicates the possible detrimental effect of this mutation on the interaction of TLR2 with TIRAP, MyD88, IRAK4, TRAF6, and the consequent signal transduction. HMGB1 has been found to upregulate the expression of TLR2 of the NK cells and promote NK cell activation mediating inflammatory responses (Qiu et al. 2014), while CD14 (a co-receptor of TLR2) accelerates the microbial ligand transfer from CD14 to TLR2, resulting in an increased TLR2 signaling (Raby et al. 2013). LY96 have been found to enhance the expression of both TLR2 and TLR4 and vice versa enabling them to generate highly sensitive responses to a broad range of microbial lipopolysaccharide (LPS) structures (Dziarski et al. 2001). Altered expression of TLR2 will invariably affect the interaction of TLR2 with these proteins thereby influencing TLR2 signaling and inflammatory responses resulting in defective immune response to some antigens such as viruses in the case of vitiligo (Karaca et al. 2013).

VitmiRS

Currently, VitmiRS has information on 41 miRNAs and 134 associated SNPs for 84 unique genes. VitmiRS provides a user-friendly interface to detailed information on disease association of miRNAs and their target genes, SNPs and their position and location, the change in alleles and the resulting amino acid change due to such

mutational events, and their respective literature reference. The users can search and access information for their respective query in the database browsing through query categories of miRNAs, SNPs, genes, and amino acid change. Further, the database interface also allows for the selection of particular attributes, such as PubMed ID, miRNA sequences, chromosome number, chromosome location, odds ratio, and *p* value; the geographical location and population in which the association of specific miRNAs and SNPs with vitiligo has been reported. Also, it incorporates the results of SNP analysis, thereby providing information on the pathogenic effect of the each SNPs as well. Thus, the database can be queried individually or in combination with any of the categories as mentioned above according to the need and interest of the user. The information available in VitmiRS may, therefore, be used for various associative studies relating to miRNAs and genetic variants to uncover their role and importance in vitiligo disease susceptibility and pathogenesis.

Discussion

An enhanced understanding of the disease causative genes and their relationship with other genes along with other diseases offers an improved resource for finding the candidate genes that mark the onset of a disease. Several unrelated diseases have been revealed to show common molecular mechanisms with strong association among them (Yu et al. 2015). As a result of such disease associations, the possibility of related diseases to occur together in an individual cannot be ruled out. Analysis of disease-gene bipartite network allowed the identification of several diseases which are under the influence of multiple genes wherein it highlighted vitiligo to be influenced by a multiplex of genes. Additionally, we also identified the genes which exhibit pleiotropy, thus accounting for multiple diseases and may play a crucial role in determining disease comorbidity. We explored some unique relationships with their previous published studies being non-existential which include the genetic association between rosacea and vitiligo, as caused by the gene BTNL2; the association between GM1-gangliosidosis and eczema, both being caused by GLB1 gene; and the association between piebaldism and urticaria pigmentosa as a result of a mutation in the KIT gene. This provides with a new perspective in understanding dermatosis opening new avenues for conducting genetic research. In the DSN analysis, we found shared SNPs between diseases xeroderma pigmentosum and keloid whose association has been previously unidentified. Also, our analysis shows a correlation between the diseases Beare–Stevenson cutis gyrata and Brooke–Spiegler syndrome. Our database, therefore, provides a fresh perspective to the possible association between these diseases, as no published literature source indicating their correlation is available as of now. However, validation of our findings through wet-lab research can further strengthen our findings.

Based on our network analysis results of disease–gene association, we further carried out an integrative systems analysis of vitiligo. Vitiligo is a result of convoluted interactions of biological, environmental, and immunological events; hence, a single concept cannot be attributable to all the conditions of functional melanocyte loss. A large-scale analysis and integration of miRNA–disease associations will offer a platform to investigate the patterns of the miRNAs and its associations with diseases. Molecular signatures of miRNAs as reported in vitiligo patients suggest that these are actively involved and have a significant role in disease pathogenesis. Having a cardinal role in maintaining physiological homeostasis and disease development and progression, miRNAs are significant for melanocyte development and survival (Mansuri et al., 2016). Our miRNA–target gene network analysis revealed seven hub miRNAs, namely, hsa-miR-99b, hsa-miR-577, hsa-miR-9, hsa-miR-155, hsa-miR-211, hsa-miR-10a, and hsa-miR-145 implicating their role in vitiligo pathogenesis. The upregulation of hsa-miR-99b reduces the cytotoxic activity (cytokine effector functions) of NK cells which are crucial for the normal BCR signaling and proliferation of B cells. This causes deregulation of genes involved in B cell maturation and development resulting in the dysfunctioning of the immune system indicating them to be important players in vitiligo immunopathogenesis (Nandagopal et al. 2014; Šahmatova et al. 2016).

TYRP1 is targeted by hsa-miR-577, and its reduced expression as induced by miR-577 leads to increased sensitivity of melanocytes to oxidative stress causing early cell death of vitiligo melanocytes (Manga et al. 2006; Sturm and Duffy 2012). Also, the downregulation of PTPN22 was observed to be influenced by miR-577 which triggers the overexpression of T cells and suppresses anti-apoptotic AKT kinase inducing melanocyte destruction, thereby, rendering susceptibility to autoimmunity in vitiligo patients (Mansuri et al., 2016). Elevated levels of SIRT1 have been reported to protect cells from oxidative stress and inflammatory microenvironment (Han et al. 2008). Increased expression of miR-9 downregulates SIRT1 resulting in melanocytes apoptosis in vitiligo (Saunders et al. 2010). SIRT1 has been shown to regulate stress-activated MAPK pathway via Akt and ASK1 in vitiligo keratinocytes (Becatti et al. 2014). Previous studies have demonstrated the influence of miR-145 on the genes involved in the pigmentation process (Dynoodt et al. 2013). The genes targeted by miR-145 also regulate MAPK pathway along with JNK and TGFB signaling pathway and are related to the functional groups that might indirectly influence cellular processes in vitiligo

wherefore they interfere with melanocytes function and viability (Šahmatova et al. 2016) suggesting the role of both miR-9 and miR-145 in the destruction of melanocytes in vitiligo.

TGFBR2 is targeted by miR-211, and downregulated miR-211 increases the expression of TGFBR2 which in turn downregulates MITF. MITF is a known primary regulator of melanocyte development and its survival (Levy et al. 2010); thus, deregulated MITF will considerably affect melanocyte development implying the role of miR-211 in vitiligo pathogenesis. Overexpression of miR-155 was found to modulate the levels of several interferon-regulated genes, such as SOCS1, IFITM1, and IRF1 that inhibits the expression of melanogenesis-associated genes, such as, TYRP1, YWHAE, SDCBP, and SOX10 in melanocytes and particularly YWHAE in keratinocytes. This suggests that upregulated miR-155 is associated with vitiligo pathogenesis which alters interferon signaling as well as targets melanogenesis-associated genes (Šahmatova et al. 2016). Both miR-155 and miR-10a are on their own largely dispensable for regulatory T cell (Treg) function and stability which is responsible for suppressing autoimmune pathology. Inhibition of miR-10a expression leads to reduced FOXP3 expression levels which subsequently decrease the stability of Treg cells (Jeker et al. 2012) resulting in the insufficient suppression of inflammation in autoimmune diseases which could likely happen in vitiligo patients.

Identifying the susceptible genes and their variants which drive the way to the onset of disease is fundamental to unravel their contribution in disease progression. Most of the vitiligo-associated genes are plausible biological candidate genes which when altered are responsible for stimulating melanocyte-specific immune responses. These candidate genes encode immunoregulatory and melanocyte proteins constituting a dense immunoregulatory network, an alteration in which highlights the systems and pathways mediating vitiligo susceptibility (Spritz 2013). Genetic variation alters or damages protein structure disrupting protein–protein interactions which are otherwise essential for regulatory processes constituting the pretext of disease development. Network-based studies of these interacting proteins may impart an insight into disease pathogenesis initiating better diagnosis and the feasibility of personalized treatment for vitiligo patients in the future. Our PPI network analysis results identified 15 hub proteins, namely, IL10, IFNG, IL4, CD44, IL1B, CTLA4, GZMB, FOXP3, TNF, IL2RA, CAT, ESR1, TLR2, HLA-A, and GSTP1 to be associated with vitiligo. The balance between pro- and anti-inflammatory cytokines plays a significant role in the pathogenesis of vitiligo. Higher concentrations of IFNG, a pro-inflammatory cytokine, enhance T cell-melanocyte attachment in the skin initiating T cell-mediated apoptosis of melanocytes in vitiligo. On the other hand, reduced concentrations of IL-10, a potent regulator of anti-inflammatory immune responses, were observed in vitiligo patients (Singh et al. 2012). An increased IL-10 concentration with an increase in the IFNG levels exhibited a positive correlation with disease duration as reported in vitiligo patients (Ala et al. 2015). IL-4, an immunomodulatory cytokine, stimulates B cell proliferation and T cell development that leads to the elevation of baseline IgE levels inducing inflammation (Del Prete et al. 1988). Polymorphisms in the IL4 gene are known to increase its expression increasing the lgE levels thereby implicating its role in autoimmunity-mediated vitiligo susceptibility (Imran et al. 2012). CTLA4 expressed by Tregs is a negative regulator of T cell function and fosters tolerance to self-antigens. Decreased levels of CTLA4 mRNA and deregulated CTLA4 expression due to genetic variations have been found in vitiligo patients (Dwivedi et al. 2011) suggesting its involvement in susceptibility to vitiligo. Also, upregulated CD44 expression in response to naive T cell proliferation as induced by autoimmune melanocyte destruction concomitantly increases T cell development implicating the complex regulation of self-reactive T cells in vitiligo (Byrne et al. 2014).

Increased mRNA levels of IL1B increases SOD levels leading to increased H_2O_2 production as observed in vitiligo patients. Genetic variability in IL1B resulting in altered IL1B transcript levels might be associated with elevated NPY levels in patients with vitiligo whose synthesis is governed by IL1B (Laddha et al. 2014). Increased NPY levels lead to epidermal and dermal hypoxia which might potentiate melanocyte death in vitiligo (Tu et al. 2001). Alterations in CAT have been reported to result in the reduction of the catalase enzyme activity and consequently evoke excess H_2O_2 accumulation in the entire epidermis of vitiligo patients (Casp et al. 2002). Although the genetic mechanisms of estrogen in increased pigment cell activity are not largely known yet, ESR1 expression on human melanocytes has been demonstrated to have specific actions in human pigmentation (Im et al. 2002). Also, genetic variation in ESR1 gene has been reported to show its association with vitiligo (Jin et al. 2004). Additionally, GSTP1 is broadly expressed in defense against oxidative stress wherein they detoxify a variety of electrophilic compounds generated by ROS-induced damaged cells (Nebert and Vasiliou 2004). Altered GSTP1 expression fails to protect cells against chemical toxicity and stress contributing to melanocyte death in vitiligo patients (Dušinská et al. 2001; Liu et al. 2009).

Effector functions of IL2RA and GZMB in the target cell killing by cytotoxic T cells (CTLs) and NK cells activation-

induced cell death terminate immune responses and mediate melanocyte killing in vitiligo (Spritz 2010). GZMB also have a role to play in cleaving melanocyte proteins that constitute vitiligo auto-antigens activating auto-antigens that initiate and propagate autoimmunity directed against melanocytes (Darrah and Rosen 2010). FOXP3, the master regulator of Treg cells, have a vital role in maintaining immune balance and its alteration triggers autoimmune diseases including vitiligo (Jahan et al. 2015). TNF downregulates MITF affecting melanocyte development and proliferation, and ultimately affecting melanogenesis. Also, TNF-α downregulates MSHR binding activity and reduces MC1-R expression, both of which are known inducers of melanogenesis (Camara-Lemarroy and Slas-Alanis 2013). TRAIL, a TNF family death receptor, activates caspases and cleaves melanocyte proteins and also promotes dendritic cell-mediated melanocyte death eliciting apoptosis of primary human melanocytes (Larribere et al. 2004). TNF, thus, acts as the central regulatory effector in the immunopathological mechanisms involved in vitiligo.

Among TLRs, TLR2 is fundamental for immune responses against mycobacterial infections, in sensing oxidative stress and cellular necrosis and, also in inducing apoptosis (Petry and Gaspari 2009). It also has the propensity to recognize a wide array of antigens evincing its instrumental role in the evolution of self-reactive diseases (Borrello et al. 2011). Altered expression and signaling due to TLR2 polymorphism have been proposed to be the reason for inadequate immune responses to viral or pathogenic antigens in vitiligo (Karaca et al. 2013; Traks et al. 2015).

The functional enrichment analysis result of the single large cluster consisting of 64 proteins demonstrated the vitiligo-associated genes to be primarily involved in immune response regulation by cytokines and oxidative stress, and apoptotic processes. Oxidative stress in the melanocytes stimulates local inflammatory responses whereby it leads to the activation of innate immune processes as a result of which melanocyte-specific cytotoxic immune responses are evoked in vitiligo patients. Vitiliginous melanocytes show increased surface expression of HLA-A, a class I MHC receptor, which enables it to present multiple autoantigens to T cells destroying skin melanocytes (Hayashi et al. 2016). Also, increased expression levels of HLA class II molecules triggers an increased production of immunostimulatory cytokines that may act as an adjuvant during the presentation of autoantigens (Cavalli et al. 2016), tying together with HLA class I molecules in the development of autoimmunity in vitiligo patients. Also, alteration in the concentration of various pro-inflammatory and anti-inflammatory cytokines such as IL-10, IL-2, TNF, and IFNG has been associated with many autoimmune disorders (Singh et al. 2012).

Apart from exhibiting pathways associated with immune responses and autoimmunity, our pathway analysis results also consisted of pathways corresponding to infectious diseases, particularly viral infections. Several studies have implicated the etiopathogenesis of vitiligo to multiple viral infections as epidermal melanocytes are important targets of viruses (Duvic et al. 1987; Grimes et al. 1996). Also, viral infectious diseases, in most cases, impair the body's systemic immune response. This explains the reason why the pathways associated with infectious diseases were also observed to be significant in the results. In the protein–pathway network, TNF was found to be involved in 24 out of 30 significant pathways indicating it to be a prime regulator of vitiligo immunopathogenesis (Birol et al. 2006).

Our SNP analysis predicted rs1801133 (MTHFR), rs5743708 (TLR2), and rs11575993 (SOD2) to be functionally significant for vitiligo susceptibility. Previous studies have shown these mutations to be associated with other diseases as well. The A222V variant of MTHFR has been reported to be associated with vascular diseases (Morita et al. 1997) and cancer (Hubner et al. 2007) The R753Q variant of TLR2 has been reported to be associated with colorectal cancer (Boraska Jelavić et al. 2006), atherosclerosis (Bielinski et al. 2011), and tuberculosis (Ogus et al. 2004). However, the L84F variant of SOD2 has only been reported in vitiligo till date (Laddha et al. 2013).

There is no definite cure available for vitiligo, and hence, the various treatment options available merely aim to improve skin appearance by repigmentation or stabilizing depigmentation without the assurance of reoccurrence or extension of depigmentation (Njoo and Westerhof 1999). Our drug–target network analysis revealed novel potential drug candidates which could be explored for improved therapeutics for vitiligo. It is noteworthy that most of the drugs defined for the protein targets, even a few hub protein targets, are not indicated to be used for the treatment of vitiligo as reported in DrugBank. This indicates a pressing need to evaluate these drugs and perform investigational studies to identify new indications and elucidate the efficiency of these drugs for the treatment of vitiligo. This would lead to significant contributions in drug discovery complementing the existing drug pipelines, thereby, improving the quality of life in vitiligo patients. Additionally, some of the hub proteins are targeted by a single drug which can be further examined to contrive better effective drugs to enhance the success rate of treatments. Interacting drug partners of a particular drug targeting a particular protein might either directly target that protein or enhance the efficacy of the drug. With this concept, we constructed the drug–similarity network and

found interacting drugs for those proteins which were previously shown to be targeted by a single drug in the drug–target network. These interacting drugs might function as an alternative to the native drug with enhanced efficacy.

Polymorphism in TLR2 (rs5743708) was found to be deleterious in our SNP analysis results indicating its potentiality to induce vitiligo. TLR2 was also found to be one of the hub protein targets for which no drug information is available yet. The R753Q mutation was identified to be located within the TIR domain, an intracellular signaling domain, which compromises the signaling capacity of TIR domain impairing MyD88–TLR2 assembly. This inactivates NF-κB signaling pathway which can invariably influence the regulation of inflammatory processes and can even impair melanogenesis suggesting its role in vitiligo pathogenesis (Karaca et al. 2013; Traks et al. 2015). Our PPI network of TLR2 shows its interacting proteins suggesting that an altered TLR2 might have an impact on its interaction with other proteins essential for many biological functions and signaling processes. This indicates the need to analyze the structural details of the protein and the effect of mutation on its structure and function, and carry out further experimental studies to discover new drugs targeting the mutated TLR2 protein associated with vitiligo.

Conclusions

Investigating the patterns of miRNAs and its associations with diseases and identifying the susceptible genes variants triggering disease onset is significant for unraveling the key factors that underpin disease manifestation. We, therefore, identified vitiligo-associated miRNAs and their targets, and susceptible genes, and carried out a comprehensive network analysis of these data which revealed the association of significant hub miRNAs and proteins with disease susceptibility. We validated their functional role and carried out SNP analysis wherein we identified mutation in TLR2 (R753Q) as deleterious. Our drug–target network and drug–similarity network unveiled novel molecular determinants and drug repositioning candidates for vitiligo. Both our databases DermaGene and VitmiRS provide authentic and relevant information on the essentialities of disease association which may facilitate researchers in identifying dermatological disorder causation. We intend to regularly update both the databases, DermaGene and VitmiRS, respectively, through a bi-annual review to ensure consistency of data and to ensure it is maintained up-to-date. The procedure for regular update would rely on identification of latest entries which may be missing in our database and merging the new data with the existing data. Our approach can provide an insight into the regulatory mechanisms of disease manifestation, thereby, implicating its role in improved therapeutic and diagnostic interventions.

Additional files

Additional file 1: Disease co-morbidities and associated SNPs. Disease comorbidity arising from shared SNPs. (XLSX 9 kb)

Additional file 2: Disease co-morbidities and associated genes. Disease comorbidity arising from shared genes. (XLSX 10 kb)

Additional file 3: DAVID functional enrichment analysis. The 9 functionally enriched clusters as found by DAVID. (XLSX 13 kb)

Additional file 4: Hub protein–pathway analysis. The significant pathways of the hub proteins in the protein–pathway network. (XLSX 10 kb)

Additional file 5: SNP analysis. The results of nsSNPs analysis using six computational platforms. (XLSX 17 kb)

Abbreviations

DAVID: The Database for Annotation Visualization and Integrated Discovery; DGN: Disease–gene bipartite network; DSN: Disease–SNP bipartite network; G23D: Genomic variant to 3D protein data; HMDD: The Human microRNA Disease Database; KEGG: Kyoto Encyclopedia of Genes and Genomes; MCC: Maximum Clique Centrality; MCL: Markov Clustering Algorithm; PROVEAN: Protein Variation Effect Analyzer; SIFT: Sorting Intolerant From Tolerant; STRING: The Search Tool for the Retrieval of Interacting Genes

Funding

This work was supported by the Department of Biotechnology, Government of India [No.BT/PR5402/BID/7/508/2012].

Availability of data and materials

The datasets generated and/or analyzed during the current study are available in the DermaGene [http://genomeinformatics.dtu.ac.in/dermagene/] and VitmiRS [http://genomeinformatics.dtu.ac.in/vitmirs/] repository.

Authors' contributions

YH conceived and designed the study. IS and RR collected data and performed the analysis for DermaGene and VitmiRS respectively. YH, RR, and IS evaluated the results and prepared the manuscript. LKG developed the web interface for both the databases. All authors read and approved the final manuscript.

Ethics approval and consent to participate

Not applicable.

Competing interests

The authors declare that they have no competing interests.

Publisher's Note

Springer Nature remains neutral with regard to jurisdictional claims in published maps and institutional affiliations.

Received: 29 December 2017 Accepted: 3 May 2018
Published online: 15 June 2018

References

Adzhubei IA, Schmidt S, Peshkin L, Ramensky VE, et al. A method and server for predicting damaging missense mutations. Nat Methods. 2010;7(4):248–9.

Agarwal V, Bell GW, Nam JW, et al. Predicting effective microRNA target sites in mammalian mRNAs. elife. 2015;4:e05005.

Ala Y, Pasha MK, Rao RN, et al. Association of IFN-γ: IL-10 cytokine ratio with nonsegmental vitiligo pathogenesis. Autoimmune Dis. 2015; https://doi.org/10.1155/2015/423490.

Bansal S, Goel A. Chilblain lupus erythematosus in an adolescent girl. Indian Dermatol Online J. 2014;(Suppl 1):30–2.

Barabasi AL, Oltvai ZN. Network biology: understanding the cell's functional organization. Nat Rev Genet. 2004;5(2):101–13.

Barateau A, Vadrot N, Vicart P, et al. A novel lamin a mutant responsible for congenital muscular dystrophy causes distinct abnormalities of the cell nucleus. PLoS One. 2017;12:1–18.

Becatti M, Fiorillo C, Barygina V, et al. SIRT1 regulates MAPK pathways in vitiligo skin: insight into the molecular pathways of cell survival. J Cell Mol Med. 2014;18(3):514–29.

Ben-Ali M, Beatrice C, Jeremy M, et al. Functional characterization of naturally occurring genetic variants in the human TLR1-2-6 gene family. Hum Mutat. 2011;32(6):643–52.
Bielinski SJ, Hall JL, Pankow JS, et al. Genetic variants in TLR2 and TLR4 are associated with markers of monocyte activation: the Atherosclerosis Risk in Communities MRI Study. Hum Genet. 2011;129(6):655–62.
Birol A, Kisa U, Kurtipek GS, et al. Increased tumor necrosis factor alpha (TNF-α) and interleukin 1 alpha (IL1-α) levels in the lesional skin of patients with nonsegmental vitiligo. Int J Dermatol. 2006;45(8):992–3.
Boisseau-Garsaud AM, Garsaud P, Calès-Quist D, et al. Epidemiology of vitiligo in the French West Indies (Isle of Martinique). Int J Dermatol. 2000;39(1):18–20.
Boraska Jelavić T, Barisic M, Drmic-Hofman I, et al. Microsatelite GT polymorphism in the toll-like receptor 2 is associated with colorectal cancer. Clin Genet. 2006;70(2):156–60.
Borrello S, Nicolo C, Delogu G. TLR2: a crossroads between infections and autoimmunity? Int J Immunopathol Pharmacol. 2011;24(3):549–56.
Brown V, Brown RA, Ozinsky A, et al. Binding specificity of Toll-like receptor cytoplasmic domains. Eur J Immunol. 2006; https://doi.org/10.1002/eji.200535158.
Byrne KT, Zhang P, Steinberg SM, et al. Autoimmune vitiligo does not require the ongoing priming of naive CD8 T cells for disease progression or associated protection against melanoma. J Immunol. 2014;192(4):1433–9.
Camara-Lemarroy CR, Slas-Alanis JC. The role of tumor necrosis factor-α in the pathogenesis of vitiligo. Am J Clin Dermatol. 2013;14(5):343–50.
Capriotti E, Fariselli P, Rossi I, et al. A three-state prediction of single point mutations on protein stability changes. BMC bioinformatics. 2008;9(2):S6.
Casp CB, She JX, McCormack WT. Genetic association of the catalase gene (CAT) with vitiligo susceptibility. Pigment Cell Melanoma Res. 2002;15(1):62–6.
Cavalli G, Hayashi M, Jin Y, et al. MHC class II super-enhancer increases surface expression of HLA-DR and HLA-DQ and affects cytokine production in autoimmune vitiligo. Proc Natl Acad Sci U S A. 2016;113(5):1363–8.
Chin C-H, Chen S-H, Wu H-H, et al. cytoHubba: identifying hub objects and sub-networks from complex interactome. BMC Syst Biol. 2014;8(4):S11.
Choi Y, Sims GE, Murphy S, et al. Predicting the functional effect of amino acid substitutions and indels. PLoS One. 2012;7(10):e46688.
Conne B, Stutz A, Vassali J-D. The 3′ untranslated region of messenger RNA: a molecular 'hotspot' for pathology? Nat Med. 2000;6(6):637.
Cordell HJ. Detecting gene-gene interactions that underlie human diseases. Nat Rev Genet. 2009;10(6):392–404.
Cresswell P, Ackerman AL, Giodini A, et al. Mechanisms of MHC class I-restricted antigen processing and cross-presentation. Immunol Rev. 2005;207(1):145–57.
Dalamon VK, Buonfiglio P, Larralde M, et al. Connexin 26 (GJB2) mutation in Argentinean patient with keratitis-ichthyosis-deafness (KID) syndrome: a case report. BMC Med Genet. 2016; https://doi.org/10.1186/s12881-016-0298-y.
Dani P, Patnaik N, Singh A, et al. Association and expression of antigen processing gene PSMB8 coding for low molecular mass protease 7 (LMP7) with vitiligo in North India: case-control study. Br J Dermatol. 2017; https://doi.org/10.1111/bjd.15391.
Darrah E, Rosen A. Granzyme B cleavage of autoantigens in autoimmunity. Cell Death Differ. 2010;17(4):624–32.
Del Prete G, Maggi E, Parronchi P, et al. IL-4 is an essential factor for the IgE synthesis induced in vitro by human T cell clones and their supernatants. J Immunol. 1988;140(12):4193–8.
Dušinská M, Ficek A, Horská A, et al. Glutathione S-transferase polymorphisms influence the level of oxidative DNA damage and antioxidant protection in humans. Mutat Res Fund Mol Mech Mut. 2001;482(1):47–55.
Duvic M, et al. Human immunodeficiency virus—associated vitiligo: expression of autoimmunity with immunodeficiency? J Am Acad Dermatol. 1987;17(4):656–62.
Dwivedi M, Rapini R, Hoots WK, et al. Cytotoxic T-lymphocyte-associated antigen-4 (CTLA-4) in isolated vitiligo: a genotype-phenotype correlation. Pigment Cell Melanoma Res. 2011;24(4):737–40.
Dynoodt P, Mestdagh P, Peer GV, et al. Identification of miR-145 as a key regulator of the pigmentary process. J Invest Dermatol. 2013;133(1):201–9.
Dziarski R, Wang Q, Miyake K, Kirschning CJ, Gupta D. MD-2 enables Toll-like receptor 2 (TLR2)-mediated responses to lipopolysaccharide and enhances TLR2-mediated responses to Gram-positive and Gram-negative bacteria and their cell wall components. J Immunol. 2001;166(3):1938–44.
Griffiths-Jones S. miRBase: the microRNA sequence database, MicroRNA protocols. Methods Mol Biol. 2006;342:129–38.
Grimes PE, Sevall JS, Vojdani A. Cytomegalovirus DNA identified in skin biopsy specimens of patients with vitiligo. J Am Acad Dermatol. 1996;35(1):21–6.
Hafner C, Groesser L. Mosaic RASopathies. Cell Cycle. 2013;12 https://doi.org/10.4161/cc.23108.
Han MK, Song EK, Guo Y, et al. SIRT1 regulates apoptosis and Nanog expression in mouse embryonic stem cells by controlling p53 subcellular localization. Cell Stem Cell. 2008;2(3):241–51.
Handa S, Kaur I. Vitiligo: clinical findings in 1436 patients. J Dermatol. 1999;26(10):653–7.
Harman M, Durdu M, Ibiloglu I. Acrokeratosis verruciformis of Hopf exhibiting Darier disease-like cytological features. Clin Exp Dermatol. 2016;41(7):761–3.
Hayashi M, Jin Y, Yorgov D, et al. Autoimmune vitiligo is associated with gain-of-function by a transcriptional regulator that elevates expression of HLA-A* 02:01 in vivo. Proc Natl Acad Sci U S A. 2016;113(5):1357–62.
Hedrich CM, Fiebig B, Hauck FH, et al. Chilblain lupus erythematosus—a review of literature. J Clin Rheumatol. 2008;27:949–54.
Howitz J, Brodthagen H, Schwartz M, et al. Prevalence of vitiligo: epidemiological survey on the Isle of Bornholm, Denmark. Arch Dermatol. 1977;113(1):47–52.
Huang DW, Sherman BT, Lempicki RA. Bioinformatics enrichment tools: paths toward the comprehensive functional analysis of large gene lists. Nucleic Acids Res. 2008;37(1):1–3.
Huang DW, Sherman BT, Lempicki RA. Systematic and integrative analysis of large gene lists using DAVID bioinformatics resources. Nat Protoc. 2009;4(1):44–57.
Huang KP, Mullangi S, Guo Y, et al. Autoimmune, atopic, and mental health comorbid conditions associated with alopecia areata in the United States. JAMA Dermatol. 2013;149(7):789–94.
Hubner RA, Lubbe S, Chandler I, et al. MTHFR C677T has differential influence on risk of MSI and MSS colorectal cancer. Hum Mol Gen. 2007;16(9):1072–7.
Im S, Lee ES, Kim W, et al. Donor specific response of estrogen and progesterone on cultured human melanocytes. J Korean Med Sci. 2002;17(1):58.
Imran M, Laddha NC, Dwivedi M, et al. Interleukin-4 genetic variants correlate with its transcript and protein levels in patients with vitiligo. Br J Dermatol. 2012;167(2):314–23.
Irvine AD, McLean WH. The molecular genetics of the genodermatoses: progress to date and future directions. Br J Dermatol. 2003;148:1–13.
Jahan P, Tippisetty S, Komaravalli PL. FOXP3 is a promising and potential candidate gene in generalised vitiligo susceptibility. Front Genet. 2015;6 https://doi.org/10.3389/fgene.2015.00249.
Jeker LT, Zhou X, Gershberg K, et al. MicroRNA 10a marks regulatory T cells. PLoS One. 2012;7(5):e36684.
Jin SY, Park HH, Li GZ, et al. Association of estrogen receptor 1 intron 1 C/T polymorphism in Korean vitiligo patients. J Dermatol Sci. 2004;35(3):181–6.
Karaca N, Ozturk G, Gerceker BT, et al. TLR2 and TLR4 gene polymorphisms in Turkish vitiligo patients. J Eur Acad Dermatol Venereol. 2013;27(1):e85.
Knox C, Law V, Jewison T, et al. DrugBank 3.0: a comprehensive resource for 'omics' research on drugs. Nucleic Acids Res. 2011;39(Database issue):D1035–41.
Krishnaram AS, Saigal A, Adityan B. Alopecia areata-vitiligo overlap syndrome: an emerging clinical variant. Indian J Dermatol Venereol Leprol. 2013;79(4):535–7. https://doi.org/10.4103/0378-6323.113100.
Kumar P, Henikoff S, Ng PC. Predicting the effects of coding non-synonymous variants on protein function using the SIFT algorithm. Nat Protoc. 2009;4(7):1073–81.
Laddha NC, Dwivedi M, Gani AR, et al. Involvement of superoxide dismutase isoenzymes and their genetic variants in progression of and higher susceptibility to vitiligo. Free Radic Biol Med. 2013;65:1110–25.
Laddha NC, Dwivedi M, Mansuri MS, et al. Association of neuropeptide Y (NPY), interleukin-1B (IL1B) genetic variants and correlation of IL1B transcript levels with vitiligo susceptibility. PLoS One. 2014;9(9):e107020.
Larribere L, Khaled M, Tartare-Deckert S, et al. PI3K mediates protection against TRAIL-induced apoptosis in primary human melanocytes. Cell Death Differ. 2004;11(10):1084–91.
Levy C, Khaled M, Iliopoulos D, Janas MM, Schubert S, et al. Intronic miR-211 assumes the tumor suppressive function of its host gene in melanoma. Mol Cell. 2010;40(5):841–9.
Lewis SN, Nsoesie E, Weeks C, et al. Prediction of disease and phenotype associations from genome-wide association studies. PLoS One. 2011;6(11):e27175.
Li Y, Qiu C, Tu J, et al. HMDD v2. 0: a database for experimentally supported human microRNA and disease associations. Nucleic Acids Res. 2014;42(D1):D1070–4.

Liu L, Li C, Gao J, et al. Genetic polymorphisms of glutathione S-transferase and risk of vitiligo in the Chinese population. J Invest Dermatol. 2009;129(11):2646–52.
Magesh R, Doss CGP. Computational pipeline to identify and characterize functional mutations in ornithine transcarbamylase deficiency. 3 Biotech. 2014;4(6):621–34.
Manga P, Sheyn D, Yang F, et al. A role for Tyrosinase-related protein 1 in 4-tert-butylphenol-induced toxicity in melanocytes: implications for vitiligo. Am J Pathol. 2006;169(5):1652–62.
Mansuri MS, Singh M, Begum R. miRNA signatures and transcriptional regulation of their target genes in vitiligo. J Dermatol. 2016; 84(1):50–8.
Marren P, Wilson C, Dawber RPR, et al. Hereditary hypotrichosis (Marie-Unna type) and juvenile macular degeneration (Stargardt's maculopathy). Clin Exp Dermatol. 1992;17:189–91.
Maruthappu T, Scott CA, Kelsell DP. Discovery in genetic skin disease: the impact of high throughput genetic technologies. Genes (Basel). 2014; 5(3):615–34.
Merx S, Neumaier M, Wagner H, et al. Characterization and investigation of single nucleotide polymorphisms and a novel TLR2 mutation in the human TLR2 gene. Hum Mol Gen. 2007;16(10):1225–32.
Mi H, Lazareva-Ulitsky B, Loo R, et al. The PANTHER database of protein families, subfamilies, functions and pathways. Nucleic Acids Res. 2005;33(suppl_1):D284–8.
Miller Z, Ao L, Bo K, Lee W. Inhibitors of the immunoproteasome: current status and future directions. Curr Pharm Des. 2013;19(22):4140–51.
Mir A, Wu T, Orlow SJ. Cutaneous features of crouzon syndrome with acanthosis Nigricans. JAMA Dermatol. 2013;149:737–41.
Mitra K, Carnuvis AR, Ramesh SK, et al. Integrative approaches for finding modular structure in biological networks. Nat Rev Genet. 2013;14(10):719–32.
Morita H, Taguchi J, Kurihara H, et al. Genetic polymorphism of 5, 10-methylenetetrahydrofolate reductase (MTHFR) as a risk factor for coronary artery disease. Circulation. 1997;95(8):2032–6.
Nanda S, Bathon JM. Etanercept: a clinical review of current and emerging indications. Expert Opin Pharmacother 2004. 2004;5(5):1175–86.
Nandagopal N, Ali AK, Komal AK, et al. The critical role of IL-15–PI3K–mTOR pathway in natural killer cell effector functions. Front Immunol. 2014;5 https://doi.org/10.3389/fimmu.2015.00355.
Nath SK, Kelly JA. Evidence for a susceptibility gene, SLEV1, on chromosome 17p13 in families with vitiligo-related systemic lupus erythematosus. Am J Hum Genet. 2001;69(6):1401–6.
Nebert DW, Vasiliou V. Analysis of the glutathione S-transferase (GST) gene family. Hum Genomics. 2004;1(6):460.
Njoo MD, Westerhof W. The development of guidelines for the treatment of vitiligo. Arch Dermatol. 1999;135(12):1514–21.
Ogus AC, Yoldas B, Ozdemir T, et al. The Arg753GLn polymorphism of the human toll-like receptor 2 gene in tuberculosis disease. Eur Respir J. 2004;23(2):219–23.
Oliveira-Nascimento L, Massari P, Wetzler LM. The role of TLR2 in infection and immunity. Front Immunol. 2012;3 https://doi.org/10.3389/fimmu.2012.00079.
Park J, Lee DS, Christakis NA, et al. The impact of cellular networks on disease comorbidity. Mol Sys Biol. 2009;5:262.
Pejaver V, Urresti J, Lugo-Martinez J, et al. MutPred2: inferring the molecular and phenotypic impact of amino acid variants. bioRxiv. 2017:134981. https://doi.org/10.1101/134981.
Petersen B, Petersen TN, Andersen P, et al. A generic method for assignment of reliability scores applied to solvent accessibility predictions. BMC Struct Biol. 2009;9(1):51.
Petry V, Gaspari AA. Toll-like receptors and dermatology. Int J Dermatol. 2009;48(6):558–70.
Picardo M, Dell'Anna ML, Ezzedine K, et al. Vitiligo. Nat Rev Dis Primers. 2015;1:15011.
Pinero J, Queralt-Rosinach N, Bravo A, et al. DisGeNET: a discovery platform for the dynamical exploration of human diseases and their genes. Database. 2015; https://doi.org/10.1093/database/bav028.
Qiu Y, Yang J, Wang W, et al. HMGB1-promoted and TLR2/4-dependent NK cell maturation and activation take part in rotavirus-induced murine biliary atresia. PLoS Pathog. 2014;10(3):e1004011.
Raby AC, Holst B, Le Boulder E, et al. Targeting the TLR co-receptor CD14 with TLR2-derived peptides modulates immune responses to pathogens. Sci Transl Med. 2013;5(185):185ra64.
Rigopoulos D, Gregoriou S, Larios G, et al. Etanercept in the treatment of vitiligo. Dermatology (Basel). 2007;215(1):84–5.
Šahmatova L, Tankov S, Prans E, et al. MicroRNA-155 is dysregulated in the skin of patients with vitiligo and inhibits melanogenesis-associated genes in melanocytes and keratinocytes. Acta Derm Venereol. 2016;96(6):742–8.
Saunders LR, Sharma AD, Tawney J, et al. miRNAs regulate SIRT1 expression during mouse embryonic stem cell differentiation and in adult mouse tissues. Aging (Albany NY). 2010;2(7):415.
Shang J, Eberle J, Geilen CC, et al. The role of nuclear factor-kappaB and melanogenesis in tumor necrosis factor-alpha-induced apoptosis of normal human melanocytes. Skin Pharmacol Physiol. 2002;15(5):321–9.
Shannon P, Markiel A, Ozier O, et al. Cytoscape: a software environment for integrated models of biomolecular interaction networks. Genome Res. 2003;13(11):2498–504.
Shen C, Gao J, Sheng Y, et al. Genetic susceptibility to vitiligo: GWAS approaches for identifying vitiligo susceptibility genes and loci. Front Genet. 2016;7:3.
Sherry ST, Ward M-H, Kholodov M, et al. dbSNP: the NCBI database of genetic variation. Nucleic Acids Res. 2001;29(1):308–11.
Singh S, Singh U, Pandey SS. Serum concentration of IL-6, IL-2, TNF-α, and IFNγ in vitiligo patients. Indian J Dermatol. 2012;57(1):12.
Smith FJD, Fisher MP, Healey E, et al. Novel keratin 16 mutation and protein expression studies in pachyonychia congenita type 1 and focal palmoplantar keratoderma. Exp Dermatol. 2000;9(3):170–7.
Solomon O, Kunik V, Simon A, et al. G23D: online tool for mapping and visualization of genomic variants on 3D protein structures. BMC Genomics. 2016;17(1):681.
Spritz RA. The genetics of generalized vitiligo: autoimmune pathways and an inverse relationship with malignant melanoma. Genome Med. 2010;2(10):78.
Srivastava I, Khurana P, Yadav M, et al. An integrative systems biology approach to unravel potential drug candidates for multiple age related disorders. Biochim Biophys Acta, Proteins Proteomics. 2017;1865:1729.
Sturm RA, Duffy DL. Human pigmentation genes under environmental selection. Genome Biol. 2012;13(9):248.
Takemura S, Braun A, Crowson C, et al. Lymphoid neogenesis in rheumatoid synovitis. J Immunol. 2001;167(2):1072–80.
Traks T, Keermann M, Karelson M, et al. Polymorphisms in Toll-like receptor genes are associated with vitiligo. Front Genet. 2015;6:278.
Tu C, Zhao D, Lin X. Levels of neuropeptide-Y in the plasma and skin tissue fluids of patients with vitiligo. J Dermatol Sci. 2001;27(3):178–82.
Vitkup D, Sander C, Church GM. The amino-acid mutational spectrum of human genetic disease. Genome Biol. 2003;4(11):R72.
Von Mering C, Jensen LJ, Snel B, et al. STRING: known and predicted protein–protein associations, integrated and transferred across organisms. Nucleic Acids Res. 2005;33:D433–7.
Wang CQ, Cruz-Inigo AE, Fuentes-Duculan J, et al. Th17 cells and activated dendritic cells are increased in vitiligo lesions. PLoS One. 2011;6(4):e18907.
Wang K, Li M, Hakonarson H. Analysing biological pathways in genome-wide association studies. Nat Rev Genet. 2010;11(12):843–54.
Werth VP, White WL, Sanchez MR. Incidence of alopecia areata in lupus erythematosus. Arch Dermatol. 1992;128:368–71.
Xiong Y, Song C, Snyder GA, et al. R753Q polymorphism inhibits Toll-like receptor (TLR) 2 tyrosine phosphorylation, dimerization with TLR6, and recruitment of myeloid differentiation primary response protein 88. J Biol Chem. 2012; 287(45):38327–37.
Yildirim MA, Goh KI, Barabasi AL, et al. Drug-target network. Nat Biotechnol. 2007; 25(10):1119–26.
Yu L, Huang J, et al. Inferring drug-disease associations based on known protein complexes. BMC Med Genet. 2015;8(2):S2.
Zonana J, Elder ME, Schneider LC, et al. A novel X-linked disorder of immune deficiency and hypohidrotic ectodermal dysplasia is allelic to incontinentia pigmenti and due to mutations in IKK-gamma (NEMO). Am J Hum Genet. 2000;67(6):1555–62.

Available online at www.sciencedirect.com

ScienceDirect

Materials Today: Proceedings 5 (2018) 15261–15266

materialstoday: PROCEEDINGS

www.materialstoday.com/proceedings

ISCAS 2017

Dielectric and absorption properties of as-grown Bilayer and Single layer graphene at the microwave frequencies

Kamlesh Patel[1,2] and Pawan K. Tyagi[1*]

[1] Department of Applied Physics, Delhi Technological University, Delhi 110042, India

[2] Department of Electronic Science, University of Delhi South Campus, New Delhi 110021, India

Abstract

The advent of two-dimensional (2-D) graphene, single atomic thick layer of graphite, has stimulated the research interest in other 2-D materials. Transition-metal dichalcogenides (TMDs) are among them. Recently, 2D materials have demonstrated a promising material from the perspective of both fundamentals as well as applications. They exhibit unique optoelectronic properties, which can be largely tuned by varying the thickness. More recently, thermal chemical vapor deposition (CVD) or HFCVD have been developed for the growth of these 2D materials. Microwave measurements have been performed in microstrip line based test fixture to obtain the real and imaginary parts of complex relative permittivity, then the loss tangent and absorption coefficients of bilayer and single layer graphene are extracted. Bilayer graphene exhibits lower absorption coefficient of 0.6 dB/cm at 26.5 GHz. We envision that reported results would help to understand the dielectric and absorption properties of as-grown graphene layer in microwave frequency range.

© 2018 Elsevier Ltd. All rights reserved.

Selection and Peer-review under responsibility of 10th NATIONAL CONFERENCE ON SOLID STATE CHEMISTRY AND ALLIED AREAS (ISCAS - 2017).

Keywords: Single layer graphene; Bilayer graphene; Relative permittivity; Microwave absorption; Microstrip line

*Email address: pawan.phy@dce.edu, pawankumartyagi@gmail.com

2214-7853 © 2018 Elsevier Ltd. All rights reserved.

Selection and Peer-review under responsibility of 10th NATIONAL CONFERENCE ON SOLID STATE CHEMISTRY AND ALLIED AREAS (ISCAS - 2017).

1 Introduction

Recently, few layer graphene (FLG) is reported to exhibit carrier mobility as high as 10^5 $cm^2/V.s$ at room temperature [1], controllable foil resistance from 100 to 8.8 Ω/sq (ohms per square), foil carrier density as high as 8.9×10^{14} cm^{-2} and carrier mean free path as large as ~ 0.6 μm [2], along with impressive flexibility and controllable conductivity. In addition, graphene is considered as a massless and gapless Dirac quasi-particle system with rough linear energy dispersion [3]. These outstanding properties of graphene have made it a potential candidate for application in sensors to terahertz (THz) devices. In addition, the characteristic of graphene has been explored for the microwave absorption and electromagnetic shielding abilities. Different materials like polymer microcellular foams, polyaniline nanorod arrays, nanoplatelet-epoxy etc. with graphene particles have been studied [4–7] and demonstrated interesting electromagnetic absorption. Such composite improves the electromagnetic wave absorption through additional relaxation processes, namely dielectric, dipole, and polarization relaxations. However, the absorption property of graphene layer is unexplored and so the present paper deals with determining the graphene absorption property in 10 MHz - 26.5 GHz frequency range. Such information could be useful for the microwave isolation of components developed using the multilayer graphene and related microwave absorption applications.

2 Graphene Samples

In the present study, single layer graphene transferred on both glass and quartz of thickness 0.7 mm and 1.0 mm, respectively of area 1″×1″ were used which was procured from Graphene Industries, USA. Bilayer graphene was grown by using Hot Filament Chemical Vapor Deposition (HFCVD) System. Commercially available Cu foil with a thickness of 25 μm were cut into 1/2″×1/4″ pieces to be used as substrate. Initially, Cu foil was ultrasonicated in acetone for 10 min, acetic acid for 10 min, and then washed with DI water. After drying the foil, it was placed in the chamber. Initially, bilayer graphene sample on Cu foil was developed by heating upto 850°C from the room temperature (RT) 27°C along with flow of H_2 at 50 sccm and pressure of 35 torr. After 10 minutes, CH_4 at a flow rate of 10 sccm and pressure of 35 torr was supplied to the processing chamber for next 10 minutes along with H_2. Then temperature is cooled down to the RT with flow of H_2. These bilayer graphene samples on Cu foil are designated as BLG/Cu, whereas the procured graphene samples are designated as SLG/glass and SLG/quartz, respectively.

3 Characterization of Graphene samples

3.1 Raman Spectroscopy

In the Raman spectra shown in Fig.1 for single layer graphene transferred on glass and quartz (a), three sharp peaks were indexed as G, 2D satellite and 2D bands. The peak position of various bands are found at ω_D ~1341.83 cm^{-1}, ω_G ~1587.12 cm^{-1}, $\omega_{2Dsatelite}$ ~2452.092 cm^{-1}, and ω_{2D} ~2688.67 cm^{-1} for graphene on glass substrate, whereas for graphene on quartz substrate, these values are at ω_D ~1341.83 cm^{-1}, ω_G ~1587.16 cm^{-1}, $\omega_{2Dsatelite}$ ~ 2452.73 cm^{-1}, and ω_{2D} ~2688.82 cm^{-1}. The insignificant D-band indicating that graphene layers are free from defects. The I_{2D}/I_G ratio is calculated as ~3.69 (on glass) and ~ 4.1 (on quartz), which has confirmed that a single layer graphene was present on both substrates. Raman spectra for bilayer graphene on Cu is shown after curve fitting in Fig. 1(b), three sharp peaks were indexed as D, G and 2D bands for as-grown graphene samples. The peak positions for BLG/Cu are found at ω_D ~1342 cm^{-1}, ω_G ~1588 cm^{-1}, and ω_{2D} ~ 2713 cm^{-1}. The I_{2D}/I_G ratio is evaluated as ~0.55 for BLG/Cu, which verified that a bilayer graphene is deposited.

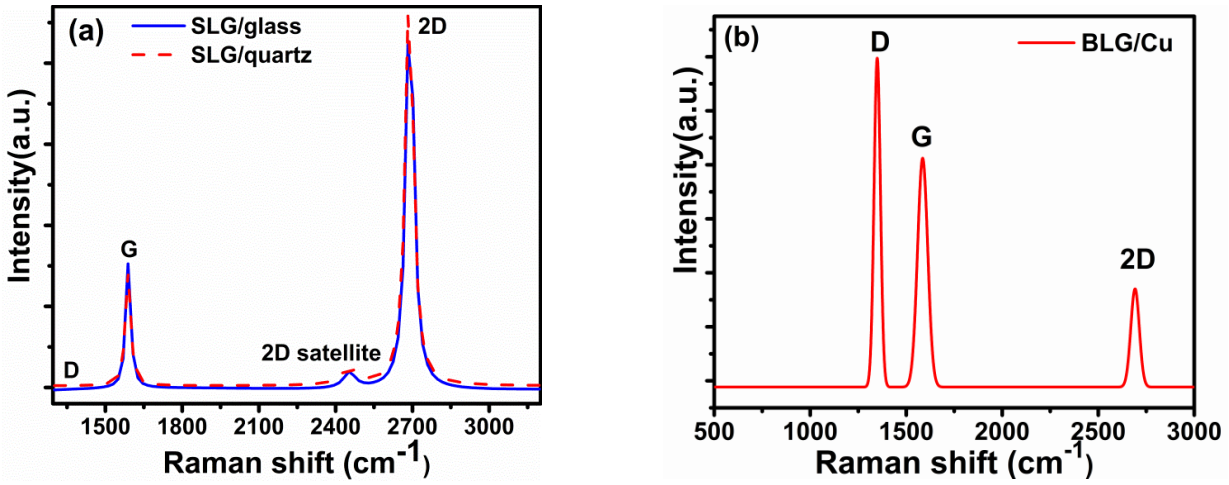


Fig. 1. Raman spectra of (a) SLG on glass and quartz, (b) BLG on Cu.

3.2 Microwave characterization of graphene samples

A 5.08 cm long microstrip line was fabricated on FR-4 substrate (ε_r = 4.4 and height= 1.5 mm). As shown in Fig. 2(a), the microstrip line with sample holder was connected between ports (A and B) of calibrated vector network analyzer model N5227A of Keysight Technologies Inc. and S-parameters were measured for unloaded microstrip line from 10 MHz to 26.5 GHz.

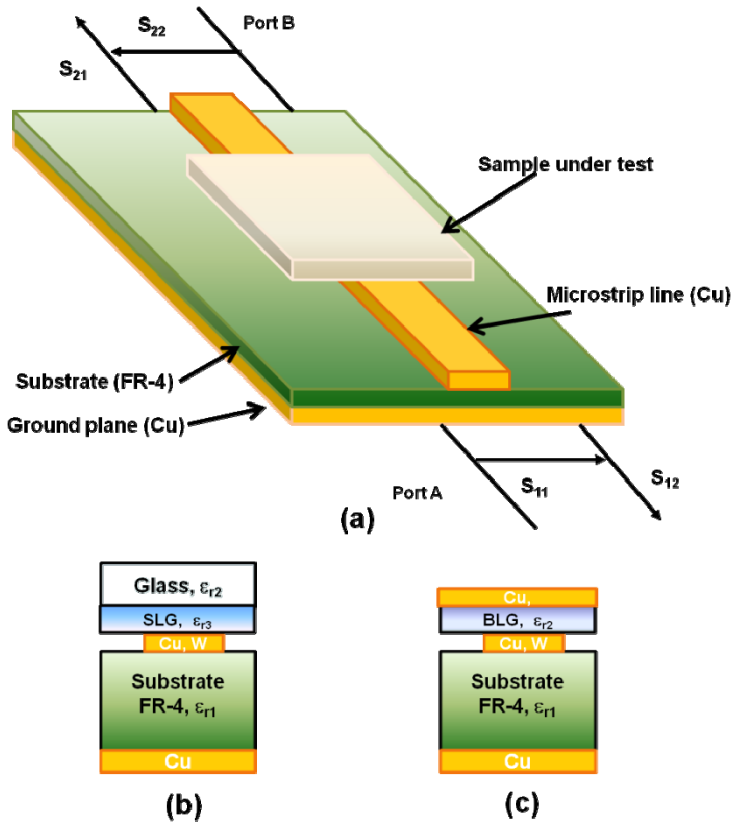
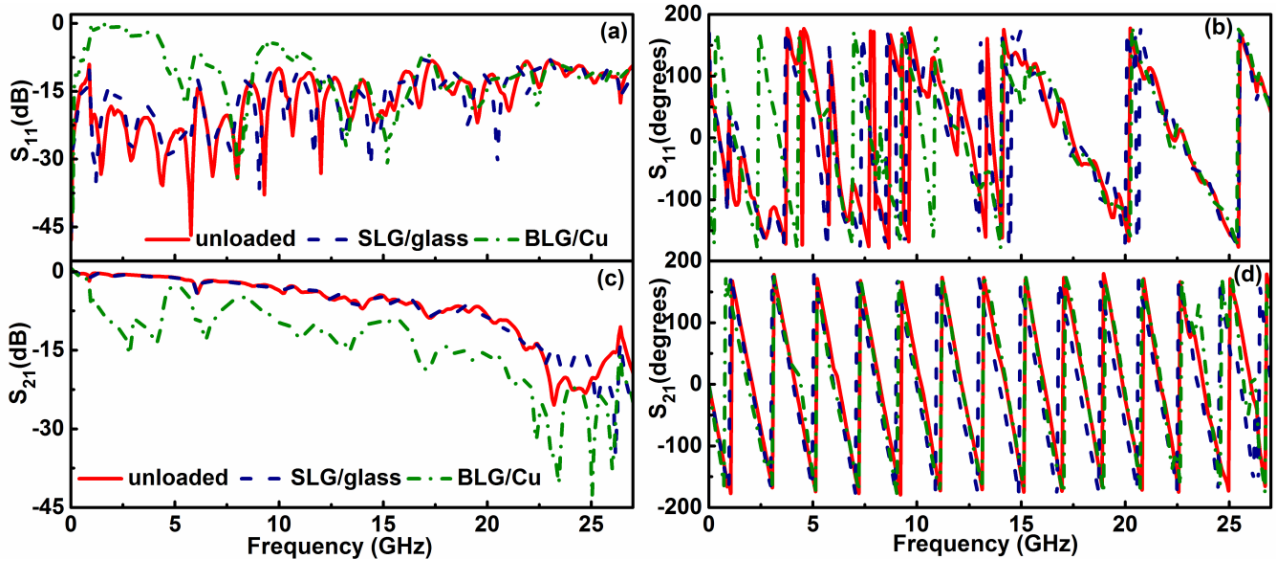


Fig. 2. Microwave measurement arrangement (a) Microstrip line based fixture, (b) Placement of SLG/glass and SLG/quartz and (c) Placement of BLG/Cu.

Then microstrip line was loaded by SLG/glass, SLG/quartz and BLG/Cu one by one and then S-parameters were measured individually. Figs. 2(b) and 2(c) show the arrangements of loading on the microstrip line for single layer graphene and bilayer graphene, respectively.



FIig. 3. Measured S-parameters of microstrip line, unloaded and loaded with SLG/glass and BLG/Cu
(a) S_{11}(dB), (b) S_{11}(degree), (c) S_{21}(dB) and (d) S_{21}(degree)

For the middle part of the microstrip line i.e. loaded by the sample, the S-parameters were obtained by using standard transmission line (ABCD) parameters based de-embedded method [8]. For unloaded microstrip line and the ones loaded with SLG/glass and BLG/Cu, the measured complex reflection (S_{11}) and transmission (S_{21}) parameters have been shown in Fig. 3(a-d). As shown in Fig. 4a, high input reflection coefficient (S_{11}) is found for SLG/glass and BLG/Cu loading in the lower frequency range up to 12 GHz. As the bilayer graphene is covered by Cu, the higher reflection in microstrip line indicates change in the effective impedance at lower frequency [9]. At higher frequency, similar S_{11} is observed for both loadings due to more field concentration in FR4 substrate after 12 GHz.
The phase of S_{11} has random shifts at lower frequencies, whereas loading shifted the peaks of phase towards lower frequencies as observed in Fig. 4(b). Differences in the phase shift amount are indicating that both graphene samples have different material properties at the microwave frequencies.
In Fig. 3(c-d), the magnitudes of forward (S_{21}) transmission parameter are found to be decreased as frequency increased, due to the lossy nature of microstrip line. Compared to unloaded microstrip line, lower S_{21} for SLG/glass and BLG/Cu, indicate loss of transmission power, the loss become more prominent with BLG/Cu (> 12 dB) upto 20 GHz. The peak values of S_{21} phase is found to be shifted towards lower frequencies with loadings in Fig. 4 (d), which is in result of dielectric kind of loading. In addition, high values > -15 dB of S_{11} suggest that unloaded microstrip line has become more reflecting at frequencies above 10 GHz.

4 Results and discussions

4.1 Complex relative permittivity of single and bilayer graphene

From the de-embedded S-parameters for microstrip line loaded with SLG/glass, SLG/quartz and BLG/Cu, the complex propagation constant (γ) is obtained [10]. The effective relative permittivity ε_{reff} of loaded middle microstrip line is evaluated as $(\gamma/\gamma_0)^2$ [11], where $\gamma_0 = j2\pi f/c$, f is operating frequency in Hz and c (= 2.998×10^8 m/s) is the velocity of light. As shown in Figs. 3(b) and 3(c), SLG is third layer and BLG is second layer in the arrangements and by applying the conformal mapping technique [12-14], the intrinsic complex relative permittivity (ε_r*) for all graphene samples have been obtained from the respective ε_{reff} values. The graphene samples are now designated as SLG_g, SLG_q and BLG and their ε_r* values are shown in Fig. 4.

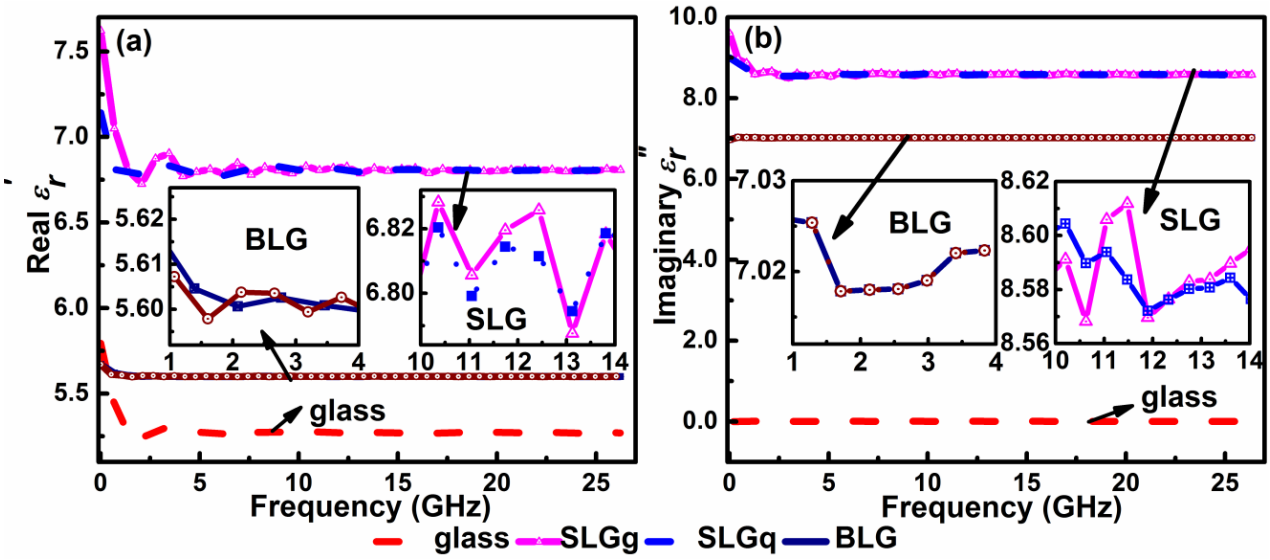


Fig. 4. (a) Real (ε_r') and (b) Imaginary (ε_r'') parts of complex relative permittivity for glass, SLG and BLG samples.

For validity of the adopted method, the complex relative permittivity of a glass is determined and the real part (ε_r') for glass substrate has been found in 5.17 – 5.30 range whereas the imaginary part (ε_r'') was in the range of 0.0001-0.01. These values are in good agreement with reported ε_r^* of supplied Corning glass substrate given by the manufacturer's specifications. The ε_r' of SLG_g and SLG_q has been found to decrease with frequency and reaches to ~6.71 @ 1.92 GHz and become constant at value ~ 6.80 till 26.5 GHz, whereas ε_r'' is decreased from ~ 9.58 @ 10 MHz to the value ~ 8.47 after 1.92 GHz. Both parts of ε_r^* were found to have slightly higher variations over most of the frequencies as seen in the insets of Fig. 4(a-b). For BLG_1/Cu and BLG_2/Cu, nearly constant ε_r' and ε_r'' are found of ~5.60 and ~7.02 for frequency >2 GHz, which is also confirmed in the insets, where both ε_r' and ε_r'' have displayed insignificant variations with frequency. Slightly lower values of ε_r' and ε_r'' for BLG than SLG suggest that BLG can absorb similar amount of microwave energy as by SLG with comparatively less dissipation (lesser ε_r') as a heat. As both parameters give a constant value for BLG, this frequency independent behavior suggests that it can be utilized as a high power microwave absorber as well as broadband substrate material for planar microwave passive components.

4.2 Absorption of single and bilayer graphene

To obtain the amount of microwave absorption, we first evaluated the loss tangent ($\tan\delta = \varepsilon_r''/\varepsilon_r'$) and then the absorption coefficient (α) is obtained by using the following formula [15].

$$\alpha = A \times \frac{\omega\sqrt{\mu_r'\varepsilon_r'}}{2c} \times \sqrt{\left[\sqrt{1+(\tan\delta)^2}\right]-1} \qquad (1)$$

where, A is adjustment factor (= 8.86/100 dB/Np), c is velocity of light, ε_r' and μ_r' are the relative permittivity and permeability of the material under test. We have taken $\mu_r' = 1$ for SLG and BLG. The evaluated parameters are shown in Fig. 5.

Fig. 5(a) shows the oscillating variation of loss tangent with frequency for SLG and BLG samples, whose values are found to be constant at nearly 1.262 in SLG and 1.253 in BLG. The absorption coefficient linearly increases with frequency from nearly zero at 10 MHz to 0.7 dB/cm in SLG and 0.6 dB/cm in BLG at 26.5 GHz, respectively. These patterns are well agreement with the graphene composite materials reported earlier [15]. We attribute the lower

absorption coefficient in BLG to the lightweight experience of photons than SLG while passing through these layers [16].

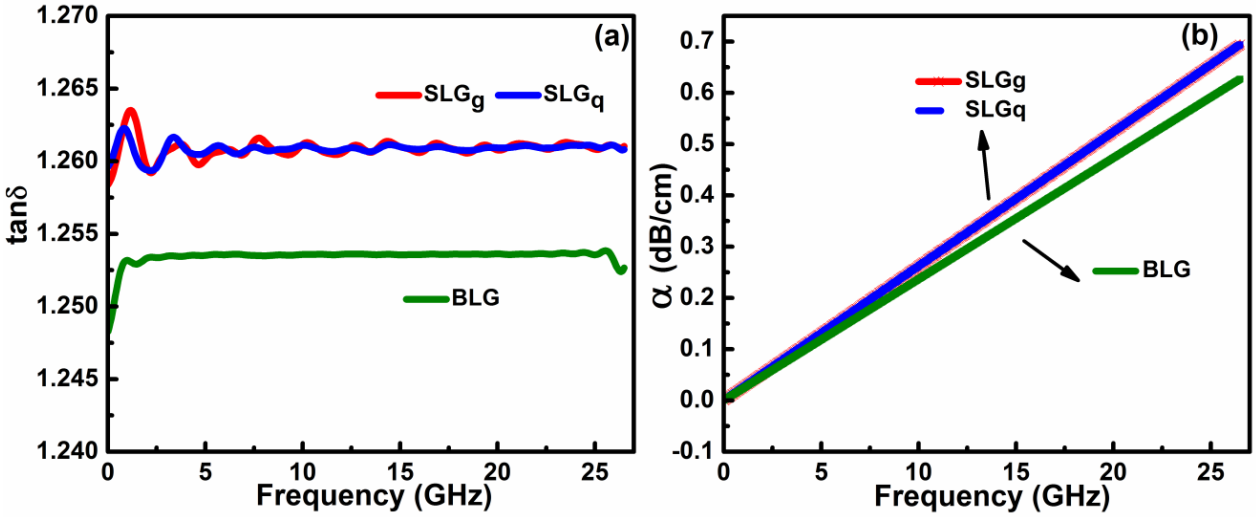


Fig.5. (a) Loss tangent (tanδ) and (b) Absorption coefficient α (dB/cm) for SLG and BLG samples.

5 Conclusions

Dielectric and absorption properties of as-grown BLG on Cu and SLG transferred on glass and quartz have been studied and compared in frequency range from 10 MHz to 26.5 GHz. Our results confirmed that BLG is a better dielectric material than the SLG as it dissipates less microwave energy and can be useful for the microwave passive component developments. Slightly lower value of absorption coefficient in BLG is led to lightweight photons than in SLG. The present analysis would encourage the application of graphene in the microwave components and as well as transparent conducting electrode in Si heterojunction solar cell.

Acknowledgements

This work is financially supported by DST-SERB, fast track Program (SR/FTP/PS-055/2012) and DST-FCT, Portugal bilateral Program (INT/PORTUGAL/P-13/2013).

References

[1].A. S. Mayorov, R. V. Gorbachev, S. V. Morozov, L. Britnell, R. Jalil, L. A. Ponomarenko, et al., Nano Lett. 11 (2011) 2396–2399
[2].I. Khrapach, F. Withers, T. H. Bointon, D. K. Polyushkin, W. L. Barnes , S. Russo, and M. F. Craciun, Novel highly conductive and transparent graphene-based conductors, Adv. Mater. 24 (2012) 2844-2849
[3].E. Tiras, S. Ardali, T. Tiras, E. Arslan, S. Cakmakyapan, O. Kazar, et al, J. Appl. Phys. 113 (2013) 43708
[4].C. Wang, X. Han, P. Xu, X. Zhang, Y. Du, S. Hu, J. Wang, X. Wang, Appl. Phys. Lett. 98 (2011) 072906.
[5].H. B. Zang, Q.Yan, W. G. Zheng, Z. He, Z. Z. Yu, ACS Appl. Mater. Interfaces 3 (2011) 918–924
[6].H. Yu, T. Wang, B. Wen, M. Lu, Z. Xu, C. Zhu, Y. Chen, X. Xue, C. Sun, M. Cao, J. Mater. Chem. 22 (2012) 21679–21685
[7].Z. Wang, J. Luo, G. L. Zhao, AIP Adv. 4 (2014) 017139
[8].J. C. Rautio, Int. J. Microwave Millimeter Wave Compter-Aided Engg. 1 (1991) 282-287
[9].D. M. Pozar, *Microwave Engineering*. 4th ed. John Wiley & Sons, Inc., USA, 2012.
[10].A. Koul, P. K. R. Anmula, M. Y. Koledintseva, J. L. Drewniak, S. Hinaga, in Proceedings of IEEE EMC Symposium,Austin, USA (2009) 191-196.
[11].Y. Wu, Y. Xu, Z. Wang, C. Xu, Z. Tang, Y. Chen, R. Xu, Appl. Phys. Lett. 101 (2012) 053110
[12].J. Sva˘cina, IEEE Trans. Microwave Theory Tech. 40 (1992) 769-772
[13].J. Sva˘cina, IEEE Microwave Guided Wave Lett. 2 (1992) 385-387
[14] C. Wan and A. Hoorfar, IEEE Microwave Guided Wave Lett. 10 (2000) 223-224
[15].K. Rubrice, X. Castel, Mohd. Himdi and P. Parneix, Materials 9 (2016) 825
[16].K. Patel and Pawan K. Tyagi, Carbon 121 (2017) 56-62

Available online at www.sciencedirect.com

ScienceDirect

Procedia Computer Science 132 (2018) 595–605

Procedia Computer Science

www.elsevier.com/locate/procedia

International Conference on Computational Intelligence and Data Science (ICCIDS 2018)

Direct Power Neuro-Fuzzy Controller Scheme of Three-Phase PWM Rectifiers for Power Quality Improvement

Mustapha Jamma[a,*], Dheeraj Joshi[b], Mohammed Akherraz[a], Abderrahim Bennassar[a]

[a]*Mohammed V University of Rabat, Mohammadia School's of Engineers, Rabat, Morocco*
[b]*Electrical Engineering Department, Delhi Technological University, Delhi, India*

Abstract

This paper investigates the design of an improvement scheme of direct power control (DPC) based on adaptive neuro-fuzzy inference system (ANFIS) for mitigation of power quality problems. The proposed control technique is performed using two ANFIS blocks. The first ANFIS block uses the grid voltage vector position, the errors of the instantaneous active and reactive powers. The second ANFIS block utilizes the dc link voltage error and its change. The purpose of the proposed control algorithm is to regulate perfectly dc link voltage, to control directly the instantaneous powers, near-sinusoidal source current waveforms and unity power factor (UPF) operation. The regulation method has been developed and simulated using MATLAB/Simulink environment. The numerical simulation results confirm the validity of the proposed control technique for three-phase PWM rectifiers and have proved excellent robustness and performance.

© 2018 The Authors. Published by Elsevier Ltd.
This is an open access article under the CC BY-NC-ND license (https://creativecommons.org/licenses/by-nc-nd/3.0/)
Peer-review under responsibility of the scientific committee of the International Conference on Computational Intelligence and Data Science (ICCIDS 2018).

* Corresponding author. Tel.: +212-616-13-31-62; fax: +212-537-77-88-53.
E-mail address:jammamustapha@gmail.com

1877-0509 © 2018 The Authors. Published by Elsevier Ltd.
This is an open access article under the CC BY-NC-ND license (https://creativecommons.org/licenses/by-nc-nd/3.0/)
Peer-review under responsibility of the scientific committee of the International Conference on Computational Intelligence and Data Science (ICCIDS 2018).
10.1016/j.procs.2018.05.013

Keywords: Direct power control; adaptive neuro-fuzzy inference system; three-phase PWM rectifiers; power quality

1. Introduction

Nowadays, the widespread utilization of power electronics based equipment is increasing. The power distribution level getting disturbed and polluted due to an increase in power electronics based loads. These loads are nonlinear and produce current harmonics, which generate electromagnetic interference, power losses, insufficient reactive power and other power quality issues[1]. A lot of solutions have been discussed in the literature to avoid the power quality problems in distribution systems. The best solution is three phase pulse with modulation rectifiers, as it has several significant advantages, including UPF condition, low total harmonic distortion (THD) in input currents, bidirectional power flow and high regulation of dc link voltage[2]. Implementation of three phase PWM rectifiers has become possible due to very fast progress in digital signal processing system and power semiconductor technology[3]. It is now possible to choose a much more advanced control scheme for this type of power converter.

Different control methods have been proposed for the regulation of the three-phase PWM rectifiers. A voltage oriented control (VOC) is used in the last few decades, this control strategy can indirectly regulate the input powers by regulating the input current vector in the d-q coordinates[4]. The main features of VOC are fixed switching frequency, good stability of the steady state and good dynamics performance. Notwithstanding its merits, the performance of this control scheme is highly depend on the tuning of the proportional-integral controller parameters. Recently, another prominent control technique of three phase PWM rectifiers is DPC. This control strategy allows a decoupled instantaneous powers control, strong robustness to parameter variations and fast dynamic response[5]. DPC is same as to direct torque control (DTC) strategy of induction motors[6]. Therefore, the DPC does not need the transformation of coordinate, separate PWM block and internal current regulation. Hence, for the improvement of the system performances, significant studies which improve the conventional DPC technique have been conducted. Among these research works, we find the decoupled control of instantaneous powers with a single cost function using model predictive control method[7], sliding mode control technique[8], and etc. Furthermore, other control algorithms based on artificial intelligent techniques have been developed recently, such as fuzzy logic (FL) approach[9], and artificial neural networks (ANN) method[10].

On the other hand, the combination of the ANN approach and the FL technique has received during those days a great interest. So, it's using in a lot of area and exactly in control of power electronic converters, in order to achieved good advantages. The ANFIS is one of the most technique combining two intelligent methods to obtain a high-performance of the control system. In the present study, an improvement DPC technique based on ANFIS for three phase PWM rectifiers is proposed. This control technique combines ANN approach and FL theory for dc link voltage control and decoupled regulation of instantaneous powers with a UPF condition. Finally, the proposed direct power neuro-fuzzy control method was tested in simulation using MATLAB/Simulink environment.

The research paper is structured as: Section 2 depicts the modeling of three-phase PWM rectifier. Section 3 explains DPC principle. The developed direct power neuro-fuzzy controller is presented in Section 4. The design of ANFIS controller is described in Section 5. Section 6 present the results and discussion. Finally, conclusion is summarized in Section 7.

Nomenclature

e_{abc}	grid voltages
S_{abc}	switching states of rectifier
C	dc- link capacitor
R_L	resistive load
L	line inductance
R	line resistor

2. Modeling of three-phase PWM rectifier

The topology of three phase PWM rectifiers is presented in Fig. 1. Each leg has two switches and two switching states; S_i = 1 and 0, where the subscript i is equal to a, b and c. In three-phase PWM rectifiers there are 3^3 = 27 switching sequences. The dynamic model of the adopted converter is given by the equation system (1)

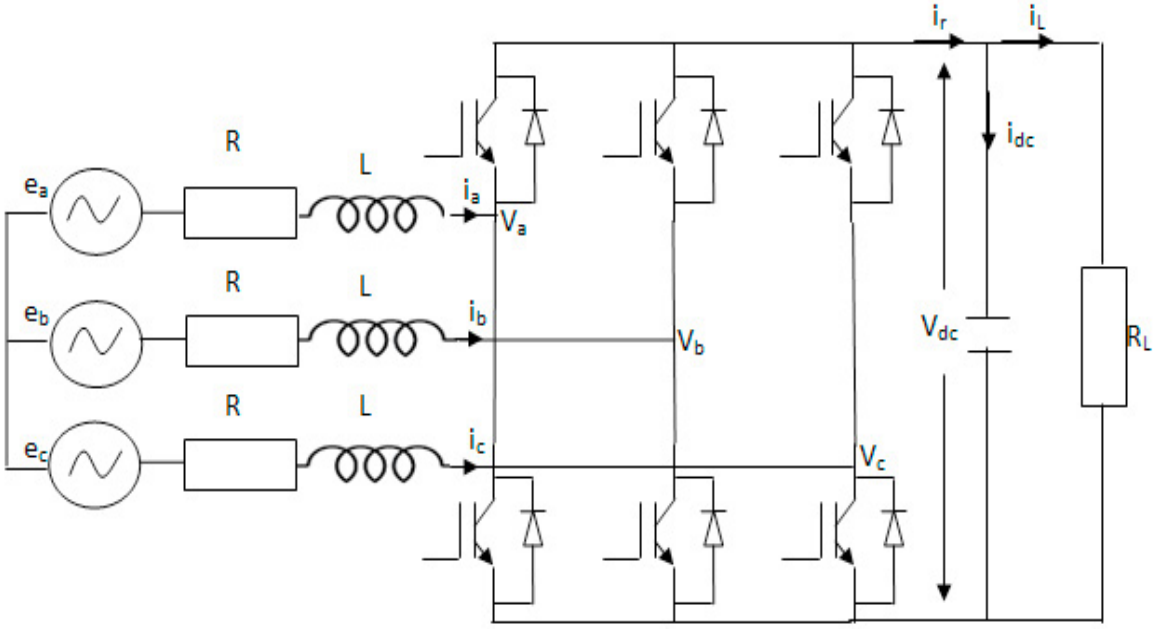


Fig. 1. Three-phase PWM rectifier circuit.

$$\begin{cases} \dfrac{di_\alpha}{dt} = \dfrac{1}{L}\left(e_\alpha - v_\alpha - Ri_\alpha\right) \\ \dfrac{di_\beta}{dt} = \dfrac{1}{L}\left(e_\beta - v_\beta - Ri_\beta\right) \\ C\dfrac{dv_{dc}}{dt} = S_\alpha i_\alpha + S_\beta i_\beta - i_L \end{cases} \tag{1}$$

3. Direct power control principle

In a DPC technique, it is possible to control directly the instantaneous powers using the selection of the appropriate voltage vectors states of the converter. The selection of these vectors is based on the made of the powers errors in the limits of the hysteresis comparators and the sector where is the position of the grid voltage vector. The application of DPC allows a decoupled control of instantaneous powers without using any current regulation loops and separate PWM block, which presents the simplicity of this regulation strategy. The conventional direct power control block diagram is given in Fig. 2.

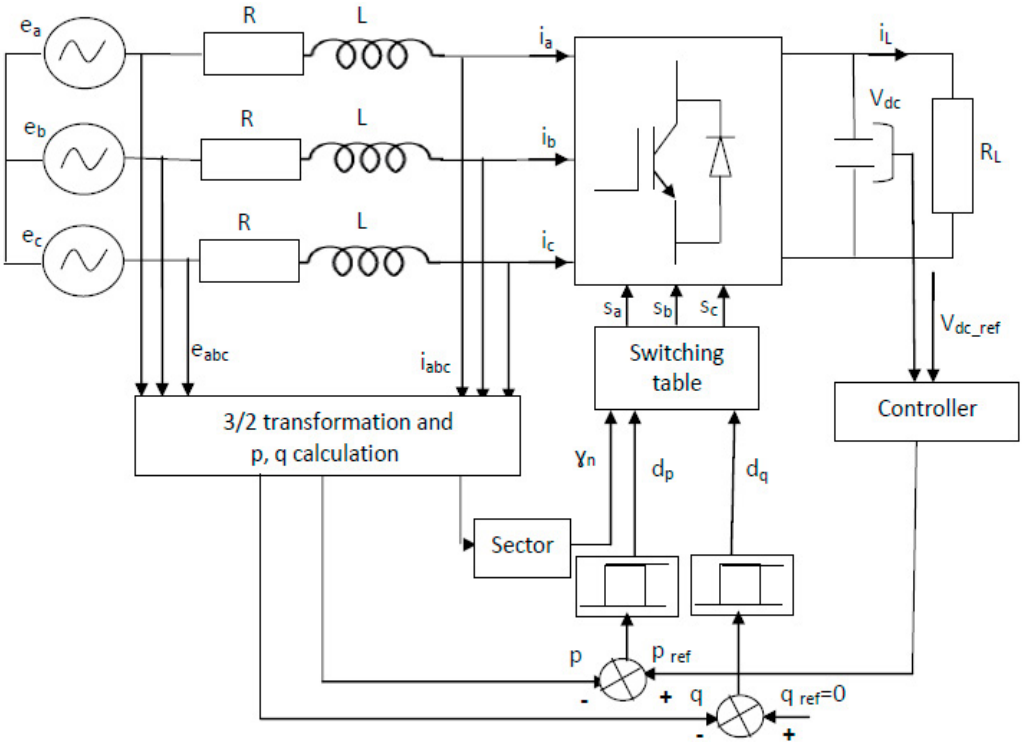


Fig. 2. Schematic diagram of conventional DPC.

The errors between the calculated and the reference powers are input into two levels hysteresis controllers. The output of these controllers given by the digitized signals d_p and d_q by following these expressions:

$$d_p = \begin{cases} 1, & p_{ref} - p \geq H_p \\ 0, & p_{ref} - p \leq -H_p \end{cases} \tag{2}$$

$$d_q = \begin{cases} 1, & q_{ref} - q \geq H_q \\ 0, & q_{ref} - q \leq -H_q \end{cases} \tag{3}$$

The position of the grid voltage vector is converted into digitized signal. Therefore, the α-β vectors plane are separated to 12 sectors, as defined in Fig. 3, it can be obtained numerically as follow:

$$(n-2)\frac{\pi}{6} \leq \gamma_n \leq (n-1)\frac{\pi}{6} \quad \text{n=1,2,...,12} \tag{4}$$

The switching table of the direct power control is given by table 1. Its inputs are the voltage vector position γ_n and the digitized errors d_p, d_q, where the switching states of the PWM rectifier are its outputs.

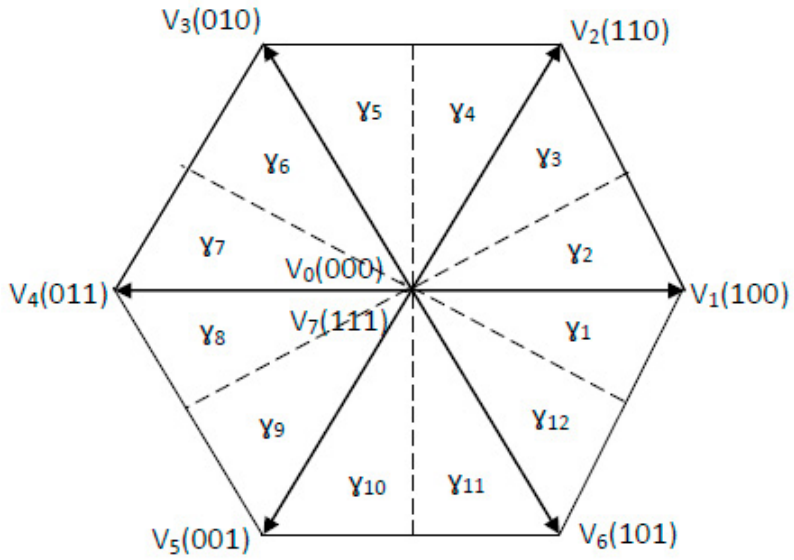


Fig. 3. Voltage vectors and 12 sectors.

Table 1. Switching table of DPC.

d_p	d_q	γ_1	γ_2	γ_3	γ_4	γ_5	γ_6	γ_7	γ_8	γ_9	γ_{10}	γ_{11}	γ_{12}
1	0	V_6	V_7	V_1	V_0	V_2	V_7	V_3	V_0	V_4	V_7	V_5	V_0
1	1	V_7	V_7	V_0	V_0	V_7	V_7	V_0	V_0	V_7	V_7	V_0	V_0
0	0	V_6	V_1	V_1	V_2	V_2	V_3	V_3	V_4	V_4	V_5	V_5	V_6
0	1	V_1	V_2	V_2	V_3	V_3	V_4	V_4	V_5	V_5	V_6	V_6	V_1

In (α-β) coordinates the instantaneous active (p) and reactive (q) powers are expressed as:

$$\begin{bmatrix} p \\ q \end{bmatrix} = \begin{bmatrix} e_\alpha & e_\beta \\ e_\beta & -e_\alpha \end{bmatrix} \begin{bmatrix} i_\alpha \\ i_\beta \end{bmatrix} \tag{5}$$

4. Proposed control algorithm

4.1. Structure of direct power neuro-fuzzy controller

The configuration of the studied system with the proposed control description is presented in Fig. 4. Indeed, two ANFIS are applied. The first one is applied instead of the hysteresis controllers and the switching table, whose inputs are the instantaneous powers errors e_p,e_q and the argument γ_n of the grid voltage. Whereas its output is the crisp value of the suitable voltage vector V_i (0,..,7), where the switching sequences of the PWM rectifier are generated using logical operation according to the table 2. The second one is applied to control the dc link voltage, whose inputs are the error of dc link voltage ($e= V_{dc_ref} - V_{dc}$) and the error change d_e, where its output is the active power current component.

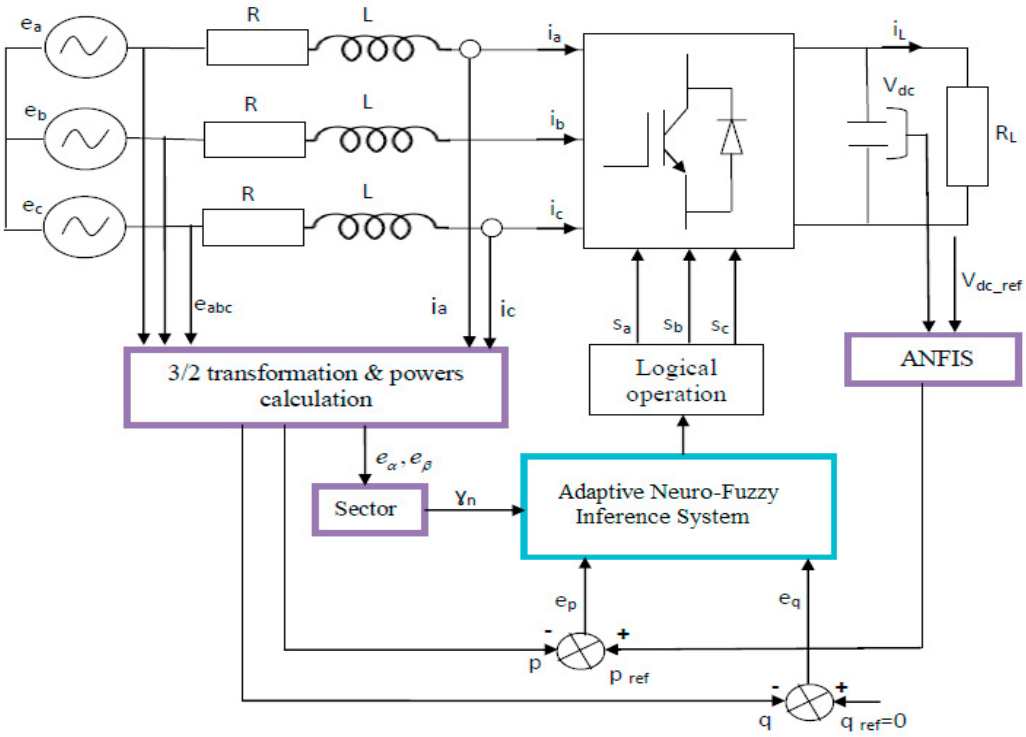


Fig. 4. Diagram and control description of proposed system.

Table 2. Different switching states.

V	S_a	S_b	S_c
0	0	0	0
1	1	0	0
2	1	1	0
3	0	1	0
4	0	1	1
5	0	0	1
6	1	0	1
7	1	1	1

4.2. Design of adaptive neuro-fuzzy controller

During the last years, genetic algorithm, artificial neural networks and fuzzy logic techniques have been intensively employed in a lot of areas, include control applications such as, process control and power converters regulation. These artificial intelligence techniques are not limited by mathematical assumptions utilized in control theories and doesn't need an exact knowledge about the studied system[11]. Indeed, the combination of ANN and FL methods are very important thanks to its advantages such as, control of non-linear system and noise rejection[12].

The ANFIS is a technique that combines two intelligent approach, artificial neural networks and fuzzy logic methods. This intelligent technique uses the fuzzy reasoning in handling uncertainties and the neural networks learning capability. The ANFIS structure based on a Takagi-Sugeno inference system is presented in Fig. 5. It contains five layers, in which the adaptive nodes are located at the first and fourth layers. The description of each layer is presented as follows:

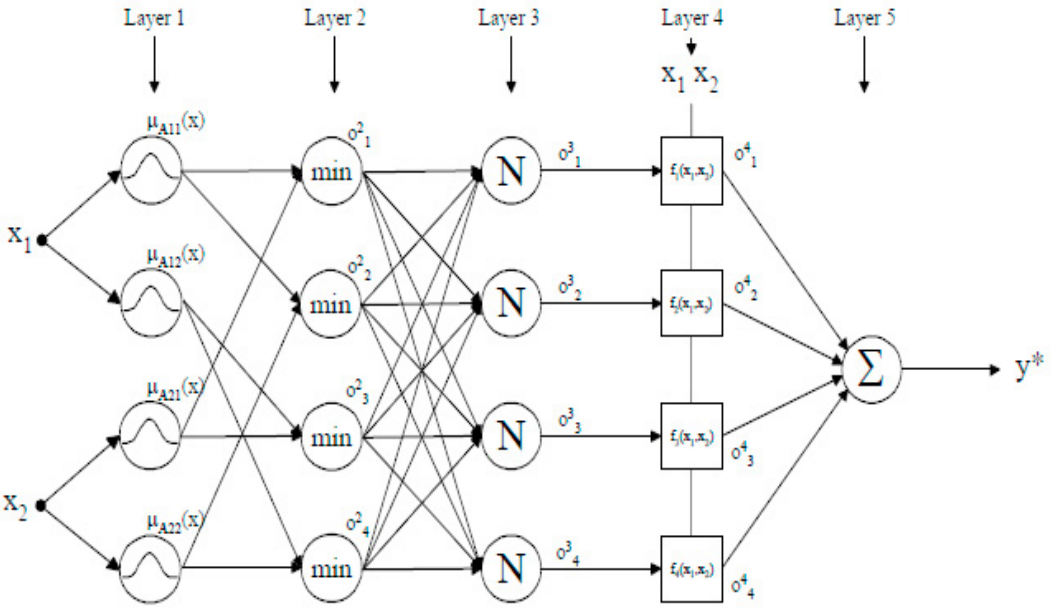


Fig. 5. ANFIS architecture.

Layer 1: is the fuzzification layer that contains the membership functions (MFs). This layer can be modeled by the following equation

$$O_k^1 = \mu_{A_{ij}}(x_i) \tag{6}$$

Where $\mu_{A_{ij}}(x_i)$ is the bell activation function, its expression is given as follow

$$\mu_{A_{ij}}(x_i) = \frac{1}{1+\left[\left(\frac{x_i - c}{a}\right)^2\right]^b} \tag{7}$$

Where x_i, j and (a, b, c) are the input signal, the number of MFs in i^{th} input, and the parameters of MFs respectively.
Layer 2: The determination of the minimum value of inputs signals is done in this layer by using the following equation:

$$O_k^2 = \min\left|\mu_{A_{ij}}(x_i), \mu_{A_{i'j'}}(x_2)\right| \tag{8}$$

Layer 3: each node of this layer determinates the normalized weight which is normalized firing strengths as follow:

$$O_k^3 = \frac{O_k^2}{\sum_{k=1}^{k} O_k^2} \tag{9}$$

Layer 4: In this layer each node is a point of connection with the node function as given in the following:

$$O_k^4 = O_k^3 f_k(x_1, x_2) = O_k^3 \sum_{i=1}^{I} P_{ik} x_i \tag{10}$$

Where P_{ik} is the consequent parameters.
Layer 5: In this layer the overall output is computes using all incoming signals as given in this expression:

$$O^5 = \sum_{k=1}^{k} O_k^4 \tag{11}$$

5. Results and discussions

To verify the effectiveness and the performance of the developed control technique, an extensive simulation study has been performed for the three-phase PWM rectifier based on the proposed direct power neuro-fuzzy controller method. The system model is simulated using MATLAB/Simulink environment. Indeed, different simulation tests under constant, variation of load and dc voltage reference are presented is this section. Table 3 gives the simulation parameters.

Table 3. Parameters of the simulation.

Sampling time	10^{-5} s
Resistance of line	0.25 Ω
Inductance of line	0.01 H
dc-link capacitor	1100 µF
Resistive load	100 Ω
Grid voltage	220 V
Frequency	50 Hz
dc-link voltage	600 V

The system responses under unity power factor condition and during a constant load (R_L=100 Ω) and constant dc voltage reference (V_{dc_ref}=600 V) are given in Fig 6. The curve of dc link voltage is shown in Fig. 6(a), it present excellent regulation to its reference with very smaller ripple. Fig. 6(b) illustrates the curves of phase voltage e_a and phase current i_a. It is clear that the phase current is nearly sinusoidal and in phase with the voltage (UPF). The behavior of instantaneous powers (p,q) shown in Fig. 6(c), present excellent control of instantaneous powers.

Fig. 7 represents the system results during a constant dc voltage reference and load variation. A resistive load (R_L=100 Ω) is applied at t=0.37 s and eliminated at t=0.6 s. It can be observed that the dc link voltage has a short transition and it is present good tracking to its reference (Fig. 7(a)). The phase current and phase voltage remains sinusoidal with clear UPF (Fig. 7(b)). The instantaneous powers present excellent decoupled regulation without any overshoot (Fig. 7(c)).

The Fig 8 shows the results under variation of dc voltage reference (V_{dc_ref} =600 V to 650 V) at t=0.5s with constant resistive load (R_L=100 Ω). We notice that the dc link voltage, the instantaneous powers (p,q) are perfectly regulated to theirs references with fast response and without any static error (Fig. 8(a) & Fig. 8(c)). It can also be noted that the line current and line voltage are increased and working under UPF condition (Fig. 8(b)).

Finally, the fast Fourier transform (FFT) analysis of phase current is illustrates in Fig. 9, where the value of THD are only 1.56%. Nevertheless, the presented control algorithm fulfils the standard IEEE STD 519-1992 recommendation.

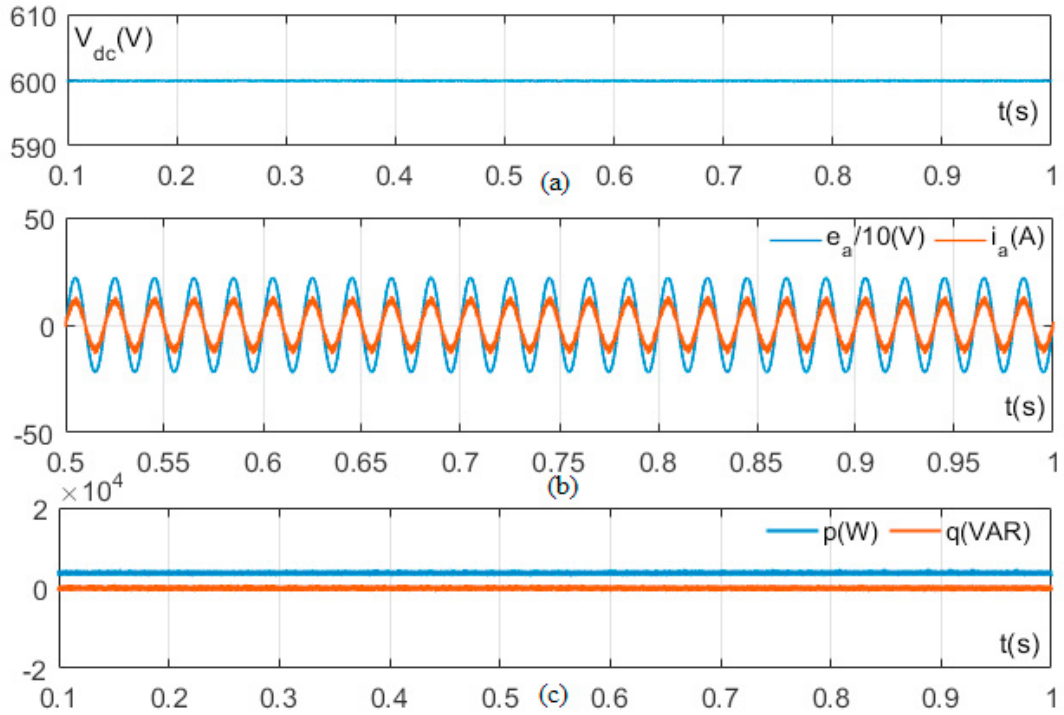


Fig. 6. Behavior of dc link voltage (a), line voltage & line current (b), active and reactive powers (c) under (V_{dc_ref}=600V; R_L=100Ω).

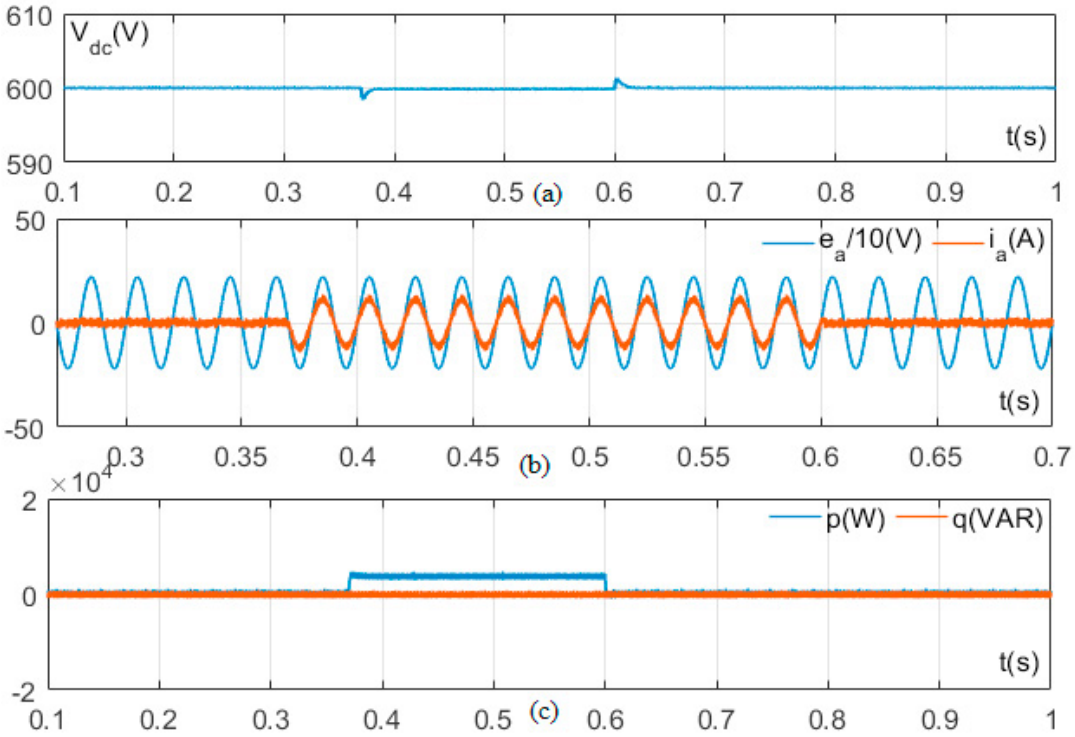


Fig. 7. Behavior of dc link voltage (a), line voltage & line current (b), active and reactive powers (c) under load variation and constant reference voltage (V_{dc_ref}=600 V).

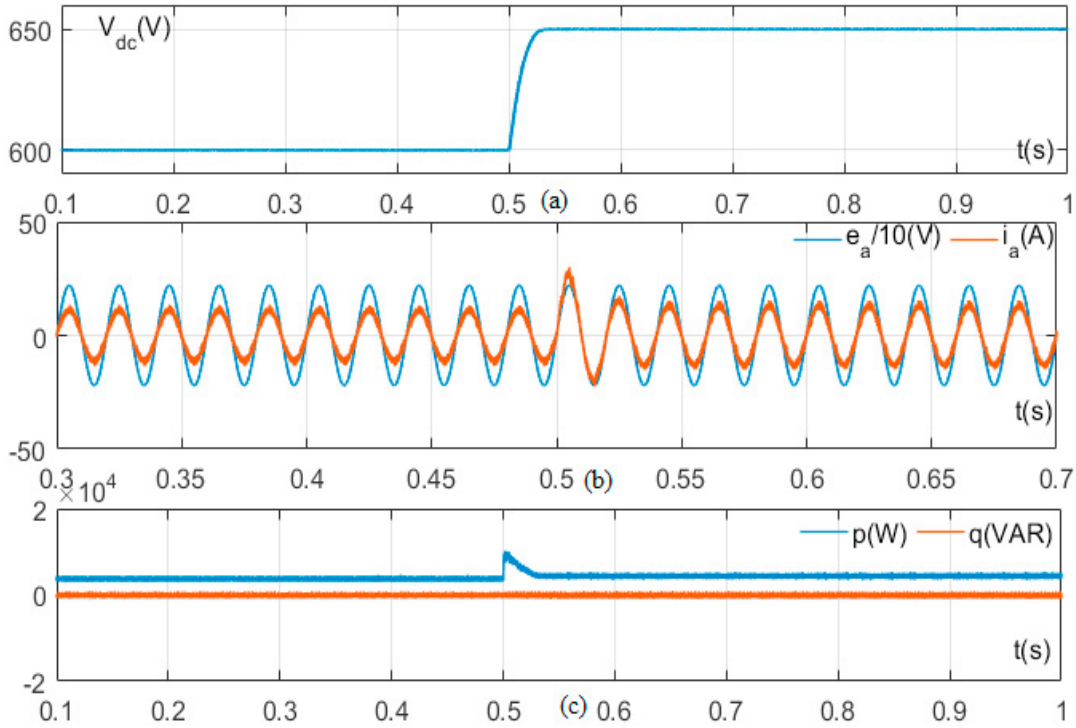


Fig. 8. Behavior of dc link voltage (a), line voltage & line current (b), active and reactive powers (c) under reference voltage variation and constant load (R_L=100 Ω)

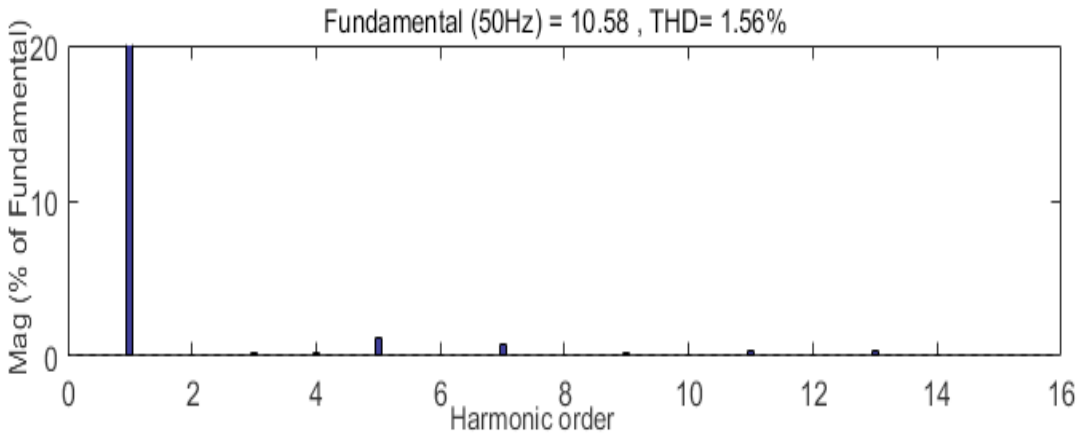


Fig. 9. Harmonics spectrum of phase current i_a.

6. Conclusion

In this work, an improvement DPC scheme based on ANFIS has been presented for three phase PWM rectifiers. The developed control technique has been successfully simulated by Matlab/Simulink environment under different operating conditions. The simulation results of the proposed control algorithm have shown fast response and excellent maintaining of dc link voltage, instantaneous powers to their references. It has also been illustrate that the current i_a and the voltage e_a are in phase (UPF) with low total harmonics distortion.

Acknowledgements

This work was carrying out in Delhi Technological University and supported by the Government of India under the C.V. Raman International scholarship.

References

[1] M. Badoni, A. Singh, and B. Singh. (2016)"Adaptive Neurofuzzy Inference System Least-Mean-Square-Based Control Algorithm for DSTATCOM." *IEEE Trans. Ind. Inform*.12(2): 483–492.

[2] M. Malinowski, M. Jasinski, and M. P. Kazmierkowski. (2004) "Simple Direct Power Control of Three-Phase PWM Rectifier Using Space-Vector Modulation (DPC-*SVM),*" *IEEE Trans. Ind. Electron 51(2): 447–454.*

[3] A. Bouafia, J.-P. Gaubert, and F. Krim. (2010)"Predictive Direct Power Control of Three-Phase Pulse width Modulation (PWM) Rectifier Using Space-Vector Modulation (SVM)," *IEEE Trans. Power Electron*. 25(1): 228–236.

[4] M. Malinowski, M. P. Kazmierkowski, and A. M. Trzynadlowski. (2003) "A comparative study of control techniques for PWM rectifiers in AC adjustable speed drives," *IEEE Trans. Power Electron* 18(6): 1390–1396.

[5] M. Jamma, M. Barara, M. Akherraz, A. Bennassar. (2017) "Comparative Study of PI and Backstepping with Integral Action Controllers Based on Direct Power Control for Three-Phase PWM Rectifier," *Int. J. Electr. Eng. Inform* 9(2): 234–243.

[6] S. M. Gadoue, D. Giaouris, and J. W. Finch. (2009) "Artificial intelligence-based speed control of DTC induction motor drives—A comparative study," *Electr. Power Syst. Res* 79(1): 210–219.

[7] S. Kwak and J.-C. Park. (2015) "Model-Predictive Direct Power Control With Vector Preselection Technique for Highly Efficient Active Rectifiers," *IEEE Trans. Ind. Inform* 11(1): 44–52.

[8] A. Djerioui, K. Aliouane, and F. Bouchafaa. (2014) "Sliding mode direct power control strategy of a power quality based on a sliding mode observer," *Int. J. Electr. Power Energy Syst.* 56: 325–331.

[9] M. Jamma, A. Bennassar, M. Akherraz, C. Fahassa, M. Barara, and M. Oproescu. (2017) "Self-tuning fuzzy PI dc-bus voltage controller and fuzzy switching sequences selection for direct power control of PWM AC/DC converter," in 9th International Conference on Electronics, Computers and Artificial Intelligence. 1–6.

[10] Shuhui Li, M. Fairbank, C. Johnson, D. C. Wunsch, E. Alonso, and J. L. Proao. (2014) "Artificial Neural Networks for Control of a Grid-Connected Rectifier/Inverter Under Disturbance, Dynamic and Power Converter Switching Conditions," *IEEE Trans. Neural Netw. Learn. Syst.* 25(4): 738–750.

[11] M. Singh and A. Chandra. (2013) "Real-Time Implementation of ANFIS Control for Renewable Interfacing Inverter in 3P4W Distribution Network," *IEEE Trans. Ind. Electron*. 60(1): 121–128.

[12] F. G. Areed, A. Y. Haikal, and R. H. Mohammed. (2010) "Adaptive neuro-fuzzy control of an induction motor," *Ain Shams Eng. J.* 1(1): 71–78.

Available online at www.sciencedirect.com

ScienceDirect

Materials Today: Proceedings 5 (2018) 15489–15491

materialstoday: PROCEEDINGS

www.materialstoday.com/proceedings

NTNM2017

Editorial Preface on the Proceedings of INN International Conference/Workshop on Nanotechnology and Nanomedicine (NTNM2017)

Masoud Mozafari*

Bioengineering Research Group, Nanotechnology and Advanced Materials Department, Materials and Energy Research Center (MERC), P.O. Box 14155-4777, Tehran, Iran

Abstract

The structural design of materials at the length scales from atomic levels to macro scales is of great importance, by which the physico-chemical characteristics of materials at nano scales fade the boundaries between physics, chemistry and biology. Nanotechnology with a considerable influence on the advancements in medical science and technology can play a vital role in human health. Based on this substantial influence of nanotechnology, an international conference/workshop on Nanotechnology and Nanomedicine (NTNM2017) was held during 2-3 May 2017 at Materials and Energy research Center (MERC), Tehran, Iran. This conference aimed to address the practical solutions that were recently offered by prominent scientists in the field of nanotechnology. It was a unique event in its type because of the participation of world-class scientists from all over the world. The multinational environment of this conference made it a perfect platform for the development of practical ideas from both academia and industry. I hope this conference will rapidly become one of the annual appointments for the scientific community interested to follow the growing advancements of nanotechnology in medicine.

© 2018 Elsevier Ltd. All rights reserved.

Selection and/or Peer-review under responsibility of INN International Conference/Workshop on "Nanotechnology and Nanomedicine'' NTNM2017.

Keywords: Tissue Engineering and Regenerative Medicine; Pharmaceutics and Drug Delivery Systems; Nanomedicine, Diagnosis, and Therapy; Nanobiodevices and Biosensors; Nanotechnology and Environmental Health; General Aspects of Nanotechnology

* Corresponding author. Tel.: +98-9126490679; fax: +98-2636280040(477).
E-mail address: mozafari.masoud@gmail.com

2214-7853 © 2018 Elsevier Ltd. All rights reserved.
Selection and/or Peer-review under responsibility of INN International Conference/Workshop on "Nanotechnology and Nanomedicine'' NTNM2017.

1. The organizer "Materials and Energy Research Center (MERC)"

The year 1971 was the beginning of a new scientific movement in all aspects of materials science and engineering when Materials and Energy Research Center (MERC) started its research activities in many subfields ranging from renewable energies and semiconductor technologies to environmental issues. This positive approach has been continued and strengthened, resulting in the development of new subfields related to the human health. Establishing an effective link between research and industry, extending the interactions between researchers inside and outside the country for transferring the needed technology, and supporting the initiatives are some of the objectives of Materials and Energy Research Center (MERC). Therefore, Materials and Energy Research Center (MERC) has developed extensive collaborations with national and international universities and industrial research institutes in recent years.

2. The Conference/Workshop NTNM2017

The “Nanotechnology and Nanomedicine” conference/workshop NTNM2017 was held on 2-3 May 2017 at Materials and Energy research Center (MERC) (see Fig. 1). The main objectives of the conference were: I) Providing a proper situation to exchange the recent scientific/technical developments, challenges and opportunities in the field of nanotechnology and nanomedicine, II) Promoting joint cooperation and advancement between scientific, research, and technology centers worldwide, III) Strengthening the relations and technological collaborations and improving transfer of experiences among researchers, IV) Transforming ideas into wealth and supporting production and development processes, V) Training of qualified human resources in the field of nano-biomedical science and technology, VI) New approaches for promoting entrepreneurship and innovation initiatives in nano-biomedical science and technology. The scope of submissions were related to "Surface Modification Strategies", "Nanomedicine, Diagnosis, and Therapy", "Pharmaceutics and Drug Delivery Systems", "Toxicology and Risk Assessment of Nanomaterials", "Tissue Engineering and Regenerative Medicine", "Nanotechnology and Environmental Health", and "Nanobiodevices and Biosensors". Among all the papers received for review, almost one hundred papers were accepted for the presentation in the conference. There were also thirty two world-class invited speakers from United States, United Kingdom, Canada, Netherlands, Norway, Japan, Australia, Kyrgyzstan, Bangladesh, Malaysia, Pakistan, India, Oman, Zimbabwean, Iraq, Turkey, and Iran.

The program highlighted recent breakthrough stories and advancements in the field of nanotechnology. It comprised six professional sessions on the main topics related to "tissue engineering and regenerative medicine", "pharmaceutics and drug delivery systems", "nanomedicine, diagnosis, and therapy", "nanobiodevices and biosensors", "nanotechnology and environmental health", and "general aspects of nanotechnology". This two-day event included invited talks, organized in different sessions each coordinated by appointed technical chairs.

There were also nine workshops held on both days of the conference which were mainly adjusted to create a knowledge exchange atmosphere for the participants. Yoshihiro Ito (Riken Institute- Japan) [Nanolayer Formation of Engineered Proteins on Materials for Biomedical Applications], Shaaker Hajati (MERC- Iran) [Nanobiomaterials Surface Characterization by X-Ray Photoelectron Spectroscopy (XPS): Chemical Composition, In-Depth Analysis and Nano-Imaging], Naveen Kumar (Delhi Technological University- India) [Role of Nanotechnology in Commercial Biodiesel Production], Fatemeh Esmaieli (University of Utah- USA) [Nanoscale Heat Transfer: Fundamentals and Engineering Aspects], Khurshid Hasanain (Quaid-i-Azam University- Pakistan) [Nanoscience and Technology in Leading OIC Countries: Prospects of New Initiatives Under the OIC Ten Year Plan of Action], Bo Örjan Gunnar Nyström (University of Oslo- Norway) [General Information about Small Angle Scattering (SAXS and SANS) and Light Scattering and Illustrating it by Given Some Examples from Polymer Science], Florence Barrère De Groot (Xpand Biotechnology- The Netherlands) [Osteoinductive Ceramics: Controlled Submicron Structures for Bone Tissue regeneration: Physico-Chemical Factors and Mechanism, Clinical and Market Applications], Mohammad Tagi Ahmadi (Universiti Teknologi Malaysia- Malaysia) [Bio sensor Modeling (DNA sensor Modeling) sensor simulation by ATK], Naveen Kumar (Delhi Technological University- India) [Role of Nanotechnology in Commercial Biodiesel Production].

This special issue of the journal "Materials Today: Proceedings" aims at providing insight into the diverse nature of nanotechnology topics for human health that were covered during NTNM2017, containing selected peer-reviewed papers presented at the conference. I hope that this selection of papers highlights the diversity of research that was presented at the meeting and that it can serve as a stimulus for future advancements.



Fig. 1. NTNM2017 photo at the end of the conference

4. Conference committee

Conference Chairman: Seyed Mohammad Mahdi Hadavi, PhD
President of MERC: Mohammad Taghi Salehi, PhD
Executive Chair: Ali Asghar Behnamghader, PhD
Executive Vice-Chair: Fatemeh Sadat Torknik, PhD
Scientific Chair: Masoud Mozafari, PhD

Acknowledgment: On behalf of the organizing committee, NTNM2017, I would like to extend my sincere thanks to all the supporters who made the event a great success. This success benefited from the help of an international scientific committee, a local organizing committee, and about thirty student volunteers who contributed to logistics during the meeting. I also acknowledge the authors for timely submission and revisions to their initial submission after reviews. In addition, special thanks to all the members under the Peer review committee who extended their timely support to complete the review process in time for publication of research articles in Materials: Today Proceedings. I extend my profound thanks to Stewart Bland, and his whole team members for accepting our appeal to publish the conference papers in this issue of Materials Today: Proceedings. The plenary and invited speakers are also acknowledged for sharing their knowledge and expertise. In conclusion, I believe that NTNM2017 was effective in bringing together a wide variety of researchers in numerous disciplines around the key issues of nanotechnology-related research and advances for human health.

Guest Editor,
Masoud Mozafari, PhD
Scientific Chair of NTNM2017

Available online at www.ijapie.org

International Journal of Advanced
Production and Industrial Engineering

IJAPIE-SI-IDCM 612 (2018) 57–61

Special Issue on

INNOVATIVE DESIGN
&
COMPUTATIONAL
MODELLING

Effect of Drive Side Pressure Angle on Load Carrying Capacity of Asymmetric Involute Helical Gear

Jairaj Gambhir[1*], Paras Kumar[2], Bhuvan Aggarwal[3], Harshit Arya[3]
[1](*Department of Mechanical Engineering, Delhi Technological University, India)*
Email: jai.gambhir@yahoo.com

Abstract *: Efficiency In this paper, the effect of drive side pressure angle on load carrying capacity of asymmetric helical gear is analyzed. The drive pressure angle of asymmetric gear tooth is varied from 20° to 40° in steps of 5° while the coast side pressure angle is kept constant (20°). Initially, the reduction in contact stress is analyzed and then the consequent increase in load carrying capacity is studied with increase in drive side pressure angle. Three dimensional model of gears are made on Solidworks®. The gears have been designed using AGMA standards. In each calculation the meshing parameters and boundary conditions are kept constant. It is found that as the drive side pressure angle increases, the contact stress on teeth reduces as compared to symmetric involute helical gear (20° drive and coast side pressure angle each). Maximum reduction in contact stress occurs in gear with drive side pressure angle of 40° with 25.4% reduction in stress. Due to maximum reduction in contact stress, the load carrying capacity of gear is increased by 34% in asymmetric gear with drive side pressure angle of 40°.*

Keywords*: Asymmetric Helical Gear, Contact Stress, Drive pressure angle, Load Capacity, AGMA*

1. INTRODUCTION

Helical gears are extensively used to transmit power by gears due to their relatively smooth operation and high load capacity. In many gear applications the gears rotate in only one direction and rarely in the reverse direction. Due to this, the pressure on loaded (drive) profile of tooth is significantly higher than that on unloaded (coast) profile of the tooth. The gear tooth design can be made more efficient by using different pressure angles on the drive and coast profile of gear tooth. Such gears with different drive and coast pressure angles are known as asymmetric gears.

The designing of asymmetric tooth gear was explained in great depth by Kapelevich [1]. He described designing of asymmetric tooth gearing, analytical and experimental comparison of symmetric and asymmetric tooth gears. Gawali et al. [2] analyzed the effect of coefficient of asymmetry on strength and contact ratio of different helical gear pairs. They further validated the results using digital strain gauge indicator mounted at the root of the gear.

Sondur et al. [3] described a method for investigation of bending stress at the critical section of asymmetric involute spur gear. They concluded that the stress was reduced by 9% which in turn can increase the load carrying capacity of gears. Anusha et al. [4] analyzed contact stress generated in symmetric helical gear by using AGMA and ANSYS. They studied the contact stress by varying pressure angle, helix angle and face width of the gear.

In the past, most of the analysis of asymmetric helical gears were focused on study of bending stress in gears but very little work has been done on study of contact stress on asymmetrical helical gear tooth. Since contact stress is one of major factor influencing pitting of gear tooth surface, thus, it is felt necessary to find out the effect of load side pressure angle on variation of contact stress in asymmetric helical gears. Further, it is important to study change in load carrying capacity of asymmetric helical gears as compared to symmetric helical gears, to ascertain advantage of asymmetric helical gears over symmetric helical gears.

2. GEAR DESIGN

Conventional involute spur gears are designed with symmetric involute tooth profiles. However the conditions of load and meshing are different for drive and coast profile of gear tooth. Application of asymmetric tooth side surfaces enables to increase the load capacity and durability for the drive tooth side. Design of Asymmetric Involute helical gear is governed by various fundamental equations as given [1].

2.1 Asymmetric Tooth Design

An Asymmetric Involute tooth is formed by two involutes with same Pitch diameter (D_p), but different pressure angle for drive and coast sides (φ_d , φ_c) and correspondingly different Base Circle diameters (D_{bd} , D_{bc}).

$$D_b = D_p * \text{Cos}(\varphi) \quad (1)$$

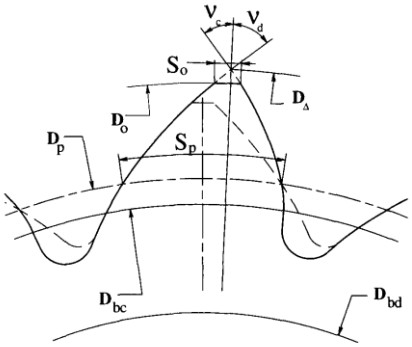


Figure 1. Asymmetric Involute tooth profile [1]

For generation of involute spur gear following parametric equations are used:

$$x(t) = D_p/2*(\cos \varphi)*[\cos(t)+ t*\sin(t)] \quad (2)$$

$$y(t) = D_p/2*(\cos \varphi)*[\sin(t)- t*\cos(t)] \quad (3)$$

where, t is angle parameter in radius;
x(t) is a function with respect to parameter t;
y(t) is a function with respect to parameter t

2.2 Gear Specifications

Various Parameters used while designing the Pinion and Gear are given in Table 1.

Table 1: Parameters for Asymmetric Helical gear design

Parameters	**Value**
Material	Structural Steel
Module (m)	4.5 mm
Gear Ratio (G)	1
Number of teeth (N)	25
Top Land Thickness Coefficient (m_o)	0.016
Drive side Pressure Angle (φ_d)	20^o, 25^o, 30^o, 35^o, 40^o
Coast side Pressure Angle (φ_c)	20^o
Helix Angle (β)	15^o
Face Width (b)	27 mm
Addendum (a)	4.5 mm
Dedendum (d)	5.625 mm
Clearance (c)	1.125 mm

3. AGMA Contact Stress Equation

A very important parameter when designing a gear pair is the maximum surface contact stress that exists between two gear teeth in mesh, as it affects surface fatigue along with gear mesh losses. The fundamental Contact Stress (σ_c) formula for gear teeth is given in ANSI/AGMA 2001-D04 [9]

$$\sigma_c = C_p \sqrt{W_t K_o K_v K_s \frac{K_m}{d} \frac{C_f}{F} \frac{}{I}} \quad (3)$$

4. Finite Element Method

The Finite Element Method (FEM) is a numerical technique used to perform Finite Element Analysis (FEA) of any given physical phenomenon. ANSYS Workbench is used for the elemental analysis of contact stress in gear. The analysis is performed on Static Structural component system in the Ansys Workbench.

The solid model is made on Solidworks® software and imported to Ansys Workbench as parasolid file. Fig. 2 to Fig. 6 show solid model of asymmetric helical gears with constant helix angle of 15° and coast side pressure angle of 20°. The drive side pressure angle is varied from 20° to 40° in steps of 5°.



Figure 2. Helical gear model for $\varphi_d = 20°$, $\varphi_c = 20°$, $\beta=15°$

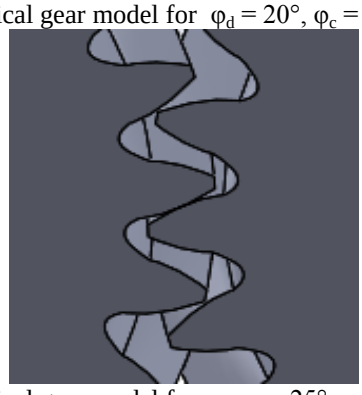


Figure 3. Helical gear model for $\varphi_d = 25°$, $\varphi_c = 20°$, $\beta=15°$

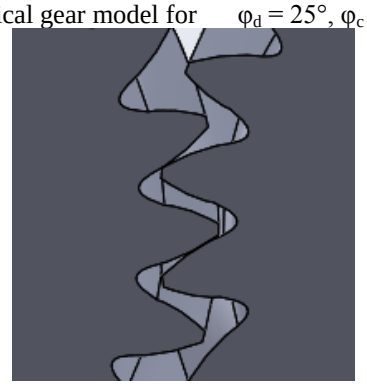


Figure 4. Helical gear model for $\varphi_d = 30°$, $\varphi_c = 20°$, $\beta=15°$ (Symmetric gear)



Figure 5. Helical gear model for $\varphi_d = 35°$, $\varphi_c = 20°$, $\beta=15°$



Figure 6. Helical gear model for $\varphi_d = 40°$, $\varphi_c = 20°$, $\beta=15°$

The meshing is done with medium relevance center and minimum edge length of 1.7mm. Total of 51,593 elements are generated with 83,059 nodes on the (20°/20°) symmetric gear with 15° helix angle. Suitable boundary conditions are given with moment load of 100 N-m and the results are calculated. The stress value is compared with theoretical AGMA stress value as shown in Table 2.

To calculate the change in load carrying capacity, the moment on pinion gear is increased till the stress value is equal to the stress induced in symmetrical (20°/20°) helical gear. The resultant load value is noted and compared with initial load to calculate the percentage increase in load carrying capacity.

5. Results and Discussion

To verify the solver settings and the boundary conditions, a test case is chosen as symmetric helical gear with 20°/20° pressure angle and 15° helix angle. The contact stress is calculated at the pitch point of gear using AGMA stress equation and then compared with the Finite Element Analysis (FEA) value. The magnitude of Contact Stress evaluated using ANSYS is found to be 393.26 MPa as compared to 393.78 MPa calculated using AGMA contact stress equation.

Table 2: Comparison of AGMA and FEA Contact Stress Values

Parameter	AGMA Value (MPa)	FEA Value (MPa)	Difference (%)
σ_C	393.78	393.26	0.13

Thus, both AGMA and FEA values are in close agreement with each other with deviation of 0.13%.

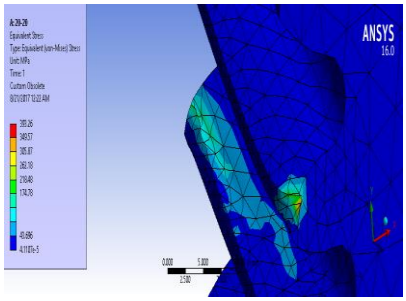


Figure 7. Contact Stress in 20°/20° Gear

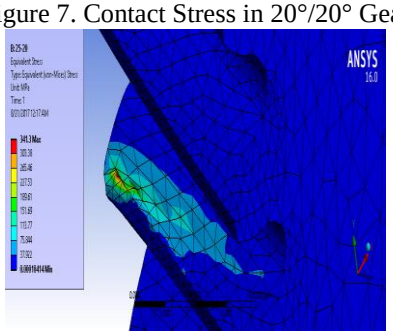
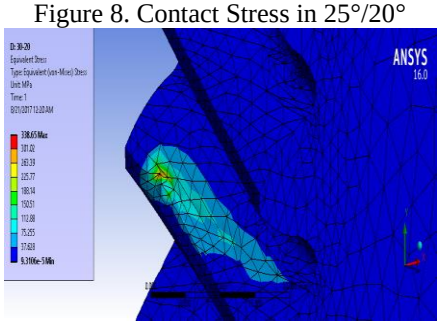


Figure 8. Contact Stress in 25°/20°



Gear Figure 9. Contact Stress in 30°/20° Gear (Symmetric gear)

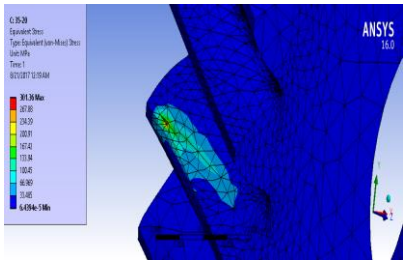


Figure 10. Contact Stress in 35°/20° Gear

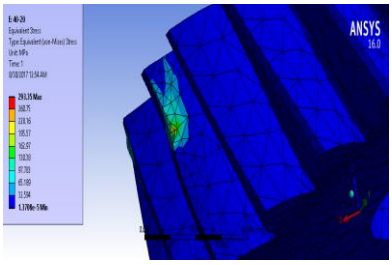


Figure 11. Contact Stress in 40°/20° Gear

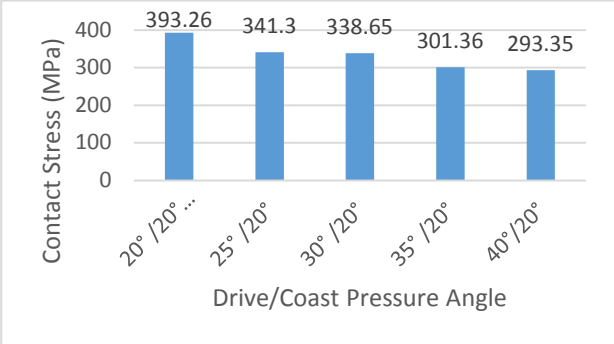


Figure 12. Variation of Contact Stress with Drive Side Pressure Angle

Table 3: Percentage Increase in Load Capacity of Gear

	Contact Stress (MPa)	Percentage reduction in contact stress (%)
20°/20° (Symmetric)	393.26	-
25°/20°	341.3	13.21
30°/20°	338.65	13.88
35°/20°	301.36	23.37
40°/20°	293.35	25.4

Fig. 7 to Fig. 11 show variation in contact stress with drive side pressure angle as obtained using finite element analysis. The contact stress continuously reduces with increase in drive side pressure angle. Fig. 12 further depicts the variation in contact stress using bar graph. The percentage reduction in contact stress on gear tooth for different values of drive side pressure angle is shown in Table 3. It is clearly seen that maximum reduction in contact stress as compared to that in symmetrical helical gear occurs in gear with drive side pressure angle of 40° with 25.4% reduction in contact stress.

Table 4: Percentage Increase in Load Capacity of Gear

	Initial Load (N-m)	Final Load (N-m)	% Increase in load
20°/20° (Symmetric)	100	100	-
25°/20°	100	115.3	15.3
30°/20°	100	116.3	16.3
35°/20°	100	130.5	30.5
40°/20°	100	134	34

Table 4 shows percentage increase in load carrying capacity of asymmetric helical gears. All asymmetric tooth profiles show considerable increase in load capacity however, the gear with 40° drive side pressure angle shows maximum increase (34%) in load capacity amongst all gears. This increase in load carrying capacity of gear is a direct result of reduction in contact stress due to increase in drive side pressure angle.

6. Conclusion

In the light of above discussions, the following conclusions are drawn –

- Contact stress in asymmetric helical gears decreases with increase in Drive side pressure angle.
- Maximum reduction in contact stress occurs in gear with drive side pressure angle of 40° with 25.4% reduction in stress.
- Load carrying capacity of gears increases remarkably with increase in dive side pressure angle.
- Gear with drive pressure angle of 40° shows 34% increase in load carrying capacity which is maximum among all.
- By increasing the drive side pressure angle in asymmetric gears, the value of contact stress on gear tooth reduces hence increasing the load carrying capacity of gears.

Thus, by using asymmetric gears in place of conventional symmetric gears in industries, load on gear can be increased to a large extent for the same amount of stress induced in them, or conversely, for the same load application the size of gear can be reduced by using asymmetric gears in place of symmetric gears.

7. Nomenclature

D_{bd} - Base circle diameter on drive side
W_t – Transmitted Load
D_{bc} - Base circle diameter on coast side
K_o -Overload Factor
D_p - Pitch circle diameter
K_v -Dynamic factor
D_o – Outside circle Diameter
K_s -Size Factor
$D_\wedge$ - Tip circle diameter
K_m -Load Distribution Factor
S_o - Tooth tip thickness
C_f -Surface Condition Factor
S_p – Tooth Thickness at Pitch diameter
F- Face width
ν_c ,ν_d - Profile angle in the intersection point
I – Geometry Factor for pitting resistance
σ_c – Contact Stress
d- operating pitch diameter of pinion
C_p –Elastic Coefficient

References

[1] Kapelevich A (2000). “Geometry and design of involute spur gears with Asymmetric teeth”, Mechanism and Machine Theory. Vol. 35, pp. 117-130

[2] Gawali S, Rahate HP, Borade RV (2017). “Effect of Coefficient of Asymmetry on Strength and Contact Ratio of Asymmetric Helical Gear”. International Journal of Scientific Research in Science, Engineering and Technology, Volume 3, Issue 1, pp.144-150

[3] Sondur VB, Dharashivkar NS (2013). "Theoretical and Finite Element Analysis of Load Carrying Capacity of Asymmetric Involute Spur Gears". International Journal of Research in Aeronautical and Mechanical Engineering, Vol.1, Issue.3, pp 67-73

[4] Anusha SS, Reddy PS, Bhaskar P, Manoj M (2014) "Contact Stress Analysis of Helical Gear by Using AGMA and ANSYS", International Journal of Science Engineering and Advance Technology, Vol 2, Issue 12

[5] Wang S, Liu GR, Zhang GY, Chen L (2011). "Accurate Bending Strength Analysis of Asymmetric Gears using the novel ES-PIM with triangular Mesh". International Journal of Automotive and Mechanical Engineering, Volume 4, pp. 373 - 396

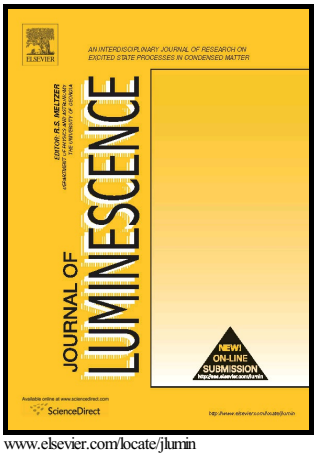
[6] Damtie S, Tilahun D (2014). "Contact stress analysis of involute spur gear by finite element method (FEM)". Journal of EEA, Vol. 32

[7] Murthy MS (2013). "Stress Analysis of Helical Gear by FEM Techniques with Variation in Face Width and Helix Angle". International Journal of Engineering Research & Technology, Vol. 2 Issue 7

[8] Karpat F, Osire SE, Cavdar K, Babalik FC (2008). "Dynamic analysis of involute spur gears with asymmetric teeth". International Journal of Mechanical Sciences, Vol. 50, pp. 1598– 1610

[9] ANSI/AGMA, (2005) "Fundamental Rating Factors and Calculation Methods for Involute Spur and Helical Gear Teeth", ANSI/AGMA 2001 –D04.

Author's Accepted Manuscript



www.elsevier.com/locate/jlumin

Enhanced red down-conversion luminescence and high color purity from flux assisted Eu^{3+} doped calcium aluminozincate phosphor

Sumandeep Kaur, A.S. Rao, M. Jayasimhadri

PII: S0022-2313(18)30136-4
DOI: https://doi.org/10.1016/j.jlumin.2018.06.015
Reference: LUMIN15677

To appear in: *Journal of Luminescence*

Received date: 24 January 2018
Revised date: 8 May 2018
Accepted date: 6 June 2018

Cite this article as: Sumandeep Kaur, A.S. Rao and M. Jayasimhadri, Enhanced red down-conversion luminescence and high color purity from flux assisted Eu^{3+} doped calcium aluminozincate phosphor, *Journal of Luminescence,* https://doi.org/10.1016/j.jlumin.2018.06.015

This is a PDF file of an unedited manuscript that has been accepted for publication. As a service to our customers we are providing this early version of the manuscript. The manuscript will undergo copyediting, typesetting, and review of the resulting galley proof before it is published in its final citable form. Please note that during the production process errors may be discovered which could affect the content, and all legal disclaimers that apply to the journal pertain.

ACCEPTED MANUSCRIPT

Enhanced red down-conversion luminescence and high color purity from flux assisted Eu^{3+} doped calcium aluminozincate phosphor

Sumandeep Kaur, A.S.Rao* and M.Jayasimhadri*
Department of Applied Physics, Delhi Technological University, Bawana Road,
New Delhi-110 042, INDIA.

Abstract

Trivalent europium ions (Eu^{3+}) doped calcium aluminozincate (CAZ) phosphors blended with various fluxes (NaF, NaCl and $Na_2B_4O_7$) have been synthesized by conventional solid-state reaction method. The structural, morphological and luminescent properties along with lifetimes have been investigated in detailed. The Judd-Ofelt (J-O) analysis has been carried out to get insights of optical properties. The X-ray diffraction (XRD) pattern confirms the single phase orthorhombic structure for Eu^{3+} doped CAZ phosphor with NaCl and $Na_2B_4O_7$ fluxes; whereas the phase purity has not been achieved in NaF assisted Eu^{3+} doped CAZ phosphor. The as-synthesized phosphor has uneven agglomerated micron sized particles. The photoluminescence (PL) studies exhibit significant enhancement in the red emission for Eu^{3+} doped CAZ phosphor with the addition of $Na_2B_4O_7$. The emission intensity has been found to increase approximately 1.5 times using NaCl and 2.5 times for $Na_2B_4O_7$ in Eu^{3+} doped CAZ phosphor as compared to the phosphor without any flux. The emission spectrum of optimized Eu^{3+} doped CAZ phosphor added with $Na_2B_4O_7$ flux has been compared the commercial Y_2O_3: Eu^{3+} phosphor. The CIE chromaticity coordinates and color purity calculated for $Na_2B_4O_7$ in Eu^{3+} doped CAZ phosphor is close to commercial red phosphor. The decay curves show bi-exponential behaviour with experimental lifetimes in the range of microseconds for the as-prepared phosphors. All these results indicate that the $Na_2B_4O_7$ flux assisted Eu^{3+} doped CAZ phosphor can serve as an efficient red phosphor under blue light for applications in white light emitting devices.

E-mail: drsrallam@gmail.com (A.S. Rao), jayaphysics@yahoo.com (M. Jayasimhadri)

Accepted manuscript

ACCEPTED MANUSCRIPT

1. Introduction

In recent years, research and development of phosphor converted white light emitting diodes (pc-WLEDs) have gained considerable interest owing to their high efficiency, long lifetime, mercury free and low power consumption [1–4]. White light emitting diodes (WLEDs) have been employed in various applications, such as illumination systems, optical communication, optical storage and sensors [5–7]. The commercial pc-WLED is an integrated assembly of high efficiency blue (InGaN) LED chip and yellow (YAG: Ce) phosphor [8,9]. The combination of blue and yellow light emits white light. Since commercial pc-WLEDs are in deficit of red component in the emission spectrum of the YAG: Ce phosphor, they have a lower color rendering index (CRI) (Ra < 80) and high correlated color temperature (CCT~7750 K) [8,10–12]. Aiming to solve this inexorable problem, a red light emitting phosphor is needed to enrich the red region in the pc-WLED to improve the CRI and CCT of the device [13–15]. At present, commercial red sulphide phosphor (Y_2O_2S: Eu^{3+}) suffers with low chemical stability and less efficient to get excited in n-UV and deep blue spectral region[16]. Nitride phosphor shows deep broad red emission and difficult to synthesize, which limit its applications [3,8,17]. Therefore, it has become important to develop a new red phosphor for pc-WLEDs. The rare earth (RE) ions enriched in f-f energy levels give abundant emission color in visible region depending upon the transition it undergoes in the host lattice [7]. Among various RE ions, Eu^{3+} serves as an excellent dopant for red light emitting phosphors to improve CRI and stability in WLEDs for optoelectronic applications [18–20].

The luminescent properties of phosphors also get influenced by some other factors such as synthesis technique, concentration of activator, use of sensitizer, and addition of flux. Among these factors, addition of flux improves the quality of phosphor by lowering calcining temperature, improving size distribution uniformity and enhancing the luminescence intensity

Accepted manuscript

ACCEPTED MANUSCRIPT

[21,22]. In general, alkali halide fluxes have been reported in literature to enhance the emission intensity, for example Na_2CO_3-SiO_2-NaF in YAG: Ce, BaF_2 and CaF_2 in $BaMgAl_{10}O_{17}$: Eu^{2+}/Mn^{2+}, H_3BO_3, NH_4Cl, NH_4F, NH_4Br, $BaCl_2$, $BaBr_2$, CaF_2 and BaF_2 in Zn_2SiO_4:Mn^{2+} [22–24]. Apart from halide fluxes, boric acid (H_3BO_3) and borax ($Na_2B_4O_7$) have also been reported in (Ca,Zn)TiO_3:Pr^{3+}, ($K_{0.5}Na_{0.5}$) NbO_3, and $SrAl_2O_4$:Eu^{2+} phosphors [25–27]. The flux had no harmful impact on the optical properties of the crystal [21]. The proper amount of flux in the synthesis process has a positive effect on the luminescent properties of the phosphor.

In this report, various fluxes, such as sodium fluoride (NaF), sodium chloride (NaCl), and borax ($Na_2B_4O_7$) have been used to synthesize Eu^{3+} doped calcium aluminozincate (CAZ) phosphor to study the enhancement of red emission in it [28]. Systematic studies on structural, morphological and PL have been carried out to analyse the suitability of the as prepared phosphors along with the optimization for better luminescence efficiency and the feasibility of using them in pc-WLEDs. J-O analysis and TR-PL were carried out for the as prepared phosphors with and without optimised flux. Confocal images and other colorimetric studies have also been analyzed for potential candidature of the flux assisted Eu^{3+} doped CAZ phosphor for visible emission.

2. Sample Preparation and characterization

The conventional solid-state reaction method used to synthesize Eu^{3+} doped CAZ phosphor by taking stoichiometric ratio of CaO, Al_2O_3, ZnO, and Eu_2O_3 precursors. The chemicals were taken in stoichiometric ratio and mixed thoroughly in a dispersing medium (acetone) and grinded in an agate mortar for an hour, to which a predetermined quantity of NaF, NaCl, and $Na_2B_4O_7$ were added separately as a flux. After sufficient grinding, samples were sintered at 1200°C with a consistent heating rate for five hours and then naturally cool

Accepted manuscript

ACCEPTED MANUSCRIPT

down to room temperature in a programmable muffle furnace. The obtained powder samples were grinded again for different characterizations. The synthesized 1.0 mol% Eu^{3+} doped CAZ phosphor with 5 wt% NaF, NaCl, and $Na_2B_4O_7$ were named as NF1, NC1, and NB1 respectively and without flux indicated as CAZ1.

The phase purity of the as prepared samples has been measured by Bruker D8-Advanced X-Ray diffraction using CuKα radiation (λ = 1.54 Å) at voltage of 40 kV and a current of 40 mA, employing a scanning rate of 0.02 $°s^{-1}$ in the 2θ range of 20–70°. The particle size and morphology of the phosphors have been examined by scanning electron microscope (SEM). The PL spectra have been recorded on Shimadzu spectrofluorophotmeter (RF-5301PC) having spectral resolution of 0.2 nm using Xenon as an excitation source. TR-PL measurements have been performed using an Edinburgh FLSP 900 spectrofluorophotometer with spectral resolution of 0.1 nm with Xenon flash lamp as an excitation source. The high-resolution PL image has been obtained from confocal microscope (Olympus, BX51) equipped with XY-piezo stage and coupled with a 410 nm Continuous Wave (CW) diode laser. All characterizations have been performed at room temperature.

3. Result and discussions

3.1. X-ray Diffraction analysis

The synthesized phosphors NF1, NC1, NB1 and CAZ1, are analysed for crystal structure and phase confirmation. X-ray diffraction patterns measured for the CAZ1, NF1, NC1, and NB1 phosphors are shown in Fig. 1. The XRD patterns of CAZ1, NC1, and NB1 phosphors are showing sharp peaks and are in complete agreement with the standard PDF4 + International Crystallographic Diffraction Database (ICDD) card no. 04-009-7304. The XRD patterns observed for NC1 and NB1 are showing single phase orthorhombic structure of $Ca_3Al_4ZnO_{10}$ (CAZ) with Pbc2 space group. However, the XRD pattern of NF1 sample does

Accepted manuscript

ACCEPTED MANUSCRIPT

not show pure phase of $Ca_3Al_4ZnO_{10}$ as shown in Fig. 1. Furthermore, the XRD pattern of NB1 shows absence of any impurity peak and also it exhibits more crystallinity when compared to other samples. This might be due to larger solubility, faster diffusion and reaction rate of reactants in NB1 phosphor. This prompted us to increase the amount of flux ($Na_2B_4O_7$) to 10, 15 and 20 wt% in the CAZ host system to optimize the amount of flux. For convenience, these samples have been designated as NB2, NB3, and NB4 for 10, 15 and 20 wt% of flux in CAZ respectively. We have employed Debye-Scherrer's equation ($D = k\lambda/\beta cos\theta$, where D is crystallite size, β is full width at half maxima, θ is bragg's diffraction angle, k is shape factor, and λ is wavelength) to estimate crystallite size of the as prepared phosphors [29]. The average crystallite size is found to be 51.6, 52.2 and 50.0 nm for CAZ1, NC1, and NB1 respectively. The reduced crystallite size for NB1 signifies the better crystallinity of that phosphor [15].

3.2. Morphology

Fig. 2 (a) and (b) are SEM images of the Eu^{3+} doped phosphor of CAZ1 and NB1, respectively. From the perspective of morphology, as appearing in Fig. 2 both the phosphors under investigation are having agglomerated cluster of particles with irregular shape and uneven particle distribution. The SEM images of CAZ1 and NB1 show that the particle size has been reduced by adding $Na_2B_4O_7$ flux to the host lattice. Different parameters such as solubility of raw materials, ionic radii of anion/cation, as well as purity of flux, have a significant effect on size and morphology of the as prepared phosphors [25]. The average size of the particle in the as prepared phosphors are found to be in the range of 2-15 μm which is comparable with the particle sizes of the commercially available phosphors [30].

3.3. Photoluminescence Properties

Fig. 3 shows the PL excitation (PLE) and emission spectra for different concentrations of Eu^{3+} doped CAZ phosphor. In Fig. 3, there are five excitation peaks in the range 350-475

Accepted manuscript

ACCEPTED MANUSCRIPT

nm which are the excitation energies of Eu^{3+} ions attributed to $^7F_0 \rightarrow {}^5D_4$, $^7F_0 \rightarrow {}^5L_7$, $^7F_0 \rightarrow {}^5L_6$, $^7F_0 \rightarrow {}^5D_3$, $^7F_0 \rightarrow {}^5D_2$ electronic transitions recorded under 615 nm emission wavelength[6]. Among all the excitations peaks, the peak at 462 nm assigned to $^7F_0 \rightarrow {}^5D_2$ transition is the most intense one and the next intense peak is assigned to $^7F_0 \rightarrow {}^5L_6$ transition at 391 nm [13]. The two excitation peaks observed at 391 and 462 nm facilitates that the as prepared phosphor can be effectively excited by both n-UV and blue LED chips. The emission spectra recorded under the intense blue excitation having several peaks in the range 550-725 nm corresponding to $^5D_1 \rightarrow {}^7F_2$, and $^5D_0 \rightarrow {}^7F_{0,1,2,3,4}$ transitions [13]. The emission spectra exhibit two intense emission bands at 588 and 615 nm assigned to $^5D_0 \rightarrow {}^7F_1$ and $^5D_0 \rightarrow {}^7F_2$ transitions respectively. Among them $^5D_0 \rightarrow {}^7F_1$ transition corresponds to the magnetic dipole (MD) and $^5D_0 \rightarrow {}^7F_2$ corresponds to the forced electric dipole (ED) in nature. The $^5D_0 \rightarrow {}^7F_1$ transition is allowed and insensitive to the crystal field environment whereas $^5D_0 \rightarrow {}^7F_2$ transition is hypersensitive to the chemical bonds in the vicinity of Eu^{3+} ions [31]. The integrated intensity ratio I_{ED}/I_{MD} is a local crystal field probe used to measure the nature of cation surroundings to estimate the degree of distortion from the inversion symmetry of the Eu^{3+} ion local environment. The intensity ratio I_{ED}/I_{MD} obtained as 1.44, 1.49, 1.52, and 1.54 speaks that, the intensity of ED transition predominantly more than MD transition, which can be seen clearly in Fig. 3. Relatively higher intensities observed for ED transitions signifies that Eu^{3+} ions are located at the sites without an inversion centre where the symmetry of crystal field is low. Higher I_{ED}/I_{MD} ratio signifies more distortion and also reflects more covalent nature of the bonds between Eu^{3+} ions and other constituents [4,11,17,32]. Further, the doping concentration of activator plays a significant role in influencing the efficiency of the phosphor. We found that, the emission intensity increases with increase in Eu^{3+} ion concentration up to 2.0 mol%, beyond which concentration quenching has been observed due to non-radiative energy transfer among Eu^{3+} ions in the as prepared phosphor. The

Accepted manuscript

ACCEPTED MANUSCRIPT

concentration quenching occurs when the distance between Eu^{3+} ions reduces to a certain level where the excitation energy is migrated to quenching centres [33]. The critical energy transfer distance can be evaluated using the relation:

$$R_c \approx 2\left[\frac{3V}{4\pi X_c N}\right]^{\frac{1}{3}} \quad (1)$$

where V is the volume of the unit cell (V = 923.438 $Å^3$), N is the number of cations per unit cell (N = 4) and X_c is the critical concentration beyond which concentration quenching has been observed (X_c = 0.02 (2.0 mol%)). The calculated value of R_c is 29.16 Å, which is far more than 5 Å, indicating non-radiative energy transfer took place via multipolar interaction among Eu^{3+} ions. According to the Dexter's theory and Reisfeld's approximation, the emission intensity (I) and concentration of the dopant ion (x) can be related as:

$$\frac{I}{x} = K\{1 + \beta(x)^{\frac{Q}{3}}\}^{-1} \quad (2)$$

where, K and β are constants for a given host lattice and Q defines the type of interaction between the dopant ions, Q = 6, 8, and 10 for dipole-dipole, dipole-quadrupole, quadrupole-quadrupole interaction, respectively [34].

Equation (2) can be approximately simplified to:

$$log\frac{I}{x} = K' - \frac{Qlog(x)}{3} \quad (3)$$

where K' is some constant. In order to identify the correct the value of Q, the graph between log(I/x) and log (x) has been plotted as shown in Fig. 4 that yields a straight-line plot having slope -Q/3. In the present study, the slope comes out to be -1.82, which gives Q = 5.46 close to 6, implying dipole-dipole interaction is the underlying mechanism for concentration quenching in Eu^{3+} doped CAZ phosphor [33].

Accepted manuscript

ACCEPTED MANUSCRIPT

3.3.1. Effect of added flux on the emission spectra

Fig. 5 shows the emission spectra of 1.0 mol% Eu^{3+} doped CAZ phosphor for CAZ1, NF1, NC1, and NB1 recorded under 462 nm excitation. The intensity variation with the addition of different fluxes can be clearly seen. From Fig. 5, it is conspicuous that, $Na_2B_4O_7$ added as a flux significantly shows intensity enhancement in Eu^{3+} doped CAZ phosphor among all fluxes. Addition of NaCl flux can only increases the emission intensity approximately 1.5 times to the CAZ1 phosphor. Whereas the emission intensity for NB1 increased approximately 2.5 times to the CAZ1 phosphor. The emission spectrum for NF1 does not show any enhancement in the emission intensity, instead there is some loss of emission intensity which might be due to impure phase formation of CAZ phosphor. Therefore, the emission intensities shown by different fluxes added to CAZ phosphor allows us to conclude that, $Na_2B_4O_7$ serve as an optimized flux to show better luminescence efficiency. Addition of $Na_2B_4O_7$ flux reduces the sintering temperature and increase the diffusion rate of Eu^{3+} in the host lattice, thereby enhancing the luminescent emission intensity [35]. Since the flux has lower melting point, it allows more particle to take part in reaction and accelerates the kinetics of formation of the phosphor by enhancing the diffusion coefficients, dissolving more reaction components and allowing larger content of reacting species to take part in reaction and improves the crystal structure and growth. When the flux melts during calcination, it removes solid-grain boundaries and make the surface of particles smooth. Among the three fluxes, $Na_2B_4O_7$ (743 °C) has lowest melting point as compared to NaCl (801 °C), and NaF (993 °C). Therefore, the possibility of $Na_2B_4O_7$ to be emerged as a good flux is more, as it can allow more reacting component to take part in reaction comparatively at lower temperature as compared to other fluxes including NaF and NaCl. Since the luminescence intensity is highest for $Na_2B_4O_7$ added in Eu^{3+} doped CAZ phosphor, it can be said that flux $Na_2B_4O_7$ emerges as an excellent flux in Eu^{3+} doped CAZ phosphor

Accepted manuscript

ACCEPTED MANUSCRIPT

[15,17]. Further, the integrated intensity ratios I_{ED}/I_{MD} for NC1 and NB1 are found to be 1.58, and 1.65 respectively. Therefore, it can be inferred from the calculated I_{ED}/I_{MD} ratio that the crystal environment of Eu^{3+} ions in NB1 is more distorted from the crystal field symmetry, and more covalent nature of the bonds between Eu^{3+} ions and other constituents [11,32]. The emission spectra also show some splitting in the emission band which can be attributed to the stark effect. The emission characteristics of RE ions in a crystal field depend on the symmetry of the coordination structure and lead to a splitting of the energy levels [28,35].

Fig. 6, shows the effect of flux dosage on the luminescent intensity of Eu^{3+} doped CAZ phosphor excited via blue (462 nm) light. The emission intensity gradually increases with increase in $Na_2B_4O_7$ amount from 5 wt% to 20 wt% (samples are named as NB1, NB2, NB3, and NB4 for 5, 10, 15 and 20 wt%, respectively) implying the enhancement in solubility of Eu^{3+} ions in the host lattice. Apart from this, as shown in the inset of Fig. 6, the emission spectral profiles of NB2, NB3 and NB4 are little deviated from the spectral profiles of NB1. To understand the plausible reason for this deviation, the structural analysis has been done again for the higher concentration of $Na_2B_4O_7$, using XRD. Fig. 7 shows the XRD pattern of variable wt% $Na_2B_4O_7$ assisted Eu^{3+} doped CAZ. It is apparent from Fig. 7, that the pure phase of CAZ has not been obtained in the 10, 15 and 20 wt % $Na_2B_4O_7$ assisted CAZ phosphor. The presence of few impurity peaks in the X-ray diffraction pattern results in impure phase formation of $Ca_3Al_4ZnO_{10}$. This might be the plausible reason for the deviation of emission spectral profiles for these phosphors. The optimal amount of flux is therefore considered to be 5 wt% of $Na_2B_4O_7$. Furthermore, the emission intensity variation is also analysed for 2.0 mol% Eu^{3+} doped CAZ phosphor with and without $Na_2B_4O_7$ (named as NB5 and CAZ2, respectively) as shown in Fig. 8. The obtained spectral profile is similar to that of NB1 and CAZ1. It is evident from Fig. 6 and 8 that, the emission intensity of $Na_2B_4O_7$ assisted Eu^{3+} doped CAZ phosphor increases more than 2.5 times approximately to that of

Accepted manuscript

ACCEPTED MANUSCRIPT

Eu^{3+} doped CAZ phosphor without flux. The emission spectrum of commercial phosphor (Y_2O_3:Eu^{3+}) has been compared with 2.0 mol% Eu^{3+} doped CAZ phosphor added $Na_2B_4O_7$ (NB5) as flux as shown in Fig. 9. The intensity ratio of the intense peak of NB5 to Y_2O_3:Eu^{3+} corresponding to $^5D_0 \rightarrow {}^7F_2$ transition is 0.81, whereas for $^5D_0 \rightarrow {}^7F_0$, $^5D_0 \rightarrow {}^7F_1$, $^5D_0 \rightarrow {}^7F_3$ and $^5D_0 \rightarrow {}^7F_4$ transition the intensity ratio is 3.9, 4.3, 2.9 and 9.5 respectively. This indicates the emission of Eu^{3+} doped CAZ phosphor added $Na_2B_4O_7$ is comparable with the commercial phosphor. Hence, $Na_2B_4O_7$ assisted Eu^{3+} doped CAZ phosphor is a potential candidate for red emitting phosphor for application in solid state lighting devices.

3.4. **Emission spectral analysis using Judd-Ofelt (J-O) theory.**

The J-O intensity parameters (Ω_λ) have been evaluated using the emission spectra of RE ions in crystal lattice using the equations given elsewhere [36]. The J-O intensity parameters (Ω_λ) evaluated can provide the information pertaining to the local structure and bonding in the vicinity of RE ions [37]. The J-O analysis is also useful in calculating the radiative transition rates between various levels of the RE ions [38–40]. The radiative transition rates for magnetic dipole and induced electric dipole transitions have been calculated using equations reported elsewhere [41–46]. The radiative transition rates ($A_{0\text{-}J}$) corresponding to the MD and ED transitions are presented in Table.1. The branching ratios (β_R) evaluated using the expression given elsewhere are listed in Table. 1 [47]. The branching ratio characterizes the lasing power of an emission transition if its value is more than 0.50 in comparison with other transitions originating from an excited level [47,48]. From Table. 1, it can be observed that $^5D_0 \rightarrow {}^7F_2$ transition has branching ratio much greater than 0.50, indicating the potentiality of the present system to serve as a good luminescent phosphor for laser applications under 462 nm excitation.

Accepted manuscript

ACCEPTED MANUSCRIPT

The J-O parameters and transition probabilities values evaluated are presented in Table. 2. The Ω_6 value cannot be evaluated in the present case, since the transition $^5D_0 \rightarrow {}^7F_6$ is missing in the emission spectra. Higher the value of Ω_2, more structural changes in the vicinity of Eu^{3+} ions and higher covalence between metal-ligand bonds [49]. Higher covalence is due to the lowering of electronic levels of free ions which in turn enhances Ω_2 value. The structural distortion is more and covalent nature is strong in $Na_2B_4O_7$ assisted Eu^{3+} doped CAZ phosphor which has been confirmed from integrated emission intensity ratio I_{ED}/I_{MD} [50,51].

3.5. Color chromaticity coordinates and color purity

To evaluate the potential of red emission in the as prepared CAZ phosphors, the CIE chromaticity coordinates can be calculated from emission spectra using color matching function $\bar{x}(\lambda)$, $\bar{y}(\lambda)$, and $\bar{z}(\lambda)$ defined in CIE 1931 and spectral power density $P(\lambda)$ of the light source [29,52]. The calculated CIE coordinates are represented in Table. 3. Fig. 10 represents the CIE color chromaticity coordinates of NB5 lies in pure red region of chromaticity diagram. The obtained CIE coordinates for all the samples are close to NTSC standard value (0.670, 0.330) for red phosphor and also to the commercial red emitting phosphor Y_2O_2S: Eu^{3+} (0.622, 0.351) [31]. The CIE coordinates on the perimeter describes the monochromaticity of the color emission. To have a better understanding about the red emission, the color purity has been calculated using the expression as follows [25]:

$$color\ purity = \frac{\sqrt{(x-x_{ee})^2+(y-y_{ee})^2}}{\sqrt{(x_d-x_{ee})^2+(y_d-y_{ee})^2}} \quad (4)$$

where (x, y) are the coordinates of the sample under consideration, (x_{ee}, y_{ee}) are the coordinates of white point, and (x_d, y_d) are the coordinates of dominant wavelength point. The color purity of the monochromatic emitters should be 100%. The calculated value of color purity for NB5 is found to be 99.09%, indicating extremely pure red emission.

Accepted manuscript

ACCEPTED MANUSCRIPT

3.6. PL decay analysis.

Fig. 11 (a-i) represents the PL decay spectral features recorded at 615 nm for all the phosphors under 462 nm excitation, namely CAZ1, CAZ2, NF1, NC1, NB1, NB2, NB3, NB4, and NB5, respectively. All the decay curves have been aptly fitted to bi-exponential equation expressed as follows [5]:

$$I_t = I_0 + A_1 \exp\left(-\frac{t}{\tau_1}\right) + A_2 \exp\left(-\frac{t}{\tau_2}\right) \quad (5)$$

where I_t and I_0 are the emission intensities at time t and 0 respectively; A_1, and A_2 are the constants; τ_1 and τ_2 are the fast and slow lifetimes for exponential components respectively. The fitting parameters, and lifetime values obtained from bi-exponential fit have been shown in Table. 1 in supplementary information. The bi-exponential fit of the decay curves indicates the presence of metal ion in two different environments due to which it has two components of lifetime [53]. The bi-exponential fitting indicates the energy transfer between the activator ions takes place via cross-relaxation process. The average lifetime (τ) has been calculated by using the formula:

$$\tau = \frac{A_1\tau_1^2 + A_2\tau_2^2}{A_1\tau_1 + A_2\tau_2} \quad (6)$$

The average value of lifetime for all the phosphors has been found to be in the range of microseconds, shown in Table. 3 The lifetime values for 1.0 and 2.0 mol% Eu^{3+} doped CAZ phosphor with and without $Na_2B_4O_7$ decreases with increase in dopant concentration shows energy transfer between Eu^{3+} ions.

4. Conclusions

Eu^{3+} doped CAZ phosphor with various fluxes (NaF, NaCl, and $Na_2B_4O_7$) has been synthesized by conventional solid-state reaction technique for the first time. The XRD pattern confirmed orthorhombic structure and pure phase of CAZ phosphor with $Na_2B_4O_7$. SEM

Accepted manuscript

ACCEPTED MANUSCRIPT

image reveals inhomogeneous agglomerated particles with average particle size of few microns. SEM image for NB1 shows reduction in particle size using $Na_2B_4O_7$ in Eu^{3+} doped CAZ phosphor. Intense red emission has been observed from Eu^{3+} doped CAZ phosphor by blue excitation. By optimizing the flux, significant enhancement of red emission has been observed in 5 wt% $Na_2B_4O_7$ assisted Eu^{3+} doped CAZ phosphor. The emission spectrum of 5 wt% $Na_2B_4O_7$ assisted Eu^{3+} doped CAZ phosphor has been compared with the commercial phosphor (Y_2O_3: Eu^{3+}). The J-O theory has been applied to analyse optical properties. The CIE chromaticity coordinates for all the studied samples are found to lie in red region and are close to the coordinates of commercial red phosphor Y_2O_2S: Eu^{3+} (x = 0.622, y = 0.351) as well as NTSC system (x = 0.670, y = 0.330). The calculated color purity found to be 99.09 % for 5 wt% $Na_2B_4O_7$ assisted 2 mol % Eu^{3+} doped CAZ phosphor which confirms the highly pure red emission from the system. The $^5D_0$ level decay curves of Eu^{3+} doped CAZ phosphor shows bi-exponential behaviour with an average lifetime of microseconds. All the aforementioned results allow us to conclude that 5wt% $Na_2B_4O_7$ assisted 2 mol% Eu^{3+} doped CAZ phosphor is a promising phosphor for intense red emission and is aptly suitable for the development of white light emitting devices.

Acknowledgement

One of the authors Ms. Sumandeep Kaur is grateful to University Grants Commission (UGC) (Ref.No: 22/06/2014(i)EU-V) for providing financial support in the form of Junior Research Fellowship (JRF) to her. The author (M. Jayasimhadri) also grateful to DST-SERB, Govt. of India for the sanction of a research project (No. SB/FTP/PS-082/2014, dt. 02/03/2015). The author (A.S. Rao) also grateful to DST-SERB, Govt. of India for the sanction of a research project (EMR/2016/007766).

Accepted manuscript

ACCEPTED MANUSCRIPT

References

[1] M. You, J. Xu, Z. Zhang, Y. Zhou, Eu3+ -doped CdWO4 phosphor for red-light emission: Hydrothermal preparation and blue light excitation, 40 (2014) 16189–16194. doi:10.1016/j.ceramint.2014.07.052.

[2] N. Guo, Y. Huang, H. You, M. Yang, Y. Song, K. Liu, Y. Zheng, Ca9Lu(PO4)7:Eu2+,Mn 2+: A potential single-phased white-light-emitting phosphor suitable for white-light-emitting diodes, Inorg. Chem. 49 (2010) 10907–10913. doi:10.1021/ic101749g.

[3] A.K. Vishwakarma, M. Jayasimhadri, Pure orange color emitting Sm3+ doped BaNb2O6 phosphor for solid - state lighting applications, J. Lumin. 176 (2016) 112–117. doi:10.1016/j.jlumin.2016.03.025.

[4] Y. Zhang, W. Gong, G. Ning, Novel red-emitting LiGd(WO4)2: Eu3+ phosphor with high thermal stability and high color purity for application in white light- emitting diodes Yang, New J. Chem. 40 (2016) 10136–10143. doi:10.1039/b000000x.

[5] J. Sun, Z. Lian, G. Shen, D. Shen, Blue–white–orange color-tunable luminescence of Ce3+/Mn2+-codoped NaCaBO3 via energy transfer: potential single-phase white-light-emitting phosphors, RSC Adv. 3 (2013) 18395–18405. doi:10.1039/c3ra42554a.

[6] G. Annadurai, S.M. Moses Kennedy, Synthesis and photoluminescence properties of Ba2CaZn2Si6O17: Eu3+ red phosphors for white LED applications, J. Lumin. 169 (2016) 690–694. doi:10.1016/j.jlumin.2015.03.007.

[7] L. Yang, Y. Wan, Y. Huang, C. Chen, H. Jin, Development of YK3B6O12 : RE (RE = Eu3+,Tb3+, Ce3+) tricolor phosphors under near-UV light excitation, J. Alloys Compd. 684 (2016) 40–46. doi:10.1016/j.jallcom.2016.04.052.

Accepted manuscript

ACCEPTED MANUSCRIPT

[8] S. Long, J. Hou, G. Zhang, F. Huang, Y. Zeng, High quantum efficiency red-emission tungstate based phosphor Sr(La 1-xEux)2Mg2W2O 12 for WLEDs application, Ceram. Int. 39 (2013) 6013–6017. doi:10.1016/j.ceramint.2013.01.013.

[9] P. Biswas, V. Kumar, G. Agarwal, O.M. Ntwaeaborwa, H.C. Swart, NaSrVO4:Sm3+ − An n-UV convertible phosphor to fill the quantum efficiency gap for LED applications, Ceram. Int. 42 (2016) 2317–2323. doi:10.1016/j.ceramint.2015.10.027.

[10] K.Y. Jung, H.W. Lee, H.K. Jung, Luminescent properties of (Sr, Zn)Al2O4:Eu 2+,B3+ particles as a potential green phosphor for UV LEDs, Chem. Mater. 18 (2006) 2249–2255. doi:10.1021/cm060003w.

[11] D.A. Hakeem, K. Park, Enhanced photoluminescence properties of red emitting Ba1-xAl2Si2O8: xEu3+ phosphors by charge compensation, New J. Chem. 39 (2015) 7768–7772. doi:10.1039/C5NJ00988J.

[12] Q. Zhang, Q. Wang, X. Wang, X. Ding, Y. Wang, Luminescence properties of Eu2+-doped BaSi2O5 as an efficient green phosphor for light-emitting devices and wide color gamut field emission displays Qiang, New J. Chem. 40 (2016) 8549–8555. doi:10.1039/b000000x.

[13] L. Zhao, J. Liu, Z. Wu, S. Kuang, Spectrochimica Acta Part A : Molecular and Biomolecular Spectroscopy Optimized photoluminescence of SrB 2 O 4 : Eu 3 + red-emitting phosphor by charge compensation, Spectrochim. Acta Part A Mol. Biomol. Spectrosc. 87 (2012) 228–231. doi:10.1016/j.saa.2011.11.043.

[14] X. Wang, G. Zhou, H. Zhang, H. Li, Z. Zhang, Z. Sun, Luminescent properties of yellowish orange Y 3 Al 5 − x Si x O 12 − x N x : Ce phosphors and their applications in warm white light-emitting diodes, J. Alloys Compd. 519 (2012) 149–155. doi:10.1016/j.jallcom.2011.12.158.

Accepted manuscript

ACCEPTED MANUSCRIPT

[15] A.K. Vishwakarma, M. Jayasimhadri, Significant enhancement in photoluminescent properties via flux assisted Eu3+ doped BaNb2O6 phosphor for white LEDs, J. Alloys Compd. 683 (2016) 379–386. doi:10.1016/j.jallcom.2016.05.052.

[16] E. Pavitra, G.S.R. Raju, J.Y. Park, L. Wang, B.K. Moon, Novel rare-earth-free yellow Ca5Zn3.92In0.08(V0.99Ta0.01O4)6 phosphors for dazzling white light- emitting diodes, Sci. Rep. 5 (2015) 10296–10309. doi:10.1038/srep10296.

[17] H. Zhang, H. Zhang, J. Zhuang, H. Dong, Y. Zhu, X. Ye, Effect of H3BO3 flux on the morphology and optical properties of Sr2MgAl22O36 : Mn4+ red phosphors for agricultural light conversion films, Ceram. Int. 42 (2016) 13011–13017. doi:10.1016/j.ceramint.2016.05.076.

[18] L. Muresan, E. Jeanne, F. Imre-lucaci, Studies on Y2O3 : Eu phosphor with different particle size prepared by wet chemical method, J. Alloys Compd. 483 (2009) 346–349. doi:10.1016/j.jallcom.2008.08.087.

[19] B. V Ratnam, M.K. Sahu, A.K. Vishwakarma, K. Jha, H. Woo, K. Jang, M. Jayasimhadri, Optimization of synthesis technique and luminescent properties in Eu3+ -activated NaCaPO4 phosphor for solid state lighting applications, J. Lumin. 185 (2017) 99–105. doi:10.1016/j.jlumin.2017.01.006.

[20] H.F. Wang, G.Z. Xing, X.Y. Wang, X.G. Bai, L. Zhang, S. Li, Tailoring photoluminescence in strontium aluminate phosphors using fluxing agent and activators : Rational synthesis via a facile microwave-assisted method, Mater. Sci. Semicond. Process. 27 (2014) 1007–1012. doi:10.1016/j.mssp.2014.09.005.

[21] H. Wu, Y. Hu, W. Zhang, H. Duan, L. Chen, X. Wang, Flux's influence on the luminescent properties of europium and dysprosium codoped melilite long afterglow phosphor, J. Non. Cryst. Solids. 358 (2012) 2734–2740.

Accepted manuscript

ACCEPTED MANUSCRIPT

doi:10.1016/j.jnoncrysol.2012.05.046.

[22] Y.E. Linqin, P. Xingping, Z. Shuihe, W. Yuhua, Photoluminescence properties of Ca-doped BaMgAl10O17: Eu2+, Mn2+ blue phosphor using BaF2 and CaF2 as co-flux, J. Rare Earths. 32 (2014) 1109–1113. doi:10.1016/S1002-0721(14)60190-3.

[23] B. Sundarakannan, M. Kottaisamy, Sol-gel derived flux assisted synthesis of fine particles YAG:Ce3+ phosphor for remote phosphor converted white light emitting diodes, Mater. Res. Bull. 74 (2016) 485–490. doi:10.1016/j.materresbull.2015.10.057.

[24] V. Sivakumar, A. Lakshmanan, Pyrolysis synthesis of Zn2SiO4: Mn2+ phosphors – effect of fuel , flux and co-dopants, J. Lumin. 145 (2014) 420–424. doi:10.1016/j.jlumin.2013.08.016.

[25] G. Swati, S. Bishnoi, P. Singh, B. Rajesh, G. Kumar, P. Seth, D. Haranath, Novel flux-assisted synthesis for enhanced afterglow properties of (Ca, Zn)TiO3: Pr3+ phosphor, J. Alloys Compd. 698 (2017) 930–937. doi:10.1016/j.jallcom.2016.12.316.

[26] K. Chen, J. Zhou, F. Zhang, X. Zhang, C. Li, L. An, Screening Sintering Aids for (K0.5Na0.5)NbO3 Ceramics, J. Am. Ceram. Soc. Ceram. Soc. 1701 (2015) 1698–1701. doi:10.1111/jace.13583.

[27] R. Sharma, U. Sharma, Influence of fluxing agent on the luminescence properties of SrAl<inf>2</inf>O<inf>4</inf>:Eu^{2+} nanophosphors, J. Alloys Compd. 649 (2015) 440–446. doi:10.1016/j.jallcom.2015.07.170.

[28] S. Kaur, M. Jayasimhadri, A.S. Rao, A novel red emitting Eu3+ doped calcium aluminozincate phosphor for applications in w-LEDs, J. Alloys Compd. 697 (2017) 367–373. doi:10.1016/j.jallcom.2016.12.150.

[29] A.K. Vishwakarma, K. Jha, M. Jayasimhadri, B. Sivaiah, B. Gahtori, D. Haranath,

Accepted manuscript

ACCEPTED MANUSCRIPT

Emerging cool white light emission from Dy3+ doped single phase alkaline earth niobate phosphors for indoor lighting applications, Dalt. Trans. 44 (2015) 17166–17174. doi:10.1039/c5dt02436f.

[30] S. Kaur, A.S. Rao, M. Jayasimhadri, Spectroscopic and photoluminescence characteristics of Sm 3+ doped calcium aluminozincate phosphor for applications in w-LED, Ceram. Int. 43 (2017) 7401–7407. doi:10.1016/j.ceramint.2017.02.129.

[31] A.K. Vishwakarma, K. Jha, M. Jayasimhadri, A.S. Rao, K. Jang, B. Sivaiah, D. Haranath, Red light emitting BaNb2O6: Eu3+ phosphor for solid state lighting applications, J. Alloys Compd. 622 (2015) 97–101. doi:10.1016/j.jallcom.2014.10.016.

[32] M. Nogami, N. Umehara, T. Hayakawa, Effect of hydroxyl bonds on persistent spectral hole burning in Eu3+-doped BaO-P2O5 glasses, Phys. Rev. B. 58 (1998) 6166–6171.

[33] P. Du, J.S. Yu, Synthesis and luminescent properties of Eu3+-activated Na0.5Gd0.5MoO4: A strong red-emitting phosphor for LED and FED applications, J. Lumin. 179 (2016) 451–456. doi:10.1016/j.jlumin.2016.07.045.

[34] D.L. Dexter, A Theory of Sensitized Luminescence in Solids, J. Chem. Phys. 21 (1953) 836. doi:10.1063/1.1699044.

[35] G. Ramakrishna, H. Nagabhushana, S.C. Prashantha, S.C. Sharma, B.M. Nagabhushana, Role of flux on morphology and luminescence properties of Sm3+ doped Y2SiO5 nanopowders for WLEDs, Spectrochim. Acta Part A Mol. Biomol. Spectrosc. 136 (2015) 356–365. doi:10.1016/j.saa.2014.09.041.

[36] L. Dacanin, S.R. Lukic, D.M. Petrovic, M. Nikolic, M.D. Dramicanin, Judd - Ofelt analysis of luminescence emission from Zn2SiO4: Eu3+ nanoparticles obtained by a

Accepted manuscript

ACCEPTED MANUSCRIPT

polymer-assisted sol - gel method, Phys. B Phys. Condens. Matter. 406 (2011) 2319–2322. doi:10.1016/j.physb.2011.03.068.

[37] Y. Tian, X. Qi, X. Wu, R. Hua, B. Chen, Luminescent Properties of Y2(MoO4)3 : Eu3+ Red Phosphors with Flowerlike Shape Prepared via Coprecipitation Method, J. Phys. Chem. C. 113 (2009) 10767–10772. doi:10.1021/jp901053q.

[38] B.R. Judd, Optical Absorption Intensities of Rare-Earth Ions, Phys. Rev. 127 (1962) 750–761.

[39] G.S. Ofelt, Intensities of Crystal Spectra of RareEarth Ions, J. Chem. Phys. 37 (1962) 511–520. doi:10.1063/1.1701366.

[40] R. Reisfeld, Luminescence and prediction of transition probabilities for solar energy and lasers, J. Less-Common Met. 112 (1985) 9–18. doi:10.1016/0022-5088(85)90003-7.

[41] K. Jha, M. Jayasimhadri, Structural and emission properties of Eu3+ -doped alkaline earth zinc - phosphate glasses for white LED applications, J. Am. Ceram. Soc. 100 (2017) 1402–1411. doi:10.1111/jace.14668.

[42] Y. Tian, B. Chen, R. Hua, J. Sun, L. Cheng, H. Zhong, X. Li, J. Zhang, Y. Zheng, T. Yu, L. Huang, H. Yu, Optical transition , electron-phonon coupling and fluorescent quenching of La2(MoO4)3: Eu3+ phosphor, J. Appl. Phys. 109 (2015) 053511–053517. doi:10.1063/1.3551584.

[43] E.E.S. Teotonio, G.P. Espı, H.F. Brito, O.L. Malta, S.F. Oliveira, D.L.A. de Faria, C.M.S. Izumi, Influence of the N - [methylpyridyl] acetamide ligands on the photoluminescent properties of Eu (III) -perchlorate complexes, Polyhedron. 21 (2002) 1837–1844.

Accepted manuscript

ACCEPTED MANUSCRIPT

[44] J. Xue, Y. Guo, B. Kee, S. Heum, J. Hyun, J. Hwan, L. Wang, Improvement of photoluminescence properties of Eu3+ doped SrNb2O6 phosphor by charge compensation, Opt. Mater. (Amst). 66 (2017) 220–229. doi:10.1016/j.optmat.2017.02.002.

[45] P. Du, X. Huang, J.S. Yu, Facile synthesis of bifunctional Eu3+-activated NaBiF4red-emitting nanoparticles for simultaneous white light-emitting diodes and field emission displays, Chem. Eng. J. 337 (2018) 91–100. doi:10.1016/j.cej.2017.12.063.

[46] P. Du, X. Huang, J.S. Yu, Ethylene glycol assisted rapid preparation of NaEuF4nanorods with splendid thermal stability for indoor illumination and optical displays, Dye. Pigment. 153 (2018) 307–315. doi:10.1016/j.dyepig.2018.02.024.

[47] C.B. Annapurna, S. Mahamuda, M. Venkateswarlu, K. Swapna, A.S. Rao, G.V. Prakash, Dy3+ ions doped single and mixed alkali fluoro tungsten tellurite glasses for LASER and white LED applications, Opt. Mater. (Amst). 62 (2016) 569–577. doi:10.1016/j.optmat.2016.11.016.

[48] M. Venkateswarlu, M.V.V.K.S. Prasad, K. Swapna, S. Mahamuda, Pr3+ doped lead tungsten tellurite glasses for visible red lasers, Ceram. Int. 40 (2014) 6261–6269. doi:10.1016/j.ceramint.2013.11.084.

[49] S. Mahamuda, K. Swapna, A.S. Rao, T. Sasikala, L.R. Moorthy, Reddish-orange emission from Pr3+ doped zinc alumino bismuth borate glasses, Phys. B Phys. Condens. Matter. 428 (2013) 36–42. doi:10.1016/j.physb.2013.07.010.

[50] K. Binnemans, C. Görller-Walrand, Are the Judd - Ofelt intensity parameters sensitive enough to reflect small compositional changes in lanthanide-doped glasses?, J. Phys. Condens. Matter. 10 (1999) L167–L170. doi:10.1088/0953-8984/10/10/002.

Accepted manuscript

ACCEPTED MANUSCRIPT

[51] R. Reisfeld, E. Greenberg, R.N. Brown, M.C. Drexhage, C.K. Jorgensen, FLUORESCENCE OF EUROPIUM(II1) 1N A FLUORIDE GLASS CONTAINING ZIRCONIUM, Chem. Phys. Lett. 95 (1983) 91–94.

[52] M. Kumar, T.K. Seshagiri, S. V Godbole, Fluorescence lifetime and Judd–Ofelt parameters of Eu3+ doped SrBPO5, Phys. B Phys. Condens. Matter. 410 (2013) 141–146. doi:10.1016/j.physb.2012.10.040.

[53] M. Mohapatra, V. Natarajan, S. V. Godbole, Speciation of "Eu" in sol-gel derived alkali barium borosilicate glass: Time resolved photoluminescence (TRPL) and Judd - Ofelt analysis, J. Non. Cryst. Solids. 386 (2014) 115–120. doi:10.1016/j.jnoncrysol.2013.12.002.

Accepted manuscript

ACCEPTED MANUSCRIPT

Figure Captions:

Fig. 1: XRD pattern of $Ca_{2.99}Al_4ZnO_{10}$: $0.01Eu^{3+}$ with and without flux along with standard diffraction pattern of $Ca_3Al_4ZnO_{10}$.

Fig. 2: SEM image of (a) CAZ1 and (b) NB1.

Fig. 3: PL Excitation (PLE) of $Ca_{2.99}Al_4ZnO_{10}$: $0.01Eu^{3+}$ and emission for $Ca_{3-x}Al_4ZnO_{10}$: xEu^{3+} (x = 0.01, 0.02, 0.03 and 0.04 mol).

Fig. 4: Plot of log(I/x) versus log(x).

Fig. 5: Emission Spectra of $Ca_{2.99}Al_4ZnO_{10}$**:** $0.01Eu^{3+}$ with different fluxes under 462 nm excitation wavelength.

Fig. 6: Emission Spectra of $Ca_{2.99}Al_4ZnO_{10}$**:** $0.01Eu^{3+}$ with different wt% of $Na_2B_4O_7$ under 462 nm excitation wavelength.

Fig. 7: XRD pattern of $Ca_{2.99}Al_4ZnO_{10}$: $0.01Eu^{3+}$ with different wt% of $Na_2B_4O_7$.

Fig. 8: Emission Spectra of $Ca_{2.98}Al_4ZnO_{10}$**:** $0.02Eu^{3+}$ without flux and with 5 wt% $Na_2B_4O_7$ under 462 nm excitation wavelength. (Inset: Enlarged emission intensity spectra from 570 nm to 644 nm).

Fig. 9: Emission spectra of commercial phosphor (Y_2O_3: Eu^{3+}), and $Ca_{2.98}Al_4ZnO_{10}$**:** $0.02Eu^{3+}$ with 5 wt% $Na_2B_4O_7$.

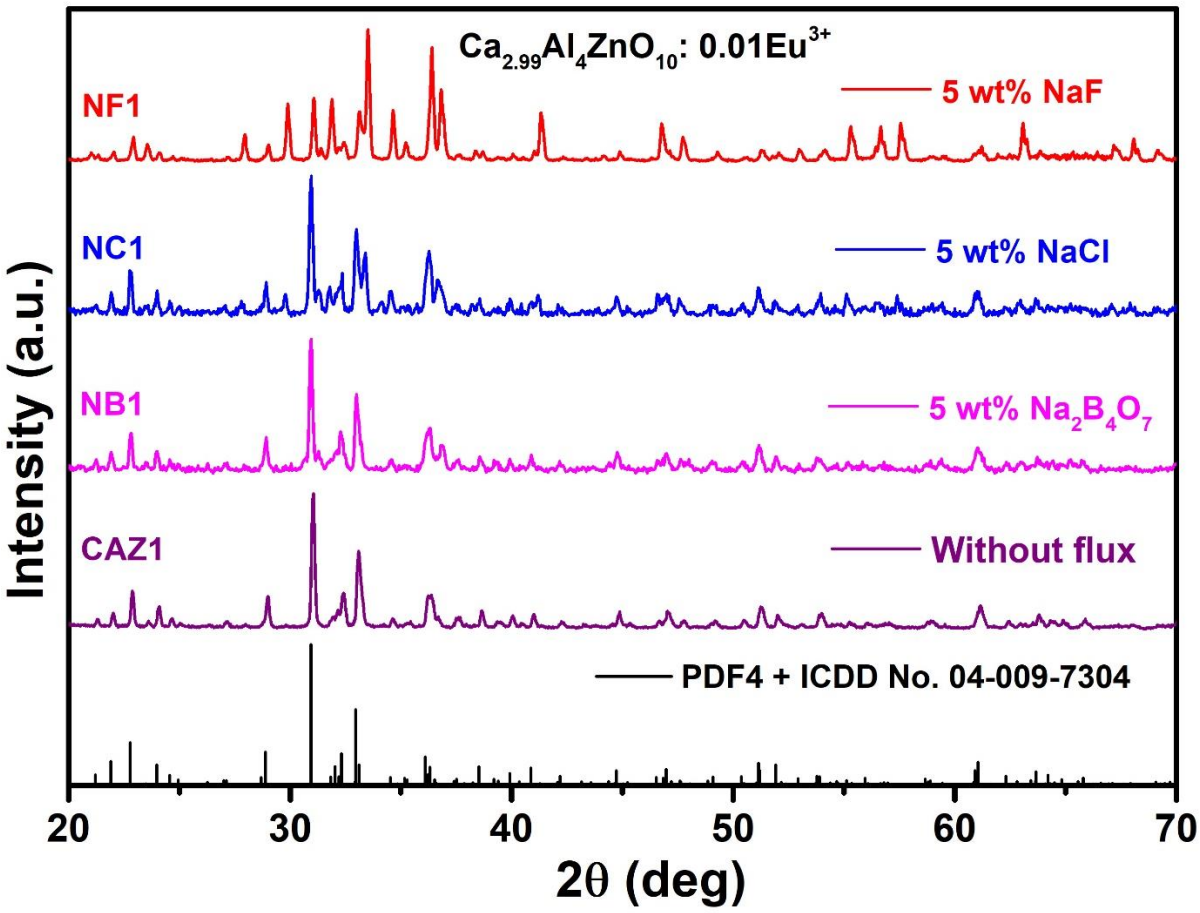
Fig. 10: CIE Chromaticity Diagram of $Ca_{2.98}Al_4ZnO_{10}$**:** $0.02Eu^{3+}$ incorporated with 5 wt% $Na_2B_4O_7$ (λ_{ex} = 462 nm) (Inset: Confocal image of $Ca_{2.98}Al_4ZnO_{10}$**:** $0.02Eu^{3+}$ incorporated with 5 wt% $Na_2B_4O_7$).

Fig. 11 (a-i): PL decay curve of all the phosphors (λ_{ex} = 462 nm and λ_{em} = 615 nm).

Accepted manuscript

ACCEPTED MANUSCRIPT

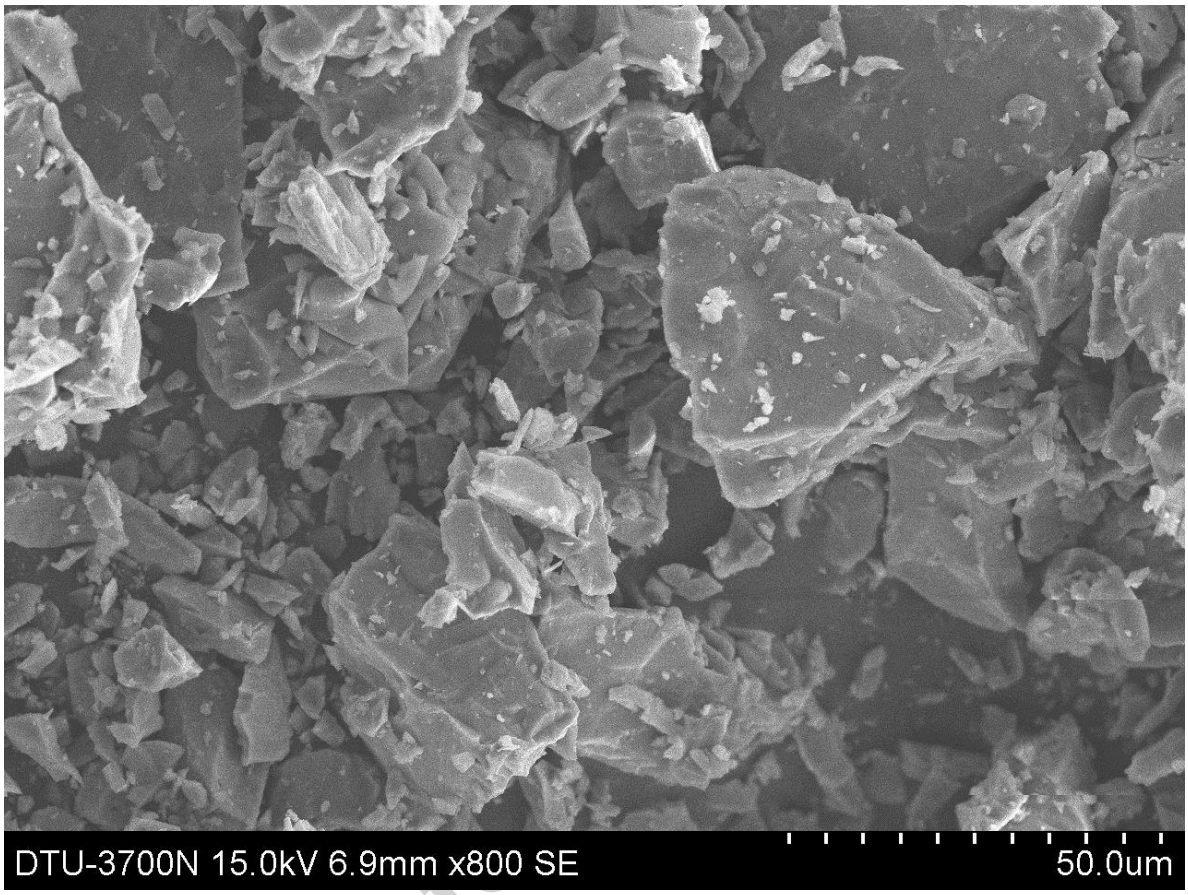
Fig. 1:



Accep

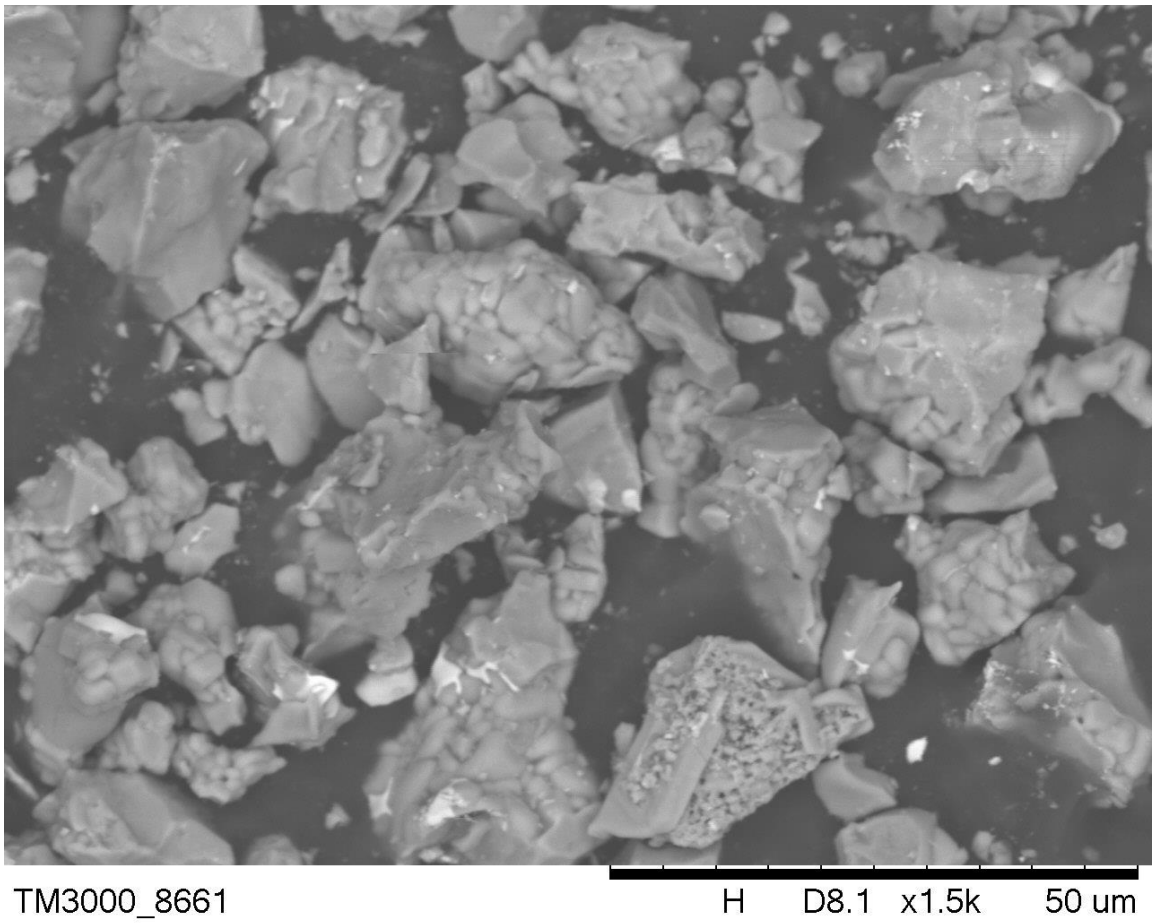
ACCEPTED MANUSCRIPT

Fig. 2a:



Accepted

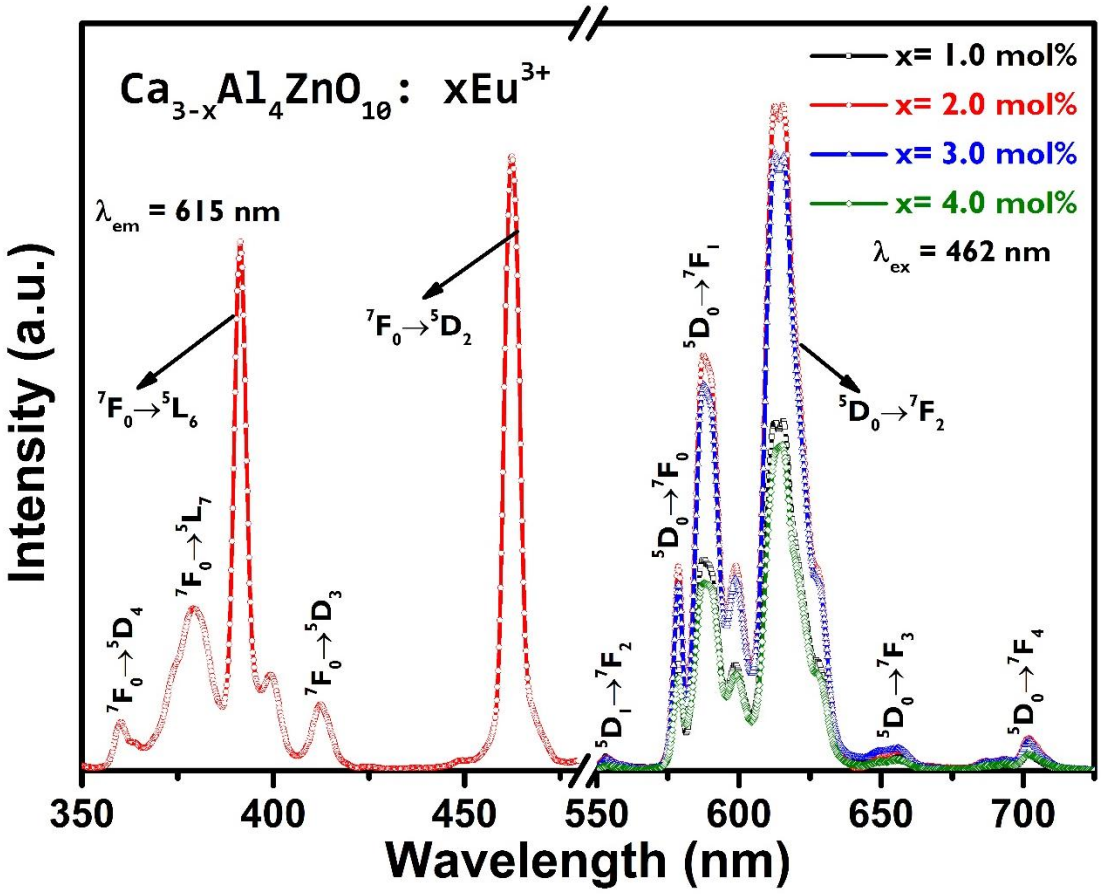
Fig. 2b:



Accep

Fig. 3:

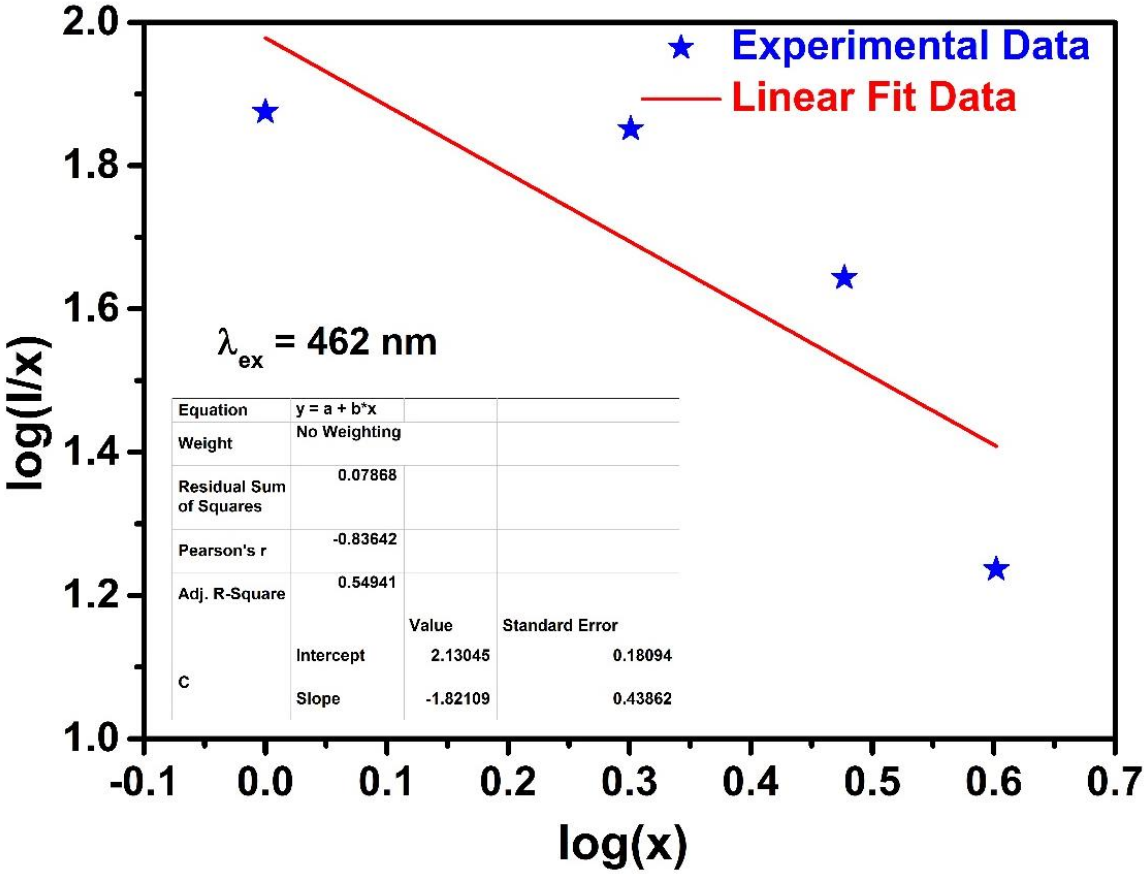
ACCEPTED MANUSCRIPT



Accepted manuscript

ACCEPTED MANUSCRIPT

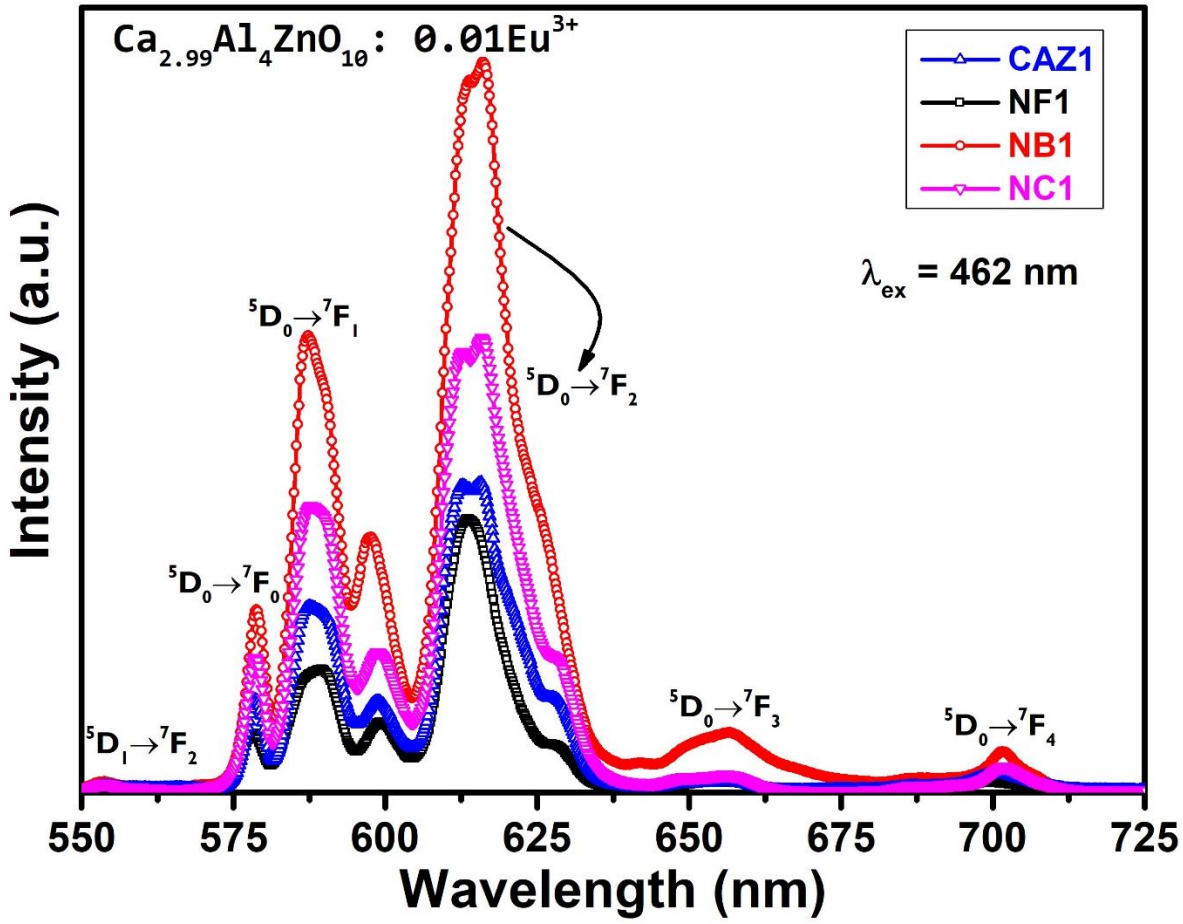
Fig. 4:



Accepted m

ACCEPTED MANUSCRIPT

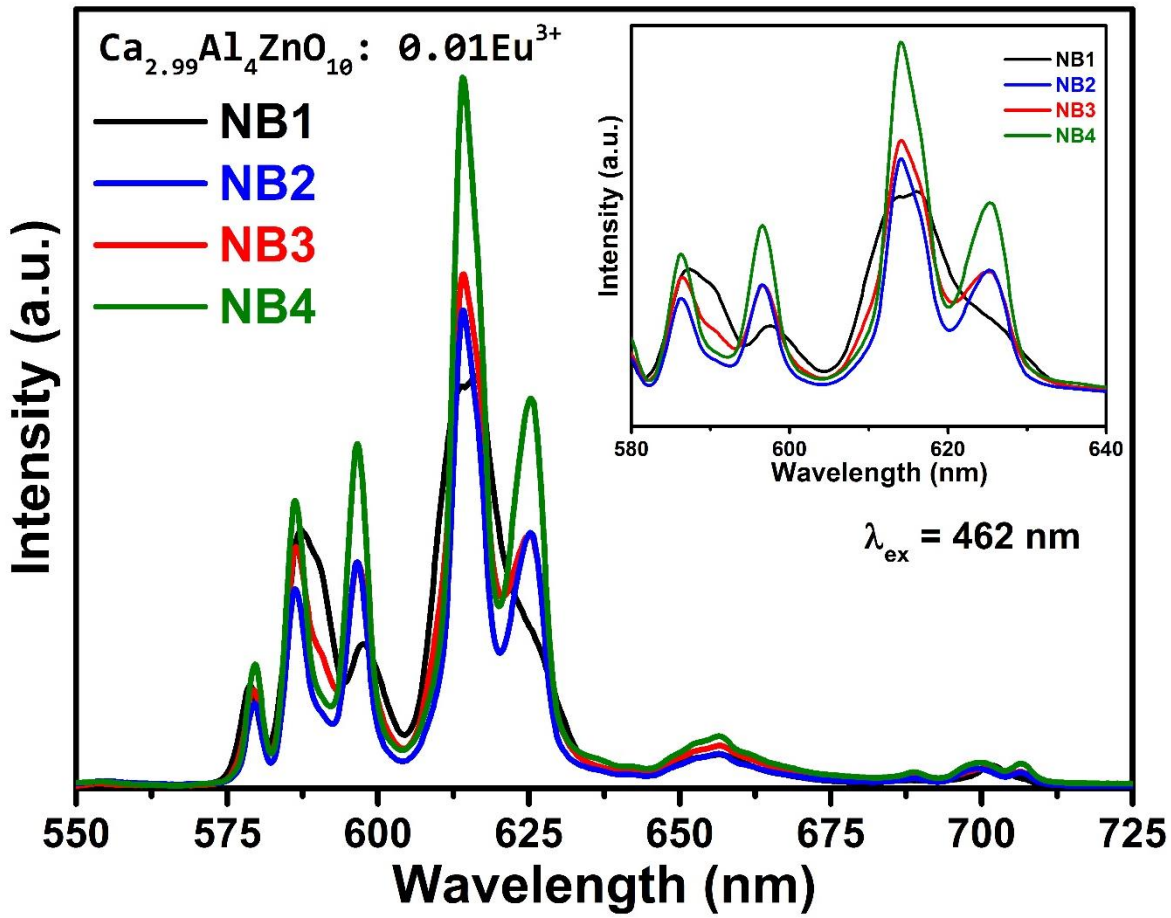
Fig. 5:



Accepted

ACCEPTED MANUSCRIPT

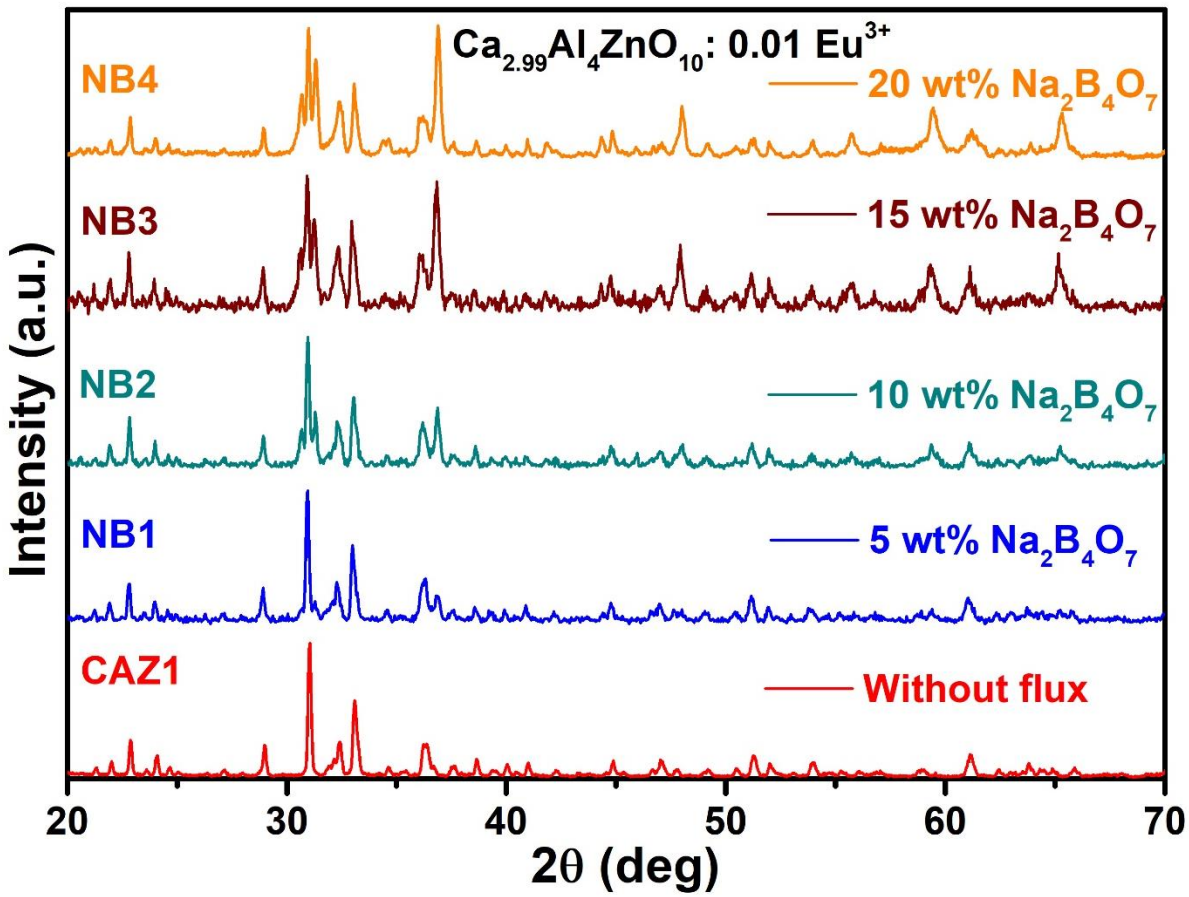
Fig. 6:



Accepted

ACCEPTED MANUSCRIPT

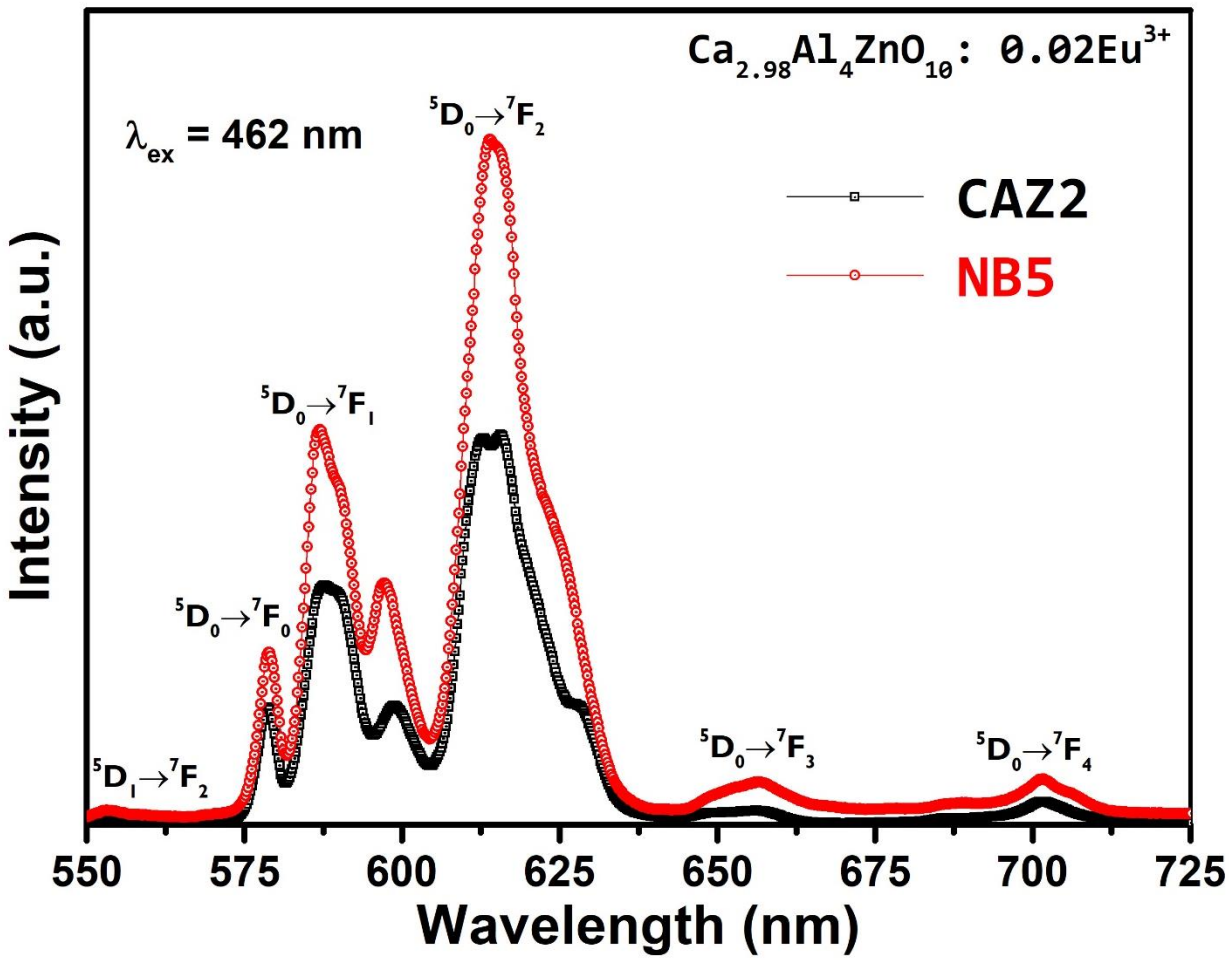
Fig. 7:



Accepted M

ACCEPTED MANUSCRIPT

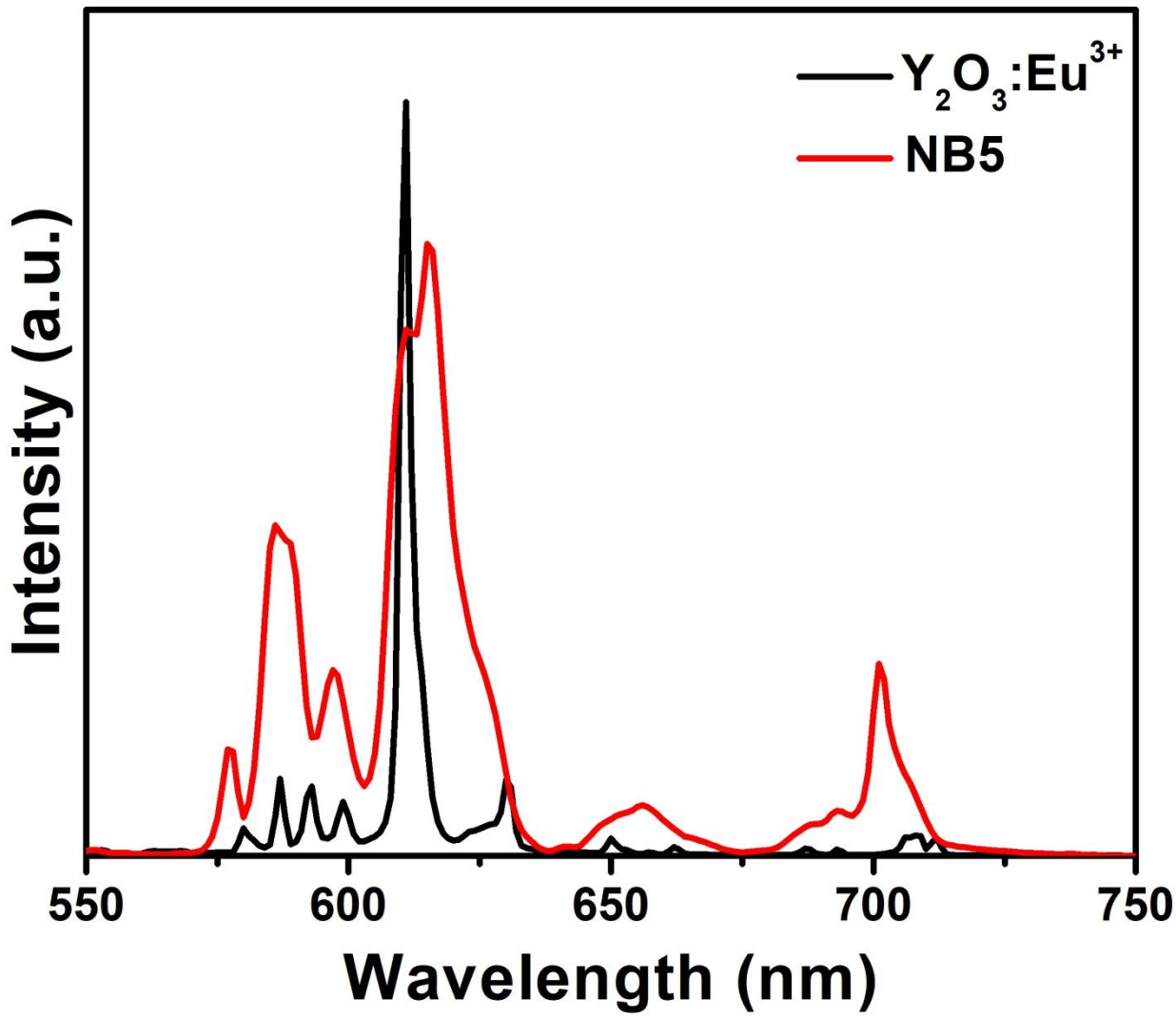
Fig. 8:



Accepted

ACCEPTED MANUSCRIPT

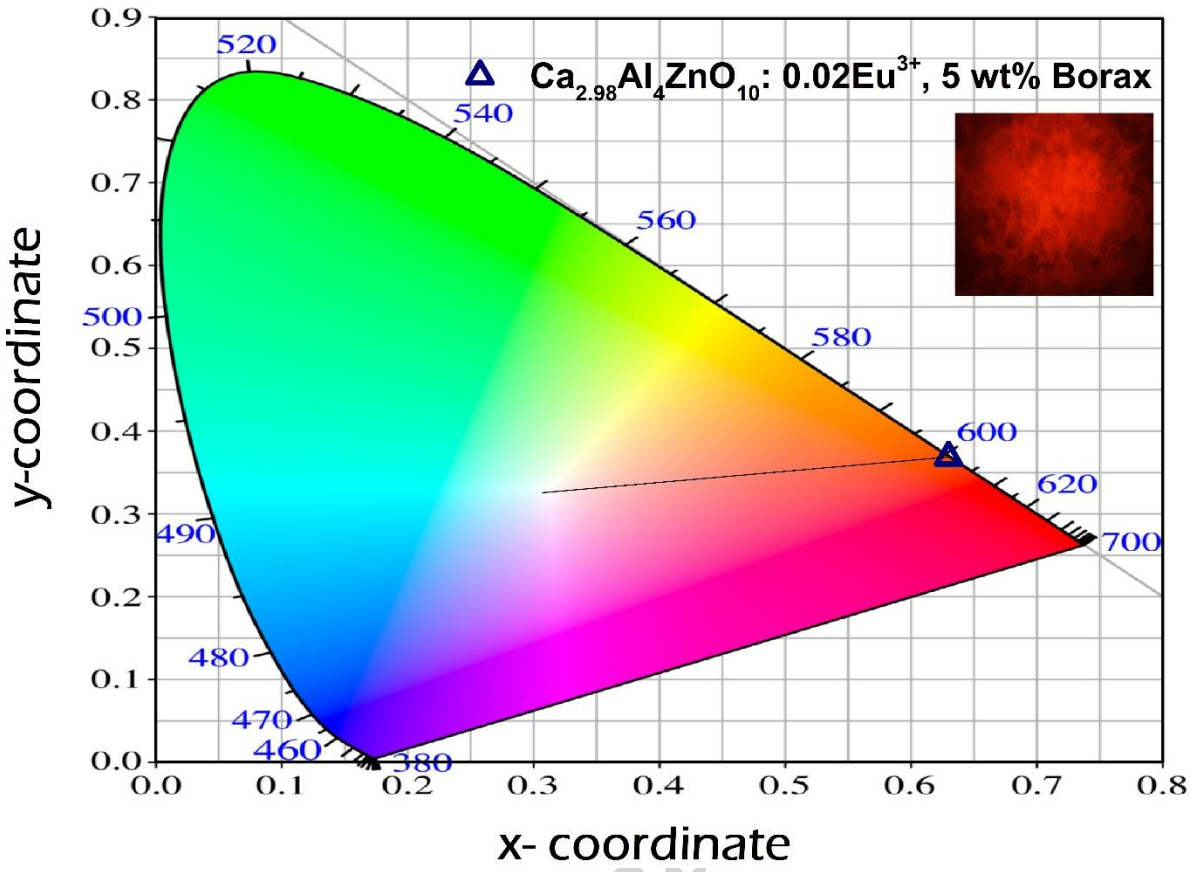
Fig. 9:



Accep

ACCEPTED MANUSCRIPT

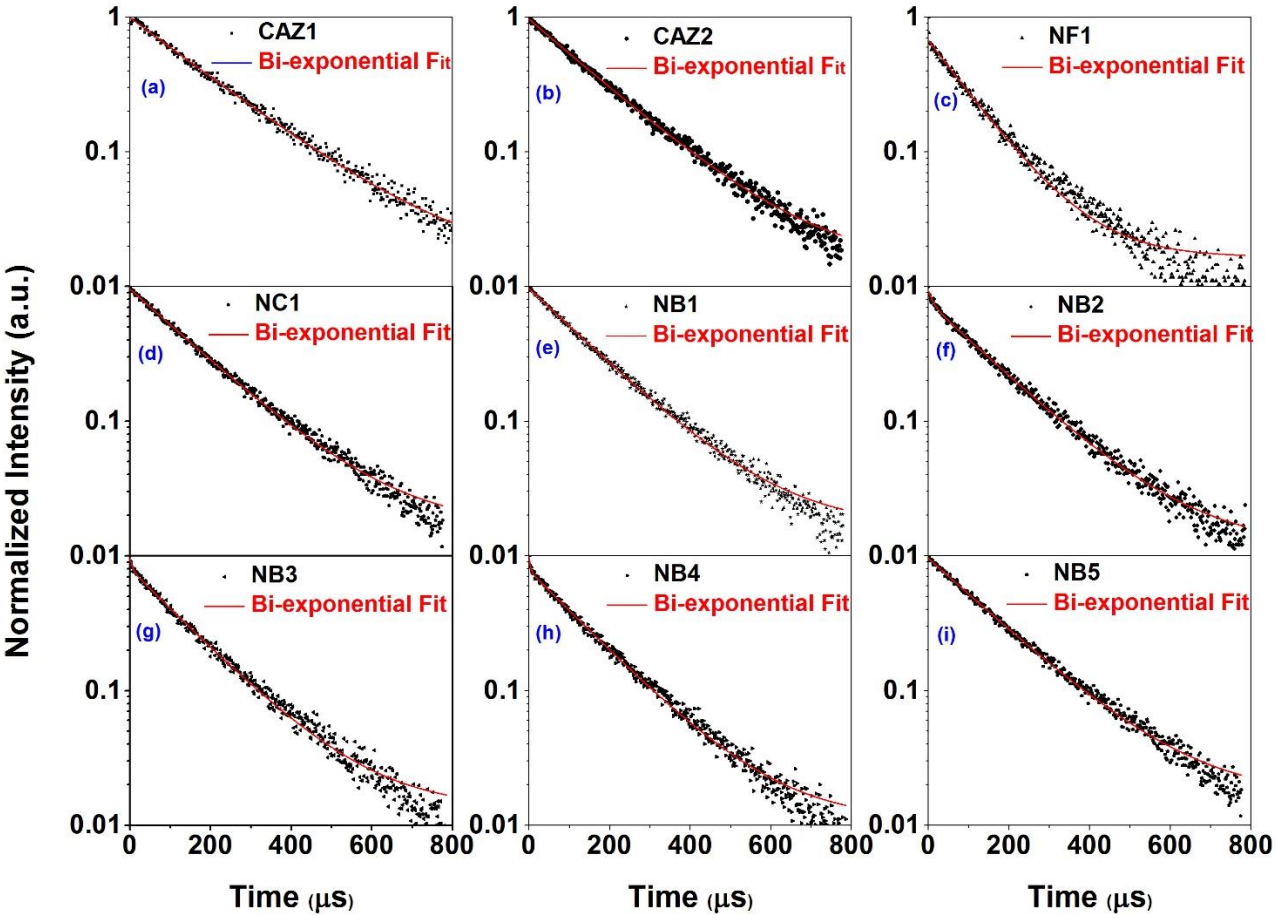
Fig. 10:



Accepted manuscript

ACCEPTED MANUSCRIPT

Fig. 11:



Accepted

ACCEPTED MANUSCRIPT

Table. 1: Energy (in cm^{-1}), radiative transition rates (A_{0-J}) and branching ratio (β_J) of NB1 and CAZ1 phosphors.

	$^5D_0$-^7F_J	Energy (cm^{-1})	A_{0-J} (s^{-1})	β_J
NB1	$^5D_0$-$^7F_1$	16893	50	0.03
	$^5D_0$-$^7F_2$	16287	1192	0.92
	$^5D_0$-$^7F_4$	14265	15	0.01
CAZ1	$^5D_0$-$^7F_1$	16893	50	0.04
	$^5D_0$-$^7F_2$	16287	1057	0.91
	$^5D_0$-$^7F_4$	14265	22	0.01

Table. 2: J-O parameters (Ω_2, Ω_4), and total radiative transition rates (A_R) of NB1 and CAZ1 phosphors.

	Ω_2 (x 10^{-20}) cm^2	Ω_4 (x 10^{-20}) cm^2	A_R (s^{-1})
NB1	4.80	0.20	1291
CAZ1	4.77	0.29	1157

Accepted manuscript

ACCEPTED MANUSCRIPT

Table. 3: CIE coordinates and decay time of all the phosphors.

Sample	CIE co-ordinates (x, y)	Decay Time (μs)
CAZ1	(0.630, 0.369)	137
CAZ2	(0.631, 0.367)	127
NF1	(0.631, 0.368)	108
NC1	(0.630, 0.368)	115
NB1	(0.632, 0.367)	126
NB2	(0.635, 0.364)	114
NB3	(0.633, 0.365)	111
NB4	(0.636, 0.362)	110
NB5	(0.630, 0.369)	119

Accepted manuscript

Journal of Pharmacognosy and Phytochemistry

Available online at www.phytojournal.com

E-ISSN: 2278-4136
P-ISSN: 2349-8234
JPP 2018; 7(3): 1336-1340
Received: 07-03-2018
Accepted: 11-04-2018

Sukirti Tiwari
Food Processing Laboratory, University School of Biotechnology, GGS Indraprastha University, Sector 16C, Dwarka, Delhi, India

Abha Sharma
Food Processing Laboratory, University School of Biotechnology, GGS Indraprastha University, Sector 16C, Dwarka, Delhi, India

Rajinder Kumar Gupta
Department of Applied Chemistry, Delhi Technological University, Shahbad Daulatpur, Bawana Road, Delhi, India

Correspondence
Rajinder Kumar Gupta
Department of Applied Chemistry, Delhi Technological University, Shahbad Daulatpur, Bawana Road, Delhi, India
Email: rkg67ap@yahoo.com

Formulation of cereal based spread using oats fermented with Baker's Yeast

Sukirti Tiwari, Abha Sharma and Rajinder Kumar Gupta

Abstract
Whole grain oats were fermented with Baker's yeast to obtain tastier, cholesterol free, low fat, cereal based spread. The phytochemical analysis showed an increase in phenolic content and antioxidant potential by 61.6% and 29.82%, respectively in the fermented oats as compared to the unfermented ones. The sensory evaluation of spread made from fermented oats gave a higher acceptance (8.67) as compared to the control spread made from unfermented oats (4.55). Furthermore, it was also observed that oats can act as fat replacers in products like spreads and marmalades as oat based spread was formulated by using only 10% fat, while on the other hand, the conventional fat based spreads are made by using 30% fat. The shelf life of fermented oat spread was found to be 21 days at refrigeration temperature with no phase separation.

Keywords: oats, fermentation, yeast, cereal spread, fat replacement

1. Introduction
Whole grain constitutes the major source of dietary protein, vitamins, minerals, fibers, carbohydrates (Blandino *et al*. 2002) [5]. The observational and clinical studies indicate that the regular consumption of whole grains can reduce the risk of various chronic diseases (Blandino and Klinken, 2014).

Among the various food grains, oats has been emerging out as excellent food grains with high health benefits and nutritional qualities. Oats (*Avena sativa*) are particularly high in soluble fiber, beta-glucan, lipids, proteins, and specific micronutrients as well as a unique source of polyphenols (Clemens and Klinken, 2014). Beta-glucan is the main functional component of cereal fibers mainly oats and barley and observed to have beneficial effects on LDL cholesterol, reduces it to 20-30% and reduces cardiovascular diseases. Beta-glucan fermentation in colon releases low molecular fatty acid, which shows its anti-carcinogenic effect (Oku, 1994; Salminen *et al*. 1998; Gallaher, 2000). Furthermore, beta-glucan also act as a prebiotic (Jaskari et al, 1998; Wood and Beer, 1998) and has high viscosity as well as water absorption capacities (Wood, 2007).

However, despite of all these health promoting benefits of oats, their consumption is not at par with other cereal grains. This is because of their bland, and unacceptable physical and organoleptic properties. Nevertheless, the physical and sensory parameters of oats can be enhanced by the process of fermentation (Martensson *et al*. 2001) [1]. Fermentation of oats with suitable microorganisms will lead to formation of flavour, acid development and consumption of carbohydrates. It was observed that the fermented oat based products have high suitability in terms of acidity, texture and overall appearance (Martensson *et al*. 2001) [1].

Furthermore, replacement of fat with dietary fiber is also drawing considerable attention these days. It has been observed that fiber can replace fat in high fat, ready to eat product, for example, bakery products (Knuckles *et al*. 1997, Lee *et al*. 2004; Lee *et al*. 2005; Brenan and Cleary, 2007; Kalingaand Mishra, 2009). Fat Replacers like fiber can replace most of the sensory and functional properties of fat, but since these are not chemically categorized as fat and therefore contribute lesser energy than fat. Cereal beta-glucan is considered as carbohydrate based fat replacer due to its water binding ability, high viscosity, and frothing and emulsion stability capacities (Barkus and Tamelli, 2000). Therefore, further research can be conducted where oats can be used as an alternative to fats in various spreads, margarines and mayonnaise.

Keeping all above in mind, the purpose of our present work is to develop a fermented oat based spread which is cholesterol free and low fat also determine its sensory, phytochemical and nutritional characteristics.

2. Materials and Methods

2.1 Starter culture

The microbial culture used in this study is *Saccharomyces cerevisae*, which is a yeast strain and was procured in the form of active dry yeast from the market. Starter culture was obtained by dissolving active dry yeast in distilled water (1:10) with a pinch of sucrose.

2.2 Oat substrate

The oat mash used as a substrate was prepared from the whole grain oats and distilled water in a ratio of 1:4 (w/v). It was then heated in temperature controlled water bath at 95 °C for 10min with stirring. The samples were brought to room temperature before the addition of required amount of starter culture.

2.3 Fermentation and storage

The oat mash was then inoculated with 0.5%, 1%, 1.5%, 2% and 2.5% (v/v) of starter culture respectively and fermentation was carried out at 25 °C for 2 days. Fermented mass was further heated again at 95 °C for 10min to stop yeast fermentation.

2.4 Spread preparation

The products were made based on a total of six components consisting of three dry ingredients (oat powder, salt, and stabilizer) and three liquid ingredients (vegetable fat, water and lemon juice). Three formulations were prepared; following the three components coordinate mixture design (Table 1).

Table 1: Formulation for spread

Ingredient	% vegetable fat	% water	% oats	% lemon juice
Fat based spread	30	60	0	10
Formulation 1 (Unfermented oats)	10	60	20	10
Formulation 2 (fermented oats)	10	60	20	10

2.5 Antioxidant analysis of DPPH radical scavenging activity

The DPPH radical scavenging method is used to measure the free radical scavenging activity of different elements (Brand-Williams *et al*. 1995). A solution of 0.1mM concentration of DPPH (Sigma-Aldrich Chemie, Steinheim, Germany) in methanol was added to 0.5ml of well diluted phenolic extracts. The change in absorbance at 517nm was measured after 30 min of incubation. Following equation can calculate the DPPH radical-scavenging activity of phenolic extract
Radical scavenging activity
(%) = (OD Blank-OD Sample*100)/OD Blank

2.6 Estimation of crude fiber

The crude fiber content of unfermented and fermented oats was estimated by digesting defatted samples first in 1.25% of H_2SO4 for ½ h, then filtered it with muslin cloth and remaining residue again digested with 1.25% NAOH for 30 min. Remaining residue was kept in oven for overnight at 105 °C. Further, it was kept in a muffle furnace for 4hr at 600 °C.
% crude fiber was calculated by following
formula Crude fiber (%) = (W2-W1)-(W3-W1)
*100/W W = weight of sample
W1 = weight of empty crucible
W2 = weight of sample + weight of empty crucible
W3 = weight of sample after ignition + weight of empty crucible

2.7 Determination of fat content

5g of fermented and unfermented samples were taken in an Erlenmeyer flask and dissolved in 50ml petroleum ether. It was further kept in shaker at 140rpm and 60 °C for overnight. The solution was filtered and the residue was re-extracted with 50ml petroleum ether. Both the filtrate was combined and evaporated at 60 °C in oven. The recovered or extracted fat in the beaker was weighted and calculated.
Fat (%) = weight of extracting fat ×100/weight of sample

2.8 Determination of protein content

Samples were dissolved in distilled water (1:10) for making sample extract, 1ml sample extract were mixed with 9ml biuret reagent. Incubate it for 20m and then absorbance was taken at 550nm. The amount of total protein content was calculated with the standard calibration curve of albumin.
Protein standard curve equation, Y = 0.1422X + 0.0634

2.9 Analysis of carbohydrate content

The clear aqueous solution is taken in a test tube and mixed with sulfuric acid and phenol. Due to interaction of carbohydrate and phenol the color of the solution will change to yellow-orange. The initial carbohydrate concentration in a sample is proportional to the absorbance at 490nm. This method determines the total sugar present in a sample by converting all non-reducing sugar to reducing sugar by means of sulfuric acid. A calibration curve is prepared using known carbohydrate concentration.
Glucose standard curve equation, Y= 24.536X-0.2714

2.10 Sensory evaluation

Sensory test is conducted by selecting a group from large population for whom the product is proposed (Meilgaard and others 1999). A panel of 10 members was selected and intensity scales were defined using 9cm lines for acidity, sweetness, consistency, oat flavour, mouth-feel, appearance, and overall acceptability. Ranking for preference was shown by noting the most desirable product according to the panelists. The panelists gave a number of the products according to their preference from 1-9 using the same sensory qualifications as in the intensity evaluation, except for oat flavor which was excluded from the test (1= dislike extremely, 5 = neither like nor dislike, 9= like extremely). Fermented oats were used for making the test spread. Unfermented product was used as control.

2.11 Shelf life evaluation

The shelf life of spread from fermented oats at refrigerated temperature was analyzed by checking for bacterial contamination at regular interval of 5 days for 25 days. Phase separation of the product was also checked after 25 days after storage at refrigerated temperature.

2.12 Statistical analysis

The experiments were done in triplicate and replicated twice. Results are expressed as average ± standard deviation (SD).

3. Result and Discussion

3.1 Starter culture concentration for fermentation of oats

The oat mash was inoculated with 0.5, 1.0, 1.5, 2.0 and 2.5% (v/v) of starter culture suspension of *S. cerevisae* separately aiming to achieve the appropriate taste, texture and flavor of the fermented substrate in minimum time. Short fermentation time is always preferable in order to minimize the risk of contamination (Blandino *et al*. 2002) [5]. Banigo *et al*. (1974), studied the manufacturing process of Ogi (traditional Nigerian fermented food) which involves the fermentation of maize, millet and sorghum with *S.cerevasie* for 24-72hrs to achieve desired texture, aroma and taste. Similarly, in the present study it was observed that 2% inoculum gave better taste, texture and aroma to the oats in 48h.

3.2 Phytochemical analysis of fermented and unfermented oats

The total increment of phenolic content in fermented oats was 61.6% as compared to unfermented oats (Table 2). This is because of yeast fermentation of oats, which released the bound phenolic compounds and free phenolic acids (Katina *et al*. 2007).

In grains, antioxidants are concentrated in the bran fraction, mainly as phenolic compounds in the form of insoluble bound ferulic acid (Hatcher and Krunger, 1997). With the aid of microbial fermentation, these bound phenolics in cereal grains can be released (Bhanja *et al*. 2007). As a consequence, the higher DPPH scavenging activity was observed in fermented oats when compared with unfermented ones (Table 3). Adom & Liu, (2002), provided strong evidence that the predominant source of antioxidant activity is derived from the phenolic compounds. The phenolic compounds in oats may be therefore able to, capture the free radicals formed in the human body, if their consumption is supported (Bryngelsson *et al*. 2002).

Table 2: Total phenolic content of fermented and unfermented oats

Samples	TPC (mg GAE g^{-1} grain)
Unfermented	195.2±0.31
Fermented	508.7±0.34

Table 3: Antioxidant activity of fermented and unfermented oats

Samples	% DPPH scavenging
Unfermented	43.02±2.44
Fermented	72.84±1.87

3.3 Nutritional analysis of fermented and unfermented oats

The nutritional profile of fermented and unfermented oats is given in Table 4. Generally, fermentation can decrease the level of carbohydrate along with some non-digestible poly or oligosaccharides (Blandino *et al*. 2002) [5]. In our study it can be seen that there is a decrease in carbohydrate content after fermentation (Table. 4). Unfermented oats have 63.6% carbohydrate while, after fermentation, it is reduced to 55.7%. Fermentation significantly improves the protein quality as well as the level of lysine in maize, millet, sorghum, and other cereals (Hamad and Fields, 1979). In our study it can be seen that there is slightly improvement in protein content of oats after fermentation. The protein content observed in unfermented oats was 7.81%, though fermented oats have 8.54% (Table. 4).

The average fat content of unfermented oats was observed to be 8.66%, which decreased to 6.46% after fermentation (Table 4). This decrease in fat is due to reduction of oleic acid content (Brindzova *et al*. 2008) [37]. Similar varietal composition of oat lipids was also reported previously (De La Roche *et al*. 1977; Saastamoinen *et al*. 1989). Oats contain a considerable amount of oleic acid. The polar lipids in the cell membranes are dominated by phospholipids and glyco-or galactolipids (Sugawara and Miyazawa, 2001).

The moisture and ash content of fermented and unfermented samples was found to be approximately same (Table 4). So, it can be said that there were no significant changes in moisture and ash content after fermentation.

Similarly, there was no significant change in crude fiber percentage after fermentation (Table 4). This indicates that beta-glucan in oats is not utilized by the yeast.

Gargi *et al*. 2017, also did nutritional analysis of fermented oats and our results were similar to them. However, we have also incorporated fermented oats into a product i.e. spread.

Table 4: Nutritional analysis of fermented and unfermented oats

Composition	Unfermented	Fermented
Fat (%)	8.66±0.115	6.46±0.305
Protein (%)	7.81±0.291	8.54±0.234
Crude fibre (%)	10.96±0.231	10.26±0.276
Carbohydrate (%)	63.6±0.256	55.7±0.249
Moisture (%)	10.77±0.189	10.55±0.129
Ash (%)	1.355±0.022	1.4±0.023
Energy (kcal)	330.02	285.84

Data is denoted as Average ± standard deviation

3.4 Formulation of spread

Oats based spread (Fig.1.) was formulated from both fermented and unfermented oats using the composition given above in Table.1. Butter based spread (Table.1.) was also made and it was observed that both fermented and unfermented oats can replace almost 60% fat in the formulated product. This is because the beta-glucan present in oats act as fat Replacers.

Kalinga (2010), shows the replacement of fat with beta glucan in bakery products. i.e. cake. Beta-glucan extracted from oats and barley and added to a cake formulation at different levels as a fat replacer.



Fig 1: Oats spread

3.5 Sensory evaluation

Generally, the panelists gave higher scores to a product made from fermented substrate.

Formulation A received the highest overall acceptability (8.67), while the control, i.e. spread made from unfermented oats was unacceptable (4.55). This indicates the importance of

fermentation in making the product (spread) from the oats acceptable.

Therefore, it can be concluded that fermentation can be used to enhance the taste and aroma of bland oats, which can thus be incorporated into different novel healthier and tastier food products.

Table 5: Average score of sensory attributes

Formulations	Appearance	Taste	Spread-ability	Smoothness	Overall acceptability
A (Spread from fermented oats)	8.9±0.251	9±0.1	7±0.152	2±0.057	8.67±0.083
Control (spread from unfermented oats)	1±0.547	2±0.547	3±0.547	6±0.456	4.55±0.404

The data is given as Average ± standard deviation and the values are based on a nine-point hedonic scale. Where 1= dislike, 5 = neither like nor dislike, 9 = like.

3.6 Estimation of shelf life

Too few to count (TFTC) colonies were seen in oat based spreads on the 25th day of refrigerated storage. Phase separation was also not seen on the 25th day of storage. So, it can be said that the product can be stored in refrigerator for more than 21 days.

4. Conclusion

In order to utilize health benefits of oats in various innovative products, like spreads and margarines, fermentation is a necessary step to improve its bland taste and flavor and thus increase consumer acceptability. The sensory evaluation showed that the spread made from fermented oats is highly acceptable (8.67 score) compared to that with the unfermented one (4.55 score). In addition to increasing the sensory characteristics, fermentation also increased the TPC and antioxidant content of the substrate. Furthermore, the beta glucan present in oats which was not utilized during the fermentation process can also be exploited as a fat replacer in conventional fat-based products by 60%.

5. References

1. Martensson O, Andersson C. Formulation of an oat based fermented product and its comparison with yoghurt. J Sci Food Agric. 2001; 81:1314-1321.
2. Angelov A, Gotcheva V. Development of new oat- based probiotic drink. International Journal of Food Microbiology. 2006; 112:75-80.
3. Das G, Maria J. Nutrient profile of fermented oats. International Journal of Food Science and Nutrition, 2017, 69-71.
   ISSN: 2455-4898,
4. Prado F, Pandey A. Trend in non-dairy probiotic beverages. Food Research International, 2007, 41.
5. Blandino A, Cantero D. Cereal based fermented foods and beverages. Food Research International. 2002; 36:527-543.
6. Thomas K, Ingledew W. Practical and theoretical consideration in the production of high concentration of alcohol by fermentation. Process Biochemistry, 1995, 0032-9592, 00073-9.
7. Cai S, Wang O, Wang W, Zhu F, Ji B, Zang D. Comparative study of the effects of solid state fermentation with three filamentous fungi on the total phenolic content, flavonoids and antioxidant activities of subfractions from oats. J Agric food chem. 2012; 60:507-513.
8. Aeschelimann A, Vonstocar U. The effect of yeast extract supplementation on the production of lactic acid from whey permeates by *Lactobacillus helveticus*. Applied microbiology and Biotechnology. 1990; 32:398-440.
9. Gupta S, Cox S, Ghannam N. Process optimization for the development of a functional beverage based on lactic acid fermentation of oats. Biochemical engineering journal, 2010.
10. Casey GP, Ingledew WM. Ethanol tolerance in yeast. CRC Crit. Rev. Biotechnol. 1986; 13:219-80.
11. Arunachalam K, Gill HS, Chandra RK. Enhancement of natural immunity functions by dietary consumption of *Bifidobacteriumlactis* HN019. European journal of clinical Nutrition, 2000, 54:1-4.
12. Ingledew WM, Casey GP. Rapid production of high concentrations of ethanol using unmodified industrial yeast. In Biotechnology and Renewable Energy, Ed. M. Moo-Young, S. Hasnain & J. Lamptey. Elsevier, New York, 1986, 246-57.
13. Scott RW, Solubilization of beta-glucan during mashing. J Inst. Brew. 1972; 78:411-2.
14. Chae HJ, Joo H, In MJ. Utilization of brewer's yeast cells for the production of food grade yeast extract. Part I: Effects of different enzymatic treatments on solid and protein recovery and flavor characteristics. Bioresource Technology. 2001; 76:253-258.
15. Anderson JW, Deakins DA, Floore TL, Smith BM, Whitis SE. Dietary fiber and coronary heart disease. Critical Reviews in Food Science and Nutrition, 1990a, 29:95-147.
16. Anderson JW, Spencer DB, Hamilton CC, Smith SF, Tietyen J, Bryant CA *et al*. Oat-bran cereal lowers serum total and LDL cholesterol in hypercholesterolemic men. American Journal of Clinical Nutrition. 1990b; 52:495-499.
17. Andersson AAM, Armo E, Grangeon E, Fredriksson H, Anderson R, Aman P. Molecular weight and structure units of (1-3, 1-4) -β-glucan in dough and bread made from hull-less barley milling fractions. Journal of Cereal Science. 2004; 40:195-204.
18. Anon. Fat Substitute Update. Food Technology. 1990; 44:92-97.
19. Anon. Food labelling: soluble dietary fibre from certain foods and coronary heart disease. Federal Register: USFDA, 1997, 67.
20. Anon. Position of the American Dietetic Association: Fat replacers. Journal of the American Dietetic Association. 1998; 98:463-468.
21. Anon. The definition of dietary fiber. Report of the dietary fiber definition committee to the board of directors of the American Association of Cereal Chemists. USA: American Association of Cereal Chemists, 2001.
22. Anon. Food Labelling: health claims; oats and coronary heart disease. Federal Register: USFDA, 2002, 62.
23. Arozarena I, Bertholo H, Empis J, Bunger A, Sousa I. Study of the total replacement of egg by white lupine protein, emulsifiers and xanthan gum in yellow cakes. European Food Research and Technology. 2001; 213:312-316.

24. Gibson GR, Roberfroid MB. Dietary modulation of the human colonic microbiota: Introducing the concept of prebiotics. Journal of Nutrition. 1995; 125:1401-1412.
25. Gill HS, Cross ML, Rutherfurd KJ, Gopal PK. Dietary probiotic supplementation to enhance cellular immunity in the elderly. British Journal of Biomedical Science. 2001; 57:94-96.
26. Bamforth CW. β-Glucan solubilizes. J Inst. Brew. 1989; 95:314-5.
27. Maisch WF. Fermentation processes and products. In Corn Chemistry and Technology, ed. S. A. Watson & E E. Ramsted. American Association of Cereal Chemists, St Paul, MN, 1987, 553-74.
28. Wood PJ. Oat β-glucan-physiochemical properties and physiological effects. Trends Food Sci Technol. 1991; 12:311-314.
29. Lambo A, Öste R, Nyman MEGL. Dietary fibre in fermented oat and barley-glucan rich concentrates. Food Chem. 2005; 89:283-293.
30. Chavan J, Kadam S. Critical reviews in food science and nutrition. Food Sci. 1989; 28:348-400.
31. Kalinga DN, Mishra VK. Pasting and sorption behavior of β-glucan and flour mixtures. In Panozzo, JF, & Black, CK. 58th Australian Cereal Chemistry Conference, 2008, 203-206.
32. Lazaridou A, Biliaderis C, Izydorczyk M. Molecular size effects on rheological properties of oat-glucans in solution and gels, Food Hydrocolloid. 2003; 17:693-712.
33. Kedia G, Wang R, Patel H, Pandiella S. Use of mixed cultures for the fermentation of cereal-based substrates with potential probiotic properties, Proc. Biochem. 2007; 42:65-70
34. Steinkraus KH. Lactic acid fermentation in the production of foods from vegetables, cereals and legumes. Antonie van Leeuwenhoek. 1983; 49:337-348.
35. Bhanja T, Kumari A, Banerjee R. Enrichment of phenolics and free radical scavenging property of wheat koji prepared with two filamentous fungi. Bioresource Technology. 2009; 100:2861-2866.
36. Hesseltine CW. The future of fermented foods. Nutrition Reviews. 1983; 41:293-301.
37. Brindzova L, Certik M, Rapta P, Zalibera M, Mikulajova A, Takacsova M. Antioxidant activity, β-glucan and lipid contents of oat varieties. Czech J Food Sci. 2008; 26:163-173.
38. Garcia K. Quality characterization of cholesterol free mayonnaise type spreads containing rice bran oil. B.S. chemical engineering, 2006, 14-22.

International Journal of Applied Engineering Research ISSN 0973-4562 Volume 13, Number 11 (2018) pp. 9627-9635
© Research India Publications. http://www.ripublication.com

Krill Herd based Optimization for Job Shop Scheduling Problems (JSSP) to Minimize Make Span Time

Vineet Kumar
Research Scholar,IKG Punjab Technical University, Jalandhar
&
Assistant Professor, Department of Mech. Engineering,
Vaish College of Engineering, Rohtak, Haryana, India.

Dr. OmPal Singh
Professor, Department of Mech. Engineering
Beant College of Engineering & Technology, Gurdaspur, Punjab, India.

Dr. Radhey Shyam Mishra
Professor and Head, Department of Mech. Engineering,
Delhi Technological University, Delhi, India.

Abstract

In conventional scheduling issues, the processing time for the given job is thought to be a consistent paying little respect to whether the job is booked before or later. In any case, the wonder named "learning impact" has widely been concentrated as of late, in which job processing times decay as laborers acquire encounter. The target of this paper is to minimize the make span time in JSSP alongside the propelled strategies. In the proposed algorithm, a few earlier standards are displayed to build the underlying populace with an abnormal state of value. This examination we have utilized four unique sorts of optimization techniques among propositions the best results acquired in Krill Herd Optimization (KHO) process. Recreation comes about on the standard test occurrences demonstrate that KHO has a superior convergence execution contrasted and single-goal existing enlivened optimization process. This proposed job accomplished 94.33% precision in KHO system contrasted with other optimization process.

Keywords: Job shop scheduling problem, make span time, optimization, objective and krill herd optimization.

INTRODUCTION

The job shop scheduling is to choose a schedule of jobs that is supplied with pre-set operation arrangement in a multi-machine environment. In the customary job shop scheduling problem (JSP), n-jobs are handled to the completing point on m-random machines. For every single assignment, innovation impediments spell out a flat out and particular routing which is set and distinguished before. What's more, processing periods are set and distinguished already. [1] Various creation assets are accessible which are used by strategies by the assignment for processing. Truth be told, every job has its own particular course in the generation site**.** Each phase of the directing is a unitary capacity performed by one/different asset (s) over the span of a predetermined processing interim. By and by, an asset is inept to do two operations all the while, at the end of the day assets are non-cumulative. [2] The issue of scheduling jobs in FJSP might be rotted into two sub-issues. The previous is the routing sub-issue that assigns each undertaking to a machine looked over among an arrangement of skilled machine, while the last is the scheduling sub-issue that incorporates scheduling the allotted errands on all machines to accomplish a practical calendar to lessen the predefined objective task [3].

For every errand there is a vocation to which it has a place, a machine on which it must be processed, a prearranged processing interim on that machine and additionally a preset processing request on the machines. The issue is to lessen the make span all the while verifying that various jobs can't be processed together on similar machine, furthermore guaranteeing that when job is initiated, it must be some way or another wrapped up. [4] But, FJSP is preferably confounded than the customary JSP, as it acquires an extra choice level notwithstanding the scheduling one, for example, the job courses. Choice at job courses incorporates deciding, for each undertaking, what machine must be utilized to process it, from among the current ones.[5] In the contemporary adaptable assembling frameworks enriched with PC computer-controlled robots, hoists, cranes, and other material processing mechanisms, setup and transport interims are vital and must be given due thought. Such transporting gadgets are plainly coordinated into the practically equivalent to scheduling models. [6].

An answer is endowed with the errand of assessing the operation arrangement on the machines to meet with specific limitations. What's more, the objectives for the most part considered in JSP are the diminishment of make span, tardiness, and mean flow interval and so forth. In this record, the lessening of make span is esteemed as the conspicuous target. It is described as the general time between the beginning of the underlying undertaking and the end of the last errand in all jobs.[7]In the make span lessening issue, they have shown that under straight crumbling the two-machine flow shop issue is intensely NP-hard, and the two-machine open shop issue is consistent NP-hard. They have additionally

exhibited that for the three-machine flow shop issue with straightforward direct disintegration, there is no polynomial-time estimation algorithm with a most pessimistic scenario proportion limited by a constant.[8] A solitary machine scheduling issue with uneven discharge interims for decreasing the make span, in which the learning impact and the breaking down jobs are correspondingly considered. Different strength guidelines and as far as possible are set up to permit the branch-and-headed algorithm for accomplishing the optimal solution.[9] In prescient receptive scheduling strategy a generation calendar is made at first and from that point overhauled in the response to an interruption of continuous occasions to lessen its impact on frameworks fabulousness, while in responsive scheduling plan just partial timetables are delivered when required for the momentary future as per the current frameworks status and confined information and limitations.[10] From times immemorial, it has been the standard practice to handle the job shop scheduling issue principally utilizing the ranch and bound , heuristic rules and shifting bottleneck processes like the taboo search, simulated annealing, genetic algorithms, neural networks and ant colony optimization which are well-equipped to usher in superlative solutions to sophisticated issues laden with exceedingly elevated expenditure.[11] When the make-span is reduction to the slightest, no less than one of the optimal arrangements gets to be dynamic all together that no undertaking can be completed without encroaching the innovative parameters. In this way, at whatever point make-span is streamlined, a calendar can be clarified by the processing requests of capacities on the machines.[12] It identifies with the way toward scheduling an arrangement of jobs on an arrangement of innovatively various machines where each machine is capable to handle one and only job at once. It might be noticed that jobs seek after differing processing techniques in the midst of the machines and it is humanly difficult to handle job by different machines simultaneously. [13] The significant issue identifies with finding the job arrangement on the machines which contribute a considerable measure to the reduction in the make-span, i.e. the greatest of the culmination times of the whole capacities. As the goal job, m mean flow time, completion time variance and total tardiness can likewise be utilized. [14] The measurement heartiness is basically sorted into two sorts, for example, quality strength and arrangement vigor. The previous is for the most part utilized to indicate the lack of care of the calendar brilliance under equivocalness in regard of the goal esteem, similar to make span and lateness while the last by and large implies the obtuseness of assignment initiation or finishing interims to the ambiguity.[15] From the job shop scheduling, the enhancement algorithm is utilized to evaluate the slightest make span interim inside the optimal timetable.

RELATED WORKS

In 2013, Suresh kumar *et al*. [16] had the credit of deliberately propelling the unordered subsequence trade cross over in genetic algorithm for lessening the make span interim in the job shop scheduling. The JSSP was, indeed, one of the critical enhancement issues in software engineering and generation situation. With an eye on diminishing the make span term and find the optimal calendar exceptional cross over system utilized the unordered subsequence exchange crossover (USXX) in genetic algorithm (GA). Utilizing the exceptional cross over system unordered subsequence trade cross over most of the standard results were evaluated and differentiated and the results accomplished were pretty much near to optimal estimation of the standard issues. From the empowering results, unmistakably the imaginative algorithm had accomplished optimal upshots of the standard issues and a few of the acknowledged results were seen in closeness to optimal and with the job of the unordered subsequence trade cross over a few benchmark issues results were acknowledged well inside the base number of emphases.

In 2013, Antonin Ponsich *et al*.[17] had accomplished name and notoriety for proposing an astounding cross over differential evolution-tabu search algorithm for the determination of job shop scheduling issues. The Differential Evolution (DE) was an Evolutionary Algorithm that had set up its one of a kind position as a profoundly capable technique for unremitting advancement; however it fizzled wretchedly to yield a magnificent execution when connected to change issue. Along these lines, an innovative cross overusing DE with Tabo Search (TS) was utilized to effectively handle the issues of the JSSP. The computational examinations in regard of cases surpassing 100 JSSP cases outlined the unchallenged certainty that the novel mixture DE–TS algorithm was equipped to yield dazzling execution when contrasted and those of the few innovative methodologies. The stunning results have shown that the certainty interims width was under 0.7% of the reference make span esteem, setting up the way that low scattering of the arrangements was figured it out.

In 2012, James C. Chen *et al.* [18] showed colossal mettle by propelling an imaginative adaptable job shop scheduling with parallel machines by method for genetic algorithm and grouping genetic algorithm. In this report, it had two modules, for example, the machine selection module (MSM) and operation scheduling module (OSM). The MSM extended some assistance to an operation to pick one of the coordinating machines to process it and the OSM was from that point utilized to arrange the arrangement of the whole operations distributed to every last machine. The mind boggling results maintained the matchless quality of the amalgamation of MSM utilizing GGA and OSM utilizing GA which continued zooming as and when the quantity of requests enlarged. The outcomes exhibited without a particle of uncertainty that the imaginative strategy utilizing GGA and GA was all around processed to apportion a machine to an operation and sort out the arrangement of operations at every machine to acquire lesser tardiness, machine idle interval, and make span than WPS was able to do.

In 2011, DarrellLochtefeld *et al*. [19] daringly propelled the helper-objective enhancement procedures for the job shop scheduling issue. The Multiple Objectives Evolutionary Algorithms (MOEAs) was executed at job Shop Scheduling Problem and it was demonstrated that they performed better than the single target Genetic Algorithms (GAs). Helper-objectives, describing portions of the major objective, were exceedingly useful in controlling MOEAs in the hunt strategy.

The arrangement in which helper-objectives were utilized were broke down which supported the way that issue particular aptitudes could be coordinated to choose an eminent helper-objectives grouping. Computational results very much displayed the way by which circumspectly sequenced helper objectives were able to venture up pursuit incredibleness. This actually brought about the outline dismissal of the customary routine of picking helper sequence construct upon a subjective request with respect to record of the insufficiency of understanding about optimal scheduling.

In 2010, Tsung-Lieh Lin *et al*. [20] were credited with presenting an imaginative strategy of particle swarm optimization for job shop scheduling. In this archive, new-fangled cross over swarm intelligence algorithm integrating particle swarm optimization simulated annealing technique and multi-type individual improvement scheme was acquainted with find feasible answers for the job shop scheduling issue. It was apparent from the remarkable results that the contrast between the MPSO's Average and the BKS were restricted to under 2% and MPSO were equipped to accomplish the optimal territory in the hunt space with lesser populace measurement and get sublime arrangements by misusing the wonderful individual improvement fitness.

Research problem

In the deterministic JSSP issue, n jobs are to be executed on m machines. Every last job is home to a pre-fixed arrangement of capacities operations, each of which must be performed without appropriation for a predetermined timeframe on a predefined machine. It is extremely hard to process the operation of the indistinguishable job correspondingly and every job is given the obligation of going by every machine just once. Every last chore must be started simply after the processing is done, if the standard capacity is as yet being executed. In such manner, a calendar speaks to a task of capacities to the time spaces on the machines.

PROPOSED METHODOLOGY

Job shop Scheduling Process (JSSP) is an inclusion of the conventional scheduling issue which empowers the errand of optimal scheduling. By scheduling issue we mean the designation of assets to execute an arrangement of exercises in an endorsed interim of time. JSSP has risen as a standout amongst the most complex combinatorial improvements. In the assembling frame jobs, a lion's share of scheduling hazards is exceptionally advanced in nature and extremely complex to be handled by exact strategies to accomplish an universal optimal schedule. The imperative capacity is to allot every last errand to a machine and to arrange the capacities on the machines, all together that the greatest length of fulfillment (make span) of the whole undertaking is decreased to the base. Every operation is to be processed on various machines, in a given request. The issue is to discover a timetable of the negligible time to finish all jobs. This exploration job examination distinctive seat marks issues are considered to minimize make span time in every jobs used to motivated diverse advancement strategies. Improvement handle consider the target job that is wellness as make span time, it's based produce the underlying answer for proposed Krill Herd Optimization (KHO) procedure. This exploration job will be executed in the MATLAB stage and the execution will be broke down through the current flow lining systems to demonstrate proposed is best so far Job scheduling process.

A. Assumptions and Constraints

This examination job taken diverse benchmark issue process and the system is pertinent with an job and process used to various four methodologies. Subsequently we need to hold up under as a primary concern that unique standard issue techniques and the strategy is fitting with any sort of job and system expect the supple job shop situation where stages may be skipped. This job the consequent supposition is being finished and they are as beneath.

- Let $J_i = \{1,2,\ldots\ldots n\}$ be a set n jobs are scheduled.
- Let $M_j = \{1,2,\ldots\ldots\ldots m\}$ be a set m machines are scheduled.
- A job should not meet the similar team more than once.
- Attendance of no superiority restraints on functions of various jobs.
- Operations ones proceeding can't be interjected.
- Each machine can do process only one job at a time.
- Each job must go completed a particular predefined order of operations

The span value to be definite as below: each job has amount of operations and each function has an explicit make value at this place.

B. Objective Functions in JSSP

This proposed job examination considers multi goals initial one is least makes span time and of various jobs performed in machines.

$$M_i = \min(M_t) \qquad (1)$$

Makes pan time is the total jobs completion time can be defined as

$$\text{Minimize } M_t = \min(\max_{j=1}^{n} T_{i-1,j}) \qquad 2)$$

In above equations M_t is the make span time, T is processing time of each i^{th} jobs based j^{th} machines order.

C. Optimization for Job shop Scheduling Problem (JSSP)

JSSP examination the make span time minimization handle distinctive propelled optimization strategies are used, for example, KHO,PSO,ABC and GA algorithm is roused by social conduct. All flow lining issues ought to have isolates reason that must be reduced or abused for accomplishing a persuaded arrangement. The target execution is the estimation of makes span or the separation recess of encoding in the

present case, this paper unmistakably talk about the KHO optimization.

D. Krill herd Optimization (KHO) for JSSP

The Krill herd algorithm is another improvement algorithm which is propelled the conduct of the krill swarms, this enhancement strategy to upgrade make span time in JSSP investigation. This KHO procedure considers two principle objectives, for example, Increasing krill density and Reaching food, so the crowding conduct of expanding thickness and discovering sustenance. Figure 1 demonstrates the flow chart of KHO process.

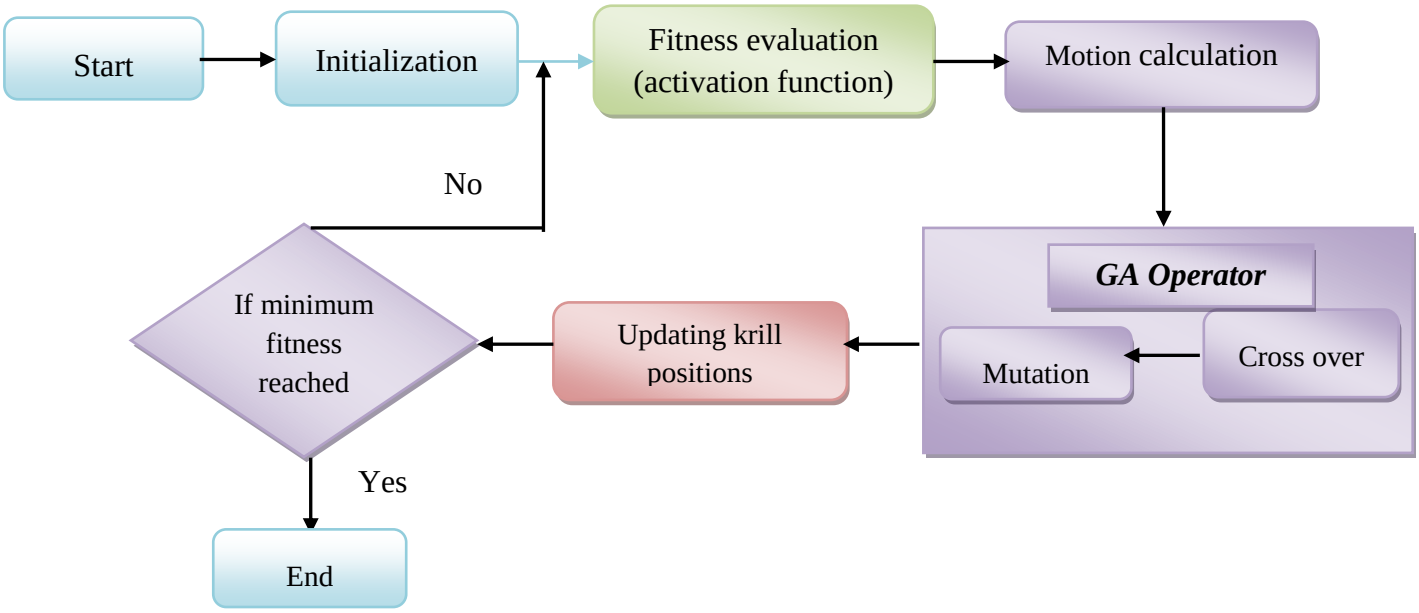


Figure 1. Flow chart for KHO

Initialization

The underlying arrangement (S_{ij}) is produced haphazardly by utilizing make span time and jobs and machine and is used as beginning arrangement by fulfilling limitations.

$$I_{ij} = \{T_{11}, T_{12}, \ldots . T_{ij}\} \quad (3)$$

Where, I is the initial solution, T is the make span time and i, j is the job and machine

Fitness computation

Fitness computation investigation the base makes span time and most extreme tardiness minimization process in JSSP examination. These destinations capacities are portrayed in area 3.2 conditions (1).

Updating Procedure

The location of a krill individual is affected by the following three factors

- Movement induced by other krill individuals
- Foraging activity
- Random diffusion

The location of krill is expressed by the following Lagrangian model

$$\frac{dA_i}{dt} = C_i + E_i + Q_i \quad (4)$$

Where C_i the motion is induced by other krill individuals; E_i is the foraging motion, and Q_i is the physical diffusion of the ith krill individuals.

Movement induced by other krill individuals

In the movement, the direction of motion of a krill individual is resolved both by the local swarm density (local effect), a target swarm density (target effect), and a repulsive swarm density (repulsive effect). The krill movement can be characterized as

$$C_i^{new} = C^{\max}\gamma_i + \omega_n C_i^{old} \quad (5)$$

Where $\alpha_i = \alpha_i^{local} + \alpha_i^{target}$ (6)

In above equation (8) individual local search and target search are calculated by as following equation.

$$\alpha_i^{local} = \sum_{j=1}^{NN} M_{ij} A_{ij} \quad (7)$$

Here

$$A_{ij} = \frac{A_j - A_i}{||A_j - A_i|| + \varepsilon} \quad (8)$$

In above conditions the documentations are clarified $C_{\max}$ similar to the maximum induced speed, is the inertia weight of the movement incited in the range [0, 1], C_i^{old} is the last motion induced, α_i^{old} is the local effect gave by the neighbors and α_i^{target} is the target direction effect gave by the best krill individual and NN is the quantities of individuals. In condition (9) the M_{ij} figured in light of the best and most exceedingly awful fitness values.

$$\alpha_i^{target} = G_{best} M_{i,best} A_{i\,best} \quad (9)$$

Where, C_{best} is the effective coefficient of the krill individual with the best fitness to the i_{th} krill individual. This coefficient is defined since α_i^{target} leads the solution to the global optima and it should be more effective than other krill individuals such as neighbors. Herein, the value of G_{best} is defined as:

$$G_{best} = 2\left(rand + \frac{IA}{IA_{\max}}\right) \quad (10)$$

Where rand is a random values between 0 and 1 and it is for enhancing exploration, IA is the actual iteration number and $IA_{\max}$ is the maximum number of iterations.

The sensing distance for each krill individual can be determined using different heuristic methods. Here, it is determined using the following formula for each iteration.

$$s_d = \frac{1}{5N} \sum_{j=1}^{N} ||A_i - A_j|| \quad (11)$$

For picking the neighbor, diverse systems can be utilized. For example, a neighborhood ratio can be essentially characterized to locate the quantity of the nearest krill individuals. Utilizing the genuine conduct of the krill individuals, a sensing distance ought to be resolved around a krill individual appeared in figure 2. Utilizing condition (11), if the separation of two krill individuals is not exactly the characterized sensing distance, they are neighbors.

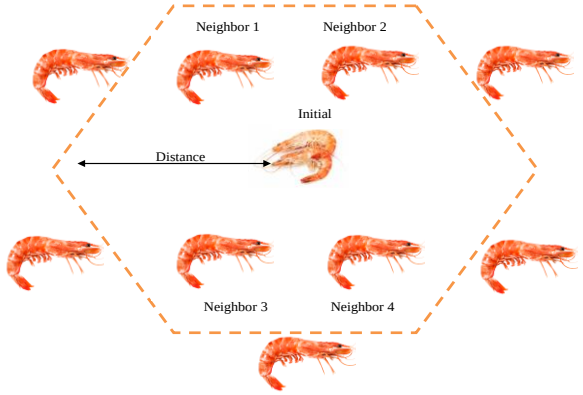


Figure 2. Schematic representation of sensing distance

Foraging motion

The foraging motion is put together in terms of two chief effective constraints. The first one is the food locality and the second one is the preceding understanding about the food location. This motion can be articulated for the i^{th} krill individual as pursue:

$$E_i = M_m \beta_i + \omega_m E_i^{old} \quad (12)$$

Where $\beta_i = \beta_i^{food} + \beta_i^{best}$ (13)

Here F_m is the foraging speed, ω_m is the inertia weight of the foraging motion in the range [0,1], is the last foraging motion, β_i^{food} is the food attractive and β_i^{best} is the effect of the best fitness of the i^{th} krill so far. According to the measured values of the foraging speed it is taken 0.02 (ms-1).

Therefore, the food attraction for the i^{th} krill individual can be determined as follows:

$$\beta_i^{food} = G^{food} M_{i\,food} A_{i\,food} \quad (14)$$

Where

$$A^{food} = \frac{\sum_{i=1}^{N} 1/M_i A_i}{\sum_{i=1}^{N} 1/M_i} \quad (15)$$

Where C^{food} is the food coefficient, because the effect of food in the krill herding decreases during the time the food coefficients is determined as

$$G^{food} = 2\left(1 - \frac{IA}{IA_{\max}}\right) \quad (16)$$

The food attraction is distinct to possibly exert a pull on the krill swarm to the global optima. Depend on this definition; the krill individuals in general herd roughly the global optima subsequent to some iteration.

The effect of the best fitness of the i^{th} krill individual is also handled using the following equation:

$$\beta_i^{best} = M_{ibest} A_{ibest} \quad (17)$$

Where M_{ibest} is the best already visited position of the krill individual.

Physical Diffusion

The physical dispersion of the krill individuals is painstaking to be a random procedure. This movement can be put across in terms of a utmost diffusion speed and a random directional vector. It can be invented as pursue:

$$Q_i = Q^{\max} \lambda \quad (18)$$

Here $Q^{\max}$ is the maximum diffusion speed, and d is the random directional vector and its arrays are random values between -1 and 1.

Motion Process of the KH

The physical diffusion performs a random search in the proposed method. Using different effective parameters of the motion during the time, the position vector of a krill individual during the interval to $t + \Delta t$ is given by following equations.

$$A_i(t + \Delta t) = A_i(t) + \Delta t \frac{dA_i}{dt} \quad (19)$$

Dt Completely depends on the search space and it seems it can be simply obtained from the following formula.

$$\Delta t = S_t \sum_{j=1}^{NN} (UB_j - LB_j) \quad (20)$$

Where NN is the total number of variables, and $UB\ and\ LB$ are lower and upper bounds of the j^{th} variables $j = 0,1,2,.....NN$ respectively. Therefore, the absolute of their subtraction shows the search space. It is empirically found that S_t is a constant number between [0, 2].

Crossover

The crossover operator is primary employed in GA as an effectual approach for global optimization. A vectorized version of the crossover is also employed in DE which can be painstaking as a additional expansion to GA. The crossover rate computation as pursue.

$$cr = 0.2 M_i \quad (21)$$

Mutation

The mutation show business an significant responsibility in evolutionary algorithms such as ES and DE. The mutation is forbidden by a mutation probability (Mr).

$$Mr = 0.5 / M_{ibest} \quad (22)$$

Using this new mutation probability, the mutation probability for the global best is equal to zero and it increases with decreasing the fitness.

Optimal Solution

In light of previously mentioned process, the new arrangements sets are accomplished. At that point, the fitness value is discovered for the new arrangements. From that, the arrangement which gives the minimized make span time is utilized as the optimal solution. Something else, the above strides are processed for the new arrangement sets.

Steps for Proposed JSSP

Step 1: Initialization the krill solutions

Step 2: Fitness Evaluation of each krill individual population

Step 3: Based on fitness updating new krill solution

Step 4: Motion calculation

Motion induced by the presence of other individuals,

Foraging motion

Physical diffusion

Motion induced in KH technique

Step 5: Genetic operator process

Step 6: Find the fitness for new updated krill solutions

Step 7: Store best minimum make span time solution

Iteration=Iteration+1

Step 8: Stop until optimal solution ($F_{optimal}$) attained

Iteration=Iteration+1

End

RESULT AND DISCUSSION

The Projected strategy is actualized in the stage of MATLAB 2015a with the framejob design is i5 processors with 4GB RAM which is utilized for make span time minimization handle in JSSP with various experiments. This proposed job results are contrasted with alternate enhancements systems like PSO, ABC and GA to proposed methods is best in JSSP process

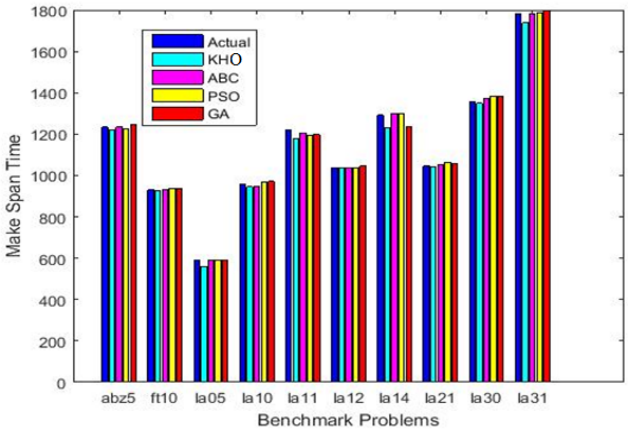


Figure 3. Comparative Analysis

Figure 3 demonstrates the near investigation in ten bench mark problems with makes span time minimization examination in various advancement procedures contrasted with genuine qualities. The above figure 3 demonstrates the ABZ5 (10X10), FT10 (10X10), LA05 (10X5), LA10 (15X5), LA11(20X5),LA12(15X10),LA14(20X5)LA21(15X10),LA30 (20X10) and LA31(30X10). In the whole bench mark problems the minimum make span time are attained in the KHO algorithm. . The genuine qualities are contrasted with the improvement of least distinction accomplished in the KHO approach in JSSP.

Table 1. Make span time for different benchmark problems (test cases)

Benchmark Problem	Size n*m	Best known solution (BKS)	Optimization Technique			
			ABC	PSO	GA	KHO (Proposed)
ABZ5	10X10	1234	1235	1223	1248	1221
FT10	10X10	930	934	938	935	928
LA05	10X5	593	591	592	591	559
LA10	15X5	958	948	968	971	945
LA11	20X5	1222	1206	1195	1198	1180
LA12	20X5	1039	1039	1039	1046	1035
LA14	20X5	1292	1301	1297	1235	1232
LA21	15X5	1046	1054	1064	1058	1041
LA30	20X10	1355	1374	1382	1382	1349
LA31	20X10	1784	1781	1786	1799	1738

Table 1 successfully displays the make traverse time of the Job shop scheduling method. In this procedure the base make traverse time is accomplished in the KHO procedure contrasted with different methods. At the start, the aggregate handling length for the entire employments are found out physically and it is assigned comparably to other the calculations. The occupation successions offer the base make traverse time for the whole employments and they contain the information having time spans which are included with those of alternate occupations. The base make traverse length is accomplished toward the end of the total operation of the whole occupations. Here, if the issue size is changed, the preparing span is additionally seen to modify as per the quantity of the machine working. For LA12 (15X10) the minimum make traverse time of the system viz. The ideal make traverse time is subjected to investigation and stood out from the perceived ideal make traverse length. It is satisfying to note that the imaginative strategy has introduced an ideal make traverse term esteem which runs as an inseparable unit with the distinguished ideal esteem. These occupation arrangements are handled to yield the minimum make traverse span. Also, the base make traverse term is accomplished in the social conduct based improvement when contrasted and the GA, ABC and PSO techniques. The distinction between the first span and novel method term is 65.23% In regard of all the twenty benchmark issues the normal contrast is observed to be 24.56% to 55.23%.

Convergence Graph

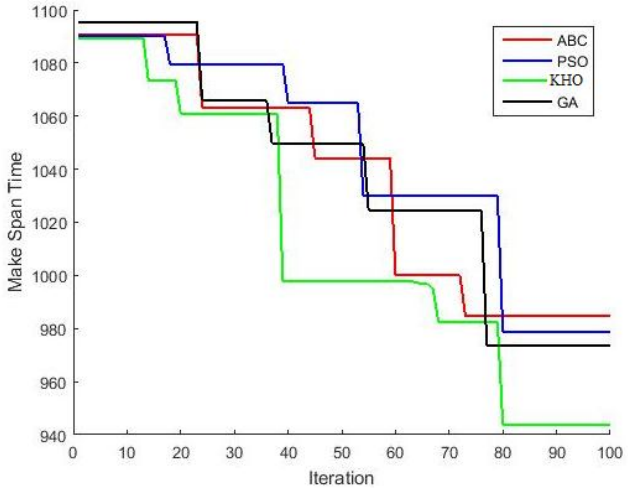


Figure 4. Convergence Graph

Figure 4 demonstrates the minimum make span time for the issue in light of the emphasis variety. When it is differentiated and the PSO the time qualification is 15 and the base time of the ABC is expert in the 91th cycle, and the PSO methodology 42 resemble the every one of the investigations. On account of the PSO likewise the base time is achieved in the 93 emphasis. In any case, on account of GA as the cycle goes up, it prompts to the reduction in the wellness esteem and finally the arrangement identified with the lower wellness is accomplished in the particular emphasis. Along these lines, the lesser wellness esteem is considered and the undifferentiated from arrangement is considered for the assignment. This joining examination the KHO method accomplished the base makes span time contrasted with other advancement systems. Hence, the lesser wellness esteem is considered and the practically equivalent to arrangement is considered for the errand.

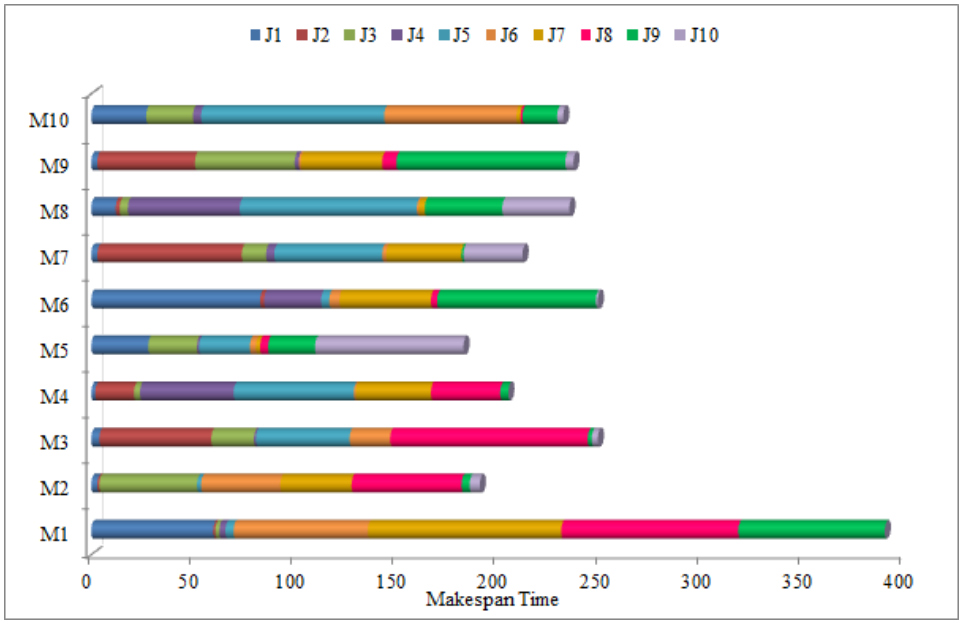


Figure 5. Make span time analysis for LA05

The Gantt chart and the make span rely on upon request in the string. The operations toward the start of the string have a higher handling need than the end. The above figure 5 obviously demonstrates the Gantt graph for string in LA05 experiment. The most ideal timetable 1 grouping is acquired from hereditary administrators with string assessment strategy.

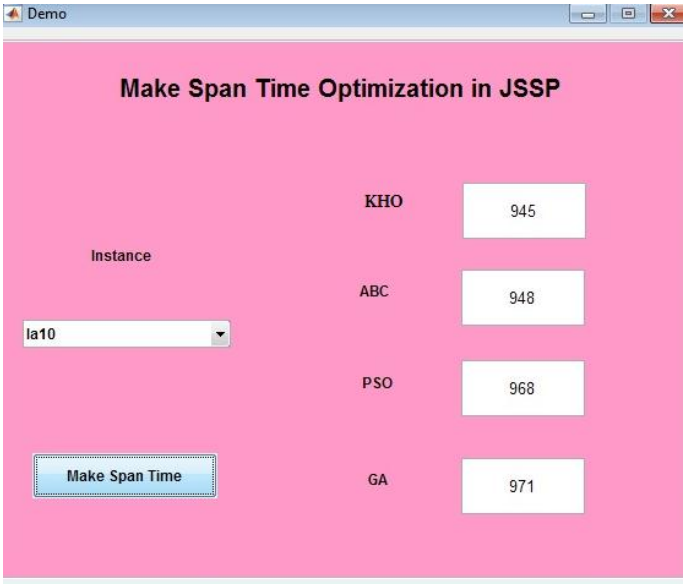


Figure 6. MATLAB output

The output part delineates 4 various constraints for the KHO, GA, PSO and ABC approaches. In the case of KHO output, the time taken is minimum value. Taking all these constraints, the output of all optimization is estimated as discussed above. Figure 6 shows the Graphical user Interface (GUI) model of the JSSP process.

CONCLUSION

Dynamic rescheduling strategy is generally utilized as a part of present day creation plant. In this paper, the JSSP is illuminated by a KHO which has an invaluable over standard procedures. The captivating results substantiate the reality the earth shattering KHO methods and some near improvement have turned out decisively by introducing minimum make-traverse interim for all the standard issues tended to. The proposed work is contrasted with other streamlining the distinction of make traverse time is 85.23%, 72.23%, 82.3% in PSO, ABC and GA strategies. In future, the specialists will use differing improvement approaches for finding the ideal arrangements with their own particular stage and minimizing the make span time. It is trusted that the inventive approach will remain in great stead by viably reassuring the up and coming specialists to find out the make span time for differing benchmark issues with their own particular exceptional strategies.

REFERENCE

[1] Parviz Fattahi, FariborzJolai, and JamalArkat, “Flexible job shop scheduling with overlapping in operations”, Elsevier Journal of Applied Mathematical Modeling, Vol.33, pp.3076–3087, 2009.

[2] D.Prot, and O. Bellenguez-Morineau, “Tabu search and lower bound for an industrial complex shop scheduling problem”, Elsevier Journal of Computers & Industrial Engineering,Vol.62,pp.1109–1118,2012.

[3] Guohui Zhang, Liang Gao, and Yang Shi, “An effective genetic algorithm for the flexible job-shop scheduling problem”, Elsevier Journal of Expert Systems with Applications, Vol.38, pp. 3563–3573, 2011.

[4] J.Heinonen, and F.Pettersson, "Hybrid ant colony optimization and visibility studies applied to a job-shop scheduling problem", Elsevier Journal of Applied Mathematics and Computation, Vol.187, pp.989–998, 2007.

[5] F.Pezzella, G.Morganti, and G.Ciaschetti, "A genetic algorithm for the Flexible Job-shop Scheduling Problem", Elsevier Journal of Computers & Operations Research, Vol.35, pp.3202 – 3212, 2008.

[6] EugeneLevner, VladimirKats, DavidAlcaide López de Pablo, and T.C.E. Cheng "Complexity of cyclic scheduling problems: A state-of-the-art survey", Elsevier Journal of Computers & Industrial Engineering, Vol.59, pp.352–361, 2010.

[7] Liang Gao, Guohui Zhang, Liping Zhang, and Xinyu Li, "An efficient memetic algorithm for solving the job shop scheduling problem", Elsevier Journal of Computers & Industrial Engineering, Vol.60, pp.699–705, 2011.

[8] Xiao-Yuan Wang, Ming-Zheng Wang, and Ji-Bo Wang, "Flow shop scheduling to minimize makespan with decreasing time-dependent job processing times", Elsevier Journal of Computers & Industrial Engineering,Vol.60,pp.840–844,2011.

[9] Yu-Hsiang Chung, and Lee-Ing Tong, "Bi-criteria minimization for the permutation flow shop scheduling problem with machine-based learning effects", Elsevier Journal of Computers & Industrial Engineering, Vol.63, pp.302–312, 2012.

[10] Li Nie, Liang Gao, Peigen Li, and Xinyu Shao, "Reactive scheduling in a job shop where jobs arrive over time", Elsevier Journal of Computers & Industrial Engineering,Vol.66,pp.389–405,2013.

[11] Leila Asadzadeh and Kamran Zamanifar,"Design and Implementation of a Design and Implementation of a Multi-Agent System for Job Shop Scheduling Problem", Journal of Computer Science and Security, Vol.5, No.2, pp.287-297, 2011.

[12] Surekha and Sumathi, "Solving Fuzzy based Job Shop Scheduling Problems using GA and ACO", Journal of Emerging Trends in Computing and information Sciences, Vol.1, No.2, pp.95-102, 2010.

[13] Tamer Abdelmaguid,"Representations in Genetic Algorithm for the Job Shop Scheduling Problem: A Computational Study", Journal of Software Engineering & Applications, Vol.3, pp.1155-1162, 2010.

[14] Miloš Šeda, "Mathematical Models of Flow Shop and Job Shop Scheduling Problems", Journal of Mathematical, Computational, Physical and Quantum Engineering, Vol.1, No.7, pp.295-300, 2007

[15] Jian Xiong, Li-ning Xing, and Ying-wu Chen, "Robust scheduling for multi-objective flexible job-shop problems with random machine breakdowns", Elsevier Journal of Production Economics, Vol.141, pp.112–126, 2013.

[16] S.Sureshkumar, G.Saravanan, and S.Thiruvenkadam "Optimizing Makespan in JSSP Using Unordered Subsequence Exchange Crossover in GA", Journal of Computer Engineering, Vol.8, No.5, pp.41-46, 2013.

[17] Antonin Ponsich, and Carlos A.Coello, "A hybrid Differential Evolution—Tabu Search algorithm for the solution of Job-Shop Scheduling Problems", Elsevier Journal of Applied Soft Computing,Vol.13,pp.462–474,2013.

[18] James C. Chen, Cheng-Chun Wu, Chia-Wen Chen, and Kou-Huang Chen, "Flexible job shop scheduling with parallel machines using Genetic Algorithm and Grouping Genetic Algorithm", Elsevier Journal of Expert Systems with Applications,Vol.39,pp.10016–10021,2012.

[19] Darrell F. Lochtefelda, and Frank W. Ciarallo, "Helper-objective optimization strategies for the Job-Shop Scheduling Problem", Elsevier Journal of Applied Soft Computing, Vol.11, pp.4161–4174, 2011.

[20] Tsung-Lieh Lin, Shi-Jinn Horng, Tzong-Wann Kao, Yuan-Hsin Chen, Ray-Shine Run,Rong-Jian Chen, Jui-Lin Lai, and I-Hong Kuo, "An efficient job-shop scheduling algorithm based on particle swarm optimization", Elsevier Journal of Expert Systems with Applications,Vol.37,2629–2636,2010

Modeling of a neural network based controller for vibration suppression of a building structure

Nilam Rathi, Harendra Pal Singh, and Surendra Kumar

Citation: AIP Conference Proceedings **1975**, 030018 (2018); doi: 10.1063/1.5042188
View online: https://doi.org/10.1063/1.5042188
View Table of Contents: http://aip.scitation.org/toc/apc/1975/1
Published by the American Institute of Physics

Articles you may be interested in

Mathematical modeling of drug delivery in tissue cells using electroporation
AIP Conference Proceedings **1975**, 030017 (2018); 10.1063/1.5042187

Cracked orthotropic interface
AIP Conference Proceedings **1975**, 030021 (2018); 10.1063/1.5042191

Heat transfer in Sisko fluid past an unsteady stretching surface with heat source/sink and viscous dissipation effects
AIP Conference Proceedings **1975**, 030026 (2018); 10.1063/1.5042196

Wave scattering by a submerged plate in a two-layer fluid of finite depth
AIP Conference Proceedings **1975**, 030032 (2018); 10.1063/1.5042202

Modelling of floating rigid dock over rectangular shelf
AIP Conference Proceedings **1975**, 030004 (2018); 10.1063/1.5042174

Modeling of a neural network based controller for vibration suppression of a building structure

Nilam Rathi[1,a)], Harendra Pal Singh[2,b)] and Surendra Kumar[3,c)]

[1]*Department of Applied Mathematics, Delhi Technological University, New Delhi, India.*
[2]*Cluster Innovation Centre, University of Delhi, New Delhi, India.*
[3]*Department of Mathematics, University of Delhi, New Delhi, India.*

[a)]rathi.nilam@gmail.com
[b)]Corresponding author: harendramaths@gmail.com
[c)]surendraiitr8@gmail.com

Abstract. This study presents a neural based control scheme for vibration suppression of a building structure against earthquakes. A priori knowledge of upper bound of model uncertainty and external disturbances is not required. The proposed control is robust to structure uncertainties and external disturbances such as strong winds, earthquakes or heavy dynamic loads. The stability of the error dynamics model is ensured by the Lyapunov stability analysis. Numerical results are carried out for a two-story uncertain building structure to show the effectiveness of the controller.

INTRODUCTION

The design of a vibration controller with high performance for passive, semi-active, active, and hybrid control of building structures is a challenging task due to model uncertainties and external disturbances. The main objective of a structural control system is to reduce the vibration of the high rise building structures when external disturbances such as strong winds, earthquakes or heavy dynamic loads act on them.

In last few decades, many control schemes such as PID, robust, adaptive, etc. have been developed to protect civil structures against earthquake excitations [1, 2, 3, 4, 5, 6]. In [7], an active robust control scheme is designed for structural systems in the presence of uncertainties. Numerical results of a four-story building structure against robust control are carried out for motion induced by the 1940 El Centro earthquake. In [8], a robust $H\infty$ control scheme is proposed to attenuate the vibrations of a building structure. The performance of the control approach is tested experimentally for a two-story building model subjected to ground acceleration using a shaker table. A new nonlinear adaptive control approach for vibration isolation of a single DOF structural system is presented in [9]. The proposed controller requires the exact information of the internal parameter of a_0 of MR damper. In[1], a robust sliding mode control scheme is proposed to attenuate the vibrations of the uncertain structures. In this scheme, a priori knowledge of the upper bounds of uncertainties is required. There are many neural network based control schemes available in the literature[10, 14]. In [15], an adaptive control scheme for nonlinear bridge models with earthquake excitation is proposed. They applied the proposed controller to a single DOF and a two-DOF bridge model. The robustness of the control systems is also investigated by applying two different earthquakes to the bridge models with same simulation scenarios. In [16], an adaptive control approach using a linearly parameterized neural network is proposed for nonlinear base-isolated structures. The control approach is based on direct adaptive control where the model response is made to follow a given motion.The estimation of upper bound of uncertainty using neural network is not found in the literature for vibration suppression of uncertain building structures.

In this paper, an adaptive neural network based controller is proposed for vibration suppression of a multi-DOF building structure. The proposed adaptive neural network based scheme has the following features:
(a) no prior information about the bound of uncertainty is required for its implementation,
(b) the controller is able to learn the bound of model uncertainties and disturbances,
(c) weight adaptive law is designed based on Lyapunov stability approach and the error converges to a desired motion

Proceedings of the International Conference on Frontiers in Industrial and Applied Mathematics (FIAM-2018)
AIP Conf. Proc. 1975, 030018-1–030018-10; https://doi.org/10.1063/1.5042188
Published by AIP Publishing. 978-0-7354-1684-0/$30.00

in a finite time interval,
(d) the proposed control is robust to model uncertainties and external disturbances such as strong winds, earthquakes or heavy dynamic loads.

This paper is organized as follows. The problem formulation is provided in Section 2. In Section 3, a novel adaptive neural network based controller is proposed for achieving robustness and asymptotic error convergence. Simulation results are presented in Section 4 to illustrate the effectiveness of the controller. Section 5 gives conclusion.

PROBLEM FORMULATION

Based on the Newton's second law, the equation of motion of a building structure with n-degree-of-freedom is given as

$$M_b\ddot{x}(t) + C_b\dot{x} + K_b x = u_b(t) \tag{1}$$

where $t \geq 0$; $x = (x_1, x_2, ..., x_n) \in R^n$ denotes the state vector of the system; $M_b \in R^{n\times n}$ represents the mass matrix; $C_b \in R^{n\times n}$ denotes the damping coefficient; $K_b \in R^{n\times n}$ represents the stiffness matrix of the building structure; $u_b(t) \in R^n$ is the control input. The mechanical structure of an n-DOF building model is shown in Fig. 1. In practice, all physical

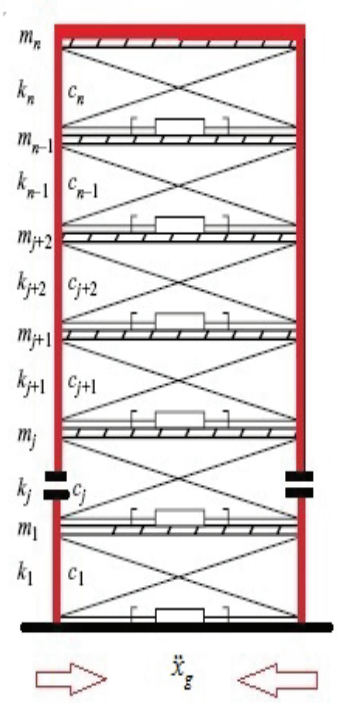


FIGURE 1. n-story building structure with active tendon control

models are subjected to system uncertainties and external disturbances during operation. Because of parameter variations and disturbances, it is assumed that the motion equation of the system presents uncertainty. Therefore, expression (1) has the following form

$$(M_b + \Delta M_b)\ddot{x} + (C_b + \Delta C_b)\dot{x} + (K_b + \Delta K_b)x = D_b(t) + u_b(t) \tag{2}$$

where ΔM_b, ΔC_b, and $\Delta K_b \in R^{n\times n}$ are parameter uncertainties of the structure. External disturbance $D_b(t) \in R^n$ disturbs the building structure and has the following form

$$D_b(t) = \lambda\ddot{x}_g \tag{3}$$

where λ is a $n \times 1$ vector for earthquake ground acceleration $\ddot{x}_g$.

Let $\dot{x}$ and $\ddot{x} \in R^n$ denote the velocity and acceleration vectors, respectively. Then the displacement and velocity errors are defined as $e = x - x_d$, and $\dot{e} = \dot{x} - \dot{x}_d$, respectively. The vector $x_d \in R^n$ denotes the desired system response.

The filtered error is given as follows

$$s = \dot{e} + \Lambda_1 e \tag{4}$$

where Λ_1 represents a diagonal gain matrix. Differentiating both sides of the Eq. (4) with respect to t and using Eq. (2), we get the following error model

$$\begin{aligned} M_d \dot{s} &= u_b(t) - C_b(s - \Lambda_1 e + \dot{x}_d) - K_b x - \Delta M_b \ddot{x} - \Delta C_b \dot{x} \\ &\quad -\Delta K_b x + D_b(t) - M_b \ddot{x}_d + M_b \Lambda_1 (r - \Lambda_1 e) \end{aligned}$$

$$\begin{aligned} M_b \dot{s} &= u_b(t) - C_b s - K_b x + C_b(\Lambda_1 e - \dot{x}_d) \\ &\quad + M_b(\Lambda_1 \dot{e} - \ddot{x}_d) - \Delta M_b \ddot{x} - \Delta C \dot{x} - \Delta K_b x + D_b(t) \end{aligned} \tag{5}$$

The expression $\Delta\varpi = C_b(\Lambda_1 e - \dot{x}_d) + M_b(\Lambda_1 \dot{e} - \ddot{x}_d) - \Delta M_b \ddot{x} - \Delta C_b \dot{x} - \Delta K_b x + D_b(t)$ represents the uncertainty for the given structure model. The expression $\Delta\varpi$ is assumed to satisfy the following condition:

$$\|M_b^{-1} \Delta\varpi\| \leq \varphi = a\|\Lambda_1 e - \dot{x}_d\| + \|\Lambda_1 \dot{e} - \ddot{x}_d\| + b\|x\| + c \tag{6}$$

where a, b, and c are the positive constants. Recently, Aghababa [1] proposed a sliding mode control method which has some potential difficulties such as (a) the upper bounds of the uncertainty terms and disturbances are assumed to be known in advance, (b) the computation of uncertainty bounds due to a tall building structure is difficult and time consuming, and (c) in case of new building structure, the whole method has to start again. The aim of this paper is to show that for a given structural system (2) with model uncertainties and external disturbances a suitable neural network controller $u_b(t)$ can be designed such that $x \to 0$ as $t \to \infty$.

NEURAL NETWORK CONTROLLER AND STABILITY ANALYSIS

Mathematical model of an one-layer neural network in terms of uncertain bound φ has the following form

$$\varphi = Z^{*T} \phi(y) + \Delta\varphi$$

and the estimate value of φ is given as

$$\hat{\varphi} = \hat{Z}^T \phi(y)$$

where $\Delta\varphi$ denotes NN approximation error satisfying $\|\Delta\varphi\| = \|Z^{*T}\phi(y) - \varphi\| < \xi$, $\phi(.)$ denotes a basis vector and $\hat{Z}$ is the estimate value of the optimal matrix Z^*. Let us assume that, the norm of $M_d^{-1}\Delta\varpi$ and φ satisfy the condition $\varphi - \|M_d^{-1}\Delta\varpi\| > \xi$.

Based on the error dynamics model and subsequent stability analysis, we design the following neural network based control scheme:

$$u_b(t) = C_b s + K_b x - M_b(\Lambda_2 s + \frac{\hat{\varphi}^2 s}{\hat{\varphi}\|s\| + \epsilon}) \tag{7}$$

where Λ_2 is a positive definite diagonal matrix, $\dot{\epsilon} = -\kappa\epsilon$, $\epsilon(0) > 0$, κ is a positive constant. The Lyapunov stability analysis of the error system is given as follows:

Theorem 3.1: Consider the uncertain building structure system (2) and control input (7). If adaptive law is given as

$$\dot{\hat{Z}} = F\|s\|\phi(y),$$

where F represents a positive definite diagonal gain matrix, then the error trajectories converge to zero asymptotically.

Proof: The Lyapunov function is defined as follows

$$V = \frac{1}{2} s^T s + \frac{1}{2} tr(\tilde{Z}^T F^{-1} \tilde{Z}) + \kappa^{-1}\epsilon \tag{8}$$

where $\tilde{Z} = Z^* - \hat{Z}, \dot{\tilde{Z}} = -\dot{\hat{Z}}$. Then, the derivative of V w.r. to t is given as

$$\dot{V} = s^T \dot{s} + tr(\tilde{Z}^T F^{-1} \dot{\tilde{Z}}) + \kappa^{-1} \dot{\epsilon}$$

Using Eq. (5), we have

$$\begin{aligned} \dot{V} &= s^T [M_b^{-1}(u_b(t) - C_b r + C_b(\Lambda_1 e - \dot{x}_d) + M_b(\Lambda_1 \dot{e} - \ddot{x}_d) - (K_b + \Delta K_b)x - \Delta M_b \ddot{x} - \Delta C_b \dot{x} + D_b(t))]s \\ &\quad + tr(\tilde{Z}^T F^{-1} \dot{\tilde{Z}}) + \kappa^{-1} \dot{\epsilon} \end{aligned}$$

Based on the control scheme (10), we have

$$\begin{aligned} \dot{V} &= s^T [M_b^{-1}(C_b s + K_b x - M_b(\Lambda_2 s + \frac{\hat{\varphi}^2 s}{\hat{\varphi}\|s\| + \epsilon}) - C_b s \\ &\quad + C_b(\Lambda_1 e - \dot{x}_d) + M_b(\Lambda_1 \dot{e} - \ddot{x}_d) - (K_b + \Delta K_b)x - \Delta M_b \ddot{x} - \Delta C_b \dot{x} + D_b(t))]s + tr(\tilde{Z}^T F^{-1} \dot{\tilde{Z}}) + \kappa^{-1} \dot{\epsilon} \end{aligned}$$

$$\dot{V} \leq -s^T \Lambda_2 s - \frac{\hat{\varphi}^2 \|s\|^2}{\hat{\varphi}\|s\| + \epsilon} + \|s\|(\|M_b^{-1} \Delta \varpi\| - \varphi) + \|s\|(Z^{*T} \phi(y) + \Delta\varphi) + tr(\tilde{Z}^T F^{-1} \dot{\tilde{Z}}) + \kappa^{-1} \dot{\epsilon}$$

$$\dot{V} \leq -\frac{1}{2} \lambda_{min}(\Lambda_2) \|s\|^2 - \frac{\hat{\varphi}^2 \|s\|^2}{\hat{\varphi}\|s\| + \epsilon} + \|s\|(-\xi + \Delta\varphi) + \|s\| Z^{*T} \phi(y) + tr(\tilde{Z}^T F^{-1} \dot{\tilde{Z}}) - \epsilon$$

$$\dot{V} \leq -\frac{1}{2} \lambda_{min}(\Lambda_2) \|s\|^2 - \frac{\hat{\varphi}^2 \|s\|^2}{\hat{\varphi}\|s\| + \epsilon} + \hat{\varphi}\|s\| + tr(\|s\| W^{*T} \phi(s) - \|s\| W^{*T} \phi(y)) - \epsilon$$

$$\dot{L} \leq -\frac{1}{2} \lambda_{min}(\Lambda_2) \|s\|^2$$

Since $V > 0$ and $\dot{V} \leq 0$ this shows s is bounded. Define a function $\Upsilon(t) = \lambda_{min}(\Lambda_2)\|s\|^2 \leq -\dot{V}$ and integrate this function with respect to time t. Then, we obtained the following results

$$\int_0^t \Upsilon(t) \leq V(0) - V(t)$$

and

$$\lim_{t \longrightarrow \infty} \int_0^t \Upsilon(t) < \infty.$$

Using Barbalat's Lemma, the error trajectories converge to zero asymptotically [10].

SIMULATION RESULTS

Consider a two-story building structure excited by unwanted earthquakes [17]. The motion equation of a two-story building structure with parameter uncertainties is given as follows

$$\begin{bmatrix} m_{11} + \Delta m_{11} & m_{12} + \Delta m_{12} \\ m_{21} + \Delta m_{21} & m_{22} + \Delta m_{22} \end{bmatrix} \begin{bmatrix} \ddot{x}_1 \\ \ddot{x}_2 \end{bmatrix} + \begin{bmatrix} c_{11} + \Delta c_{11} & c_{12} + \Delta c_{12} \\ c_{21} + \Delta c_{21} & c_{22} + \Delta c_{22} \end{bmatrix} \begin{bmatrix} \dot{x}_1 \\ \dot{x}_2 \end{bmatrix} + \begin{bmatrix} k_{11} + \Delta k_{11} & k_{12} + \Delta k_{12} \\ k_{21} + \Delta k_{21} & k_{22} + \Delta k_{22} \end{bmatrix} \begin{bmatrix} x_1 \\ x_2 \end{bmatrix} = D(t) + u(t)$$

where

$$m_{11} = 0.136, m_{12} = 0, m_{21} = 0, m_{22} = 0.066, c_{11} = 0.0572, c_{12} = -0.0198, c21 = -0.0198, c22 = 0.0313,$$
$$k_{11} = 75, k_{12} = -44.3, k_{21} = -44.3, k_{22} = 44.3.$$

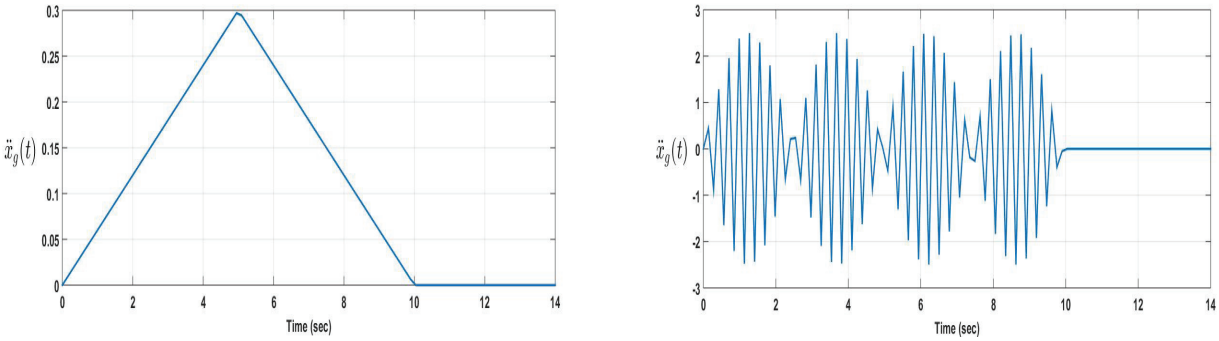


FIGURE 2. Excitations applied to the building structure [15]

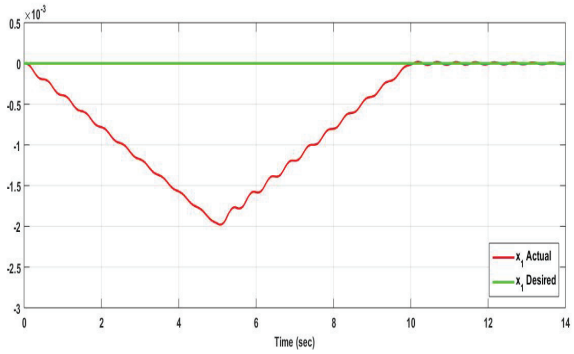


FIGURE 3. Response of variable x_1 without any controller

Parameter uncertainties values for simulation are defined as follows

$$\Delta m_{11} = -0.05, \Delta m_{12} = cos(t)x_1, \Delta m_{21} = 0.01, \Delta m_{22} = cos(t)x_2, \Delta c_{11} = -0.0005, \Delta c_{12} = cos(t)x_1,$$
$$\Delta c_{21} = 0.01, \Delta c_{22} = cos(t)x_2, \Delta k_{11} = 2, \Delta k_{12} = sin(t)x_1, \Delta k_{21} = -2, and \Delta k_{22} = sin(t)x_2.$$

External disturbance term is given as $D_b(t) = \lambda \ddot{x}_g$, where $\lambda = -[0.136 \quad 0.066]^T$. Let us assume that ground acceleration $\ddot{x}_g$ disturbs the model dynamics and has the following shapes.

For simulation results, we have two cases. Case (i): Performance of the system under ground acceleration 1 is shown in Figs. 3-9. Case (ii): Performance of the system under ground acceleration 2 is shown in Figs. 10-16.

The numerical results are shown for 14 sec. The desired system response x_d is 0. The controller parameters are selected as $F = 10I_{10}$, $\gamma = 0.01$, $\Lambda_1 = I_{10}$, and $\Lambda_2 = I_{10}$. In both cases, the effectiveness of a neural network to learn the bound of uncertain vibration control is shown in Figs. 4, 6, 8, 9, 11, 13, 15 and 16. Response of the system without any controller is shown in Figs. 3, 5, 7, 10, 12 and 14. Against the earthquake excitation, the performance of the state variables is found to be smoother and less oscillatory than the uncontrolled system. Control inputs under both ground accelerations are presented in Figs. 9 and 16.

CONCLUSION

In this study, an adaptive controller is designed to solve the problem of vibration suppression of an uncertain multi-DOF structural system. Neural network is employed to learn the parameter vibrations and disturbances. The stability analysis of the error dynamic model is achieved using the Lyapunov function. The simulation results are carried out for a two-story structure suffered by an earthquake. It can be concluded from the above simulation results that the proposed controller has more robust stability and performance characteristics than the without any controller.

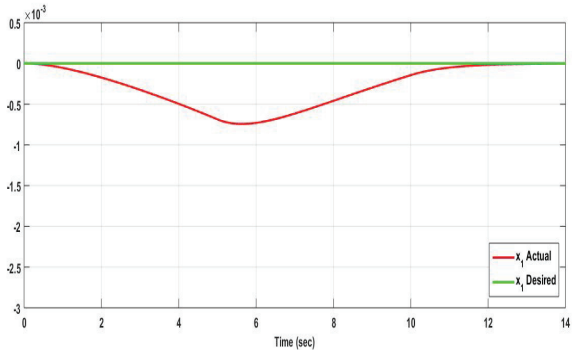


FIGURE 4. Response of variable x_1 with a neural network based controller

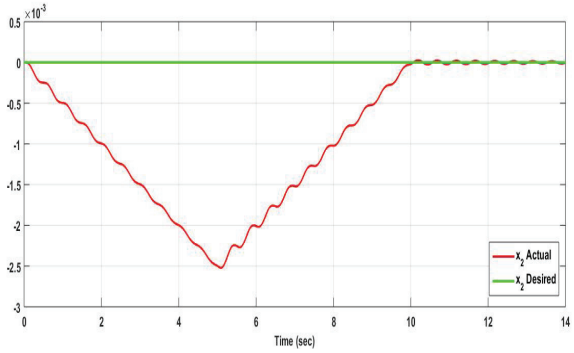


FIGURE 5. Response of variable x_2 without any controller

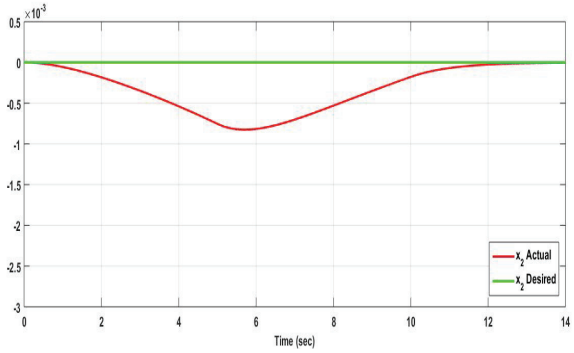


FIGURE 6. Response of variable x_2 with a neural network based controller

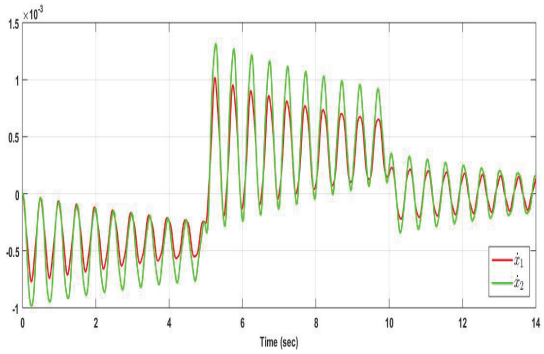


FIGURE 7. Response of velocities without any controller

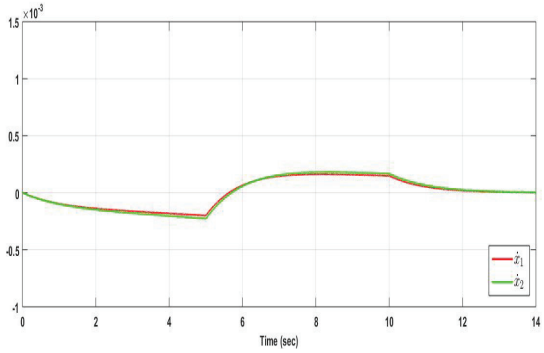


FIGURE 8. Response of velocities with a neural network based controller

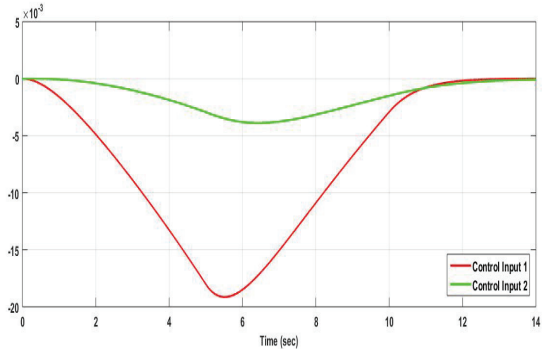


FIGURE 9. Response of controller inputs

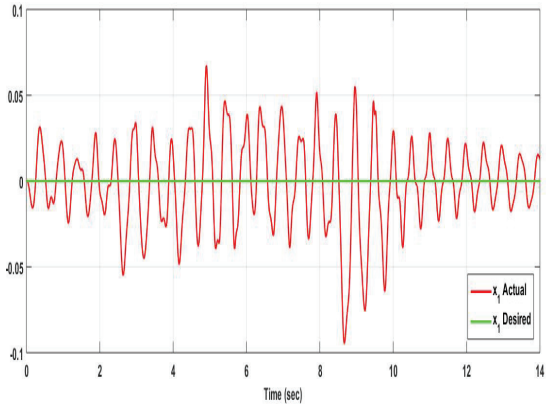


FIGURE 10. Response of variable x_1 without any controller

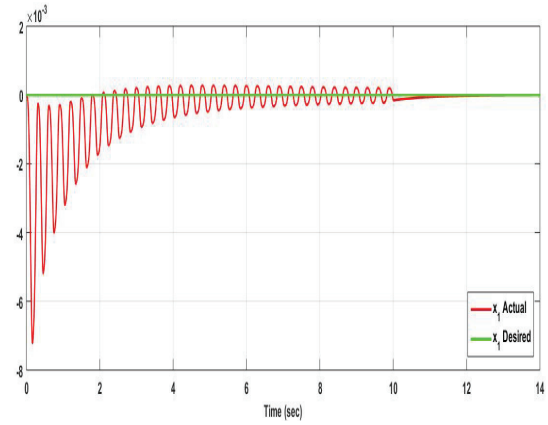


FIGURE 11. Response of variable x_1 with a neural network based controller

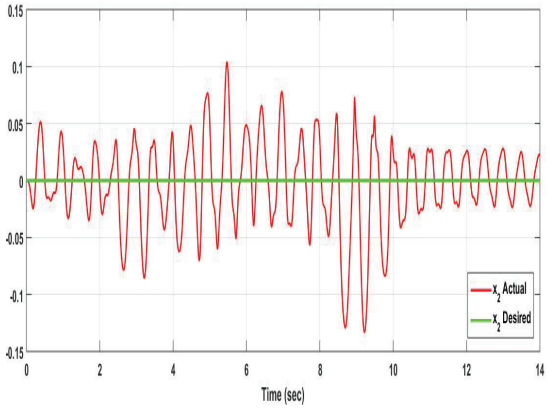


FIGURE 12. Response of variable x_2 without any controller

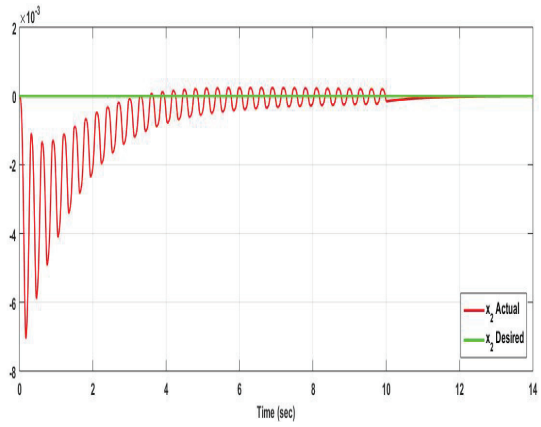


FIGURE 13. Response of variable x_2 with a neural network based controller

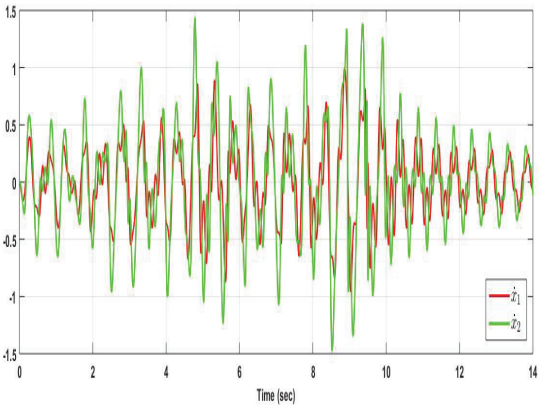


FIGURE 14. Response of velocities without any controller

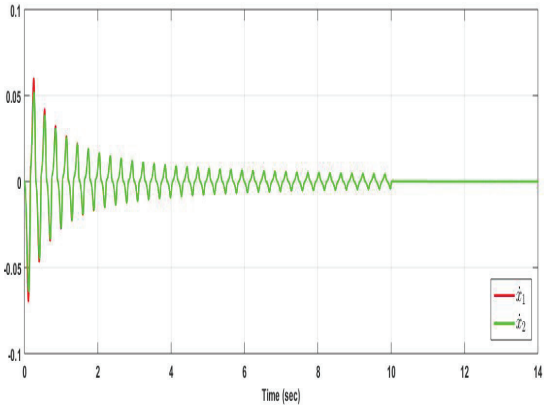


FIGURE 15. Response of velocities with a neural network based controller

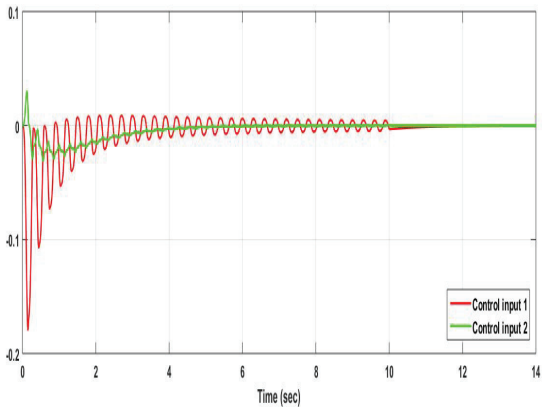


FIGURE 16. Response of controller inputs

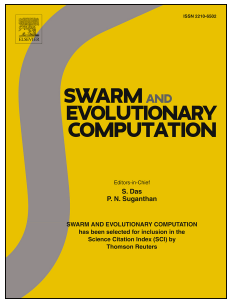
ACKNOWLEDGMENTS

The author acknowledges the financial support by UGC (F.No. 30-317/2016), New Delhi, India to carry out the reported research work.

REFERENCES

[1] M. P. Aghababa, ISA Transactions **52**, 881-887 (2013).
[2] G. W. Housner, T. T. Soong, S. F. Masri, World conference on structural control (Los Angeles, 1994).
[3] Y. L. Xu, W. L. Qu, B. Chen, Journal of Sound and Vibration **261**, 277-296 (2003).
[4] R. Guclu, Mathematical and Computer Modelling **44**, 210-217 (2006).
[5] N. R. Fisco, H. Adeli, Scientia Iranica **18**, 285-295 (2011).
[6] Suresh Thenozhi, Wen Yu, Annual Reviews in Control **37**, 346-364 (2013).
[7] S. G.Wang, H. Y. Yeh, P. N. Roschke, Nonlinear Dynamics and Systems Theory **4**, 195-216 (2004).
[8] G. L. C. M. Abreu, V. Lopes Jr., M. J. Brennan, ISMA2010 including USD2010, 215-226 (2010).
[9] S. Cetin, E. Zergeroğlu, S. Sivrioğlu, İ. Yöksek, 18th IEEE International Conference on Control Applications, (Saint Petersburg, Russia, 2009),pp. 60-65.
[10] F. L. Lewis, A. Yesildirek, K. Liu, IEEE Transactions on Neural Networks **7**, 388-399 (1996).
[11] H. P. Singh, N. Sukavanam, International Journal of Intelligent Engineering Informatics **1**, 142-155 (2011).
[12] H. P. Singh, N. Sukavanam, ISA Transactions **51**, 105-110 (2012).
[13] H. P. Singh, International Journal of Nonlinear Sciences and Numerical simulation **15**, 181-188 (2014).
[14] H. P. Singh, S. Kumar, P. Kumar, A. Mahajan, Virtual Experimental Analysis of Redundant Robot Manipulators Using Neural Networks, in Soft Computing: Theories and Applications, Advances in Intelligent Systems and Computing, edited by M. Pant, K. Ray, T. Sharma, S. Rawat, A. Bandyopadhyay (Springer, Singapore, 2018), pp. 21-30.
[15] H. C. Cho, M. S. Fadali, M. S. Saiidi, K. S. Lee, International Journal of Control, Automation, and Systems **3**, 202-210 (2005).
[16] S. Suresh, S. Narasimhan, American Control Conference (USA, 2011), pp. 3129-3133.
[17] F. Y. Cheng, H. Jiang, K. Lou, Smart structures: Innovative systems for seismic response control, CRC Press/Taylor and Francis Group (2008).

Accepted Manuscript



Nature Inspired Power Optimization in smartphones

Nirmal Pandey, O.P. Verma, Amioy Kumar

PII: S2210-6502(17)30812-X

DOI: 10.1016/j.swevo.2018.06.006

Reference: SWEVO 417

To appear in: *Swarm and Evolutionary Computation BASE DATA*

Received Date: 8 October 2017

Revised Date: 7 May 2018

Accepted Date: 3 June 2018

Please cite this article as: N. Pandey, O.P. Verma, A. Kumar, Nature Inspired Power Optimization in smartphones, *Swarm and Evolutionary Computation BASE DATA* (2018), doi: 10.1016/j.swevo.2018.06.006.

This is a PDF file of an unedited manuscript that has been accepted for publication. As a service to our customers we are providing this early version of the manuscript. The manuscript will undergo copyediting, typesetting, and review of the resulting proof before it is published in its final form. Please note that during the production process errors may be discovered which could affect the content, and all legal disclaimers that apply to the journal pertain.

ACCEPTED MANUSCRIPT

Nature Inspired Power Optimization in Smartphones

Nirmal Pandey[1], O.P. Verma[2], Amioy Kumar[3]

Abstract

Good battery backup has always been one of the most desirable features of smartphones since inception. Key subsystems of smartphones include powerful processors (application processors - CPU, communication processors - modem and graphics processors - GPU), large displays and high-speed networks. All these subsystems are very demanding on smartphone battery. Popular smartphone use cases, such as high-resolution video streaming, networked gaming, video calling etc., are power hungry. Due to increased security concerns, smartphone manufacturers have added biometric security features such as fingerprint, IRIS and face recognition etc. in smartphones. There is additional current consumption ranging from 300 milliampere (mA) to 400 milliampere (mA) each time smartphone user unlocks the device using any one of these security features. Therefore, it will be in the fitness of the things that smartphone battery lifetime is increased as much as possible. Due to irregular nature of mobile network traffic, it is very difficult to accurately predict battery lifetime or set a deadline up to which battery should last. In this paper, we have addressed both these problems. Here, we present a novel power optimization system called NIPO (Nature Inspired Power Optimization). Our contributions are – i) Present a novel client server based power optimization System, called NIPO. ii) Use nature inspired algorithms - particle swarm optimization (PSO), ant colony optimization (ACO), and cuckoo search algorithm (CSA) with Levy Flights, for power optimization in smartphone displays for the first time. iii)

[1] Nirmal Pandey (writetonirmal@gmail.com), Delhi Technological University (DTU), Shahbad Daulatpur, Main Bawana Road, Delhi, 110042
[2] Prof O.P. Verma (opverma@dce.ac.in), Delhi Technological University (DTU), Shahbad Daulatpur, Main Bawana Road, Delhi, 110042Delhi
[3] Amioy Kumar (amioy.iitd@gmail.com), Delhi Technological University (DTU), Shahbad Daulatpur, Main Bawana Road, Delhi, 110042Delhi

Develop a mathematical model of power consumption for OLED (Organic Light Emitting Diode) displays in smartphones. iv) Implement NIPO system on Android based smartphone and Windows server to validate the effectiveness of proposed system.

For experimental purposes, the proposed NIPO system was implemented on smartphone running Android OS for client side and a Windows server for server side. The experimental results validate the effectiveness of the proposed NIPO system. NIPO system successfully meets user defined time-to-last requirement of battery lifetime.

Index Terms: – *Energy Efficiency; smartphones; nature inspired algorithms; power optimization.*

I. INTRODUCTION

The smartphone user base is expanding at an ever-increasing pace. According to one estimate, total number of mobile users has already surpassed the human population[4]. The processing power of smartphones is always on the rise, following Moore's law[5]. Nowadays smartphones with eight-core CPU (Central Processing Unit) are very common. At the same time, high speed networks (4G and beyond) have been rolled out in most of the countries[6]. High processing power coupled with high speed data networks enable many new use cases in smartphones such as FHD (Full High Definition)/HD content streaming, Video/Wi-Fi calling, high end local/networked gaming, content sharing, large size content downloads, to name a few. In emerging countries, due to large customer base and unstable cellular networks,

[4] Ericsson Mobility Report, Nov 2016, available at: https://www.ericsson.com/mobility-report

[5] Moore's Law: http://www.mooreslaw.org/

[6] Deloitte Mobile Consumer Survey 2016, available at:https://www2.deloitte.com/global/en/pages/technology-media-and-telecommunications/articles/global-mobile-consumer-survey.html

frequent cases of call-drops as well as data disconnect have been reported. This requires lot of retransmission and extra communication between network and smartphones involving RF (Radio Frequency). All of these put smartphone battery under severe pressure, thereby drastically reducing battery lifetime.

A. Motivations

Smartphone users are conscious about limited battery lifetime of the device. The users lack in proper know-how about power consumption features and capabilities of the device [1]. Therefore, there is need to have a system that can take care of power optimization without much user intervention. Several attempts have been made to optimize power using software based profiling information. However, usage pattern profiling-based methods are not suitable as these tend to increase power consumption overhead due to the need for additional processing [2]. Usage pattern-based power optimization systems with client server architecture have also been proposed [3]. However, if fine grained profiling is done to improve system accuracy and all profiling data is sent to server, it may have privacy issues.

Battery lifetime prediction has also been investigated by various researchers. A battery lifetime prediction method that makes use of activities and the time spent in these activities and various applications as the basis for lifetime computation has been proposed in literature [4] – [5]. However, it is also equally important that smartphone user should be able to set a duration deadline up to which the battery of his device should last without having any charging opportunity for that duration.

B. Contributions

In this paper, our main contributions are: -

i) Proposed a novel client server based power optimization System. Computation of optimum value of parameters that impact power consumption involve high amount of

CPU processing. This CPU processing in turn also consumes lot of battery power. Therefore, it is prudent that such type of CPU hungry processing is offloaded to a server. In this paper, we present architecture of a system that involves both – a client software running on the smartphone and a power optimization engine running on the server.

ii) This work, to the best of our knowledge, for the first time utilizes nature inspired algorithms for solving power optimization problem in smartphones. In this work, we chose to utilize few popularly available nature inspired algorithms - Ant Colony Optimization (ACO) which is inspired by behaviour of ants, Particle Swarm Optimization (PSO) which is inspired by movement of swarms/birds, and Cuckoo Search algorithm (CSA) with Levy flight for battery power optimization. We further compared these three optimization techniques for power optimization. For optimization purposes, the total power consumed becomes the cost function of nature inspired algorithms. In the current work, we have taken power consumed by OLED (Organic Light Emitting Diode) display of the smartphone as the cost function, which is dependent upon transparency, brightness, and colour (Red, Green and Blue) intensity of the pixels.

iii) Develop a mathematical model of power consumption for OLED displays in smartphones. OLED displays are now quite common in mid to high range smartphones. Power consumption characteristics of these displays have been investigated on the real device. A mathematical model for screen level power consumption in OLED based devices has been proposed.

iv) Implement and validate the proposed system - on Android smartphone for the client side and Windows machine for the server side. Its efficacy has been validated with experimental test results.

Rest of the paper is organized as below. In section II, we present a survey of prior research done related to smartphone power optimization. Mathematical model of screen level power

consumption in OLED displays is detailed under Section III. The proposed Nature Inspired Power Optimization (NIPO) system is presented in Section IV. The experimental setup and test results are provided under Section V. Under Section VI, conclusion of the work done is given and scope for future research outlined.

II. STATE OF THE ART

Power conservation has been investigated and improved by various researchers since the advent of smartphones. Linux kernel[7], which forms the basis of popular smartphone OS (Operating System) called Android, implements power saving framework using dynamic voltage frequency scaling (DVFS) and idle governor. Android OS provides power conservation with "Doze" mode[8]. This mode gets activated when display is off and device is not charging.

In a study involving more than 350 subjects distributed over different countries, Rahmati et al. [1] found that 80% of the mobile users were concerned with the battery life of the device. Various researchers have investigated power consumption in smartphones [6] – [10]. Various components of smartphones that consume most of the power have been identified. These include processors (application and communication processors), graphical processing unit (GPU), Radios (2G/3G/4G/Wi-Fi), display, memory and audio subsystems. Mobile devices with large screen sizes (up to 6") are becoming very common. Large displays consume more power. With live video streaming in high resolution use cases increasing it is imperative that power conservation in displays should be investigated.

[7] Linux Kernel, available at: www.kernel.org
[8] Android 7.0 Changes in Doze Mode, available at: https://developer.android.com/about/versions/nougat/android-7.0-changes.html

Cloud and client software components/functionality distribution has also been utilized to conserve power [11]. Power hungry functionality is transferred to server and functions which are light on battery are executed on the device [12]. However, the main pain point here is difficulty in designing software such that the functionalities can be split between server and client.

According to a recent survey[9], one of the top concerns of the smartphone users was related to security of the device. Smartphone manufacturers have tried to address this concern in various ways. The most common among these is introduction of biometric enabled security features such as fingerprint, face and iris recognition[10]. However, addition of any feature or functionality on the device results in some impact on the power consumption. To understand the impact of biometric security features on power consumption of the device, we conducted test using Samsung Note 7 smartphone as DUT (Device under Test) and a power monitor tool[11]. Galaxy Note 7 has inbuilt front facing fingerprint scanner as well as iris scanner. If we observe Galaxy Note 7 power consumption test results as given in figure 1, we can see that for each unlock operation 300 to 400 milliampere (mA) extra current is consumed if we make use of iris or fingerprint scanner for unlocking the device in comparison to unlocking with finger swipe. Thus, biometric enabled security features reduce number of hours a smartphone can be used without charging. This reflects the severity of the power consumption problem in smartphones.

[9] Deloitte Global Mobile Consumer Survey2015, available at: https://www2.deloitte.com/content/dam/Deloitte/us/Documents/technology-media-telecommunications/us-tmt-global-mobile-executive-summary-2015.pdf

[10] Samsung Galaxy Note 7 with inbuilt Iris scanner. https://news.samsung.com/global/everything-you-need-to-know-about-the-galaxy-note7s-iris-scanner

[11] Monsoon Solution Inc., “Power Monitor": www.msoon.com/LabEquipment/PowerMonitor/

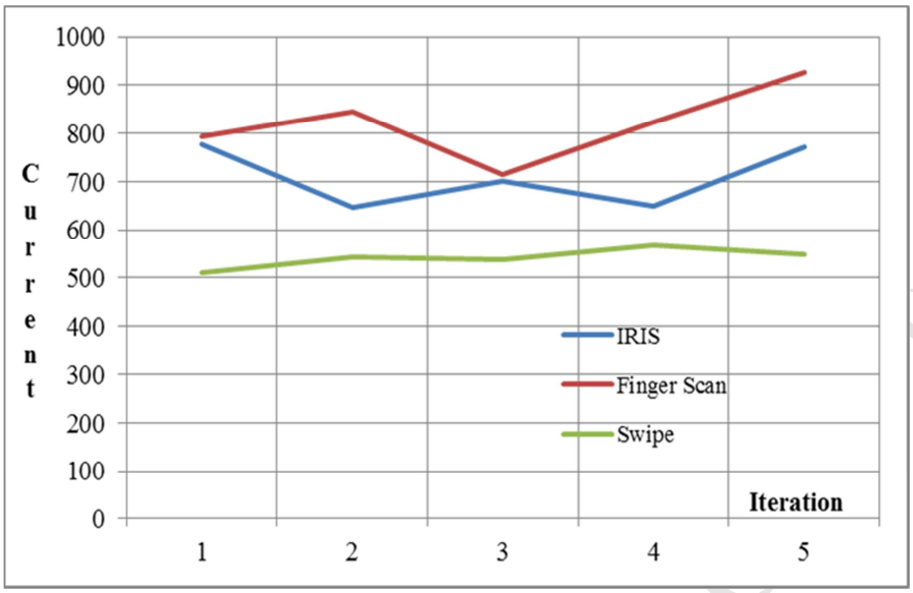


Fig 1: Power Consumption for Biometric Sensor Use cases

OLED displays have also been subject of several power conservation studies. Over the years, various researchers have proposed many techniques to optimize power in OLED displays. All these techniques broadly fall in to two categories – First category of techniques involves dynamic voltage scaling to save power. Second category of techniques involves exploiting various properties of OLEDs related to luminosity (LUMA) and chroma to save the power [13]. Driving voltage needed for glowing OLEDs can be reduced to reduce overall power requirement of display. This fact has been exploited by some researchers [14] – [16] to achieve varying degree of power savings. However, these hardware specific changes are not suitable to already manufactured smartphone devices.

Many researchers focused on power-aware graphical user interface (GUI) and colour transformation to save power in displays. Valerio [17] proposed the concept of Energy Efficient GUI (E2GUI). They proposed that the overall power consumption of the device depends upon GUI elements as well as on the human response which is dependent upon perceptual capacity, cognitive speed and motor speed of the user. This method is useful

during the GUI design stage and the content to be displayed must be known a priori. Dong et al. [18] – [19] demonstrated that the power consumed by OLED varies differently for different colours (Red, Blue and Green) and colour intensity has a non-linear relationship with the consumed power. Therefore, it is possible to minimise energy consumption in OLED based devices by suitably designing colour combinations that consume less power than other colours. However, their method is only suitable for GUI screens and will have quality of experience issues where fidelity of the displayed contents cannot be compromised. Dong [20] applied colour transformation to the browser. They developed a modified web browser called Chameleon. This modified browser dynamically changes colours of displayed content to optimize power consumption.

The state of the art review shows that, the earlier attempts mostly considered color intensity (red, blue, and green components) and brightness [21] [22] as main parameters for battery power optimization. Further, there has been very little or no attempt on optimization of battery power of smartphones using nature inspired optimizations system which can provide efficient optimization to battery power. In this work, we choose transparency, brightness, and colour intensity as optimization parameters to save power for a given battery level. To the best of our knowledge, there is no work which has used nature inspired algorithms like PSO, ACO, or CSA for power optimization.

III. MATHEMATICAL MODEL for OLED DISPLAY

At static content and simple applications, power model and energy estimation in OLED displays can be presented through pixel level [21] as well as image level as: -

$$P_{pixel}(R, G, B) = f(R) + h(G) + k(B) \quad (1)$$

Where f(R), h(G), k(B) are power consumptions of red, green and blue components of the pixel respectively. The power consumption of an OLED display with n pixels can therefore be represented as:

$$P = C + \sum_{i=1}^{n} \{f(Ri + h(Gi) + k(Bi)\} \quad (2)$$

Where C is a constant that is equal to the power consumption of OLED screen when it is fully black i.e. R, G, B = 0 at constant brightness level.

Further, the brightness can also be included in order to compute overall power consumption of OLED display [22]. The modified power model by reflecting both the sum of RGB values and the brightness level in the original model can be as follows:

$$P = C + Br * \sum_{i=1}^{n} \{\beta R \,.\, Ri + \beta G \,.\, Gi + \beta B \,.\, Bi\} + eRi\ Gi\ Bi \quad (3)$$

Here Br is the brightness level ranging from 0 to 1, f(r), h(G), and k(B) used in previous model [21], are represented by βR , βG, and βB coefficients. Here, e is the power consumption function for red, blue, and green pixel colours.

The above two equations (proposed in [21] and [22] respectively) have not included one of the important parameters, referred as transparency (Alpha value) for OLED display. The transparency factor controls the opacity of OLED display layers. It can vary from full transparent ($\alpha = 255$) to complete opaque ($\alpha = 0$). It is important to note that, when transparency factor is zero, the displayed content becomes completely black. This makes battery consumption minimal and hence the transparency factor should be included as one of the important parameters in battery power optimization of smartphones. We have shown in *Section V (A)* that transparency factor could be an important parameter for power optimization in smartphones.

Therefore, any screen level power model for OLEDs should take all these three parameters – colour intensity, brightness and transparency factor, into consideration. The model presented in [21] does not consider brightness and alpha values, whereas the one presented in [22], does not take in to account alpha. The screen level power consumption model for OLED can be proposed as below.

$$P = C + \alpha * Br \{ \sum_{i=1}^{n} \{fr(Iri) + fg(Igi) + fb(Ibi)\} \quad (4)$$

Where C is constant, α is the screen transparency (Alpha) value. I_{ri} is the intensity of Red colour in pixel, $I_{gi\ is}$ the intensity of Green colour in pixel, and I_{bi} is the intensity of Blue colour in pixel. The transparency parameter of the screen serves as an important tool in changing power consumed by the OLED display of a smartphone without have much impact on the fidelity of the contents displayed on the screen.

IV. NATURE INSPIRED POWER OPTIMIZATION SYSTEM

A. The Proposed NIPO System

The proposed NIPO system aims to optimize power consumption in smartphones in such a way so that the smartphone battery lasts for a given period of time. The NIPO system is generic in nature in the sense that it can be applied to any smart device or any subsystem of the device for power optimization. It can be noted that, the power consumed by the device is dependent upon various parameters. This power function can be used as a cost function for nature inspired algorithms that need to be optimized. It has client-server based system architecture. Some of its components are resident on server whereas some are on the device.

The main components of the proposed system on the device side are – 1.) User Interface module, 2.) Battery Monitoring module, 3.) Power State Monitoring module, 4.) Time Monitoring module, and 5.) Server Interface module. On the server side, the two main

components of the system are – 1.) Device Interface module and 2.) Power Optimization Engine. The figure 2 depicts the proposed NIPO system.

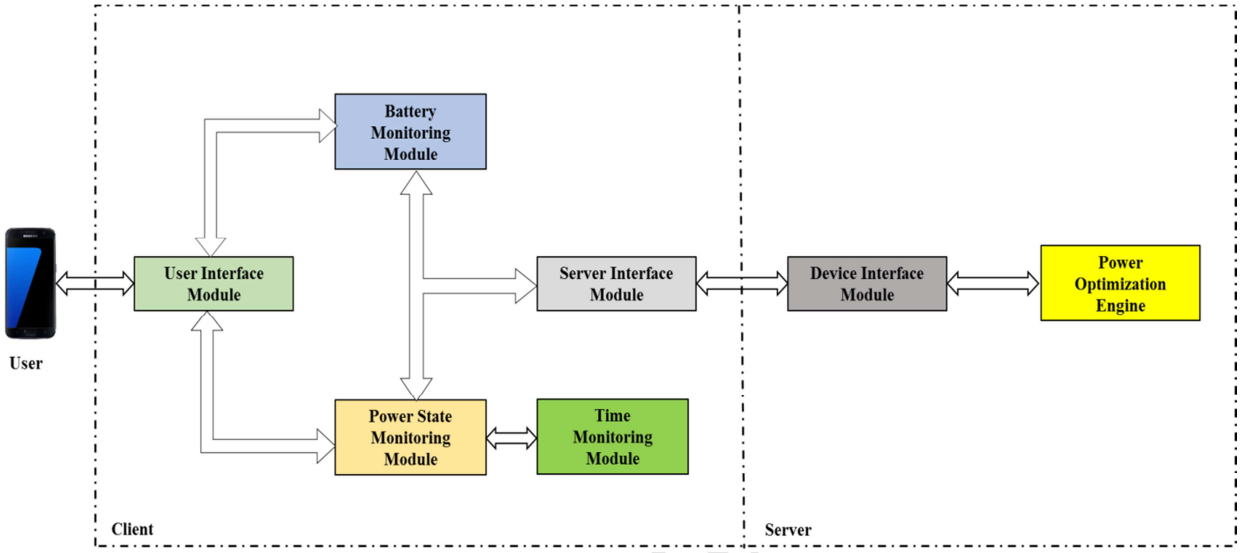


Fig 2: Nature Inspired Power Optimization System Block Diagram

The purpose of User Interface module is to interact with the user of the smartphone. It takes duration (in terms of number of hours) as input from the user. This duration refers to the period up to which user wants the battery of his smartphone to last. UI module also helps user to set the battery level water mark in terms of percentage of total battery capacity. Once this water mark is crossed, NIPO system is triggered automatically. UI module displays the decision of system i.e. whether battery can last up to asked-for duration. UI module also helps user in enabling/disabling NIPO system. This module is resident on the device.

The Battery Monitoring module keeps track of battery discharge level of the device. It keeps track of NIPO system trigger water mark. As soon as this water mark is crossed, it indicates to Power State Monitoring module to check whether power optimization should be started. It also periodically sends battery discharge level information to Power State Monitoring module. It resides on the device.

The Power State Monitoring (PSM) module takes battery level as input from Battery Monitoring module. This information along with display parameters such as brightness, color intensity, transparency etc. is sent to server via server interface module. It also updates the display setting parameters such as brightness and intensity based on the optimization decisions done by the power optimization engine. This module interacts with Time Monitoring module to get the trigger at every 30 minutes. This enables PSM module to periodically fetch battery discharge information.

The purpose of Time Monitoring (TM) module is to keep track of time. It gives triggers to PSM module at every half an hour which is used to constantly optimize power consumption as needed. This module stays on the device. The Server Interface (SI) module on the device handles the full duplex communication between device and the server. It maintains a connection with the server. Device power status is sent to server via SI module. The optimized power parameters are received by SI module from server.

The purpose of Device Interface (DI) module is to handle the communication between device and the server from the server perspective. It maintains a connection with the device. It receives various device related information from the device. The optimized power parameters are sent by DI module to the device. It is resident on the server. The Power Optimization Engine (POE) is the heart of NIPO system. It resides on the server. It makes use of nature inspired algorithms to optimize power. In this work, we have used nature inspired algorithms such as ACO, PSO and CSA to compute optimum power consumption level by modifying display parameters such as color intensity, brightness level or transparency level (Detailed in Section III). These optimized parameters are sent to PSM module on the device to control battery power. The experimental results are given in Section V.

B. Ant Colony Optimization

Ant colony optimization (ACO), first introduced by Marco Dorigo, is a class of optimization algorithms applicable to the problems seeking optimal paths [23]. The ACO algorithm relies on the pheromone-based probabilities to search for the optimal paths [23]. While searching, the moving ants (probable solutions) deposit some pheromone which evaporates over a trail period on the chosen paths. Any ant encountering a previous trail decides to follow a path having a high concentration of pheromone meaning thereby many ants had already tread that path. As a result, the collective behavior emerging from several trails is a kind of positive feedback for the selection of an optimal path. The pheromone evaporation prevents the premature convergence as no single ant can ever dictate a path; and the selected path is a collective judgment.

The population in ACO is initialized in the D-dimensional space. An ant can be represented as Xmd = (*xm*1, *xm*2… *xm*D), where the first subscript m represents a m^{th} solution, and *D* denotes the dimension (X is a vector). In the proposed framework, each ant has *five* dimensions. The first dimension is screen transparency value (α), the next three values are pixel intensities of color, i.e. I_{ri} for Red colour, I_{gi} for Green colour, and I_{bi} for Blue colour {Eq (4)}. The fifth dimension is screen brightness (*Br*) as given in Eq (3). An ant thus represents a parameter vector as follows:

$$\text{Xmd} = \{ \alpha, I_{ri}, I_{gi}, I_{bi}, Br\}, \qquad (5)$$

The ants are initialized as in Eq. (5). Initially, each ant deposits an equal amount of pheromone level. Now, the objective function G can be computed using Eq. (4) is given below:

$$\text{G} = \text{Min}\,[\text{C} + \alpha * Br\,\{\sum_{i=1}^{n}\{fr(Iri) + fg(Igi) + fb(Ibi)\}\,] \qquad (6)$$

The objective function G is evaluated for each ant. The updated pheromone level τ_i^{t+1} at $(t+1)^{th}$ iteration where i denotes the i^{th} ant is given by

$$\tau_i^{t+1} = \rho \times \tau_i^i + \frac{Q}{G}, \text{ if } i^{th} \text{ ant minimizing the G}$$

$$\tau_i^{t+1} = \rho \times \tau_i^i, \text{ Otherwise} \quad (7)$$

If any of the ants (newly computed solutions) participates in the minimization of the objective function (G), the value of the pheromone level increases by Q/G; where Q is a constant chosen by trial and error in the range [0.005, 0.01]. A value of 0.01 is found to be appropriate here. Along with the update of the pheromone levels, the probability of the i^{th} ant is computed for the next iterations as:

$$\text{Pi} = \frac{\tau_i^{(t)}}{\sum_{k=1}^{D} \tau_k^{(t)}} \quad (8)$$

The probability of selecting ants which minimizes G gets better than that of other ants in Eq. (8) in the next iteration where the pheromone levels are comparatively less. One important parameter of ACO is the evaporation factor (ρ) in Eq. (7) that influences the probability in Eq. (8). The ACO suffers from the problem of saturation of the pheromone level for small values of ρ (close to 0) forcing the ants getting stuck on a particular path. On the other hand, if ρ is close to 1, every path will have equal probability with no scope for optimization. To overcome this, ρ is set to 1 initially and subsequently decreased in steps of 0.005. This

strategy not only prevents the ants from being dragged on any non-optimal path but also allows them to navigate to an optimal path.

C. Particle Swarm Optimization

Particle swarm optimization (PSO) [24] algorithm is a computational technique which tends to optimize the solution of a problem iteratively, in turn improving a possible solution with each iteration. The solution space is searched with the speed of participating particles. As the iterations progress, only the particle with best fitness value is allowed to transmit parameters to the other particles. Therefore, the collective behavior tends to move the swarm toward the optimum solution.

In PSO each particle has some velocity according to which it moves in the multi-dimensional solution space and it also has memory to keep information of its previous visited space; hence its movement is influenced by two factors: the local best solution due to itself and the global best solution due to all particles participating in the solution space. The particle's motion is affected by its own best position denoted by Pos_{id} and the global best position denoted by Pos_{gd}. The velocity of a particle at *k*th iteration is updated by:

$$V_{id}^{k+1} = \omega V_{id}^{k} + r_1\alpha\left(Pos_{id} - X_{id}^{k}\right) + r_2\beta\left(Pos_{gd} - X_{id}^{k}\right) \tag{9}$$

The corresponding position of the particle is updated by:

$$X_{id}^{k+1} = X_{id}^{k} + V_{id}^{k+1} \tag{10}$$

where i = 1,2,3….*M*; *M* being the number of swarms and d=1,2, 3…. *N* is the dimension of a swarm; and are the positive constants, called cognitive parameter and social parameter respectively. In PSO, the parameters used are: inertia weight (W) = 1.2, the social (ψ_1) and

the cognitive (ψ_2) parameters are 1.2 and 0.9 respectively. The particle and velocity update for PSO is given in Eq (*9*) and Eq (*10*) respectively.

The number of swarms is 15 whose initialization is the same as that of ants (See Section *IV-B*).

D. Cuckoo Search Algorithm via Levy Flight

Cuckoo search is a relatively recent inclusion in the family of nature inspired algorithms. It was first proposed by Yang and Deb [25] [26] who studied the breeding behaviour of cuckoos laying eggs in the nest of other host bird, commonly referred as brood parasitism [27]. They further combined it with Levy Flight behaviour of some birds which is a mathematically designed model [28].

In recent literature, some researchers have shown that, the cuckoo search algorithms (CSA) can outperform some of nature inspired parameter estimation methods such as genetic algorithm (GA) and PSO [25] [26] [29] [30]. The work in [26] has shown that, CSA can outperform GA and PSO in finding global optima. Wang et al. [30] has pointed out that, GA and PSO algorithms may be trapped into local best solution which may affects the quality of the solution. They have further shown that, the improved CSA can outperform both the GA and PSO algorithms. In this work, we utilize the CSA proposed by Yang and Deb [26][12]. The CSA algorithm utilized in this work is given below:

The CSA algorithm [26] starts with three main assumptions: 1.) one cuckoo can lay one egg at a time and can randomly choose one nest to dump the egg. 2.) Only the best nests with high quality solution will be carried out to the next generation. 3.) The number of host nest is fixed and the probability of a host bird discovers the cuckoo's egg in her nest can be

[12] MATLAB code available at: https://in.mathworks.com/matlabcentral/fileexchange/29809-cuckoo-search--cs--algorithm

assumed as $p_\alpha \in [0,1]$. Once a host bird recognizes the cuckoo's egg, she can either throw it out or abandon the nest and go for next nest. For the sake of convenience, it is assumed that the host bird will abandon that particular nest and go for entirely new nest with a fraction of p_α of the *n* nests. In this work, the solution space is five dimensional: first dimension is brightness, second to fourth dimensions represent RGB colours, fifth dimension is transparency (as detailed in Section III). The cuckoo egg in a nest represents the current solution and the aim is to check if the newly chosen solution can be a better solution and replace the eggs (earlier solution) in the nest. Let a new solution $S^{(t+1)}$ at iteration *t* be generated for a cuckoo *i* chosen randomly with Levy flight walk as:

$$S_i^{t+1} = S_i^t + \alpha \oplus \text{Levy}(\lambda) \quad (11)$$

Here α>0 is known as step size and is related to scales of the problem of interests and the symbol $\oplus$ represents entry-wise multiplications [26]. The use of Levy flight is advantageous in exploring new solutions and is drown through Levy distribution as:

$$\text{Levy} \sim u = t^{-\lambda}, (1< \lambda \leq 3) \quad (12)$$

One of the advantage of CSA is that it needs to adjust only one parameter: p_α. We empirically choose *n* = 15, α = 1, and p_α = 0.25.

E. The NIPO Algorithm

The final NIPO algorithm is given below:

i. Step 1: Take NIPO system trigger battery level watermark and time-to-last duration of the battery as input from the user. If user disables the optimization or device is connected to charger, exit.

ii. Step 2: Compare current battery level with the trigger level. If battery level is less than trigger level, go to next step else go to Step 1.

iii. Step 3: Read current brightness, transparency, colour intensity values and send these values along with battery level, trigger level to power optimization Engine on the server.

iv. Step 4: Power Optimization Engine calculates the current consumption value using nature inspired algorithms (ACO, PSO, CSA) so that battery could last up to time-to-last duration provided by the user.

v. Step 5: If solution is possible in Step 4, the optimized parameters are sent to Power State Monitoring module on the device. PSM module applies these parameters by making suitable changes in display settings.

vi. Step 6: If solution is not possible in Step 4, inform user that device battery can't last up to time-to-last duration with current charge level of battery.

vii. Go to Step 1.

Refer to figure 3 for the flow chart depicting the flow of algorithm.

In this work, we considered different battery levels and computed optimal parameters in order to maintain time-to-last battery hours. We put a threshold of 50% battery level for the proposed NIPO system to be triggered. As the battery level decreases from 50% to 5%, the PSO/ACO/CSA choose different optimized values of parameters (Brightness, Transparency, and R, G, B values) in order to meet the desired time-to-last battery life. The time-to-last battery life denotes the duration for which the battery power is required to sustain without charging. In this work, we chose a variation in time-to-last from 8 hours to 20 hours in order to test robustness of the proposed work. In this work, maintaining the desired battery level can be considered as constraint while achieving the time-to-last battery life can be considered as objective function for ACO/PSO/CSA.

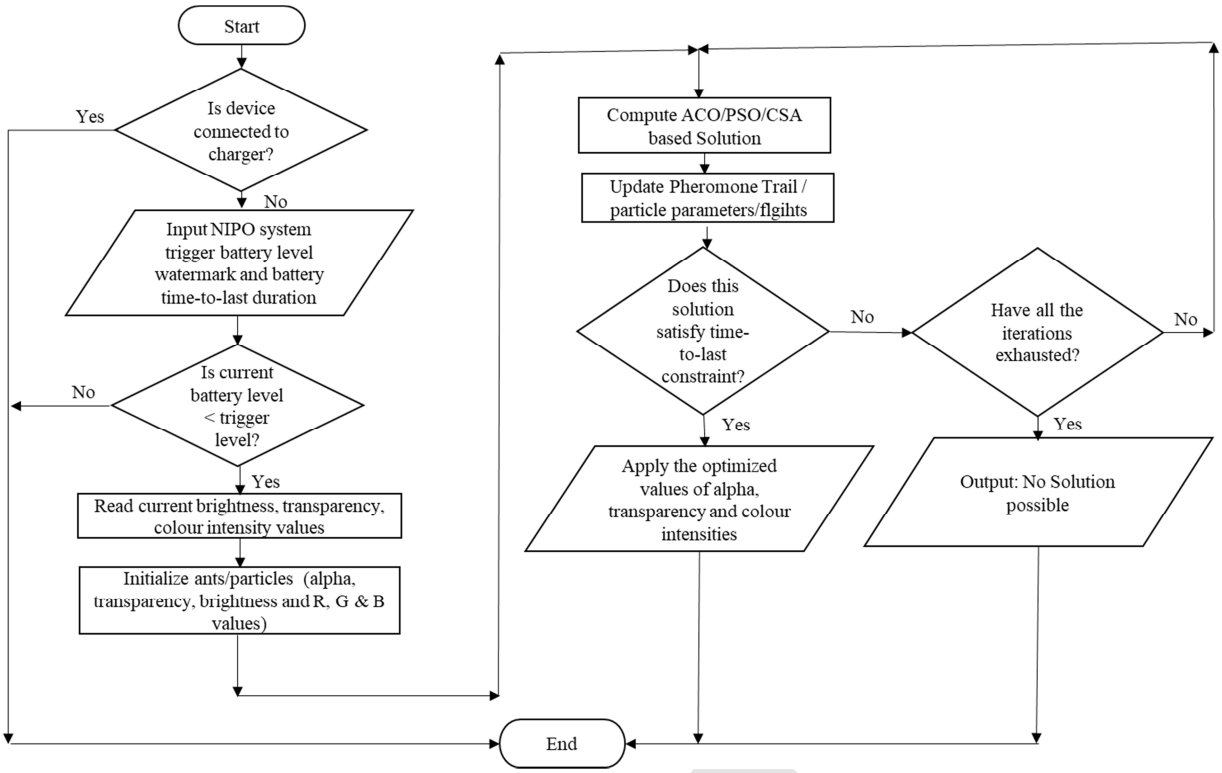


Fig 3: Nature Inspired Power Optimization Algorithm Flow Chart

V. EXPERIMENTAL SETUP & RESULTS

The experimental results provided in two sections. In first section, we provide experiments on proposed mathematical model for model optimization. In next section, we summarize results conducted on battery optimization using ACO, PSO and CSA.

A. Results on Proposed Power Model

Power consumption aspects of OLED display on mobile device were tested using Samsung Galaxy Note 3[13] device. The test set up is shown in figure 4. Below components were used in our experimental set up.

Device *under test (DUT):* A Samsung Galaxy Note 3 running Google Android 4.3 (Jelly Bean Plus) software. The Specifications of the device are given in Table 1. Power Monitor

[13] Samsung Galaxy Note 3. Specs available at: http://www.samsung.com/levant/consumer/mobile-devices/smartphones/galaxy-note/SM-N9000ZKEXSG/

(FTA22D) from M/S Monsoon Solution Inc. MS Windows Laptop connected with power monitor running Power Tool software



Fig 4: Test Setup

Table 1: DUT Specifications

Chipset (CPU)	OCTA 1.9GHz Quad + 1.3GHz Quad
Memory	3 GB RAM & 32 GB Internal Storage
Display	FHD (1920 x 1080), sAMOLED, 14.4cms
Camera Rear	13MP
Sensors	Gyro, Ambient light sensor, Accelerometer, Proximity Barometer etc.
Battery	3,200mAh
Location	AGPS
Wireless Connectivity	2G/3G,HSPA+, Wi-Fi, BT, NFC
OS	Android 4.3 (Jelly Bean Plus)

Test Methodology

We adapted Galaxy Note 3 settings so that we could get power consumption readings as accurately as possible.

- The device was put in Flight mode so that there is no radio communication related power consumption.
- All but one CPU cores were put to sleep.
- All background services and processes were stopped.
- DUT was supplied constant voltage (3.8V) at VBAT pin directly connected to power monitor.

We measured the power for various scenarios. We developed an Android application which takes R, G, B, Alpha and brightness values as input and changes display parameters accordingly. We measured current consumption values for RGB values set to zero i.e. fully back screen with constant brightness. After that we took multiple readings of power consumption for R, G and B at all intensity levels (0 to 255) with constant brightness. We studied power consumption behaviour of DUT for various Alpha values (0 to 255) for each colour (R, G, and B) at constant brightness level. We also studied power consumption behaviour of DUT for various brightness levels, varying from 0 to 1.

Power Consumption in OLED Displays

The figures 5, 6 and 7 below represent various current consumption relationships with colour intensity, brightness and Alpha values.

ACCEPTED MANUSCRIPT

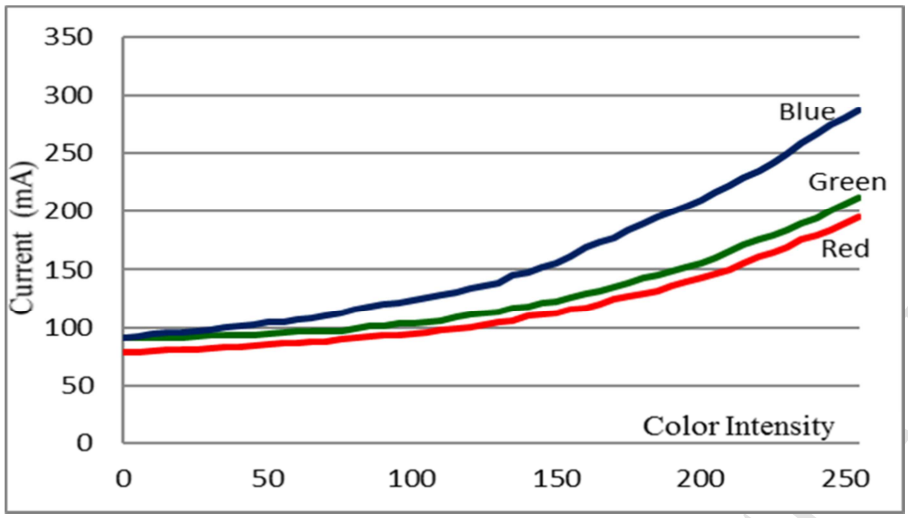


Fig 5: Colour Intensity Vs Current consumption

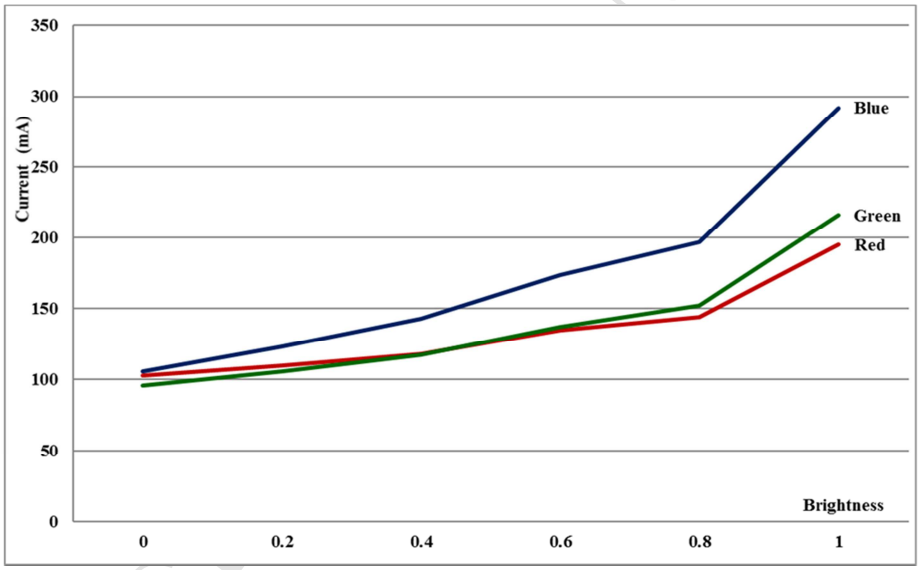


Fig 6: Brightness vs Current consumption

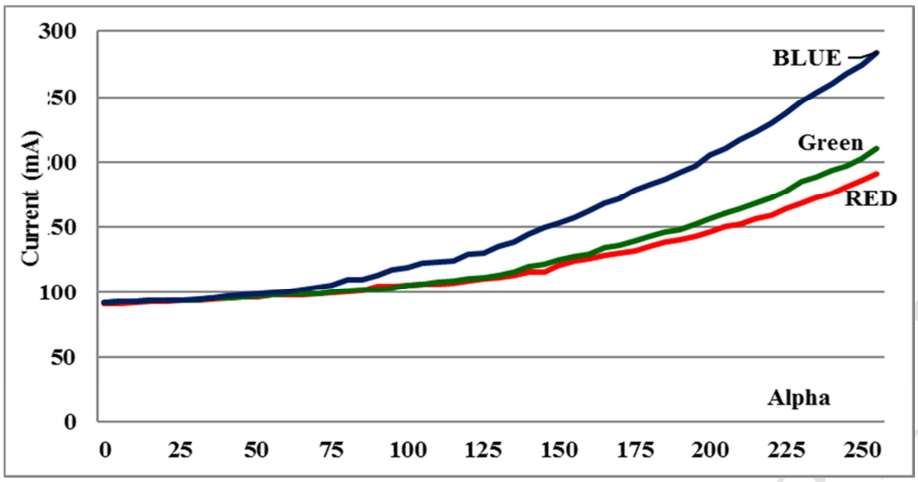


Fig 7: Alpha vs Current consumption

The results from above experiments can be summarised as follows: -

1. Power consumption is minimum for Red colour and maximum for Blue colour for a given brightness and alpha.
2. Power consumption does not increase linearly with colour intensity / alpha.
3. Power consumption does not have linear relationship with Brightness for a particular colour.
4. Power consumption shoots up if brightness is increased beyond 80%.
5. Significant power consumption could be saved by suitably adjusting Alpha value, brightness as well as R, G, B colour values.
6. In smartphones, which have OLED display, transparency parameter can be used to control power consumed by the display.

B. Results on NIPO Systems

Camera Setup

For experimental purpose, we focused on power consumed by OLED display in Samsung Galaxy Note 3 device running Android OS. The relationship between various display related parameters such as R, G, B, brightness and transparency that was established in the previous

section, is utilized to find optimum value of these parameters to reach to a given power consumption level of display. Here we use Ant Colony Optimisation (ACO), Particle Swarm Optimization (PSO) and Cuckoo Search Algorithm (CSA) for determining optimum value of parameters.

For test purpose, static content was displayed on the device screen. The screen was divided in to three sections with R, G and B colours respectively. Initially, colour intensities of all three colours, brightness and transparency values were kept at maximum value. NIPO system trigger level water mark was set at 50% of battery level. As soon as battery level is less than 50%, NIPO system is triggered. From 50% battery level to 25% battery level, ACO, PSO and CSA algorithms in Power Optimization engine make use of transparency and brightness parameters for power optimization. When battery level goes below 25% but remains above 5%, colour intensity of the pixels is also adjusted to control the consumed power. As soon as battery level reaches below 5%, all colours are changed to grey scale to optimize power. This is shown in table 2 below.

Table 2: Display Parameters for Optimization

Current Battery Level	**Parameters (Particles)**
> 50 %	No change
25 - 50 %	Transparency and Brightness
5 - 25 %	R, G, B, Transparency and Brightness
< 5%	Change colours to Grey Scale, with minimum brightness and minimum transparency

Test results

In the experiment, NIPO system trigger level battery water mark was set at 50% of battery level. As soon as battery level reaches less than 50%, NIPO system is triggered. In the first experiment, time-to-last duration for battery was set at 8 hours and test was repeated with different battery levels – 50%, 40%, 30% and 20%. Both ACO as well as PSO optimization algorithms were able to optimize parameters as per table 2 above and NIPO system was able to meet user defined time-to-last battery requirement without the need for charging the system. Figure 8 below shows the test results.

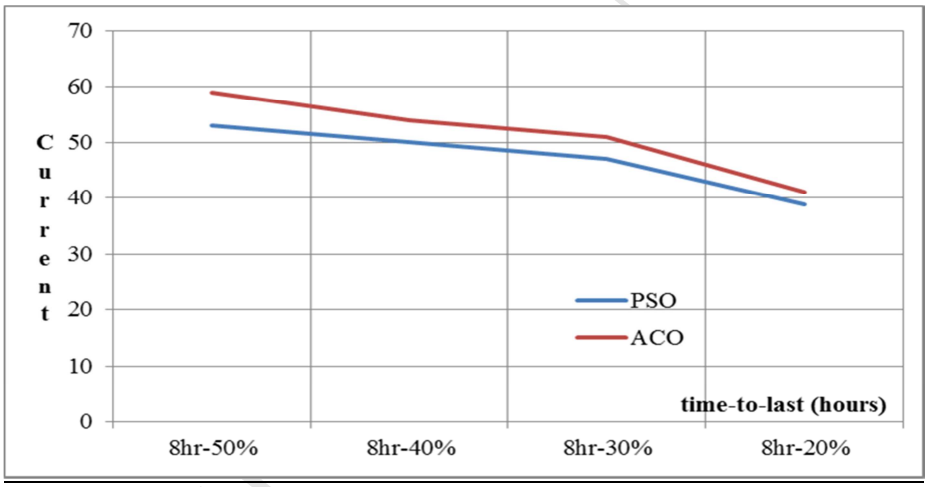


Fig 8: ACO vs PSO Power Consumption (time-to-last: 8 hours)

In the second experiment, time-to-last duration for battery was increased to 12 hours, therefore requiring more optimization. The test was repeated with different battery levels – 50%, 40%, 30% and 20%. For this requirement also, NIPO system was able to meet user defined time-to-last battery requirement without the need for charging the system. Figure 9 below shows the test results.

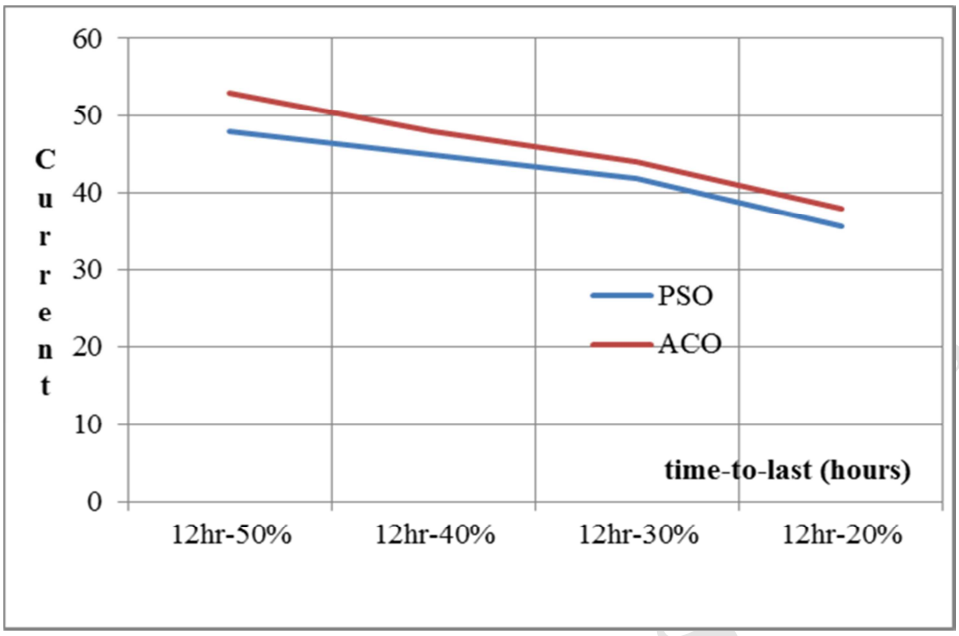


Fig 9: NIPO System Power Consumption (time-to-last: 12 hours)

Comprehensive test results are given in Table 3 below. For test results explanation, let's consider serial number 4. For this test iteration, initial battery level is 40% and time-to-last requirement for battery are 8, 12, 16 and 20 hours. ACO and PSO algorithms consider values of transparency and brightness as optimizing parameters. As we can see, NIPO system is able to optimize current consumption successfully for 8 hours and 12 hours' time-to-last requirements. It can be observed that, when time-to-last requirement is 8 hours, the PSO chose the values of T and B as 0.9 and 151 respectively (For ACO T=0.82 and B=156). However, when time-to-last requirement changes to 12 hours, these values change to 0.85 and 77 respectively (for ACO 0.75 and 87 respectively). However, there is no solution possible for 16 and 20 hours of time-to-last requirements. The observations in Table 3 confirm the optimal selection of parameters in order to satisfy the constraint time-to-last battery life. Thus, from the test results we can see that NIPO system is able to successfully optimize power consumption in such a way that time-to-last requirement of the battery is met.

Table 3: NIPO Composite Test Results

Sr. No.	Start Battery Level (%)	Time-to-last	Parameters (Ants / Particles)	PSO Optimized Value	ACO Optimized Value
1	90	-	None	Same as before	Same as before
2	51		None	Same as before	Same as before
3	50	8 hrs	Brightness (B) and Transparency (T)	T : 0.9 ; B : 151	T : 0.82 ; B : 156
		12 hrs		T : 0.85 ; B : 77	T : 0.75 ; B : 87
		16 hrs		T : 0.8 ; B : 35	T : 0.9 ; B : 41
		20 hrs		Solution not possible	Solution not possible
4	40	8 hrs	Brightness (B) and Transparency (T)	T : 0.7 ; B : 108	T : 0.67 ; B : 118
		12 hrs		T : 0.68 ; B : 48	T : 0.60 ; B : 58
		16 hrs		Solution not possible	Solution not possible
		20 hrs		Solution not possible	Solution not possible
5	30	8 hrs	Brightness (B) and Transparency (T)	T : 0.6 ; B : 62	T : 0.69 ; B : 72
		10 hrs		T : 0.4 ; B : 34	T : 0.48 ; B : 39
		16 hrs		Solution not possible	Solution not possible
6	20	6 hrs	Brightness (B) and Transparency (T), R, G, B	R:84 , G:68 ,B:98 , T : 0.6 ; B : 52	R:89 , G:78 ,B:88 , T : 0.54 ; B : 59
		8 hrs		R:61 , G:46 ,B:69 , T : 0.51 ; B : 44	R:71 , G:56 ,B:59 , T : 0.41 ; B : 54
		16 hrs		Solution not possible	Solution not possible
7	5	-	Change to Grey Scale	-	-

It can be noted that, the proposed algorithm provides power optimization in the terms of five variables (transparency, brightness, and colour intensities for R, G, and B pixels). However, these five variables will be considered for optimization as per battery power level. In Table 3, it can be seen that, till the battery power level 30% only transparency and brightness are optimized. However, when the power level decreases from 30% the R, G, B intensities are also considered for optimization. This approach can save unnecessary change in colour fidelity of device. The colour intensity values are optimized when extremely needed (battery power less than 30%).

In the third set of experiments, the proposed NIPO algorithm is evaluated by using CSA algorithm (Detailed in Section *IV*-D). Similar to first and second sets of experiments, we

tested the CSA algorithm by setting battery time to last requirement as 8 hours and 12 hours. With time to last requirement of 8 hours, test is repeated with different battery levels – 50%, 40%, 30% and 20%. The CSA algorithm is able to optimize parameters and the system is able to meet user defined time-to-last battery requirement without the need for charging the system. The optimization by CSA algorithm in comparison to ACO and PSO is shown in Fig. 10. It can be observed that both ACO and CSA algorithms are able to operate on similar trend to optimize the battery power. However, the PSO of performance can be considered as a bit inferior to both ACO and CSA. This may be due to the PSO getting stuck in local minima and not able to select the truly optimized display parameters.

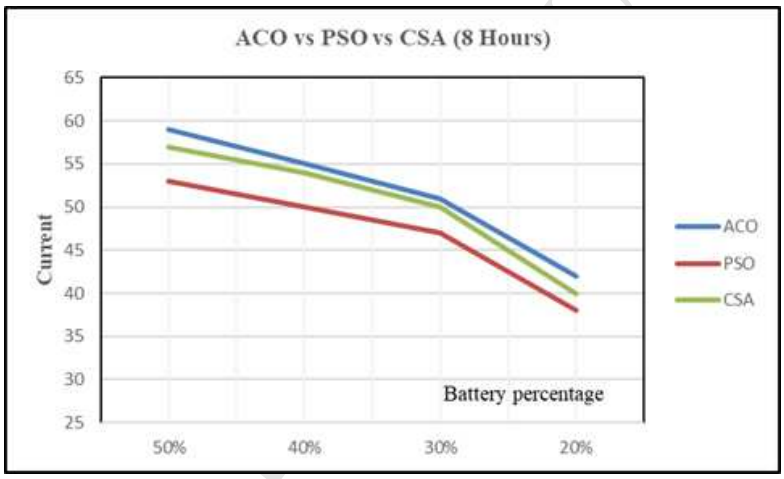


Fig 10: NIPO System Power Consumption (time-to-last: 8 hours)

For 12 hours of time to last battery requirement with varying battery level from 50% to 20%, similar trend could be observed from Fig 11. All the three algorithms are able to optimize parameters to maintain time to last requirement. The ACO and CSA algorithms operate on similar trends to save power and achieve time to last battery requirement.

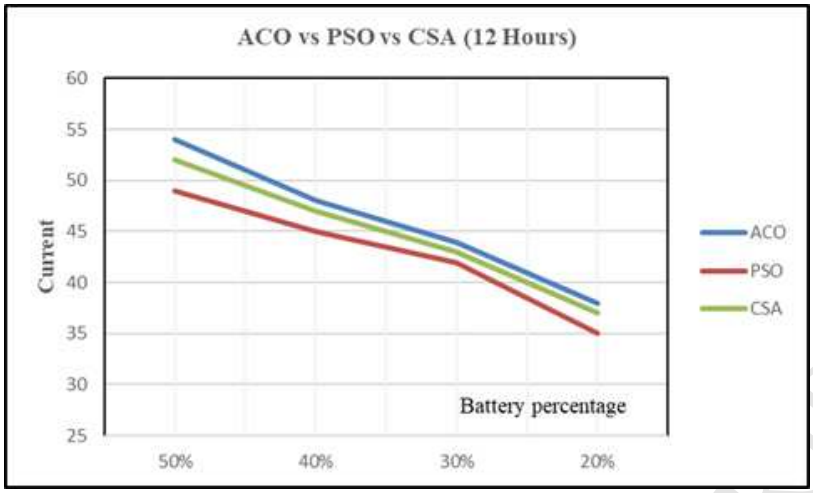


Fig 11: NIPO System Power Consumption (time-to-last: 12 hours)

In this work, the convergence of ACO/PSO is all about satisfying the time-to-last criteria for battery duration. The results from table 3 show that both PSO and ACO achieve the desired optimization, i.e. time-to-last hours of battery life. This automatically proves the convergence of nature inspired algorithms (ACO/PSO/CSA) to the desired results. As evident from Table 3, when battery level reaches at 50% the proposed algorithm is triggered. As the battery level decreases from 50% to 20%, the PSO/ACO/CSA choose different optimized values of parameters (Brightness, Transparency, and R, G, B values) in order to meet the desired battery time-to-last. Further, for some cases (for ex- 16hrs or 20hrs battery life with 40% available battery level) when solution is not possible, the algorithm automatically stops as all the iterations exhaust.

VI. CONCLUSION AND FUTURE WORK

Power optimization is key aspect of smartphones. The technology in fabrication has kept pace with the times following Moore's Law, however, battery technology has lagged behind. Therefore, power optimization plays a key role in giving mobile users satisfaction. In this work, we have two main contributions: 1.) *we proposed transparency factor as one of the important factor that needs to be included in battery power optimization* (Section III). 2.) *A*

new framework using NIPO system (ACO, PSO and CSA) which can optimize the parameters mentioned in the above proposed mathematical model. A new mathematical model is proposed including transparency factor for power consumption in OLED displays. In this work, we considered different battery levels and computed optimal parameters in order to maintain time-to-last battery hours. As observed by table 3, for a battery level say 50% (varying in the range of 50% to 5%) we have different battery requirements, such as: 8 hours, 12 hours, 16 hours, and 20 hours. The task of the system is to choose the optimal parameters (Brightness and Transparency) in order to meet these time-to-last requirements by maintaining the specified battery level. As can be observed from table 3 that till battery power level is above 30%, the battery power is optimized by manipulating the transparency and brightness. So, the addition of brightness in the power optimization variables provides a better power management using ACO/PSO/CSA.

In this work, we have shown power optimization in display subsystem of smartphone. For NIPO system, we have made use of ACO, PSO and CSA. Future work may involve power optimization in other subsystems of smartphone.

REFERENCES

[1] Rahmati A, Qian A, Zhong L, “Understanding human-battery interaction on mobile phones”. *In: Proceedings of the 9th international conference on human computer interaction with mobile devices and services*, ACM, Singapore, Sept 9 – 12, 2007.

[2] Kjærgaard MB, Blunck H, "Unsupervised power profiling for mobile devices", *Mobile and ubiquitous systems: computing, networking, and services*, Berlin, Heidel-berg: Springer; 138–49, 2012.

[3] Datta Soumya Kanti, Bonnet Christian, Nikaein Navid, "Personalized Power Saving Profiles Generation Analyzing Smart Device Usage Patterns", *7th IEEE IFIP Wireless and Mobile Networking Conference (WMNC 2014)*, Vilamoura, Portugal, 20-22 May 2014.

[4] Joon-Myung Kang, Sin-seok Seo and James Won-Ki Hong, "Personalized Battery Lifetime Prediction for Mobile Devices based on Usage Patterns", *Journal of Computing Science and Engineering*, Vol. 5, No. 4, pp. 338-345, December 2011.

[5] Chandra Krintz, Y. Wen, and R. Wolski, "Application-level prediction of battery dissipation," *Proceedings of the International Symposium on Lower Power Electronics and Design*, Newport Beach, CA, pp. 224-229, 2004.

[6] R. Balani, "Energy Consumption Analysis for Bluetooth, Wi-Fi and Cellular Networks", *White Paper*, Tech Republic, December 2007.

[7] G.P. Perrucci, F.H.P. Fitzek and J. Widmer, "Survey on Energy Consumption Entities on the Smartphone Platform," in *73rd IEEE Vehicular Technology Conference (VTC)*, Yokohoma, Japan, 1–5 May 2011.

[8] A. Carroll, "An Analysis of Power Consumption in a Smart-Phone," in *Proc. USENIX Annual Technical Conference*, Boston, MA, USA, 23–25 June 2010.

[9] K. Paul, and T.K. Kundu, "Android on Mobile Devices: An Energy Perspective," in 10th *IEEE International Conference on Computer and Information Technology (CIT)*, Bradford, UK, 29 June – 1 July 2010.

[10] A. Rice and S. Hay, "Decomposing Power Measurements for Mobile Devices," in *IEEE International Conference on Pervasive Computing and Communications*, Manheim, Germany, 29 March – 2 April 2010.

[11] Abolfazli S, Sanaei Z, Ahmed E, Gani A, Buyya R, "Cloud-based augmentation for mobile devices: motivation, taxonomies, and open challenges", *IEEE Commun Surv Tutor2*;16:337–68, 2014.

[12] Cuervo E, Balasubramanian A, Cho D-k, Wolman A, Saroiu S, Chandra R, et al, "MAUI: making smartphones last longer with code offload", *In: Proceedings of the 8th international conference on mobile systems, applications, and services:* ACM, p.49–62, 2010.

[13] D. Shin, Y. Kim, N. Chang and M. Pedram, “Dynamic Voltage Scaling of OLED Displays,” in *Proc. 48th Design Automation Conference (DAC)*, San Diego, USA, 5–9 June 2011.

[14] Xiang Chen, Jian Zeng, Yiran Chen, Wei Zhang, Hai Li, "Fine-grained Dynamic Voltage Scaling on OLED Display", *IEEE*, Pages 807-812, 2012.

[15] Xiang Chen. Jian Zheng, Yiran Chen, Mengying Zhao, Chun Jason Xue, “Quality-retaining OLED Dynamic Voltage Scaling for Video Streaming Application on Mobile Device", *DC 2012 USA* Pages 1000-1005, June 2012.

[16] Qingyu Cui, Chen Jiang, Guangyu Yao, Xiaoli Xu, Wenjiang Liu and Xiaojun Guo "Dynamic Supply Voltage Scaling of Pixel Circuits for Static Power Reduction in AMOLEDs", *SID 2013 Digest*, China, Pages 1040 – 1043, 2013.

[17] Keith S Vallerio, Lin Zhong, Niraj K. Jha, "Energy -Efficient Graphical User Interface Design" Published by *IEEE Transaction on Mobile Computing*, Vol. 5, No.7, Pages 846-859, Published on 16 May 2006.

[18] Mian Dong, Yung-Seok Kevin Choi, Lin Zhong, "Power Modelling of Graphical User Interfaces on OLED Displays", *DAC'09*, USA, Pages 652-657, July 2009.

[19] M. Dong, Y. S. K. Choi, and L. Zhong, “Power-Saving Colour Transformation of Mobile Graphical User Interfaces on OLED-based Displays”, in *Proc. 14th ACM/IEEE International Symposium on Low Power Electronics and Design*, 19–21 August 2009.

[20] M. Dong and L. Zhong, “Chameleon: A Colour-Adaptive Web Browser for Mobile OLED Displays” *Technical Report* 2010-1212.

[21] Mian Dong, Lin Zhong, "Power Modelling and Optimization for OLED Displays", Published by *the IEEE CS, CASS, ComSoc, IES, &SPS*, VOL 11, NO 9, 9/1/2012.

[22] Dongwon Kim, Wonwoo Jung, Hojung Cha, "Run time Power Estimation of Mobile AMOLED Displays", *EDAA* Year 2013.

[23] Dorigo M., G. Di Caro and L. M. Gambardella “Ant Colony System: A Cooperative Learning Approach to the Traveling Salesman Problem” IEEE transactions on evolutionary computation, vol. 1, no. 1, April 1997.

[24] J. Kennedy and R. C. Eberhart, “PSO optimization,” Proc. IEEE Int. Conf. Neural Networks, pp.1941–1948, 1995.

[25] Yang, X.-S., and Deb, S., “Engineering Optimisation by Cuckoo Search”, Int. J. Mathematical Modelling and Numerical Optimisation, Vol. 1, No. 4, 330–343, 2010.

[26] Yang, X. S. and Deb, S., “Cuckoo search via L´evy flights”, Proceedings of World Congress on Nature & Biologically Inspired Computing (NaBIC 2009, India), IEEE Publications, USA, pp. 210-214, 2009.

[27] Reynolds, A. M. and Frye, M. A.,“Free-flight odor tracking in Drosophila is consistent with an optimal intermittent scale-free search”, PLoS One, 2, e354, 2007.

[28] Pavlyukevich, I., ‘L´evy flights, non-local search and simulated annealing’, J. Computational Physics, 226, 1830-1844, 2007.

[29] Md. Akhtaruzzaman Adnan and M. A. Razzaque, “A Comparative Study of Particle Swarm Optimization and Cuckoo Search Techniques Through Problem-Specific Distance Function”, International Conference of Information and Communication Technology (ICoICT), Indonesia, 2013.

[30] Jun Wang, Bihua Zhou, & Shudao Zhou, “An Improved Cuckoo Search Optimization Algorithm for the Problem of Chaotic Systems Parameter Estimation”, Computational Intelligence and Neuroscience, Article No 8, Vol. 2016, 2016.

ACCEPTED MANUSCRIPT

Int. J. Electron. Commun. (AEÜ) 93 (2018) 182–190

Contents lists available at ScienceDirect

Int. J. Electron. Commun. (AEÜ)

journal homepage: www.elsevier.com/locate/aeue

Regular paper

New realization of third order sinusoidal oscillator using single OTRA

Gurumurthy Komanapalli, Neeta Pandey*, Rajeshwari Pandey

Dept. of Electronics and Communication Engg, Delhi Technological University, Delhi, India

A B S T R A C T

In this paper, a new, single operational transresistance amplifier (OTRA) based third order sinusoidal oscillator is presented. The nonideal behavior of proposed structure has been analyzed using single and double pole models of the OTRA. It is observed that for high-frequency applications the effect of nonidealities may be eliminated through self-compensation. Active and passive sensitivities are computed for the proposed structure and are found to be less than unity rendering proposed circuit insensitive to component variations. Workability of the proposed oscillator is verified through Analog Design Environment (ADE) spectre tool provided by cadence virtuoso using 0.18 µm CMOS process parameters. Monte Carlo analysis is also carried for the proposed structure. Total harmonic distortion (THD) is found to be less than 2.6%. Post layout simulations; experimental results are also included to validate the theory.

1. Introduction

Sinusoidal oscillators play a vital role in control, power electronics, instrumentation, measurement, standard test and carrier signals for communications and other electronic systems [1]. It is a well-established fact that for such applications the third-order sinusoidal oscillators (TOSOs) are a better choice [2,3] over second-order oscillators, as they provide better frequency response with low harmonic distortion. A comparative study of existing TOSOs [4–37] has been presented in Table 1. These TOSOs are either single phase [10,22,33,35–37] or quadratureoscillators (QOS) [4–9,11–21,23–32,34]. These existing structures have been designed using op-amp [12,35,36], operational transconductance amplifier (OTA) [10,11], second generation current conveyor (CCII) [5,13,21], current controlled conveyor (CCCII) [15,22,24]. The structures proposed in [18,19,23] use differential voltage current conveyor (DVCC) whereas the design of [4] utilizes differential voltage current conveyor transconductance amplifier (DVCCTA). The current difference transconductance amplifier (CDTA) based TOSOs are available in [14,16] while current controlled current conveyor transconductance amplifier (CCCCTA) based oscillator is presented in [30]. Voltage difference transconductance amplifier (VDTA) and Modified current controlled current follower transconductance amplifier (MCCCFTA) based oscillators are discussed in [8,9,31,32] respectively. The designs proposed in [6,7,17,20,33,34,37] are based on OTRA [38]. Some of the structures are designed using mixed ABBs [25–29] The structure of [25] is designed using OTA and CCCCTA whereas [26] uses OTA and differential difference current conveyor (DDCC). Combination of OTA and current controlled current difference transconductance amplifier (CCCDTA) is reported in [27]. Ref. [28] proposes DDCC and VDTA based TOSO and oscillator presented in [29] is based on CCII and Universal voltage conveyor (UVC).

The comparative table suggests that existing structures

- use excessive ABBs such as two [4–9,31,35,36], three [10,11 (see Fig. 7(b))–21, 33] and four [11 (see Fig. 11),23–25]
- use mix of ABBs [25–29]
- are designed using operational amplifiers (OpAmps) [12,35,36] and have restricted performance at higher frequencies is due to gain bandwidth dependency and slew limitation of opamps [1].
- provide either single (S) [10,22,33,35–37] or quadrature (Q) response [4–9,11–21,23–32,34].
- provide only voltage [6,7,11–13,17,20–23,26,33–37]/current [9,10,14,24,25,28,30–32]/both [4,5,8,15,16,18,19,27,29] outputs.

It may, therefore, be concluded that there is a lean presence of single ABB based TOSO in literature, which led authors to present a single ABB based TOSO structure. It is pertinent to mention here that only [36,37] provides voltage output at low impedance. The proposed topology also provides voltage output at low impedance and uses single OTRA and six passive components namely three resistors three capacitors. However, the component spread in CO is much smaller in the proposed configuration, compared to [37], which is desirable for functional accuracy, performance and IC chip area viewpoint [39].

Having highlighted salient features of the proposed design, it is

* Corresponding author.
E-mail address: n66pandey@rediffmail.com (N. Pandey).

https://doi.org/10.1016/j.aeue.2018.06.005
Received 16 February 2018; Accepted 1 June 2018
1434-8411/ © 2018 Published by Elsevier GmbH.

Table 1
Comparison of TOSOs.

Ref.	No. of ABBs used	No. of R + C Floating (F)/Grounded (G)	Control of FO without affecting CO	Electronic tuning	Output phase	Realization/ supply voltage	THD/sensitivity of FO w.r.t R,C	Hardware implementation	Highest measured frequency	Layout design	O/p Type Voltage (V)/ Current/(I)/ both(B)
[4]	2DVCCTA	Fig. 4a.1(G) + 3(G) Fig. 4b.2(G) + 3(G)	Y	Y	Q	CMOS/ ± 1.25 V	≤2%/–	Y	1.59 MHz	N	B
[5]	2 CCII	3(1F,2G) + 3(G)	Y	N	Q	CMOS/ ± 1.25 V	2.95%/–	N	~950 kHz	N	B
[6]	2 OTRA	4(F) + 3(F)	Y	Y	Q	CMOS/ ± 1.5 V	6.3%/–	N	159 kHz	N	V
[7]	2 OTRA	Fig. 2d.3(F) + 3(F) Fig. 3d.3(F) + 3(F)	Y	N N	Q	CMOS/ ± 1.5 V	1.54%/ ≤ 0.5 –/ ≤ 0.5	Y	29.07 kHz 5.04 kHz	N	V
[8]	2 VDTA	0 + 3(G)	Y	Y	Q	CMOS/ ± 1 V	2.98%/	N	2 MHz	N	B
[9]	2 VDTA	0 + 3(G)	Y	Y	Q	CMOS/ ± 2 V	1.8%/0.5	N	1.10 MHz	N	I
[10]	3 OTA 3 OTA	Fig. 3a.0 + 3(G) Fig. 3b.0 + 3(G)	Y Y	Y	S S	CMOS/ ± 1.85 V	–/ ≤ 0.5	N	500 kHz	N	I
[11]	3 OTA 4 OTA	Fig. 7b.0 + 3(G) Fig. 11.1(G) + 3(G)	Y	Y	Q	CMOS/ ± 3 V	~35 dB/–	Y	3 MHz 4 MHz	N	V
[12]	3OPAMP	Fig. 1.5(F) + 3(F) Fig. 2 .3(F) + 5(F)	Y	N N	Q	LF351/ ± 10 V	–/ ≤ 0.5	Y	~160 kHz	N	V
[13]	3 CCII	Fig. 1. 5(G) + 3(G) Fig. 2.3(G) + 5(G) Fig. 3.5(4G,1F) + 3(G)	Y Y Y	N N N	Q	AD844/ ± 12 V	–/ ≤ 0.5	Y	370.3 kHz 215.5 kHz 4.92 kHz	N	V
[14]	3 CDTA	0 + 3(G)	Y	Y	Q	CMOS/ ± 1.25 V	2.5%/ ≤ 0.5	N	~9kHz	N	I
[15]	3 CCCII	0 + 3(G)	Y	Y	Q	CMOS/ ± 2.5 V	3%/–	Y	34 MHz	N	B
[16]	3 CDTA	0 + 3(G)	Y	Y	Q	CMOS/ ± 1.25 V	10.39%/–	N	~1MHz	N	B
[17]	3 OTRA	Fig. 2.5(F) + 3(F) Fig. 3.5(F) + 3(F)	Y Y	Y Y	Q	CMOS/ ± 1.5 V	0.57%/– 0.7%/–	N	159 kHz 159 kHz	N	V
[18]	3 DVCC	3(G) + 3(G)	Y	Y	Q	CMOS/ ± 1.5 V	1%/0.5	N	796 kHz	N	B
[19]	3 DVCC	3(1F,2G) + 3(G)	Y	N	Q	CMOS/ ± 2.5 V	≤2%/0.5	N	10.62 MHz	N	B
[20]	3 OTRA	5(F) + 3(F)	Y	Y	Q	CMOS/ ± 2.5 V	4.82%/–	N	318.3 kHz	N	V
[21]	3 CFOA	Fig. 3b.4(2G,2F) + 3(G)	Y	N	Q	CMOS/ ± 1.5 V	–/–	N	–	N	V
	3CCII-	Fig. 4.5(G) + 3(G)	Y	N					0.8 MHz		
[22]	4 CCCII	1(G) + 3(G)	Y	Y	S	CMOS/ ± 1.25 V	2.9%/–	N	10 MHz	N	V
[23]	4 DVCC	3(F) + 3(G)	Y	N	Q	CMOS/ ± 2.5 V	1.8%/–	Y	2.5 MHz	N	V
[24]	4 CCCII	0 + 3(G)	Y	Y	Q	NR100N, PR100N	≤1%/–	Y	1.47 MHz	N	I
[25]	1 CCCTA 1 OTA	0 + 3(G)	Y	Y	Q	CMOS/ ± 1.5 V	1.8%/ ≤ 0.5	N	1.22 MHz	N	I
[26]	1 DDCC 1 OTA	1(G) + 3(G)	Y	Y	Q	CMOS/ ± 1.25 V	1.75%/–	N	1.69 MHz	N	V
[27]	1CCCDTA,1OTA	0 + 3(G)	Y	Y	Q	CMOS/ ± 1.5 V	1.8%/0.5	N	1.38 MHz	N	B
[28]	1 DDCC, 1VDTA	1(G) + 3(G)	Y	Y	Q	CMOS/ ± 1.25 V	2.95%/–	N	1 MHz	N	I
[29]	2CCII, 1 UVC	3(G) + 3(G)	Y	N	Q	CMOS/ ± 1.2 V	0.86%/	N	1.439 MHz	N	B
[30]	2 CCCCTA	0 + 3(G)	Y	Y	Q	ALA40/ ± 1.5 V	1.10%/–	Y	489.7 kHz	N	I
[31]	1MCCCFTA	0 + 3(G)	Y	Y	Q	CMOS/ ± 1 V	4.59%/0.5	N	12.15 MHz	N	I
[32]	1MCCFTA	0 + 3(G)	Y	Y	Q	CMOS/ ± 1V	0.85%/0.5	Y	3.25 MHz	N	I
[33]	3 OTRA	6(F) + 3(F)	Y	Y	S	CMOS/ ± 1.5 V	0.631%/–	N	275 kHz	N	V
[34]	2 OTRA	3(F) + 3(F)	Y	Y	Q	CMOS/ ± 1.5 V	1.83%/0.5	Y	18.85 MHz	N	V
[35]	2 OPAMP	3(1G,2F) + 3(1G,2F)	Y	N	S	μA741/15 V	6.3%/–	Y	~160 kHz	N	V
[36]	1 OPAMP	3(1G,2F) + 3(1G,2F)	Y	N	S	–	–/–	N	–	N	V
[37]	1 OTRA	3(F) + 3(1F,2G)	Y	N	S	CMOS/ ± 2.5 V	1.9%at 100 KHz/ ≤ 1	Y	1.08 MHz	N	V
Proposed	1 OTRA	3(F) + 3(2F,1G)	Y	N	S	CMOS/ ± 0.9 V	< 2.6%/ ≤ 1	Y	15.92 MHz	Y	V

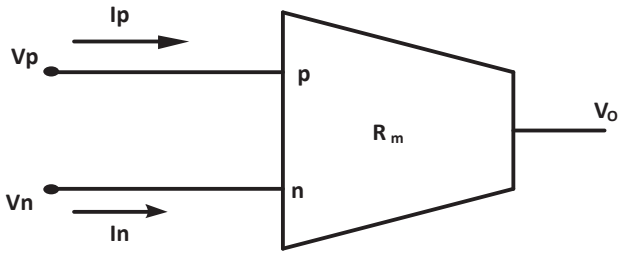


Fig. 1. OTRA circuit symbol.

relevant to mention that our design has few limitations as well such as the use of floating components, component matching requirement and lack of electronic tunability. However, the effect of parasitics introduced due to floating capacitances can be mitigated to some extent using top-quality IC technologies of today. Further, following various layout rules component matching may be achieved to acceptable limits.

The rest of the paper is organized as follows: Section 2 describes the proposed circuit. In Section 3 nonideality analysis is carried out by considering a single and double pole models of OTRA. Sensitivity analysis is discussed in Section 4. Workability of the proposed topology is verified through simulation in Section 5 which is followed by layout design and post-layout simulation results. The experimental results, wherein the circuit is breadboarded using off the shelf ICs AD844, are presented in Section 6. The paper is concluded in Section 7. In Appendix A single ABB TOSO structures based on Current difference buffered amplifier (CDBA) [40]/Current follower- voltage follower (CF-VF) [42]/Extra-X second-generation current conveyor (EXCC-II) [42] are proposed which are similar to the design of this communication.

2. Proposed configuration

The OTRA is a high gain, current input voltage output analog building block [38]. The input terminals of OTRA are internally grounded, thereby eliminating response limitations due to parasitic capacitances and resistances and hence is a suitable choice for high-frequency applications. The circuit symbol of OTRA is shown in Fig. 1, and the port characteristics are given by (1), where R_m is transresistance gain of OTRA

$$\begin{bmatrix} V_p \\ V_n \\ V_o \end{bmatrix} = \begin{bmatrix} 0 & 0 & 0 \\ 0 & 0 & 0 \\ R_m & -R_m & 0 \end{bmatrix} \begin{bmatrix} I_p \\ I_n \\ I_o \end{bmatrix} \tag{1}$$

Ideally, the transresistance gain R_m approaches infinity making two input currents equal. The proposed TOSO is shown in Fig. 2. It uses a single OTRA and six passive components. The characteristic equation for Fig. 2 is obtained by performing routine analysis assuming OTRA to be ideal and is given by

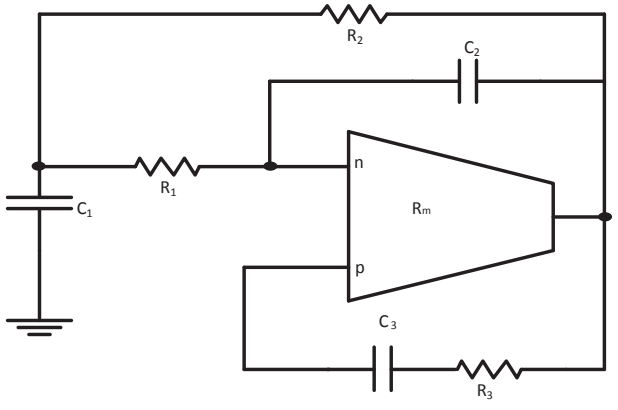


Fig. 2. Proposed TOSO circuit.

$$\begin{aligned} &s^3C_1C_2C_3R_1R_2R_3 \\ &\quad + s^2 \\ &\quad \left[\begin{array}{c} C_1C_2R_1R_2 + C_2C_3R_1R_3 + \\ C_2C_3R_2R_3 - C_1C_3R_1R_2 \end{array} \right] \\ &\quad + s[C_2R_1 + C_2R_2 + C_3R_3 - C_3R_1 - C_3R_2] + 1 = 0 \end{aligned} \tag{2}$$

Assuming $C_1 = C_2 = C_3 = C$, $R_1 = R_2 = R$ characteristic Eq. (2) reduces to

$$s^3C^3R^2R_3 + 2s^2C^2RR_3 + sCR_3 + 1 = 0 \tag{3}$$

Therefore FO and CO are given by

$$\text{FO: } f_o = \frac{1}{2\pi RC} \tag{4a}$$

$$\text{CO: } 2R_3 = R \tag{4b}$$

From above equations, it is clear that FO can be tuned using C without affecting CO. Similarly CO can be adjusted using R_3. In practice, frequency tuning via capacitor variation is difficult. However, the capacitors may be replaced by a capacitor bank formed by parallel connection of a capacitor and a series switch. The value of capacitance may be varied by appropriate switch settings.

3. Nonideal analysis

3.1. Nonideal analysis using one pole model of an OTRA

The performance of the proposed oscillator may deviate from the original results because of the OTRA nonidealities. As already discussed Section 2 because of internally grounded input terminals most of the parasitics affecting the performance of OTRA can be ignored. Ideally, R_m is assumed to approach infinity. However, practically its value is a frequency dependent.

Considering a single pole model, R_m can be expressed as

$$R_m(s) = \left(\frac{R_o}{1 + \frac{s}{\omega_o}} \right) \tag{5}$$

where R_o represents the dc transresistance gain. For high-frequency applications, the $R_m(s)$ reduces to

$$R_m(s) = \frac{1}{sC_p} \quad \text{where} \quad C_p = \frac{1}{R_o\omega_o} \tag{6}$$

Using single pole model for Rm the characteristic equation given in (2) modifies to

$$\begin{aligned} &s^3C_1C_3R_1R_2R_3(C_2 + C_p) + s^2[(C_2 + C_p)(C_3R_3(R_1 + R_2) + C_1R_1R_2) \\ &\quad - C_1C_3R_1R_2] + s[(R_1 + R_2)(C_2 + C_p) - C_3(R_1 + R_2 - R_3)] + 1 = 0 \end{aligned} \tag{7}$$

and the FO and CO change to

$$\text{FO: } f_o = \frac{1}{2\pi}\sqrt{\frac{(R_1 + R_2)(C_2 + C_p) - C_3(R_1 + R_2 - R_3)}{C_1C_3R_1R_2R_3(C_2 + C_p)}} \tag{8}$$

$$\text{CO: } \left[\frac{(R_1 + R_2)(C_2 + C_p) - C_3(R_1 + R_2 - R_3)}{C_1C_3R_1R_2R_3(C_2 + C_p)} \right] = \frac{1}{(C_2 + C_p)(C_3R_3(R_1 + R_2) + C_1R_1R_2) - C_1C_3R_1R_2} \tag{9}$$

The effect of C_p can be eliminated by pre-adjusting the value of capacitor C_2, thus achieving self-compensation. By choosing equal capacitance and resistor values except for R_3 the FO and CO are reduced to (4a), (4b).

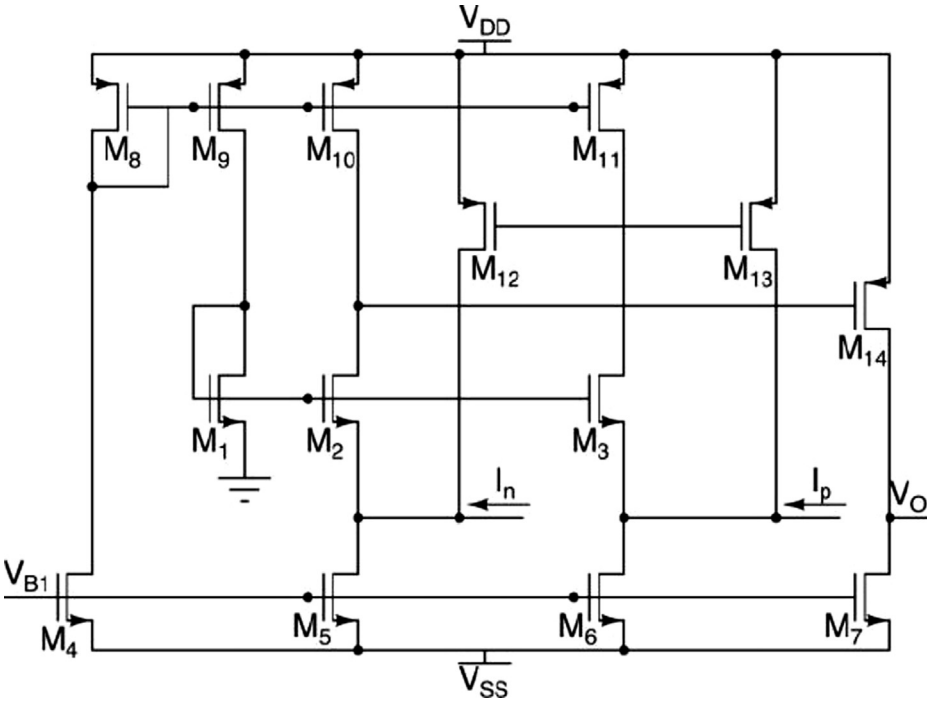


Fig. 3. CMOS OTRA [38].

3.2. Nonideal analysis using two-pole model of an OTRA

Considering a two pole model for OTRA [43] the transresistance gain, can be expressed as

$$R_m(s) = \frac{R_o}{\left(1 + \frac{s}{\omega p_1}\right)\left(1 + \frac{s}{\omega p2}\right)} \tag{10}$$

The above expression for $R_m(s)$ can be written as

$$R_m(s) = \frac{1}{C_p\left(s + \frac{1}{C_pR_o}\right)\left(1 + \frac{s}{\omega_{p_2}}\right)} \tag{11}$$

If the operating frequency is in between the range $\omega_{p_1} << \omega << \omega_{p_2}$, (11) can be approximated as (5). The characteristic Eq. (2) of Fig. 2 by considering (11) is given by

$$X_1s^4 + X_2s^3 + X_3s^2 + X_4s^4 + X_5 = 0 \tag{12}$$

where

$$X_1 = C_1C_2C_3R_1R_2R_3\{(sC_pR_0 + 1) + C_pR_0\omega_{p_2}\} - C_pR_0(C_1C_3R_1R_2 - C_2C_3R_3(R_1 + R_2) - C_1C_2R_1R_2)$$

$$X_2 = C_1C_2C_3R_1R_2R_3\omega_{p2} - (1 + C_p\omega_{p2}R_0)(C_1C_3R_1R_2 - C_2C_3R_3(R_1 + R_2) - C_1C_2R_1R_2) - C_pR_0(C_3(R_1 + R_2) - C_3R_3 - C_2(R_1 + R_2))$$

$$X_3 = C_1C_3R_0R_1R_2R_3\omega_{p2} - (1 + C_p\omega_{p2}R_0)(C_3(R_1 + R_2) - C_3R_3 - C_2(R_1 + R_2)) - \omega_{p2}(C_1C_3R_1R_2 - C_2C_3R_3(R_1 + R_2)) - C_1C_2R_1R_2 + C_pR_0$$

$$X_4 = R_0\omega_{p2}(C_1R_1R_2 + C_3R_3(R_1 + R_2) + R_1 + R_2) + \omega_{p2}(C_3(R_1 + R_2 - C_3R_3 - C_2(R_1 + R_2)) + 1 + C_p\omega_{p2}$$

$$X_5 = \omega_{p2}$$

By choosing frequency much below $\frac{1}{C_pR_o}$, ignoring higher order terms s^5 and equating real and imaginary parts of (12) gives CO and FO as

$$\text{CO:}\frac{X_1X_4}{X_2} + \frac{X_5X_2}{X_4} = X_3; \quad \text{FO: } f_1 = \frac{1}{2\pi}\sqrt{\frac{X_4}{X_2}} \tag{13}$$

$$f_1 = f_o\sqrt{\frac{R_o\omega_{p_2}(R^2C + 2R(1 + CR_3)) - \omega_{p_2}(R_3C - C_p) + 1}{C_pR_o\left(\frac{R_3}{R^2C}\right) + \omega_{p_2}R_3C - (1 + C_p\omega_{p2}R_3R_o)\left(\frac{2R_3}{R}\right)}} \tag{14}$$

The percentage error in the frequency of oscillation can be found using the expression, and the approximate error function is given as

$$\%\text{Error} = \omega_{p_2}R_o(R^2C + 2R(1 + CR_3)) - (R_3C - C_p) + \frac{1}{\omega_{p_2}} - C_pR_o\left(\frac{R_3}{R^2C\omega_{p_2}}\right) - R_3C + \frac{2R_3}{R}\left(\frac{1}{\omega_{p_2}} + C_pR_3R_o\right) \times 100\% \tag{15}$$

Hence it is found that C_p affects the FO and CO. Therefore at high operating frequencies the FO may slightly deviate from the ideal value. The percentage deviation may be determined through simulations.

4. Sensitivity analysis

The sensitivity is a significant performance criterion of any network [1]. The sensitivity of FO (f_o) concerning circuit parameters, say Y is given by

$$S_Y^{f_o} = \frac{\partial f_o}{\partial Y}.\frac{Y}{f_o} \tag{16}$$

Using this definition, the sensitivity of FO(f_o) for the circuit w.r.t R, C are given as

$$|S_C^{f_o}| = |S_R^{f_o}| = 1;\ |S_{R_3}^{f_o}| = 0 \tag{17}$$

From (17), it is observed that all passive sensitivities for Fig. 2 are less than or equal to unity in magnitude. Therefore it ensures that the sensitivity performance is satisfactory. Sensitivities of the proposed structure by considering nonidealities (8) and component setting of $C_1 = C_2 = C_3 = C$, $R_1 = R_2 = R$ are given by

Table 2
Aspect ratios of transistors.

Transistor	W (μm)/L(μm)
M1–M3	36/0.9
M4	3.6/0.9
M5, M6	10.8/0.9
M7	3.6/0.9
M8-M11	18/0.9
M12, M13	36/0.9
M14	18/0.18

$$|S_R^{f_o}| = \frac{RC_p + R_3C}{2RC_p + R_3C};\ |S_{R_3}^{f_o}| = \frac{R_3C + 4RC_p}{4RC_p + 2R_3C};\ |S_C^{f_o}|$$
$$= \frac{R_3C(C + C_p) - (2RC_p + R_3C)(3C + 2C_p)}{2(2RC_p + R_3C)(C + C_p)};\ |S_{Cp}^{f_o}|$$
$$= \frac{RC_p(C + C_p) - (2RC_p + R_3C)C_p}{(2RC_p + R_3C)(C + C_p)} \quad (18)$$

It is found that with $C_p \to 0$ the above active and passive sensitivities reduces to $|S_C^{f_o}| = 1$, $|S_{R_3}^{f_o}| \to {}^1/_2$, $|S_R^{f_o}| \to 1$, $|S_{C_p}^{f_o}| \to 0$ likewise, even for $C_p = 5.03$ fF all the sensitivity coefficients are observed to be small.

5. Simulation results and layout design

The proposed circuit is verified through simulations using Cadence Virtuoso analog design Environment (ADE) tool at 0.18 μm CMOS technology. The OTRA schematic [38] is used for proposed TOSO realization is shown in Fig. 3. The voltages V_{DD}, V_{SS}, and V_B taken are +0.9 V, −0.9 V and −0.3 V respectively. The transistor aspect ratios used are shown in Table 2.

The OTRA of Fig. 3 [38] is simulated, and the post layout DC open loop transresistance gain (Ro) for OTRA is obtained as 157 dB Ω. The gain-bandwidth product, parasitic capacitance, and power dissipation are obtained as 440 GHz Ω, 5.03 fF, and 226.26 μW respectively. As a next step the proposed oscillator was simulated and the simulated FO for the component values $C_1 = C_2 = C_3 = C = 1.8$ pF and $R_1 = R_2 = 10$ kΩ, $R_3 = 5$ kΩ was observed to be 8.82 MHz against the calculated value of 8.84 MHz. The corresponding output waveform, FFT spectrum are shown in Fig. 4(a) and (b) respectively. It may be noted that the simulated and theoretical values of FO are in close agreement.

The robustness of the proposed circuit is examined by carrying out Monte Carlo simulations by considering the result of ten samples for 3% variations in R_3. Fig. 5(a) and (b) shows that although CO is altered slightly by modifying R_3, the circuit is well operated. Fig. 5(b) shows the histogram in which the value of FO remain close to its standard value 8.84 MHz. The FO variation w.r.t R and C are shown in Fig. 6(a) and (b) respectively. In Fig. 6(a) capacitor value is fixed at 100 pF and R is varied from 0.5 kΩ to 25 kΩ. For Fig. 6(b) resister values are set at 10 kΩ and capacitor is varied from 1 pF to 10 nF. The highest frequency measured is 15.92 MHz, and lowest frequency is 1.59 kHz.

The %THD variation with respect to R and C are shown in Fig. 7(a) and (b) respectively. The highest %THD obtained as 2.6. The proposed TOSO is also laid out and verified through post-layout simulations. The typical values of the passive components as $R_1 = R_2 = 10$ kΩ, $R_3 = 5$ kΩ, and $C_1 = C_2 = C_3 = C = 1.8$ pF are considered. The resultant theoretical FO is found to be 8.84 MHz. The complete layout of proposed TOSO is shown in Fig. 8.

The physical verification checks such as DRC (Design Rule Check), LVS (Layout vs. Schematic check), RC parasitic extraction and post-layout simulation results authenticate the layout implemented. The total active die area occupied by the oscillator is 3085.7959 μm^2 (51.37 μm × 60.07 μm). The post-layout simulated waveform and FFT response are shown in Fig. 9(a) and (b) respectively. The simulated FO

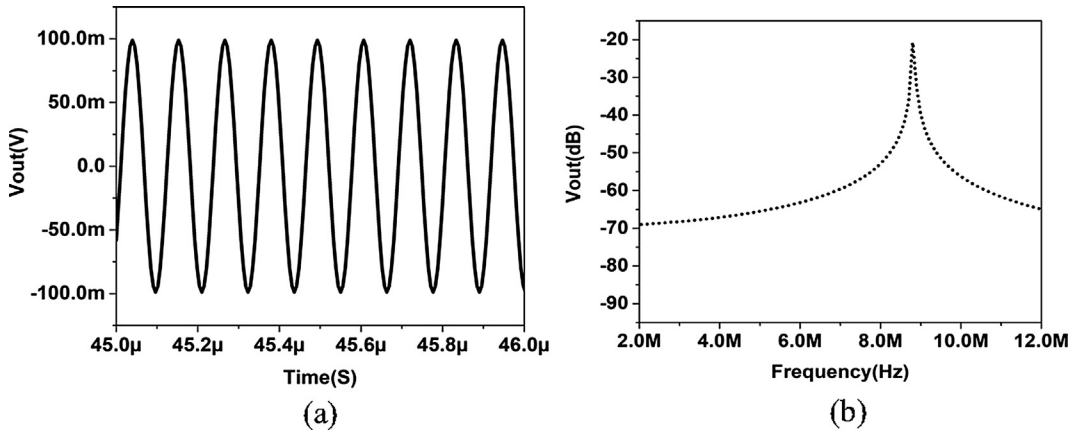


Fig. 4. (a) Transient output (b) frequency spectrum of proposed circuit.

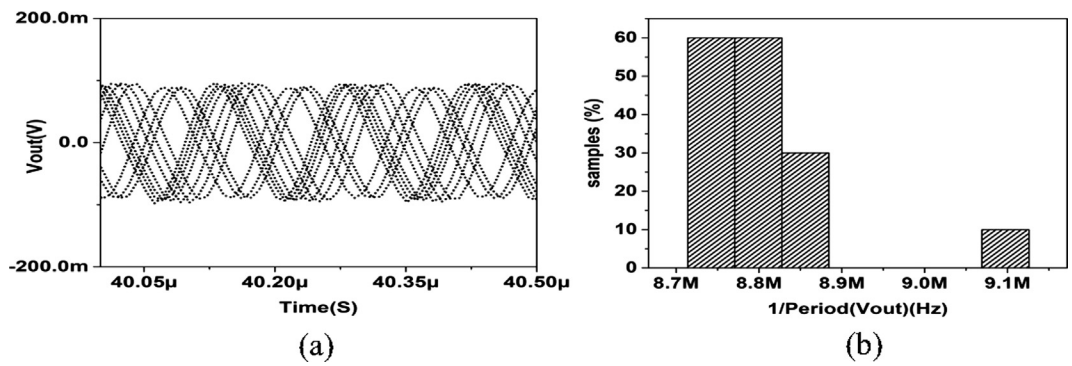


Fig. 5. (a) Monte Carlo simulation (b) histogram of proposed circuit after Monte Carlo simulation.

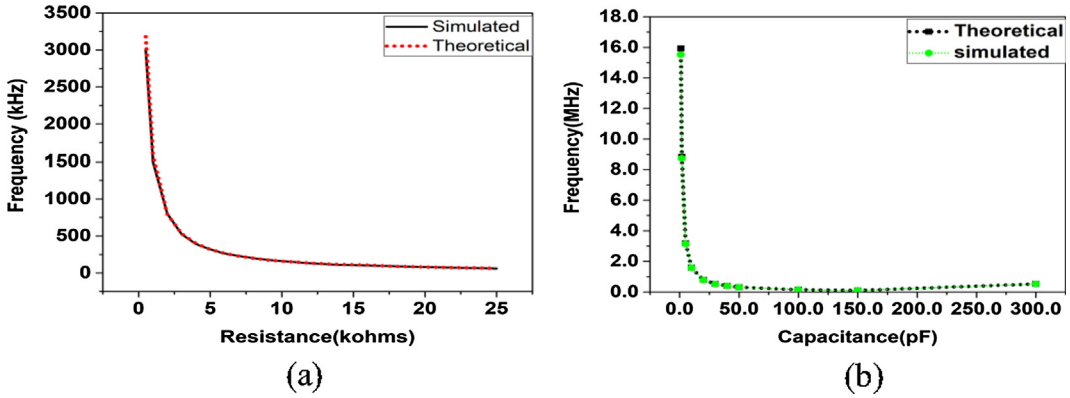


Fig. 6. Frequency tuning with (a) resistance (b) with capacitance for circuit.

is obtained as 8.79 MHz which accords well with the theoretical value thus confirm the validity of the proposed configuration.

The proposed design has floating passive components in its topology, Although grounded capacitors are preferred from fabrication viewpoint, to lower the effects of the top plate and bottom plate parasitic capacitances of (C_2 and C_3) on the proposed oscillator they can be implemented using top-quality IC technology of today, which offers metal–insulator– metal (MIM) or metal–oxide–metal (MOM), double poly (poly1–poly2) capacitor processes [44,45],.

6. Experimental results

The proposed oscillator is also verified experimentally by breadboarding using off shelf IC's AD844 [46]. Fig. 10 shows OTRA implementation using AD844 with a supply voltage of ± 8 V.

The proposed TOSO is modeled with resistor values $R_1 = R_2 = 10\,k\Omega$, $R_3 = 5\,k\Omega$, and capacitor values $C_1 = C_2 = C_3 = C = 100\,pF$ for which the calculated FO is 159.2 kHz. The experimental steady-state response, FFT spectrum are shown in Fig. 11(a) and (b) respectively, and the practical FO is found to be 160 kHz.

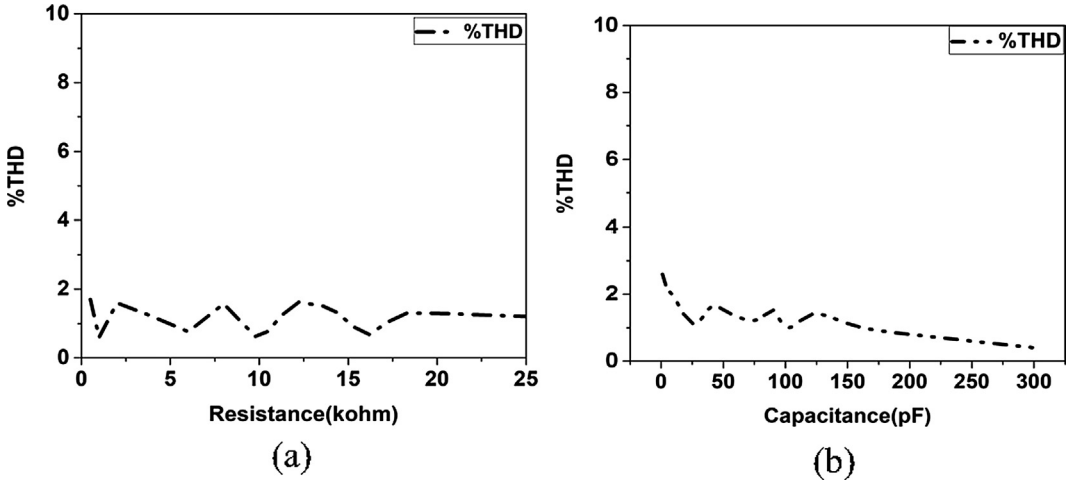


Fig. 7. % THD variation with (a) resistance (b) capacitance for circuit.

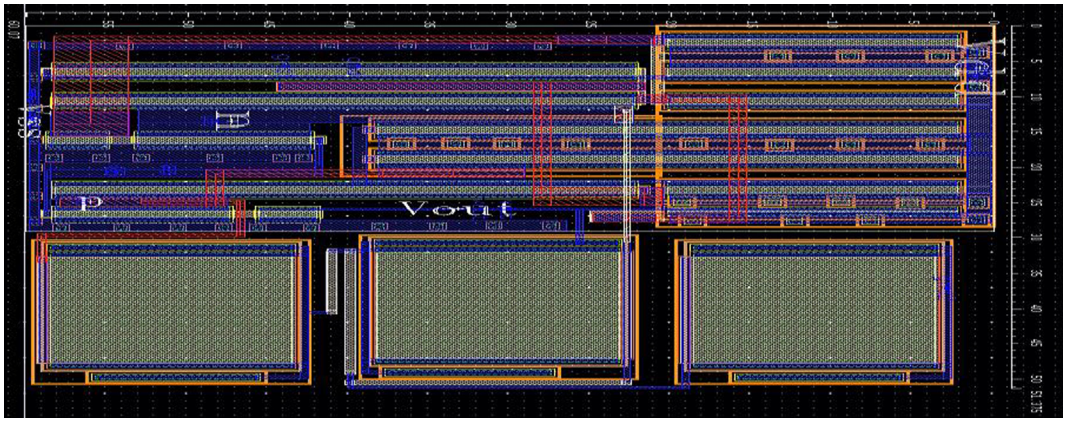


Fig. 8. The complete physical layout of proposed TOSO.

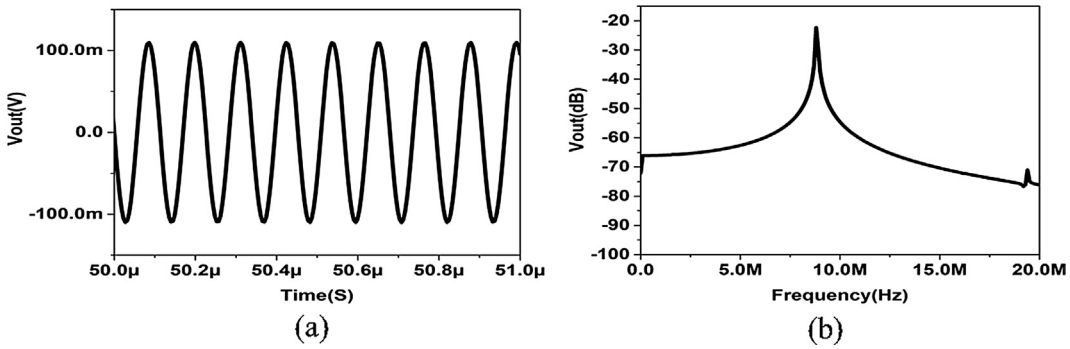


Fig. 9. (a) Simulated output waveform and (b) frequency spectrum of proposed TOSO.

The proposed circuit has also been simulated in SPICE in which OTRA has been realized using IC AD 844. Fig. 12(a) and (b) shows the simulated and experimental results for FO and THD variation of FO by varying R from 1 kΩ to 10 kΩ while keeping C = 100 pF and by changing from 20 pF to 10 nF with R fixed at R = 1 kΩ. Simulated and experimental FOs achieved are found to be in close agreement. It is observed that the highest experimental THD obtained as 3% which is considered to be low.

7. Conclusion

A new realization of OTRA based third order oscillator is presented in this paper. The functionality of proposed structure is verified through ADE tool provide by cadence virtuoso using 0.18 µm technology parameters. Moreover, the layout of the proposed structure is also presented. The simulation and experimental results are found to be in close agreement with theoretical propositions. The effect of non-idealities of OTRA has been analyzed by considering single and double poles. Which suggest that for high-frequency applications self-compensation can be used. The sensitivity of ω w.r.t passive components is also examined, and values found out to be less than or equal to unity in magnitude. This topology is further tested experimentally wherein the OTRA is realized using off the shelf CFOA IC AD844.

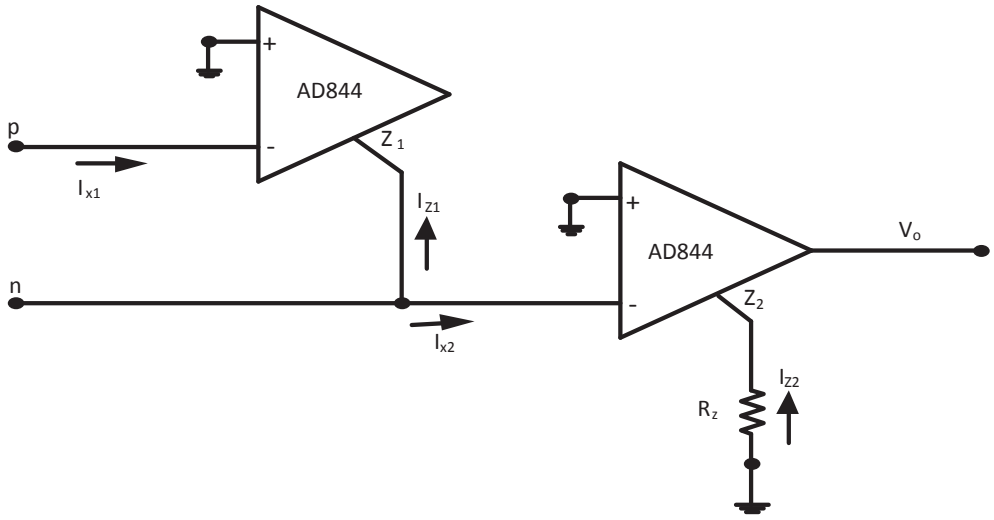


Fig. 10. OTRA implementation using IC AD 844 [37].

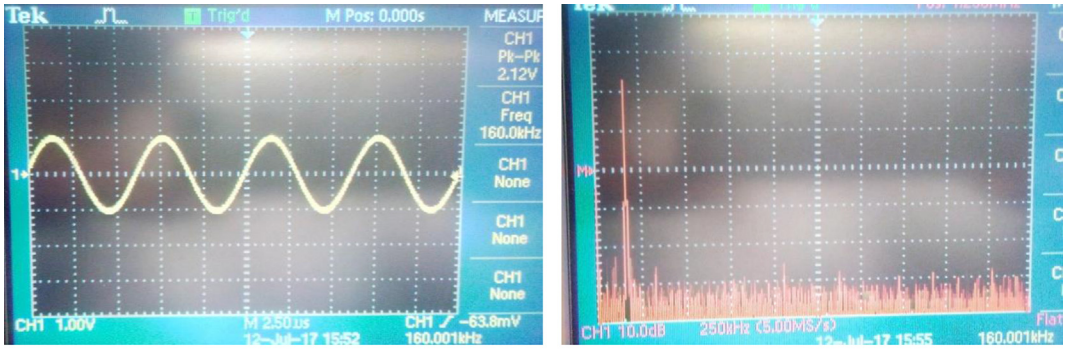


Fig. 11. Experimental (a) steady-state output and it's (b) frequency spectrum.

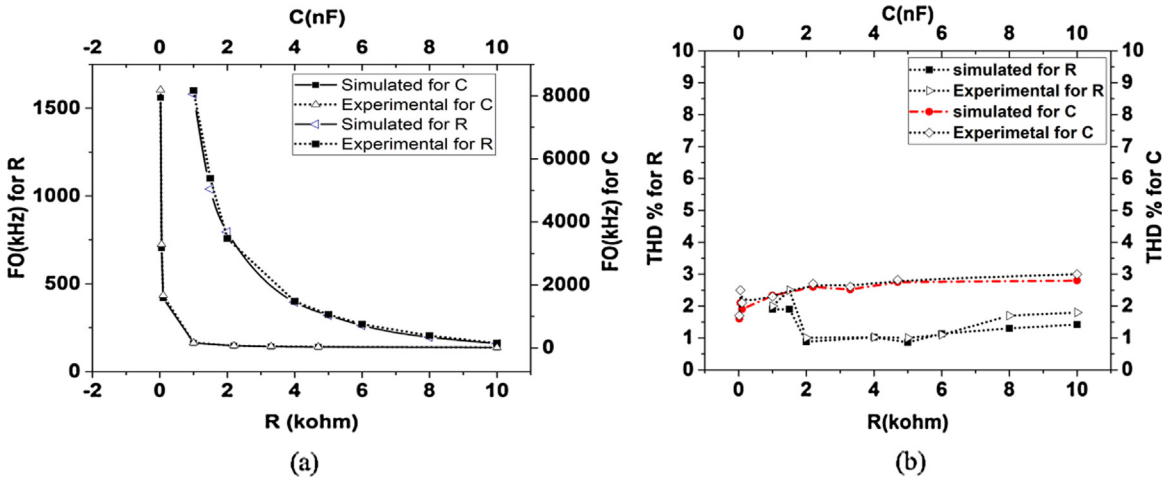


Fig. 12. (a) Frequency tuning with R and C (b) %THD variation with R and C.

Appendix A

It has been observed from the literature review that similar structures using CDBA [41]/CF-VF[42]/EXCC-II [42] are not available. Authors have designed the circuits using listed ABBs which are shown in Figs. A.1–A.3. The characteristic equation for circuits of Figs. A.1–A.3 remains same as (3) of the proposed design.

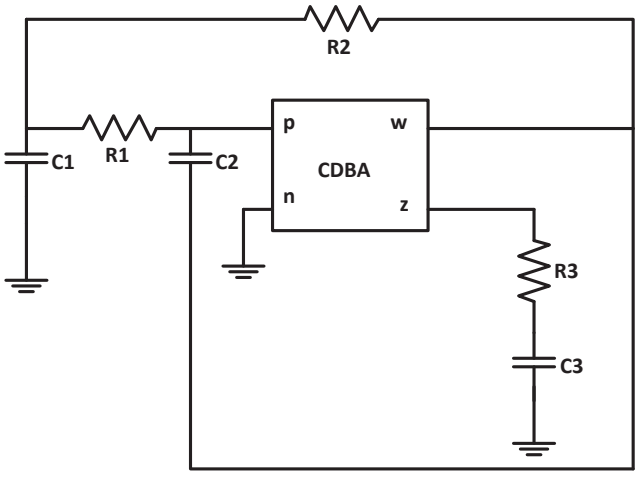


Fig. A1. Proposed CDBA based TOSO.

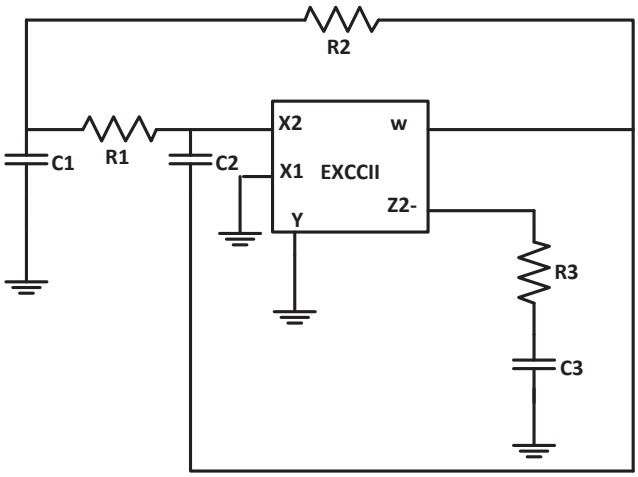


Fig. A2. Proposed EXCC-II based TOSO.

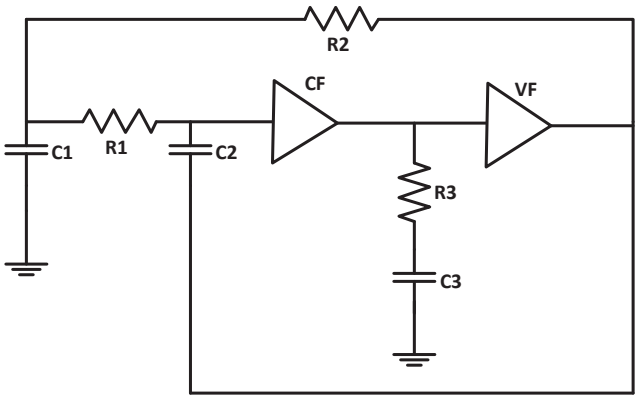


Fig. A3. Proposed CF-VF based TOSO.

References

[1] Sedra AS. smith. Microelectronic circuits. 4th ed. Oxford University Press; 2004.
[2] Senani R, Bhaskar DR, Singh VK, Singh VK. Sinusoidal oscillators and waveform generators using modern electronic circuit building blocks. Springer International Publishing; 2015. pp. 1–622.
[3] Hajder T. Higher order loops improve phase noise of feedback oscillators. Appl Microwave Wirel 2002:24–31.
[4] Pandey R, Pandey N. Approach for third order quadrature oscillator realisation. IET Circuits, Devices Syst 2015;9:161–71.
[5] Horng JW. Current/voltage-mode third order quadrature oscillator employing two multiple outputs CCIIs and grounded capacitors. Indian J Pure Appl Phys 2011;49:494–8.
[6] Pandey R, Pandey N, Paul SK. MOS-C Third order quadrature oscillator using OTRA. In: 2012 Third Int Conf Comput Commun Technol; 2012. p. 77–80.
[7] Nagar BC, Paul SK. Voltage mode third order quadrature oscillators using OTRAs. Analog Integr Circuits Signal Process 2016;88:517–30.
[8] Channumsin O, Jantakun A. Third-order sinusoidal oscillator using VDTAs and grounded capacitors with amplitude controllability. In : 4th joint international conference on information and communication technology, electronic and electrical engineering; 2014. p. 4–7.
[9] Phatsornsiri P, Lamun P, Kumngern M, Torteanchai U. Currentmode third order quadrature oscillator using VDTAs and grounded capacitors. In: 4th joint international conference on information and communication technology, electronic and electrical engineering; 2014. p. 23–6.
[10] Tsukutani T, Sumi Y, Fukui Y. Electronically controlled currentmode oscillators using MO-OTAs and grounded capacitors. Frequenz 2006;60:220–3.
[11] Prommee P, Dejhan K. An integrable electronic controlled quadrature sinusoidal oscillator using CMOS operational transconductance amplifier. Int J Electron 2002;89:365–79.
[12] Horng JW. Quadrature oscillators using operational amplifiers. Act Passiv Electron Compon 2011;2011:1–4.
[13] Horng JW, Hou CL, Chang CM, Chung WY, Tang HW, Wen YH. Quadrature oscillators using CCIIs. Int J Electron 2005;92:21–31.
[14] Horng JW. Current-mode third-order quadrature oscillator using CDTAs. Act Passiv Electron Compon 2009;2009:1–4.
[15] Maheshwari S. Current-mode third-order quadrature oscillator. IET Circuits, Devices Syst 2010;4:188.
[16] Horng JW, Lee H, Wu JY. Electronically tunable third-order quadrature oscillator using CDTAs. Radioengineering 2010;19:326–30.
[17] Pandey R, Pandey N, Gurumurthy K, Anurag R. OTRA based voltage mode third order quadrature oscillator. ISRNElectronics Hindawi Publishing Corporation 2014; 2014.
[18] Maheshwari S. Quadrature oscillators using grounded components with current and voltage outputs. IET Circuits, Devices Syst 2009;3:153–60.
[19] Chaturvedi B, Maheshwari S. Third-order quadrature oscillator circuit with current and voltage outputs. ISRN Electron 2013;2013:1–8.
[20] Kumngern M, Kansiri I. Single-element control third-order quadrature oscillator using OTRAs. In: Int Conf ICT Knowl Eng; 2015. p. 24–7.
[21] Soliman AM. Generation of third order quadrature oscillator circuits using NAM expansion. J Circuits, Syst Comput 2013;22:1–13.
[22] Maheshwari S, Verma R. Electronically tunable sinusoidal oscillator circuit. Act Passiv Electron Compon 2012;2012:1–6.
[23] Maheshwari S. Analogue signal processing applications using a new circuit topology. IET Circuits, Devices Syst 2009;3:106–15.
[24] Maheshwari S, Khan IA. Current controlled third order quadrature oscillator. In: IEE Proc Circuits, Devices Syst, vol. 152; 2005. p. 605–7.
[25] Duangmalai D, Jaikla W. Realization of current-mode quadrature oscillator based on third order technique. ACEEE Int J Electr Power Eng 2011;2:46–9.
[26] Kwawsibsam A, Sreewirote B, Jaikla W. Third-order voltage-mode quadratrue oscillator using DDCC and OTAs. In: 2011 Int Conf Circuits, Syst Simul; 2011. p. 317–21.
[27] Kumngern M, Junnapiya, S. Current-mode third-order quadrature oscillator using minimum elements. In: Int Conf on Electrical Engineering and Informatics; 2011. p. 1–4.
[28] Phanruttanachai K, Jaikla W. Third order current-mode quadrature sinusoidal oscillator with High Output. Int Sch Sci Res Innov 2013;7:472–5.
[29] Koton J, Herencsar N, Vrba K. Current and voltage-mode third-order quadrature oscillator. In: International conference on optimization of electrical and electronic equipment; 2012. p. 1203–6.
[30] Lawanwisut S, Siripruchyanun M. High output-impedance current-mode third-order quadrature oscillator based on CCCCTAs. In: IEEE Region 10 annual international conference; 2009. p .8–11.
[31] Kumngern M, Torteanchai U. A current-mode four phase third-order quadrature oscillator using a MCCCFTA. In: 2012 IEEE Int Conf Cyber Technol Autom Control Intell Syst Cyber; 2012. p.156–9.
[32] Khawngam K, Kumngern M, Khateb F. Mixed-mode third-order quadrature oscillator based on single MCCFTA. Radioengineering 2017;26:522–35.
[33] Gurumurthy K, Pandey N, Pandey R. OTRA based second and third order sinusoidal oscillators and their phase noise performance. AIP Conference Proc 2017;1859:020017.
[34] Nagar BC, Paul SK. Realization of OTRA-based quadrature oscillator using third-order topology. In: Konkani A, Bera R, Paul S, editors. Advances in systems, control and automation. Lecture Notes in Electrical Engineering. Singapore: Springer; 2018. p. 375–86.
[35] Senani R. New Rc-active oscillator configuration employing unity-gain amplifiers. Electron Lett 1985;21:953–4. http://dx.doi.org/10.1049/el:19850627.
[36] Boutin N. Synthesis of oscillator circuits employing only one unity-gain amplifier. Electron Lett 1986;22:22–3.
[37] Chien H. Third-order sinusoidal oscillator using a single CMOS operational transresistance amplifier. J Appl Sci Eng 2016;19:187–96.
[38] Mostafa BH, Soliman AM. A modified CMOS realization of the operational transresistance amplifier (OTRA). Frequenz 2006;60:3–4.
[39] Moschytz G. Trade-offs in sensitivity, component spread and component tolerance in Active filter design. In: Toumazou C, Moschytz G, Gilbert B, Kathiresan G, editors. Trade-offs in analog circuit design. MA, Boston: Springer; 2002. p. 315–39.
[40] Acar C, Ozoguz S. A new versatile building block: current differencing buffered amplifier suitable for analog signal-processing filters. Microelectronics J 1999;30:157–60.
[41] Biolek D, Senani R, Biolkova V, Kolka Z. Active elements for analog signal processing: Classification, review, and new proposals. Radioengineering 2008;17:15–32.
[42] Maheshwari S. Current conveyor all-pass sections: brief review and novel solution. ScientificWorldJournal 2013;2013:429391.
[43] Raj S, Singh AK, Gupta A, Bhaskar DR. Simple simulated inductor, Low-Pass/Band-Pass filter and sinusoidal oscillator using OTRA. Circuits Syst 2016;7:83–99.
[44] Nagar BC, Paul SK. Lossless grounded FDNR simulator and its applications using OTRA. Analog Integr Circuits Signal Process 2017;92:507–17.
[45] Jacob Baker J.CMOS circuit design, layout, and simulation, 3rd ed. Newyork; 2010.
[46] AD844 Current Feedback Op-Amp Data Sheet. Norwood, NJ, USA: Analog Devices Inc.; 1990.

Available online at www.sciencedirect.com

ScienceDirect

Procedia Computer Science 132 (2018) 1562–1569

Procedia Computer Science

www.elsevier.com/locate/procedia

International Conference on Computational Intelligence and Data Science (ICCIDS 2018)

Particle Swarm Optimization based Automatic Generation Control of Interconnected Power System incorporating Battery Energy Storage System

Nidhi Gupta [1], Narendra Kumar[2]

[1]MSIT, GGSIPU, Delhi, India

[2] Delhi Technological University, Delhi, India

Abstract

This paper deals with Automatic Generation Control (AGC) of three area multi source interconnected power system assimilating Battery Energy Storage System (BESS). The plant is designed with Particle Swarm Optimization (PSO)tuned Integral controller (IC) which is carried out on three different sources, thermal, gas and hydro interconnected power system with and without BESS. Further computational intelligent technique, has been used to optimize the parameters of IC for different area by considering the objective function as integral square error (ISE). BESS provides fast active power compensation and manage sudden demand of power requirement in load, thus effectively dampening the frequency oscillations due to large disturbances in load. Dynamic performances of the system and objective function are analysed and compared for considered model. Analysis reveals that with the use of BESS, there is effective improvement in deviation of frequency of load disturbances.

© 2018 The Authors. Published by Elsevier Ltd.
This is an open access article under the CC BY-NC-ND license (https://creativecommons.org/licenses/by-nc-nd/3.0/)
Peer-review under responsibility of the scientific committee of the International Conference on Computational Intelligence and Data Science (ICCIDS 2018).

*Keywords:*Automatic Generation Control,Battery Energy Storage System, Thermal-gas-hydro Interconnected Power System, Integral controller, Particle Swarm Optimization.

1. Introduction

The power system comprises of large number of generators interconnected by network of transmission lines which provide power to the consumers at rated voltage and frequency. Generally, the interconnected power system contains thermal and hydro power generation as a research. Deviation in frequency occurs due to real power dispatch among generator and load, while the cause of voltage variations is reactive power imbalance in the power system. According to the definition of AGC, active power balance is achieved by controlling power generation [1]. The characteristics of governors, and its effect on tie line power and frequency are considered for electric power system [2]. Further, AGC of two area hydro thermal interconnected power system incorporating various controllers were elucidated [3]. If a real power mismatch, frequency and tie line power exchanges between interconnected power systems are significant variables. A single variable called Area control Error(ACE) weighs these variables together[4]. Additionally,the impactof including load generation participation factors for AGC of two area multi source power system wasanalyzed [5]. Some important aspects of multi source as thermal, hydro and gas interconnected power systemwere considered for single or maximum two areas[6]. Due to shortage of resources, it is difficult to combine multi source in one area.

Corresponding author: nidhi@msit.in

1877-0509 © 2018 The Authors. Published by Elsevier Ltd.
This is an open access article under the CC BY-NC-ND license (https://creativecommons.org/licenses/by-nc-nd/3.0/)
Peer-review under responsibility of the scientific committee of the International Conference on Computational Intelligence and Data Science (ICCIDS 2018).
10.1016/j.procs.2018.05.120

So, in a realistic power system there is a need to consider different sources as an individual area which is further interconnected to make a power system.

BESS creates interest in utilities and transmission system operators. Incremental block diagram of a BESS was operated to the two area thermal power system[7]. Previous study shows that few studies has been devoted to the AGC of interconnected three area thermal- gas-hydro power system with BESS.
In this paper effect of BESS on AGC of multi source interconnected power generation is analyzed. Hence, it is seen that BESS in multi source generation system improves performance of the system and reduces overshoots of dynamic frequency deviation under load disturbances.

Nomenclature

ΔF_i	Deviation in powerSystem frequency
T_P	Power system Time constant
R	Speed regulation
K_{RT}	Gain of reheat turbine
K_P	Power system gain
T_g	Time constant of thermal governor
T_W	Time constant for hydraulic turbine
ΔP_{GC}	Changein system generated power
ΔP_{dc}	Load disturbances change
ΔP_{cc}	Speedgovernor change
ΔP_M	Hydraulic turbine mechanical power
T_{tt}	Time constant of thermal turbine
ΔP_{tieij}	Tie-line power deviation
T_{ij}	Tie-linesynchronizing coefficient
ΔX_E	Governor valve position change.
x	State vector of system
u	Control vector of system
p	Disturbance vector of system
r_b	Overvoltage resistance
r_{BPC}	Self discharge resistance
$\propto$	Firing angle
c_{BPC}	Battery capacitance
K_{BESS}	Control gain parameter
T_{BESS}	Time constant of control loop
V_i^k	Velocity at iteration k
w_w	Inertia factor
c	Weighting factor
X_n^m	Current position
Iterm	maximum value of iteration number

2. Description Of Battery Energy Storage System

Schematic description of BESS plant consists of 12 pulse bridge converter coupled to 3 phase transformer, battery cells and control scheme [8, 9] is given in Fig.1.

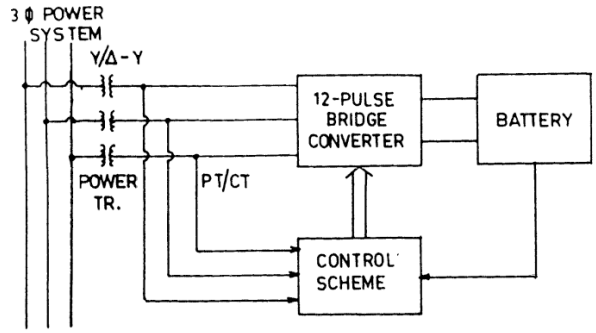


Fig.1. A schematic description of a BESS plant.

A converter is linked to an equivalent battery. It can be represented as an equivalent circuit of the BESS which is shown in Fig.2. The no load d.c. voltage is given as

$$E_{do} = E_{do1} + E_{do2} = \frac{6\sqrt{6}}{\pi} E_{tc} \quad (1)$$

where E_{tc} is the line to neutral voltage. The terminal voltage of battery isattained from,

$$E_{bt} = E_{do} \cos \propto^{0} - R_c \, I_{BESS} \quad (2)$$

$$E_{bt} = \frac{3\sqrt{6}}{\pi} E_t (cos \propto^{10} + cos \propto^{20}) - \frac{6}{\pi} X_{co} I_{BESS} \quad (3)$$

Where, $\propto^{k0}$ is delay angle of k converter, $I_{BESS}$is the current flowing into battery, X_{co} is commutating resistance.
In Fig.2, d.c. current flowing into the battery can be specified as

$$I_{BESS} = \frac{(E_{bt} - E_{boc} - E_b)}{r_{bt} + r_{bs}} \quad (4)$$

Where E_b is battery over voltage, E_{boc} is battery voltage at open circuit, r_{bt} and r_{bs} are connecting and standard internal resistances, C_{bc} is overvoltage capacitance.
Power absorbed byBESS with respect to converter circuit analysis is written as,

$$P_{BESS} = \frac{3}{\pi}\sqrt{6}\, E_{tc} I_{BESS} (cos \propto^{10} + cos \propto^{20}) \quad (5)$$

$$Q_{BESS} = \frac{3}{\pi}\sqrt{6}\, E_{tc} I_{BESS} (sin \propto^{10} + sin \propto^{20}) \quad (6)$$

For *P*-modulation control strategy, active power considered in AGC of the interconnected power system is presented as

$$\propto^{10} = -\propto^{20} = \propto^{0} \quad (7)$$

Therefore,

$$P_{BESS} = \frac{6}{\pi}\sqrt{6}\, E_{tc} I_{BESS} cos \propto^{0} \quad (8)$$

$$P_{BESS} = E_{do} I_{BESS} cos \propto^{0} \quad (9)$$

$$Q_{BESS} = 0 \quad (10)$$

Let us assume

$$E_{co} = E_{do} \cos \propto^{0} \quad (11)$$

where E_{co} is d.c. voltage without overlap
So,

$$P_{BESS} = E_{co} I_{BESS} \quad (12)$$

Linearizing the above equation, the incremental BESS power [10]as,

$$\Delta P_{BESS} = E_{co}{}^{\circ}\Delta I_{BESS} + I_{BESS}{}^{\circ}\Delta E_{co} \quad (13)$$

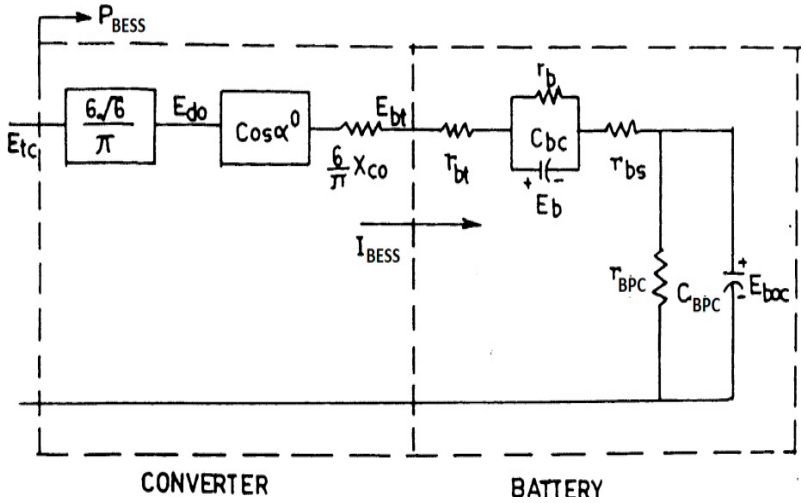


Fig.2. Equivalent circuit diagram of BESS.

By adjusting the firing angle for AGC with BESS, d.c. voltage without overlap works in constant power mode, which are further separated into voltage deviation and responded voltage after system disturbances.

$$\Delta E_{co} = \Delta E_d + \Delta E_p \quad (14)$$

Now,

$$\Delta P_{BESS} = E_{co}{}^{\circ}\Delta I_{BESS} + I_{BESS}{}^{\circ}\Delta E_p + I_{BESS}{}^{\circ}\Delta E_d \quad (15)$$

For smooth functioning of AGC with BESS

$$E_{co}{}^{\circ}\Delta I_{BESS} + I_{BESS}{}^{\circ}\Delta E_p = 0 \quad (16)$$

$$\Delta E_p = -E_{co}{}^{\circ}(\Delta I_{BESS}/I_{BESS}{}^{\circ}) \quad (17)$$

$$\Delta E_p = -E_{do}\cos \propto {}^{\circ}(\Delta I_{BESS}/I_{BESS}{}^{\circ}) \quad (18)$$

Therefore,

$$\Delta P_{BESS} = I_{BESS}{}^{\circ}\Delta E_d \quad (19)$$

Thus to provide a damping effect in AGC of interconnected power systems incorporating BESS is attained by considering Δsignal as an input to the BESS. Input signal to BESS is the ACE of the reheat thermal power system [11].

Now,

$$\Delta E_d = (K_{BESS}/1 + s\,T_{BESS})\ \Delta signal \quad (20)$$

During peak load period, energy is provided by BESS during discharging mode. At discharging mode, BESS operates at (β°=$\pi - \propto^0$) as an ignition angle for the converter.

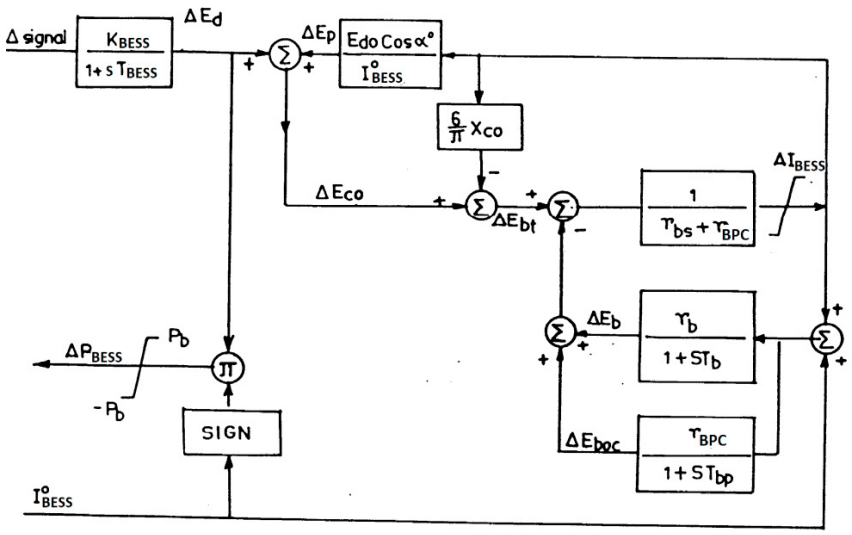


Fig.3. The incremental block diagram of BESS.

3. Power system model

In the present work, the model consists of multi source interconnected power generation. It consists of three areas namely reheat thermal, gas and hydropower generating units as shown in Fig. 4.Parameters of reheat thermal system, gas and hydro are given in Appendix A. In this paper 10MW/40MWh BESS is applied and implemented to area 1(thermal power system) of interconnected power system. PSO tuned IC gain parameters is considered for three area in thermal, gas and hydro interconnected power system incorporating BESS under 1% step increase of load disturbances in the system. Changes in load can bring about intolerable dynamic frequency changes in the system. Supervising of frequency amends the speed changer setting automatically. Area Control Error (ACE) from frequency deviation of respective area is provided through an integrator to the speed changer.

$$ACE_i = \Delta P_{tieii}(t) + b_i \Delta F_i \quad (21)$$

$$\Delta P_{tieii}(t) = T_{ij} [\Delta F_i(t) - \Delta F_j(t)] \quad (22)$$

Where, *i != j and i,j= 1,2,*3 for thermal, gas and hydro power generation respectively.

The motor signal will be of the form

$$\Delta Pcc_i(t) = - K_{Ii} \int (ACE_i)\, dt \quad (23)$$

where, K_{Ii} is IC gain for area i.
Dynamic model in state variable form can be is written as:-

$$x^o = Ax+Bu+Rp \quad (24)$$

where A, B and R are constant matrices whose size is influenced by system parameters and operating point. An objective function depending on integral square error (ISE) criterion is an effective measurement of dynamic performances. ISE has a property of penalizing large error greatly and low errors slightly which is given as

$$J=\int(ACE_1^2(t)+ACE_2^2(t)+ACE_3^2(t))dt \quad (25)$$

PSO is applied to tune IC for better dynamic responses of AGC with BESS and without BESS.

4. Overview of particle swarm optimization technique

Nonlinear and continuous optimization problem can be solved easily with modern heuristic algorithms. As compared to otheroptimization techniques, PSO isa population influenced optimization technique. It has less possibility to get trapped on localoptima. PSO is recognized as an analogy of swarm of bird and school of fish [12]. Its mechanism is inspired by the social and

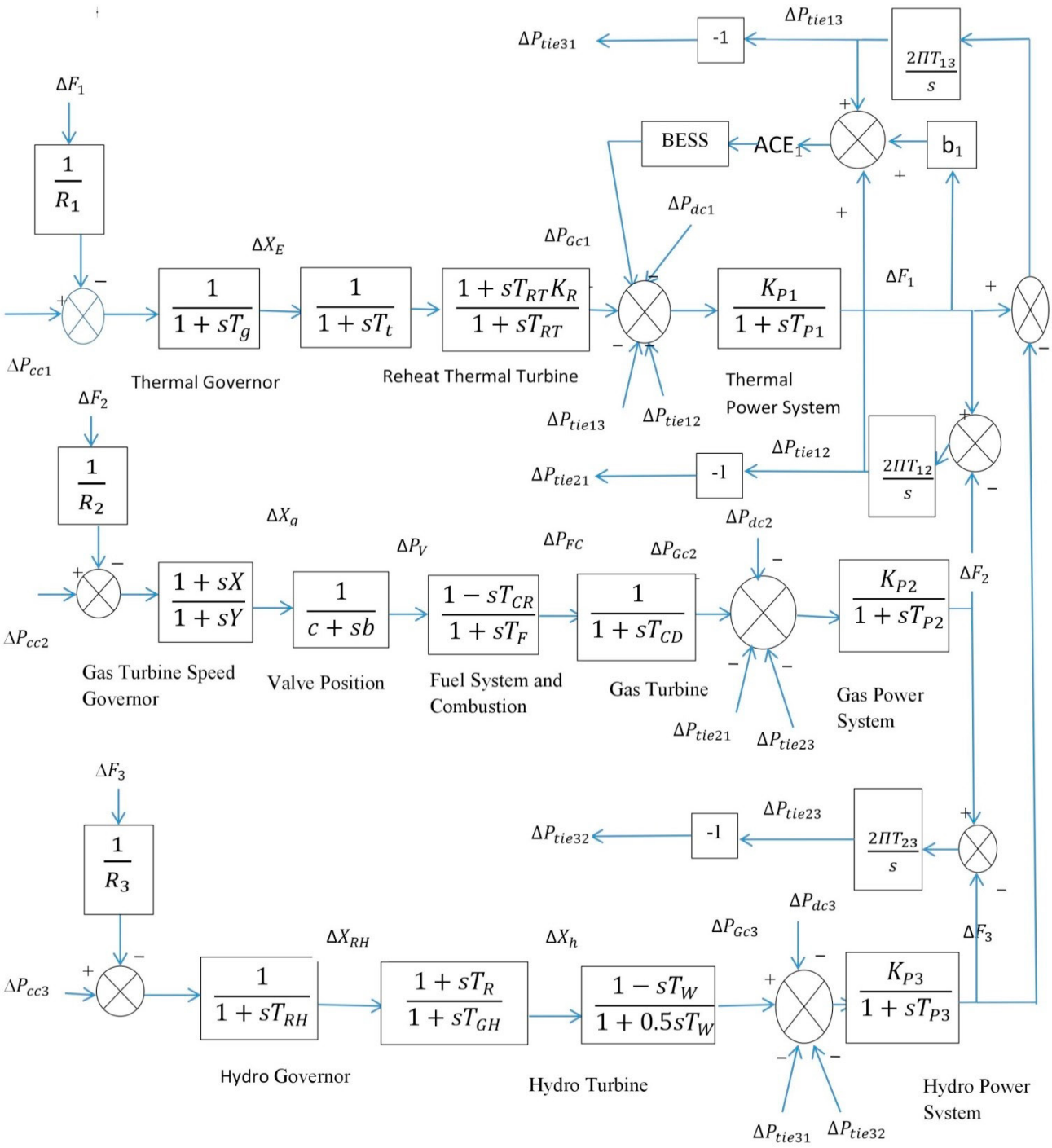


Fig.4. Transfer function model of three areas controlled thermal-gas-hydro interconnected power generation.

cooperative nature of flying birds. In PSO, decisions are made on the basis of its own and the other's experience [13]. Each individual's velocity is adjusted as per its own flying experience as well as its companion's. Particles record the recent best fitness value coordinates. This value is known as $X_{pbest}$for position best value, X_{gbest} as global best value, obtained so far by the recent iterations. Each individual's velocity is adjusted as per its own flying experience as well as its companions. The following equation represents the modification of the particles velocity as:-

$$V_n^{m+1} = w * V_n^m + c_1 * ran_1 * \left(X_{pbest\,n} - X_n^m\right) + c_2 * ran_2 * (X_{gbest\,n} - X_n^m) \quad (26)$$

where ran is uniformly distributed random numbers in the range of 0 to 1, w_{mx} is maximum weight , n is current iteration number and w_{mn} is minimum weight.

$$w = w_{mx} - [(w_{mx} - w_{mn}) * n]/\text{Iterm} \quad (27)$$

If value of w is large then it facilitates the global search, whereas if the value is small then it facilitates a local search. Now the position of particle is updated

$$X_n^{m+1} = X_n^m + V_n^{m+1} \quad (28)$$

5. Results and discussions

The BESS has been implemented in PSO based AGC of multi sourceinterconnected power generation systemunderload disturbances and parameters used in thescheme are given in Appendix A. BESS is designed as a subsystem and connected to reheat thermal area 1of model. Each area of the interconnected power system model represents a different power generation as thermal gas and hydro of the same capacity. Analysis is now made to investigate the performance of considered model incorporating BESS at 1% step increase of load disturbances in each area which further comparewith the model without using BESS. For both the comparisons, PSO technique is applied to tune IC parameters for AGC of interconnected power systems in each area. It is inferred from the responses of AGC of multi source interconnected power generation system incorporating BESS that it settles at less time when compared to AGC of multi area interconnected power generation systemwithout BESS as depicted in Fig. 5.

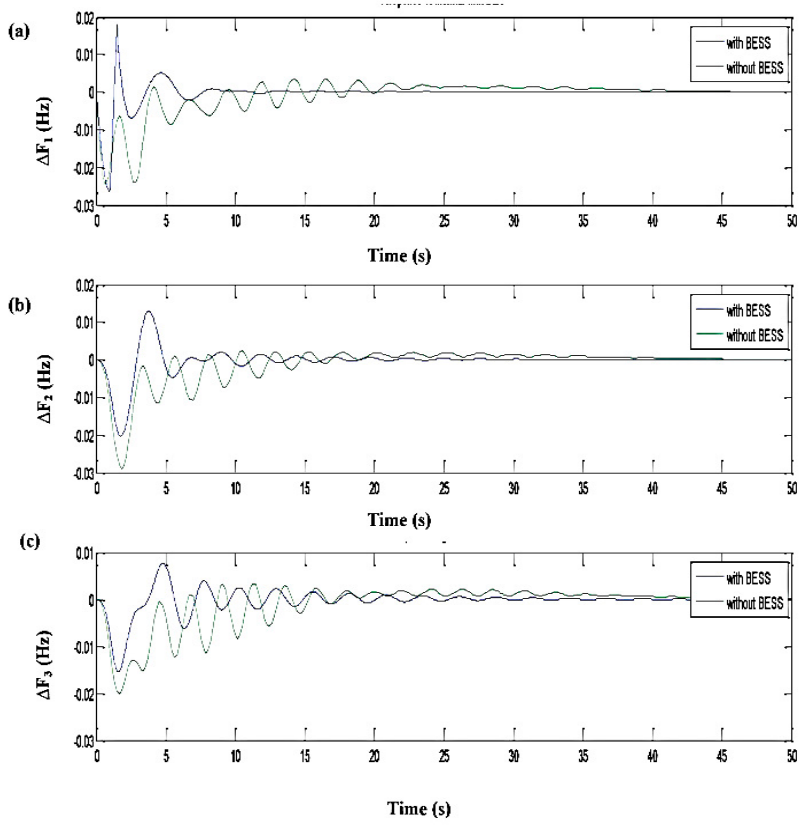


Fig.5. System dynamic response of frequency deviation at 1% step increase of load in each area a) area 1; b) area2 ; c) area 3.

The proposed IC controller for the power system model incorporating BESS with cost function as ISE accomplished better system characteristics as shown in Table II. The least possible value of the objective function is greatly improvedin case of considered model with BESS is 0.000357 whereas for AGC without BESS is 0.001157.The parameter tuned value of IC for power system model without BESS is 0.1 and power system modelwith BESS is 0.12.
Hence, BESS assimilationof the power system with PSO tuned IC helps in substantiallyimproving the response of system for1% step increase of load disturbanceand maintain a good Automatic Generation Control.

Table 1 System Characteristics of Interconnected Model with and without BESS.

System Modes	Without BESS			With BESS+ACE		
	ΔF_1	ΔF_2	ΔF_3	ΔF_1	ΔF_2	ΔF_3
SettlingTime	41.44	40.32	43.68	13.59	27.81	31.75
Peak	0.02	0.03	0.02	0.02	0.02	0.01
PeakTime	0.62	1.848	1.67	0.59	1.76	1.58

6. Conclusion

The effect of BESS on AGC of multi source thermal-gas-hydro interconnected power system is investigated using PSO. The areas of interconnected power systems are reheat thermal, gas and hydro turbines. To reveal the performance of PSO based AGC tuned IC parameter is optimized by considering minimum performance index criterion. The effectiveness of BESS with ISE as an objective function for three area interconnected power systems under 1% step increase of load disturbances in each area is demonstrated. The system dynamic response method is applied to obtain analysis result. Since BESS offers rapid active power compensation in power system, improved system performance of PSO based AGC for multi-source incorporating BESS in an area is considered.System response characteristics show an appreciable improvement in settling time, peak time and peak amplitude.It has been observed that the dynamic system performances are significantly improved by using BESS to multi source interconnected power system Sensitivity analysis shows that the system gets degraded when there is a disturbance in hydro generation plant. Moreover, these degradations of dynamic responses are considerably improved by applying BESS in area1of interconnected power system. It can be concluded that application of PSO based AGC of interconnected, multi source power system incorporating BESS provides significant improvement in system dynamic responses.

Appendix A : Power system data

$P_{r1}=P_{r2}=P_{r3}=2000$MW, Frequency of system =60Hz, $R_1=R_2=R_3=$ 2.4Hz /p.u. MW ,b_i=0.425p.u.MW/Hz, K_{pi}=120,T_{pi}=20s, P_{tieij}=200MW, T_{ti}=0.3s, T_{ggi}=0.08s, ΔP_{dci}=0.01 p.u. MW,$2\Pi T_{12}$= 0.15 p.u. MW, $2\Pi T_{23}$= 0.15 p.u. MW, $2\Pi T_{31}$= 0.15 p.u. MW, T_w=1s, T_{RH}=48.7s, a=1,b=0.05s, c=1, X=0.6s, Y=1, BESS data is taken from [7].

References

[1] Carpentier, J.(1985) "'To be or not to be modern'that is the question for automatic generation control (point of view of a utility engineer)." International journal of electrical power & energy systems 7, no. 2: 81-91.

[2] C. Concordia and LK Kirchmayer(1954)"Tie-line power & frequency control of electric power system: Part II", AISE Trans, III-A, vol. 73, pp. 133-146.

[3] Nanda, J., and B. L. Kaul.(1978) "Automatic generation control of an interconnected power system." In Proceedings of the Institution of Electrical Engineers, vol. 125, no. 5, pp. 385-390. IET Digital Library, 1978.

[4] Kundur, Prabha, Neal J. Balu, and Mark G. Lauby. (1994) Power system stability and control. Vol. 7. New York: McGraw-hill.

[5] Ramakrishna, K. S. S., and T. S. Bhatti.(2008) "Automatic generation control of single area power system with multi-source power generation." Proceedings of the Institution of Mechanical Engineers, Part A: Journal of Power and Energy 222, no. 1: 1-11.

[6] Challa, Kiran Kumar, and PS Nagendra Rao.(2010) "Analysis and design of controller for two area thermal-hydro-gas AGC system." In Power Electronics, Drives and Energy Systems (PEDES) & 2010 Power India, IEEE ,2010 Joint International Conference on, pp. 1-4.

[7] Aditya, S. K., and D. Das.(2001) "Battery energy storage for load frequency control of an interconnected power system." Electric power systems research 58, no. 3: 179-185.

[8] Walker, Loren H.(1990) "10-MW GTO converter for battery peaking service." IEEE Transactions on Industry Applications 26, no. 1: 63-72.

[9] Chatzinikolaou, Efstratios, and Daniel J. Rogers.(2017) "A comparison of grid-connected battery energy storage system designs." IEEE Transactions on Power Electronics 32, no. 9 :6913-6923.

[10]Lu, Chun-Feng, Chun-Chang Liu, and Chi-Jui Wu. (1995) "Effect of battery energy storage system on load frequency control considering governor deadband and generation rate constraint." IEEE Transactions on Energy Conversion 10, no. 3: 555-561.

[11]Biswas, S., and P. Bera. (2012) "GA Application to Optimization of AGC in Two-Area Power System Using Battery Energy Storage." In Communications, Devices and Intelligent Systems (CODIS),IEEE, 2012 International Conference on, pp. 341-344.

[12]Kennedy, James, and Russell Eberhart.(1995) "PSO optimization." In Proc. IEEE Int. Conf. Neural Networks, vol. 4, pp. 1941-1948. IEEE Service Center, Piscataway, NJ.

[13]AlRashidi, Mohammed R., and Mohamed E. El-Hawary. (2009): "A survey of particle swarm optimization applications in electric power systems." IEEE transactions on evolutionary computation 13, no. 4 : 913-918.

Accepted Manuscript



Potential application of multi-walled carbon nanotubes/activated carbon/bamboo charcoal for efficient alcohol sensing

Vinay Kumar, Pawan K. Tyagi

PII: S0925-8388(18)32244-8

DOI: 10.1016/j.jallcom.2018.06.123

Reference: JALCOM 46459

To appear in: *Journal of Alloys and Compounds*

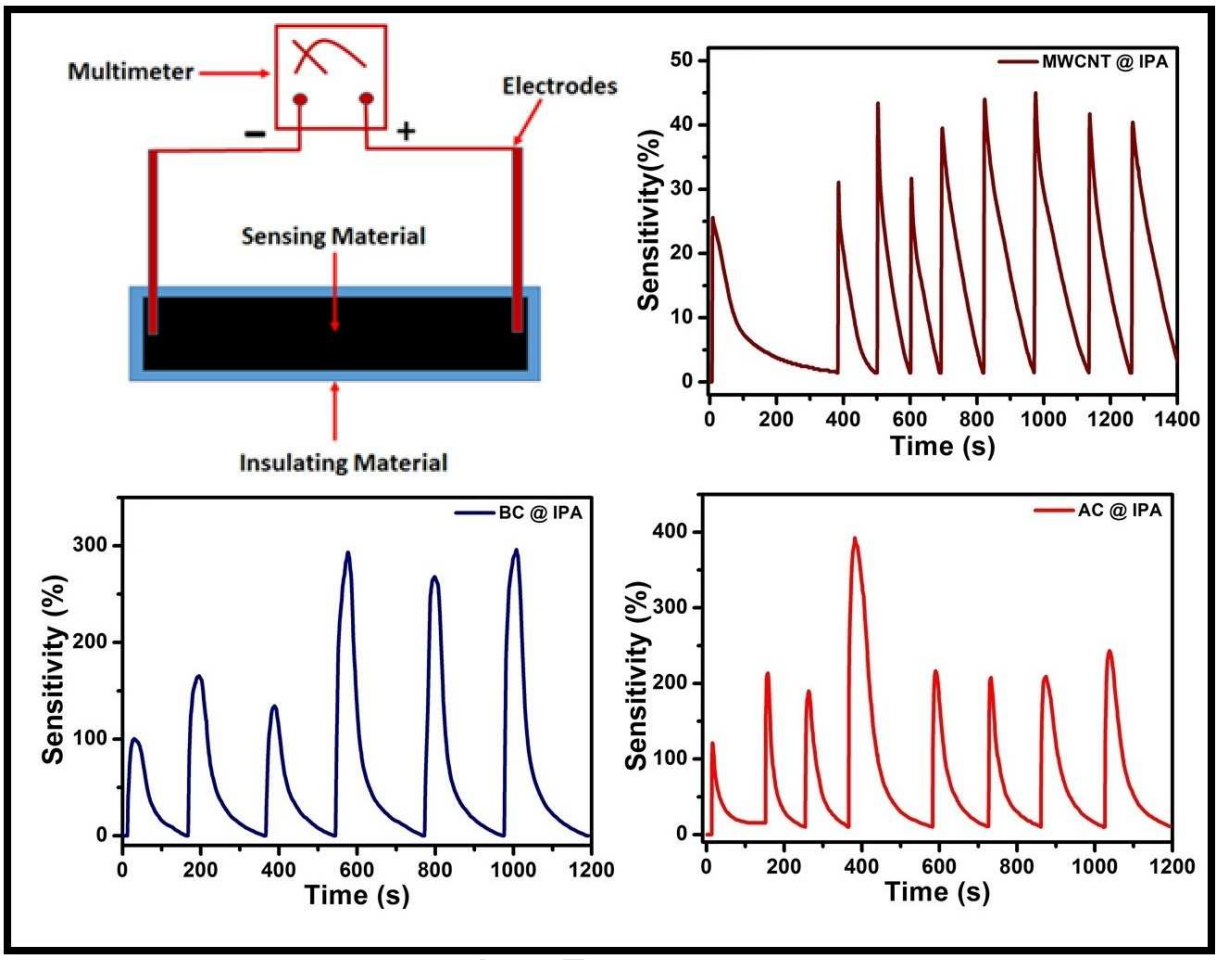
Received Date: 27 February 2018

Revised Date: 9 June 2018

Accepted Date: 12 June 2018

Please cite this article as: V. Kumar, P.K. Tyagi, Potential application of multi-walled carbon nanotubes/ activated carbon/bamboo charcoal for efficient alcohol sensing, *Journal of Alloys and Compounds* (2018), doi: 10.1016/j.jallcom.2018.06.123.

This is a PDF file of an unedited manuscript that has been accepted for publication. As a service to our customers we are providing this early version of the manuscript. The manuscript will undergo copyediting, typesetting, and review of the resulting proof before it is published in its final form. Please note that during the production process errors may be discovered which could affect the content, and all legal disclaimers that apply to the journal pertain.



ACCEPTED MANUSCRIPT

ACCEPTED MANUSCRIPT

Potential application of multi-walled carbon nanotubes/activated carbon/bamboo charcoal for efficient alcohol sensing

Vinay Kumar[1], Pawan K. Tyagi[1#]

[1]Department of Applied Physics, Delhi Technological University, Delhi-110042, India

Abstract

In the present work, multi-walled carbon nanotubes (MWCNTs), bamboo charcoal (BC) and activated carbon (AC) have been synthesized via thermal CVD technique by adopting fixed catalyst route and by simple pyrolysis, respectively. A two-terminal device has been fabricated using either MWCNTs, BC or AC as sensing material which was kept between the two terminals. This fabricated device was used for alcohol sensing at room temperature. In order to determine the sensitivity and detection limit, one droplet (~ 10 μL) of alcohol (CH_3OH, C_2H_5OH and IPA) as well as IPA/water mixture was drop casted on the sensing material and the variation of resistance with respect to time has been monitored. The plausible explation of detection has also been proposed taking into account the carriers tunneling between two disordered regions which was being wetted by alcohol molecules. We envision that the fabricated device might be a cost effective solution for the detection of pure as well as dilute isopropyl alcohol.

Keywords: Carbon nanotubes, activated carbon, bamboo charcoal, transmission electron microscopy, alcohol sensing

1. Introduction:

Recently, for alcohol detection many types of sensors such as optical, resistive, piezo-resistive, capacitive, gravimetric and magneto-elastic [1-5] have been demonstrated. In all reported devices, one basic perspective being high sensitivity towards physisorption of

#pawantyagi@dtu.ac.in, pawankumartyagi@gmail.com

alcohol molecules and other being selectivity. This originates from the susceptibility of electronic structure of sensing element towards absorbing molecules. Due to high surface area with high areal defect density, carbon nanomaterials have emerged as fascinating materials [6-13] for sensing applications. Among them, particularly carbon nanotubes (CNTs) have been successfully used for the sensing of gases such as NH_3, H_2, CH_4, NO, NO_2, etc. [14-17]. In these reports, variation in sensitivity was reported to be due to the charge transfer between CNT and an absorbed gas molecule. In reported devices, usually either surface modified, oxidized or functionalized CNTs has been used [10]. Besides CNTs, other carbon nano materials (CNMs) have also been used in wide range of sensing applications mainly due to their sensitivity towards any physical and chemical change occurring locally [18]. In recent reports, Polanyi theory is adpoted to describe adsorption of molecules from gas as well as aqueous phases on carbon materials such as activated carbon, charcoal and CNTs [19-21]. According to this theory, adsorption capacity and affinity of carbon materials towards absorbents have two main aspects: one being limited by the potential space available on adsorbate for adsorbents and other being the strength of the net attractive forces between adsorbate and adsorbent. These attractive forces include van der Waals force as well as other forces caused due to hydrophobic effect, π–π electron-donor-acceptor interaction (EDA), hydrogen bonds, covalent and electrostatic interaction. Furthermore, in carbon materials the volume of adsorbent at a particular location depends upon the adsorption potential, i.e. energy required to remove the molecule from the location where attractive forces get minimized and on the effective separation between adsorbing molecule and surface atoms. Furthermore, in case of alcohol adsorption, the –OH group forms hydrogen bonds with graphite sheets of CNMs, where the benzene rings of graphite sheet act as the hydrogen–bonding acceptor [19, 22]. It has also been reported that hydrogen bonds can also be formed between an organic molecule and CNMs if functional groups such as –COOH and –OH are present on the

surface of CNMs [23, 24]. These functional groups act as hydrogen-bonding donors. In further advances, hydrogen-bonding between a water molecule and functional groups present on CNMs was reported to be stronger than that between organic molecules and CNMs [19, 24, 25]. Previously, it was reported that covalent interaction between alcohol and CNMs occurs if they have functional groups such as –COOH, –OH and $–NH_2$. This bonding interaction is much stronger than above-mentioned interactions.

Furthermore, bamboo charcoal (BC) has emerged as promising adsorbent material due to its cost-effectiveness, renewability and environment-friendly nature [26]. In recent advances, due to their porous structure and large surface area as-produced and modified BC can adsorb many contaminants such as antibiotics [27], dibenzothiophene [28], nitrate-nitrogen [29], N-vinylpyrrolidone [30] in wastewater. Previously, Liao *et.al* [31] reported that BC and microwave assisted modify BC can be used for the adsorption of methylene blue (MB) as well as acid oragne7 (AO7) in water. They found that hydrophobic, π-π and electrostatic interactions are mainly responsible for the adsorption of dyes instead of surface area, pore volume and H-bond interaction. As reported that in carbon-based absorbents, π-π interaction plays an important role in governing the adsorption of molecules which either accept or donate π-electron to graphene surfaces. Since, both AC and BC have a large fraction of graphene surface, therefore can be explored in sensing application. Recently, Lucky Krishnai *et.al* [32] have reported that various carbonaceous structures such as 3D nanographene oxide (3D-NGO), graphite nanodots (GNDs), carbon nanotubes (CNTs), and carbon onions are present in activated carbon (AC) which was produced from pyrolysis of sugarcane bagasse. Their reported field emission studies reveal that as-pyrolyzed AC has semiconducting nature. In other application, S.C. Rabelo *et al.* [33] reported the usage of sugarcane bagasse for the production of bioethanol, methane and heat production in a bio-refinery but till date it is not used for alcohol sensing. In another report, Jiangtao Zhu *et al.*

[34] demonstrated the synthesis of MWCNTs from bamboo charcoal and investigated the role minerals in CNT growth.

In this work, we have successfully demonstrated that detection of alcohol such as iso-propyl alcohol, methanol and ethanol using a simple device fabricated with MWCNTs/BC/AC as a sensing element. The plausible explanation of detection is explained taking into account Polanyi theory and carrier's tunneling between two disordered regions which was being wetted by alcohol molecules. The comparative study reveals that BC and AC have higher sensitivity in comparison to MWCNTs whereas MWCNTs exhibit faster response and recovery time.

2. Experimental details:

2.1 Synthesis of MWCNTs:

MWCNTs were grown by using thermal chemical vapour deposition (Thermal-CVD) technique. Details of Thermal-CVD system have been reported elsewhere [35]. In our procedure, 25 mL solution of ferrocene/toluene mixture was taken. In this solution ferrocene was dissolved in toluene at a ratio of 0.02 g mL^{-1} and then sonicated before feeding into a pre-heating zone with a rate of 0.2 mL/minute. In order to ensure vapors of the mixture passed in reactor, hydrogen was used as carrier gas and flow rate was optimized and kept at 100 sccm. The growth temperature was kept at 840°C. After completation of the growth process, system was allowed to cool down upto 200 $^{\circ}$C in the presence of H_2 and then as-deposited MWCNTs were scratched from the wall of quartz reactor and characterized by using SEM (Hitachi S3700 N) and high-resolution transmission electron microscope (JEOL JEM 2010 operated at 200 kV).

2.2 Pyrolysis of bamboo charcoal:

Fresh bamboo was collected from a tree grown in Delhi region. The culms of bamboo were cut in the pieces of 5 mm wide by using a knife. Outer coverings of culms were

removed and only the inner part of bamboo stem used in the pyrolysis process. In the pyrolysis process, self-thermochemical decomposition of bamboo culms at high temperature (1250 °C) for 12 hrs was carried out in an argon atmosphere. A heating rate was kept at 5°C/min to minimize the thermal stress that may occur during the pyrolysis. The produced charcoals were allowed to cool down to 200 °C naturally in the inert atmosphere. More details of process have been reported elsewhere [36].

2.3 Pyrolysis of activated carbon:

Activated carbon was produced by the pyrolysis of crushed powder of extracted sugarcane bagasse. Pyrolysis was carried out at 550 °C in the presence of argon atmosphere. More details of process are given in Ref. [32].

2.4 Device fabrication and sensing measurement:

To fabricate the device, initially small amount of used carbonaceous structures were dispersed uniformly on a non-conducting flexible substrates (adhesive plastic tape) of the same area i.e.1 cm × 1 cm. Areal densities of MWCNTs, AC and BC in coated film was kept 15 mg/cm^2. In order to make firmly adhered film, coating of used carbon materials have been done adhesive plastic tape and adherence was further tested with sudden jerking of the carbon film. Schematic representation of the steps involved in device fabrication and sensing is shown in Figure 1. As shown in Fig. 1, black region between two copper electrodes is either MWCNTs, BC or AC. The electrical contacts were made on the top of film using cello tape, and crocodile clip and then fabricated device was used for resistivity measurement. Initially, resistance (R_0) was measured to insure the connectivity and then 1-10 μL pure alcohol was drop casted using syringe pump between two electrodes.

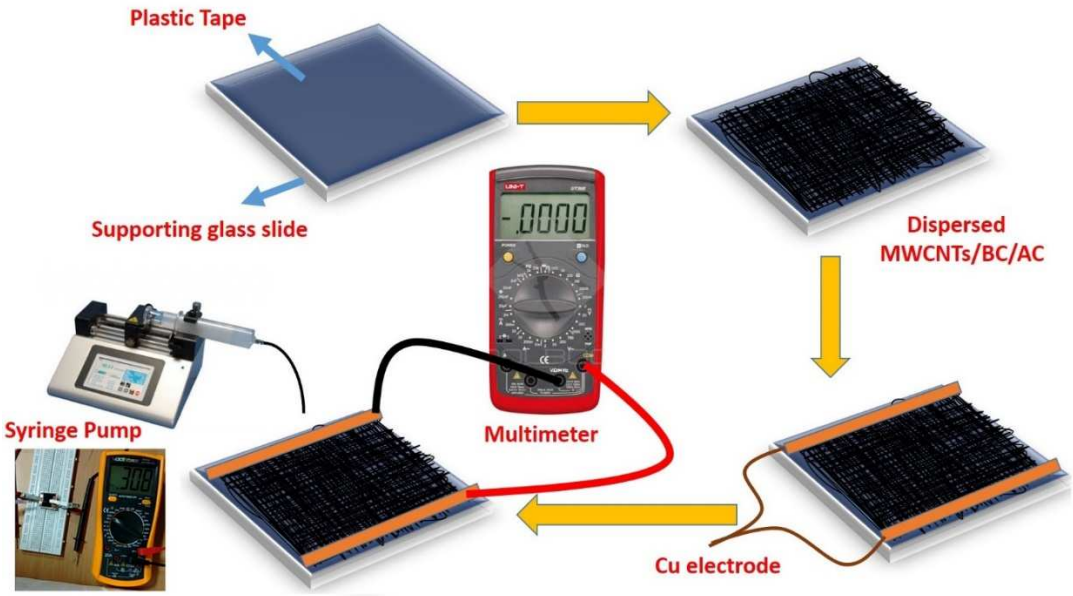


Figure. 1: Schematic representation of the steps involved in device fabrication and sensing.

3. Result and Discussion:

3.1 Characterization of carbon materials:

The surface morphology of MWCNTs, BC and AC was examined and SEM micrographs have been shown in Figs. 2a, 3a and 4a, respectively. As shown in Fig. 2a, most of the as-grown MWCNTs possesses a uniform diameter and length. The diameter of MWCNTs was found to be in the range of 25-35 nm whereas length in micron. SEM micrograph of BC (Fig.3a) reveals that BC is porous in nature and observed particles were identified as silicon oxide which were either embedded or present in the pores. These particles were spherical in shape with a diameter in the range of 2-5 µm. As shown in Figs.4a &b, SEM micrographs of as-prepared AC were taken at different magnification and reveal that the AC possesses non-uniform sheet-like structure. These samples were further characterized via EDX for elemental analysis. The colored version in the lower part of Fig. 2, Fig. 3 and Fig. 4 are the EDX spectral mapping images of MWCNTs, BC, and AC, respectively. The elemental mapping of MWCNTs reveals that rich carbon contents were present with iron either as a catalyst impurity or filler inside the CNT core in the form of Fe_3C. Mapping of BC in lower panels in Fig. 3 reveals that carbon and silicon were the major

contents along with some impurities like potassium (K) and magnesium (Mg). Similarly, we have performed the spectral mapping on AC as shown in lower part of Fig. 4 confirming the presence of carbon along with potassium (K) and calcium (Ca). Bright field TEM micrograph of MWCNT (Fig.2b) reveals that few CNTs is partially filled with Fe_3C as confirmed by lattice imaging and XRD analysis (results not shown), and TEM micrograph of BC (Fig, 3b) reveals that spherical nanoparticles of Si have diameter in range 0.5-2 μm and distributed uniformly in BC.

ACCEPTED MANUSCRIPT

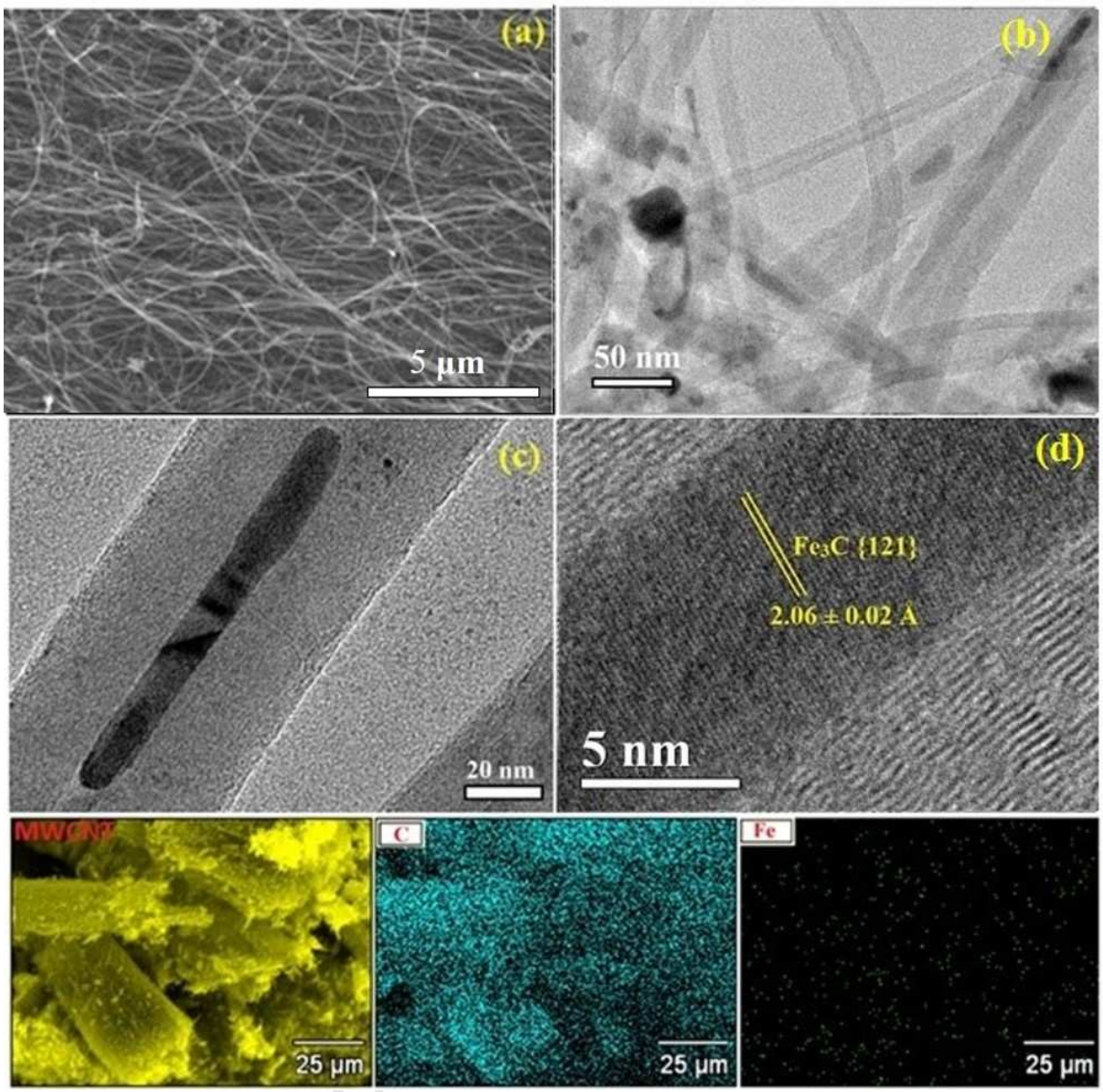


Figure 2: (a) Scanning electron microscopy image of MWCNTs used for device fabrication, (b) Bright field (BF) transmission electron microscopy image of un-filled MWCNTs, (c) BF image of filled-MWCNT, (d) high-resoluation lattice image illustarting lattice of both catalyst and MWCNT. In the lower panel EDX spectral mapping of MWCNT has been shown.

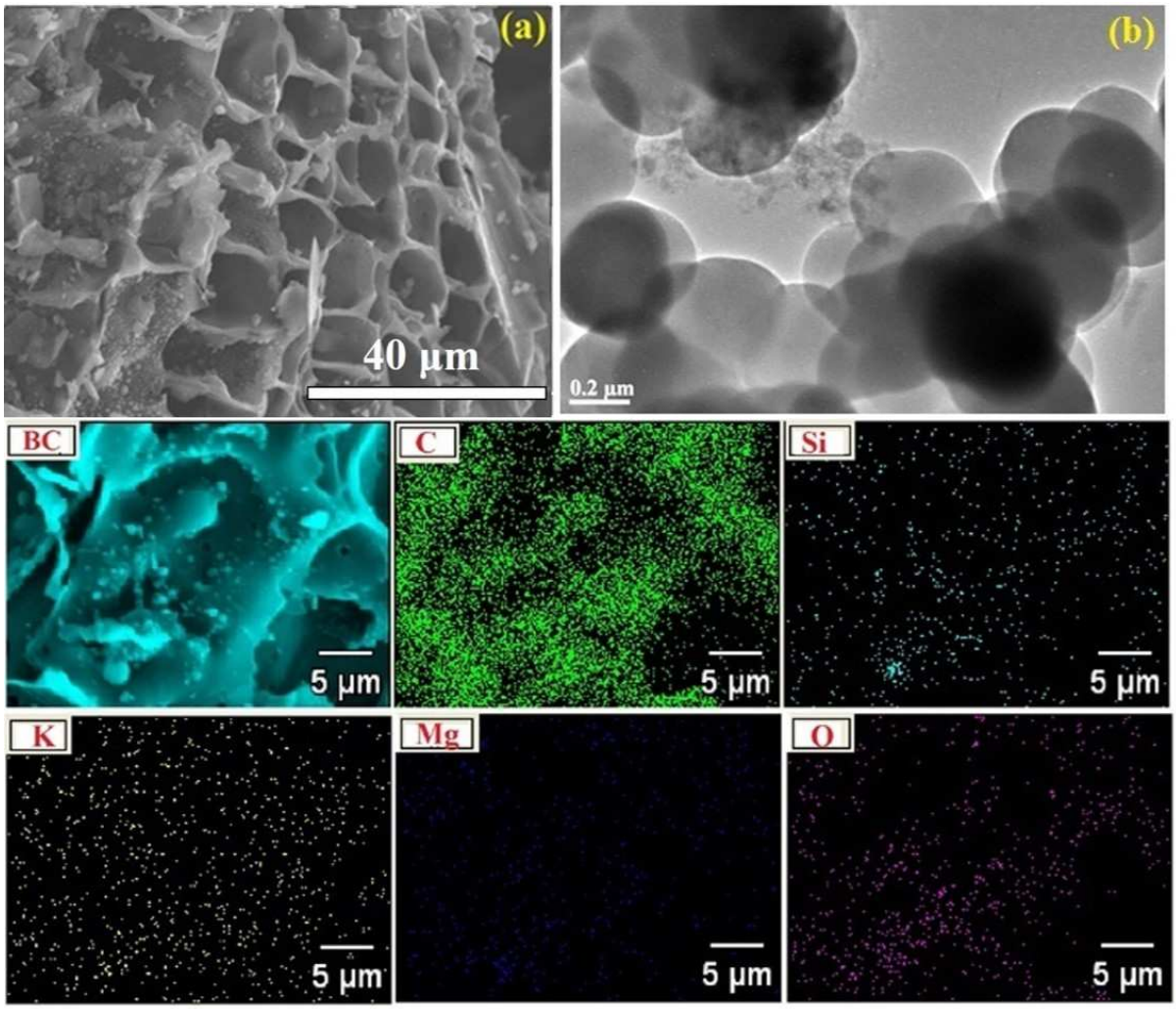


Figure 3: (a) SEM micrograph of bamboo charcol (BC) used for device fabrication, (b) Bright field (BF) transmission electron microscopy image of SiO_2 particle embeded in BC. In the lower panel EDX spectral mapping of BC illustartion the distribution of mapped elements.

ACCEPTED

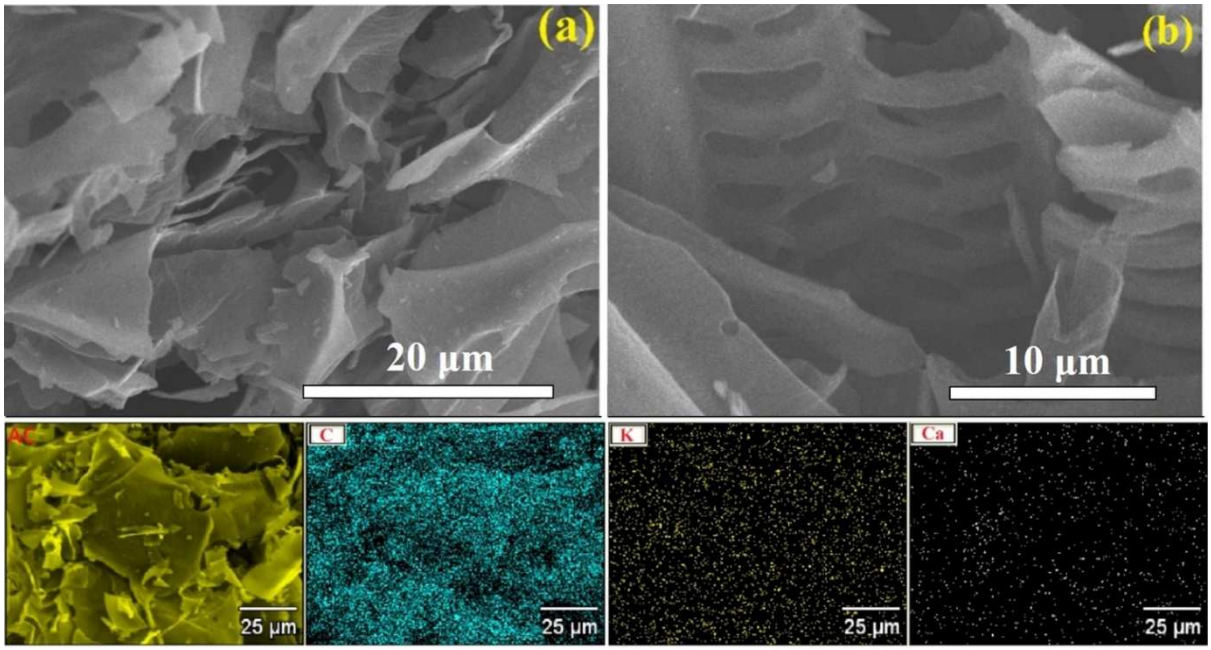


Figure 4: (a-b) SEM micrographs of activated carbon captured different magnification. In the lower panel EDX spectral mapping of BC illustartion the distribution of mapped elements.

3.2 Sensing measurement:

Sensitivity was monitored taking into account the variation of resistance with time as shown in Figs. 5 (a, c & e) for MWCNTs, BC and AC, respectively. Here, sensitivity is defined as:

$$\text{Sensitivity (S)} = \frac{\Delta R}{R_0} \times 100 = \frac{(R - R_0)}{R_0} \times 100$$

Where, R_0 and R are the resistance before or after adsorption of alcohol, respectively. High sensitivity (~ 200 %) was observed in AC which is approximately five time higher than that for crystalline and ordered sp^2 bonded network of MWCNTs. In the present case, the sensor is working on the principle of adsorption and desorption of alcohol molecules on the surface of the used carbonaceous structures. This can be evidenced by the fast recovery time of ~ 90 s, 150 s and 100 s in MWCNTs, BC, and AC, respectively as shown in Figs. 5 b, d & f. There is a possibility that evaporation of IPA might change integrity of film but this possibility is negligible as evidenced by nearly 100 % recovery of resistivity as shown in Fig. 5. Therefore,

we presume that resistance increases either due to charge transfer between sensing material and alcohol molecules, carrier's scattering with alcohol molecule or electron tunneling at the CNT-CNT junctions. Considering first case, if charge transfer is taking place then resistance will not change after desorption of IPA molecules. Post-desorption reduction in resistance is only possible if scattering occurs. As per our observation when IPA is drop casted, first resistance increases linearly and then decreases exponentially. This exponential decrement can be understood as when volume of adsorbed IPA molecules reduces due to desorption. This reduction depends exponentially on the adsorption potential as well as the strength of attractive field forces. As reported by Daria Samazna *et.al* [37] and Ritu Malik *et.al* [38] charge transfer between absorbent like alcohol and volatile organic compounds (VOCs) on Buckminsterfullerene and carbon nanomaterials occurred which enhances optical and electrical properties of the host. This enhancement in electrical conductivity has been monitored to detect the VOCs. Our observation was in well agreement with these reports. In our case, the response (R/Ro) is found to be 4 for ethanol detection using BC which is nearly equivalent to 5 as reported in graphitic carbon nitride [38]. Furthermore, all the measurements have been repeated and found to be consistent. In order to check the reusality of device after one year IPA sensing was again performed using the same device and perfornace was found to be consistant (Fig.6).

ACCEPTED MANUSCRIPT

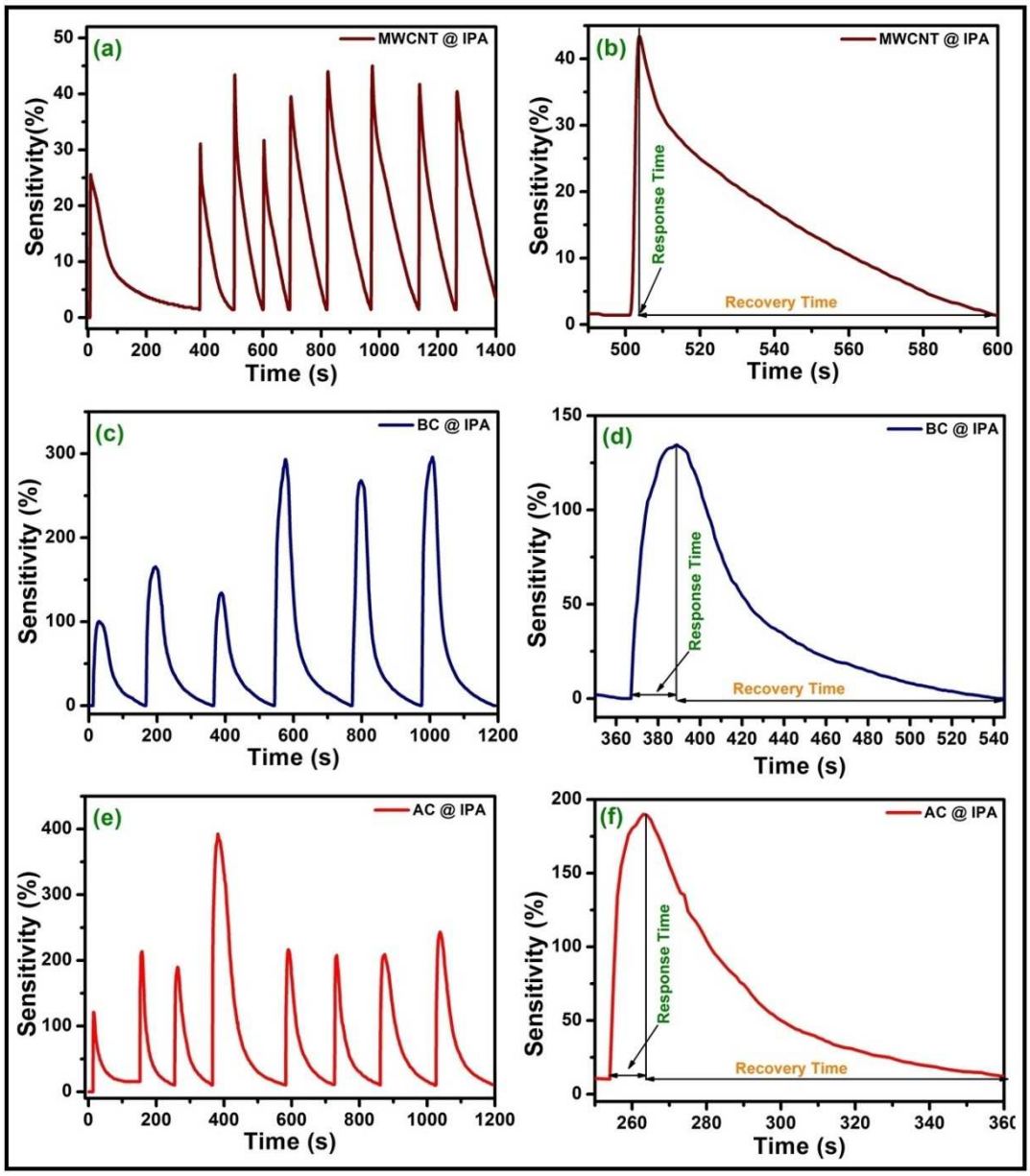


Figure 5: (a, c & e) Sensitivity plot depicted performance of device fabricated using MWCNTs, BC and AC, respectively. (b, d & f) Response as well as recovery time was illustrated.

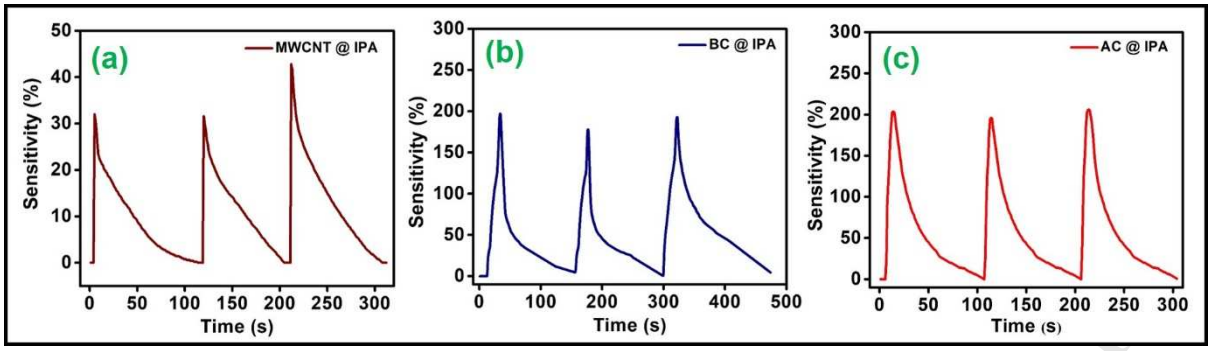


Figure 6: IPA sensing using same device fabricated with (a) MWCNTs, (b) BC and (c) AC for reusability test.

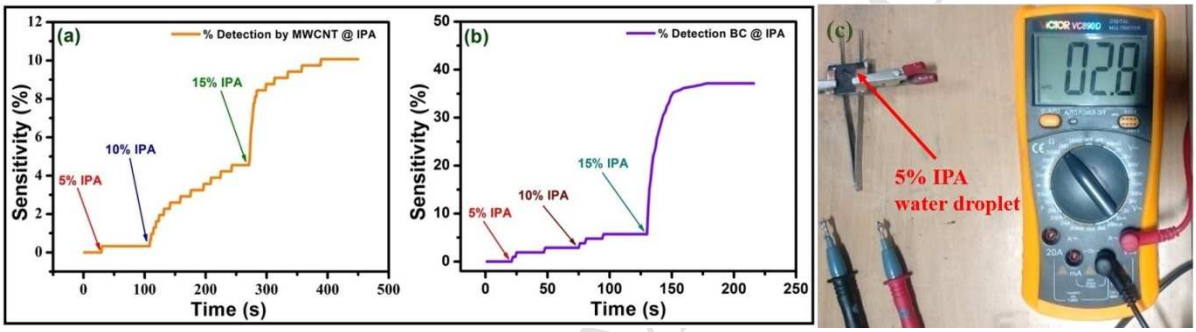


Figure 7: Plot representing percentage detection limit of device fabricated using (a) MWCNT, (b) BC. and (c) optical image of the device displaying resistance increases from 2.6 KΩ to 2.8 KΩ after drop casting 5% IPA/water mixture on BC as a film.



Figure 8: (a-b) Variation of resistance in device fabricated using BC before and after casting of pure water, respectively. (c) Variation after drop casting on AC

As reported by Fabian Schutt et.al [18] in MWCNTs film highly conductivity pathways formed on surface of film. Therefore, an explicit interpretation of resistance variation can be given as: initially, as liquid was drop casted on the sensing element (MWCNTs/AC/BC) it starts percolating through the CNT-CNT junction and through the pores in case of BC and AC. Consequently effective separation at CNT-CNT junction and pore interface increases. J. Lee *et. al*. [39] reported that the resistance variation occurs due to the number of formed CNT-CNT junctions as well as percolated pathway through which electrons must tunnel. During electron tunneling, barrier at CNT-CNT and pore interface increases [39] and reduces the tunneling probability. This finally increases the resistance of network. In the present case, the observed fast response time is dependent on the percolation rate whereas recovery time depends on desorption rate. In order to determine the detection limit IPA was diluted to 5 % (~0.05µL) and then sensing performance was monitored as shown in Figs.7 (a-c). We have further tested the device for pure water, and it was observed that resistance does not change in case of MWCNTs as well as BC as shown in Figs. 8(a&b). This might be due to the hydrophobic nature of these materials. Contrarily, resistance increased in case of AC which may be due to its hydrophilic nature. Hence, it can be concluded that 5 % IPA diluted in pure water can be easily detected using this device. Furthermore, as evident from Fig. 7 (c), after drop casting 5% IPA/water mixture on BC resistance increases from 2.66 kΩ to 2.8 kΩ. This confirms that IPA-water mixture does not make the short circuit in BC films. The device was further tested for sensing of ethanol and methanol. As shown in Fig. 9, for device made of MWCNT and BC the sensitivity was found to nearly equal for both ethanol and methanol whereas in case of AC it decreased to 50 % than that observed for IPA. These result confirm that device can used for other alcohols too.

Table 1: Tabulation of sensing parameters for each sensing element

Sensing Material	Response Time (s)	Recovery Time (s)	Sensitivity (%)
MWCNT	1.3	95.7	40
Activated carbon (AC)	9.7	97.5	200
Bamboo charcoal (BC)	22	152.6	175-200

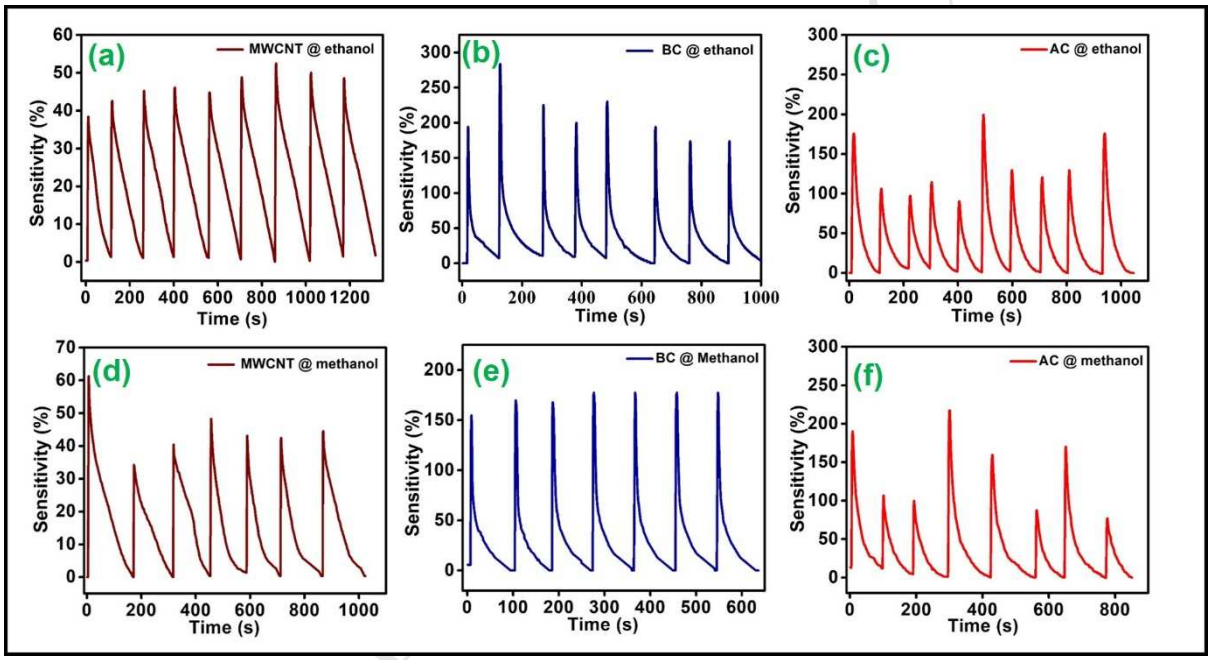


Figure 9: Sensitivity plot depicted performance of device fabricated using MWCNTs, BC and AC (a, b &c) for ethanol and (d, e & f) for methanol respectively.

Conclusion:

In summary, a simple device has been fabricated for sensing of alcohol by using a film of MWCNTs/BC/AC (sensing element) deposited on a non-conducting plastic substrate. The fabricated device was operated at room temperature and atmospheric pressure. Sensitivity was found to be high in case of AC and BC in comparison to MWCNTs whereas in terms of detection limit MWCNTs prove to be the superior ones. The present concept of device fabrication using these carbon materials as sensing elements is two-fold. Firstly, it would

improve the detection limit of various alcohols diluted in water and in the other hand it would explore the potential application of these low-cost new materials (AC and BC) as sensing elements.

Acknowledgements:

We would like to thank Mr. Sandeep Mishra, Advanced instrumentation lab DTU for obtaining SEM images, EDX mapping, and XRD.

Conflicts of Interest

The authors declare no conflicts of interest.

References:

[1] A.R. Zarei, B. Ghazanchayi, Design and fabrication of optical chemical sensor for detection of nitroaromatic explosives based on fluorescence quenching of phenol red immobilized poly (vinyl alcohol) membrane, *Talanta.* 150 (2016) 162–168.

[2] P.X. Zhao, Y. Tang, J. Mao, Y.X. Chen, H. Song, J.W. Wang, Y. Song, Y.Q. Liang, X.M. Zhang, One-Dimensional MoS_2-Decorated TiO_2 nanotube gas sensors for efficient alcohol sensing, *J. Alloys Compd.* 674 (2016) 252–258 .

[3] L. Janovák, D. Kovács, A. Sápi, D.G. Dobó, Á. Kukovecz, Z. Kónya, I. Dékány, Room temperature ethanol sensor with sub-ppm detection limit : Improving the optical response by using mesoporous silica foam, *Sensors and Actuators B: Chem.* 243 (2017) 1205–1213.

[4] M.S. Hosseini, S. Zeinali, M.H. Sheikhi, Fabrication of capacitive sensor based on Cu-BTC (MOF-199) nanoporous film for detection of ethanol and methanol vapors, *Sensors Actuators: B Chem.* 230 (2016) 9–16.

[5] V. Mahendran, J. Philip, A methanol sensor based on stimulus-responsive magnetic nanoemulsions, *Sensors and Actuators: B chemical* 185 (2013) 488– 495

[6] M. Penza, G. Cassano, P. Aversa, F. Antolini, A. Cusano, M. Consales, M. Giordano, L. Nicolais, Carbon nanotubes-coated multi-transducing sensors for VOCs detection, *Sensors and Actuators B* 112 (2005) 171–180.

[7] J. Kong, N.R. Franklin, C. Zhou, Nanotube Molecular Wires as Chemical Sensors, *Science*, 287 (2000) 622–625.

[8] H. Dai, Carbon Nanotubes : Synthesis , Integration , and Properties, *Acc. Chem. Res* 35 (2002) 1035–1044.

[9] M. Penza, F. Antolini, M.V. Antisari, Carbon nanotubes as SAW chemical sensors materials, *Sensors and Actuators B. chemical.* 100 (2004) 47–59.

[10] J. Choi, E.J. Park, D.W. Park, S.E. Shim, MWCNT – OH adsorbed electrospun nylon 6 , 6 nanofibers chemiresistor and their application in low molecular weight alcohol vapours sensing, *Synthetic Metals* 160 (2010) 2664–2669.

[11] K.P.S.S. Hembram, Origin of structural defects in multiwall carbon nanotube, *Materials Letters* 72 (2012) 68–70.

[12] H.J. Choi, J. Ihm, S.G. Louie, M.L. Cohen, Defects , Quasibound States , and Quantum Conductance in Metallic Carbon Nanotubes, *Phy. Rev. Lett.* 84 (2000) 2917–2920.

[13] Y. V Shtogun, L.M. Woods, Electronic and magnetic properties of deformed and defective single wall carbon nanotubes, *Carbon* 47 (2009) 3252–3262.

[14] S. Abdulla, T.L. Mathew, B. Pullithadathil, Highly sensitive, room temperature gas sensor based on polyaniline-multiwalled carbon nanotubes (PANI/MWCNTs) nanocomposite for trace-level ammonia detection, *Sensors Actuators, B Chemical*. 221 (2015) 1523–1534.

[15] U. Yaqoob, A.S.M.I. Uddin, G. Chung, Sensors and Actuators B : Chemical Foldable hydrogen sensor using Pd nanocubes dispersed into multiwall carbon nanotubes-reduced graphene oxide network assembled on nylon filter membrane, *Sensors and Actuators B: Chemical* 229 (2016) 355–361.

[16] Z. Li, J. Li, X. Wu, S. Shuang, C. Dong, M.M.F. Choi, Sensors and Actuators B : Chemical Methane sensor based on nanocomposite of palladium/multi-walled carbon nanotubes grafted with 1,6-hexanediamine, *Sensors and Actuators B: Chemical* 139 (2009) 453–459.

[17] Y. Li, M. Hodak, W. Lu, J. Bernholc, Mechanisms of NH_3 and NO_2 detection in carbon-nanotube-based sensors : An ab initio investigation, *Carbon* 101 (2016) 177–183.

[18] F. Schütt, S. Signetti, H. Krüger, S. Röder, D. Smazna, S. Kaps, S.N. Gorb, Y.K. Mishra, N.M. Pugno, R. Adelung, Hierarchical self-entangled carbon nanotube tube networks , Nat. Commun. 8 (2017) 1215.

[19] K. Yang, B. Xing, Adsorption of organic compound by carbon nanomaterials in aqueous phase: Polanyi theory and its application, *Chemical Review* 110 (2010) 5989-6008.

[20] Manes, M. In: Encyclopedia of environmental analysis and remediation; Meyers, R. A., Eds.; John Wiley & Sons: New York, 1998; p 26.

[21] J. C. Crittenden, S. Sonongraj, J. L. Bulloch, D. W. Hand, T. F. Speth, M. Ulmer, Corelation of aqueous-phase adsorption isotherm, *Environ. Sci. Technol* 33(1999), 2926-2933.

[22] K. Yang, W. Wu, Q. Jing, L. Zhu, Aqueous adsorption of aniline, phenol, and their substitutes by multi-walled carbon nanotubes, *Environ. Sci. Technol* 42 (2008), 7931–7936.

[23] M. Franz, H. A. Arafat, N. G. Pinto, Effect of chemical surface heterogeneity on the adsorption mechanism of dissolved aromatics on activated carbon, *Carbon* 38 (2000), 1807-1819.

[24] F. Ahnert, H. A. Arafat, N. G. Pinto, A study of the influence of hydrophobicity of activated carbon on the adsorption equilibrium of aromatics in non-aqueous media, *Adsorption*, 9 (2003), 311-319.

[25] E. A. Muller, L. F. Rull, L. F. Vega, K. E. Gubbins, Adsorption of water on activated carbons: a molecular simulation study, J. Phys. Chem.,100 (1996), 1189-1196.

[26] P. Liao, S. Yuan, W. Xie, W. Zhang, M. Tong, K. Wang, Adsorption of nitrogen-heterocyclic compounds on bamboo charcoal: Kinetics, thermodynamics, and microwave regeneration, *Journal of Colloid and Interface Science*, 390 (2013) 189–195.

[27] Y. Fan, B. Wang, S. Yuan, X. Wu, J. Chen, L. Wang, Adsorptive removal of chloramphenicol from wastewater by NaOH modified bamboo charcoal, *Bioresource Technology* 101 (2010) 7661–7664.

[28] D. Zhao, J. Zhang, E. Duan, J. Wang, Adsorption equilibrium and kinetics of dibenzothiophene from n-octane on bamboo charcoal, *Applied Surface Science* 254 (2008) 3242–3247.

[29] K. Mizuta, T. Matsumoto, Y. Hatate, K. Nishihara, T. Nakanishi, Removal of nitrate-nitrogen from drinking water using bamboo powder charcoal, *Bioresource Technology* 95 (2004) 255‑257.

[30] S. Li, D. Umereweneza, Adsorption of N-Vinylpyrrolidone from polyvinylpyrrolidone solution onto bamboo-based activated carbon, *Separation Science and Technology*, 47 (2012) 104-111.

[31] P. Liao, Z. M. Ismael, W. Zhang, S. Yuan, M. Tong, K. Wang, J. Bao, Adsorption of dyes from aqueous solutions by microwave modified bamboo charcoal, *Chemical Engineering Journal* 195–196 (2012) 339–346

[32] L. Krishnia, B.S. Yadav, U. Palnitkar, P. V Satyam, B. Kumar, N.A. Koratkar, P.K. Tyagi, As-pyrolyzed sugarcane bagasse possessing exotic field emission properties, Appl. Surf. Sci. 443 (2018) 184–190.

[33] S.C. Rabeloa, H. Carrere, R. Maciel Filho, A.C. Costa, Production of bioethanol, methane and heat from sugarcane bagasse in a biorefinery concept, *Bioresource Technology*, 102, (2011) 7887-7895

[34] Jiangtao Zhu, Juncai Jia, Fung Luen Kwong, Dickon Hang Leung Ng, Sie Chin Tjong, Synthesis of multiwalled carbon nanotubes from bamboo charcoal and the roles of minerals on their growth, *Biomass and Bioenergy* 36 (2012) 12–19

[35] R. Kumari, L. Krishnia, V. Kumar, S. Singh, H. K. Singh, R. K. Kotnala, R. R. Juluri, U. M. Bhatta, P. V. Satyam, B. S. Yadav, Z. Naqvi, P. K. Tyagi, Fe_3C-filled carbon nanotubes: permanent cylindrical nanomagnets possessing exotic magnetic properties, *Nanoscale*, 8 (2016) 4299-4310.

[36] V. Kumar, P. Tiwari, L. Krishnia, R. Kumari, A. Singh, A. Ghosh, Green route synthesis of silicon/silicon oxide from bamboo, *Advacced Material Letters* 7 (2016) 271–276.

[37] S. Shree, V. Postica, G. Neubüser, A.F. Martins, N. Ben Sedrine, N.K. Jena, L. Siebert, F. Schütt, O. Lupan, R. Ahuja, M.R.P. Correia, T. Monteiro, L. Kienle, Y. Yang, Y.K. Mishra, R. Adelung, Buckminsterfullerene Hybridized Zinc Oxide Tetrapods: Defects and Charge Transfer Induced Optical and Electrical Response, Nanoscale,10 (2018) 10050-10062.

[38] R. Malik, V. K. Tomer, T. Dankwort, Y. K. Mishra and L. Kienle, Cubic mesoporous Pd-WO3 loaded graphitic carbon nitride (g-CN) nanohybrids: Highly sensitive and temperature dependent VOCs sensors Materials Chemistry A, (2018).

[39] J. Lee, I.Y. Stein, M.E. Devoe, D.J. Lewis, N. Lachman, S.S. Kessler, T. Samuel, B.L. Wardle, networks Impact of carbon nanotube length on electron transport in aligned carbon nanotube networks, 106 (2015) 53110.

ACCEPTED MANUSCRIPT

Research Highlights

Highlights of submitted work are as following:

- In fabricated device, MWCNTs, bamboo charcoal or activated carbon was used as sensing material.
- This fabricated device was used for alcohol (CH_3OH, C_2H_5OH and IPA) sensing.
- Taking into account carriers tunneling between disordered regions alcohol detection explained.
- Higher sensitivity was found for AC and BC in comparison to MWCNTs.
- The fabricated device might be a cost effective for the detection of pure as well as dilute IPA.

ACCEPTED MANUSCRIPT

Available online at www.sciencedirect.com

ScienceDirect

Procedia Computer Science 132 (2018) 563–571

Procedia Computer Science

www.elsevier.com/locate/procedia

International Conference on Computational Intelligence and Data Science (ICCIDS 2018)

Realization of class – A chopper using dSPACE

Akshat Jain[a,*], Dheeraj Joshi[a]

[a]Electrical Engineering Department, Delhi Technological University, Shahabad Daulatpur, New Delhi-110042, India

Abstract

This paper describes the designing and analysis of a class – A Chopper in open loop as well as closed loop control. This paper aims to put up the results based on software as well as hardware simulation. DC chopper is realized by using dSPACE DS1104 for open loop operation of class – A chopper with resistive load. In this paper, computed values are compared with measured values and accordingly error is calculated. In closed loop control of chopper, voltage control strategy is implemented using MATLAB 2016a. Improved results illustrate the effectiveness of closed loop control strategy.

© 2018 The Authors. Published by Elsevier Ltd.
This is an open access article under the CC BY-NC-ND license (https://creativecommons.org/licenses/by-nc-nd/3.0/)
Peer-review under responsibility of the scientific committee of the International Conference on Computational Intelligence and Data Science (ICCIDS 2018).

Keywords: Class – A DC Chopper; dSPACE 1104; Ripple Factor; RMS voltage; Output Average Voltage; Voltage Control

1. Introduction

Digital Signal Processing (DSP) has entangled its root in almost all parts of world. It has become an integral part of various developments across the world. In earlier practice there were a lot of switching schemes for switching of fast devices. Lot of commutations was implemented in those switching schemes. These switching schemes can be made much easier by using the applications of Digital Signal Processing. Implementation of Digital Signal Processing is slowly replacing the conventional switching schemes of power devices.

* Telephone: +91-9729038102
Email address: akshat21jain@gmail.com

1877-0509 © 2018 The Authors. Published by Elsevier Ltd.
This is an open access article under the CC BY-NC-ND license (https://creativecommons.org/licenses/by-nc-nd/3.0/)
Peer-review under responsibility of the scientific committee of the International Conference on Computational Intelligence and Data Science (ICCIDS 2018).
10.1016/j.procs.2018.05.010

There are many researches that are done on DC choppers and their closed loop control. In 1980, Takahiko Iida and group used the thyristor based DC chopper for DC motor control [3]. In 2004, ripple of DC converters was analysis [5]. In 2007, Huangsheng Xu, used DC chopper to control speed and current of universal motors using microcontroller [8]. In 2012, Anupam Agarwal designed a DC chopper to minimize the voltage ripple [1]. Then in 2014, Shun Takeuchi used current control technique for closed loop DC chopper. Then in 2017, Yifan Lang and group implemented the closed loop buck chopper with more refined outputs by triggering again by microcontroller 8052.

This paper includes the interfacing of MATLAB Simulink with dSPACE DS1104 R&D Controller Board, analyzing its applications and further using these applications for the switching of different converters. In this paper, author will implement Class – A DC Chopper by triggering it through dSPACE. Operation of Class – A DC chopper is done both in open loop as well as in closed loop, and finally the error is compared and calculated at different values.

2. Block diagram and circuit diagram

Operation of a Class – A DC chopper is generally based on the operation of a single power electronic switch like MOSFET, IGBT, Thyristor, GTO, BJT, etc. One needs to select the switch from the available choices depending upon the circuit requirement. For example, IGBTs are used for high power requirement devices and MOSFETs are used in circuits where high switching frequency is required. Thyristor can also be used in such a condition, but implementation of a thyristor controlled converter is a complex and tedious process as it requires a commutation circuit and thyristor operation support circuit for its operation. Instead of using such a tedious circuit, best practice is to use a single switch instead. Here as high frequency carrier wave is used for PWM signal generation as well as the circuit is operating with low power requirement, so MOSFET is used as a switch in the chopper.

2.1 Open Loop Class – A DC Chopper

Main objective of DC Chopper is to change the DC voltage level, either by stepping up the voltage or by stepping down the voltage. Class – A chopper is used to step down the DC voltage and is the most basic type of choppers used. It operates in first quadrant of V-I plane, which means both voltage as well as current will remain positive throughout the operation.

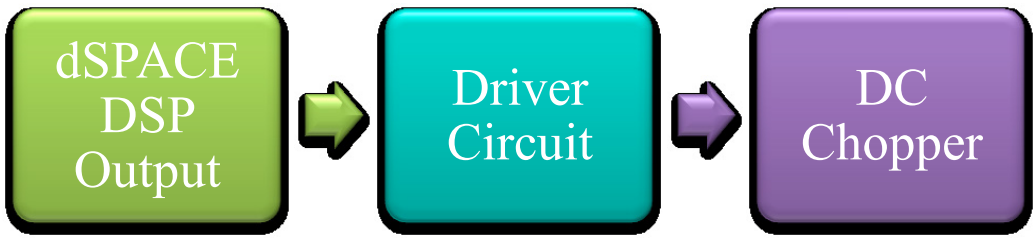


Figure 1: Block Diagram of open loop DC Chopper

Fig. 1 shows the block diagram of DC chopper operated in open loop mode. A constant input DC power supply is connected to the switch and then the output is obtained from the switch. For getting the desired output one needs to change the operating state of that switch as per the requirement, so accordingly switch has to be triggered by using some external medium. This external medium can be – microcontroller output, DSP kit output, dSPACE output, bistable or monostable operation of 555 IC, PWM generation ICs (LM5045, SG3525 and UC3843), etc. Here for this paper author has used dSPACE 1104 as the triggering medium as it has many advantages as compared to other triggering mediums. dSPACE 1104 have many PWM outputs, ADC inputs, DAC outputs and Digital input/output. It also provides the user with serial communication port (RS232 and RS485). Above all, it facilitates

the user with real time simulation and control of converter unlike other triggering mediums. It is required to connect a driver circuit between the output of dSPACE and the gate terminal of switch in order to isolate the dSPACE from hardware circuit such that any residual current may not damage the dSPACE. Driver circuit is also responsible for bringing the input voltage at gate to desired voltage level.

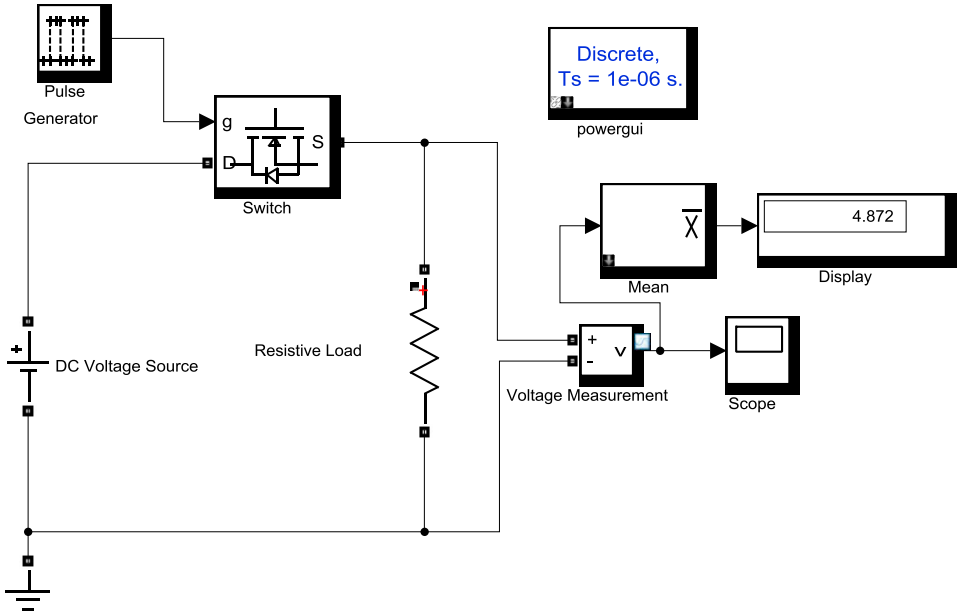


Figure 2: Schematic Diagram of open loop DC Chopper

As seen in figure 2, input DC voltage is connected at Drain terminal of MOSFET and load is connected at source terminal of MOSFET and to reference ground. A DC voltmeter is connected across the load to measure the average output voltage across the load. Gate terminal of MOSFET is receiving triggering signal. For convenience, instead of dSPACE block, a pulse generator block is used with exactly the same parameters defined as dSPACE block does not work in the absence of hardware circuit that is to be attached.

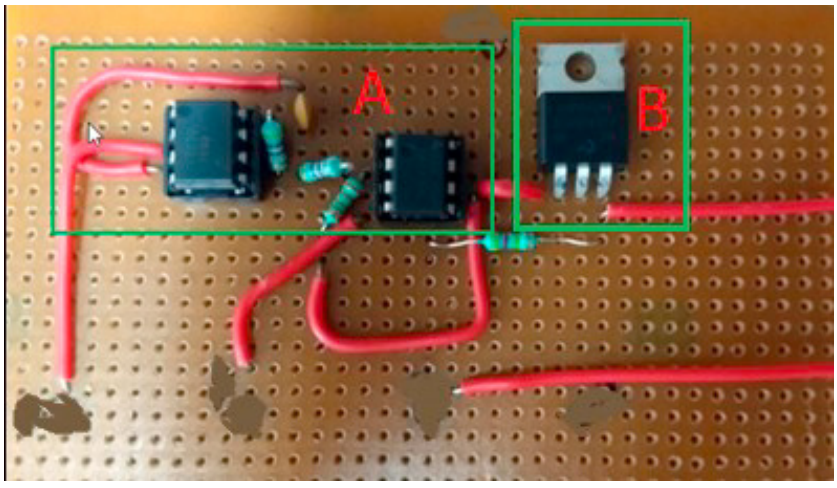


Figure 3: DC Chopper Circuit
A: Driver Cicuit; B: MOSFET IRF640N

Figure 3 shows the circuit of DC Chopper made on a general purpose PCB where details of A and B are shown in Appendix. In this circuit, a part of circuit is enclosed in a green box which is indicating the driver circuit. In this driver circuit, left IC is an optocoupler which is used for isolating the dSPACE from chopper circuit to prevent any reverse flow of current. It gives an output of magnitude between 3volts – 5volts and 180^0 out of phase. But to drive the given MOSFET at least 10V is recommended, so the output of optocoupler is fed to an OPAMP connected as an

inverting amplifier. This will not only amplify the voltage but also will bring the final output in phase of the dSPACE output.

2.2 *Closed Loop Class – A DC Chopper With Voltage Control*

Open loop DC chopper does not gives required error correction, so one needs to give error as feedback to input, forming a closed loop control strategy. Here, instead of taking a PWM signal for gate triggering, feedback signal is used for gate triggering. A voltage sensor is used to measure the output voltage of DC chopper. This measured value is then compared with some reference value to calculate error. This error is then fed back to the input through some appropriate controller, in order to minimize that error and finally obtaining the most accurate output possible. Block diagram of closed loop operation of class – A chopper is shown in figure 4.

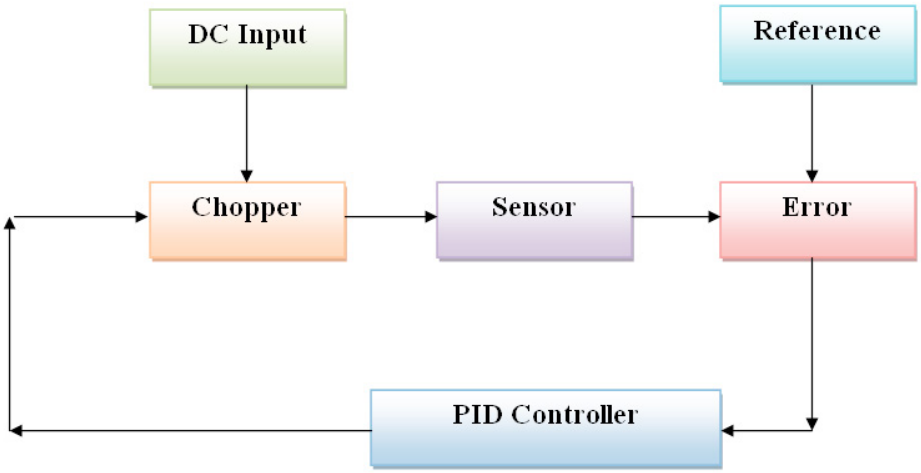


Figure 4: Block Diagram of Closed Loop DC Chopper

This chopper circuit is receiving some DC input through Drain terminal of MOSFET. Output of chopper is measured across the load by connecting a voltage sensor between Source terminal of MOSFET and reference ground. This output is now compared with some reference signal by using a comparator which will be the error in output. Now, the error signal is fed back to the gate terminal of MOSFET through a PI controller. Controller parameters are adjusted for optimum performance parameters. Output of PI controller is compared with a triangular wave of high frequency, so that number of samples increases in order to provide further better output.

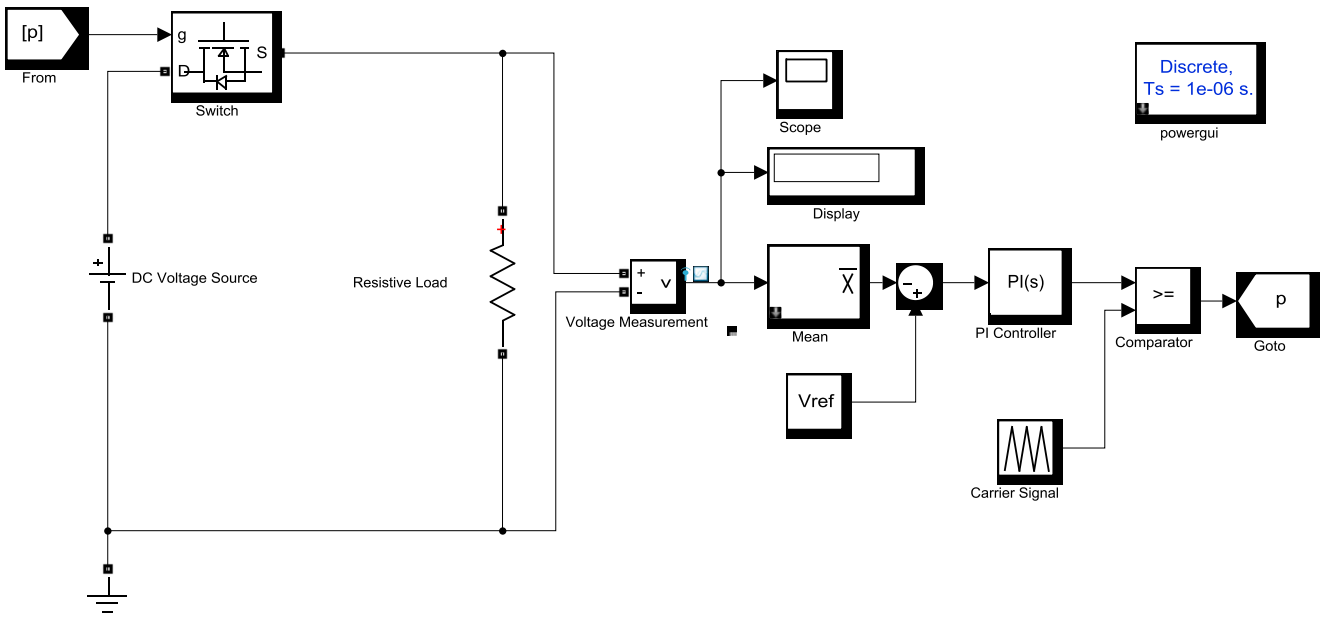


Figure 5: Schematic Diagram of Closed Loop DC Chopper

While implementing the schematic diagram (as shown in figure 5) on hardware, the same open loop DC chopper circuit (as shown in figure 3) can be used along with a voltage sensor connected across load. Output of voltage sensor is now fed to dSPACE through either its ADC terminal or Digital Input terminal. Further task of error calculation, PI control implementation and finally sampling is done through computer. In short dSPACE is not only facilitating an individual to trigger the switch but it is also reducing the complexity of the circuit by minimizing the hardware. It is also providing an inbuilt PI controller due to which need of external PI controller and its manual tuning has been eliminated. Output of the relational operator can be taken out of dSPACE through DAC terminal or Digital Output terminal of dSPACE workbox. This signal is further fed to Gate terminal of MOSFET for its triggering. Hardware implementation of closed loop control will be done later when closed loop control strategy will be finalized.

3. Results and calculations

3.1 Calculations

Mean value of a DC chopper is taken as output because the output obtained is a DC and for DC voltage, mean voltage is considered. So below are the necessary calculations that are done to calculate the error.

Duty cycle (D) = 50%

$$Mean\ Voltage\ (V_0) = Input\ DC\ Voltage\ (V_{in}) \times D \tag{1}$$

$$Mean\ Voltage\ (V_0) = Input\ DC\ Voltage\ (V_{in}) \times 0.5 \tag{2}$$

$$Relative\ Error = (Measured\ value - Calculated\ value) \tag{3}$$

$$Error = \frac{(Measured\ value - Calculated\ value) \times 100}{\text{Calculated value}} \tag{4}$$

Here is the error calculation for Open Loop DC Chopper,

Table 1: Error calculation for open loop DC chopper

Sr.No.	Actual Value (V)	Measured Value (V)	Relative Error (V)	Percentage Error (%)
1.	12	11.170	-0.830	-6.917
2.	11	10.240	-0.760	-6.909
3.	10	9.306	-0.694	-6.940
4.	9	8.375	-0.625	-6.944
5.	8	7.445	-0.555	-6.938
6.	7	6.514	-0.486	-6.943
7.	6	5.584	-0.416	-6.933
8.	5	4.653	-0.347	-6.940

As we can see in table 1, percentage error at all values lies from -6.905% to -6.945%. Generally, error should lie in ±5% tolerance but this error is more than the specified range. Negative sign signifies that measured value is less than the calculated value. Error calculation for closed loop control of DC chopper with voltage control strategy is tabulated below.

Table 2: Error calculation for closed loop DC chopper

Sr.No.	Actual Value (V)	Measured Value (V)	Relative Error (V)	Percentage Error (%)
1.	12	12.010	0.010	0.083
2.	11	11.030	0.030	0.273
3.	10	10.070	0.070	0.700
4.	9	9.074	0.074	0.822
5.	8	8.093	0.093	1.163
6.	7	7.111	0.111	1.586
7.	6	6.130	0.130	2.167
8.	5	5.150	0.150	3.000

After applying closed loop control to DC – chopper, it can be observe from table 2 that the percentage error has reduced to great extent and lies between 0.083% and 3%. It can be observed that as the reference voltage is getting decreased, percentage error is getting increased. It is also lying in ±5% tolerance band, which is acceptable.

3.2 Results

On running the simulation of open loop class – A DC chopper, one should obtain a waveform such that the amplitude should be positive and must be equal to DC input voltage (V_{in}) when switch is ON and output should be zero when the switch is OFF. Here, duty cycle (D) is 50%, so switch will be ON for half cycle and OFF another half.

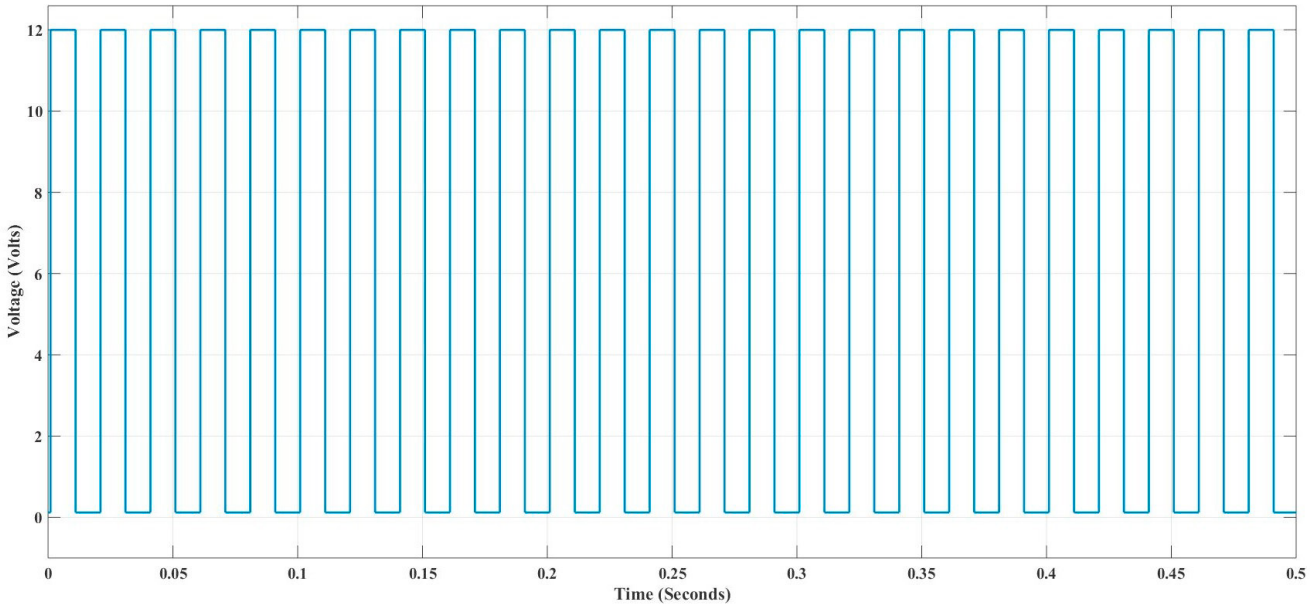


Figure 6: Output of open loop DC chopper

As it can be clearly seen from the output waveform of open loop DC chopper in (figure 6), when switch is ON output is +12V which is exactly equal to V_{in} and when switch is OFF output is slightly more than zero. Duty cycle is also 50% as observed from the waveform.



Figure 7: Output of hardware of open loop DC chopper

For an input of 18V, output should be 9V and it can be seen in figure 7, 9.05V is obtained as mean voltage. This value is very near to 9V as a result 0.555% error only. Spikes seen in the waveform are switching transients which will be removed by connecting some adequate filter later.

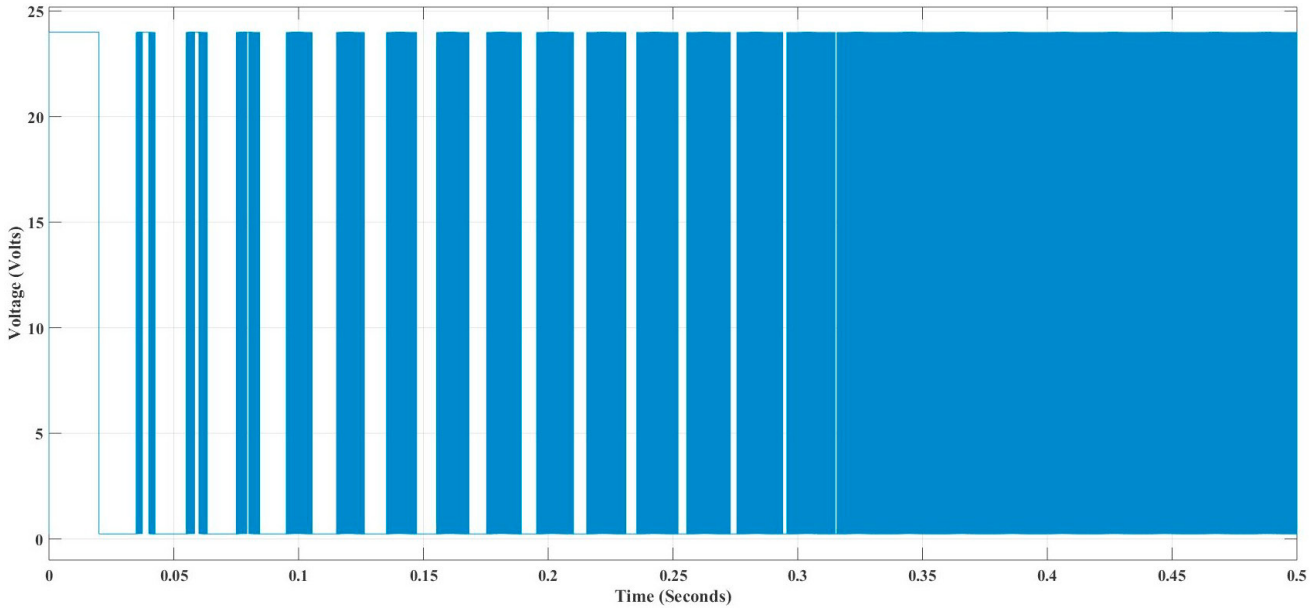


Figure 8: Output of closed loop DC chopper

As it can be seen from the waveform in figure 8, amplitude is of 24V. This is because input DC voltage of chopper is 24V itself but as reference value of 6V is taken, so the mean output obtained will be approximately 6V. Varying duty cycle is observed in this waveform, because PI controller is bringing the output close to 6V cycle by cycle.

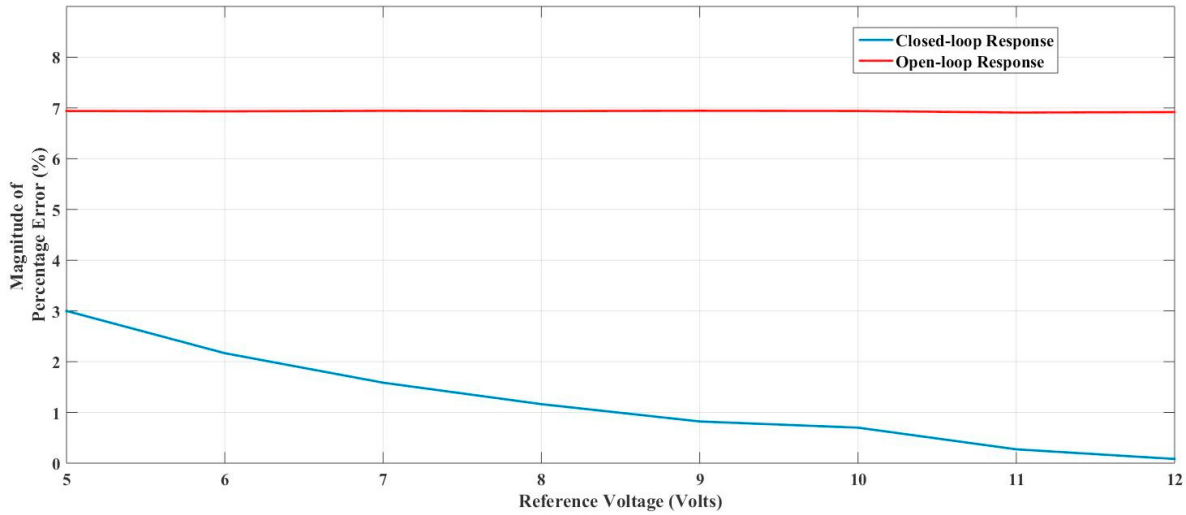


Figure 9: Comparison of open loop and closed loop errors

In figure 9, author has compared the percentage error obtained in open loop class – A chopper with percentage error obtained in closed loop class – A chopper. Blue line denotes the percentage error from open loop chopper while red shows the percentage error shown in closed loop chopper.

4. Conclusion

After analyzing all the calculations and results, it can be seen that percentage error in open loop DC chopper is out of ±5% tolerance range. Now in order to reduce the error, closed loop control of DC chopper was employed whose output must have lied in ±5% tolerance range. After analyzing the results of closed loop chopper, it can be seen that it is actually fulfilling the criteria. Hence, it can be concluded that closed loop control is efficient in reducing the error in output. After going through the error waveform it can also be seen that open loop error is more or less constant but closed loop error is varying with change in values because in closed loop output is continuously monitored and better output is achieved.

Chopper is generally a single switch circuit. As the author is able to analyze the single switch based convertor using dSPACE, some multi-switch convertor (like single phase inverters, 3-phase inverter, multi-level inverters etc.) circuits can also be implemented using the same with different switching strategies. In future, author will try to implement other control strategies for chopper to further reduce the error. Researcher will also implement single phase as well as 3-phase inverters using dSPACE and further will choose the best control strategy for inverters after implementing various voltage as well as current control strategies.

References

[1] Agarwal Anupam and Dheeraj Joshi. (2012) "Design of Class-A Chopper for Minimizing Load Voltage Ripple." in *5th India International Conference on Power Electronics*. Delhi, India, 6-8 Dec. 2012: IEEE

[2] Bimal K. Bose, "Power Electronics and AC Drives", Prentice-Hall,'' NJ, USA, 2002.

[3] Iida Takahiko, Hideo Iwamoto, Hisao Oka and Shigeru Funakawa (1980) "New DC Chopper Circuits Using Fast-Switching Reverse- Conducting Thyristors for Low-Voltage DC Motor Control." in *IEEE Transactions on Industry Applications* (Volume: IA-16, Issue: 1, Jan. 1980). Jan. 1980: IEEE; 111 - 118.

[4] Lang Yifan, Xin Ge, Runan Gu and Yuanyuan Zhang (2017) "The Closed-Loop Design for Buck Chopper Circuit." in *2017 International Conference on Circuits, Devices and Systems*. Chengdu, China, 5-8 Sept. 2017: IEEE; 38-43.

[5] Mihajlovic Zoric, Brad Lehman and Chunxiao Sun. (2004) "Output Ripple Analysis of Switching DC-DC Converters." in *IEEE Transactions on Circuits and Systems I: Regular Papers* (Volume: 51, Issue: 8, Aug. 2004), 16 August 2004: IEEE; 1596 - 1611.

[6] Muhammad H. Rashid, "Power electronics circuits, devices and applications", 2nd ed, Prentice-Hall, 1993.

[7] Takeuchi Shun and Keiji Wada. (2014) "Experimental Verification of Noiseless Sampling for Buck Chopper Circuit with Current Control." in *Power Electronics Conference (IPEC-Hiroshima 2014 - ECCE-ASIA).* Hiroshima, Japan, 18-21 May 2014: IEEE; 3646 - 3651.

[8] Xu Huangsheng, Kevin King and Yashvant Jani. (2007) "High Performance DC Chopper Speed and Current Control of Universal Motors Using a Microcontroller." in *Industry Applications Conference, 2007. 42nd IAS Annual Meeting. Conference Record of the 2007 IEEE.* New Orleans, LA, USA, 23-27 Sept. 2007: IEEE; 701 - 705.

Appendix

A. Driver circuit

It has an optocoupler (6N137) and an OPAMP (uA741). Output of 6N137 is cascaded to inverting input of uA741 as shown in figure 10.

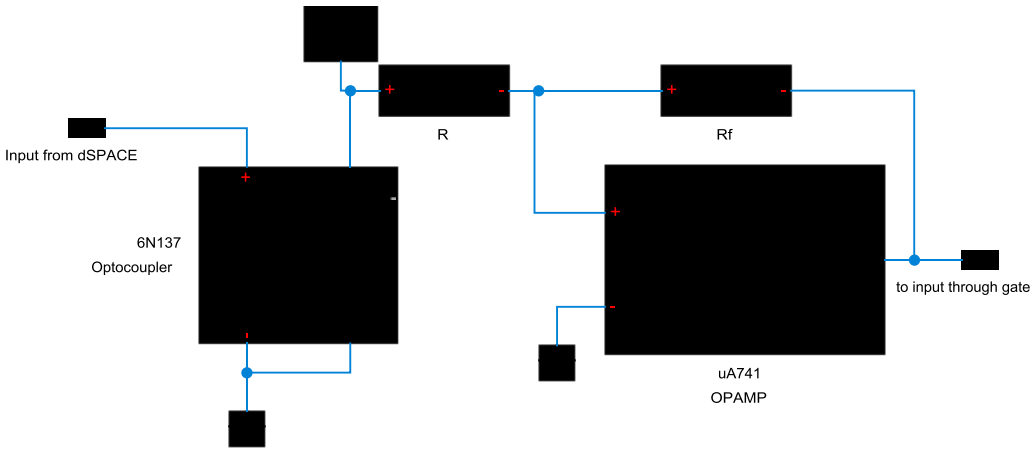


Figure 10: Circuit diagram of driver circuit

- 6N137 have following features:
  - Enable input voltage = V_{cc} + 0.5V
  - Enable input current = 5mA
  - Output voltage = 7V
  - Output current = 50mA
- uA741 have following features:
  - Supply voltage = -18V to 18V
  - Operating temperature = 0^0C to 70^0C

B. MOSFET

MOSFET used here is IRF640N and its features are:

- Gate-to-source voltage = ±20V
- Power dissipation at 25^0C = 150W
- Turn-ON delay time = 10ns
- Rise time = 19ns
- Turn-ON delay time = 23ns
- Fall time = 5.5ns
- Drain-to-source breakdown voltage = 200V

Realization of Recursive Algorithm for One-Dimensional Discrete Cosine Transform and Its Inverse

- Authors
- Authors and affiliations
- Pragati DahiyaEmail author
- Priyanka Jain

Conference paper
First Online: 09 June 2018

- 6Downloads

Part of the Lecture Notes in Electrical Engineering book series (LNEE, volume 509)

Abstract

In this paper, recursive algorithm for the computation of discrete cosine transform (DCT) and inverse discrete cosine transform (IDCT) has been proposed. This algorithm has been implemented using recursive structure, i.e., infinite impulse response (IIR) filter. Further, any desired output kernel can be computed independently which is an added attraction of the proposed design. Besides being recursive, this algorithm requires less multiplier and adders than other DCT algorithms. The suggested scheme is time efficient as it provides output in $N/2$ computational cycles, where N is the length of the input sequence. Therefore, the proposed algorithm is both time and hardware efficient. Further, the recursive property of proposed algorithm results in a regular and modular structure which results in easier VLSI implementation.

Keywords

Discrete Cosine Transform (DCT) Recursive structures Infinite impulse response filter (IIR)

1 Introduction

Real and orthogonal discrete cosine transform (DCT) [1] and discrete sine transform (DST) [2] are members of sinusoidal unitary transforms [3] having numerous applications in field of digital signal processing and image processing

especially in data compression, digital filtering, feature extractions, and recognition. Modified form of DCT and DST are used in MPEG-1 and MPEG-2 (moving picture expert group) for audio coding. DCT and DST are used in standard JPEG for image compression/decompression [4]. When transform of highly correlated signal in time domain like speech signal is computed, it gets decorrelated in frequency domain such that most of the transform coefficients are near to zero value and maximum information gets stored in few transform coefficients which can be encoded with less number of bits as compared to original signal. DCT-II has shown performance identical to Karhunen–Loeve transform (KLT) which is an optimal transform in terms of decorrelation and energy compaction based on value of the correlation coefficient [5]. For highly correlated signal, DCT operates similar to KLT, whereas for low correlated signal DST operates similar to KLT [6]. The basis vectors of DCT and DST are independent of input signal statistics; hence, development of fast algorithm for these transform is an easy task as compared to KLT whose basis vector gets altered with the change in input. Different authors have used different methods to simplify the DCT computation which can be broadly classified as (1) indirect approach [7] in which other transforms like FFT, Walsh–Hadamard transforms are used to compute DCT of a signal, (2) direct factorization of transform matrix using sparse matrix factorization method [8], (3) recursive approach [9, 10, 11, 12] in which lower-order transform coefficient values are used to compute higher-order transform coefficient values. This paper is aimed to reduce the multiplication and additions required for DCT and inverse discrete cosine transform (IDCT) computation. The proposed algorithm provides improved results in terms of number of mathematical operation and time required to compute the transform coefficients as compare to [13, 14, 15, 16, 17, 18], and also, the proposed recursive structures show saving in terms of hardware.

2 Recursive Algorithm for Computation of DCT-II

DCT-II for input sequence $x(n) for n=0,1,\ldots,(N-1) x(n) for n=0,1,\ldots,(N-1)$ where N has even value is given by following equation:

$$X(k)=A_k 2N\sqrt{}\sum_{n=0}^{N-1} x(n)\cos[(2n+1)k\pi 2N], k=0,1,\ldots,N-1 X(k)=Ak2N\sum n=0N-1 f_0 x(n)\cos f_0[(2n+1)k\pi 2N], k=0,1,\ldots,N-1 \quad (1a)$$

where

$$A_k=\{12\sqrt{},1,k=0 k=1,2\ldots,N-1 Ak=\{12,k=01,k=1,2\ldots,N-1 \quad (1b)$$

Omitting the scalar multiplier $A_{k2N}\sqrt{}Ak2N$ from (1a) as it is constant so not included in derivation procedure.

$$X(k)=\sum_{n=0}^{N-1}x(n)\cos[(2n+1)k\pi/2N],k=0,1,\ldots,N-1X(k)=\sum n=0N-1x(n)\cos[(2n+1)k\pi/2N],k=0,1,...,N-1 \quad (2)$$

2.1 Input Folding Recursive (IFR) Transform Algorithm

Equation (2) can be expressed as (3a, 3b) by folding input sequence:

$$X(k)=\sum_{n=0}^{N2-1}w_k(n)\cos[(2n+1)k\pi/2N],k=0,1,\ldots,N-1X(k)=\sum n=0N2-1wk(n)\cos[(2n+1)k\pi/2N],k=0,1,...,N-1 \quad (3a)$$

where

$$w_k(n)=\{x(n)+(-1)^k x(N-1-n)\}wk(n)=\{x(n)+(-1)kx(N-1-n)\} \quad (3b)$$

Replacing n by $(N/2 - n)$ in Eq. (3a), we obtain

$$X(k)k=\sum_{n=1}^{N/2}w_k(N2-n)[\cos(k\pi2)\cos[(2n-1)k\pi/2N]+\sin(k\pi2)\sin[(2n-1)k\pi2N],=0,1,\ldots,N-1X(k)=\sum n=1N/2wk(N2-n)[\cos(k\pi2)\cos[(2n-1)k\pi/2N]+\sin(k\pi2)\sin[(2n-1)k\pi2N],k=0,1,...,N-1 \quad (4)$$

In next subsection, Kernels for even and odd values of k are developed as follows.

2.1.1 IFR Kernel for *k* Even

When k is even, Eq. (4) can be written as

$$X_1(k)=(-1)^{k/2}\sum_{n=1}^{N/2}w_k(N2-n)\cos[(2n-1)k\pi/2N],k=0,2,\ldots,N/2X1(k)=(-1)k/2\sum n=1N/2wk(N2-n)\cos[(2n-1)k\pi/2N],k=0,2,...,N/2 \quad (5)$$

Let

$$P_{kn}=\cos[(n-1/2)\phi_k]\cos(\phi_k/2),\phi_k=k\pi N,k\text{even}Pnk=\cos[(n-1/2)\phi k]\cos(\phi k/2),\phi k=k\pi N,k\text{ even} \quad (6a)$$

$$P_{kn+1}=\cos[(n+1/2)\phi_k]\cos(\phi_k/2),k\text{even}Pn+1k=\cos[(n+1/2)\phi k]\cos(\phi k/2),\text{keven} \quad (6b)$$

$$X_1(k)=(-1)^{k/2}\cos(\phi_{k2})\sum_{n=1}^{N/2}w_k(N2-n)P_{kn},k\text{even}X1(k)=(-1)k/2\cos(\phi k2)\sum n=1N/2wk(N2-n)Pnk,\text{keven} \quad (7)$$

Equation (6b) can be rewritten using the following trigonometric identity

$$\cos(t\phi_k)=2\cos[(t-1)\phi_k]\cos\phi_k-\cos[(t-2)\phi_k]\cos(t\phi k)=2\cos[(t-1)\phi k]\cos\phi k-\cos[(t-2)\phi k] \quad (8)$$

$$\sin(t\emptyset_k)=2\sin[(t-1)\emptyset_k]\cos\emptyset_k-\sin[(t-2)\emptyset_k]\sin(t\emptyset k)=2\sin[(t-1)\emptyset k]\cos\emptyset k-\sin[(t-2)\emptyset k] \tag{9}$$

$$P_{kn+1}=2\cos[(n-1/2)\emptyset_k]\cos\emptyset_k-\cos[(n-3/2)\emptyset_k]\cos(\emptyset_k/2),\text{keven}P_{n+1k}=2\cos[(n-1/2)\emptyset k]\cos\emptyset k-\cos[(n-3/2)\emptyset k]\cos(\emptyset k/2),\text{keven} \tag{10}$$

$$P_{kn+1}=2P_{kn}\cos\emptyset_k-P_{kn-1},\text{keven}P_{n+1k}=2P_{nk}\cos\emptyset k-P_{n-1k},\text{keven} \tag{11}$$

Assume

$$S_{kN2}=\sum_{n=1}^{N2}w_k(N2-n)P_{kn},\text{keven}SN2k=\sum_{n=1}^{N2}wk(N2-n)Pnk,\text{keven} \tag{12}$$

Above equation can be rewritten by substituting value $P_{k1}=1P1k=1$

$$S_{kN/2}=w_k(N2-1)+\sum_{n=1}^{N2-1}w_k(N2-n-1)P_{kn+1},\text{keven}SN/2k=wk(N2-1)+\sum_{n=1}^{N2-1}wk(N2-n-1)Pn+1k,\text{keven} \tag{13}$$

Using recursive relation Eq. (11), above equation can be expressed as:

$$S_{kN/2}=w_k(N2-1)+\sum_{n=1}^{N2-1}w_k(N2-n-1)[2P_{kn}\cos\emptyset_k-P_{kn-1}],\text{keven}SN/2k=wk(N2-1)+\sum_{n=1}^{N2-1}wk(N2-n-1)[2Pnk\cos\emptyset k-Pn-1k],\text{keven} \tag{14}$$

Or

$$S_{kN/2}=w_k(N2-1)-w_k(N2-2)+2\cos\emptyset_k\sum_{n=1}^{N2-1}w_k(N2-n-1)P_{kn}-\sum_{n=2}^{N2-1}w_k(N2-n-1)P_{kn-1},\text{keven}SN/2k=wk(N2-1)-wk(N2-2)+2\cos\emptyset k\sum_{n=1}^{N2-1}wk(N2-n-1)Pnk-\sum_{n=2}^{N2-1}wk(N2-n-1)Pn-1k,\text{keven} \tag{15}$$

Using above equation, we get following recursive relation:

$$S_{kN/2}=w_k(N2-1)-w_k(N2-2)+2\cos\emptyset_kS_{kN2-1}-S_{kN2-2},\text{keven}SN/2k=wk(N2-1)-wk(N2-2)+2\cos\emptyset kSN2-1k-SN2-2k,\text{keven} \tag{16}$$

We get Eq. (17) used to compute the even coefficient of DCT-II by substituting (12) in (7)

$$X_1(k)=(-1)^{k/2}A_{k2N}--\sqrt{}\cos(\emptyset_{k2})S_{kN2},k=0,2,\ldots,N/2X1(k)=(-1)k/2Ak2N\cos(\emptyset k2)SN2k,k=0,2,...,N/2 \tag{17}$$

$X_1(k)X1(k)$ can be realized using infinite impulse response (IIR)-filters structure as shown in Fig. 1. Thus, $S_{kN/2}SN/2k$ is available at $n=N2.n=N2$. For a specific value $k=k_1,k=k1$, say, the computation of DCT

coefficient X(k1)X(k1) takes N2N2 clock cycles. In other word, the full X(k)X(k) for even kernel is computed in (N/2)(N/2). (N/2)(N/2) clock cycles.

Open image in new window

Fig. 1

Filter structure for calculating *N*-point DCT-II

2.1.2 IFR Kernel, *k* Odd

Let

$$Q_{kn}=\sin[(n-12)\emptyset k]\sin(\emptyset k2),\text{kodd}Q_{nk}=\sin f_0[(n-12)\emptyset k]\sin f_0(\emptyset k2),\text{kodd} \quad (18)$$

$$Q_{kn+1}=2\sin[(n+12)\emptyset k]\sin(\emptyset k2),\text{kodd}Q_{n+1k}=2\sin f_0[(n+12)\emptyset k]\sin f_0(\emptyset k2),\text{kodd} \quad (19)$$

When *k* is odd, Eq. (4) can be written as

$$X2(k)=(-1)^{(k-1)/2}\sin(\emptyset k/2)\sum_{n=1}^{N/2}w_k(N2-n)Q_{kn},k=1,3,\ldots,NX2(k)=(-1)(k-1)/2\sin f_0(\emptyset k/2)\sum n=1N/2f_0wk(N2-n)Qnk,k=1,3,...,N \quad (20)$$

By algebraic manipulation and by using Eq. (9), Eq. (19) can be expressed in following recursive form:

$$Q_{kn+1}=2Q_{kn}\cos\emptyset k-Q_{kn-1},\text{kodd}Q_{n+1k}=2Q_{nk}\cos\emptyset k-Q_{n-1k},\text{kodd} \quad (21)$$

Assume

$$U_{kN/2}=\sum_{n=1}^{N/2}w_k(N2-n)Q_{kn},\text{kodd}U_{N/2k}=\sum n=1N/2f_0wk(N2-n)Qnk,\text{kodd} \quad (22)$$

Above equation can be rewritten by substituting value of $Q_{k1}=1$ $Q1k=1$ [obtained from Eq. (18)]

$$U_{kN/2}=w_k(N2-1)+\sum_{n=2N/2}w_k(N2-n)Q_{kn},\text{kodd}U_{N/2k}=wk(N2-1)+\sum n=2N/2f_0wk(N2-n)Qnk,\text{kodd} \quad (23)$$

$$U_{kN/2}=w_k(N2-1)+\sum_{n=1}^{N2}w_k(N2-n-1)Q_{kn+1},\text{kodd}U_{N/2k}=wk(N2-1)+\sum n=1N2f_0wk(N2-n-1)Qn+1k,\text{kodd} \quad (24)$$

Using recursive relation obtained from Eq. (21), above equation can be expressed as:

$$U_{kN/2}=w_k(N2-1)+\sum_{n=1}^{N2-1}w_k(N2-n-1)[2Q_{kn}\cos\emptyset k-Q_{kn-1}],\text{kodd}U_{N/2k}=wk(N2-1)+\sum n=1N2-1f_0wk(N2-n-1)[2Qnk\cos f_0\emptyset k-Qn-1k],\text{kodd} \quad (25)$$

Or

$$U_{kN/2}=w_k(N2-1)+w_k(N2-2)+2\cos\emptyset_k U_{kN2-1}-U_{kN2-2},k\text{odd}U_{N/2k}=w_k(N2-1)+w_k(N2-2)+2\cos f_0\emptyset_k U_{N2-1k}-U_{N2-2k},k\text{odd} \quad (26)$$

Using Eqs. (20), (22), and (26), we get odd coefficient of DCT-II

$$X_2(k)=(-1)^{(k-1)/2}A_{k2N}--\sqrt{}\sin(\emptyset_{k2})U_{kN2},k\text{odd}X_2(k)=(-1)(k-1)/2Ak2N\sin f_0(\emptyset k2)UN2k,k\text{odd} \quad (27)$$

Using above equation, recursive filter structure is realized as shown in Fig. 1. When *k* is odd, computation time for X(k)X(k) is again the same (i.e.,(N2).(N2)(N2).(N2)) as for even case. Equations (16) and (26) show that the equations are same in the feedback path so the feedback structures are same for both the cases. These equations are different in feed-forward path; i.e., it is implemented by a control unit (MUX, DEMUX1 and DEMUX2) and select line as represented in Fig. 1. This control unit is used to select the inputs for the recursive structure to get any desired output coefficient. The selection is done through a mode selector switch, *S*, mode 0 provides even coefficients of the output, and mode 1 gives the odd coefficients of *k*. Therefore, the proposed structure can compute any desired output coefficient independently.

2.2 Recursive Output Folding Algorithms (OFR) for Inverse DCT

IDCT-II of
sequence X(k)fork=0,1,2,…,(N−1)X(k)fork=0,1,2,...,(N−1) where *N* has even value is given by following equation:

$$x(n)=A_{k2N}--\sqrt{}\sum_{k=0}^{N-1}X(k)\cos[(2n+1)k\pi/2N],n=0,1,\ldots,N-1x(n)=Ak2N\sum k=0N-1 f_0X(k)\cos f_0[(2n+1)k\pi/2N],n=0,1,...,N-1 \quad (28)$$

Following Eqs. (29) and (30) are obtained by folding the data from above equation in which value of x(n)+x(N−1−n)x(n)+x(N−1−n) is obtained for even values of *k* and of x(n)−x(N−1−n)x(n)−x(N−1−n) is obtained for odd values of *k*.

$$x(n)+x(N-1-n)=\sum_{k=0}^{N-1}X(k)\{1+(-1)^k\}\cos[(2n+1)k\pi 2N],n=0,1,\ldots,N2-1x(n)+x(N-1-n)=\sum k=0N-1 f_0X(k)\{1+(-1)k\}\cos f_0[(2n+1)k\pi 2N],n=0,1,...,N2-1 \quad (29)$$

$$x(n)-x(N-1-n)=\sum_{k=0}^{N-1}X(k)\{1-(-1)^k\}\cos[(2n+1)k\pi 2N],n=0,1,\ldots,N2-1x(n)-x(N-1-n)=\sum k=0N-1 f_0X(k)\{1-(-1)k\}\cos[(2n+1)k\pi 2N],n=0,1,...,N2-1 \quad (30)$$

We now proceed to obtain the folded output (LHS) of Eqs. (29) and (30) for the even and odd values of k.

2.2.1 OFR Kernel for the Even Index Sequence X(k)X(k)

When k is even, Eq. (29) may be written as

$$x(n)+x(N-1-n)n=2\sum k=0N2-1X(2k)\cos[(2n+1)k\pi N],=0,1,2,\ldots,N2-1x(n)+x(N-1-n)=2\sum k=0N2-1 f_0 X(2k)\cos f_0 [(2n+1)k\pi N],n=0,1,2,...,N2-1 \quad (31)$$

Replacing k by $(N/2 - k)$

$$x(n)+x(N-1-n)n=2(-1)n\sum k=1N2X(N-2k)\sin(k\beta n),=0,1,\ldots,N2-1x(n)+x(N-1-n)=2(-1)n\sum k=1N2 f_0 X(N-2k)\sin f_0 (k\beta n),n=0,1,...,N2-1 \quad (32a)$$

where

$$\beta n=(2n+1)\pi N\beta n=(2n+1)\pi N \quad (32b)$$

Equation (32a) can also be written as

$$x(n)+x(N-1-n)n=2(-1)n\sin(\beta n)\sum k=1N2X(N-2k)Dnk,=0,1,2,\ldots,N2-1x(n)+x(N-1-n)=2(-1)n\sin f_0 (\beta n)\sum k=1N2 f_0 X(N-2k)Dkn,n=0,1,2,...,N2-1 \quad (33a)$$

where

$$Dnk=\sin(k\beta n)\sin(\beta n),n=0,1,2,\ldots,N2-1Dkn=\sin f_0 (k\beta n)\sin f_0 (\beta n),n=0,1,2,...,N2-1 \quad (33b)$$

Equation (33b) can be mathematically manipulated using Eq. (9) as

$$Dnk+1=2\cos\beta nDnk-Dnk-1,n=0,1,2,\ldots,N2-1Dk+1n=2\cos\beta nDkn-Dk-1n,n=0,1,2,...,N2-1 \quad (34)$$

Assume

$$LnN/2=\sum k=1N2X(N-2k)Dnk,n=0,1,2,\ldots,N2-1LN/2n=\sum k=1N2 f_0 X(N-2k)Dkn,n=0,1,2,...,N2-1 \quad (35)$$

Above equation can be rewritten by substituting value of $Dn1=1D1n=1$ obtained from Eq. (33b)

$$LnN/2=X(N-2)+\sum k=1N2X(N-2k-2)Dnk+1,n=0,1,2,\ldots,N2-1LN/2n=X(N-2)+\sum k=1N2 f_0 X(N-2k-2)Dk+1n,n=0,1,2,...,N2-1 \quad (36)$$

Or

$$LnN/2=X(N-2)+2\cos\beta nLnN2-1-LnN2-2,n=0,1,2,\ldots,N2-1LN/2n=X(N-2)+2\cos\beta nLN2-1n-LN2-2n,n=0,1,2,...,N2-1 \quad (37)$$

Even coefficient of IDCT-II can be obtained by substituting (34) in (32a)

$$x(n)+x(N-1-n)n=2(-1)^{n}A^{k}2N---\sqrt{}\sin(\beta n)L^{nN2},=0,1,2,\ldots,N2-1x(n)+x(N-1-n)=2(-1)nAk2N\sin f_0(\beta n)LN2n,n=0,1,2,...,N2-1 \tag{38}$$

Filter structure is used to realize Eq. (38) as shown in Fig. 2 marked A. Thus, thereafter we can determine the value of x(n)+x(N−1−n)x(n)+x(N−1−n) by using even-indexed X(k).X(k).

Open image in new window

Fig. 2

Recursive filter structure for calculating *N*-point IDCT-II

2.2.2 OFR Kernel for the Odd Index Sequence X(k)X(k)

When *k* is odd, Eq. (30) may be written as

$$x(n)-x(N-1-n)=2\sum_{k=0}^{N2-1}X(2k+1)\cos[(2n+1)(2k+1)\pi 2N],n=0,1,2,\ldots,N2-1x(n)-x(N-1-n)=2\sum k=0N2-1f_0X(2k+1)\cos f_0[(2n+1)(2k+1)\pi 2N],n=0,1,2,...,N2-1 \tag{39}$$

Replacing *k* by (*N*/2 − *k*), we get following equation

$$x(n)-x(N-1-n)=2(-1)^{n}\sum_{k=1}^{N/2}X(N-2k+1)\sin((2k-1)\alpha n),n=0,1,2,\ldots N2-1x(n)-x(N-1-n)=2(-1)n\sum k=1N/2f_0X(N-2k+1)\sin f_0((2k-1)\alpha n),n=0,1,2,...N2-1 \tag{40a}$$

where

$$\alpha n=(2n+1)\pi 2N\alpha n=(2n+1)\pi 2N \tag{40b}$$

$$x(n)-x(N-1-n)n=2(-1)^{n}\sin(\alpha n)\sum_{k=1}^{N/2}X(N-2k+1)Fnk,=0,1,2,\ldots N2-1x(n)-x(N-1-n)=2(-1)n\sin f_0(\alpha n)\sum k=1N/2f_0X(N-2k+1)Fkn,n=0,1,2,...N2-1 \tag{41a}$$

where

$$Fnk=\sin((2k-1)\alpha n)\sin(\alpha n),n=0,1,2,\ldots N2-1Fkn=\sin f_0((2k-1)\alpha n)\sin f_0(\alpha n),n=0,1,2,...N2-1 \tag{41b}$$

It may be seen after applying the trigonometric identity

$$Fnk+1=2\cos 2\alpha nFnk-Fnk-1,n=0,1,2,\ldots N2-1Fk+1n=2\cos f_0 2\alpha nFkn-Fk-1n,n=0,1,2,...N2-1 \tag{42}$$

Assume

$$MnN/2=\sum_{k=1}^{N/2}X(N-2k+1)Fnk,n=0,1,2,\ldots N2-1MN/2n=\sum k=1N/2f_0X(N-2k+1)Fkn,n=0,1,2,...N2-1 \tag{43}$$

Above equation can be rewritten by substituting value of $F_{n1}=1 F_{1n}=1$ obtained from (41b)

$$M_{nN/2}=X(N-1)+\sum_{k=1}^{N2-1}X(N-2k-1)F_{nk+1}, n=0,1,2,\ldots N2-1 M_{N/2n}=X(N-1)+\sum_{k=1}^{N2-1}X(N-2k-1)F_{k+1n}, n=0,1,2,\ldots N2-1 \quad (44)$$

Using recursive relation Eq. (42), above equation can be expressed as:

$$M_{kN2}n=X(N-1)+\sum_{k=1}^{N2-1}X(N-2k-1)[2F_{nk}\cos 2\alpha_n-F_{nk-1}], =0,1,2,\ldots N2-1 M_{N2k}=X(N-1)+\sum_{k=1}^{N2-1}X(N-2k-1)[2F_{kn}\cos 2\alpha n-F_{k-1n}], n=0,1,2,\ldots N2-1 \quad (45)$$

or

$$M_{kN2}n=X(N-1)+X(N-3)+2\cos 2\alpha_n M_{nN2-1}-M_{nN2-2}, =0,1,2,\ldots N2-1 M_{N2k}=X(N-1)+X(N-3)+2\cos 2\alpha n M_{N2-1n}-M_{N2-2n}, n=0,1,2,\ldots N2-1 \quad (46)$$

We get Eq. (47) which is used to compute the odd coefficient of IDCT-II by substituting (43) in (40a)

$$x(n)-x(N-1-n)n=2(-1)^n A_k 2N\sqrt{\sin(\alpha_n)}M_{kN2}, =0,1,2,\ldots N2-1 x(n)-x(N-1-n)=2(-1)nAk2N\sin(\alpha n)MN2k, n=0,1,2,\ldots N2-1 \quad (47)$$

Filter structure is used to realize Eq. (47) as shown in Fig. 2 marked B. Thus, thereafter we can determine the value of $x(n)+x(N-1-n)x(n)+x(N-1-n)$ by using odd-indexed $X(k)X(k)$

By adding and subtracting Eqs. (38) and (47), we get $x(n)x(n)$ and $x(N-1-n).x(N-1-n)$. Clearly, having computed the values of $x(n)+x(N-1-n)x(n)+x(N-1-n)$ and $x(n)-x(N-1-n)x(n)-x(N-1-n)$ for $n=0,1,2,\ldots N2-1, n=0,1,2,\ldots N2-1$, we obtain all the values of $x(n)n=0,1,\ldots,N.x(n)n=0,1,\ldots,N$. Refer to Fig. 2 for its realization.

3 Performance Comparison and Discussion

A comparison of proposed algorithm with available recursive algorithms [13, 14, 15, 16, 17, 18] is done on the basis of data throughput per transformation (DTPT) and computation speed and hardware complexity. Following observations are made on the basis of Table 1:

Table 1

Hardware complexity of different DCT/IDCT algorithms

	No. of multipliers	No. of adders	No. of latches	DTPT	Number of computation cycles
[13]	4/4	6/7	4/4	2/2	$(N/2)/(N/2)$
[15]	2/2	3/2	3/2	1/1	$(N)/(N)$

	No. of multipliers	No. of adders	No. of latches	DTPT	Number of computation cycles
[16]	6/7	11/14	4/6	2/4	$(N/4)/(N/2)$
[18]	3/2	3/2	3/2	1/1	$(N)/(N)$
Proposed	2/4	3/7	3/4	1/2	$(N/2)/(N/2)$

- Though the number of computation cycles is equal to N (maximum) among available algorithms [15] and [18], these use minimum hardware for realization.
- Number of computation cycles in proposed algorithm for IDCT is same as those in [13, 16] but hardware requirement is far less.
- The proposed DCT algorithm requires two multipliers, three adders, and three latches which is similar to [15], but the former is far better in terms of number of computation cycles.
- The data throughput per transformation (DTPT) of proposed IDCT algorithm is twice of that [15, 18], while DTPT of the suggested algorithm for DCT is less as compared to [16].
- The speed of proposed algorithm may be increased by replicating the proposed hardware. The hardware complexity with this enhancement is far less than those given in [16].
- Computational speed of the proposed algorithm is better as compare to [15, 18]; however, this translates into hardware penalty.

Another comparison is made on the basis of the number of addition and multiplication operation per transformation among different algorithms for DCT computation enlisted in Table 2. It is noted that proposed algorithm requires $N/2$ multiplication and $(2N - 4)$ addition per transformation which is minimum among available DCT algorithms. Table 3 summarizes the findings related to requirement of multiplication/addition per transformation for IDCT with previously reported recursive algorithms [13, 15]. The number of multiplications requirement in the proposed algorithm is N and addition $(5/2N - 6)$, which is same as that [13] and less than that of [15]. Through the proposed structure, two coefficients are obtained simultaneously, whereas in [15] only one output coefficient is obtained. Therefore, saving in time/high throughput can be achieved by proposed algorithm for realization of DCT/IDCT.

Table 2
Comparison of number of multiplications/additions required for DCT algorithms

N	[13] (*N*)/(2*N* − 4)	[14]		[15] (*N*)/(3*N* − 4)	Proposed (*N*/2)/(2*N* − 4)
		Even output (*N*/2)/(*N* − 1)	Odd output (3*N*/2)/(2*N* − 1)		
4	4/4	2/3	6/7	4/8	2/4
8	8/12	4/7	12/15	8/20	4/12
16	16/28	8/15	24/31	16/44	8/28
32	32/60	16/31	48/63	32/92	16/60
64	64/124	32/63	96/127	64/188	32/124

Table 3
Comparison of number of multiplications/additions required for IDCT algorithms

N	[13] (*N*)/(^{52}N−6)(52N−6)	[15] (*N*)/(2*N* − 3)	Proposed (N)/(^{52}N−6)(N)/(52N−6)
4	4/4	4/5	4/4
8	8/14	8/13	8/14
16	16/34	16/29	16/34
32	32/74	32/61	32/74
64	64/154	64/125	64/154
DTPT	2	1	2

4 Conclusion

In this paper, computationally efficient recursive algorithms for DCT and IDCT have been proposed. The proposed algorithms are implemented using recursive structures. The necessary formulas required for the recursive structures have been derived using mathematical manipulations. The number of addition, multiplications and computation cycles required in the recursive algorithms for DCT/IDCT is less in comparison with some existing structures. Therefore, saving in time, hardware can be achieved by the proposed algorithm for DCT/IDCT in its realization. The realized structures can be easily implemented in VLSI due to their regular, modular, and parallel structures. Moreover, any desired output kernel is computed independently. No complex multiplication is an added advantage of the design.

Notes

Acknowledgements

The authors wish to acknowledge research fellowship from University Grants of commission, Government of India.

References

1. 1.

N. Ahmed, T. Natrajan, K.R. Rao, Discrete cosine transform. IEEE Trans. Comput. **C-23**(1), 90–93 (Jan 1974)MathSciNetCrossRefGoogle Scholar

2. 2.

P. Jain, A. Jain, Regressive structures for computation of DST-II and its inverse. Int. Sch. Res. Netw. ISRN Electron., pp. 1–4 (2012)CrossRefGoogle Scholar

3. 3.

A.K. Jain, A sinusoidal family of unitary transforms. IEEE Trans. Pattern Anal. Mach. Intell. **PAMI-1**(4), 356–365 (Oct 1979)CrossRefGoogle Scholar

4. 4.

C.H. Chen, B.D. Liu, J.F. Yang, Recursive architectures for realizing modified discrete cosine transform and its inverse. IEEE Trans. Circuit Syst. II Anal. Digit. Signal Process. **50**(1) (Jan 2003)Google Scholar

5. 5.

Z. Wang, B. Hunt, The discrete cosine transform—a new version, in *IEEE International Conference on ICASSP'83 Acoustics, Speech, and Signal Processing*, vol. 8, pp. 1256–1259 (Apr 1983)Google Scholar

6. 6.

P. Jain, B. Kumar, S.B. Jain, A general design for one dimensional discrete sine transform. Analog Integr. Circuits Signal Process **61**(2), 211–214 (Nov 2009)CrossRefGoogle Scholar

7. 7.

D. Hein, N. Ahmed, On a real-time Walsh-Hadamard cosine transform image processor. IEEE Trans. Electromagn. Compat. **1**(EMC-20), 453–457 (Aug 1978)CrossRefGoogle Scholar

8. 8.

Z. Wang, Fast algorithms for the discrete W transform and for the discrete Fourier transform. IEEE Trans. Acoust. Speech, Signal Process. **ASSP-32**, 803–816 (Aug 1984)Google Scholar

9. 9.

J.-F. Yang, C.-P. Fan, Recursive discrete cosine transforms with selectable fixed-coefficient filters. IEEE Trans. Circuits Syst. II: Analog Digit. Signal Process. **46**(2), 211–216 (Feb 1999)Google Scholar

10. 10.

Z. Cvetkovic, M.V. Popovic, New fast recursive algorithms for the computation of discrete cosine and sine transforms. IEEE Trans. Signal Process. **40**(8), 2083–2086 (Aug 1992)CrossRefGoogle Scholar

11. 11.

P. Lee, F.Y. Huang, Reconstructed recursive DCT and DST algorithms. IEEE Trans. Signal Process. **42**(7), 1600–1609 (1994)CrossRefGoogle Scholar

12. 12.

L.-P. Chau, W.-C. Siu, Recursive algorithm for the discrete cosine transform with general lengths. Electron. Lett. **30**(3) (Feb 1994)CrossRefGoogle Scholar

13. 13.

J.L. Wang, C.B. Wu, B.D. Liu, J.F. Yang, Implementation of the Discrete Cosine Transform and its inverse by recursive structures, in *SiPS 99. 1999 IEEE Workshop on Signal Processing Systems, 1999*, pp. 120–130 (Oct 1999)Google Scholar

14. 14.

M.N. Murthy, Radix-2 algorithms for implementation of type-II discrete cosine transform and discrete sine transform. Int. J. Eng. Res. Appl. **3**(3), 602–608 (May–June 2013)Google Scholar

15. 15.

M.N. Murthy, Recursive algorithms and systolic architectures for realization of type-II discrete cosine transform and inverse discrete cosine transform. Int. J. Eng. Res. Appl. **4**(4), 24–32 (Apr 2014)Google Scholar

16. 16.

C.-H. Chen, J.-F. Yang, J.-L. Wang, Efficient recursive structures for forward and inverse discrete cosine transform. IEEE Trans. Signal Process. **52**(8), 2665–2669 (Sept 2004)MathSciNetCrossRefGoogle Scholar

17. 17.

P. Lee, Restructured recursive DCT and DST algorithms. IEEE Trans. Signal Process. **42**(7), 1600–1608 (July 1994)Google Scholar

18. 18.

Z. Wang, G.A. Jullien, W.C. Miller, Implementation of the discrete cosine transform and its inverse by digital filtering, in *Proceedings of the 37th Midwest Symposium on Circuits and Systems*, vol. 23, pp. 821–824 (5 Aug 1994)Google Scholar

IUST Iran University of Science and Technology

Iranian Journal of Electrical and Electronic Engineering

Journal Homepage: ijeee.iust.ac.ir

Recognition of Multiple PQ Issues using Modified EMD and Neural Network Classifier

M. K. Saini*(C.A.) and R. K. Beniwal*

Abstract: This paper presents a new framework based on modified EMD method for detection of single and multiple PQ issues. In modified EMD, DWT precedes traditional EMD process. This scheme makes EMD better by eliminating the mode mixing problem. This is a two step algorithm; in the first step, input PQ signal is decomposed in low and high frequency components using DWT. In the second stage, the low frequency component is further processed with EMD technique to get IMFs. Eight features are extracted from IMFs of low frequency component. Unlike low frequency component, features are directly extracted from the high frequency component. All these features form feature vector which is fed to PNN classifier for classification of PQ issues. For comparative analysis of performance of PNN, results are compared with SVM classifier. Moreover, performance of proposed methodology is also validated with noisy PQ signals. PNN has outperformed SVM for both noiseless and noisy PQ signals.

Keywords: Empirical Mode Decomposition, Neural Network, Power Quality, Wavelet Transform.

Nomenclature

PQ	Power Quality
EMD	Empirical Mode Decomposition
IMF	Intrinsic Mode Function
DWT	Discrete Wavelet Transform
PQD	Power Quality Disturbance
FFT	Fast Fourier Transform
STFT	Short-Time Fourier Transform
CWT	Continuous Wavelet Transform
DWPT	Discrete Wavelet Packet Transform
PNN	Probabilistic Neural Network
SVM	Support Vector Machine
PLL	Phase Locked Loop
ICA	Independent Component Analysis
HHT	Hilbert Huang Transform
WT	Wavelet Transform

Iranian Journal of Electrical & Electronic Engineering, 2018.
Paper first received 01 April 2017 and accepted 26 December 2017.
* The authors are with the Electrical Engineering Department, DCR University of Science & Technology, Sonipat, India.
E-mails: manishkumar.ee@dcrustm.org and mail.rajendera@gmail.com.
Corresponding Author: M. K. Saini.

1 Introduction

CONCERN towards PQ has become the sine-qua-non for the industrial, domestic and commercial domains. In today's world, proliferation in the application of nonlinear loads like fluorescent lamps with electronic ballasts, switched mode power supplies, solid state control devices, power converters etc. has drawn more attention towards PQ. All these nonlinear loads, capacitor switching banks, short-circuit faults, starting of large machines, and renewable energy integration with grid cause PQ disturbances [1]. PQD is any distortion in the standard voltage and current. PQ limits are given by the international standards, for instance, IEC-61000, IEEE-1159 and EN50160 to keep PQ parameters within acceptable limits. PQ disturbances like sag, swell, harmonics, transient, flickers, interruption etc., pose risk to the life and efficiency of end user equipments like computers, TV, refrigerators, highly sensitive control equipments, tubelights, microwaves etc. and also cause interference to communication lines. Prior detection and continuous monitoring are necessary to mitigate the aftermaths of PQ disturbances [2].

Profuse attempts have been undertaken for the analysis of these disturbances. The most primary

technique used in PQ analysis is Fast Fourier Transform but it is unsuccessful in case of non-stationary transient signal. To overcome the limitation of FFT, STFT and WT started being used. There are many variants of WT, being employed by the researchers like CWT, DWT, DWPT and many others [3-5]. In [6], authors have implemented DWPT using polyphase-decomposition based wavelet filters on Xilinx Artix-7 field-programming gate array AC701 board for estimation of power system harmonics. This hardware design facilitates reduction in computational requirements and memory resources. To deal with problem of spectral leakage in WT, authors [7] utilized modified WT, i.e., generalized empirical wavelet transform for estimation of PQ indices like instantaneous values of fundamental amplitude, root mean square, frequency variation, THD, form factor, normalized distortion energy index, and K-factor. Another variant of WT, i.e., Tunable-Q wavelet transform has been applied by Karthik Thirumala et al. [8] for accurate decomposition of signal into different components among which one is fundamental and others are harmonic components. Authors have tuned the wavelet depending upon the inter-harmonics present near fundamental frequency for better analysis of both single and combined disturbances.

Suhail Khokhar et al. [9] have proposed DWT for feature extraction from sixteen PQD signals. They have optimized the features using Ant Bee Colony optimization before feeding them to PNN whose spread constant has also been optimized using the same technique. DWT-PNN based method has been also tested on the noise-ridden signals having Gaussian noise of 20 dB, 30 dB and 40 dB. In [10] also, authors implemented DWT using Daubechies family filter banks for better feature extraction from PQDs. They have determined the unique adaptive threshold for the decomposed PQDs depending upon their value of energy and entropy. The intersection of thresholds and curves of decomposed PQD signals has provided the automatic segmentation of PQ signals. DWT using modified wavelets called fraclets have also been proposed by some authors to further improve wavelet decomposition results for having correct classification of PQ disturbances [11, 12].

Like other techniques, WT have their own limitations like time-frequency uncertainty relation, caution needed while choosing the mother wavelet, interference terms, border distortion, energy leakage etc. Another technique used by the researchers for time-frequency analysis of PQDs is S-transform. M. V. Reddy and Ranjana Sodhi [13] have improved the usability of S-transform for PQ assessment by designing its rule-base using statistical entropy measure for selecting the suitable window. Twelve features have been computed from magnitude and phase values of ST matrix; these features have been fed to AdaBoost classifier using decision stump also. Authors have improved the performance of the classifier by using adaptable initial weights to avoid over-fitting of the classifier. Offering more robustness and less computational complexity, double resolution S-transform has been implemented by J. Li et al. in a digital signal processor for effective feature analysis of PQDs with the help of reduced instruction set of processor [14]. Features provided by double resolution S-transform have been accurately classified into PQ issues by directed acyclic graphs-SVM.

Raj Kumar et al. [15] have opted a different strategy for detection of PQ issues, namely, transients, flickers, interruption, sag, harmonics, swell, spikes and notch. They have implemented the method based on symmetrical components of PQD signals on a digital signal processor, i.e., dSPACE 1104. PLL has been used to generate two other ideal phases to have symmetrical components of all three phases whose positive and negative sequence components have been used for identification of PQ issues. ICA is used to statistically decompose a multivariate signal into independent components. In [16], authors have applied single-channel ICA for detection of transient. This method has been compared with other methods used for transient detection, e.g., average fundamental waveform analysis, notch and high-pass filters, cycle-by-cycle difference etc.

Many analysis works have been carried out depending upon the threshold values without the use of classifiers. For instance, in [17], authors present a modified potential function based technique to detect the PQ disturbances having short duration, e.g., sag, swell and transient. This technique computes a diffusion matrix having threshold values, as per the proposed algorithm which is used for fast real-time tracking and detection. PQ events have been successfully classified by using the concept of neural networks in different forms. Manjeevan Seera et al. [18] have developed PQ analysis model by modifying the basic concepts of fuzzy min–max clustering neural network. Voltage harmonics and total harmonic distortion have been extracted from all three phases of acquired PQD signals. Fuzzy min-max clustering network have been applied upon those features due to their individual capabilities of online learning and prediction explanation respectively. This method can have setback due to increasing complexity while learning due to increase in number of clusters. Another neural network based approach using conjugate gradient back-propagation algorithm has been adopted by Chetan B. Khadse et al. [19] for detection and classification of sag and swell in LabVIEW. This technique recognizes PQ events from their odd and even harmonic components extracted using FFT.

Another main technique for time-frequency localization of PQ events is Hilbert-Huang Transform which comprises of EMD and then Hilbert spectral analysis. Many researchers have relied upon EMD for decomposition of PQD signals to have effective feature extraction. Since, EMD has certain drawbacks like envelope undershoot or overshoot due to the cubic

spline interpolation, negative effects at the boundary and the mode mixing [20]; noise-assisted ensemble EMD has been proposed but it also lacks somewhere due to drastic increase in computational burden. Therefore, David Camarena-Martinez et al. [20] have fused the down-sampling stage and spline-cubic interpolation to the standard EMD process to have more adequate IMF extraction and less computational burden. This method extracts the first IMF as the fundamental component and rest information that is mainly of PQDs lies in other IMFs. This technique facilitates elimination of overshoots, undershoots and mode mixing problem with fundamental component of PQD.

To address the limitations of traditional EMD, for instance, intermittence, mode-mixing, and undesirable IMFs, authors have proposed new framework utilizing modified EMD in this work. Ideally, every IMF should have one single oscillatory mode or frequency component. But, as PQD signal has numerous harmonics and time-varying amplitude and frequency, there are chances that each IMF computed by EMD has multiple frequency components. Hence, to ward off this improper decomposition of PQD signal, a pre-processing stage has been introduced before the process of EMD. That pre-processing stage is DWT in this paper. The combination of DWT and EMD is named as modified EMD. Modified EMD has been applied on eleven PQ signals, simulated by parametric equations, i.e., normal, swell, sag, flicker, interruption, harmonics, swell with harmonics, sag with flicker, sag with harmonics, swell with flicker and interruption with harmonics. DWT has been used to split PQ signal into two narrow bands, i.e., low frequency and high frequency components. Only low frequency components are further treated with EMD since main frequency components of PQ signal reside in low frequency region. Eight statistical features such as mean, root mean square, standard deviation, variance, skewness, kurtosis, energy and entropy have been further calculated from the obtained IMFs. The same features have been computed from the high frequency component of PQ signal to also utilize the high frequency information of PQ signal. These features have been used as the characteristics of PQ issues and employed in the training of PNN for automatic classification of PQ issues. PNN has been adopted in this work on account of its faster training procedure and has been also proved superior to SVM for classification of single and multiple PQ issues.

Rest of the paper is organized as follows: Section 2 contains proposed methodology for the classification of PQ issues. Section 3 briefs theoretical background of DWT, modified EMD, and PNN classifier, and Section 4 presents results and discussion followed by conclusion of the proposed technique with the future directions in Section 5.

2 Proposed Methodology

Detection and classification of PQ issues (sag, swell, flicker, interruption, harmonics, sag with harmonics, swell with harmonics, sag with flicker, swell with flicker and interruption with harmonics) have been illustrated in this section. The proposed technique considers the analysis of both single and multiple PQ issues. Single PQ issues include sag, swell, flicker, interruption and harmonics; whereas multiple PQ issues are sag with harmonics, swell with harmonics, sag with flicker, swell with flicker and interruption with harmonics. This method is based mainly on the application of modified EMD and PNN. The block diagram of the proposed methodology is presented in Fig. 1. Different steps of block diagram have been discussed as follows.

2.1 Simulation of PQ Issues

Proposed methodology starts with simulation of PQ input signal which undergoes the detection and classification process. Input signals with PQ issues are generated in MATLAB by varying the parameters of parametric equations as per IEEE-1159 standard. The parametric equations used for simulating PQ issues considered in this work are given in Table 1. Both single and multiple PQ issues such as sag, swell, flicker, interruption, harmonics, sag with harmonics, swell with harmonics, sag with flicker, swell with flicker and interruption with harmonics, have been simulated in this work.

2.2 Signal Decomposition using Modified EMD

This stage explains the application of signal processing technique for transforming the signal into a form which contains significant recognizable information to characterize PQ issue. For this purpose, modified EMD is proposed in this work. Modified EMD presents application of DWT on input

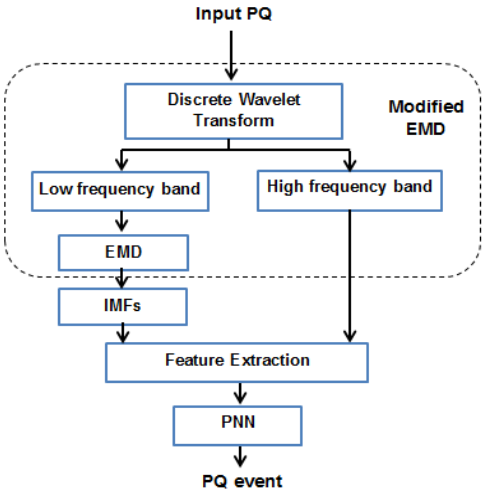


Fig. 1 Proposed methodology for detection and classification of PQ issues.

PQ signal first and then EMD of resultant low frequency signal. For applying DWT, db4 wavelet is used which divides signal into low frequency and high frequency components. EMD is then applied only on low frequency signal and produces IMFs from the low frequency part of PQ issue. All these IMFs now obtained have single oscillatory modes, thus overcoming the problem of mode-mixing.

2.3 Feature Extraction

Feature extraction implies the process of transforming the signal into a set of features. Signal obtained after EMD is too big to be dealt with, so, it is transformed into set of features which represents its characteristic information. Eight statistical features such as mean, root mean square (RMS), standard deviation, variance, skewness, kurtosis, energy and entropy, are calculated from IMFs having useful signal information. These features have also been extracted from the high frequency component of PQ signal to extract the signal information hidden in high frequency component. These features are introduced in Table 2 with their labels. In PQ analysis, feature extraction is a prominent step. More the features are relevant; more is the classification accuracy for PQ issues.

Table 1 Parametric equations used for PQ issues generation.

PQ Issue	Class	Parametric Equation	Parameters
Normal signal	C1	$s(t) = A_m \sin(wt)$	$A_m = 1pu, w = 2\pi * 50$
Voltage Sag	C2	$s(t) = A_m \left(1 - \beta\left(u(t-t_1) - u(t-t_2)\right)\right)\sin(wt)$	$0.1 \le \beta \le 0.9;$ $T \le t_2 - t_1 \le 9T$
Voltage Swell	C3	$s(t) = A_m \left(1 + \beta\left(u(t-t_1) - u(t-t_2)\right)\right)\sin(wt)$	$0.1 \le \beta \le 0.8;$ $T \le t_2 - t_1 \le 9T$
Interruption	C4	$s(t) = A_m \left(1 - \beta\left(u(t-t_1) - u(t-t_2)\right)\right)\sin(wt)$	$0.9 \le \beta \le 1;$ $T \le t_2 - t_1 \le 9T$
Harmonics	C5	$s(t) = A_m \left(\beta_1 \sin(wt) + \beta_3 \sin(3wt) + \beta_5 \sin(5wt)\right)$	$0.05 \le \beta_3, \beta_5 \le 0.15;$ $\sum \beta_i^2 = 1$
Flicker	C6	$s(t) = A_m \left[1 + \beta_1 \sin(\beta_2 wt)\right]\sin(wt)$	$0.1 \le \beta_1 \le 0.2;$ $5 \le \beta_2 \le 20Hz$
Sag with Harmonics	C7	$s(t) = A_m \left(1 - \beta\left(u(t-t_1) - u(t-t_2)\right)\right)\left(\beta_1 \sin(wt) + \beta_3 \sin(3wt) + \beta_5 \sin(5wt)\right)$	$0.1 \le \beta \le 0.9;$ $T \le t_2 - t_1 \le 9T;$ $0.05 \le \beta_3, \beta_5 \le 0.15;$ $\sum \beta_i^2 = 1$
Swell with Harmonics	C8	$s(t) = A_m \left(1 + \beta\left(u(t-t_1) - u(t-t_2)\right)\right)\left(\beta_1 \sin(wt) + \beta_3 \sin(3wt) + \beta_5 \sin(5wt)\right)$	$0.1 \le \beta \le 0.8;$ $T \le t_2 - t_1 \le 9T;$ $0.05 \le \beta_3, \beta_5 \le 0.15;$ $\sum \beta_i^2 = 1$
Interruption with Harmonics	C9	$s(t) = A_m \left(1 - \beta\left(u(t-t_1) - u(t-t_2)\right)\right)\left(\beta_1 \sin(wt) + \beta_3 \sin(3wt) + \beta_5 \sin(5wt)\right)$	$0.9 \le \beta \le 1;$ $T \le t_2 - t_1 \le 9T;$ $0.05 \le \beta_3, \beta_5 \le 0.15;$ $\sum \beta_i^2 = 1$
Sag with Flicker	C10	$s(t) = A_m \left[1 + \beta_1 \sin(\beta_2 wt)\right]\sin(wt)\left(1 - \beta\left(u(t-t_1) - u(t-t_2)\right)\right)$	$0.1 \le \beta \le 0.9;$ $T \le t_2 - t_1 \le 9T;$ $0.1 \le \beta_1 \le 0.2;$ $5 \le \beta_2 \le 20Hz$
Swell with Flicker	C11	$s(t) = A_m \left[1 + \beta_1 \sin(\beta_2 wt)\right]\sin(wt)\left(1 + \beta\left(u(t-t_1) - u(t-t_2)\right)\right)$	$0.1 \le \beta \le 0.8;$ $T \le t_2 - t_1 \le 9T;$ $0.1 \le \beta_1 \le 0.2;$ $5 \le \beta_2 \le 20Hz$

Table 2 Characteristic features of PQ signal.

Feature Label	Features	Expression	Feature Label	Features	Expression
F1	Mean	$\mu = \frac{1}{N}\sum X$	F5	Skewness	$X_{\text{skew}} = \frac{1}{N}\sum\left(\frac{X-\mu}{X_{\text{rms}}}\right)^3$
F2	RMS	$X_{\text{rms}} = \sqrt{\frac{1}{N}\sum X^2}$	F6	Kurtosis	$X_{\text{kurt}} = \frac{1}{N}\sum\left(\frac{X-\mu}{X_{\text{rms}}}\right)^4$
F3	Standard Deviation	$\sigma = \sqrt{\frac{\sum(X-\mu)^2}{N}}$	F7	Energy	$X_{\text{energy}} = \sum_N \lvert X\rvert^2$
F4	Variance	$\sigma^2 = \frac{\sum(X-\mu)^2}{N}$	F8	Entropy	$X_{\text{entropy}} = \sum X\ \log(X)$

2.4 Classification of PQ Issues

Features have been extracted from all the samples of PQ signals to form the corresponding feature vector. The feature vectors of randomly selected PQ issue samples are used for training of PNN. PNN is a feed forward neural network based on the Bayesian network. The spread constant is adjusted by hit and trial method in order to achieve maximum classification accuracy. PNN gets trained with all the feature vectors in one go facilitating fast response. Trained PNN has been employed for the automatic classification of PQ issues. Test samples are randomly selected for testing of trained classifier.

3 Theoretical Background

3.1 Discrete Wavelet Transform

Discrete wavelet transform (DWT) is one of the most prominently used tool for time-frequency localization of the signal. DWT has been adopted instead of CWT due to the redundancy present in continuous wavelet transform [23]. DWT utilizes the analysis filter-bank to split the signal into approximation and detail information of the signal. Coarse (or approximation) information of the signal is present in low frequency components and detail information of the signal is present in high frequency components. The analysis filter bank for DWT is presented in Fig. 2. DWT of a signal is represented mathematically as below in (1) [24]:

$$DWT(p,n) = \frac{1}{\sqrt{s^p}}\sum_k i(n)\psi\left(\frac{n-kbs^p}{s^p}\right) \quad (1)$$

where $i(n)$ represents the discrete version of $i(t)$, the continuous PQ signal; s and b are constant real values and p and n are the integers. $\psi(n)$, the wavelet function is the mother wavelet that is used to extract signal information at different scaling level, s and translation level, bs^p. Here, p decides the resolution level of the decomposition. There are many mother wavelets used in DWT, e.g., Daubechies, Morlet, Haar, Mexican etc. In this work, 'db4', a member of Daubechies wavelet family has been utilized as the wavelet function. 'db4' wavelet has low-pass, $h[n]$ and high-pass filter coefficients, $g[n]$ as given in equation (2).

$$\begin{bmatrix} h[n] \\ g[n] \end{bmatrix} = \begin{bmatrix} \frac{1+\sqrt{3}}{4} & \frac{3+\sqrt{3}}{4} & \frac{3-\sqrt{3}}{4} & \frac{1-\sqrt{3}}{4} \\ \frac{1-\sqrt{3}}{4} & \frac{-3+\sqrt{3}}{4} & \frac{3+\sqrt{3}}{4} & \frac{-1-\sqrt{3}}{4} \end{bmatrix} \quad (2)$$

DWT utilizes the principle of multiresolution analysis (MRA) to decompose signal under analysis to different resolution levels. Approximation signal obtained from first level decomposition is further decomposed to have approximation and detail coefficients at second level, as per Mallat's algorithm. This process is continued till the signal gets splitted into desired frequency bands. Though, DWT provides time-frequency information of signal simultaneously, but it is limited by Heisenberg uncertainty [21]. Moreover, choice of mother wavelet is also a task to be done carefully which demands prior knowledge of signal. Hence, DWT has not been relied upon by authors as the single and only technique for PQ analysis.

3.2 Modified Empirical Mode Decomposition

Modified empirical mode decomposition is only the preferment of traditional EMD as the only difference between EMD and modified EMD is the pre-processing stage in modified EMD before application of EMD. Pre-processing stage includes application of DWT on PQ signal. The genesis of modified EMD lies in the shortcomings of traditional EMD like mode mixing and intermittence according to Gibbs phenomenon [25]. Sometimes, EMD decomposes the signal into intrinsic mode functions (IMFs) which are not having single oscillatory modes, representing frequency mixing in IMFs. This situation doesn't allow the proper representation of the signal into mono-components. Hence, modified EMD has been adopted which proposes application of DWT to decompose PQ signal into narrow bands, prior to the application of EMD for IMF generation. EMD of the

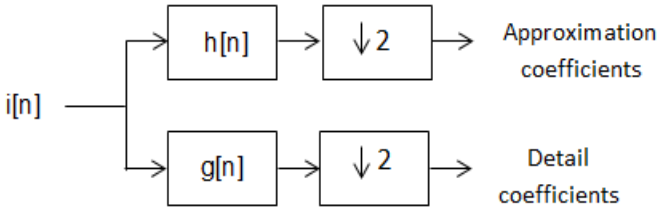


Fig. 2 DWT analysis filter bank.

narrow band signals results into IMFs having only single oscillatory modes.

EMD is the process that deals with both non-stationary and nonlinear signal and provides adaptive time-frequency localization. The concept of EMD is similar to wavelet transform which decomposes the signal in higher and lower frequency band. In EMD, the first IMF having the highest frequency is followed by other IMFs having decreasing frequency components. The basis of empirical mode decomposition is the sifting process in which mean of upper and lower envelope of the signal is repetitively subtracted from the original signal [26]. This sifting process extracts the highest frequency component from the signal in the repetitive manner.

An oscillating signal is called as an intrinsic mode function if it satisfies following two conditions [25]:

i. Number of extrema and zero crossing must be equal or vary by one only.
ii. The mean of envelope which is defined by local maxima and local minima is zero.

The process of EMD is progressed as per the flowchart presented in Fig. 3.

i. Calculate maxima and minima of the signal and apply cubic spline to get upper and lower envelope.
ii. Calculate mean $m(t)$ of the envelopes and subtract it from input signal $i(t)$, define it as in (3):

$$d_1(t) = i(t) - m(t) \tag{3}$$

iii. Check whether $d_1(t)$ satisfies two conditions of IMF, if yes then $d_1(t)$ is first IMF otherwise repeat steps i-iii by considering $d_1(t)$ as input signal and define the next component as in (4):

$$d_{11}(t) = d_1(t) - m_1(t) \tag{4}$$

iv. The process of sifting is replicated j times until first IMF $d_{1j}(t)$ is obtained and residue is calculated as per (5):

$$r_1(t) = i(t) - d_{1_j}(t) \tag{5}$$

v. Consider $r_1(t)$ as input and repeat steps i-iv to get second IMF.

This algorithm is executed g times to get g IMFs. If $r_g(t)$ is monotonic, then no further decomposition is possible and the process is stopped here.

After this process, the original signal $i(t)$ can be represented by (6),

$$i(t) = r_g(t) + \sum_{k=1}^{g} IMF_k(t) \tag{6}$$

In this way, g IMFs are extracted from the original input signal $i(t)$. These IMFs are used for analysis of PQ signals, as these IMFs depict the varying amplitude and frequency of non-stationary PQ signals. EMD also offers freedom from Heisenberg uncertainty thus facilitating better time-frequency representation.

3.3 Probabilistic Neural Network Classifier

There are many variants of classifiers based on neural network, for instance, artificial neural network, back propagation neural network, multi-layer perceptron, deep neural network and PNN. D. F. Specht proposed probabilistic neural network in the early 1990s, which was a feed forward neural network based on Bayesian network [27]. PNN comprises of four layers of neurons which are input layer, pattern layer, summation layer and output layer. The architecture of PNN is presented in Fig. 4. Feature vector is presented at the input layer and neurons in pattern layer computes the distance of feature vector from training patterns according to Gaussian function. The summation unit simply sums the input from the pattern units that corresponds to the category from which the training pattern is selected. Summation layer contains as much neurons as the number of classes of training patterns. At the end, output layer uses the principle of maximum a posteriori to produce the final class to which feature vector belongs.

The classification process of PNN can be described as a two class problem. Let the state of a variable δ be either δ_A or δ_B . Decision of whether it is δ_A or δ_B, depends on the set of measurements captured by p-dimensional vector [25],

$$Y^t = \left[Y_1, Y_2, Y_3, \ldots, Y_j, \ldots, Y_p\right] \tag{7}$$

then Bayes decision rule becomes as (8) and (9),

$$d(Y) = \delta_A \quad \text{if} \quad h_A I_A f_A(Y) > h_B I_B f_B(Y) \tag{8}$$

$$d(Y) = \delta_B \quad \text{if} \quad h_B I_B f_B(Y) > h_A I_A f_A(Y) \tag{9}$$

where $f_A(Y)$ and $f_B(Y)$ gives probability density function for categories A and B respectively, I_A and I_B are loss function of decisions, h_A is prior probability of having pattern of category A and h_B is prior probability of having pattern of category B. Thus, the boundary between the regions given by Bayes decision, is represented as in (10),

$$f_A(Y) = K f_B(Y) \quad \text{where} \quad K = \frac{h_B I_B}{h_A I_A} \tag{10}$$

One of the various advantages of PNN is that it does not require any weight initialization. Addition or removal of training patterns is very easy in PNNs as addition and removal of training samples just demands addition or removal of neurons of pattern layer, hence minimal efforts are required for retraining PNN, if needed [28]. PNN is much faster and accurate than multilayer perceptron networks. The higher learning speed of PNN makes it suitable for signal classification and fault diagnosis problems. In this work, PNN classifier has been relied upon for the classification of PQ issues due to its capability of being trained by all the features in one go only. High dimensional feature set obtained from modified EMD is used for the training and testing of PNN in this work.

4 Results and Discussions

The proposed methodology has been validated in this section with the experimental results and discussions. The results of various stages from PQ issue generation to classification have been discussed below.

4.1 PQ Signal Generation

The proposed methodology has been investigated by using 100 patterns of each desired PQ issue. These issues are simulated by using MATLAB software expressions given in Table 1 [21,22]. The controlling parameters in these equations are illustrated in the same table. For the harmonic issue, fundamental component and the two other harmonic components are required. In this study, 3rd and 5th harmonic components are used.

4.2 Detection of PQ Issues

Synthetic signals used for the analysis of PQ issues are obtained from the mathematical equations in MATLAB. Normally, a signal consists of multiple oscillatory components which represent its physical properties. If these components are extracted from the signal, then the interpretation of the signal becomes much easier. Hence for extracting the information from these signals, modified EMD is applied. As PQ signals have multiple oscillatory modes, therefore, DWT has been first applied on PQ signal using 'db4' wavelet. The lower frequency narrow band obtained from wavelet decomposition has been used as the input for EMD rather than the original PQ signal. On applying EMD, IMF components and residue (last IMF) are obtained. In this work, five single and multiple PQ issues each, along with normal signal have been worked upon. Results of three single and two multiple PQ disturbances, i.e., sag, swell, flicker, sag with harmonics, and swell with harmonics are presented in this subsection.

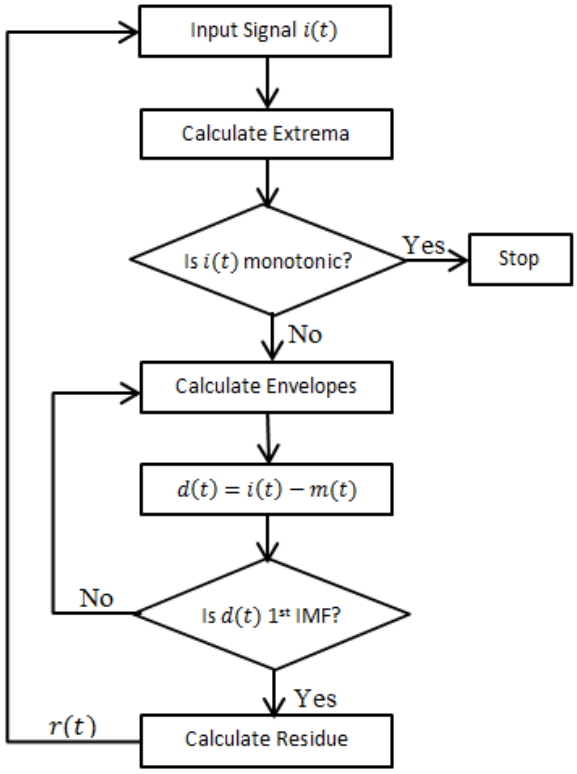


Fig. 3 Flowchart of EMD.

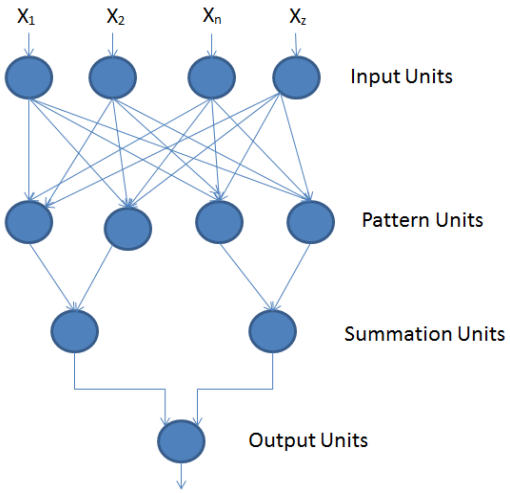


Fig. 4 Basic structure for classification of patterns into categories.

Three single PQ issues are here discussed, which are sag, swell and flicker. All these issues are shown in Fig. 5. Sag is dip in the voltage or current for a short duration, as shown in Fig. 5(a) which represents PQ signal with voltage sag of amplitude 0.7 p.u. Voltage sag signal has been decomposed using wavelet 'db4'. The approximation and detail coefficients of the voltage sag signal have been shown in Fig. 6 corresponding to low frequency and high frequency bands. Among these narrow bands obtained from wavelet decomposition, low frequency part is selected for further empirical mode decomposition to analyse the primary frequency components of PQ signal. IMF components for low frequency component

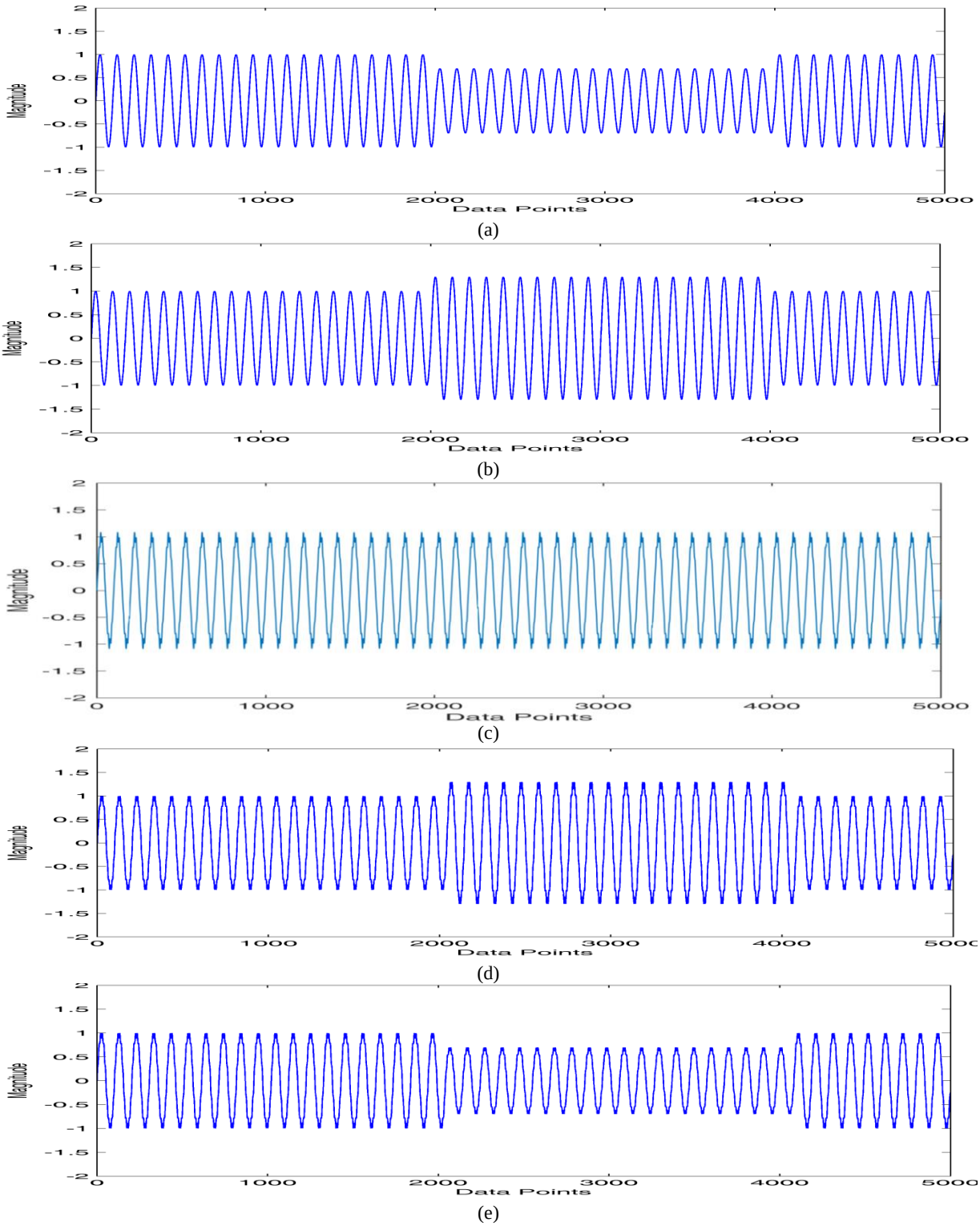


Fig. 5 Power quality signals a) sag, b) swell, c) flicker, d) swell with harmonics and e) sag with harmonics.

are depicted in Fig. 7.

The portion specified by *A* in Fig. 7, represents the presence of sag in signal and *B* represents the posterior event. First IMF preserves the frequency and phase of signal, and the little change is observed during the occurrence and termination of sag. During the voltage sag, the voltage amplitude becomes 0.7 p.u. First IMF component contains the highest frequency information. It is clearly visible from the Fig. 7 that the frequency content gets reduced from first IMF component to last IMF component. The last component (fifth IMF) obtained from EMD process is known as residue. After residue, no mono-component is derived. Residue contains no important information about the signal. Hence, only (*N*-1) IMFs, i.e., four in the case of voltage sag signal, are useful for extracting the time-frequency information of PQ signal; *N* is the number of mono-components obtained from EMD of sag signal and N^{th} mono-component is treated as residue.

For getting significant information about PQ issue in compact form, eight features mentioned in Table 2 have been computed from first four IMFs. There is also some remnant information of PQ issue in the high frequency component obtained from DWT. So, both components are used to provide various characteristic features of the signal. The same features have also been calculated from high frequency component of PQ signal. The feature vector formed is presented in Fig. 8. In this way, forty features have been computed for the voltage sag. These features form a feature vector as shown in Fig. 8, which has been used to train PNN for voltage sag. Next single disturbance presented is voltage swell.

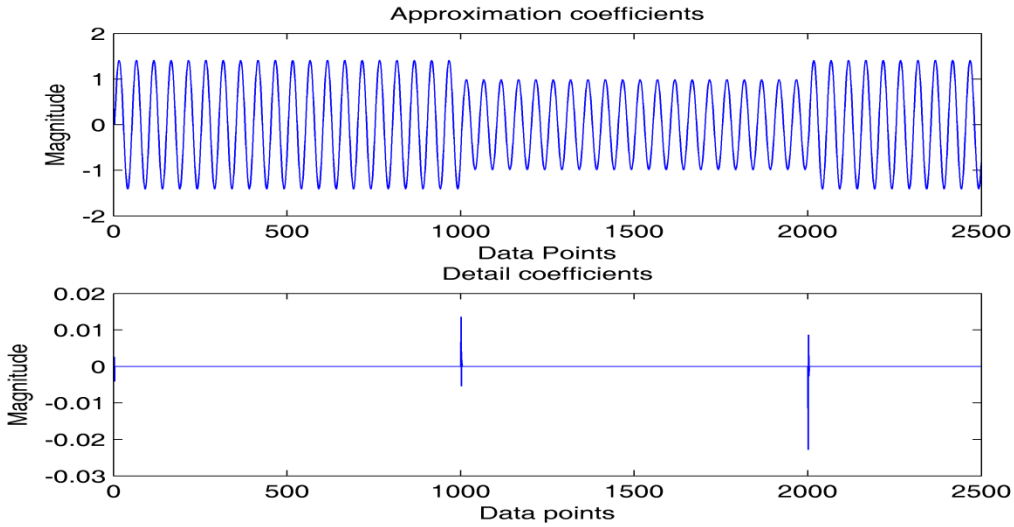


Fig. 6 Low and high frequency components of voltage sag.

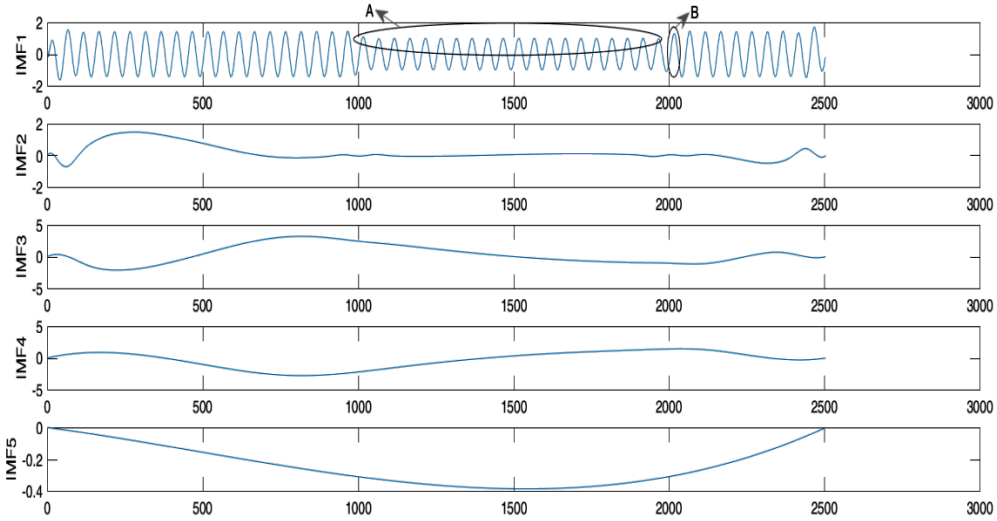


Fig. 7 IMF components and residue of low frequency component of voltage sag.

Voltage swell signal of amplitude 1.3 has been generated as presented in Fig. 5(b). DWT has been applied on the swell signal using wavelet 'db4'. The resultant low frequency and high frequency decomposed bands of the swell signal are represented by the approximation and detail coefficients, Fig. 9. Then, IMFs have been extracted from this low frequency component as given in Fig. 10.

EMD of low frequency band of swell signal has generated seven mono-components among which seventh mono-component is treated as residue. Like sag signal, same features have been computed from first four IMFs and from the higher frequency component of the swell signal.

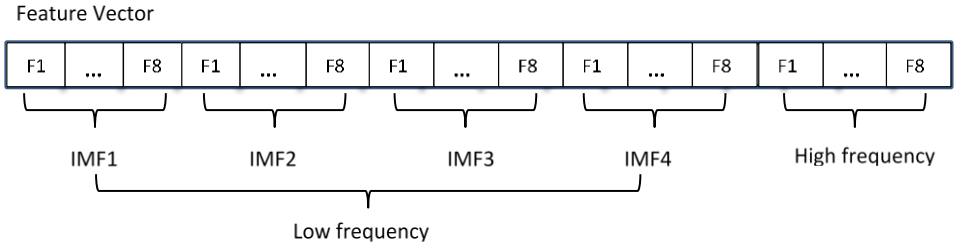


Fig. 8 Feature vector formed for voltage sag.

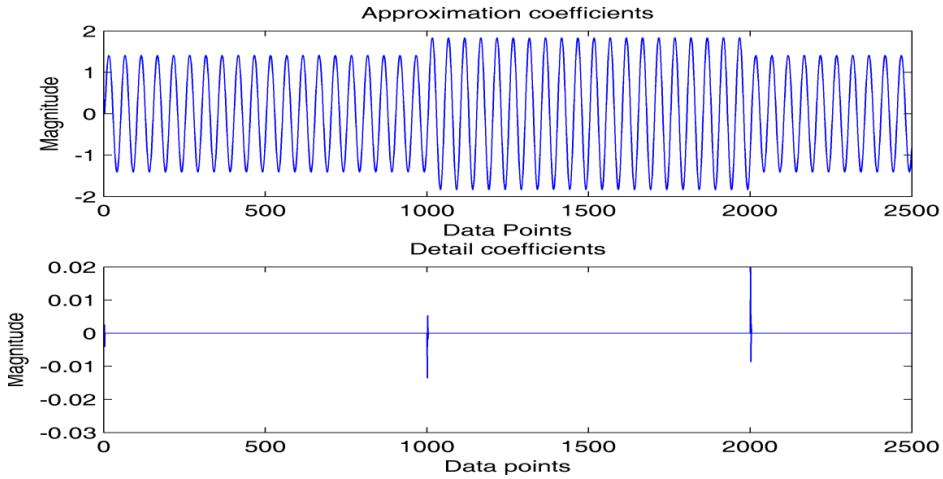


Fig. 9 Low and high frequency components of voltage swell.

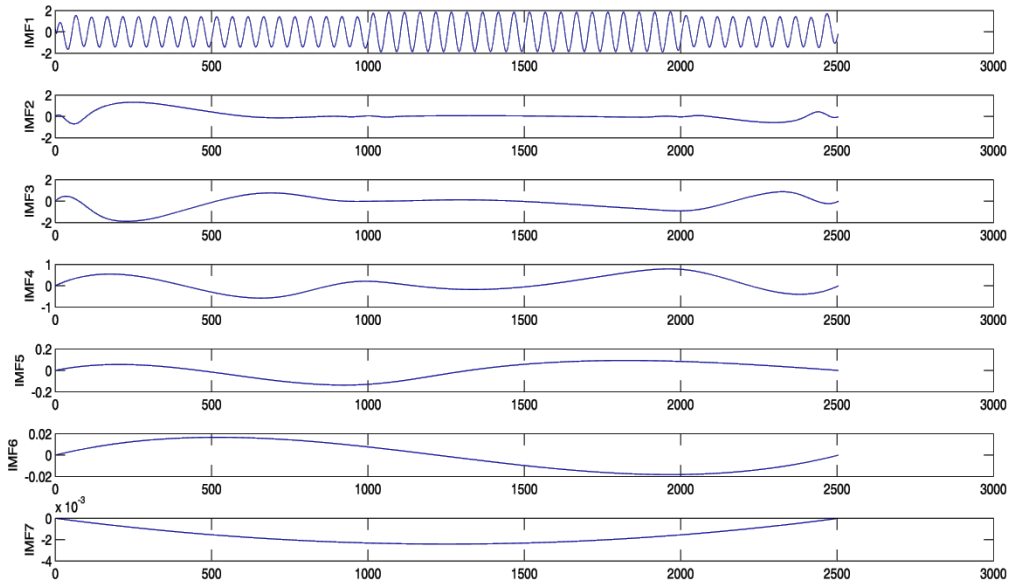


Fig. 10 IMF components and residue of low frequency component of voltage swell.

All these features collectively form the feature vector representing the unique swell signal for training the classifier.

Third single PQ issue is flicker which is the distortion in the magnitude, waveform and frequency of the voltage signal, as shown in Fig. 5(c). Flicker signal is decomposed into low frequency and high frequency bands using wavelet 'db4' which results into approximation and detail coefficients plotted in Fig. 11. The low frequency signal is further decomposed into IMFs using EMD as shown in Fig. 12. Flicker signal has six IMF other than one residue. Characteristic features have been extracted from first four IMFs and also from the high frequency band of the flicker signal to tap the high frequency information of flicker signal.

Multiple PQ issues represent the occurrence of more than one PQ disturbance simultaneously. Five multiple PQ disturbances, namely, sag with harmonics, swell with harmonics, interruption with harmonics, sag with flicker and swell with flicker have been worked upon according to the proposed technique of modified EMD. Sag with harmonics and swell with harmonics have been discussed here. Fig. 5(d) depicts PQ signal having harmonics of third and fifth order with swell. This PQ signal is first decomposed using wavelet 'db4' upto first level and the decomposed signals are shown in Fig. 13.

EMD has been carried out for the lower frequency band. Resultant IMF components for swell with harmonics are presented in Fig. 14. The first IMF component contains the highest frequency information and the last IMF, i.e., seventh IMF contains lowest frequency due to the subtraction of local mean from the signal during various iterations. The last component obtained from EMD process (residue) has no inherent information. The frequency content is very much high in first IMF. In similar fashion, characteristic features have been extracted from first four IMFs of low frequency component and from high frequency component of PQ signal.

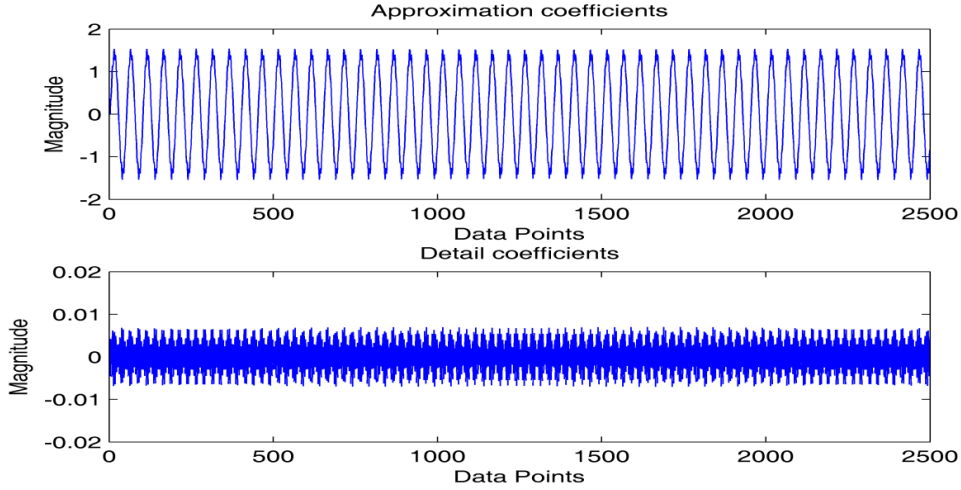


Fig. 11 Low and high frequency components of voltage flicker.

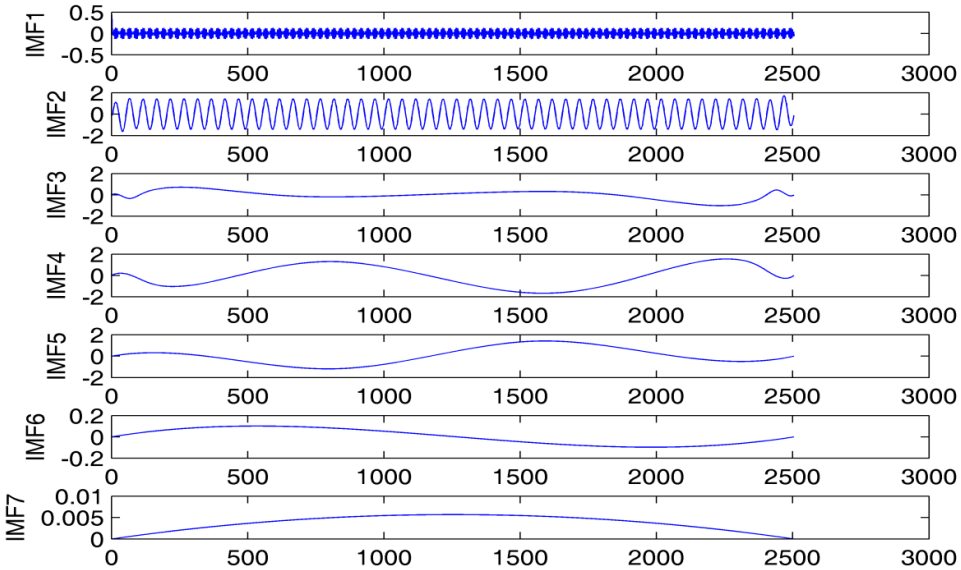


Fig. 12 IMF components and residue of low frequency component of voltage flicker.

Sag with harmonics is another major PQ issue that is simulated as in Fig. 5(e). Harmonics of third and fifth order occurs simultaneously with sag. 'db4' wavelet has been used for decomposing PQ signal into low and high frequency bands to further apply EMD on low frequency band. Fig. 15 presents the approximation and detail coefficients of PQ signal showing the low and high frequency component of PQ signal respectively. EMD of low frequency band of sag with harmonics signal has generated seven IMFs and one residue, that does not signify any information about the PQ issue. Characteristic features have been computed from first four IMFs (as more significant information lies in initial IMFs of the PQ signal), given in Fig. 16, and the high frequency band of PQ signal.

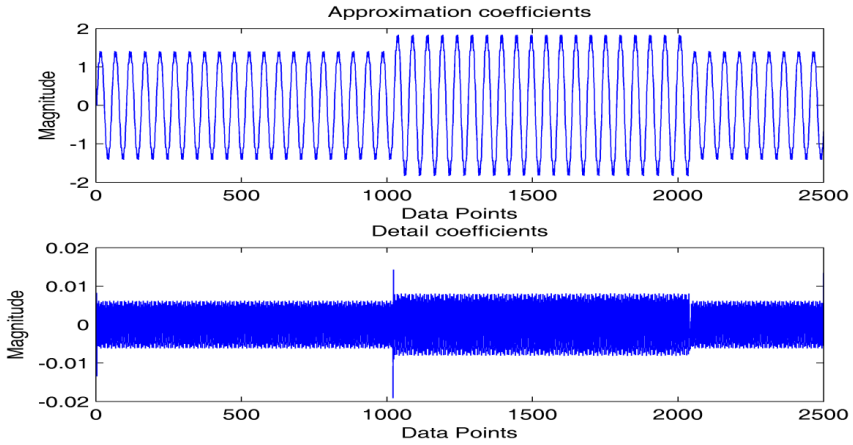


Fig. 13 Low frequency and high frequency components of swell with harmonics.

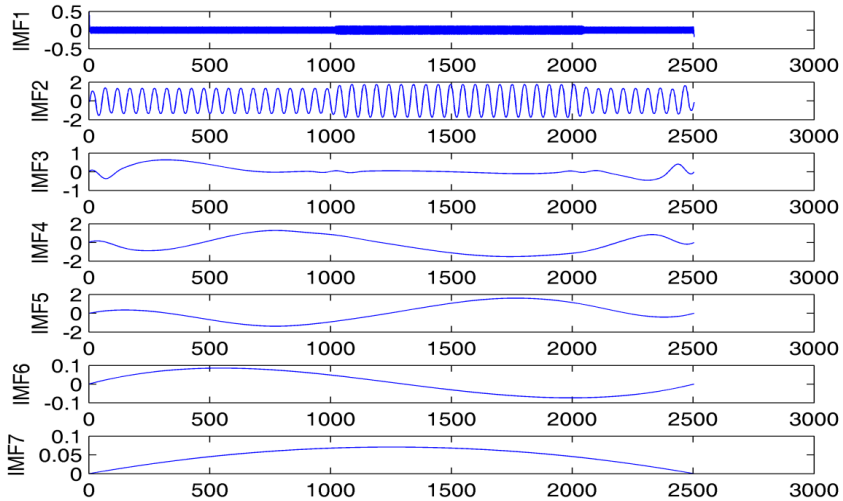


Fig. 14 IMF components and residue of low frequency component of voltage swell with harmonics.

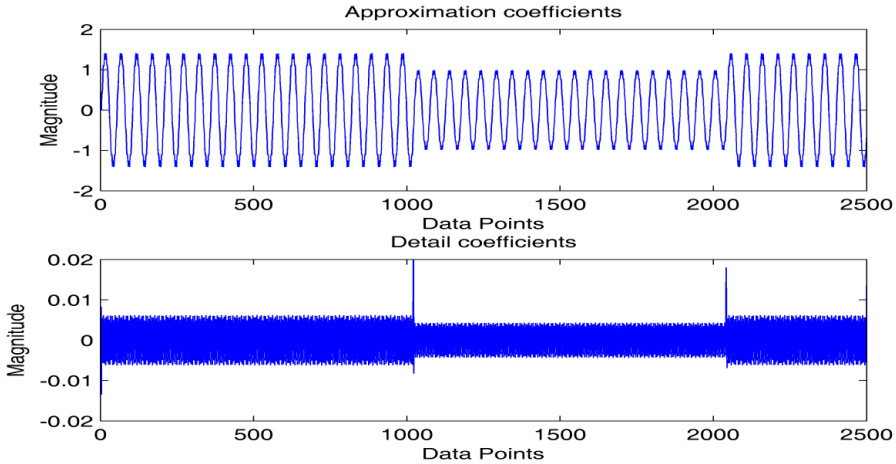


Fig. 15 Low frequency and high frequency components of sag with harmonics.

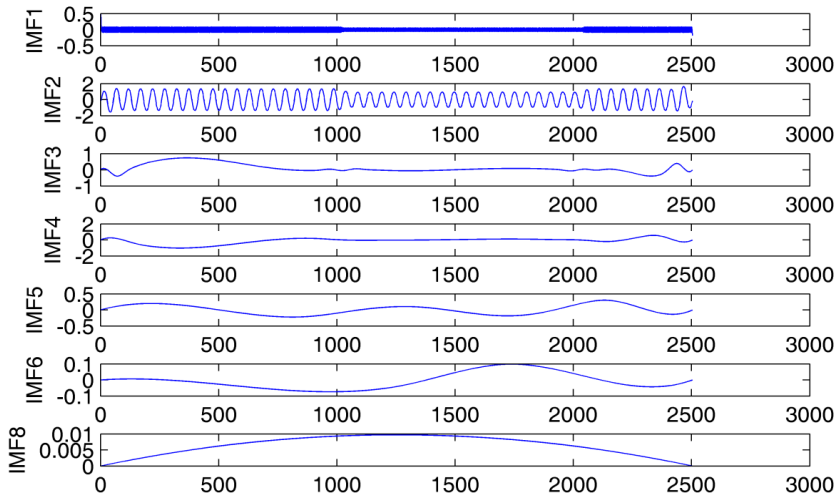


Fig. 16 IMF components and residue of low frequency component of voltage sag with harmonics.

Feature vector has been formed corresponding to all the samples of PQ issues. These feature vectors have been used for training PNN for classification of both single and multiple PQ issues.

4.3 Classification of PQ Issues using PNN

PNN classifier is proposed for classification of single and multiple PQ issues. For classification, eleven classes for ten different PQ issues and normal signal are defined and these classes are such that C1 represents normal, C2 represents sag, C3 represents swell, C4 represents interruption, C5 represents harmonics, C6 represents flicker, C7 represents sag with harmonics, C8 represents swell with harmonics, C9 represents interruption with harmonics, C10 represents sag with flicker and C11 represents swell with flicker. Feature vectors obtained for some randomly selected disturbance samples corresponding to each PQ issue have been utilized for training PNN. Spread constant of PNN has been selected randomly to achieve good classification accuracy. Classification performance of trained PNN has been evaluated by using randomly selected 50% samples of PQ issues as the test samples.

The classification accuracy of PNN corresponding to all PQ issues has been presented in Table 3. The effectiveness of proposed classifier has been investigated for noisy PQ signals also. For this purpose, uniform Gaussian noise has been added to PQ signals at different SNR level. The classification accuracy for PQ signals having SNR of 20 dB, 30 dB and 40 dB has been presented in Table 3. The classification performance of PNN has been compared with that of support vector machine (SVM) using Gaussian kernel. SVM has also been used for the classification of all PQ issues, in both the cases, i.e., noiseless and noisy PQ signals. Though, both PNN and SVM are based on Gaussian function; in the case of PQ issue classification, PNN outperforms SVM in this work due to high-dimensional set of features. SVM has shown average 97.58% accuracy in recognition of noiseless PQ signals. PNN has resulted into average accuracy of 99.64% for noiseless PQ signals. As the SNR of PQ signal decreases, recognition accuracy decreases for both the classifiers. SVM and PNN give 91.09% and 93.25% accuracy respectively for SNR of 20 dB.

The classification accuracy obtained with the proposed work has been compared with some state-of-the-art techniques in the same field of PQ issues recognition in Table 4. Table 4 illustrates the classification accuracy of other established techniques compared with our proposed technique particularly for noiseless PQ signals. These results focus on the better performance of the proposed technique for the classification of PQ issues.

5 Conclusions

This paper presents the application of modified EMD for the analysis of single and multiple PQ issues which are nonlinear and non-stationary. Various types of single and multiple PQ issues such as sag, swell, interruption, harmonics, flicker, sag with harmonics, swell with harmonics, interruption with harmonics, sag with flicker and swell with flicker have been considered in this work for automatic classification. For the detection of these PQ issues, a signal processing technique, modified EMD has been proposed which has DWT preceding traditional EMD. DWT has been applied on PQ signal to split the signal into low and high frequency components. EMD of low frequency component has been carried out producing certain IMFs which represents the oscillatory modes of PQ signal. To extract distinctive information from IMFs, eight characteristic features are extracted from first four IMFs. High frequency component has also been used for the feature extraction. These extracted features are used to train PNN classifier and further test the classification performance of PNN classifier into eleven classes of PQ issues including normal voltage signal.

PNN has remarkably performed the classification of PQ signals even with varying levels of noise. The performance of proposed method is compared with SVM classifier; the results of PNN highlight the outperformance of PNN over SVM.

The current study has tried to implement a signal decomposition technique (EMD) for the detection of PQ anomalies and a neural network for their classification of PQ anomalies. Further, the work can be extended by using optimization techniques for having more suitable features for the classification process. The proposed method is in the process of being tested on the real time PQ issues caused by different faults in the power system.

Table 3 Performance comparison of PNN and SVM under different SNR.

Issue Class	PQ Issue	SVM				PNN			
		Noiseless	40 dB	30 dB	20 dB	Noiseless	40 dB	30 dB	20 dB
C1	Normal	100	97.7	96.4	91.2	100	97.8	97.5	92.2
C2	Sag	99.1	98.4	97.3	90.6	99.9	98.6	96.6	94.2
C3	Swell	99.2	98.1	96.3	90.1	99.8	98.5	97.3	95.1
C4	Interruption	99.8	96.7	95.4	91.1	99.9	97.1	96.9	93.5
C5	Harmonics	97.5	96.1	95.2	90.1	99.8	96.8	95.7	92.4
C6	Flicker	97.2	96.4	94.1	91.5	99.9	97.6	95.5	93.8
C7	Sag with Harmonics	96.9	95.8	93.2	91.3	99.7	97.4	95.1	92.9
C8	Swell with Harmonics	96.2	95.1	93.1	90.4	99.6	96.4	94.8	92.5
C9	Interruptions with Harmonics	96.9	95.8	94.2	92.7	98.8	96.9	95.1	93.9
C10	Sag with Flicker	95.4	94.8	93.2	91.7	99.2	95.9	94.7	92.5
C11	Swell with Flicker	95.2	94.7	92.2	91.3	99.4	95.2	93.1	92.8
Average Accuracy		97.58	96.33	94.60	91.09	99.64	97.11	95.66	93.25

Table 4 PQ issue classification performance of other state-of-the-art techniques.

Ref.	Feature Extraction	Classifier	No. of PQ issue	Classification Accuracy (%)
[30]	S-Transform	MPNN	6	96.17
		SVM	6	97.67
[31]	Wavelet Packet Transform	SVM	8	98.33
[8]	Tunable-Q Wavelet Transform	Dual Multiclass SVM	14	98.78
[29]	Hilbert Huang Transform	PNN	1	98.63
Proposed method	DWT and EMD	PNN	11	99.64

References

[1] R. Kapoor and M. K. Saini, "Hybrid demodulation concept and harmonic analysis for single/multiple power quality events detection and classification," *International Journal of Electrical Power & Energy Systems*, Vol. 33, No. 10, pp. 1608–1622, 2011.

[2] M. H. J. Bollen and I. Y. H. Gu, "Signal processing of power quality disturbances," *John Wiley and Sons*, Vol. 30, 2006.

[3] M. K. Saini and R. Kapoor, "Classification of power quality events-A review," *International Journal of Electrical Power & Energy Systems*, Vol. 43, No. 1, pp. 11–19, 2012.

[4] J. Barros, R. I. Diego and M. D. Apraiz, "Applications of wavelets in electric power quality: Voltage events," *Electric Power Systems Research search*, Vol. 88, pp. 130–136, 2012.

[5] R. Kapoor and M. K. Saini, "Multi wavelet transform based classification of PQ events," *International Transactions on Electrical Energy Systems*, Vol. 22, No. 4, pp. 518–532, 2012.

[6] V. K. Tiwari and S. K. Jain, "Hardware implementation of polyphase-fecomposition-based wavelet filters for power system harmonics estimation," *IEEE Transactions on Instrumentation and Measurement*, Vol. 65, No. 7, pp. 1585–1595, 2016.

[7] K. Thirumala, Shantanu, T. Jain and A. C. Umarikar, "Visualizing time-varying power quality indices using generalized empirical wavelet transform," *Electric Power Systems Research*, Vol. 143, pp. 99–109, 2017.

[8] K. Thirumala, M. S. Prasad, T. Jain and A. C. Umarikar, "Tunable-Q wavelet transform and dual multiclass SVM for online automatic detection of power quality disturbances," *IEEE Transactions on Smart Grid*, Vol. 99, pp. 1–11, 2016.

[9] S. Khokhar, A. A. M. Zin, A. P. Memon and A. S. Mokhtar, "A new optimal feature selection algorithm for classification of power quality disturbances using discrete wavelet transform and probabilistic neural network," *Measurement*, Vol. 95, pp. 246–259, 2017.

[10] L. C. M. Andrade, M. Oleskovicz and R. A. S. Fernandes, "Adaptive threshold based on wavelet transform applied to the segmentation of single and combined power quality disturbances," *Applied Soft Computing*, Vol. 38, pp. 967–977, 2016.

[11] M. K. Saini and R. K. Beniwal, "Optimum fractionally delayed wavelet design for PQ events detection and classification," *International Transactions on Electrical Energy Systems*, Vol. 27, No. 10, pp. 1–15, 2017.

[12] M. K. Saini and R. K. Beniwal, "Design of modified wavelet design using lagrange interpolation," *2016 Second International Innovative Applications of Computational Intelligence on Power, Energy and Control with their impact on Humanity, Ghaziabad*, pp. 264–268, 2016.

[13] M. V. Reddy and R. Sodhi, "A rule-based-S-transform and adaBoost based approach for power quality assessment," *Electric Power Systems Research*, Vol. 134, pp. 66–79, 2016.

[14] J. Li, Z. Teng, Q. Tang and J. Song, "Detection and classification of power quality disturbances using double resolution S-transform and DAG-SVMs," *IEEE Transactions on Instrumentation and Measurement*, Vol. 65, No. 10, pp. 2302–2312, 2016.

[15] R. Kumar, B. Singh and D. T. Shahani, "Symmetrical components based modified technique for power quality disturbances detection and classification," *IEEE Transactions on Industry Applications*, Vol. 52, No. 4, pp. 3443–3450, 2016.

[16] D. D. Ferreira, J. M. de Seixas, A. S. Cerqueira, C. A. Duque, M. H. J. Bollen and P. F. Ribeiro, "Extracting the transient events from power system signals by independent component analysis," *International Transactions on Electrical Energy Systems*, Vol. 26, No. 4, pp. 884–900, 2016.

[17] R. Kapoor and M. K. Saini, "Detection and tracking of short duration variation of power system disturbances using modified potential function," *International Journal of Electrical Power & Energy Systems*, Vol. 47, pp. 394–401, 2013.

[18] M. Seera, C. P. Lim, C. K. Loo and H. Singh, "Power quality analysis using a hybrid model of the fuzzy min-max neural network and clustering tree," *IEEE Transactions on Neural Networks and Learning Systems*, Vol. 27, No. 12, pp. 2760–2767, 2016.

[19] C. B. Khadse, M. A. Chaudhari and V. B. Borghate, "Conjugate gradient back-propagation based artificial neural network for real time power quality assessment," *Electrical Power and Energy Systems*, Vol. 82, pp. 197–2016, 2016.

[20] D. Camarena-Martinez, M. Valtierra-Rodriguez, C. A. Perez-Ramirez, J. P. Amezquita-Sanchez, R. D. J. Romero-Troncoso and A. Garcia-Perez, "Novel down-sampling empirical mode decomposition approach for power quality analysis," *IEEE Transactions on Industrial Electronics*, Vol. 63, No. 4, pp. 2369–2378, 2016.

[21] A. M. Gargoom, N. Ertugrul and W. L. Soong, "Automatic classification and characterization of power quality events," *IEEE Transactions on Power Delivery*, Vol. 23, No. 4, pp. 2417–2425, 2008.

[22] Z. Moravej, M. Pazoki and A. A. Abdoos, "Wavelet transform and multi-class relevance vector machines based rec0ognition and classification of power quality disturbances," *International Transactions on Electrical Energy Systems*, Vol. 21, No. 1, pp. 212–222, 2011.

[23] A. N. Akansu and R. A. Haddad, *Multi resolution signal decomposition, transforms sub bands, and wavelets, Second Edition, Academic Press*, 1992.

[24] I. Daubechies, *Ten lectures on wavelets*. Philadelphia, USA: CBMSNSF, Regional Conference Series, SIAM, Vol. 61, 1992.

[25] N. E Huang and S. S P Shen, *Hilbert–Huang transform and its applications*, World Scientific Publishing Co., 2005.

[26] A. Baccigalupi and A. Liccardo, "The Huang Hilbert transform for evaluating the instantaneous frequency evolution of transient signals in non-linear systems," *Measurement*, Vol. 86, pp. 1–13, 2016.

[27] D. F. Specht, "Probabilistic neural networks," *Neural Networks*, Vol. 3, No. 1, pp. 109–118, 1990.

[28] C. H. Chen, *Fuzzy Logic and Neural Network Handbook*, New York: McGraw Hill Publishing Company, 1996.

[29] M. Manjula, S. Mishra and A.V. R. S. Sarma, "Empirical mode decomposition with Hilbert transform for classification of voltage sag causes using probabilistic neural network," *Electrical Power and Energy Systems*, Vol. 44, No. 1, pp. 597–603, 2013.

[30] S. R. Mohanty, "Classification of disturbances in hybrid DG system using modular PNN and SVM," *Electrical Power and Energy Systems*, Vol. 44, No. 1, pp. 764–777, 2013.

[31] K. Manimala, K. Selvi and R. Ahila, "Optimization techniques for improving power quality data mining using wavelet packet based support vector machine," *Neurocomputing*, Vol. 77, No. 1, pp. 36–47, 2012.



M. K. Saini was born in Rohtak, Haryana (INDIA), on Oct. 2, 1981. He did his B.E., M.E. in Electrical Engineering from Maharshi Dayanand University, Rohtak, Haryana (INDIA) with Honors. He did his Ph.D. in Electronics and Communication Engineering from Delhi College of Engineering, New Delhi (INDIA). He is currently associated with Department of Electrical Engineering in DCR University of Science and Technology, Sonepat. His field of interest includes digital signal processing, power quality, image processing and power system. He has been the author of more than 50 papers in different journals and conferences in the area of interest.



R. K. Beniwal received his Bachelor of Technology in Electrical and Electronics Engineering from Kurukshetra University, Kurukshetra, Haryana (INDIA). He received his Master of Technology in Instrumentation and Control Engineering from Maharshi Dayanand University, Rohtak, Haryana (INDIA). Presently, he is pursuing PhD in Electrical Engineering from DCR University of Science & Technology, Sonepat, Haryana (INDIA). His research interests include power quality, signal processing, system design and microcontroller-based instrumentation. He has around fifteen publications in journals and conferences.

Available online at www.ijapie.org

INTERNATIONAL JOURNAL OF ADVANCED PRODUCTION AND INDUSTRIAL ENGINEERING

IJAPIE-2018-04-222, Vol 3 (2), 06-12

IJAPIE
Connecting
Science & Technology
with Management.

A Journal for all
Products & Processes.

Review on Different Types of 3D Watermarking

Akshay Mool[1], Pran Swarup Borah[2], Ramjan Ali[2], Dr. Jeebananda Panda[2]
([1]Department of Information Technology, [2]Department of Electronics and Communication, Delhi Technological University, Delhi, India)
Email: akkmool@gmail.com, pran.swarup@gmail.com, ramjan494@gmail.com, jpanda@dce.ac.in

Abstract : In this paper, an attempt has been made to summarise the work done related to 3D watermarking in past years. Here, the different types of watermarking methodology for 3D models have been presented. Focus on the 3D watermarking is ensured, ranging from the earliest time till present, regarding their nature and robustness against various attacks.

Keywords: Digital Watermarking, 3D models, 3D watermarking, Robustness

I. INTRODUCTION

WATERMARKING in the field of 3D models made in virtual space using various software like Computer-Aided Drafting (CAD) is still in a very less developed stage due to less or no research work done regarding this field of interest. However, there are still many important works done in this field. This paper tries to summarize the few important works done by people regarding this topic, starting from the beginning of the idea of 3D watermarking to the recent change in trends. Comparison between different types of watermarking based on their properties and robustness against various attack has been made in this paper.

This paper is organized as follow: Section 2 presents the related work that has been done in other fields. Section 3 present extensive review regarding the different types of watermarking

II. RELATED WORK IN OTHER FIELDS

Watermarking has been used in other field of work like images, audios etc. for the purpose of copyright related problems like- copyright protection, broadcasting monitoring. These digital watermarking methods have achieved new heights of development making the watermark more robust and imperceptible. These watermarking methods are also commercially available e.g. – Digimarc company.

In the past few years digital watermarking for 3Dimensional models has made noticeable progress. Unlike other digital watermarking schemes, several parameters have been made for 3D watermarking for measuring the imperceptibility for the watermark.

III. DIFFERENT TYPES OF WATERMARKING

A. Watermarking Three-Dimensional Polygonal Models through Geometric and Topological Modifications (1988)

This is the one the earliest watermarking scheme for 3D models. In this paper, [1] Ryutarou proposed technique of embedding data into the 3D polygonal models of geometry. Basically, data embedded into either their vertex coordinates, their vertex topology (connectivity), or both. A “polygonal model” containing one or more of the following geometrical primitives: points, lines, polygons, connected polygons, polyhedrons, and connected polyhedrons is required for the method.

In this paper, the author has given three algorithms for embedding of data in 3D model.

The Triangle Similarity Quadruple (TSQ) algorithm gives a quadruple of adjacent triangles that share edges in the configuration as embedding primitives. TSQ doesn’t require the original cover 3D model for extraction. TSQ can withstand translation, rotation, and uniform-scaling transformations of the stego-3-D-model, resection and local deformation.

Tetrahedral volume ratio (TVR) uses ratio of the volumes of a pair of tetrahedrons is the embedding primitive. TVR algorithm does not require a cover-3-D-model for extraction. The watermarks that it produces survive affine transformation, but are destroyed by topological modifications such as remeshing, randomization of vertex

coordinates and geometrical transformations that are more general than affine transformation (e.g., projection transformation), among other disturbances.

Mesh density Pattern, algorithm tessellates given curved surfaces. It embeds a visible pattern by modulating the sizes of triangles in the output mesh. This pattern is hardly visible if displayed with a smooth shading (e.g., Gouraud shading) using proper vertex normal vectors calculated from the original curved surfaces, but becomes visible when displayed by using wire mesh rendering. This watermark withstands practically every geometrical transformation. The algorithm is resistant but not immune to polygonal simplification and other topological manipulations.

Combining multiple embedding methods, each with their own strengths and weaknesses, is a possible approach to increasing the utility of data embedding. However, they are not robust enough, for example, to prove that a theft has occurred. They lack many qualities, the most important of which is robustness, that are considered necessary for most applications of data embedding.

B. Geometry-based watermarking of 3D models (1999)

In this paper, [2] Oliver has proposed a watermarking system for a private watermarking. The idea is to use collections of surfaces as an embedding primitive.

The system proposed in this article introduces modifications in object-model normal distribution to achieve independence from one particular mesh representation. It requires a mesh representation of a 3D model consisting entirely of triangle patches as input. The watermark data is embedded in this mesh by performing certain displacements of points, which in turn introduces specific changes in mesh surface normal distribution. The resulting mesh again consists of triangle patches, with no topological or adjacency (vertices or faces) changes with respect to original mesh.

The system uses a collection of surfaces as an embedding primitive. These collections are generated by grouping model normal into distinct sets called bins. A bin is the entity for embedding one bit of watermark data. The bins can be constructed in a general way by tessellating the unit sphere.

The embedding and retrieval processes consist of several stages, as follows:

General outline of the embedding procedure: (El) Calculate consistent surface patch normals (E2) Sample model normals to bins

(E3) Apply core watermark embedding algorithm.
General outline of retrieval procedure:

(R1) Calculate consistent surface patch normals

(R2) Transform model into spherical representation (EGI) and adjust model orientation

(R3) Sample model normals to bins
(R4) Apply core watermark retrieval algorithm

The algorithm showed promising potential with respect to robustness against mesh simplifications. One drawback of the algorithm is the large amount of a priori data needed before watermark retrieval. For private watermarks, this is tolerable.

C. Wavelet-Based Blind Watermarking of 3D Models (2004)

In the given paper, [3] Uccheddu proposed a novel multi resolution mesh watermarking algorithm particularly designed to work with semi-regular meshes with subdivision connectivity. The algorithm embeds by the watermark modifying the wavelet coefficients of 3D models obtained by decomposing the host mesh by means of the algorithm proposed by Lansbury. Particular attention is paid to ensure that the embedding algorithm preserves the visual integrity of the models. The watermark is recovered by means of a correlation detector designed according to statistical detection theory. Their system does not require that the original non-marked mesh is available at the detector, thus resulting in a much more flexible system easily adaptable to practical applications.

The algorithm embeds the watermark by modifying the position of the mesh vertices in a transformed domain, i.e. wavelet domain. The 3D watermarking system presented in this paper embeds a numeric code into a semi-regular mesh with subdivision connectivity using multi-resolution framework. The algorithm presented in this paper belongs to the category of detectable watermarks. The watermarking embedding algorithm works according to three parameters (a secret key, the resolution level and coefficient determining the strength of the watermark.)

WATERMARK EMBEDDING

1) A particular watermark-dependent structure called watermarking map is generated according to Key.

2) The input model is decomposed into a set of wavelet coefficients and a base domain.

3) The vertices of the model and the wavelet coefficients at the same level are used by the embedding algorithm to embed the watermark by altering the modulus of a subset of the wavelets coefficients.

4) The watermarked wavelet coefficients and the other sets of wavelets are used to reconstruct the watermarked full resolution model.

WATERMARK DETECTION

The detection procedure works as follows: the user specifies the numeric key and the level of resolution where he wants to

verify the presence of Key and the detector provides a positive or negative answer i.e.-if watermark is present or not.

The models used in the experiments are the semi-regular meshes made available to the public by the Multi-resolution Modelling Group of Caltech University. One of the main problems of 3D watermarking is the wide variety of different attacks possible on a polygonal mesh. The technique is specific for semi-regular meshes with subdivision connectivity, thus do not take into account those attacks that alter these properties of the mesh such as re-triangulation, simplifications or re-meshing. Instead the robustness of the algorithm against additive noise, low pass filtering, geometric manipulations, cropping and a combination of the above are tested.

D. Efficient Spectral Watermarking of Large Meshes with Orthogonal Basis Functions (2005)

In this paper, [4] Jianhua presented a novel spectral watermarking scheme using a new set of orthogonal basis functions derived from radial basis functions. The watermarking scheme embeds the digital watermarks by modifying the low-frequency components of a given shape in the spectral domain.

The watermark embedding phase computes a small set of new orthogonal basis functions. Then the geometry of the original mesh is projected to these basis functions spanning the spectral domain to acquire a set of corresponding spectral coefficients. Watermarks will be encoded into the leading coefficients which can be used later to reconstruct the watermarked mesh together with the unmodified coefficients. Thus, compared to related approaches, the algorithm runs much faster by two orders of magnitude, hence leading to efficient watermarking of very large models. Also as the watermarking scheme only modifies the "low-frequency" component of a given shape, the visual differences between the original mesh and the watermarked mesh are almost imperceptible.

As already told that watermarking scheme embeds the digital watermarks by modifying the low-frequency components of a given shape in the spectral domain. The new orthogonal basis functions derived via singular value decomposition will be used to decompose the input mesh into a spectral representation, and then the coefficients of the leading part of the spectrum which are more robust against attacks can be modulated. The watermarked mesh is later produced with an inverse transform using the same basis functions and is ready to be distributed.

After registration and resampling, the watermarked mesh is spectral analyzed to get a set of coefficients to extract the watermark.

The algorithm is robust against Similarity Transform, Cropping, Simplification, Additive noise, Remeshing and Smoothing.

E. An Oblivious Watermarking for 3-D Polygonal Meshes Using Distribution of Vertex Norms (2007)

In this paper, [5] *Cho* proposed two statistical watermarking methods for 3D polygonal mesh models, which modify the distribution of vertex norms via changing respectively the mean and the variance of each bin by Histogram mapping function for embedding of watermarking bit. Histogram mapping function are introduced to modify the distribution.

The two methods are proposed, one method is shifting the mean of distribution and another is to shift change of its variance.
In addition, *Cho* proposed an oblivious watermarking detection scheme, which can extract the watermark without referring to the cover mesh model.

Cho modified the distribution of vertex norm instead of normal distribution by *O.Benedens* to hide watermark information.

3D mesh polygonal model has no unique representation i.e. No implicit order and connectivity of vertices, while image data is represented by brightness (or amplitude of RGB component in the case of color images) of pixels sampled over a regular grid in two dimensions.

We analyze two parameters that can be adjusted to improve the robustness of the proposed methods. One is the watermark strength factor alpha, another is the size of bin**.** However, watermark transparency should be also carefully considered and the use of larger bins limits the number of watermark bits.

The methods show robustness against various kind of distortion attack such as addition noise, simplification, smoothing, re-meshing, and clipping and so on.

F. A New Approach of 3D Watermarking Based on Image Segmentation (2008)

In this paper, [6] *Saoussen Ben* proposed a robust 3D triangular mesh watermarking algorithm based on 3D segmentation, new approach of 3D image watermarking which combines three classes of insertion. This combination allows benefiting from the multiple advantages of each class. This is realized by segmenting the 3D image in unrefined regions having different values of curvature and by adapting every region to a class of insertion to obtain the maximum of invisibility of the mark.

The methods use the two possible domains of insertion:

spatial (geometric and topologic), and spectral domain

The segmentation decomposes a 3D mesh into connected subsets of mesh. The chosen algorithm that was implemented was proposed by L.Guillaume. It decomposes the object into almost constant curvature triangle regions with precise edge boundaries.

Firstly, discrete curvature is calculated for each vertex according to the work of Meyer et al. Then, vertices are classified into clusters according to their principal curvatures values. A region growing algorithm is then processed assembling triangles into connected labeled regions according to the vertex clusters.

Holes between regions are filled taking into account boundary criteria. Finally, a region adjacency graph is processed and reduced in order to merge similar regions according to several criteria (curvature similarity, size, common perimeter).

For robustness, to get the maximum efficiency, their idea was to profit from the advantages of many classes of watermarking. So, they choose to use three schemes in one algorithm.

(1) Geometric (2) Topologic (3) spectral scheme. First scheme permits getting robustness against geometric attacks, the second permits the signature to be robust against remeshing and simplification and the last scheme allows obtaining robustness against filtering and compression.

A quantitative evaluation in terms of "SNR" was used to measure the quality of the marked image. The robustness of new method was verified after application of various types of attacks such as RST transformations (rotation, scaling and translation), smoothing, random noise added to vertex coordinates, cropping vertices, simplification and remeshing.

G. A New Watermarking Method for 3D Models Based on Integral Invariants (2009)

In this paper, [7] *Yu-Ping et al.* proposed semi-fragile watermarking method based on integral invariants. It is a spatial domain method robust against rigid transformations and noise attacks and improves our algorithm by increasing its embedding capacity, currently limited to two integral invariants.

One solution would be using multi-resolution analysis methods to simplify the model and embed a watermark at the corresponding simplified model vertex. Another solution would be to find a method to simultaneously change four kinds of integral invariants.

It is desired that the hidden data be robust to unintentional changes like model compression, rigid transformation, and random noise originating from format conversion, similar to image watermarking nomenclature. They have characteristic watermarking algorithms showing this property as semi-fragile.

With each vertex that will undergo watermarking, the integral invariants of the unwatermarked model are calculated. These invariants are then slightly changed to embed the watermark image parts. In order to change the integral invariants to the new value, the positions of the vertex and its neighbors are modified.

The method is robust against rigid transformations and noise attacks. The method can recover only a fraction of the watermark, when model is cropped.

H. Constrained Optimization of 3D polygon mesh watermarking by Quadratic Programing (2009)

In this paper, [8] *Roland* propose a blind and robust watermarking method for 3D polygonal meshes by minimizing the mean square error between the original mesh and the watermarked mesh under several constraints using Quadratic programming.

In this paper, a histogram-based watermarking algorithm by globally optimizing distortions between the watermarked mesh and the original mesh is proposed, with several constraints to be satisfied. We take similar approaches as in the paper given by *cho* to modify the distribution of vertex norms, but the modification is executed by incorporating quadratic programming (QP) into the watermarking scheme to minimize the mean square error (MSE) between the original mesh and the watermarked mesh.

Three constraints are applied to ensure that the embedded watermarking bits are correctly decoded later. The first constraint ensures that the points belonging to the nth bin still belong to that bin after the watermarking process. The second constraint ensures that the mean of the transformed vertex norms in the nth bin is greater (or smaller) than a reference value when the embedded watermarking bit $\omega n = +1$ (or $\omega n = -1$). This constraint must be satisfied to ensure that the embedded watermarking bits could be correctly extracted later. Another constraint (3^{rd} constraint) was proposed, to guarantee that the centre of gravity of the watermarked mesh is the same as the original one.

Thus, the problem of assigning distortions to an optimization problem is changed, with a quadratic objective function and three constraints. This is exactly a quadratic programming problem. The theory of convex optimization guarantees that such kind of problems can be solved reliably and efficiently, even in very large scales.

Compared with the watermarking schemes in paper given by *cho*, this method performs better in resisting Gaussian noise, thus potentially is a better watermarking algorithm. However, this method has difficulties in dealing with large meshes because of the complexity limitations of computers and existing QP solvers.

I. A novel semi-blind-and-semi-reversible robust watermarking scheme for 3D polygonal models (2010)

In this paper, [9] *Chao-Hung Lin* has introduced a novel semi-blind-and-semi-reversible robust watermarking scheme for three-dimensional (3D) polygonal models. The proposed approach embeds watermarks in the significant features of 3D models in a spread-spectrum manner. In this paper, novel semi-blind robust watermarking scheme for 3D polygonal models. Rather than requirement of the original models, only a small amount of information is needed to detect watermarks. The method embeds a watermark in the significant features of the models, which are detected by the proposed similarity-invariant curvature estimation approach. The approach embeds the watermark by deforming the significant features with shape constraints and successfully leads to imperceptible watermark embedding. Moreover, it can semi-recover the original models by deforming the watermarked models back using only a little information relative to the original models.

Embedding procedure
To consider perceptual invisibility, the watermark is embedded in significant patches, a curvature estimation approach to determine these embedding patches is proposed. To determine the embedding order, the embedding patches are sorted by geodesic distances that are insensitive to various aforementioned attacks. Finally, each bit of watermark is embedded in one embedding patch by a feature-preserving deformation approach

Detection procedure
In the detection procedure, the embedding positions and embedding order of the suspected models can be obtained in the same steps. The watermark is then extracted by comparing the embedding patch curvatures in the suspected model with the stored curvature information.

Model recovery
The proposed approach can semi-recover the original models after extracting the watermarks. It is achieved by deforming the watermarked model back.

The experimental results show that our approach is robust against a wide variety of attacks, including similarity transformation, noise addition, smoothing, cropping, vertex reordering, simplification, and even pose deformation. In addition, this approach has the ability to semi-recover the original models.

Currently, the proposed approach has the following two limitations. It is not suitable to handle the models that have smooth shapes as well as few protrusive patches, such as sphere and knot, since we select protrusive patches, i.e., high curvature patches, to embed watermarks. The other limitation is that our approach cannot resist the attacks of non-uniform scaling, shearing, and even free-form deformation since these attacks could cause severe alteration to the surface curvature.

J. Blind 3D model watermarking based on Multi-resolution and Fuzzy logic

In the paper, [10] Prof. Sharvari proposed a blind and robust watermarking system based on wavelet transform, a fuzzy inference system and a multi-resolution representation (MRR) of the 3d model. The method presented here is a combination of two algorithms proposed by Saeed K. Amirgholipour and Mukesh Motwani with some modifications. Paper given by Xavier represented a novel blind watermarking algorithm based on a joint DWT-DCT for 2D digital image. The idea of inserting watermark in the combined transform was based on the fact that, the joint transform can eliminate the drawback of each other and then, an effective watermark is embedded in the most

robust and imperceptible parts of the image. Watermarking is done with embedding the watermark in the special middle frequency coefficient sets of 3-levels DWT transformed of a host image, followed by computing 4×4 block-based DCT on the selected DWT coefficient sets. Paper has proposed a non-blind watermarking algorithm based on wavelets and fuzzy logic, which inserts 8-bit grey scale image as a watermark into the 3D model.

The algorithm used in this paper embeds the watermark by modifying the wavelet coefficients of the 3 D model at third level and by using Mamdani's fuzzy inference system, thus enhancing the robustness and making it more imperceptible as compared with other existing algorithms. Particular attention would be paid to ensure that the embedding algorithm preserves the visual integrity of the models.

Watermarking embedding
Haar wavelet transform on the 3d model is applied and four coefficients are generated, then Haar wavelet transform is applied again and again to generate level 2 approximation, level 3 approximations and detail coefficients. Total 16 matrices are generated in this process. Watermark image is converted into binary format and scramble watermark with Arnold transform Inputs (like Curvature, Area and Bumpiness) of 3d model are computed and Fuzzy Inference system (FIS) is applied and decide weight depending upon rules. Modify coefficients to embed the watermark into the model where the corresponding weighting factor has the values either high or higher. The watermark is inserted by adjusting the remainder of wavelet coefficient vector. Apply inverse DWT on the modified coefficients set up to level 3.

Watermarking extraction
Watermark can be extracted from the 3D watermarked model by using a blind method. Algorithm for extracting the watermark is as follows:

Step 1: Perform the first three steps of insertion process on 3d watermarked model.

Step 2: Use the same FIS as used in the embedding process and calculate the remainder of the coefficients for high and

higher weight values of FIS. If the remainder of the coefficient is greater than reference value then the extracted watermark bit is 1 otherwise it is 0.

Step 3: The scrambled watermark is reconstructed using the extracted watermark bits with Arnold transform and calculate the correlation between original and extracted watermark.

The system has been proved to be robust against smoothing, similar transformations (Rotation, Translation and Scaling), noise and cropping attacks.

K. Optimized 3D Watermarking for Minimal Surface Distortion

In this paper, [11] Adrian has proposed a new 3D watermarking methodology which minimizes the object surface distortions by using the Levenberg–Marquardt optimization method for vertices represented in spherical coordinates. The proposed method is statistical, blind and robust 3D watermarking method.

The Watermark is embedded into histograms of distances from the object centre to vertices on its surface by slightly displacing the location of the vertices. The proposed method considers an error function consisting of three components measuring the distortion with respect to the original surface, the watermarked surface (updated surface) and the Euclidean distance from the original vertex location. This error function ensures both a minimal distortion with respect to the original surface as well as enforces smoothness in the object surface resulting after watermarking.

We provide a study of minimal object watermark embedding and a study of the watermark security for the proposed methodology. Here safety detection difference (SSD) represents the normalized difference between the distribution of the distance from the watermarked object surface to the center, and that of the uniform distribution. This SSD characterizes the level of distortion that the watermark object may undergo during an attack.

The security of the watermark can be improved if additional key-generated parameters would be added. the proposed watermarking methodology is better than other method like method proposed by Cho *et al.*, and the method using quadric error metric (QSP) has high robustness against common mesh attacks like additive noise, Laplacian smoothing, mesh simplification, quantization and uniform resampling, while ensuring object centre doesn't change. It can be observed that the distortion is increased when either Embedding Strength Factor α or the embedding capacity is increased.

L. Triangle Surface Mesh Watermarking Based on a Constrained Optimization Framework

In this paper, [12] Xavier Rolland proposed generalizing framework for 3D mesh watermarking, where the embedding process is formulated as a quadratic programming (QP) problem. This paper introduced three different extensions to the baseline system:

(i) The revision of the mathematical framework to support integral definitions of the centre of mass of a mesh.

(ii) The relaxation of the constraint on the direction of alteration to allow displacements deviating from the radial direction.

(iii) The integration of perceptual components in the cost function to better account for human perception during the minimization process.

Surface meshes are approximations of the surface boundary of 3D objects by M.Botsch and most 3D watermarking methods focus on the popular triangle mesh representation.

Non-blind 3D watermarking methods exhibit satisfactory robustness, but blind watermarking detection cannot leverage on recent advances in shape matching, which could help for registration e.g. when dealing with different poses of a model. Moreover, Xavier et al. review relevant state of art technique for 3D watermarking through special care to highlight their limitation. And introduce a mathematical framework that will serve to formulate our baseline 3D watermarking system as a quadratic programming problem.

M. Perceptual 3D watermarking using Mesh Saliency (2017)

In this paper, [13] *Jeongho Son* has proposed a novel blind and robust 3D Watermarking method which focuses on preserving the appearance of watermarking model using Mesh saliency. This paper used the vertex norm distribution and solved the quadratic error minimization problem to insert watermark bits.

It captures the visual appearance by preserving regions having high saliency by combining spatial domain- based watermarking and frequency-based weight map.

The proposed method shows a better result in terms of distortion metrics (The mesh Structural Distortion Measure [MSDM] and The Fast Mesh Perceptual Distance [FMPD]) compared to other methods like method proposed by *cho* and *Xavier*.

The proposed method shows good performance compared to the existing method in terms of robustness against Additive noise, Laplacian smoothing, Quantization and Mesh simplification in terms of averages of Bit error ratio (BER).

IV. CONCLUSIONS

This paper discusses and reviews various methods that have been introduced for 3D watermarking over the years, and discusses their merits and limitations in context to modern day technology.

REFERENCES

[1] Ryutarou Ohbuchi, Hiroshi Masuda, Masaki Aono. "Watermarking Three-Dimensional Polygonal Models through Geometric and Topological Modifications." IEEE Journal on Selected Areas in Communications (Volume:16, Issue:4, May 1998), pp.561-560, 1998.Prasad SV Asthana R. (2004). Aluminum Metal-Matrix Composites for Automotive Applications: Tribological Considerations. *Tribology Letters 17:445-453*.

[2] Oliver Benedens. "Geometry-based watermarking of 3D models." IEEE Computer Graphics and Applications (Volume:19, Issue:1, Jan/Feb 1999), pp.46-55, 1999.

[3] F. Uccheddu, M. Corsini, M. Barni. "Wavelet-Based Blind Watermarking of 3D Models." MM&Sec '04 Proceedings of the 2004 workshop on Multimedia and security, pp.143-154, 2004.

[4] Jianhua Wu, Leif Kobbelt. "Efficient Spectral Watermarking of Large Meshes with Orthogonal Basis Functions." The Visual Computer, Volume 21, Issue 8–10, pp.848–857, 2005.

[5] Jae-Won Cho, Rémy Prost, Ho-Youl Jung. "An Oblivious Watermarking for 3-D Polygonal Meshes Using Distribution of Vertex Norms." IEEE Transactions on Signal Processing (Volume:55, Issue:1, Jan. 2007), pp.142-155, 2006.

[6] Saoussen Ben Jabra, Ezzeddine. "A New Approach of 3D Watermarking Based on Image Segmentation." Computers and Communications, 2008. ISCC 2008. IEEE Symposium on, 2008.

[7] Yu-Ping Wang, Shi-Min Hu. "A New Watermarking Method for 3D Models Based on Integral Invariants."IEEE Transactions on Visualization and Computer Graphics (Volume:15, Issue:2, March-April 2009), pp.285-294, 2008.

[8] Roland Hu, Patrice Rondao-Alface, Benoıt Macq. "Constrained Optimisation of 3D polygon mesh watermarking by Quadratic Programing." Acoustics, Speech and Signal Processing, 2009. ICASSP 2009. IEEE International Conference on, 2009.

[9] Chao-Hung Lin, Min-Wen Chao, Chan-Yu Liang, Tong-Yee Lee. "A novel semi-blind-and-semi-reversible robust watermarking scheme for 3D polygonal models." The Visual Computer, Volume 26, Issue 6–8, pp 1101–1111, 2010.

[10] Sharvari C. Tamane, Ratnadeep R. Deshmukh. "Blind 3D model watermarking based on Multi-resolution and Fuzzy logic." International Journal of Computer Science & Information Technology (IJCSIT) Vol 4, No 1, pp.117-126, 2012.

[11] Adrian G. Bors, Ming Luo. "Optimized 3D Watermarking for Minimal Surface Distortion." IEEE Transactions on Image Processing (Volume:22, Issue:5, May 2013), pp.1822-1835, 2012.

[12] Xavier Rolland-Nevière, Gwenael Doerr. "Triangle Surface Mesh Watermarking Based on a Constrained Optimization Framework." IEEE Transactions on Information Forensics and Security (Volume:9, Issue:9, Sept. 2014), pp.1491-1501, 2014.

[13] Jeongho Son, Dongkyu Kim, Hak-Yeol Choi, Han-Ul Jang, Sunghee Choi. "Perceptual 3D watermarking using Mesh Saliency." International Conference on Information Science and Applications: Information Science and Applications, pp.315-322,2017.

Robust Object Tracking with Crow Search Optimized Multi-cue Particle Filter

Kapil Sharma[a], Gurjit Singh Walia[b], Ashish Kumar[a], Astitwa Saxena[c], Kuldeep Singh[d]

[a]*Delhi Technological University, Delhi, India*
[b]*Defence Research and Development Organization, Ministry of Defence, India*
[c]*Netaji Shubhas Institute of Technology, Delhi, India*
[d]*Bharat Electronics Ltd., Central Research Laboratory, Government of India, Ghaziabad, India*

Abstract

Particle Filter(PF) is used extensively for estimation of target Non-linear and Non-gaussian state. However, its performance suffers due to inherent problem of sample degeneracy and impoverishment. In order to address this, we propose a novel resampling method based upon Crow Search Optimization to overcome low performing particles detected as outlier. Proposed outlier detection mechanism with transductive reliability achieve faster convergence of proposed PF tracking framework. In addition, we present an adaptive fuzzy fusion model to integrate multicue extracted for each evaluated particle. Automatic boosting and suppression of particles using proposed fusion model not only enhances performance of resampling method but also achieve optimal state estimation. Performance of the proposed tracker is evaluated over 12 benchmark video sequences and compared with state-of-the-art solutions. Qualitative and quantitative results reveals that the proposed tracker not only outperforms existing solutions but also efficiently handle various tracking challenges. On average of outcome, we achieve CLE of 7.98 and F-measure of 0.734.

Keywords: Particle Filter, COA, object tracking, fusion model

1. Introduction

Object tracking is a vital research area in computer vision due to its promising applications in the field of military surveillance, augmented reality, robotics, medical imaging and human-computer interaction. It aims at keeping track of targeted object in a video sequence. Initially, target is localized either manually or through a detection algorithm and subsequently its trajectory is traced over the period of time. Keeping path of target's trajectory in a video sequence is

Email address: kapil@ieee.com (Kapil Sharma)

challenging due to its scale and pose variations, fast and abrupt motion, background clutters and full or partial occlusion [1].

Generally, object tracking methods can be categorized into either stochastic framework or deterministic framework. Stochastic framework include probabilistic methods in the Bayesian framework for state estimation. Under stochastic framework, linear and gaussian state estimation was addressed using kalman filter [2], extended kalman filter and unscented kalman filter [3]. Whereas non- linear and non-gaussian state can be estimated using particle filter (PF) [4], condensation filter [5] and boot strap filter [6]. On the other hand, deterministic framework viz. mean shift [7], fragment based tracker [8] and multi-stage tracker [9] employs target search in each frame to maximize similarity between the target and search space. These methods used less spatial information of the target and hence, were vulnerable to occlusion and background clutters. How- ever, stochastic methods reduced target sampling patches during tracking and were able to address the challenges occurred due to similar backgrounds and occlusion.

Under stochastic methods, PF has shown better results than other methods but its performance is severely degraded due its inherent problem of particle degeneracy and impoverishment [10]. Particle degeneracy occurs due to updation of particles with insignificant weight. These particles dispense less towards the state estimation and their usage for subsequent estimation leads to wastage of computational efforts. In order to address this, resampling techniques such as sequential resampling [11], adaptive resampling [12], dynamic resampling [13], spline resampling [14] were proposed. But implication of these methods in PF leads to sample impoverishment whereas all the particles converge to a single end leading to drastic degradation in tracker's performance. Recently, particle impoverishment is solved using nature-inspired and evolutionary optimization viz. Particle Swarm Optimization [15], Firefly Algorithm [16], Spider Monkey [17], Social Spider [18], Cuckoo Search [19], Modified Galaxy based Search [20], Bat Algorithm [21]. The exploitation and exploration characteristics of these methods introduce randomness in search space through diversification of particles. The optimal particles generated through these optimization not only achieved fast convergence rate but also enhanced the accuracy of PF frame- work. However, most of PF based tracking solution were proposed using only single feature and hence, leading to degradation in performance under dynamic environment.

Multicue based tracking framework have been discussed and reviewed mostly under deterministic methods [22]. Recently, under stochastic methods multicue based tracking framework were investigated [23], [24], [20]. In these work, multiple complementary cue are integrated to overcome individual cue limitations. In [23] author used color, texture and edge cue for the object representation and integrated them using an adaptive weighting scheme. Walia and Kapoor [24] exploited color, thermal and motion feature for object representation and integrated their scores using PCR-5 rules. In [20], authors calculated color histogram and histogram of orientation gradient (HOG) for each particle. Resampling was performed using modified galaxy based search algorithm. However,

adaptive integration of multicue was not addressed. In addition, resampling methods proposed in previous work require the processing of all evaluated particles and hence, require more computational power. Hence, future tracking solutions should consider adaptive fusion of multicue to handle dynamic environmental challenges along with efficient resampling method for real time applications.

In this paper, we propose a muliticue object tracking framework based on PF with a novel nature inspired resampling method. An adaptive fuzzy based fusion model is proposed for automatic suppression and boosting of particles weights. Outlier detection mechanism is also utilized to detect low performing particles to improve the performance of resampling method. To summarize, the main contributions of our research work are as follows:

- We propose an object tracking framework in which target is represented by complementary multi-cue viz. color and texture for each particle. Color cue is sensitive to illumination variations, similar background and occlusion while texture cue can handle these variations effectively. On the other hand, texture cue fails during scale variations while color cue maintain tracker's efficiency under this challenge.

- We also propose a novel resampling method based on Crow Search Optimization (COA). COA maintain diversity in the search space by considering awareness probability. It improves performance by distributing particles in the high likelihood region to address sample degeneracy. Unimportant particles detected as outlier were resampled to reduce computational complexity of the proposed tracker.

- An outlier detection mechanism is proposed to identify unimportant particles (having negligible weight). Particle consistency in subsequent frames is exploited for detecting the particles which contribute less towards the state estimation. In addition, this mechanism improves performance of the proposed resampling technique and ensures faster convergence.

- An adaptive fuzzy fusion model is proposed for integration of multi cues. This model resolve conflict among the particles and takes decision on the basis of fuzzy inference rule. It either boost or suppress the particles for their optimal contribution in the state estimation. It creates clear decision boundaries between significant particles and low performing particles. Model is made adaptive through a transductive reliability calculated through correlation among the particles.

The rest of this paper is organized as follows. In Section II, we review the literatures closely related to our work. Section III discusses the architecture of the proposed multicue object tracking framework. Detailed design of resampling model and fusion model is also presented. Core design of proposed tracker is highlighted further in section IV. Qualitative and quantitative results along- with their comparison with existing methods is presented in section V. Finally, concluding remarks and future directions are drawn in section VI.

2. Related Work

Object tracking under PF framework has been extensively investigated due to its potential applications in video surveillance, military and robotics. However, PF inherent problem viz. sample impoverishment and degeneracy limit its performance of object tracking. Many solutions have been proposed to address these problems and reviewed in [10]. In this section, we examine the closely related work of contemporary solutions for object tracking under PF framework. In [16], author used firefly algorithm (FA) before resampling to improve particle distribution. FA converged particles rapidly to optimal solution by changing their positions. Use of optimization generate significant particles which leads to accurate target state estimation. However, performance of this method de- graded when FA trapped in local minimum. Walia and Kapoor [19] presented a resampling method based on improved cuckoo search (ICS) with levy flight for object tracking under PF framework. ICS abandoned the particles with lesser weight to avoid the local minimum trap. However, optimal selection of step size for levy flight was not addressed. In [17], authors utilized spider mon- key optimization as resampling method in PF based tracking framework. The particle's position was updated on the basis of experience of local and global leader. Use of optimization improved quality of particles and converge them in high likelihood region. Resampling method based on immune genetic algorithm (IGA) for object tracking under PF framework was discussed [25]. IGA used crossover and mutation process to generate new particles in search region. IGA's regulatory mechanism viz. promotion and suppression ensured particles diversity. In [26] author used Pearson correlation coefficient as resampling under PF framework. Similarly, In [27] authors explored resampling method based on backtracking search optimization (BSA). But both of these methods were not evaluated on video sequences. Ahmadi and Salari [18] applied social spider optimization (SSO) as resampling method for tracking framework based on PF. SSO grouped the particles as male and female to increase randomness in search space. If target was lost, optimization ensured diversity by forcing the redistribution of particles. However, most of the methods under PF framework consider only single cue for particle evaluation. However, single cue is not sufficient to handle dynamic environments. Hence, particles need to be evaluated over multicue and subsequently fused for compensating various tracking challenges.

In [15], authors exploited color histogram and HOG for evaluation of each particle and PSO is applied as resampling technique. But this method is computationally complex due to multilevel evaluation of each particles with multiple cues. In [20], authors used color histogram and HOG cue with resampling method based on modified galaxy based search. Adaptive appearance model with multiple parameters were used at each time step to detect and handle occlusion. Due to this, method was considerably slow. Similarly, Sardari and Moghaddam [28] used color and motion cue for likelihood calculation of particles. The resampling method based on modified galaxy based search algorithm was proposed to obtain optimum state of the object. In [24], authors exploited color, thermal and motion cue for each particle evaluation. The particles were

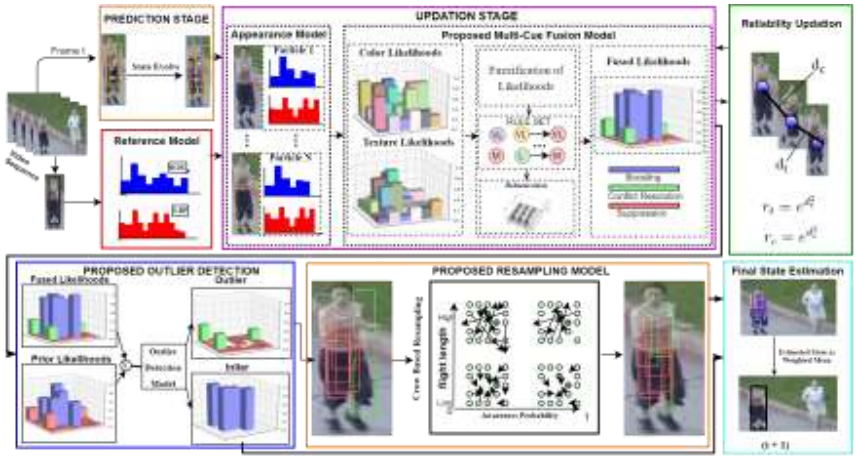


Figure 1: Overview of the proposed Tracker. N particles are evolve using multi component state model. Predicted particles are updated through multicue evaluation and adaptive fusion of evaluated particles. Detected outlier are resampled to overcome sample degeneracy. Targeted state is determined as weighted mean of N particles.

fused using Dezert-Smarandache Theory. Generally, resampling mechanism for PF consider all the particles to ensure optimal state estimation. This needs high computational power for desired convergence. Methodology to relocate the lost target has not been explored much. Moreover, adaptive fusion of particles in multi cue object tracking based on PF is limitedly addressed.

Review of closely related literatures indicate that future research in multicue object tracking based on PF should consider adaptive fusion of particles for efficient tracking. In addition, unimportant particles needs to be detected not only to reduce computation but also for efficient resampling. The next section will detail architecture of the proposed tracker.

3. Architecture of Proposed Tracker

The Proposed tracker is developed under PF based probabilistic tracking framework with multicue evaluation for each and every particle. Extracted color cue (H_C) and texture cue (H_T) for each evaluated particle are integrated using the proposed fuzzy based adaptive fusion model. Fusion model is made adaptive through online calculation of transductive reliability metric for each cue. The particle level multicue fusion is performed considering boosting of good particles and simultaneously suppressing of the low performing particles. In each frame, low performing particles are detected using the proposed outlier detection mechanism. These particles are relocated to their optimum position using the proposed resampling method based on Crow Search Optimization (COA) [29]. Architecture of the proposed tracker is depicted in Fig 1. As shown, at k = 1, the target is segmented using Gaussian Mixture Model (GMM) [30] and N particles are initialized around the detected centroid of the target. These initialized

particles are evolved using the Multi component state model to obtain the predicted particles. Each predicted particle is evaluated over two complementary cues and weights are assigned through comparison of extracted features with the corresponding reference model. Further, these weights are integrated using the multicue fuzzy fusion model to obtain fused weight w_t for each evaluated particles. Based upon their fused weights particles are classified into outlier (O) and inlier (I) using the proposed outlier detection mechanism which is based on Markov process. Only the outliers O are processed through the proposed resampling method to relocate them in high likelihood area. Resampling mechanism considers outlier as initial population for COA. The diversity of the particles is maintained through the awareness probability. On the other hand, search region is controlled through the flight length to obtain the optimal resampled particles. High convergence rate of COA achieves real time realization of the proposed tracker. At each time step, transductive reliabilities r_c and r_t associated with the cues are evaluated to discount the particle in concurrence with the cue performance. These reliability ensures quick adaptation of the pro- posed tracker to the dynamic environment. Finally, target state is determined as weighted sum of inlier as well as resampled outlier particles. The detailed design of the proposed tracker is follows in turn.

3.1. Multicue Particle Filter

Proposed tracker is designed using Particle Filter [6] which is a probabilistic recursive Bayesian framework used for estimation of Non-linear and Non- Gaussian state. Particle filter has been exploited for multicue tracking frame- work to precisely localize the target under dynamic environment. Aim is to approximate PDF $p(S_k|w_k)$ of the target state given its prior PDF $p(S_{k-1}|w_{k-1})$, where S_k and S_{k-1} are state vectors represented by N particles and w_k and w_{k-1} are set of measurements at time instant k and $k-1$.

In the proposed model, we consider state vector for each particle as $S_k = (X_k, X_k^j, Y_k, Y_k^j, r_k, \theta_k)$. X_k and Y_k are cartesian coordinates of the center of bounding box, X_k^j and Y_k^j are velocities in respective direction, r_k and θ_k are rotation and scaling components of the particle. Measurement is obtained for each particle using complementary multicue viz. color and texture extraction and their score fusion using proposed multicue fusion model. Particles are evolved using the state model as Eq.(1).

$$S_k = f_k(S_{k-1}, r_{k-1}) \tag{1}$$

Where,r_{k-1} is zero mean white noise and f_k: R^p R^q R^p is a multicomponent transition function which includes constant velocity model and random walk model [23].

The PDF of target state S_k i.e. $p(S_k|w_k)$ is obtained recursively into two stages viz. prediction and update. The initial PDF of the target $p(S_{k-1}\, w_{k-1})$ at time $k = 2$ is manually obtained through random placement of particles. In the subsequent estimate prior PDF of the target at time instant k is obtained using

Eq.(2).

$$p(S_k|w_{k-1}) = \int p(S_k|S_{k-1})p(S_{k-1}|w_{k-1})dS_{k-1} \quad (2)$$

Where, multicomponent state model is used to evolve the particles to obtain predicted particle represented PDF $p(S_k|S_{k-1})$. Further, the predicted particles representing| PDF $p(S_k|S_{k-1})$ are updated by assignment of multicue measurement and fusion as discussed in Section B. The updation of these particles is performed using Bayes rule using Eq. (3).

$$p(S_k|w_k) = \frac{p(w_k|S_k)p(S_k|w_{k-1})}{p(w_k|w_{k-1})} \quad (3)$$

In Eq(3) normalizing denominator factor $p(w_k|w_{k-1})$ is obtained as:

$$p(w_k|w_{k-1}) = \int p(w_k|S_k)p(S_k|w_{k-1})dS_k \quad (4)$$

Where, $p(w_k|S_k)$ is obtained through multicue evaluation of each particle and their subsequent fusion using proposed mulitcue fusion model.

Posterior PDF $p(S_k|w_k)$ is represented by N updated particles and used to determine the state of the target as their weighted mean. In the iterative process of particle filter these updated particles are used as prior initialization for the next stage estimation. Details of the proposed tracker updation model is discussed in the next section.

3.2. Proposed Updation Model

Proposed tracker is realized through online detection of target through GMM [30] where N particles are initialized. Each particle state S_k is evolved through multi component state model to achieve predicted particles. Particles updation consists of mainly: a) multicue evaluation and b) adaptive fusion of likelihoods. For this, each particle is evaluated over two complementary cues viz. color and texture. Color cue is invariant to scale variations and occlusion but sensitive to illumination variations and background clutters. On the other hand, texture cue is robust to illumination variations and background clutters. Hence, complementary color and texture cue compensate for each other during tracking process.

The color cue is calculated using RGB color histogram model. Color histogram (H_c) for each t^{th} particle with pixel location p (a_n, b_n), is determined by Eq. (5).

$$H_c = Z\sum_{t=1}^{N} B(a_i, b_i), c = 1,2 \dots M_b \quad (5)$$

where, $B(.)$ represents binning function that assign pixel (a_i, b_i) to one of the M_b histogram bins and normalizing factor Z is calculated as $\sum_{c=1}^{M_b} H_c = 1$.

Unlike color cue, texture cue is used to extract low level features from the image. It is determined for each particle by considering rotation invariant Local

Binary Pattern (LBP) [31]. The LBP of t^{th} particle is calculated from central pixel (a_c, b_c) with radius z and with equally spaced pixels p. The uniform pattern in image region used multi-resolution gray scale rotation for separating target texture information. It is represented as $U\,(LBP_{z,p}((a_c, b_c))$ and determined using Eq. (7).

$$LBP_{(z,p)}(a_c, b_c) = \begin{cases} \sum_{j=0}^{p-1} T\left(\left(u_j(a_j, b_j) - u_c(a_c, b_c)\right)\right), if\ U(LBP_{z,j}(a_c, b_c)) \le 2 \\ j+1,\ \ otherwise \end{cases} \quad (6)$$

$$U(LBP_{(z,p)}(a_c, b_c)) = |T\left(u_{j-1}(a_{j-1}, b_{j-1}) - u_c(a_c, b_c)\right) - T(u_0(a_0, b_0) - u_c(a_c, b_c)) + \sum_{j=0}^{p-1} |T\left(u_j(a_j, b_j) - u_c(a_c, b_c)\right) - T\left(u_{j-1}(a_{j-1}, b_{j-1}) - u_c(a_c, b_c)\right)| \quad (7)$$

Using this LBP operator, normalized histogram are determined for each particle by mapping uniformity measure of every pixel and represented as H^t . Further, $_T$ weights are assigned to each particle through estimation of similarity between predicted particles histogram and corresponding references histograms. This is achieved through Bhattacharyya distance [32]. For this, Bhattacharyya coefficient is determined using Eq. (8).

$$\beta_{t,i}(H_i^R, H_i^t) = \sum_{r=1}^{N} \sqrt{(H_i^R)^r \times (H_i^t)^r} \quad (8)$$

Where, H_i^R represents reference histogram, $i \in C$, T and H^t denotes the histogram of considered cue for t^{th} particle. Using Eq. (8) Bhattacharyya distance is calculated for color and texture cue as illustrated in Eq. (9).

$$BD_{t,i}(H_i^R, H_i^t) = \sqrt{1 - \beta_{t,i}(H_i^R, H_i^t)} \quad (9)$$

Using this, likelihoods for each particle are determined using Eq. (10).

$$\alpha_{t,i}(H_i^R, H_i^t) \propto e^{\left(-\frac{(BD_{t,i}(H_i^R, H_i^t))^2}{2\sigma_i^2}\right)} \quad (10)$$

Where σ_i denotes standard deviation and $I \in (C, T)$.

The color and texture likelihoods so calculated are subjected to the proposed adaptive multicue fusion model. The proposed model is designed considering boosting of concordant particles, suppressing of discordant particles and on- line conflict resolving among the conflicting particles. In order to achieve quick adaptation of tracker, individual likelihoods are discounted with the transductive reliability of the respective cue as determined in the previous frame. For this, particle likelihoods $\alpha_{t,i}$ are multiplied with the corresponding cue reliability as depicted in Eq (11).

$$\gamma_{t,i} = r_i \times \alpha_{t,i}(H_i^R, H_i^t) \tag{11}$$

Where, r_i is transductive cue reliability determined in the previous frame and $i \in (C, T)$. Proposed fuzzy fusion model achieves precise decision boundary among high performing particles and low performing particles under complex environment. Fuzzy logic can induce human being inferences in the fused model [33]. It was reported that human sensing system consist of multi cue framework with online adaptation to dynamic environment [34]. Considering this, fuzzy set is defined as: $S = \{VS, S, M, L, VL\}$representing Very Small, Small, Medium, Large and Very Large likelihood value for the particle. Membership value for the evaluated particle $\gamma_{t,i}$ are determined in each fuzzy set element using Eqs. (12-16):

$$\delta_{VS}(x) = \frac{1}{1+e^{-c_{VS}(x-f_{VS})}} \tag{12}$$

$$\delta_S(x) = e^{\frac{-(x-d_S)^2}{f_S^2}} \tag{13}$$

$$\delta_M(x) = e^{\frac{-(x-d_M)^2}{f_M^2}} \tag{14}$$

$$\delta_L(x) = e^{\frac{-(x-d_L)^2}{f_L^2}} \tag{15}$$

$$\delta_{VL}(x) = \frac{1}{1+e^{-c_{VL}(x-f_{VL})}} \tag{16}$$

Where, $c_{VS} = 80$, $f_{VS} = 0.15$, $d_S = 0.3$, $f_S = 0.12$, $d_M = 0.5$, $f_M = 0.12$, $d_L = 0.7$, $f_L = 0.12$, $c_{VL} = 80$ and $f_{VL} = 0.15$ and $x \in (\gamma_{t,i}, w_t)$, $i \in (C, T)$.

The functional mapping $R_{m,n}$ between the color and the texture likelihood is presented in the Table 1, where m and n represent the fuzzy set value assigned to each evaluated particle. This mapping ensures boosting of high performing particles and suppression of low performing particles, creating a precise decision boundary for the proposed outlier detection mechanism.

m/n	VS	S	M	L	VL
VS	VS	VS	VS	M	L
S	VS	VS	S	M	L
M	VS	S	M	M	L
L	M	M	M	VL	VL
VL	L	L	L	VL	VL

Table 1: Fuzzy inference Model ($R_{m,n}$)

Further to achieve crisp fused value of particle likelihood, defuzzification using Center of Gravity (COG) method has been considered for obtaining optimal results. The crisp COG value for a pair of fuzzy set elements m, n is defined as:

$$COG_{R_{m,n}} = \frac{\int_0^1 \delta_{R_{m,n}(x)} x dx}{\int_0^1 \delta_{R_{m,n}(x)} dx} \tag{17}$$

Where $R_{m,n}$ is determined using Table 1 and $\gamma_{t,i}$, w_t). The weighted mean, Eq. (18), of COG values being determined over pair (m,n) $\in$ S and used for estimation of final fused weight for each evaluated particle.

$$w_t = \frac{\sum_m \sum_n \pi_{m,n}(\gamma_{t,C},\gamma_{t,T}) \times COG_{R_{m,n}}}{\sum_m \sum_n \pi_{m,n}(\gamma_{t,C},\gamma_{t,T})} \tag{18}$$

Where, $\pi_{m,n}$ is fuzzy control rule calculated using Eq. (19).

$$\pi_{m,n}(\gamma_{t,C},\gamma_{t,T}) = \min(\delta_m(\gamma_{t,C}),\delta_n(\gamma_{t,T})) \tag{19}$$

3.3. Proposed Resampling Method

Proposed multicue fusion model creates precise decision boundaries between low performing particles and high performing particles. Keeping low performing particle for subsequent iteration not only requires high computation but also impairs tracker accuracy. This problem of sample degeneracy has been solved using conventional techniques like adaptive resampling [12], sequential resampling [11], cuckoo search [19]. However, most of the resampling methods consider all the particles for resampling process which requires high computational requirement. In order to realize the tracker in real time scenario, we determine the recurrently low performing particles as outliers which are subjected to the proposed resampling method. We assume that outliers are those particles which are either drifted off the target or highly affected by the dynamic environment. Generally, environments affect the target particles in consequent frames. This has been exploited by assuming that individual particle state estimation as a Markov process and helps us in design of proposed outlier detection mechanism. Proposed outlier detection mechanism is designed by considering particles performance in previous frame along with their current estimation. The particles likelihood for the current state (w^k), t 1...N_t are fused with their previously estimated likelihoods (w^{k-1}). These likelihoods for each particle are adaptively fused using the proposed multicue fusion model as discussed in Section B. For this, we consider the fuzzy set S for the two likelihood value for each particle and membership values ($\delta_m(.)$) are determined using Eqs. (12-16). Further, final score for the t_{th} particle for its classification as outlier or inlier is calculated using Eq. (20).

$$\kappa_t = \frac{\sum_m \sum_n \pi_{m,n}(w_t^k,w_t^{k-1}) \times COG_{R_{m,n}}}{\sum_m \sum_n \pi_{m,n}(w_t^k,w_t^{k-1})} \tag{20}$$

Where, $\pi_{m,n}$ is fuzzy control rule calculated using Eq. (21) and used for weighing the COG values.

$$\pi_{m,n}(w_t^k, w_t^{k-1}) = \min(\delta_m(w_t^k), \delta_n(w_t^{k-1})) \tag{21}$$

Using the fused score for each particle, outlier and inlier are classified by comparing their fused score with predefined threshold value κ_{th}. The particles are classified as outliers using Eq. (22) and as inliers using Eq. (23)

$$O = \{S_k^t, \forall\ t \quad where\ \kappa_t \leq \kappa_{th}\} \tag{22}$$

$$I = \{S_k^t, \forall\ t\ where\ \kappa_t > \kappa_{th}\} \tag{23}$$

Precise decision boundary determined through proposed outlier detection mechanism aids proposed resampling mechanism to eliminate particle degeneracy. Only the particles classified as outliers are resampled using the proposed resampling technique. The resampling technique is based on crow search optimisation which diversifies the outliers in the search space. The crow search optimization is a meta-heuristic optimization approach proposed in [29]. The outlier particle set O_k obtained through Eq. (22) are initialized as the crow population. Position of the crow population is updated as shown in Eq. 24.

$$O_v = \begin{cases} O_v + r \times fl \times (M_v^r - O_v), & r \geq AP \\ random\ redistribution, & otherwise \end{cases} \tag{24}$$

where $r \in [0, 1]$, $v \in (X, Y)$, fl represents the flight length and AP denotes the awareness probability and $M_{k,v}^r$ represents the global best location of each crow. This iterative process is performed for J iterations to achieve the optimal solution. Finally, the optimally localized outliers with updated weights are used for determining the target state. Proposed tracker state estimation is depicted

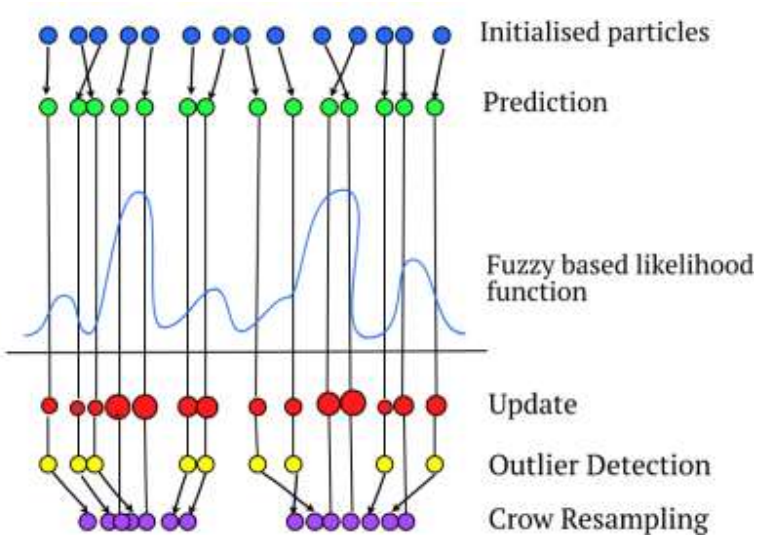


Figure 2: Optimal particle localization using resampling process

in Fig. 2 where particle marked as outlier are detected and resampled. After

Algorithm 1: Proposed Tracker

Function Multicue Tracker()**:**
  for *each frame k* **do**
    if $k==1$ **then**
      Intialise N particles on the detected target
      $r_C, r_T \leftarrow 1,1$
    else
      $S_k = f_k(S_{k-1}, w_{k-1})$
      Obtain $\alpha_{t,i}$ using Eq. (10)
      $\gamma_{t,i} \leftarrow r_i \times \alpha_{t,i}$, $i \in (C, T)$
      Calculate w_t using Eq. (19)
      Obtain κ_t using Eq. (20)
      I,O$\leftarrow \varphi$
      for t *in* S_k **do**
        if $\kappa_t > \kappa_{th}$ **then**
          I=I$\cup$ S_t^k
        else
          O=O$\cup$ S_t^k
        end
      end
      for j *from 1 to* J **do**
        for c *from 1 to* $|O|$ **do**
          r $\leftarrow$ U(0,1)
          R $\leftarrow$ Uint(J)
          if $r \geq AP$ **then**
            $O_{v,c} \leftarrow O_{v,c} + r \times fl \times (M_v^R - O_{v,c})$
          else
            $O_{v,c} \leftarrow O_{v,c} + N(0, 1)$
          end
          Update M_v^c
        end
      end
      Obtain updated w_t using Eq. (19)
      Calculate S^F , S^F, S^F using Eqs. (25-27)
      calculate $d_C = \sigma(S_k^F, S_k^R)$
      calculate $d_T = \sigma(S_k^F, S_k^T)$
      Obtain r_C, r_T using Eqs. (28-29)
    end
  end
  return $S_1, S_2, \ldots, S_k$
Mt

resampling the outliers are positioned appropriately for improvement in their performance for state estimation. The final state estimation is described in the following section.

3.4. State Estimation and Reliability Updation

The final state of the object (S_k^F) is estimated by using the updated fused likelihoods w_t as weights for inlier states ($I_{k,v}$) and resampled outlier states ($O_{k,v}$). This is depicted in Eq. (25).

$$S_k^F = \frac{\sum_u w_u \times O^u + \sum_v w_v \times I^v}{\sum_{t=1}^{N} w_t} \tag{25}$$

where $|u \cup v| = N$

For quick adaptation of the proposed tracker against environment challenges, reliability values are calculated for each cue individually. For this, the state is estimated using color and texture likelihoods and depicted in Eqs. (26-27).

$$S_k^R = \frac{\sum_u \gamma_{u,C} \times O^u + \sum_v \gamma_{v,C} \times I^v}{\sum_{t=1}^{N} \gamma_{v,C}} \tag{26}$$

$$S_k^T = \frac{\sum_u \gamma_{u,T} \times O^u + \sum_v \gamma_{v,T} \times I^v}{\sum_{t=1}^{N} \gamma_{v,T}} \tag{27}$$

The reliability values are obtained through Eqs. (28,29), which are further passed on to the next frame iteration.

$$r_C \propto e^{-\hat{d}_C} \tag{28}$$

$$r_T \propto e^{-\hat{d}_T} \tag{29}$$

where d_C, d_T are the Euclidean distance between the final state and the state estimated for color and texture cue respectively and is given by Eqs. (30-31)

$$d_C = \sigma(S_k^F, S_k^R) \tag{30}$$

$$d_T = \sigma(S_k^F, S_k^T) \tag{31}$$

The pseudocode of the proposed tracker is depicted in Algorithm 1. Updated inliers (I^v) and Outliers (O^u) are used as a prior for next state estimation. These particles are further evolved using the state model Eq.(1). Predicted particles are updated using the multicue framework as discussed in Section B. In addition, transductive reliabilities estimated at (k) state are used for discounting the particles weights at (k + 1) state. This iterative process will continue till the detected target is present in the scene. Once the target is lost, the automatic detection mechanism using GMM will redetect the new target and the particles are re-initialized in the iterative process. Details of experimental validation of the proposed tracker along with the comparison with state-of-the-art is presented in the next section.

4. Experimental Validation

In this section, we demonstrated experimental validation of the proposed method and compare the results with 9 other state-of-the-art trackers viz. ASLA [35], CT [36], MIL [37], IVT [38], FRAG [8], WMIL [39], PF [6], PF-PSO [15] and PF-BSA [27] . In order to gauge robustness and reliability of the proposed method, we have evaluated our tracker over 12 benchmarked video sequences, encompassing various tracking challenges such as illumination variations, scale variations, full or partial occlusion, background clutters, object's deformation and rotation. Qualitative and quantitative analysis of results is performed using standard performance metrics. Proposed algorithm is implemented in Python2 and executed on a 2.4 GHz quad core processor with 6 GB RAM. Proposed tracker is initialized with $N = 49$ particles on pre-detected target using GMM [30] segmentation technique. Probabilistic nature of PF is handled by iterating the algorithm 10 times and taking the mean value of the results. 1-D and 2-D tracking work of Bhateja et al. [27] has been extended for video sequences to compare its performance with the proposed method. In the next section, the qualitative analysis of the proposed method is demonstrated.

4.1. Qualitative analysis

4.1.1. Illumination and Scale variations

The challenging video sequence *CarScale* frames under illumination and scale variations have been illustrated in Fig. 3 (a). From frames #180 to #240, under prominent variation in the target's scale, the trackers viz ASLA, CT, MIL, WMIL and IVT totally deflected from the target. Due to their appearance model, these trackers fail to handle the large-scale variations of the target but our tracker can efficiently track the target. Proposed multicue fuzzy fusion model suppresses the low performing particles during the large-scale variations and hence, maintains tracker's efficiency. In Fig. 3(b) sample frames for sequence *Dog* are shown. At #126 frame, when the targeted object encounters scale variations PF-PSO, IVT and PF drifted away while ours successfully tracked the marked object. The representative frames for the sequence *Human8* are illustrated in Fig. 3(c), target has significant change in illumination from frame #100 to #124. Only the proposed tracker keeps track of the target. This is mainly attributed to multi component state model where scaling factor is included in the state vector. There is a sudden change in illumination at frames #41, #132 and #229 for sequence *Singer2* as depicted in Fig. 3(d). Discriminative trackers CT and MIL are not able to handle the drastic change in illumination. These trackers considered Haar like features for object representation which are prone to illumination variations. However, the proposed tracker is robust to illumination variations as it considers complementary cues viz. color and texture. When RGB color histogram performance degrades due to illumination and scale variations, the scale invariant LBP texture histogram will compensate. In addition, the particles which are affected by the illumination and scale variations are suppressed by the proposed multicue fuzzy fusion model and hence, enhances the tracking accuracy.

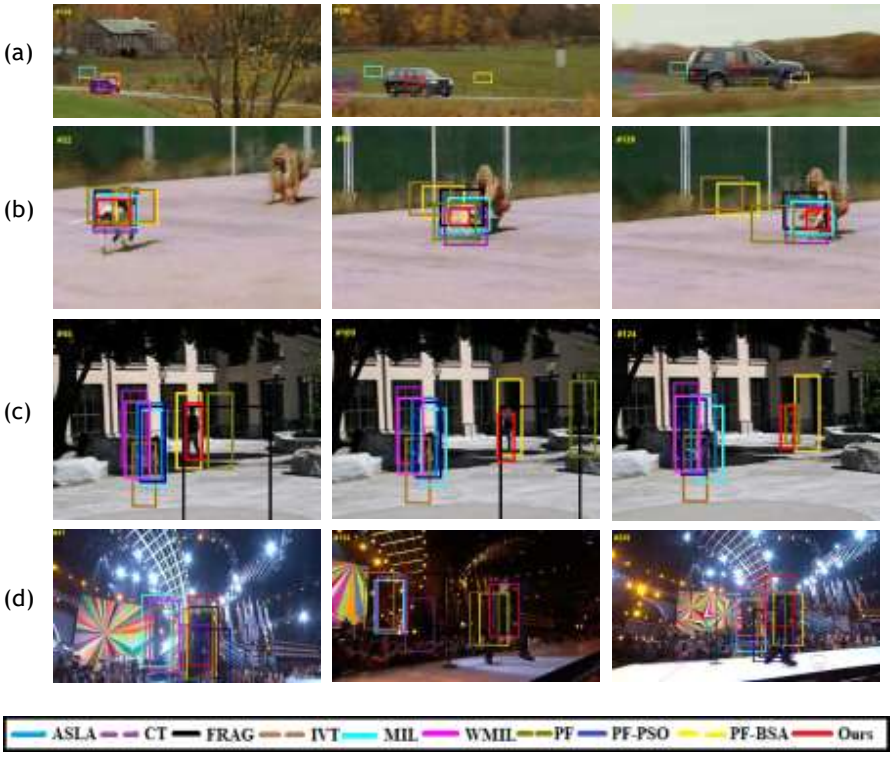


Figure 3: Critical frames with Illumination and Scale variations video sequences: a) *CarScale b) Dog* c) *Human8* d) *Singer2*

4.1.2. Full or Partial Occlusion

The sample frames for video sequences considered under this challenge are presented in Fig.4. The *Bolt* sequence has several full and partial occlusions as shown in Fig. 4(a). ASLA, CT, MIL, WMIL, PF-PSO, PF-BSA and IVT fail to track the target when it undergoes full occlusion at frame #126 and #275 while ours perform comparatively better. Fig 4(b) depicts partial occlusions of the target at frame #190. CT, MIL and Frag has shown unsatisfied performance under partial occlusion. On the other hand, our tracker with adaptive multicue fuzzy fusion model boost the high performing particles during occlusion and hence, prevents drift. At frame #70 target has full occlusion by the pillar as shown in Fig. 4(c). The trackers viz. ASLA, MIL, WMIL, CT, FRAG, IVT and PF are not sufficiently able to handle this challenge as they are not able to alleviate from drift. Whilst ours perform effectively under this challenge. Critical frames for *Subway* sequence are shown in Fig. 4(d). At frame #90 ASLA and WMIL lost the target when it is partially occluded by the other person. Ours along with MIL and WMIL has shown relatively good performance in comparison to the other trackers. Proposed tracker performance improvement under

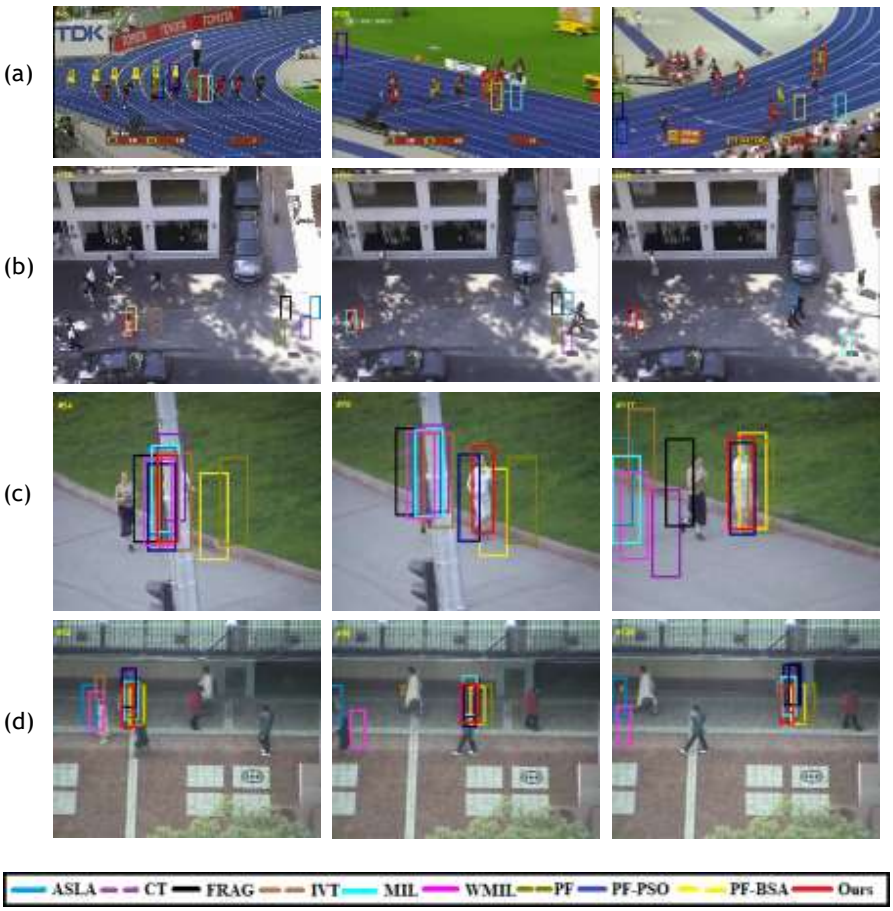


Figure 4: Critical frames with Full or partial Occlusion for video sequences: a) *Bolt* b) *Crowds c) Jogging-2* d) *Subway*

full or partial occlusion is mainly attributed to the outlier detection mechanism and the proposed resampling technique. The particles affected due to occlusion are identified by the outlier detection mechanism. The proposed resampling technique diversified these particles in the search space in order to improve their placement. This helps in maintaining the tracker's efficiency under full or partial occlusion.

4.1.3. Background clutters

We have considered challenging video sequences under this challenge and certain frames are presented in Fig. 5. In *Walking* video sequence at frame #125 PF drift away from the target as shown in Fig 5(a). PF-BSA and ASLA also drift away from the target as they have no mechanism to relocate the target

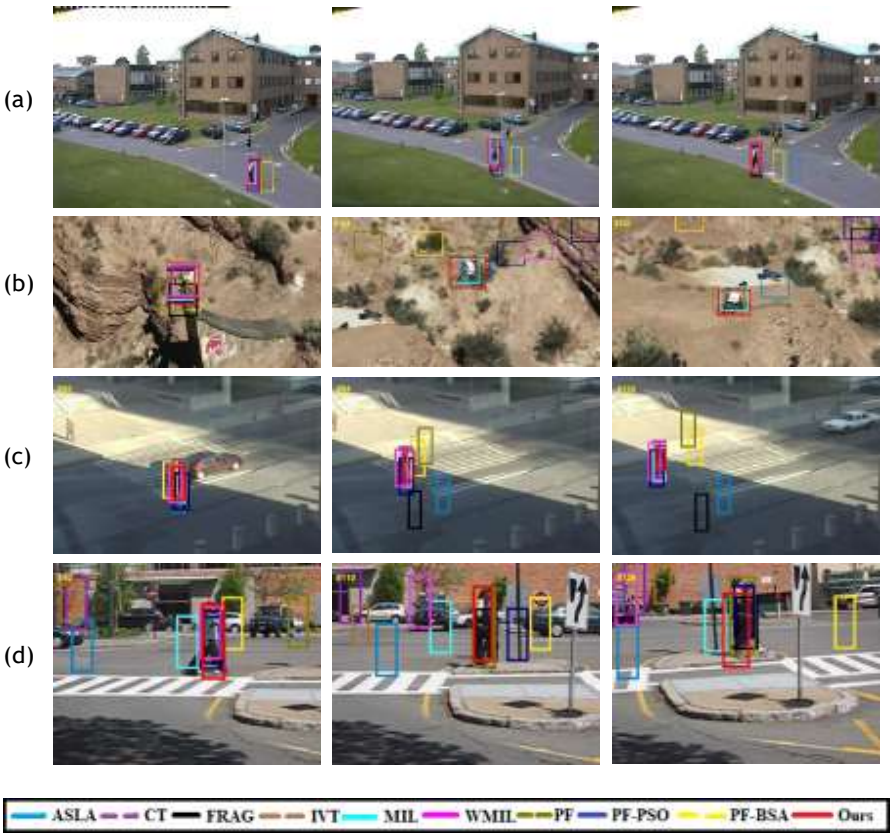


Figure 5: Critical frames with background clutters for video sequences: a) *Walking* b) *MountainBike* c) *Crossing* d) *Couple*

Video Sequence	ASLA	CT	FRAG	IVT	MIL	WMIL	PF	PF-PSO	PF-BSA	Ours
CarScale	79.80	75.14	31.21	11.58	70.97	70.33	40.26	38.08	96.86	7.26
Dog	9.21	8.33	-	46.81	13.42	25.13	25.44	13.51	37.26	8.98
Human8	65.56	82.65	55.65	90.01	62.77	79.26	32.70	71.90	30.12	5.96
Singer2	193.91	121.21	88.44	171.09	161.69	160.98	34.26	140.23	56.49	13.76
Bolt	379.76	376.24	333.81	367.76	383.71	370.01	68.07	91.14	64.09	9.39
crowds	295.40	380.72	-	11.04	261.56	249.34	110.91	10.49	146.51	5.83
Jogging2	143.90	116.98	37.42	132.33	134.43	141.62	16.05	13.48	24.68	7.06
Subway	145.04	11.58	8.50	117.19	6.70	136.73	9.71	11.34	5.73	4.06
Walking	247.76	8.55	9.54	2.30	4.38	8.63	81.70	15.72	45.08	8.15
Mountainbike	21.73	192.44	206.90	7.21	7.78	107.11	165.75	94.76	85.63	8.31
Crossing	33.41	5.37	38.50	3.18	3.16	5.12	22.66	12.23	16.19	3.19
Couple	96.23	79.30	8.94	100.50	27.68	39.78	38.81	65.10	42.78	13.77
Average	142.64	121.54	81.89	88.42	94.85	116.17	53.86	48.16	54.28	7.98

Table 2: Centre Location Error (in pixels). The best results are shown in red, blue and green respectively.

but ours, MIL and FRAG successfully track the target. In Fig. 5(b) critical frames for *MountainBike* sequences are shown. MIL, WMIL, CT, FRAG, PF



Figure 6: Critical frames with Object's deformation and rotation for video sequences: a) *Singer2* b) *Bolt* c) *Dog* d) *Couple*

Video Sequence	ASLA	CT	FRAG	IVT	MIL	WMIL	PF	PF-PSO	PF-BSA	Ours
CarScale	0.460	0.432	0.471	0.002	0.172	0.474	0.176	0.353	0.348	0.786
Dog	0.500	0.492	-	0.109	0.481	0.378	0.202	0.487	0.244	0.610
Human8	0.130	0.063	0.218	0.049	0.071	0.087	0.379	0.156	0.384	0.733
Singer2	0.053	0.138	0.246	0.049	0.048	0.064	0.395	0.331	0.417	0.867
crowds	0.071	0.004	-	0.075	0.059	0.005	0.056	0.602	0.280	0.777
Jogging2	0.133	0.092	0.569	0.158	0.138	0.133	0.177	0.651	0.483	0.852
Subway	0.194	0.699	0.757	0.183	0.801	0.189	0.321	0.605	0.572	0.687
Bolt	0.020	0.028	0.019	0.008	0.013	0.015	0.168	0.207	0.129	0.709
Walking	0.069	0.643	0.684	0.874	0.685	0.659	0.037	0.493	0.091	0.498
Mountainbike	0.633	0.222	0.149	0.840	0.821	0.436	0.171	0.428	0.211	0.845
Crossing	0.380	0.779	0.349	0.401	0.837	0.660	0.327	0.596	0.447	0.829
Couple	0.056	0.237	0.692	0.081	0.100	0.526	0.367	0.484	0.138	0.617
Average	0.225	0.319	0.415	0.236	0.352	0.302	0.231	0.449	0.312	0.734

Table 3: F-Measure. The best results are shown in red, blue and green respectively.

and PF-BSA are inefficient to handle the similar background. However, ours, ASLA and MIL is able to track the target. In our tracker, the outlier detection mechanism identified the unimportant particles due to similar background and

hence, prevents false updation of particles in our tracker. *Crossing* critical frames are presented in Fig. 5(c). At frame #94 after the car passes in front of the target, ASLA, FRAG, PF-BSA and PF deflected away from the target. On the other hand, our tracker has shown substantially good performance in the sequence as proposed adaptive multicue fuzzy fusion supports boosting of good particles during the background clutters. The frames for sequence *Couple* are shown in Fig. 5(d). After frame # 90 when the target passes by the similar car in the background then only ours with FRAG able to track the target efficiently. The tranductive reliability values of the color and texture prevents the drift of target during background clutters and the redetection strategy also supports in enhancing the tracking accuracy.

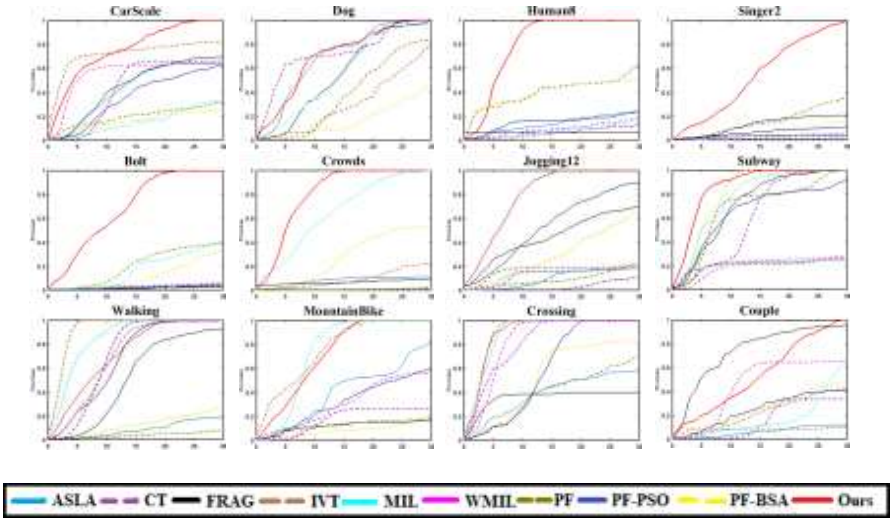


Figure 7: Precision Plot *vs* CLE threshold (in pixels) under various visual tracking challenges: i) Illumination and Scale variations (*CarScale, Dog, Human8, Singer2*) ii) Full and Partial Occlusion (*Bolt, Crowds, Jogging-2, Subway*) iii) Background Clutters (*Walking, MountainBike, Crossing, Couple*) iv) Object's Deformation and Rotation (*Singer2, Bolt, Dog, Couple*)

4.1.4. Object's Deformation and Rotation

The sample frames for the challenging video sequences under this challenge are presented in Fig. 6. In *Singer2* video sequence at frames #89 and #132 the target deformed due to its sudden pose variations and subsequent rotation. MIL, CT, WMIL, ASLA, CT and PF-BSA has lost the target. However, ours has shown better results. In Fig. 6(b) critical frames for *Bolt* sequences are shown. Non-rigid deformation occurs in the target due to its in-plane rotation at frames #274 and #340. Most of the trackers are unable to handle this deformation. Only our tracker manages to handle the target's deformation. The sample frames for *Dog* sequence are shown in fig. 6(c). At frames #12 and #46 the target has deformation due its fast motion and rotation. MIL, FRAG, PF and

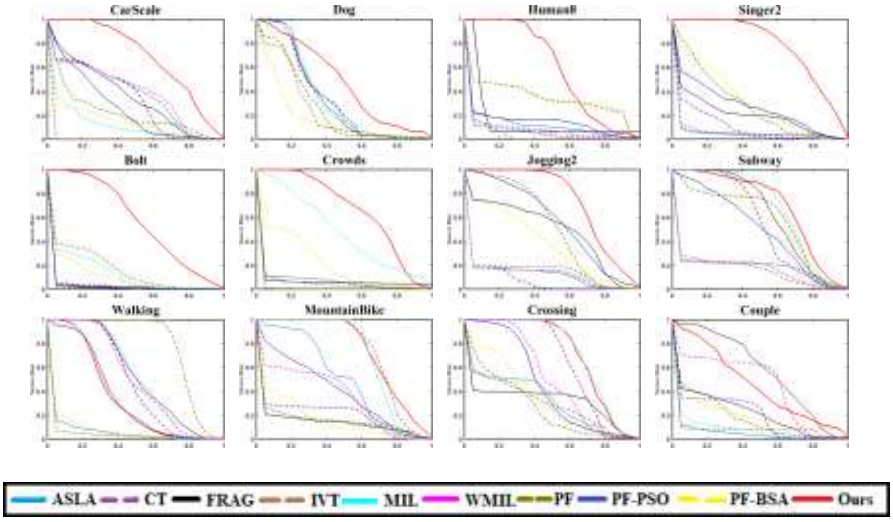


Figure 8: Success *vs* Percent Overlap Threshold (%) Plot under various visual tracking challenges: i) Illumination and Scale variations (*CarScale*, *Dog*, *Human8*, *Singer2*) ii) Full and Partial Occlusion (*Bolt*, *Crowds*, *Jogging-2*, *Subway*) iii) Background Clutters (*Walking*, *MountainBike*, *Crossing*, *Couple*) iv) Object's Deformation and Rotation (*Singer2*, *Bolt*, *Dog*, *Couple*)

PF-BSA are slightly drifted from the target whilst ours, ASLA and CT perform efficiently. *Couple* whose sample frames are presented in Fig. 5(d). At frame #100 ASLA, CT and PF-BSA fail to keep track of the target as deformation occurs due to sudden camera movement. Ours, FRAG and IVT keep track of the target. However, at frame #108 only our tracker is able to locate the target. It is mainly due to the rotational component which is incorporated in the state vector of the multi component state model. In addition, the low performing particles due to object's deformation are suppressed by the multicue fuzzy fusion model to cater this challenge.

4.2. Quantitative analysis

The quantitative performance of proposed tracker is analyzed by considering multiple evaluation metrics which includes Centre location error(CLE), F-Measure [40] and plots as: Precision vs Location error threshold and Success rate vs overlap threshold [41]. CLE is calculated as the distance between tracker bounding box and the center of the ground truth. F-Measure is defined as $\frac{2\times pr\times rl}{pr+rl}$

Where pr is precision and calculated as $(B_R \cap B_G)/B_R$; rl is recall and given as: $\frac{B_R \cap B_G}{B_G}$. B_R is tracker bounding box and B_G ground truth bounding box. Precision plot illustrates the mean precision at various location error thresholds (in pixels). The Success plot represents the percent success over various overlap thresholds (in %).

We have achieved an average CLE of 7.98 and average F-Measure of 0.734

when evaluated on 12 challenging video sequences taken from benchmark datasets. The mean CLE and mean F-Measure are tabulated in Table 2 and Table 3 respectively. Fig.(7) represents the percentage overlap of successful frames from a given threshold from the ground truth. Fig.(8) illustrates the success rate over overlap threshold. As shown in Fig. (7), for 20 location error threshold (in pixels) we achieve an average precision of 0.90 for illumination and scale variations, 0.98 for full or partial occlusion, 0.91 for background clutters and 0.82 for object's deformation and rotation. As depicted in Fig.(8), at 0.2 overlap threshold (in %) our tracker manages average success rate 0.99 for illumination and scale variations as well as for full or partial occlusion, 0.97 for background clutters and 0.95 for object's deformation and rotation. High values of precision and success rate reveals that our tracker can handle various dynamic environment challenges. On the other hand, generative tracker such as ASLA [35] are not robust against full or partial occlusion as its appearance model do not consider background information. Discriminative trackers viz. CT[36] and MIL[37] fail to keep track of target in background clutter and illumination variation. WMIL[39] is considered random Haar like features for object representation and hence, not able to tackle sudden illumination and scaling variations. IVT[38] performance is limited by the large number of parameters used for developing appearance model of the target. PF based trackers such as PF[6], PF-PSO[15], PF-BSA[27] are not efficient enough to address dynamic challenges, mainly due to limited solution to sample degeneracy and impoverishment problem. Our tracker has exploited CSA as a resampling technique which ensures the diversity in the search space with two parameters: awareness probability and flight length. The outlier detection mechanism helps in identifying the low performing particles. The complexity of the proposed resampling technique is reduced as it resampled only the low performing particles detected by the outlier. In addition, the proposed multicue fuzzy based fusion model not only boost the high performing particles but also, suppresses the low performing particles. Hence, achieve high accuracy and robustness against dynamic challenges is achieved.

5. Conclusion

In this paper, we propose a robust tracker based on multicue particle filter framework which comprises of adaptive multicue fuzzy based fusion model and a novel resampling method to overcome particle degeneracy. Complementary multicue viz. RGB color and LBP texture are considered to enhance the tracker accuracy under illumination variation, occlusion, background clutters, object's deformation and rotation. The adaptive mulitcue fuzzy fusion model either boosts or suppresses the particles in order to ensure clear decision boundary between the unimportant particles and the significant particles. Nevertheless, an outlier detection mechanism is also proposed to classify the unimportant particles from the significant one. Proposed tracker is computationally efficient as only the unimportant particles are resampled by the proposed resampling technique. Quick adaptation of tracker is ensured through online estimation of transductive reliability of each cue. Qualitative and quantitative analysis on

12 challenging video sequences from benchmark infer that the proposed tracker perform favorable against the state-of-the-art trackers.
In future, we look forward to integrate more multimodal features in the proposed tracking framework. Inclusion of user defined source importance in the proposed fusion model is another direction for future undertaking. We would also like to extend our work for tracking multiple people in video sequences. Online model for guiding particles under uncertain conditions can also be investigated.

References

[1] X. Wang, Z. Hou, W. Yu, L. Pu, Z. Jin, X. Qin, Robust occlusion-aware part-based visual tracking with object scale adaptation, Pattern Recognition (2018).

[2] S.-K. Weng, C.-M. Kuo, S.-K. Tu, Video object tracking using adaptive kalman filter, Journal of Visual Communication and Image Representation 17 (6) (2006) 1190–1208.

[3] N. Gordon, B. Ristic, S. Arulampalam, Beyond the kalman filter: Particle filters for tracking applications, Artech House, London 3 (2004) 1077–2626.

[4] M. S. Arulampalam, S. Maskell, N. Gordon, T. Clapp, A tutorial on particle filters for online nonlinear/non-gaussian bayesian tracking, IEEE Trans. on signal processing 50 (2) (2002) 174–188.

[5] M. Isard, A. Blake, Condensation—conditional density propagation for visual tracking, Inter. J. of Comp. Vis. 29 (1998) 5–28.

[6] N. J. Gordon, D. J. Salmond, A. F. Smith, Novel approach to nonlinear/non-gaussian bayesian state estimation, in: IEE Proceedings F (Radar and Signal Processing), Vol. 140, IET, 1993, pp. 107–113.

[7] D. Comaniciu, V. Ramesh, P. Meer, Kernel-based object tracking, IEEE Trans. on patt. analy. & mach. intelli. 25 (2003) 564–577.

[8] A. Adam, E. Rivlin, I. Shimshoni, Robust fragments-based tracking using the integral histogram, in: Comp. visi. and pattern recog., 2006 IEEE CS Conf. on, Vol. 1, 2006, pp. 798–805.

[9] G. S. Walia, S. Raza, A. Gupta, R. Asthana, K. Singh, A novel approach of multi-stage tracking for precise localization of target in video sequences, Expert Sys. with App. 78 (2017) 208–224.

[10] T. Li, S. Sun, T. P. Sattar, J. M. Corchado, Fight sample degeneracy and impoverishment in particle filters: A review of intelligent approaches, Expert Sys. with app. 41 (8) (2014) 3944–3954.

[11] M. Bolić, P. M. Djurić, S. Hong, Resampling algorithms for particle filters: A computational complexity perspective, EURASIP Journal on Advances in Signal Processing 2004 (15) (2004) 403686.

[12] Z. Wang, Z. Liu, W. Liu, Y. Kong, Particle filter algorithm based on adaptive resampling strategy, in: Electronic and Mechanical Engineering and In- formation Technology (EMEIT), 2011 International Conference on, Vol. 6, 2011, pp. 3138–3141.

[13] J. Zuo, Dynamic resampling for alleviating sample impoverishment of particle filter, IET Radar, Sonar & Navi. 7 (2013) 968–977.

[14] G. Choe, T. Wang, F. Liu, S. Hyon, J. Ha, Particle filter with spline resampling and global transition model, IET Comp. Vis. 9 (2) (2014) 184–197.

[15] J. Zhao, Z. Li, Particle filter based on particle swarm optimization resampling for vision tracking, Exp. Sys. with App. 37 (2010) 8910–8914.

[16] M.-L. Gao, L.-L. Li, X.-M. Sun, L.-J. Yin, H.-T. Li, D.-S. Luo, Firefly algorithm based particle filter method for visual tracking, Optik-Int. J. for Light and Elect. Optics 126 (2015) 1705–1711.

[17] R. Rohilla, V. Sikri, R. Kapoor, Spider monkey optimisation assisted parti- cle filter for robust object tracking, IET Comp. Vis. 11 (3) (2016) 207–219.

[18] K. Ahmadi, E. Salari, Social-spider optimised particle filtering for tracking of targets with discontinuous measurement data, IET Computer Vision 11 (3) (2016) 246–254.

[19] G. S. Walia, R. Kapoor, Intelligent video target tracking using an evolutionary particle filter based upon improved cuckoo search, Expert Systems with Applications 41 (14) (2014) 6315–6326.

[20] F. Sardari, M. E. Moghaddam, A hybrid occlusion free object tracking method using particle filter and modified galaxy based search meta-heuristic algorithm, App. Soft Comp. 50 (2017) 280–299.

[21] N. Khasnabish, K. P. Detroja, A stochastic resampling based selective particle filter for visual object tracking, in: Indian Control Conference (ICC). 2018, IEEE, 2018, pp. 42–47.

[22] G. S. Walia, R. Kapoor, Recent advances on multicue object tracking: a survey, Artificial Intelli. Review 46 (2016) 1–39.

[23] P. Brasnett, L. Mihaylova, D. Bull, N. Canagarajah, Sequential monte carlo tracking by fusing multiple cues in video sequences, Image and vision computing 25 (8) (2007) 1217–1227.

[24] G. S. Walia, R. Kapoor, Robust object tracking based upon adaptive multi-cue integration for video surveillance, Multimedia Tools and Applications 75 (23) (2016) 15821–15847.

[25] H. Han, Y.-S. Ding, K.-R. Hao, X. Liang, An evolutionary particle filter with the immune genetic algorithm for intelligent video target tracking, Comp. & Maths. with App. 62 (2011) 2685–2695.

[26] H. Zhou, Z. Deng, Y. Xia, M. Fu, A new sampling method in particle filter based on pearson correlation coefficient, Neurocomputing 216 (2016) 208–215.

[27] A. Bhateja, G. S. Walia, R. Kapoor, Non linear state estimation using particle filter based on backtracking search optimization, in: Comp., Comm. and Automation, Inter. Conf. on, 2016, pp. 342–347.

[28] F. Sardari, M. E. Moghaddam, An object tracking method using modified galaxy-based search algorithm, Swarm and Evolutionary Computation 30 (2016) 27–38.

[29] A. Askarzadeh, A novel metaheuristic method for solving constrained engineering optimization problems: crow search algorithm, Computers & Structures 169 (2016) 1–12.

[30] C. Stauffer, W. E. L. Grimson, Adaptive background mixture models for real-time tracking, in: Computer Vision and Pattern Recognition, 1999. IEEE CS Conf. on., Vol. 2, 1999, pp. 246–252.

[31] T. Ojala, M. Pietikainen, T. Maenpaa, Multiresolution gray-scale and rotation invariant texture classification with local binary patterns, IEEE Trans. on pattern analy. and machine intelli. 24 (7) (2002) 971–987.

[32] A. Bhattacharyya, On a measure of divergence between two statistical populations defined by their probability distributions, Bull. Calcutta Math. Soc. 35 (1943) 99–109.

[33] Y. Bai, D. Wang, Fundamentals of fuzzy logic controlfuzzy sets, fuzzy rules and defuzzifications, in: Advanced Fuzzy Logic Technologies in Industrial Applications, Springer, 2006, pp. 17–36.

[34] R. R. Murphy, Biological and cognitive foundations of intelligent sensor fusion, IEEE Transactions on Systems, Man, and Cybernetics-Part A: Systems and Humans 26 (1) (1996) 42–51.

[35] X. Jia, H. Lu, M.-H. Yang, Visual tracking via adaptive structural local sparse appearance model, in: Com. vis. and pattern recog. (CVPR), IEEE Conf. on, IEEE, 2012, pp. 1822–1829.

[36] K. Zhang, L. Zhang, M.-H. Yang, Real-time compressive tracking, in: European conf. on computer vision, Springer, 2012, pp. 864–877.

[37] B. Babenko, M.-H. Yang, S. Belongie, Robust object tracking with online multiple instance learning, IEEE transactions on pattern analysis and machine intelligence 33 (8) (2011) 1619–1632.

[38] D. A. Ross, J. Lim, R.-S. Lin, M.-H. Yang, Incremental learning for robust visual tracking, Inter. journal of comp. vis. 77 (1-3) (2008) 125–141.

[39] K. Zhang, H. Song, Real-time visual tracking via online weighted multiple instance learning, Pattern Recog. 46 (2013) 397–411.

[40] N. Lazarevic-McManus, J. Renno, D. Makris, G. A. Jones, An object-based comparative methodology for motion det. based on the f-measure, Comp. Vis. and Image Un. 111 (2008) 74–85.

[41] Y. Wu, J. Lim, M.-H. Yang, Online object tracking: A benchmark, in: IEEE Conf. on Comp. Vis. and Pattern Recog., 2013, pp. 2411–2418.

Available online at www.sciencedirect.com

ScienceDirect

Materials Today: Proceedings 5 (2018) 15416–15420

materialstoday: PROCEEDINGS

www.materialstoday.com/proceedings

ISCAS 2017

Role of Different Etchants on the Growth of Catalyst Nanoparticles During the Plasma Processing of Metal Catalyst Thin Film

Ravi Gupta[1*], Suresh C. Sharma[1], and Neha Gupta[1]

[1] Department of Applied Physics, Delhi Technological University (DTU), Shahbad Daulatpur, Bawana Road, Delhi 110042, India

Abstract

An analytical model is developed to investigate the role of different etchants (plasma composition) on the growth of catalyst nanoparticles during the plasma pretreatment of metal catalyst thin film. The model accounts the kinetics of all plasma species (i.e., electrons, positively charged ions, and neutrals), energy balance on the film surface placed over the substrate, energy fluxes of various plasma species, etching and sputtering of the metal catalyst thin film, and growth of catalyst nanoparticle. In our investigation, it is found that the catalyst nanoparticle size decreases catalyst film is treated with hydrogen + nitrogen plasma as compared to the pure hydrogen plasma. Moreover, we found that number density of catalyst nanoparticles (i.e., the number of catalyst particle per unit area) increases when nitrogen is added to hydrogen plasma. This work can be extended to enhance the catalyst-assisted growth of carbon nanostructures and their field emission properties. The theoretical predictions are in concurrence with the experimental observations.

© 2018 Elsevier Ltd. All rights reserved.
Selection and Peer-review under responsibility of 10th NATIONAL CONFERENCE ON SOLID STATE CHEMISTRY AND ALLIED AREAS (ISCAS - 2017).

Keywords: Plasma, Catalyst, nanoparticle, thin film, hydrogen, nitrogen, and plasma pretreatment.

*Email address: ravigpt0709@gmail.com

2214-7853 © 2018 Elsevier Ltd. All rights reserved.
Selection and Peer-review under responsibility of 10th NATIONAL CONFERENCE ON SOLID STATE CHEMISTRY AND ALLIED AREAS (ISCAS - 2017).

1 Introduction

The intriguing properties and potential utilization of carbon nanostructures have brought about plenty latest studies on their formation mechanism. Plasma enhanced chemical vapor deposition (PECVD) is the commonly used technique to synthesize vertically aligned carbon nanostructures [1], in which graphitic structures are shaped from the disintegration of carbon-containing gases on the metallic catalyst nanoparticle surface [2]. These catalyst nanoparticles act as the nucleation sites for the nucleation and growth of carbon nanostructures and can be formed on the substrate surface by plasma etching [3] or by thermal annealing [4] of deposited thin metal catalyst film before the nanostructures growth. The initial size of the catalyst nanoparticle influences the shape, alignment and crystalline structure of the nanostructure [5].

Amid plasma pretreatment of the metal catalyst film, plasma parameters affect the catalyst particle size. Chang et al. [6] pretreated the nickel catalyst thin film with unadulterated hydrogen plasma to segregate it into nanoparticles and found that catalyst particle size decreases with increase in plasma power. Other than plasma parameters, plasma compositions also influence the catalyst particle. Yang et al. [7] utilized hydrogen, nitrogen and oxygen plasma for pretreatment and reported the formation of nickel nitride that can enhance the nanostructures growth. Chang et al. [8] pretreated catalyst film with hydrogen + nitrogen plasma and found that hydrogen/nitrogen proportion has giant impact on the morphology of the catalyst particle. In this paper, we portrayed the general plasma-based model to foresee the formation of nanoparticles from nanofilms.

2 Analytical Model

In the present paper, an analytical model to explain the effects of the catalyst film plasma pretreatment on the growth of the catalyst nanoparticle has been developed. The present model considers the plasma composed of electrons, ions (H^+, H_2^+, N^+, N_2^+) and neutrals (H, H_2, N, N_2) of hydrogen and nitrogen. The electric field due to plasma sheath is assumed to be vertically downward direction, and sheath kinetic of all plasma species are taken into account [11-13], the main equations of the present model are:

$$\frac{\partial Z}{\partial t} = \sum_j I_{ij} + \sum_j K_{ij} - \gamma_e \left(I_e + K_e \right), \tag{1}$$

$$\frac{\partial n_e}{\partial t} = \sum_j \beta_j n_j - \sum_j \alpha_j n_e n_{ij} - \gamma_e \frac{n_{cnf}}{\lambda_d} \left(I_e + K_e \right), \tag{2}$$

$$\frac{\partial n_{ij}}{\partial t} = \beta_j n_j - \alpha_j n_e n_{ij} - \frac{n_{cnf}}{\lambda_d} \left(I_{ij} + K_{ij} \right), \tag{3}$$

$$\frac{\partial n_j}{\partial t} = \alpha_j n_e n_{ij} - \beta_j n_j + \frac{n_{cnf}}{\lambda_d} \left(1 - \gamma_{ij} \right) \left(I_{ij} + K_{ij} \right) - \frac{n_{cnf}}{\lambda_d} \gamma_j \left(I_j + K_j \right) + IF_j - OF_j, \tag{4}$$

where Z is the charge number, n_e, n_j, and n_{ij} are the number density of electrons, neutrals, and ions in the bulk plasma I_{ij} and K_{ij} are the ion collection currents at the CNF tip and curved surface, respectively [11] (*j* refers to the ions of hydrogen or nitrogen). β_j is the coefficient of ionization of positively charged ions, α_j is the coefficient of recombination of positively charged ions and electrons, n_{cnf} is the number density of the carbon nanofibers, λ_d is the plasma sheath width. γ_e, γ_j, γ_{ij} are the sticking coefficient of electrons, neutrals and ions, respectively. IF_j and OF_j are the inflow and out flow rates of the j^{th} species into the plasma chamber.

The Eq. (1) denotes the charge developed on the CNF surface due to the accumulation of positively charged species and electrons on the surface of the CNF. The Eq. (2) represents the rate of electron number density variation in the reactive plasma system on account of ionization of neutral atoms, recombination of electrons and ions, and electron collection current on the CNF surface.
The Eq. (3) represents the rate of positively charged species number density variation in the reactive plasma due to ionization of neutral atoms, electron-ion recombination, ion collection current at the surface of CNF. The Eq. (4) is the particle balance equation for neutrals that represents the growth rate of neutral atom number density. First and third terms show the increase in growth rate of neutral density due to electron-ion recombination and neutralization of ions collected at the surface of CNF, respectively. The second and fourth terms symbolize the decay rate of neutral density due to ionization and accumulation of neutrals on the surface of CNF, respectively.

3 Nanostructuring of thin catalyst film

Catalyst nanoparticles are nucleating seed for the carbon nanostructure growth. Their number density and size strongly influence the growth characteristics and resulting structure on the nanostructure. These nucleating seeds are formed by the plasma pre-treatment of the predeposited thin metal catalyst film over the silicon substrate. The heavy bombardment of plasma species (ions and neutrals) from dense plasma fragments the thin film into many nanoislands (nanoparticle). The morphological characteristics and number density of these nanoparticles strongly depend on plasma composition. The general power balance at the surface of the catalyst film placed over the silicon substrate in the presence of plasma is given by the following equation [14].

$$\dot{E}_{in} = \dot{E}_{gain} + \dot{E}_{loss} \ , \tag{5}$$

$$\dot{E}in = A_f \sigma \left[\in_{env} \left(T_{env}\right)^4 - \in_f \left(T_S\right)^4 \right] + \left[I_{ef} \varepsilon_e^f + \sum_j I_{i2f} \varepsilon_{i2}^f + \sum_j I_{2f} \varepsilon_2^f \right] + \frac{3}{2} k_B T_S \sum_j (1-\gamma_{ij}) I_{ijf} , \tag{6}$$

$$\dot{E}_{gain} = \frac{d}{dt}\left(m_f C_f T_S\right) = A_f C_f \rho_f \left[d_f \frac{dT_s}{dt} + T_s n_a \frac{d}{dt}\left(\frac{1}{6}\pi D^3\right) \right] \tag{7}$$

$$\dot{E}_{loss} = \sigma A_f \left(\in_f T_s^4 - \in_{env} T_{env}^4 \right) + \delta_{ef}(1-\gamma_e)\left(\varepsilon_{ef}^S - \frac{3}{2} k_B T_S \right) I_{ef} + \left[\upsilon_0 \sigma_{ads} U_B + y_d(E_i)(1-\theta_t) \sum_{ij} J_{ij} \right] A_f , \tag{8}$$

where $\dot{E}_{in}$, $\dot{E}_{gain}$ and $\dot{E}_{loss}$ are the total input plasma power, power gained and power loss during plasma pretreatment, respectively. A_f is the area of the metal catalyst film, $\sigma\left(= 5.67 \times 10^{-5} \text{ ergs cm}^{-2} \text{ s}^{-1} \text{ K}^{-4}\right)$ is the Stefan's constant, $\in_{env} (\approx 1)$ is the emissivity of the environment, $\in_f \left(=0.12 \text{ for Nickel}\right)$ is the emissivity of the material of the metal catalyst film, T_S is the substrate temperature, T_{env} is the temperature of the plasma environment, ε_e^f, ε_{i2}^f, and ε_2^f are the mean energies collected by metal catalyst film surface due to electrons, ions, and neutral atoms, respectively [15] and given by $\varepsilon_k^f = \left[\left(\frac{2 - Z\gamma_k}{1 - Z\gamma_k} \right) - Z\gamma_k \right] k_B T_k$ and $\gamma_k = \frac{E_b}{k_B T_k}$, where *k* can be ion, electron or neutral atom. E_b is the energy barrier at the catalyst film surface, I_{i2f}, I_{ef}, and I_{2f} are the collection currents at the metal catalyst film surface due to ions of type 2, electrons, and neutrals of type 2, respectively [10], m_f is the mass of the catalyst film, d_f is the thickness of the film, $C_f \left(= 0.104 \text{ cal g}^{-1} \ {}^0C^{-1}\right)$ is the specific heat of the film, ρ_f is the density of catalyst film material, *D* is the diameter of the catalyst

nanoparticle and n_a is the number of catalyst nanoparticle per unit area, where $\delta_{ef} = 2\left(m_e / m_f\right)$ is the fraction of energy lost during the collision with film, $\varepsilon_{ef}^{S} = 2k_B T_e$ is the mean energy of electrons collected by the surface film [15], υ_0 is the number of sites available, $\sigma_{ads}\left(= 6.8\times10^{-16}\ \text{cm}^2\right)$ is the cross section for the reaction of atomic hydrogen [16], $J_j = n_j\left(k_B T_j / m_j\right)^{1/2}$ is the neutral atom flux, $J_{ij} = n_{ij}\left(k_B T_{ij} / m_{ij}\right)^{1/2}$ is the hydrogen ion flux [17] (here j is 2 for a hydrogen atom), U_B (= 3.74 eV for the nickel) is the surface binding energy of the material (sputter target), γ_d is the sputtering yield [18], and θ_t is the total surface coverage.

The first term in Eq. (6) denotes the heat radiation per unit time towards the surface of the film from the surrounding. The second term represents the energy per unit time collected by the film surface due to electrons, ions and neutral atoms, and the last term is the energy gained per unit time due to the formation of neutrals at the film surface. The Eq. (7) represents the power gained during the nanostructuring of the thin film. The applied plasma power fragments the catalyst film into the catalyst nanoparticles [19] and during this plasma treatment, the temperature of the substrate increases and attains the constant value after some time [20]. Similarly to the power input, various processes contribute to the power loss (power out) during plasma pretreatment of the catalyst film. The first term of Eq. (8) represents the radiative energy per unit time from the surface to the surrounding. The remaining terms denote the energy loss due to sticking and elastic collision of electrons with the surface, energy loss due to chemical etching, and energy loss due to sputtering [21], respectively.

4 Results and discussion

This plasma-based model correlates the thickness of the film, plasma parameters, and diameter and number density of the catalyst nanoparticles. With the aid of Mathematica software, we have solved the first order differential equations simultaneously for the default set of glow discharge parameters.

Figure1 shows the time advancement of catalyst particle diameter obtained from plasma pretreatment of the thin film. From Fig.1, it can be seen that size of the catalyst nanoparticle increases with time and achieves the saturation after some time. Additionally, the Fig.1 indicates that one can obtain lesser particle size when hydrogen + nitrogen plasma is utilized contrasted to the pure hydrogen plasma. This is imputable to the fact that nitrogen is more massive than hydrogen, and also acts as the etching agent, therefore, lesser particle size can be obtained as a result of higher etching of the film.

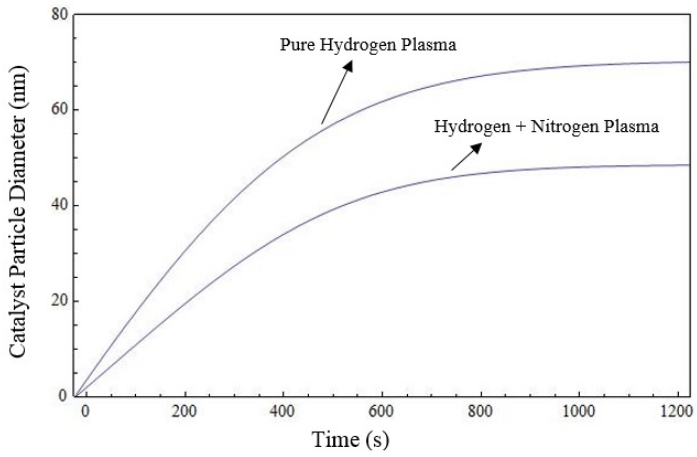


Fig.1 Time evaluation of catalyst particle diameter for (a) pure hydrogen and (b) hydrogen + nitrogen plasma, respectively.

Figure 2 represents that number of catalyst particle per unit area increases when nitrogen is introduced in the pretreatment process. This can be clarified in the way that particles with lesser diameters are formed when hydrogen/nitrogen plasma is used (cf. fig.1) and consequently more particles are formed. These theoretical findings comply with the experimental observations of Chang et al. [8]

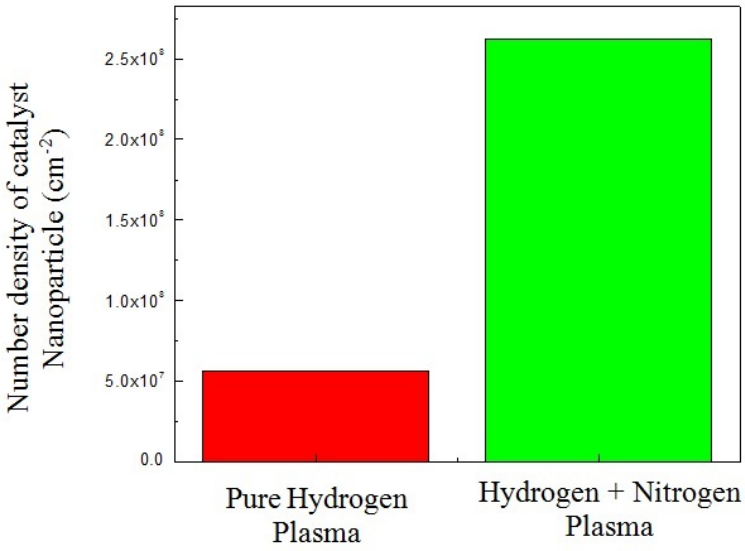


Fig.2 Variation of a number of catalyst particle per unit area for various plasmas.

5 Conclusions

In the present paper, the effect of plasma composition on the nanostructuring of the thin film has been investigated through the plasma kinetics based analytical model. We observed that the presence of nitrogen in the reactive plasma strongly affects the nanoparticle size and their number density. The present work can be extended to study the nucleation and growth of carbon nanostructures in the reactive plasma containing nitrogen species.

References

[1]P. Nath, P.K. Sarker, Constr.Build. Mater. 66 (2014) 163–171
[1]H. W. Wei, K. C. Leou, M. T. Wei, Y. Y. Lin, and C. H. Tsai. J. Appl. Phys. 98 (2005) 044313
[2]N. M. Rodriguez. J. Mater. Res. 8 (1933) 3233
[3]M. Yudasaka, R. Kikuchi, T. Matsui, Y. Ohki, S. Yoshimura and E. Ota. Appl. Phys. Lett. 67 (1995) 2477
[4]C. H. P. Pao, S. J. Henley, G. Y. Chen, A. A. D. T. Adikaari, G. E. Giusca, and S. R. P. Silvaa. J. Appl. Phys. 97 (2005) 114308
[5]R. T. Yang, and J. P. Chen. J. Catal 115 (1989) 52
[6]S. C. Chang, T. C. Lin, and C. Y. Pai, Microelectron. J. 38 (2007) 657
[7]D. J. Yang, Q. Zhang, and S. F. Yoon. Surf. Coat. Technol. 167 (2003) 288
[8]S. C. Chang, T. C. Lin, T. S. Li, and S. H. Huang. Microelectron. J.39 (2008) 1572
[9]H. Kersten, H. Deustch, H. Steffen, G. M. W. Kroesen, R. Hippler, Vacuum 63 (2001) 385
[10]S. C. Shrama and N.Gupta. Phys. Plasmas 22 (2015) 123517
[11]H. Mehdipour, K. Ostrikov, and A. E. Rider. Nanotechnology 21 (2010) 455605
[12] M. A. Lieberman, and A. J. Lichtenberg, Principles of Plasma Discharges and Material Processing (New York:Wiley-Interscience), (1994)
[13]R. Gupta, S. C. Sharma, and R. Sharma. Plasma Sources Sci. Technol. 26 (2017) 024006
[14]H. Kersten, H. Deutsch, H. Steffen, G. M. W. Kroesen, and R. Hippler. Vacuum 63 (2001) 385
[15]M. S. Sodha and S. Guha. Physics of Colloidal Plasmas A. Simon and W. B. Thomson (New York: John Wiley & Sons) (1971) p 219
[16]I. Denysenko and K. Ostrikov. J. Phys. D: Appl. Phys. 42 (2009) 015208
[17]S. Hofmann, G. Csanyi, A. C. Ferrari, M. C. Payne, and J. Robertson. PRL 95 (2005) 036101
[18]R. T. K. Baker, M. A. Barber, R. J. Waite, P. S. Harris, and F. S. Feates. J. Catal. 26 (1972) 51
[19]H. Cui, X. Yang, M. L. Simpson, D. H. Lowndes, and M. Varela. Appl. Phys. Lett. 84 (2004) 20
[20] S. K. Srivastava, A. K. Shukla, V. D. Vankar, and V. Kumar. Thin Solid Films. 492 (2005) 124
[21]N. V. Mantzaris and E. Gogolides. J. Appl. Phys. 79 (1996) 3718

Available online at www.sciencedirect.com

ScienceDirect

Materials Today: Proceedings 5 (2018) 15466–15472

materialstoday: PROCEEDINGS

www.materialstoday.com/proceedings

ISCAS 2017

Role of Dust Grains in Beam-Driven Instabilities

S. C. Sharma[1], VedPrakash[2] and Ruby Gupta[3*]

[1]*Department of Applied Physics, Delhi Technological University, Shahbad Daulatpur, Bawana Road, Delhi-110 042, India*

[2]*India Meteorological Department, Ministry of Earth Sciences, Lodi Road, New Delhi-110 003, India*

[3]*Department of Physics, Swami Shraddhanand College, University of Delhi, Alipur, Delhi-110 036, India*

Abstract

The interaction of beam with magnetized plasma can lead to the excitation of many instabilities which are useful for understanding the stability, confinement and heating of the plasma. In the present work, we investigate the electromagnetic surface plasma waves, lower hybrid waves and ion cyclotron waves in three component dusty plasmas. The presence of charged dust grains modifies the dispersion relation of plasma waves. The charge and number density of dust grains and external magnetic field significantly modify the dispersion properties of these waves. It is shown that in the absence of beam, the plasma mode damps due to dust charge fluctuations and an additional damping dust charge fluctuation mode is induced in plasma. The beam propagating parallel or perpendicular to the magnetic field drives the plasma waves to instability via Cerenkov and cyclotron interaction. Using the analytical and numerical results the influence of the number density of negatively charged dust grains on growth rate of instabilities is studied.

© 2018 Elsevier Ltd. All rights reserved.
Selection and Peer-review under responsibility of 10th NATIONAL CONFERENCE ON SOLID STATE CHEMISTRY AND ALLIED AREAS (ISCAS - 2017).

*Keywords:*Instability, Dispersion, Cerenkov, Cyclotron, Growth rate

*Email address: *rubyssndu@gmail.com*

2214-7853© 2018 Elsevier Ltd. All rights reserved.
Selection and Peer-review under responsibility of10th NATIONAL CONFERENCE ON SOLID STATE CHEMISTRY AND ALLIED AREAS (ISCAS - 2017).

1 Introduction

The studies of instabilities are of great importance because they are helpful for understanding the origin of enhanced fluctuations as well as dust voids and nonlinear dust oscillations in space and laboratory dusty plasmas. There are several mechanisms by which the plasma waves can be driven to instability when free energy sources are available in dusty plasma system. For example, dusty plasmas can be subjected to the influence of external force fields, spatial variation of pressure or intensity of dc electric and magnetic fields, laser/electron/ion beams, etc. The transfer of energy from a beam of particles into electromagnetic wave energy has been given considerable attention in various fields of physics. Beam-energy extraction requires that phase matching between waves and particles is maintained for as long as possible. It is well known that Cerenkov and cyclotron resonances have this desirable property of maintaining synchronization. A number of new plasma modes in magnetized dusty plasma and their instabilities have been investigated in recent years. D'Angelo [1] has investigated the dispersion relation for low-frequency electrostatic waves in magnetized dusty plasma. In the presence of negatively charged dust grains, he has found that the mode frequencies increased as the density ratio of negatively charged dust grains to positive ions is increased. Torney*et al.*[2] have studied the effect of a dust grain population on the growth of the electrostatic waves and explained why no X-ray emission was detected from the optically bright, dusty comet Halebopp.

In the present article, we review the electron/ion beam driven instabilities such as surface plasma wave [3-6], lower hybrid wave [7,8] and ion cyclotron wave [9,10] in magnetized dusty plasma. A dispersion relation and the growth rate of the waves have been derived in the presence of beam and the effect of dust grain number density, dust grain charge and dust grain size is studied. We consider a dusty plasma with equilibrium electron, ion and dust particle densities being given as n_{eo}, n_{io} and n_{do}, respectively, immersed in a static magnetic field B_s in the z-direction. The charge, mass and temperature of the three species are denoted by (-e, m_e, T_e), (e, m_i, T_i) and (-Q_{do}, m_d, T_d), respectively. The response of plasma electrons, plasma ions, beam electrons/ions and negatively charged dust particles is governed by the equations of motion and continuity, which on linearization yield number density perturbations. The dust response is usually taken as unmagnetized as $\omega \gg \omega_{cd}$. The quasi-neutrality condition in a dusty plasma is given by

$$en_{i1} \pm en_{b1} = en_{e1} + Q_{do}n_{d1} + Q_{d1}n_{d0} \qquad (1)$$

where the subscript 1 refers to a perturbed quantity due to electrostatic perturbation. A + sign in beam term stands for ion beam and a – sign stands for an electron beam.

Applying probe theory to a dust grain, the charge on a dust grain is known to be balanced with plasma currents on the given surface, and following Jana *et al.* [11], we obtain the dust charge fluctuation as

$$Q_{d1} = \frac{i|I_{eo}|}{(\omega + i\eta)}\left(\frac{n_{i1}}{n_{io}} - \frac{n_{e1}}{n_{eo}}\right). \qquad (2)$$

where $\beta = \frac{|I_{eo}|}{e}\frac{n_{do}}{n_{eo}}$ is the coupling parameter given as $\beta = 0.1\pi a^2 n_{do} v_{te}$, $\eta = 0.01\omega_{pe}\frac{n_{eo}}{n_{io}}\frac{a}{\lambda_D}$ is the time scale of delay, a is the dust grain radius, λ_D is the Debye length and $v_{te} = \left(\frac{2T_e}{m_e}\right)^{1/2}$ is the electron thermal velocity.

For electromagnetic waves such as surface plasma wave, the perturbed electron beam current density is obtained using the relation

$$J_{b1} = -e\, n_{b0} v_{b1} - e\, n_{b1} v_{b0}. \qquad (3)$$

The values obtained above are then substituted in the following wave equation to obtain the dispersion relation of the electromagnetic wave.

$$\nabla^2 \mathbf{E} - \nabla(\nabla \cdot \mathbf{E}) + \frac{\omega^2}{c^2}\mathbf{E} = -\frac{4\pi i\omega}{c^2}\mathbf{J}. \qquad (4)$$

For electrostatic waves, the perturbed quantities are substituted in the quasi-neutrality condition to obtain the dispersion relation of the electrostatic waves such as lower hybrid wave, ion cyclotron wave, upper hybrid wave, etc. The electron, ion, dust and beam plasma frequencies are respectively given as

$$\omega_{pe}=\left(\frac{4\pi n_{eo}e^2}{m_e}\right)^{1/2},\ \omega_{pi}=\left(\frac{4\pi n_{io}e^2}{m_i}\right)^{1/2},\ \omega_{pb}=\left(\frac{4\pi n_{bo}e^2}{m_e}\right)^{1/2},\ \omega_{pd}=\left(\frac{4\pi n_{do}Q_{do}^2}{m_d}\right)^{1/2}$$

2 Electron beam driven surface plasma wave (SPW) instability [3]

An electron beam drives surface plasma waves to instability on a vacuum magnetized dusty plasma interface and in a magnetized dusty plasma cylinder via Cerenkov and fast cyclotron interaction. These waves play a crucial role in laser ablation, high sensitivity sensorsand are being explored for their potential in subwavelength optics, magento-optic data storage, microscopy and solar cells. Using first order perturbation theory, the dispersion relation of SPW has been obtained in the presence of electron beam and negatively charged dust grains as

$$(\omega^2-\omega_1^2)(\omega^2-\omega_2^2)=-\omega_{pb}^2\,k_Z\,\omega^3\,v_{b0}\left(\frac{\in+1}{\in}\right)\left[\frac{1}{[(\omega-k_Zv_{b0})^2-\omega_{ce}^2]}-\frac{1}{(\omega-k_Zv_{b0})^2}\right] \tag{5}$$

where ω_1^2 and ω_2^2 are two roots of ω^2, given as

$$\omega_1^2=\frac{1}{2}k_Z^2c^2\left(\frac{\in+1}{\in}\right)\pm\frac{k_Zc}{2}\left[k_Z^2c^2\left(\frac{\in+1}{\in}\right)^2+4\left(\frac{\in+1}{\in}\right)\frac{\omega_{pe}^2\,\omega_{ce}^2}{(\omega^2-\omega_{ce}^2)}\frac{i\beta}{(\omega+i\eta)}\right]^{\frac{1}{2}},\ \text{and} \tag{6}$$

$$\omega_2^2=\frac{-k_Z^2c^2\left(\frac{\in+1}{\in}\right)\frac{\omega_{pe}^2\,\omega_{ce}^2}{(\omega^2-\omega_{ce}^2)}\frac{i\beta}{(\omega+i\eta)}}{\omega_1^2}. \tag{7}$$

For Cerenkov interaction, $(\omega-k_Zv_{b0})^2\approx 0\Rightarrow\omega\ \square\ k_Zv_{b0}$. Assuming perturbed quantities, the growth rate is obtained as

$$\gamma=\frac{\sqrt{3}}{2}\left[\frac{\omega_{pb}^2\,\omega_1^2\,k_Z\,v_{b0}}{2\left(\omega_1^2-\omega_2^2\right)}\left(\frac{\in+1}{\in}\right)e^{-2k_2a}\right]^{1/3}. \tag{8}$$

In Cyclotron interaction $(\omega-k_Zv_{b0})^2\approx\omega_{ce}^2$, the growth rate for fast cyclotron interaction is obtained as

$$\gamma=\left[\frac{\omega_{pb}^2\,\omega_1^2\,k_Z\,v_{b0}}{4\omega_{ce}\left(\omega_1^2-\omega_2^2\right)}\left(\frac{\in+1}{\in}\right)e^{-2k_2a}\right]^{1/2}. \tag{9}$$

The unstable wave frequencies and the axial wave vector k_z (cm^{-1}) of the surface plasma waves in presence of dust grains have increased. The growth rate of the unstable mode also increases with an increase in the number density of dust grains, in Cerenkov as well as cyclotron interaction.The growth rate in finite geometry is less than the growth rate in infinite geometry, which should be observed as the growth is bounded by the dimensions of the dusty plasma cylinder. The above explanation can also be justified by the fact that as we increase the radius of the cylinder, the growth rate increases. For all values of dust grain number density, the growth rate is less in finite geometry as compared to the growth rate in infinite geometry. The rate of increase of growth rate in finite geometry is also less than the rate of increase of growth rate in infinite geometry. In cyclotron interaction, only fast cyclotron interaction is found to excite the surface plasma waves and provide them a growth. The velocity of the beam for slow cyclotron interaction is such that it cannot interact with the surface plasma waves. Mathematically also, the growth rate in slow cyclotron interaction is found to be zero in both the infinite and finite geometries.

3 Electron beam driven lower hybrid wave (LHW) instability [7]

An electron beam propagating through a magnetized dusty plasma drives electrostatic lower hybrid waves to instability via Cerenkov interaction and cyclotron interaction. Lower hybrid waves play an important role in space and laboratory plasmas due to their ability to interact efficiently with electrons propagating along the magnetic field

and with ions in the transverse plane. Thus LHWs may transfer energy from the perpendicular motion of ions to the parallel motion of electrons or vice versa, either accelerating the electrons or heating the ions[1-3]. Using first order perturbation theory, the dispersion relation of LHW has been obtained in the presence of electron beam and negatively charged dust grains as

$$\left(\omega^2-\omega_1^2\right)\left(\omega^2-\omega_2^2\right)\left(\omega+i\eta+i\beta_1+i\beta_2+i\beta_3\right)=-\left(i\beta_1+i\beta_2+i\beta_3\right)\left(\omega_1^2\omega^2+\omega_2^2\omega^2-\omega_1^2\omega_2^2\right)$$
$$+\omega_{pb}^2\omega^2\left(\omega^2-\omega_{ci}^2\right)(\omega+i\eta)\frac{1}{K}\left[\frac{k_x^2}{k^2}\frac{1}{\left(\bar{\omega}^2-\omega_{ce}^2\right)}+\frac{k_z^2}{k^2}\frac{1}{\bar{\omega}^2}\right] \quad (10)$$

where $\omega_1^2=\omega_{ci}^2+\omega_{lh}^2\left(1+\frac{k_z^2}{k^2}\frac{m_i}{m_e}\frac{1}{\delta}+\frac{\omega_{pd}^2}{\omega_{pi}^2}\right)$, (11)

$$\omega_2^2=\frac{\omega_{ci}^2\left(\frac{k_z^2}{k^2}\frac{m_i}{m_e}\frac{1}{\delta}+\frac{\omega_{pd}^2}{\omega_{pi}^2}\right)}{\left(1+\frac{k_z^2}{k^2}\frac{m_i}{m_e}\frac{1}{\delta}+\frac{\omega_{pd}^2}{\omega_{pi}^2}\right)}, \quad \text{and} \quad \omega_{lh}^2=\omega_{pi}^2\Big/\left(1+\frac{k_x^2}{k^2}\frac{\omega_{pe}^2}{\omega_{ce}^2}\right).$$

In the dispersion relation given by Eq. (10), the first bracket on the left hand side describes the lower hybrid mode with dust particles having frequency ω_1, the second bracket corresponds to the ion-cyclotron mode with frequencyω_2, and the third bracket indicates the damped low-frequency dust fluctuation mode. The first term on the right hand side can be interpreted as a coupling term which is proportional to the dust charge fluctuation and the second term is the beam term. Aperturbative solution of Eq. (10) in the absence of beam yields two roots:

$$\omega=\omega_1-i\beta'\frac{\omega_1^2}{2(\omega_1^2-\omega_2^2)}, \quad (12)$$

$$\text{and } \omega=-i\eta\left(1+\eta^3\beta'/\omega_1^2\omega_2^2\right), \quad (13)$$

$$\text{where } \beta'=\beta\left[1-\frac{\omega_{ci}^2}{\omega^2}\left(1+\frac{m_i}{m_e}\right)\right]$$

Eq. (12) represents the LH mode damping due to dust charge fluctuations and Eq. (13) represents the damping dust charge fluctuation mode.

For Cerenkov interaction, the maximum growth rate of the unstable mode is obtained as

$$\gamma_{max}=\text{Im }\alpha=\frac{\sqrt{3}}{2}\left[\frac{\omega_{pb}^2}{2K}\frac{k_z^2}{k^2}\frac{\left(\omega_+^2-\omega_{ci}^2\right)}{\left(\omega_1^2-\omega_2^2\right)}\omega_1\right]^{1/3}. \quad (14)$$

The LH wave frequency and hence the phase velocity increases with an increase in the dust grain number density. The effects of dust charge fluctuations become negligible when the frequency of LH mode approaches the plasma ion frequency. It is found that the instability has the largest growth rate when the velocity of electron beam in the direction of the magnetic field is comparable to the parallel phase velocity of the mode. An increase in the dust population enhances the growth rate of the LH wave instability through the effect of capturing electrons. However, the maximum growth rate decreases with an increase in the velocity of the beam travelling parallel to the magnetic field.

4 Ion beam driven lower hybrid wave (LHW) instability [8]

An ion beam drives lower hybrid waves to instability in a magnetized dusty plasma via Cerenkov interaction. A dispersion relation and the growth rate of the lower hybrid waves has been derived taking into account the dust charge fluctuations. Using first order perturbation theory, the dispersion relation of LHW has been obtained in the presence of electron beam and negatively charged dust grains as

$$\left(\omega^2-\omega_l^{\,2}\right)\left(\omega+i\eta+i\beta_1+i\beta_2\right)=-\omega_l^2\left(i\beta_1+i\beta_2\right)+\frac{k_x^2}{k^2}\frac{1}{K}\frac{\omega_{pb}^2\omega^2(\omega+i\eta)}{(\omega-k_x v_{b0})^2} \tag{15}$$

where $$\omega_l^2=\omega_{lh}^2\left(\frac{k_x^2}{k^2}+\frac{k_z^2}{k^2}\frac{m_i}{m_e}\frac{1}{\delta}+\frac{\omega_{pd}^2}{\omega_{pi}^2}\frac{k_x^2}{k^2}\right). \tag{16}$$

In the dispersion relation given by Eq. (15), the first bracket on the left hand side describes the LH mode with dust particles having frequency $\omega_l$and the second bracket indicates the damped low-frequency dust charge fluctuation mode. The first term on the right hand side is the coupling term which is proportional to the dust charge fluctuation and the second term is the beam term. A perturbative solution of Eq. (15) in the absence of beam yields:

$$\omega=-i\eta\left(1+\frac{\eta(\beta_1+\beta_2)}{\omega_l^{\,2}}\right) \tag{17}$$

Eq. (17) represents the damping dust charge fluctuation mode with the LH mode in plasma.
For Cerenkov interaction, the maximum growth rate of the unstable mode is obtained as

$$\gamma_{max}=\mathrm{Im}\,\alpha=\frac{\sqrt{3}}{2}\left[\frac{\omega_{pb}^2}{2K}\frac{k_x^2}{k^2}\omega_l\right]^{1/3}. \tag{18}$$

The frequency of the LH increases with an increase in the number density of negatively charged dust grains. An increase in the dust population enhances the growth rate of the LHWs through the effect of capturing electrons, modifying the dispersion properties of LHWs in plasmas. As the number density of negatively charged dust grains increases, the electron plasma density n_{eo} decreases with respect to ion plasma density n_{io}. Thus, the ions have an effective mass that is less than m_i, and their greater mobility leads to increased wave generation. As the beam velocity increases, an increase in the most unstable frequency of LH mode is observed, in accord with the results obtained in Sec. 3. It is again found that the instability had the largest growth rate when the velocity of beam is comparable to the phase velocity of the LH mode. The growth rate is maximum when the parallel-wave phase velocity of the LHWs is approximately of the order of the electron thermal velocity, therefore we expect efficient energy transport from the perpendicular ion beam to the bulk of the electrons via Landau damping, accelerating the electrons or heating them. The emission caused by this energetic electron component could explain the observed X-ray spectra [12]. The presence of dust particles can modify the instability, as in the case of cometary emission [13].
Comparing the results of Sec. 3 and Sec. 4, it is found that the maximum growth rate decreases as the parallel electron beam velocity increases, but it increases with an increase in perpendicular ion beam velocity. This is because the maximum growth rate is proportional to one-third power of the unstable wave frequency in both the cases and the unstable frequency decreases with an increase in parallel electron velocity but increases with an increase in perpendicular ion beam velocity.

5 Ion beam driven ion cyclotron wave (ICW) instability [10]

An ion beam propagating parallel to the magnetic field drives ion cyclotron waves to instability via Cerenkov interaction. In a plasma with an ion beam injected parallel to the magnetic field, electrostatic ICWs can have a fairly large parallel phase velocity and can easily be destabilized. ICWs are observed in a wide variety of situations, ranging from laboratory experiments to space plasmas. The electrostatic waves heat the electrons and ions via Landau and cyclotron damping, respectively. Using first order perturbation theory, the dispersion relation of LHW has been obtained in the presence of electron beam and negatively charged dust grains as

$$\left(\omega^2-\omega_l{}^2\right)\left(\omega+i\eta+i\beta'\right)=-i\omega_l{}^2\beta'+\frac{\omega_{pb}^2 v_{te}^2}{\omega_{pe}^2}\left(\omega^2-\omega_{ci}^2\right)(\omega+i\eta)\left[\frac{k_x^2}{\left[\left(\omega-k_z v_{b0}\right)^2-\omega_{ci}^2\right]}+\frac{k_z^2}{\left(\omega-k_z v_{b0}\right)^2}\right], \quad (19)$$

where

$$\omega_l{}^2=\omega_{ci}^2+k^2C_s^2\frac{n_{io}}{n_{eo}}\left(1+\frac{\omega_{pd}^2}{\omega_{pi}^2}\right), \quad (20)$$

$\omega_2{}^2=\omega_{ci}^2+k^2C_s^2$, $\beta'=\beta\left(\omega^2-\omega_2{}^2\right)\Big/\omega^2$ and $C_s=\sqrt{\frac{T_e}{m_i}}$ is the ion acoustic speed.

In the dispersion relation given by Eq. (19), the first bracket on the left hand side represents the IC mode with dust particles having frequency $\omega=\omega_l$ and the second bracket indicates the damped low-frequency dust charge fluctuation mode. The first term on the right hand side is a coupling term proportional to the dust charge fluctuation and the second term describes the beam mode with Cerenkov and cyclotron terms.

A perturbative solution of Eq. (19) in the absence of beam yields two roots

$$\omega=\omega_l-i\beta'/2, \quad (21)$$

and $$\omega=-i\eta\left(1+\eta\beta'\Big/\omega_l{}^2\right), \quad (22)$$

where Eq. (21) represents the ion cyclotron mode damping due to dust charge fluctuations and Eq. (22) represents the damping dust charge fluctuation mode. The growth rate of the unstable mode is also obtained in Cerenkov and cyclotron interaction. The sizes of dust particles, which are observed in tokamaksTEXTOR, TFTR etc. range from 100 nm to 100 μm, therefore we have observed the variation of growth rate with the dust grain size for a maximum dust grain size of 100 μm. The unstable frequency of the excited waves gradually increases with an increase in the number density of dust grains.

6 Discussion and Conclusion

It is well established that the presence of dust grains can considerably change the collective properties of plasma. The growth rate of the instabilities is found to be dust-dependent.The effect of dust charge fluctuations is directly related to the parameters βand η. β is the coupling parameter which is like an effective collision frequency of electrons with the dust grains. The β terms arise due to coupling of the ion cyclotron mode with the dust charge fluctuations which result as a response to collective plasma perturbations. The charge fluctuations on dust particles have a natural decay rate of order η. Physically, the charge fluctuations decay because any deviation of the grain potential from the equilibrium floating potential is opposed by electron and ion currents into the grains. For appreciable dust charge fluctuations, the beam effect and the dust charge fluctuation effect both need to be considered. When the beam enters the dusty plasma, it interacts with the dust grains and releases secondary electrons due to impact ionization. This reduces the average dust grain charge Q_{do} and thus leads to a decrease in growth rate.The growth rate decreases with an increase in the dust grain number density. It is because an increase in the dust grain number density means that the dust grains together have a large apetite for the electrons, but the number of available electrons per dust grain decreases. This reduces the average dust grain charge Q_{d0}, and thus leads to a decrease in growth rate.The maximum growth rate [cf. Eq.(8), Eq.(9), Eq.(14) &Eq.(18)] is independent of the dissipative mechanisms in the dusty plasma. For a collisionless plasma, it can be mode conversion into a short wavelength mode, as in the present article, the LH mode with frequency ω_{lh} is converted into a high frequency mode with frequency ω_l [cf. Eq. (11)&Eq.(16)]. An additional unique dissipative mechanism in the presence of dust grains is the dust charging process [14]. The dust charging induces the existence of an additional short wavelength highly damped mode [cf. Eq. (13), Eq. (17) &Eq.(22)]. Our theoretical results could be useful and valid for smaller nano-sized dust particles (e.g., a ~ 10-100 nm) as two limits $a \ll \lambda_{De} \ll \lambda$ (where λ_{De} is the electron Debye length and λ is the wavelength of the fluctuation fields) and $a \ll \rho_L$ are satisfied in the present calculations. Our results are sensitive to the material of dust particles [Mass of dust grains (as appears in ω_{pd}) $m_d=4\pi a^3\rho_d/3$, where a is the dust grain radius and ρ_d is the dust grain density].

References

[1]. N. D'Angelo, Planet. Space Sci. 38 (1990) 1143-1146.
[2]. M. Torney, C. Marmolino, U. De Angelis, A. Forlani and R. Bingham, J. Plasma Phys. 71, (2005) 475-486.
[3]. V. Prakash and S.C. Sharma, Phys. Plasmas, 16 (2009) 093703(1)-093703(9).
[4]. R. Gupta, S.C. Sharma and V. Prakash, Phys. Plasmas, 17 (2010) 112701(1)-112701(5).
[5]. R. Gupta, S.C. Sharma and V. Prakash, Phys. Plasmas, 17 (2010) 122105(1)-122105(6).
[6]. R. Gupta, S.C. Sharma and V. Prakash, Phys. Plasmas, 18 (2011) 053704(1)-053704(6).
[7]. V. Prakash, Vijayshri, S.C. Sharma and R. Gupta, Phys. Plasmas, 20 (2013) 053701(1)-053701(6).
[8]. V. Prakash, Vijayshri, S.C. Sharma and R. Gupta, Phys. Plasmas, 20 (2013) 063701(1)-063701(6).
[9]. V. Prakash, S.C. Sharma, Vijayshri and R. Gupta, Phys. Plasmas, 21 (2014) 033701(1)-033701(7).
[10]. V. Prakash, S.C. Sharma, Vijayshri and R. Gupta, Progress in Electromagnetics Research M, 36 (2014) 161-168.
[11]. M.R. Jana, A. Sen and P.K. Kaw, Phys. Rev. E 48 (1993) 3930-3933.
[12]. R. Bingham, J. M. Dawson and V. D. Shapiro, J. Plasma Phys. 68 (2002) 161-172.
[13]. P. K. Shukla and A. A. Mamun, *Introduction to Dusty Plasma Physics* (Bristol :IOP, 2002)
[14]. S. V. Vladimirov, Phys. Plasmas 1 (1994) 2762-2767.

Available online at www.sciencedirect.com

ScienceDirect

Materials Today: Proceedings 5 (2018) 15409–15415

www.materialstoday.com/proceedings

ISCAS 2017

Solid Flavinium perchlorate salt as catalyst for Bayer-Villiger Oxidation: Effect of N^{10} chain length

Ram Singh[1*], Deepshikha Rathore[1], Geetanjali[2] and Richa Srivastava[1]

[1]Department of Applied Chemistry, Delhi Technological University, Delhi- 110 042, India

[2]Department of Chemistry, Kirori Mal College, University of Delhi, Delhi- 110 007, India

Abstract

Biomimetic reactions have been used for many transformations in organic synthesis. The synthetic isoalloxazines (or flavins) mimic the oxygenation reactions carried out by Flavin-containing monooxygenases (FMOs) including Baeyer−Villiger (BV) oxidationreactions. Here, we studied the effect of chain length at N^{10} position of isoalloxazines during their use as the metal-free organocatalyst. The study suggested that the chain length of 5 to 6 carbon atoms at the N^{10}-position has been ideal to carry out the BV oxidation.

© 2018 Elsevier Ltd. All rights reserved.

Selection and Peer-review under responsibility of 10th NATIONAL CONFERENCE ON SOLID STATE CHEMISTRY AND ALLIED AREAS (ISCAS - 2017).

*Keywords:*Biomimetic reaction, Baeyer-Villiger oxidation, FMOs, BVMOs, Isoalloxazine, Flavin

*Email address: ramsingh@dtu.ac.in

2214-7853© 2018 Elsevier Ltd. All rights reserved.

Selection and Peer-review under responsibility of10th NATIONAL CONFERENCE ON SOLID STATE CHEMISTRY AND ALLIED AREAS (ISCAS - 2017).

1. Introduction

Baeyer−Villiger (BV) oxidation is a widely used transformation in organic synthesis having more than 100 years of history [1,2].In this oxidation reaction, lactones or esters are obtained directly from the corresponding ketones. The reaction utilizes hydrogen peroxide, percarboxylic acid, 3-5-dinitroperbenzoic acid, *meta*-chloroperbenzoic acid etc. as oxygen donor [1]. The reactions where percarboxylic acids used as oxygen donor, the formation of corresponding carboxylic acid or its salt remains as waste. Many metal catalysts have been employed for this transformation leading to the generation of waste containing metal ions which are not environmental friendly [3-5]. The development of better catalysts for this type of transformation is still a focus of research.

The application of biocatalysisalong with biomimetic reactions are excellent alternative for many transformations in organic synthesis including BV oxidation [6,7]. The Baeyer-Villiger monooxygenases (BVMOs) are the flavoenzymes that catalyse the nucleophilic oxygenation of ketones leading to BV oxidation product [8]. Theisoalloxazine (orflavin) derivatives are the prosthetic groups for BVMOs and other flavoenzymes that have been used as synthetic chemical models to mimic the reactions carried by FMOs [9-12].The present work is based on the catalytic cycle of BVMOs for the Baeyer−Villiger (BV) oxidation. The cycle has been modified with the synthesized prosthetic group of FMOs. The effect of chain length at N^{10} position of isoalloxazines has been studied during their use as the metal-free organocatalyst.

2. Experimental

Melting points were determined on a laboratory capilary melting apparatus and are uncorrected. Electronic spectra were recorded on a Perkin-Elmer UV-260 spectrophotometer and absorption maxima have been expressed in nanometers (nm). FTIR spectra were recorded on a Perkin Elmer 1710 FTIR spectrophotometer and the ν_{max} are expressed in cm^{-1}. ^1H NMR was recorded on a Bruker Avance-300 spectrophotometer (300 MHz) and the chemical shifts were expressed in ppm. The abbreviations s, d, t, q, m and bs stand for singlet, doublet, triplet, quartret, multiplet and broad singlet respectively.

The solvents and reagents were purchased from reputed company and were used without further purifications. Alloxan monohydrate was obtained from Acros (Belgium), substituted amines were obtained from Fluka (Switzerland). The 1-chloro-2-nitrobenzene, metal salts and other related reagents were obtained from s.d. Fine chemicals (India) and other reputed Indian companies.

***General procedure for synthesis of 10-substituted isoalloxazines*(4)**

The 10-substituted isoalloxazines were synthesized by using the literature procedure [13-15]. To a solution of N-substituted-2-nitroaniline (**3**, 5 mmol) in dry ethanol (40 mL) in paar hydrogen bottle, Pd/C (20 %) (0.02 g) was added and the reaction mixture was hydrogenated at ambient pressure and temperature till the colour of the solution disappears (for 15-24 h). When the quantitative amount of hydrogen was absorbed and the reaction mixture became almost colourless, glacial acetic acid (2 mL) was added to the reaction mixture and the catalyst was filtered off. The alloxan monohydrate (5 mmol), conc. HCl (2 mL) were added to the filtrate, and the reaction mixture was refluxed for 1 h. The reaction mixture was allowed to cool to room temperature and kept overnight in refrigerator. The resulting precipitate was filtered off to give 10-substituted isoalloxazines (**4**).

10-Ethylisoalloxazine **(4a)**

Mp. 299 ^oC; UV-visible (CH_3OH) λ_{max}: 266, 335, 440 nm; FTIR (KBr): 3400, 3100, 1715, 1660, 1572, 1423, 1281, 1266, 1180, 1093, 881, 860 cm^{-1}; ^1H NMR ($CDCl_3$): 1.27 (t, 3H, CH_3), 4.13 (q, 2H, N^{10}-CH_2), 7.64-7.69 (m, 2H, H-8 & H-9), 7.92-7.97 (m, 1H, H-7), 8.33-8.36 (m, 1H, H-6), 8.58 (s, 1H, NH).

10-Propylisoalloxazine **(4b)**

Mp. 293-294 ^oC; UV-visible (CH_3OH) λ_{max}: 268, 338, 449 nm; FTIR (Nujol): 3399, 3320, 2922, 1714, 1664, 1547, 1460, 1272, 1196, 1090, 880, 875 cm^{-1}; ^1H NMR (DMSO-d_6): 1.10 (t, 3H, CH_3), 1.81-1.89 (m, 2H, CH_2), 4.62 (t, 2H, N^{10}-CH_2), 7.96-8.05 (m, 3H, H-9, H-7 & H-8), 8.40 (d, 1H, H-6, J = 9.12 Hz), 8.71 (s, 1H, NH).

10-Butylisoalloxazine **(4c)**

Mp.: 294-296 ^oC (dec.); UV-visible (CH_3OH) λ_{max}: 269, 333, 441 nm; FTIR (KBr): 3469, 3225, 2955, 1720, 1664, 1549, 1503, 1400, 990, 773 cm^{-1}; ^1H NMR ($CDCl_3$): 0.93 (t, 3H, CH_3), 1.33-1.78 (m, 4H, 2×CH_2), 4.69 (t, 2H, $N^{10}CH_2$), 6.99 (d, 1H, H-9, J = 7.90 Hz), 7.64-7.79 (m, 2H, H-7 & H-8), 7.99 (d, 1H, H-6, J = 8.01 Hz), 8.40 (bs, 1H, N^3H).

10-Pentylisoalloxazine **(4d)**
Mp.: 274-275 °C; UV-visible (CH_3OH) λ_{max}: 273, 338, 447 nm; FTIR (KBr): 3459, 3222, 2956, 1721, 1663, 1541, 1500, 1401, 993, 773 cm^{-1}; ^1H NMR ($CDCl_3$): 0.91 (t, 3H, CH_3), 1.13-1.79 (m, 6H, 2×CH_2), 4.59 (t, 2H, $N^{10}CH_2$), 7.01 (d, 1H, H-9, J = 7.93 Hz), 7.66-7.81 (m, 2H, H-7 & H-8), 8.11 (d, 1H, H-6, J = 8.11 Hz), 8.44 (bs, 1H, N^3H).
10-Hexylisoalloxazine **(4e)**
Mp.: 254-256 °C; UV-visible (CH_3OH) λ_{max}: 266, 335, 440 nm; FTIR (KBr): 3466, 3220, 2925, 1723, 1674, 1549, 1503, 1404, 990 and 771 cm^{-1}; ^1H NMR ($CDCl_3$): 0.92 (t, 3H, CH_3), 1.36-1.49 & 1.85-2.18 (m, 8H, 4×CH_2), 4.71 (t, 2H, $N^{10}CH_2$), 7.64-7.69 (m, 2H, H-7 & H-9), 7.97 (dd, 1H, H-8, J = 7.66 & 1.40 Hz), 8.36 (d, 1H, H-6, J = 7.88 Hz), 8.50 (bs, 1H, N^3H).

General procedure for synthesis of the catalyst (5-ethyl-3-methylflavinium perchlorate salt) **(6)**

The synthesis of the catalyst **6**was achieved using the reported procedure [16,17].10-Substituted-3-methylisoalloxazine (**5**, 1 mmol) and Pd/C (10%) were suspended in ethanol (15 mL). The mixture was purged with nitrogen. Concentrated HCl (1.5 mL) and freshly distilled acetaldehyde (1.5 mL) were added to the mixture and was hydrogenated at room temperature. The mixture was filtered to give yellow colour solution. Since this compound as reported is very sensitive towards air, it was not isolated. This was further dissolved in 10 mL of dithionite containing ammonia and filtered. The filtrate was added to 70% $HClO_4$ solution (15 mL). Further, $NaNO_2$ (7 mmol) and $NaClO_4$ (4 mmol) were added to the reaction mixture. The reaction mixture was stirred at 10°C for 2 h. The resulting light purple precipitate was filtered, washed with water, CH_3OH, ether and $CHCl_3$ to yield flavinium perchlorate salt (**6**).
5,10-Diethyl-3-methylflavinium perchlorate salt **(6a)**
^1H NMR (CD_3CN): 0.96 (t, 3H, CH_3), 1.11 (t, 3H, CH_3), 1.81 (m, 2H, CH_2), 3.21 (s, 3H, N^3CH_3), 3.92 (t, 2H, $N^{10}CH_2$), 7.34 (d, 1H, H-9, J = 7.91), 7.67-7.68 (m, 2H, H-7 & H-8), 7.96 (d, 1H, H-6, J = 7.88 Hz).
5-Ethyl-3-methyl-10-propylflavinium perchlorate salt **(6b)**
^1H NMR (CD_3CN): 0.98 (t, 3H, CH_3), 1.17 (t, 3H, CH_3), 1.71 (m, 2H, CH_2),1.91 (m, 2H, CH_2), 3.16 (s, 3H, N^3CH_3), 3.93 (t, 2H, $N^{10}CH_2$), 7.33 (d, 1H, H-9, J = 7.71), 7.77-7.88 (m, 2H, H-7 & H-8), 7.91 (d, 1H, H-6, J = 7.78 Hz).
10-Butyl-5-ethyl-3-methylflavinium perchlorate salt **(6c)**
^1H NMR (CD_3CN): 0.91 (t, 3H, CH_3), 1.09 (t, 3H, CH_3), 1.22–1.92 (m, 6H, 3×CH_2), 3.25 (s, 3H, N^3CH_3), 4.02 (t, 2H, $N^{10}CH_2$), 7.31–7.41 (m, 2H, H-7 & H-9), 7.77-7.79 (m, 1H, H-8), 8.06 (d, 1H, H-6, J = 7.99 Hz).
5-Ethyl-3-methyl-10-pentylflavinium perchlorate salt **(6d)**
^1H NMR (CD_3CN): 1.01 (t, 3H, CH_3), 1.16 (t, 3H, CH_3), 1.19–1.99 (m, 8H, 4×CH_2), 3.22 (s, 3H, N^3CH_3), 3.86 (t, 2H, $N^{10}CH_2$), 7.39 (d, 1H, H-9, J = 8.11 Hz), 7.55–7.68 (m, 2H, H-7 & H-8), 7.86 (d, 1H, H-6, J = 7.79 Hz).
5-Ethyl-10-hexyl-3-methylflavinium perchlorate salt **(6e)**
^1H NMR (CD_3CN): 0.96 (t, 3H, CH_3), 1.11 (t, 3H, CH_3), 1.20–2.01 (m, 10H, 5×CH_2), 3.21 (s, 3H, N-CH_3), 3.92 (t, 2H, $N^{10}CH_2$), 7.34–7.41 (m, 2H, H-7 & H-9), 7.67-7.68 (m, 1H, H-8) & 7.86 (d, 1H, H-6, J=7.88 Hz).

BV oxidation with the catalyst prepared

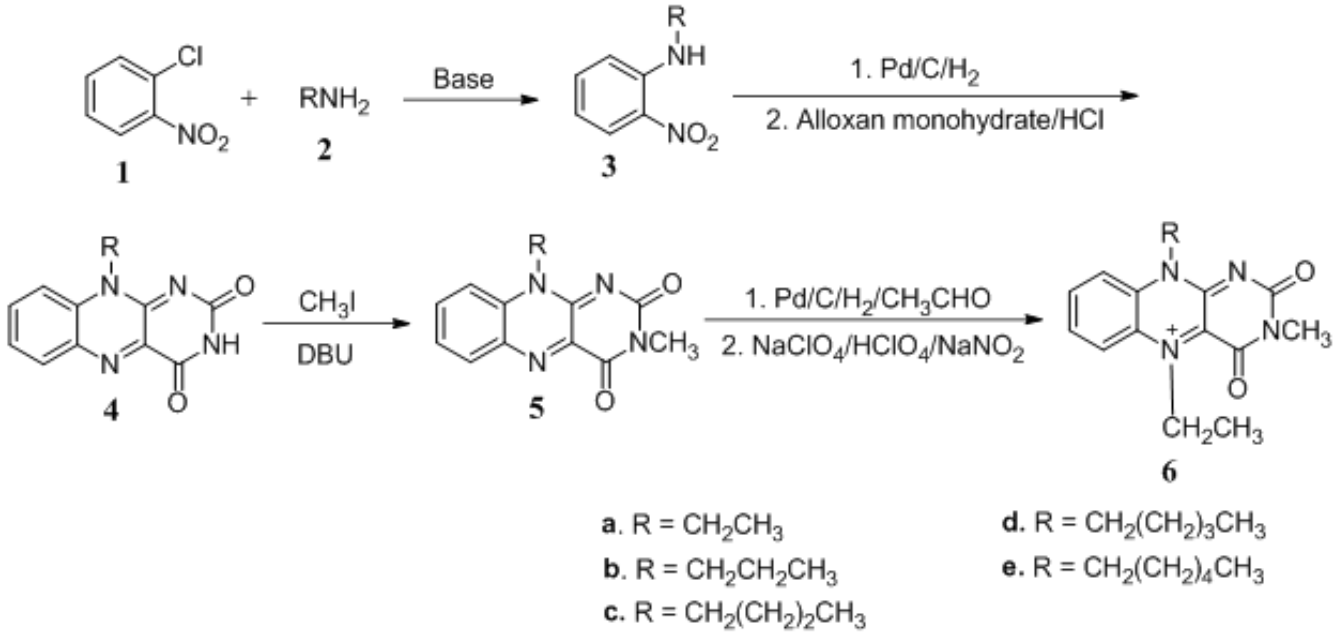
Ketone (**7**, 5 mmol) and the catalyst **6** (100 mg) were dissolved in *t*-BuOH (10 mL), and 1 mL of 35% H_2O_2/water solution was added *via* syringe in a 50mL round bottom flask. The mixture was stirred at nitrogen atmosphere at room temperature for 24 h. The progress of the reaction was monitored with TLC using authentic sample. The evaporation of the solvent under reduced pressure afforded the lactones (**8**).

3. Results and Discussion

Synthesis of 5-ethyl-3-methylflavinium perchlorate salt **(6)**
The reaction of 1-chloro-2-nitrobenzene (**1**) with aliphatic amines (**2**) in the presence of base gave N-substituted-2-nitroaniline (**3**) in 40-45% yield.The reduction of **3** with Pd/C/H_2 gives the required diamino compound, which on subsequent cyclocondensation with alloxan monohydrate afforded 10-substituted isoalloxazines (**4**)in33-54% yields [13-15]. The formation of **4** has been confirmed by various spectroscopic data including UV-visible, FTIR and ^1H NMR spectroscopy. In a typical case, the absorption maxima in the UV-visible spectrum of 10-ethylisoalloxazine (**4a**) has been observed in methanol at 266, 335 and 440 nm, which are characteristic of the isoalloxazine moiety

[18]. In the FTIR spectra of **4a**, the appearance of peaks at 1660 and 1715 cm^{-1} indicated the presence of two carbonyl groups at 2- and 4-positions respectively, which are also characteristics of the isoalloxazine moiety [18-20]. The structure has further been confirmed by ^1H NMR spectroscopy.In the ^1H NMR spectrum of **4a** recorded in $CDCl_3$, a triplet at 1.27 for three protons and a quartet at 4.13 ppm have been assigned to the methyl group and $N^{10}CH_2$ protons. Other multiplets in the aromatic regions have been consistent with the ^1H NMR spectrum of flavin moiety [18,19].The reaction of 10-substituted isoalloxazines (**4**) with methyl iodide using DBU (1,8-diazabicyclo[5.4.0]undec-7-ene) as a base in dry benzene at room temperature gave 3,10-disubstituted isoalloxazines (**5**) in 87-97% yields (Scheme 1) [21].The alkylation at N-3 position in **5a** has been confirmed by ^1H NMR where an additional singlet appeared at 3.33 ppm. The other peaks have been observed in agreement with the isoalloxazine moiety.

The synthesis of the catalyst **6**was achieved using the reported method (Scheme 1) [16,17]. The flavin **5** on reductive alkylation with Pd/C (10%) and acetaldehyde and further treatment without isolation with $HClO_4$/ $NaClO_4$ in the presence of $NaNO_2$ gave a purple colour compound **6**.This catalyst was used for the oxidation of lactones. These cationic isoalloxazines are known to give an intermediate isoalloxazine hydroperoxide on reaction with hydrogen peroxide (H_2O_2), which is an active oxygen donor [17].

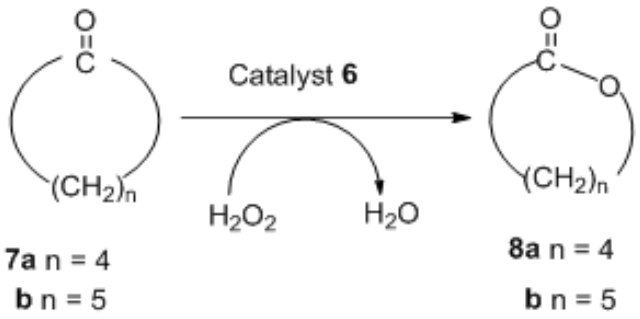


Scheme 1: Synthesis of 10-substituted 5-ethyl-3-methylflavinium perchlorate (**6**)

Baeyer-Villiger oxidation of lactones with synthesized catalyst

The reaction of cyclopentanone (**7a**) with hydrogen peroxide solution (35% w/w) in the nitrogen atmosphere and the flavin catalyst **6** in *t*-butanol resulted in the conversion of cyclopentanone (**7a**) to δ-valerolactone (**8a**) in 89% yields after 24 hours of the reaction at room temperature (Scheme 2). The progress of reaction was monitored with thin layer chromatography (TLC) using authentic sample of **8a**. The formation of the product was confirmed by FTIR spectroscopy. The decrease in the frequency has been observed for carbonyl group in lactones. To check the utility of catalyst, the reaction was performed under same condition without the use of catalyst **6**. In the first 24 hours, no product was obtained as observed from TLC. The reaction was allowed to run for further 48 hours. No product was obtained even after 48 hours. The TLC of the reaction mixture showed the presence of unreacted **7a**(entry 5, table 1). The reaction was also repeated with cyclohexanone (**7b**) and found the similar results.

The reaction with respect to the use of solvent was also optimized for the biomimetic reaction leading to BV oxidation (Table 1). Four solvents were tried, water, methanol, acetonitrile and *t*-butanol. The reaction in *t*-butanol gave the best yield and hence was chosen as the appropriate solvent for the reaction. The role of hydrogen peroxide (H_2O_2) was also confirmed as oxygen donor as no reaction was observed without its presence (Table 1, entry 6). However, when reaction was performed with H_2O_2 but in the presence of molecular oxygen, about 30% conversion observed.



Scheme 2: BV oxidation of cyclic ketones

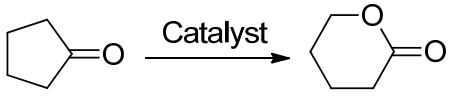
To check the biomimetic prospects of the reaction, catalyst with different chain length at N^{10}-position, which were prepared, have been applied for the BV oxidation with the substrates, **7a** and **7b** (Table 2). The reaction with the catalyst 10-hexyl-5-ethyl-3-methylflavinium perchlorate salt) (**6e**) gave better yield in both the cases. Also, the difference in yield between the catalysts **6e** and **6d** was found to be very low (Table 2). This suggests that the chain length of 5 to 6 carbon atoms at the N^{10}-position is ideal to carry out this BV oxidation using metal-free organocatalyst based on the reaction pathways of BVMOs.

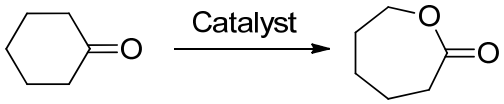
Table1: Optimization of reaction conditions for BV oxidation of **7a**

S. No.	Reaction conditions used[#]	Isolated % Yield of 8a
1.	**7a**/**6a**/ H_2O_2/water	30
2.	**7a**/**6a** /H_2O_2/methanol	40
3.	**7a**/**6a** /H_2O_2/acetonitrile	60
4.	**7a**/**6a** /H_2O_2/*t*-butanol	89
5.	**7a**/ H_2O_2/ *t*-butanol	No reaction
6.	**7a**/**6a** /*t*-butanol	No reaction
7.	**7a**/**6a**/mol O_2 /*t*-butanol	30

#stirred for 24 h in nitrogen atmosphere at room temperature

Table 2: Comparative yield of cyclic ketones with catalysts **6**

S. No.	Catalyst	Yield (%, Isolated)
		
7a	**8a**	
1	**6a,** N^{10}-ethyl	78
2	**6b,** N^{10}-propyl	78
3	**6c,** N^{10}-butyl	80

4	**6d**, N^{10}-pentyl	87
5	**6e,** N^{10}-hexyl	89
7b  **8b**		
6	**6a,** N^{10}-ethyl	80
7	**6b,** N^{10}-propyl	80
8	**6c,** N^{10}-butyl	82
9	**6d**, N^{10}-pentyl	89
10	**6e**, N^{10}-hexyl	91

4. Conclusions

This work has been performed for the synthesis of lactones using chemical methods based on biomimetic approach. The results supported the existing thought that the isoalloxazine derivatives can be used as chemical models for BVMOs for catalyzing the BV oxidation of ketones. The reaction can be run in a very simple fashion at room temperature using hydrogen peroxide as a cheap oxidant using metal-free organocatalysts.Further, the study suggested that the chain length of 5 to 6 carbon atoms at the N^{10}-position is ideal to carry out this BV oxidation based on the reaction pathways of BVMOs.

Acknowledgements

The author DR is thankful to Delhi Technological University, New Delhi, India for the financial supports.

References

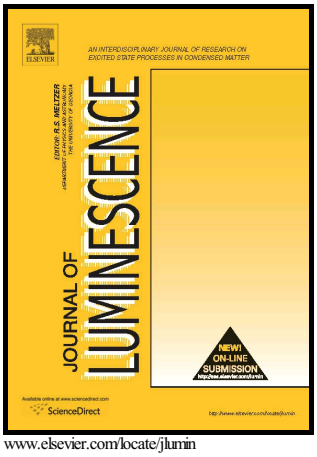
1. M. Renz, B. Meunier, Eur. J. Org. Chem. 1 (1999) 737-750.
2. G.-J.ten Brink, W.C.E. Arends, R.A. Sheldon, Chem. Rev. 104 (2004) 4105–4123.
3. C. Bolm, O. Beckmann, Chirality 12 (2000) 523-525.
4. A.M. Phillips, C. Romao, Eur. J. Org. Chem.64 (1999) 1767-1770.
5. G.J.T. Brink, J.M. Vis, I.W.C.E. Arends, R.A. Sheldon, J. Org. Chem. 66 (2001) 2429-2433.
6. R.A. Sheldon, P.C. Pereira, Chem. Soc. Rev. 46 (2017), 2678-2691.
7. L. Marchetti, M. Levine,ACS Catal. 1 (2011) 1090–1118.
8. V. Alphand, G. Carrea, R. Wohlgemuth, R. Frustoss, J.M. Woodley, Trends Biotech. 21 (2003) 318-323.
9. R. Singh,Geetanjali, S.M.S. Chauhan, Bioorg. Chem.32 (2004) 140-169.
10. R. Singh, Geetanjali, C.R. Babu, Chem. Biodiver.2 (2005) 429-446.
11. Geetanjali, R. Singh, Arch. Appl. Sci. Res. 5(2013) 259-262.
12. Geetanjali, R. Singh,Heterocycl.Commun. 19(2013) 261-263.
13. S.M.S. Chauhan, Geetanjali, R. Singh, Ind. J. Heterocycl. Chem.10 (2000) 157-158.

14. S.M.S. Chauhan, R. Singh,Geetanjali, Synth. Commun.33(2003) 1179-1184.
15. D. Rathore, R. Srivastava, R. Singh, Ind. J.Heterocycl. Chem.27 (2017) 13-16.
16. K. Bergstad, J.E. Backvall, J. Org. Chem. 63 (1998) 6650-6655.
17. D. Rathore, R. Singh, Geetanjali, R. Srivastava, Appl.Biochem. Biotech. 174(2014) 1151-1156.
18. K.H. Dudley, A. Ehrenberg, P. Hemmerich, F. Muller, Helv. Chim. Acta. 47 (1964) 1354-1383.
19. I. Hazekawa, Y. Nishina, K. Sato, M. Shichiri, R. Miura, K. Shiga, J. Biochem. 121 (1997) 1147-1154.
20. S. Shinkai, H. Nakao, I. Kuwahara, M. Miyamoto, O. Manaha, J. Chem. Soc. Perkin Trans I, (1988) 313-319.
21. Geetanjali, R. Singh, S.M.S. Chauhan, Synth. Commun. 33 (2003) 613-620.

Author's Accepted Manuscript

Synthesis and enhancement of photoluminescent properties in spherical shaped Sm^{3+}/Eu^{3+} co-doped $NaCaPO_4$ phosphor particles for w-LEDs

Mukesh K. Sahu, M. Jayasimhadri, Kaushal Jha, B. Sivaiah, A.S. Rao, D. Haranath



www.elsevier.com/locate/jlumin

PII: S0022-2313(18)30555-6
DOI: https://doi.org/10.1016/j.jlumin.2018.06.002
Reference: LUMIN15664

To appear in: *Journal of Luminescence*

Received date: 27 March 2018
Revised date: 29 May 2018
Accepted date: 2 June 2018

Cite this article as: Mukesh K. Sahu, M. Jayasimhadri, Kaushal Jha, B. Sivaiah, A.S. Rao and D. Haranath, Synthesis and enhancement of photoluminescent properties in spherical shaped Sm^{3+}/Eu^{3+} co-doped $NaCaPO_4$ phosphor particles for w-LEDs, *Journal of Luminescence,* https://doi.org/10.1016/j.jlumin.2018.06.002

This is a PDF file of an unedited manuscript that has been accepted for publication. As a service to our customers we are providing this early version of the manuscript. The manuscript will undergo copyediting, typesetting, and review of the resulting galley proof before it is published in its final citable form. Please note that during the production process errors may be discovered which could affect the content, and all legal disclaimers that apply to the journal pertain.

ACCEPTED MANUSCRIPT

Synthesis and enhancement of photoluminescent properties in spherical shaped Sm^{3+}/Eu^{3+} co-doped $NaCaPO_4$ phosphor particles for w-LEDs

Mukesh K. Sahu[1], M. Jayasimhadri*[,1], Kaushal Jha[1], B. Sivaiah[1,2], A.S. Rao[1], D. Haranath[2]

[1]*Luminescent Materials Research Lab, Department of Applied Physics, Delhi Technological University, Delhi 110 042, India*

[2]*CSIR-National Physical Laboratory, Dr. K.S. Krishnan Road, New Delhi 110 012, India*

***Corresponding author:** Tel: +91- 9013553360. jayaphysics@yahoo.com (M. Jayasimhadri)

Abstract

A series of Sm^{3+} doped and Sm^{3+}/Eu^{3+}co-doped $NaCaPO_4$ phosphors have been successfully synthesized via molten salt method. The structural, morphological, optical, photoluminescence and decay properties of the synthesized phosphors were investigated. Sm^{3+} doped phosphor exhibits excellent emission properties in the orangish-red region under n-UV excitation (403 nm), and the optimized doping concentration of Sm^{3+} was found to be 1.0 mol%. The excitation spectrum confirms that Sm^{3+}/Eu^{3+} co-doped $NaCaPO_4$ phosphors can be efficiently excited by both n-UV and blue LED chips. In the co-doped $NaCaPO_4$:Sm^{3+}/Eu^{3+} phosphors, the intensity of main characteristic emission peaks of Sm^{3+} decreased and Eu^{3+} increased with increasing Eu^{3+} ion concentration. The energy transfer (ET) from Sm^{3+} to Eu^{3+} was demonstrated to be quadrupole-quadrupole in nature by applying Dexter's ET formula and Reisfeld's approximation. Commission Internationale de l'Eclairage (CIE) chromaticity coordinates for co-doped samples lie in the red region. The decay time for the $^4G_{5/2}$ level of Sm^{3+} decreases with increasing Eu^{3+} concentration, which also indicate the energy transfer from Sm^{3+} to Eu^{3+}. These

Accepted manuscript

ACCEPTED MANUSCRIPT

results indicate that Sm^{3+} and Eu^{3+} co-doped $NaCaPO_4$ multifunctional phosphor is a promising and an attractive potential candidate for n-UV and blue excitation based w-LEDs.

Keywords: Photoluminescence, Orthophosphate, Phosphor, Rietveld refinement, white LEDs, Energy transfer.

1. Introduction

In recent years, white light emitting diodes (w-LEDs) have received significant attention in the field of solid-state lighting as compared with the incandescent and fluorescent lamps [1–3]. White LEDs offer many prominent advantages such as small size, energy-saving, robustness, high brightness, fast switching, longer lifetime (>100 000 h) and environmental friendliness [4–6]. Due to these superior properties, w-LEDs can be used for indoor and outdoor lighting applications, full-color displays, traffic signals, automotive displays and cellular phone illumination etc. [7–9].

Currently, two different techniques have been implemented to obtain white light from LED sources. The first one is RGB method, which combines individual red, green and blue (RGB) emitting LED chips to obtain white light. In the second technique, ultra-violet (UV)/ near ultra-violet (n-UV)/ blue LED source with single (yellow)/ multiple (RGB) fluorescent materials are used [10,11]. This approach has fluorescent material in the form of powder known as phosphor (host material + activator) and thus termed as phosphor converted white light emitting diodes (pc-w-LEDs). The first commercial method to obtain the pc-w-LED involves the combination of a blue LED chip with yellow emitting cerium doped yttrium aluminium garnet (YAG: Ce^{3+}) phosphor [12]. However, this technique has several drawbacks like halo effect due to the separation of blue-yellow color, thermal quenching, and poor color rendering index (R_a<

Accepted manuscript

ACCEPTED MANUSCRIPT

65~70) [5,13,14]. To accomplish better white light with improved R_a, RGB phosphors with n-UV LED chip as an excitation source is required [15]. However, in this approach, the efficiency of red phosphor is very poor as compared to the green and blue phosphors. Therefore, it is essential to synthesize efficient red phosphor material having many distinguished properties such as chemically stable, environmental friendly and highly efficient n-UV/blue excited fluorescent material to use in pc-w-LED [16,17].

Rare earth ions can act as sensitizer as well as an activator in the host lattices to extend the excitation wavelength region of phosphor [18–21]. Sm^{3+} as a sensitizer can be excited by n-UV and blue light with energy level close to that of Eu^{3+} ion, which acts as an activator in the same lattice. Therefore, the co-doped phosphor covers the large portion of emission of the n-UV LED (InGaN) chip due to energy transfer from sensitizer to activator, which enhances the emission intensity and also the n-UV absorption of the phosphor [22–24].

Rare earth doped alkali-alkaline earth orthophosphates have emerged as an excellent inorganic host material for many optoelectronic applications due to their excellent luminescent properties along with many distinguished properties such as large optical band gap, low phonon energy, high thermal as well as chemical stability [16,25]. In alkali-alkaline earth orthophosphate group with general formula $ABPO_4$ (where A = alkali and B = alkaline earth metal), $NaCaPO_4$ has been emerged as an incomparable host lattice for the potential applications in pc-w-LEDs [26]. Rare-earth doped $NaCaPO_4$ possess some unique properties such as strong UV absorption, high conversion efficiency with low-cost, lower synthesis temperature, higher physical and chemical stability [27–30].

Various synthesis methods such as solid state reaction (SSR), sol-gel, hydrothermal, combustion and solvothermal have been used to synthesize phosphors [31–33]. Among all

Accepted manuscript

ACCEPTED MANUSCRIPT

methods, SSR method is an easy and commercially acceptable technique to synthesize the variety of powder materials and phosphors [34]. However, SSR has some drawbacks such as complex post annealing at high temperature for a long duration, which degrade the structural and morphological properties of the synthesized materials [35]. Few researchers used metal salt mixture along with raw materials to provide a better medium for diffusion in solid state reaction and this method is generally known as a molten salt method. In the molten salt method, the alkali metal salts are added to the precursor raw mixture during the grinding process [36]. These alkali metal salt plays a crucial role in molten state and provides favorable reaction medium, which may improve the kinetics of formation of the product. The molten salt method offer advantages like increasing the reaction rate and the degree of homogeneity, simultaneously lower the reaction temperature, controlling the particle size and shape and preventing the agglomeration of particles [37].

In the present research work, Sm^{3+} doped and Sm^{3+}/Eu^{3+} co-doped $NaCaPO_4$ phosphors were synthesized via the molten salt method. The structural, optical, morphological, luminescence and decay properties along with energy transfer mechanism between Sm^{3+} and Eu^{3+} have been discussed in detail. Especially, orthophosphate $NaCaPO_4$ phosphor synthesized with the uniform spherical particle size in this work. The phosphor exhibit orange and red emission from Sm^{3+} doped and Sm^{3+}/Eu^{3+}co-doped $NaCaPO_4$ phosphors under n-UV/blue excitations, which recommends the possibility of utilizing the synthesized phosphors for phosphor-converted w-LEDs.

2. Experimental

2.1. Materials and Synthesis

Accepted manuscript

ACCEPTED MANUSCRIPT

A series of $NaCaPO_4$: x Sm^{3+} (x = 0.5, 1.0, 1.5 and 2.0 mol%) doped and $NaCaPO_4$: x Sm^{3+}/y Eu^{3+} (x = 1.0 mol% y = 0.5, 1.0, 2.0, 3.0 and 5.0 mol%) co-doped phosphors were synthesized via molten salt method. Na_2CO_3 (Fisher Scientific, 99.9%), $CaCO_3$ (Fisher Scientific, 99.9%), $(NH_4)_2HPO_4$ (Fisher Scientific, 99.9%), Sm_2O_3 (Sigma-Aldrich, 99.99%) and Eu_2O_3 (Sigma-Aldrich, 99.99%) chemicals have been used as starting materials.

In molten salt method, high purity eutectic mixture of NaCl and KCl in equal weight ratio were blended to synthesize $NaCaPO_4$ compound. The ratio of molten salt mixture [NaCl + KCl] and starting material [Na_2CO_3 + (1-x-y) $CaCO_3$ + $(NH_4)_2HPO_4$ + x Sm_2O_3 + y Eu_2O_3] were maintained as 5:1 weight percent. The stoichiometric ratio of the molten salt mixture and starting material were ground in an agate mortar for an hour with ethanol as wetting medium. The mixture was kept in an alumina crucible and placed in a programmable muffle furnace at 800 °C for 3 h. Then the samples were naturally cooled to room temperature. Further, samples were washed several times with hot deionized water and dried in an oven at 150 °C for 24 h to obtain the desired phosphor.

2.2. Characterization Techniques

The phase purity of the synthesized samples was identified by using Bruker D8 Advanced Powder X-ray diffractometer with Cu-Kα radiation (λ = 1.54 Å, 40 kV, 40 mA) source in the 2θ range of 20° to 80°. The morphology and elemental analysis of the samples were observed via scanning electron microscopy (SEM) (Hitachi, Model- S-3700N). Diffuse reflectance spectra of synthesized samples were recorded using UV–Vis spectrophotometer (Cary-300 UV-Vis) (Agilent Technologies) at room temperature. The excitation and emission spectra of the samples were recorded at room temperature by a Spectrofluorophotometer (Shimadzu RF-5301PC) with a

Accepted manuscript

ACCEPTED MANUSCRIPT

xenon lamp as an excitation source. The decay measurements were performed using an Edinburgh FLS900, where xenon flash lamp was used as an excitation source.

3. Results and discussion

3.1. Phase identification and Rietveld refinement

Fig.1 (a-e). shows the X-ray diffraction (XRD) patterns of the standard (JCPDS 76-1456), synthesized pure, 1.0 mol% Sm^{3+}, 1.0 mol% Eu^{3+} doped, 1.0 mol% Sm^{3+} and 1.0 mol% Eu^{3+} co-doped $NaCaPO_4$ powder samples. All the diffraction peaks of the samples are well matched with the standard JCPDS card no. 76-1456 has an orthorhombic structure with a space group of $Pn2_1a$ (33). A few minute unknown peaks were present in the as-prepared $NaCaPO_4$ sample at 2θ ~ 22°, 25°, 30° and 32°. These minute impurity peaks may be due to the potassium salt present in the sample, which was also detected during EDS analysis as presented in succeeding section. No impurity/extra peaks were found related to doping and co-doping in $NaCaPO_4$, which confirms the effective doping of rare-earth ions in the host lattice. The average crystallite size of the pure, doped and co-doped samples were estimated by using Debye-Scherer's formula [38].

$$D = \frac{K\lambda}{\beta cos\theta}$$

where D is the average crystallite size, K is the shape factor (typically~0.91), λ (1.54 Å) is the X-ray wavelength, β and θ are the full-width at half-maximum (FWHM) and the diffraction angle of the X-ray diffraction peak, respectively. The average crystallite sizes of pure, doped and co-doped samples were found to be in the range of 40 to 48 nm.

The Rietveld analysis was performed for the pure $NaCaPO_4$ sample. The peak shape and the background were described by pseudo-voigt function and the mode of linear interpolation

Accepted manuscript

ACCEPTED MANUSCRIPT

between a set background points, respectively. The raw, fitted, the difference between them and Bragg position of $NaCaPO_4$ samples are shown in Fig. 2. The refinement parameters indicate that the diffraction pattern exhibits good agreement with the standard JCPDS data without an anonymous peak. The calculated lattice parameters and goodness of fit (GOF) (χ^2) have been provided in Table 1. The crystal structure of $NaCaPO_4$ indicates that three Na^+ and three Ca^{2+} cations are located at 4a sites. The atom Ca (Ca1, Ca2 and Ca3) is connected with eight O atoms forming eight folded polyhedral coordinates. Whereas each Na atom is surrounded by ten O atoms, forming ten-folded coordinates. There are three different P (P1, P2 and P3) site, each P atom is connected with four O atoms, forming the PO_4 tetrahedral structure. The final atomic coordinates of atoms are listed in Table 2.

3.2. Morphological Study

The surface morphology of the synthesized pure $NaCaPO_4$ and $NaCaPO_4$: x Sm^{3+}/y Eu^{3+} (x = y =1.0 mol%) co-doped samples were presented in Fig. 3 (a, b) and Fig. 3 (c), respectively. The SEM images of pure and co-doped samples indicate the regular spherical morphology with particles size in the range of 3-8 μm. It might be due to the molten salt (NaCl + KCl), which plays a crucial role in the formation of spherical shape particle. In this method, the particle morphology is mainly depending on the dissolution precipitation of starting materials in the molten salt medium [39]. When the starting materials and salts are fired at a temperature above the melting point of the salts, the starting materials rearrange and diffuse quickly in a liquid state [40,41]. In the molten state, ionic salt (K^+, Na^+ and Cl^- ions) provides the medium to prevent particle agglomeration, which may affect the crystallization and growth orientation of the particles [42].

Accepted manuscript

ACCEPTED MANUSCRIPT

The energy dispersive spectrum (EDS) of pure $NaCaPO_4$ is shown in the Fig. 3 (d). Elemental analysis confirms that the synthesized sample comprises of sodium, calcium, phosphorous, and oxygen, which confirmed the successful synthesis of $NaCaPO_4$ sample. There are two minute peaks at 3.2 and 3.5 keV which are related to K^+ ions present in sample.

3.3. DRS spectra and band gap Measurement

Diffuse reflectance spectra of Sm^{3+} doped and Sm^{3+}/Eu^{3+} co-doped $NaCaPO_4$ phosphor samples are presented in Fig 4. The samples exhibit peaks in the range of 250 to 500 nm due to characteristic transitions of Sm^{3+} and Eu^{3+} ions, which matches well with the photoluminescence excitation spectrum of $NaCaPO_4$: *x* Sm^{3+} (*x* = 1.0 mol%) and $NaCaPO_4$: *x* Sm^{3+}/*y* Eu^{3+} (*x* = *y* =1.0 mol%) (Fig.5 and Fig.6 discussed in subsequent section). The optical band gap has been estimated according to the equation mentioned below [43,44].

$$[F(R)h\nu]^n = A(h\nu - E_g)$$

where *h, ν, A* and E_g are Plank's constant, frequency of light, constant and optical band gap, respectively. The value of *n* depends on the type of transition, which is 1/2, 2, 1/3 and 3 for direct allowed, indirect allowed, direct forbidden and indirect forbidden transitions, respectively. The *F(R)* is Kubelka-Munk function [13,45]

$$F(R) = \frac{(1-R)^2}{2R} = \frac{\alpha}{S}$$

where *R, α* and *S* are reflectance, absorbance and scattering coefficient, respectively. Since the *S* is independent of wavelength, *F(R)* is proportional to *α*. The E_g value was calculated by extrapolating the linear region of the plot $[F(R)h\nu]^2$ versus energy (hν) as shown in the inset of

Accepted manuscript

ACCEPTED MANUSCRIPT

Fig. 4 (a) & Fig. 4 (b). The band gap of $NaCaPO_4$: *x* Sm^{3+} (*x* = 1.0 mol%) and $NaCaPO_4$: *x* Sm^{3+}/*y* Eu^{3+} (*x* = *y* =1.0 mol%) were estimated to be about 4.489 and 4.472 eV, respectively.

3.4. Photoluminescence study

3.4.1. Photoluminescence properties of Sm^{3+} doped $NaCaPO_4$ phosphor

The photoluminescence excitation (PLE) and emission spectra of $NaCaPO_4$: *x* Sm^{3+} (*x* = 1.0 mol%) phosphor are presented in Fig. 5. PLE spectrum was recorded in the range of 300 to 500 nm with the emission fixed at 599 nm. The excitation spectrum consist of several peaks centered at 318, 345, 362, 376, 403, 417, 441 and 475 nm corresponding to $^6H_{5/2} \rightarrow {}^4P_{1/2}$, $^6H_{5/2} \rightarrow {}^4H_{9/2}$, $^6H_{5/2} \rightarrow {}^4D_{3/2}$, $^6H_{5/2} \rightarrow {}^4D_{1/2}$, $^6H_{5/2} \rightarrow {}^4F_{7/2}$, $^6H_{5/2} \rightarrow {}^4M_{19/2}$, $^6H_{5/2} \rightarrow {}^4G_{9/2}$ and $^6H_{5/2} \rightarrow {}^4I_{11/2} + {}^4I_{13/2} + {}^4M_{15/2}$ electronic transitions of Sm^{3+} ion, respectively. The intensity of excitation peak at 403 nm was the most intense compared with others, which has been selected as an excitation wavelength to record the emission spectra. The emission spectra revealed three emission bands centered at 562, 599 and 644 nm attributed to $^4G_{5/2} \rightarrow {}^6H_{5/2}$, $^4G_{5/2} \rightarrow {}^6H_{7/2}$ and $^4G_{5/2} \rightarrow {}^6H_{9/2}$ transitions of Sm^{3+} ion, respectively. The $^4G_{5/2} \rightarrow {}^6H_{5/2}$ corresponds to the magnetic dipole transition whereas $^4G_{5/2} \rightarrow {}^6H_{9/2}$ corresponds to the forced electric dipole transition of Sm^{3+} ions [46]. The emission peak intensity increases with an increase in the concentration of Sm^{3+} ions up to 1.0 mol% in $NaCaPO_4$, beyond this concentration, the emission intensity decreases due to the concentration quenching, which indicates the resonant energy and cross relaxation transfer take place between Sm^{3+} ions [47].

3.4.2. Photoluminescence properties of Eu^{3+} doped and Sm^{3+}/Eu^{3+} co-doped $NaCaPO_4$ phosphor

Accepted manuscript

ACCEPTED MANUSCRIPT

Fig. 6 represents the excitation and emission spectrum of $NaCaPO_4$: y Eu^{3+} (y = 1.0 mol%) phosphor, the excitation peaks were observed at 318, 360, 380, 392 415 and 462 nm corresponding to the $^7F_0 \rightarrow {}^5H_6$, $^7F_0 \rightarrow {}^5D_4$, $^7F_0 \rightarrow {}^5L_7$, $^7F_0 \rightarrow {}^5L_6$ $^7F_0 \rightarrow {}^5D_3$ and $^7F_0 \rightarrow {}^5D_2$ transitions, respectively. The emission spectrum consists of several peaks centered at 576, 590, 619, 650 and 700 nm corresponding to the $^5D_0 \rightarrow {}^7F_0$, $^5D_0 \rightarrow {}^7F_1$, $^5D_0 \rightarrow {}^7F_2$, $^5D_0 \rightarrow {}^7F_3$ and $^5D_0 \rightarrow {}^7F_4$, which are the characteristic transitions of Eu^{3+} ions. The $^5D_0 \rightarrow {}^7F_1$ and $^5D_0 \rightarrow {}^7F_2$ are magnetic dipole (MD) and forbidden electric dipole (ED) transition of Eu^{3+} ions, respectively. ED transition is hypersensitive in nature and the emission intensity of this transition is strongly affected by the crystal field of ligand atoms whereas MD transition is insensitive to the crystal environment. It is observed that the emission intensity of ED transition is dominant than the MD transition for the Eu^{3+} doped $NaCaPO_4$ phosphor. The intensity ratio of ED to MD transition reveals the degree of distortion from the inversion symmetry of doping ions in the lattice, known as asymmetric ratio. The asymmetric ratio is more than 1, which indicates a higher degree of covalence and Eu^{3+} ions are located at high-symmetry sites with an inversion center [48–50]. According to the refinement result, activator (Eu^{3+}) ions can occupy three different Ca^{2+} cations at 4a site in the $NaCaPO_4$. This means that the activator (Eu^{3+}) ions could occupy randomly the three Ca^{2+} cations site in the $NaCaPO_4$ sample. The occurrence of the doublet for the transition from $^5D_0 \rightarrow {}^7F_0$ is due to Eu^{3+} ions occupying more than one site of Ca^{2+} cations in $NaCaPO_4$ lattice [51,52].

The PLE spectrum of $NaCaPO_4$: x Sm^{3+}/y Eu^{3+} (x = y =1.0 mol%) co-doped phosphor is represented in the inset of Fig.7, which was obtained by monitoring emission at 619 nm. In PLE spectrum, most of the observed peaks are due to Eu^{3+} along with few other peaks due to Sm^{3+} ions. The observed Sm^{3+} ions peaks at 345, 403, 441 nm and broad band from 457 to 495 nm, correspond to the $^6H_{5/2} \rightarrow {}^4H_{9/2}$, $^6H_{5/2} \rightarrow {}^4F_{7/2}$, $^6H_{5/2} \rightarrow {}^4G_{9/2}$ and $^6H_{5/2} \rightarrow {}^4I_{11/2} + {}^4I_{13/2} + {}^4M_{15/2}$

Accepted manuscript

ACCEPTED MANUSCRIPT

transition, respectively. The inset of Fig. 7 represents the PLE spectra of $NaCaPO_4$: *x* Sm^{3+} (*x* = 1.0 mol%) and $NaCaPO_4$: *y* Eu^{3+} (*y* = 1.0 mol%) phosphor by monitoring the fixed intense emission at 599 and 619 nm respectively. Based on the excitation spectra shown in the inset of Fig.7, emission spectra for Sm^{3+} and Eu^{3+} co-doped $NaCaPO_4$ phosphors were recorded at four wavelengths (373, 403 and 463 nm).

Fig. 8 (a-c) represents the emission spectra of Sm^{3+} and Eu^{3+} co-doped $NaCaPO_4$ phosphors at 373, 403 and 463 nm excitations, respectively for fixed 1.0 mol% Sm^{3+} and for varied Eu^{3+} (0.5, 1.0, 2.0, 3.0 and 5.0 mol%) concentrations. The emission spectra (Fig. 8 a) of Sm^{3+} (*x* = 1.0 mol%) and Eu^{3+} (*y* = 0.5, 1.0, 2.0, 3.0 and 5.0 mol%) co-doped $NaCaPO_4$ phosphors under the excitation wavelength of 373 nm. There are several emission peaks in visible range from 550 to 750 nm. Among these peaks, three peaks are due to the $^4G_{5/2}\rightarrow{}^6H_{5/2}$, $^4G_{5/2}\rightarrow{}^6H_{7/2}$ and $^4G_{5/2}\rightarrow{}^6H_{9/2}$ transition of Sm^{3+} ions, while other peaks correspond to the $^5D_0\rightarrow{}^7F_0$, $^5D_0\rightarrow{}^7F_1$, $^5D_0\rightarrow{}^7F_2$, $^5D_0\rightarrow{}^7F_3$ and $^5D_0\rightarrow{}^7F_4$, transitions of Eu^{3+} ions in $NaCaPO_4$. It can be observed from Fig.8 (a) that the intensity of the emission bands originated from Sm^{3+} ions decreases while that of the Eu^{3+} increases with increasing concentration of the Eu^{3+} ions [53]. In Figs. 8 (b-c), similar trend was observed that with increasing Eu^{3+} ion concentration, the intensity of emission peaks related to Sm^{3+} ion decreased, while that of Eu^{3+} ion increased simultaneously. The above mentioned emission results clearly suggest the energy transfer form Sm^{3+} to Eu^{3+} ions.

The mechanism of energy transfer (ET) can be explained from the energy level diagrams of Sm^{3+} and Eu^{3+} ions as shown in the Fig. 9. It can be observed from the energy level diagram, that the energy of the $^4G_{5/2}$ level (~17924 cm^{-1}) of Sm^{3+} ion is slightly higher than that of $^5D_0$ level (~17277 cm^{-1}) of Eu^{3+} ion. The energy difference between $^4G_{5/2}$ and $^5D_0$ is 647 cm^{-1}, which

Accepted manuscript

ACCEPTED MANUSCRIPT

indicates that Sm^{3+} act as an efficient sensitizer for the Eu^{3+} ion. Thus, Sm^{3+} ion transfers a part of energy to the Eu^{3+} ion. [53,54].

The ET mechanism from the Sm^{3+} ion (sensitizer) to Eu^{3+} ion (activator) may take place via exchange or multipolar interaction. Based on Dexter's ET formula for multipolar interaction and Reisfeld's approximation, a relation can be obtained as [55,56]:

$$\frac{\eta_0}{\eta} \propto C^{n/3}$$

where η_0 and η are the luminescent quantum efficiency of the Sm^{3+} ion (sensitizer) in the absence and presence of the Eu^{3+} ion (activator), *C* is the sum of the mol% of the $Sm^{3+}$and Eu^{3+} ions, and *n* refers to the nature of multipolar interaction, which can be 6, 8 and 10 corresponding to dipole-dipole, dipole-quadrupole, and quadrupole-quadrupole interaction, respectively. The η_0/η value can be approximately calculated by the ratio of related luminescence intensities as [57]:

$$\frac{I_{SO}}{I_S} \propto C^{n/3}$$

where I_{SO} is the luminescence intensity of Sm^{3+} and I_S is the luminescence intensity of Sm^{3+} ion in the presence of Eu^{3+} ion. Fig. 10 represents the plot between the I_{SO}/I_S versus $C^{n/3}$ for the value of n=6, 8 and 10 under 403 nm excitation wavelength. The best linear fit was obtained for n=10, which indicates that the ET from the Sm^{3+} to Eu^{3+} is due to the non-radiative quadrupole-quadrupole interaction [53].

3.5. CIE coordinates

The CIE chromaticity coordinates were calculated based on the emission spectra for Sm^{3+}/Eu^{3+} co-doped $NaCaPO_4$ phosphors are listed in Table 3. The CIE chromaticity coordinates

Accepted manuscript

ACCEPTED MANUSCRIPT

for $NaCaPO_4$: *x* Sm^{3+}/ *y* Eu^{3+} (*x* = 1.0 mol% & *y* = 0.5, 1.0, 2.0, 3.0, 5.0 mol%) can be modulated from orange to red with the variation in the Eu^{3+} concentration.

The CIE chromaticity coordinates for Sm^{3+} (*x* = 1.0 mol%) doped under 403 nm excitation and *x* Sm^{3+}/*y* Eu^{3+} (*x* = 1.0 mol% & *y* = 5.0 mol%) co-doped $NaCaPO_4$ phosphor under 463 nm excitation were (0.578, 0.402) and (0.631, 0.368), respectively as shown in Fig.11 (a & b). The calculated CIE chromaticity coordinates for Sm^{3+} doped $NaCaPO_4$ are in close to Nichia Corporation developed Amber LED NSPAR 70BS (0.570, 0.420) [58]. The calculated CIE chromaticity coordinates for Sm^{3+}/Eu^{3+} co-doped $NaCaPO_4$ phosphor was close to coordinates of commercial red phosphor, Y_2O_2S: Eu^{3+} (0.622, 0.351) [59]. Hence, it can be concluded that the tunable emission obtained from orange to red via orange -reddish light in $Sm^{3+}$and Eu^{3+} co-doped $NaCaPO_4$ phosphors confirms that Sm^{3+} and Eu^{3+} doped $NaCaPO_4$ phosphor is a suitable candidate for w-LEDs.

Accepted manuscript

3.6. Decay measurements

Fig. 12 represents the decay curves for 1.0 mol% Sm^{3+} and Eu^{3+} (*y* = 0.0, 0.5, 1.0, 2.0, 3.0 and 5.0 mol%) ions in $NaCaPO_4$ phosphor for $^4G_{5/2}$ level of Sm^{3+} ion at 599 nm under the excitation of 403 nm. The decay time gives a deeper insight about the energy transfer process from Sm^{3+} to Eu^{3+} ion. The decay curves were fitted with different exponential equations and the best fit was obtained for bi-exponential equation as [60]

$$I = I_0 + A_1 exp\left(-\frac{t}{\tau_1}\right) + A_2\, exp\left(-\frac{t}{\tau_2}\right)$$

ACCEPTED MANUSCRIPT

where I and I_0 represent the luminescence intensities at time t and 0, τ_1 and τ_2 represent the two components of the lifetime, corresponding to the fast and slow lifetimes for exponential components, respectively; A_1 and A_2 are fitting constants, and t is the time. The average value of the lifetimes for different $NaCaPO_4$:x Sm^{3+}/y Eu^{3+} (x = 1.0 mol% & y = 0.0, 0.5, 1.0, 2.0, 3.0 and 5.0 mol%) co-doped phosphor samples were calculated using the formulae [61]

$$\tau_{avg} = \frac{A_1\tau_1^2 + A_2\tau_2^2}{A_1\tau_1 + A_2\tau_2}$$

The average decay time for co-doped phosphor samples are tabulated in Table 4. It can be seen from Fig. 12, the average value of lifetime for $^4G_{5/2}$ level of the sensitizer (Sm^{3+}) decreases with increase in the activator (Eu^{3+}) concentration, which is strong evidence of energy transfer from Sm^{3+} to Eu^{3+} [27, 60].

The ET efficiency (η_T) values can be evaluated from the below mentioned equation [54]

$$\eta_T = 1 - \frac{\tau_d}{\tau_{d0}}$$

where, τ_{d0} and τ_d represents the decay time of the Sm^{3+} ions in the absence of Eu^{3+} ions and in the presence of the Eu^{3+} ions, respectively. The values of the energy transfer efficiencies(η_T) are given in the Table 4. The values of energy transfer efficiency increase with Eu^{3+} ion concentration which indicates energy transfer from Sm^{3+} to Eu^{3+} ions and this value increase two times as the concentration of Eu^{3+} increased from 0.5 to 5.0 mol% in the Sm^{3+}/Eu^{3+} co-doped $NacaPO_4$ phosphor.

4. Conclusion

Sm^{3+} doped and Sm^{3+}/Eu^{3+}co-doped $NaCaPO_4$ phosphors were successfully prepared via molten salt method. Under n-UV excitation (403 nm), the Sm^{3+} doped $NaCaPO_4$ phosphor show three intense emission bands at 562, 599 nm and 644 nm are attributed to $^4G_{5/2} \rightarrow {}^6H_{5/2}$,

Accepted manuscript

ACCEPTED MANUSCRIPT

$^4G_{5/2} \rightarrow {}^6H_{7/2}$ and $^4G_{5/2} \rightarrow {}^6H_{9/2,}$ respectively. The energy transfer from sensitizer Sm^{3+} to activator Eu^{3+} takes place in $NaCaPO_4$ phosphors due to electric quadrupole-quadrupole interaction, which was confirmed by applying Dexter and Reisfeld's theory of luminescence spectra. The lifetime value for the $^4G_{5/2}$ level, decreased for Sm^{3+} and Eu^{3+} co-doped $NaCaPO_4$ phosphor with an increase in the concentration of the Eu^{3+}. The decrease in the lifetime value further suggests energy transfer process from Sm^{3+} to Eu^{3+}. The value of the CIE chromaticity coordinates for 1.0 mol% Sm^{3+} and 5.0 mol% Eu^{3+} co-doped phosphors under 463 nm are (0.631, 0.368) falling in the red region. The above mentioned results strongly suggest the utility of Sm^{3+} doped and Sm^{3+}/Eu^{3+}co-doped $NaCaPO_4$ phosphor for fabrication of w-LEDs using n-UV LED chips.

Acknowledgements:

The author (Dr. M. Jayasimhadri) would like to thank DST-SERB, Govt. of India for sanctioning the research project (No. SB/FTP/PS-082/2014, dt. 02/03/2015).

References:

[1] P.-P. Dai, C. Li, X.-T. Zhang, J. Xu, X. Chen, X.-L. Wang, Y. Jia, X. Wang, Y.-C. Liu, A single Eu^{2+}-activated high-color-rendering oxychloride white-light phosphor for white-light-emitting diodes, Light Sci. Appl. 5 (2016) e16024.

[2] M.-H. Fang, C. Ni, X. Zhang, Y.-T. Tsai, S. Mahlik, A. Lazarowska, M. Grinberg, H.-S. Sheu, J.-F. Lee, B.-M. Cheng, R.-S. Liu, Enhance Color Rendering Index via Full Spectrum Employing the Important Key of Cyan Phosphor, ACS Appl. Mater. Interfaces. 8 (2016) 30677–30682.

[3] J. Chen, W. Zhao, J. Wang, N. Wang, Photoluminescence properties and thermal stability

Accepted manuscript

ACCEPTED MANUSCRIPT

of $RbBaPO_4:Eu^{3+}$ phosphor, J. Mater. Sci. Mater. Electron. 27 (2016) 237–244.

[4] N. Guo, Y. Huang, H. You, M. Yang, Y. Song, K. Liu, Y. Zheng, $Ca_9Lu(PO_4)_7:Eu^{2+},Mn^{2+}$: A potential single-phased white-light-emitting phosphor suitable for white-light-emitting diodes, Inorg. Chem. 49 (2010) 10907–10913.

[5] X. Li, J.D. Budai, F. Liu, J.Y. Howe, J. Zhang, X. Wang, Z. Gu, C. Sun, R.S. Meltzer, Z. Pan, New yellow $Ba_{0.93}Eu_{0.07}Al_2O_4$ phosphor for warm-white light-emitting diodes through single-emitting-center conversion, Light Sci. Appl. 2 (2013) e50.

[6] A.K. Vishwakarma, K. Jha, M. Jayasimhadri, B. Sivaiah, B. Gahtori, D. Haranath, Emerging cool white light emission from Dy^{3+} doped single phase alkaline earth niobate phosphors for indoor lighting applications, Dalt. Trans. 44 (2015) 17166–17174.

[7] C. Feldmann, T. Justel, C.R. Ronda, P.J. Schmidt, Inorganic luminescent materials: 100 Years of research and application, Adv. Funct. Mater. 13 (2003) 511–516.

[8] C.-H. Chiu, C.-H. Liu, S.-B. Huang, T.-M. Chen, White-Light-Emitting Diodes Using Red-Emitting $LiEu(WO_4)_{2-x}(MoO_4)_x$Phosphors, J. Electrochem. Soc. 154 (2007) J181–J184.

[9] L. Mishra, A. Sharma, A.K. Vishwakarma, K. Jha, M. Jayasimhadri, B. V Ratnam, K. Jang, A.S. Rao, R.K. Sinha, White light emission and color tunability of dysprosium doped barium silicate glasses, J. Lumin. 169 (2016) 121–127.

[10] E.F. Schubert, J.K. Kim, Solid-State Light Sources Getting Smart, Science (80). 308 (2005) 1274–1278.

[11] J. McKittrick, L.E. Shea-Rohwer, Review: Down conversion materials for solid-state

Accepted manuscript

ACCEPTED MANUSCRIPT

lighting, J. Am. Ceram. Soc. 97 (2014) 1327–1352.

[12] S. Nakamura, Blue-green light-emitting diodes and violet laser diodes, MRS Bull. 22 (1997) 29–35.

[13] Z. Xia, Y. Zhang, M.S. Molokeev, V. V. Atuchin, Structural and Luminescence Properties of Yellow-Emitting $NaScSi_2O_6$:Eu^{2+} Phosphors: Eu^{2+} Site Preference Analysis and Generation of Red Emission by Codoping Mn^{2+} for White-Light-Emitting Diode Applications, J. Phys. Chem. C. 117 (2013) 20847–20854.

[14] F. Kang, Y. Zhang, M. Peng, Controlling the energy transfer via multi luminescent centers to achieve white light/tunable emissions in a single-phased X2-type Y_2SiO_5:Eu^{3+},Bi^{3+} phosphor for ultraviolet converted Leds, Inorg. Chem. 54 (2015) 1462–1473.

[15] C. Zhao, Z. Xia, M. Li, Eu^{2+} -activated full color orthophosphate phosphors for warm white light-emitting diodes, RSC Adv. 4 (2014) 33114–33119.

[16] G. Zhu, Z. Ci, Y. Shi, M. Que, Q. Wang, Y. Wang, Synthesis , crystal structure and luminescence characteristic of a novel red phosphor $Ca_{19}Mg_2(PO_4)_{14}$: Eu^{3+} for light emitting devices and field emission displays, J. Mater. Chem. C. 1 (2013) 5960–5969.

[17] V.R. Bandi, B.K. Grandhea, K. Jang, D.-S. Shin, S.-S. Yi, J.-H. Jeong, An investigation on photoluminescence and energy transfer of Eu^{3+}/Sm^{3+} single-doped and co-doped $Ca_4YO(BO_3)_3$ phosphors, Mater. Chem. Phys. 140 (2013) 453–457.

[18] V. Singh, G. Sivaramaiah, J.L. Rao, N. Singh, A.K. Srivastava, H.D. Jirimali, J. Li, H. Gao, R.S. Kumaran, P.K. Singh, S.J. Dhoble, Eu^{2+} and Mn^{2+} Co-doped $BaMgAl_{10}O_{17}$ Blue- and Green-Emitting Phosphor: A Luminescence and EPR Study, J. Electron. Mater.

Accepted manuscript

ACCEPTED MANUSCRIPT

45 (2016) 2776–2783.

[19] D. Geng, M. Shang, Y. Zhang, H. Lian, J. Lin, Color-tunable and white luminescence properties via energy transfer in single-phase $KNaCa_2(PO_4)_2$:A (A = Ce^{3+}, Eu^{2+}, Tb^{3+}, Mn^{2+}, Sm^{3+}) phosphors., Inorg. Chem. 52 (2013) 13708–18.

[20] A. Watras, P.J. Dereń, R. Pązik, Luminescence properties and determination of optimal RE^{3+} (Sm^{3+} , Tb^{3+} and Dy^{3+}) doping levels in the KYP_2O_7 host lattice obtained by combustion synthesis, New J. Chem. 38 (2014) 5058–5068.

[21] N. Singh, V. Singh, G. Sivaramaiah, J.L. Rao, P.K. Singh, M.S. Pathak, S.J. Dhoble, M. Mohapatra, blue – green light emitting powder phosphors, J. Lumin. 178 (2016) 479–486.

[22] W.W. Holloway, M. Kestigian, Energy Transfer between the Sm^{3+}, Eu^{3+}, Tb^{3+}, and Dy^{3+} Ions in Sodium Rare-Earth Tungstates, J. Opt. Soc. Am. 56 (1966) 1171–1174.

[23] M. Xie, R. Pan, Improving electrochemical performance of $Li_3V_2(PO_4)_3$ in a thiophene-containing electrolyte, J. Alloys Compd. 551 (2013) 48–52.

[24] Y.-C. Fang, S.-Y. Chu, P.-C. Kao, Y.-M. Chuang, Z.-L. Zeng, Energy Transfer and Thermal Quenching Behaviors of $CaLa_2(MoO_4)_4$:Sm^{3+},Eu^{3+} Red Phosphors, J. Electrochem. Soc. 158 (2011) J1–J5.

[25] J. Chen, W. Zhao, J. Zhong, L. Lan, J. Wang, N. Wang, Synthesis and luminescence properties of Ce^{3+}-doped $RbBaPO_4$, Ceram. Int. 40 (2014) 15241–15248.

[26] C.C. Lin, Z.R. Xiao, G.-Y. Guo, T.-S. Chan, R.-S. Liu, Versatile Phosphate Phosphors $ABPO_4$ in White Light-Emitting Diodes: Collocated Characteristic Analysis and Theoretical Calculations, J. Am. Chem. Soc. 132 (2010) 3020–3028.

Accepted manuscript

ACCEPTED MANUSCRIPT

[27] Z. Yang, G. Yang, S. Wang, J. Tian, X. Li, Q. Guo, G. Fu, A novel green-emitting phosphor $NaCaPO_4:Eu^{2+}$ for white LEDs, Mater. Lett. 62 (2008) 1884–1886.

[28] C. Qin, Y. Huang, L. Shi, G. Chen, X. Qiao, H.J. Seo, Thermal stability of luminescence of $NaCaPO_4:Eu^{2+}$ phosphor for white-light-emitting diodes, J. Phys. D. Appl. Phys. 42 (2009) 185105.

[29] B. V. Ratnam, M. Jayasimhadri, K. Jang, H.S. Lee, White light emission from $NaCaPO_4:Dy^{3+}$ phosphor for ultraviolet-based white light-emitting diodes, J. Am. Ceram. Soc. 93 (2010) 3857–3861.

[30] B. V. Ratnam, M. Jayasimhadri, G.B. Kumar, K. Jang, S.S. Kim, Y.I. Lee, J.M. Lim, D.S. Shin, T.K. Song, Synthesis and luminescent features of $NaCaPO_4:Tb^{3+}$ green phosphor for near UV-based LEDs, J. Alloys Compd. 564 (2013) 100–104.

[31] Y. Chen, J. Wang, M. Gong, Q. Su, Comparative study on the synthesis, photoluminescence and application in InGaN-based light-emitting diodes of $TAG:Ce^{3+}$ phosphors, J. Solid State Chem. 180 (2007) 1165–1170.

[32] R.K. Tamrakar, D.P. Bisen, N. Bramhe, Influence of Er^{3+} concentration on the photoluminescence characteristics and excitation mechanism of $Gd_2O_3:Er^{3+}$ phosphor synthesized via a solid-state reaction method, J. Radiat. Res. Appl. Sci. 7 (2014) 550–559.

[33] P. Godlewska, A. Matraszek, L. Macalik, K. Hermanowicz, M. Ptak, P.E. Tomaszewski, J. Hanuza, I. Szczygieł, Spectroscopic and structural properties of $Na_3RE(PO_4)_2$:Yb orthophosphates synthesised by hydrothermal method (RE = Y, Gd), J. Alloys Compd. 628 (2015) 199–207.

Accepted manuscript

ACCEPTED MANUSCRIPT

[34] D. Jugović, D. Uskoković, A review of recent developments in the synthesis procedures of lithium iron phosphate powders, J. Power Sources. 190 (2009) 538–544.

[35] Y.L. Chen, Y.J. Cui, Y. Zhang, C.H. Cheng, Y. Zhao, Molten Salt Synthesis of $BaPb_{1-x}Bi_xO_3$ Powder at Low Temperatures, J. Supercond. Nov. Magn. 26 (2013) 327–332.

[36] G. Hu, W. Li, G. He, J. Wang, Y. Zhao, Y. Zhang, Molten salt synthesis of $Zn_{1.8}Mn_{0.2}SiO_4$ luminescent materials in NaCl – $ZnCl_2$ eutectic salt, Ceram. Int. 42 (2016) 7852–7856.

[37] X. Wang, J. Li, P. Shi, W. Guan, H. Zhang, High dispersibility and enhanced luminescence properties of $BaMgAl_{10}O_{17}: Eu^{2+}$ phosphors derived from molten salt synthesis, Opt. Mater. (Amst). 46 (2015) 432–437.

[38] L. Alexander, H.P. Klug, Determination of crystallite size with the x-ray spectrometer, J. Appl. Phys. 21 (1950) 137–142.

[39] T. Kimura, Molten Salt Synthesis of Ceramic Powders, Adv. Ceram. - Synth. Charact. Process. Specif. Appl. (2011) ISBN:978-953-307-505-1.

[40] C. Mao, G. Wang, X. Dong, Z. Zhou, Y. Zhang, Low temperature synthesis of $Ba_{0.70}Sr_{0.30}TiO_3$ powders by the molten-salt method, Mater. Chem. Phys. 106 (2007) 164–167.

[41] K.H. Yoon, Y.S. Cho, D.H. Kang, Molten salt synthesis of lead-based relaxors, J. Mater. Sci. 33 (1998) 2977–2984.

[42] S. Zhang, D.D. Jayaseelan, G. Bhattacharya, W.E. Lee, Molten salt synthesis of magnesium aluminate ($MgAl_2O_4$) spinel powder, J. Am. Ceram. Soc. 89 (2006) 1724–1726.

Accepted manuscript

ACCEPTED MANUSCRIPT

[43] R. Lopez, R. Gomez, Band-gap energy estimation from diffuse reflectance measurements on sol-gel and commercial TiO_2: A comparative study, J. Sol-Gel Sci. Technol. 61 (2012) 1–7. =

[44] R. Köferstein, L. Jäger, S.G. Ebbinghaus, Magnetic and optical investigations on $LaFeO_3$ powders with different particle sizes and corresponding ceramics, Solid State Ionics. 249–250 (2013) 1–5.

[45] J. Zhou, Z. Xia, M. Yang, K. Shen, High efficiency blue-emitting phosphor: Ce^{3+}-doped $Ca_{5.45}Li_{3.55}(SiO_4)_3O_{0.45}F_{1.55}$ for near UV-pumped light-emitting diodes, J. Mater. Chem. 22 (2012) 21935.

[46] B.J. Chen, L.F. Shen, E.Y.B. Pun, H. Lin, Sm^{3+}-doped germanate glass channel waveguide as light source for minimally invasive photodynamic therapy surgery, Opt. Express. 20 (2012) 879.

[47] B. V Ratnam, M. Jayasimhadri, K. Jang, Spectrochimica Acta Part A : Molecular and Biomolecular Spectroscopy Luminescent properties of orange emissive Sm^{3+} -activated thermally stable phosphate phosphor for optical devices, Spectorchimica Acta Part A Mol. Biomol. Spectrosc. 132 (2014) 563–567.

[48] D. Tu, Y. Liang, R. Liu, Z. Cheng, F. Yang, W. Yang, Photoluminescent properties of $LiSrxBa_{1-x}PO_4:RE^{3+}$ (RE = Sm^{3+}, Eu^{3+}) f-f transition phosphors, J. Alloys Compd. 509 (2011) 5596–5599.

[49] A.K. Vishwakarma, M. Jayasimhadri, Significant enhancement in photoluminescent properties via flux assisted Eu^{3+} doped $BaNb_2O_6$ phosphor for white LEDs, J. Alloys

Accepted manuscript

ACCEPTED MANUSCRIPT

Compd. 683 (2016) 379–386.

[50] K. Jha, M. Jayasimhadri, Structural and emission properties of Eu^{3+} -doped alkaline earth zinc - phosphate glasses for white LED applications, J. Am. Ceram. Soc. (2017) 1402–1411.

[51] L. Shi, Y. Huang, H.J. Seo, Emission red shift and unusual band narrowing of Mn^{2+} in $NaCaPO_4$ phosphor, J. Phys. Chem. A. 114 (2010) 6927–6934.

[52] Y. Peng, Y. Su, R. Yang, The charge transfer transition phenomenon and microstructure of Eu^{3+}-doped $NaCaPO_4$ phosphors sintered with NH_4Cl flux via solid-state reaction, Mater. Res. Bull. 48 (2013) 1946–1951.

[53] X. Min, Z. Huang, M. Fang, Y. Liu, C. Tang, X. Wu, Energy Transfer from Sm^{3+} to Eu^{3+}in Red-Emitting Phosphor $LaMgAl_{11}O_{19}$: Sm^{3+} , Eu^{3+} for Solar Cells and Near-Ultraviolet White Light-Emitting Diodes, Inorg. Chem. 53 (2014) 6060–6065.

[54] K. Jha, M. Jayasimhadri, Effective sensitization of Eu^{3+} and energy transfer in Sm^{3+}/Eu^{3+} co-doped ZPBT glasses for CuPc based solar cell and w-LED applications, J. Lumin. 194 (2018) 102–107.

[55] G. Li, D. Geng, M. Shang, C. Peng, Z. Cheng, J. Lin, Tunable luminescence of Ce^{3+}/Mn^{2+}-coactivated $Ca_2Gd_8(SiO_4)_6O_2$ through energy transfer and modulation of excitation: potential single-phase white/yellow-emitting phosphors, J. Mater. Chem. 21 (2011) 13334.

[56] K. Jha, A.K. Vishwakarma, M. Jayasimhadri, D. Haranath, Multicolor and white light emitting Tb^{3+}/Sm^{3+} co-doped zinc phosphate barium titanate glasses via energy transfer

Accepted manuscript

ACCEPTED MANUSCRIPT

for optoelectronic device applications, J. Alloys Compd. 719 (2017) 116–124.

[57] C.-H. Huang, T.-S. Chan, W.-R. Liu, D.-Y. Wang, Y.-C. Chiu, Y.-T. Yeh, T.-M. Chen, Crystal structure of blue–white–yellow color-tunable $Ca_4Si_2O_7F_2$:Eu^{2+},Mn^{2+} phosphor and investigation of color tunability through energy transfer for single-phase white-light near-ultraviolet LEDs, J. Mater. Chem. 22 (2012) 20210.

[58] G.S.R. Raju, J.S. Yu, J.Y. Park, H.C. Jung, B.K. Moon, Photoluminescence and Cathodoluminescence Properties of Nanocrystalline $Ca_2Gd_8Si_6O_{26}$:Sm^{3+} Phosphors, J. Am. Ceram. Soc. 95 (2012) 238–242.

[59] Y.R. Do, Y.D. Huh, Optical Properties of Potassium Europium Tungstate Phosphors, J. Electrochem. Soc. 147 (2000) 4385.

[60] K. Jha, M. Jayasimhadri, Spectroscopic investigation on thermally stable Dy^{3+} doped zinc phosphate glass for white light emitting diodes, J. Alloys Compd. 688 (2016) 833–840.

[61] Q. Wang, Z. Ci, Y. Wang, G. Zhu, Y. Wen, Y. Shi, Photoluminescence of Ce^{3+} in haloapatites $Ca_5(PO_4)_3$ X, Mater. Res. Bull. 48 (2013) 1065–1070.

[62] F. Kang, Y. Hu, H. Wu, Z. Mu, G. Ju, C. Fu, N. Li, Luminescence and red long afterglow investigation of Eu^{3+}- Sm^{3+} CO-doped $CaWO_4$ phosphor, J. Lumin. 132 (2012) 887–894.

Accepted manuscript

ACCEPTED MANUSCRIPT

Parameters	Standard data JCPDS (76-1456)	$NaCaPO_4$ Pure
a (Å)	20.3970	20.4032
b (Å)	5.4120	5.4038
c (Å)	9.1610	9.1696
$\alpha = \beta = \gamma$	90°	90°
Cell Volume ($Å^3$)	1011.27	1010.97
GOF (χ^2)	-	1.22

Table:1 The unit cell refined parameters compared with the standard JCPDS data.

Table:2 The final atomic coordinates of atoms resulted from the Rietveld refinement.

Atoms	x	y	z
Ca1	0.00013	0.20797	0.53406
Ca2	0.17243	0.29328	0.52672
Ca3	0.33324	0.20378	0.54442
Na1	0.4383	0.07698	0.03408
Na2	0.27392	0.42493	0.05184
Na3	0.11129	0.08239	0.04813
P1	0.0923	0.41733	0.01581
P2	0.26115	0.09259	0.03577
P3	0.41872	0.40847	0.05168
O1	0.16631	0.4442	0.05453
O2	0.0569	0.51279	0.06812
O3	0.07771	0.30408	0.30352
O4	0.07749	0.3201	0.8106
O5	0.32346	0.06259	0.0444
O6	0.2853	0.43181	0.58532
O7	0.24674	0.18586	0.259
O8	0.2656	0.65597	0.29234

Accepted manuscript

ACCEPTED MANUSCRIPT

O9	0.01219	0.04792	0.05493
O10	0.12757	0.06176	0.55177
O11	0.40177	0.32256	0.284
O12	0.0893	0.84562	0.38352

Table:3 Colorimetric properties of $NaCaPO_4$: *x* Sm^{3+}/ *y* Eu^{3+} (*x* = 1.0 mol % & *y* = 0.5, 1.0, 2.0, 3.0, and 5.0 mol%) for different excitation wavelength.

Sample $NaCaPO_4$:*x* Sm^{3+}/*y* Eu^{3+} (*x* = 1.0 mol%)	CIE (x, y)		
	λ_{ex} = 373 nm	λ_{ex} = 403 nm	λ_{ex} = 463 nm
y = 0.5 mol %	(0.591, 0.406)	(0.589, 0.408)	(0.597, 0.403)
y = 1.0 mol %	(0.580, 0.414)	(0.588, 0.408)	(0.600, 0.398)
y = 2.0 mol %	(0.606, 0.392)	(0.597, 0.400)	(0.609, 0.389)
y = 3.0 mol %	(0.605, 0.392)	(0.595, 0.402)	(0.616, 0.383)
y = 5.0 mol %	(0.608, 0.389)	(0.596, 0.400)	(0.631, 0.368)

Table:4 The average value of decay lifetime (ms) of $NaCaPO_4$:*x* Sm^{3+}/y Eu^{3+} (x = 1.0 mol % & *y* = 0.0, 0.5, 1.0, 2.0, 3.0, and 5.0 mol%) co-doped phosphors.

Sample $NaCaPO_4$: *x* Sm^{3+}/ *y* Eu^{3+} (*x* = 1.0 mol%)	Average Decay time (ms)	Energy Transfer Efficiency (η_T)
y = 0.0 mol %	1.282	---
y = 0.5 mol %	1.168	8.872
y = 1.0 mol %	1.158	9.704
y = 2.0 mol %	1.150	10.328
y = 3.0 mol %	1.106	13.759
y = 5.0 mol %	1.071	16.488

Accepted manuscript

Fig. 1: X-ray diffraction pattern of $NaCaPO_4$ for (a) Standard JCPDS (76-1456), (b) synthesized $NaCaPO_4$ pure (c) $NaCaPO_4$: *x* Sm^{3+} (*x* = 1.0 mol%) (d) $NaCaPO_4$: *y* Eu^{3+} (*y* = 1.0 mol%) doped and (d) $NaCaPO_4$: *x* Sm^{3+}/*y* Eu^{3+} (*x* = y = 1.0 mol%) co-doped sample.

Fig. 2: Rietveld refinement of synthesized $NaCaPO_4$ pure sample.

Fig. 3: SEM images of pure synthesized $NaCaPO_4$ sample (a & b), (c) $NaCaPO_4$: *x* Sm^{3+}/*y* Eu^{3+} (*x* = *y* = 1.0 mol%) co-doped sample (d) EDS images of $NaCaPO_4$ pure sample.

ACCEPTED MANUSCRIPT

Fig. 4: Diffuse reflectance spectra of 1.0 mol% Sm^{3+} doped $NaCaPO_4$ and *x* Sm^{3+}/*y* Eu^{3+} (*x* = *y* = 1.0 mol%) co-doped $NaCaPO_4$ (Inset: Represent the optical band gap of (a) $NaCaPO_4$: *x* Sm^{3+} (*x* = 1.0 mol%), (b) $NaCaPO_4$:*x* Sm^{3+}/*y* Eu^{3+} (*x* = *y* = 1.0 mol%) co-doped sample.

Fig. 5: PLE spectrum of $NaCaPO_4$: *x* Sm^{3+} (*x* = 1.0 mol%) phosphor and emission spectra of $NaCaPO_4$: *x* Sm^{3+} (*x* = 0.5, 1.0, 1.5, 2.0 mol%) phosphors.

Fig. 6: PLE and emission spectra of $NaCaPO_4$: *y* Eu^{3+} (*y* = 1.0 mol%) phosphors

Fig. 7: Excitation spectrum of $NaCaPO_4$:*x* Sm^{3+}/*y* Eu^{3+} (*x* = *y* = 1.0 mol%) co-doped phosphors. (Inset: Represent the excitation spectrum of $NaCaPO_4$: *x* Sm^{3+} (*x* = 1.0 mol%) and $NaCaPO_4$: *y* Eu^{3+} (*y* = 1.0 mol%) phosphors).

Fig. 8: Emission spectra of $NaCaPO_4$: *x* Sm^{3+}/*y* Eu^{3+} (*x* = 1.0 mol% & *y* = 0.5, 1.0, 2.0, 3.0, and 5.0 mol%) phosphors under different excitations (λ_{ex} = 373, 403 and 463 nm)

Fig. 9: Energy level diagram showing energy transfer involved in Sm^{3+} and Eu^{3+}ions co-doped $NaCaPO_4$ phosphors.

Fig. 10: Dependence of I_{SO}/I_S of Sm^{3+} on (a) $(C_{Sm+Eu})^{6/3}$, (b) $(C_{Sm+Eu})^{8/3}$ and (c) $(C_{Sm+Eu})^{10/3}$ in the $NaCaPO_4$: *x* Sm^{3+}/*y* Eu^{3+} (*x* = 1.0 mol% & *y* = 0.5, 1.0, 2.0, 3.0, and 5.0 mol%) phosphors for 403 nm excitation.

Fig. 11: CIE color coordinates of (a) $NaCaPO_4$: *x* Sm^{3+} (*x* = 1.0 mol%) under excitation wavelength of 403 nm and (b) $NaCaPO_4$:*x* Sm^{3+}/*y* Eu^{3+} (*x* = 1.0 mol% & *y* = 5.0 mol%) under excitation wavelength of 463 nm.

Fig. 12: Decay profile of $NaCaPO_4$: *x* Sm^{3+}/*y* Eu^{3+} (*x* = 1.0 mol% & *y* = 0.0, 0.5, 1.0, 2.0, 3.0, and 5.0 mol%) phosphors under excitations and emission of λ_{ex} = 403 nm and λ_{em} = 599 nm.

Accepted manuscript

ACCEPTED MANUSCRIPT

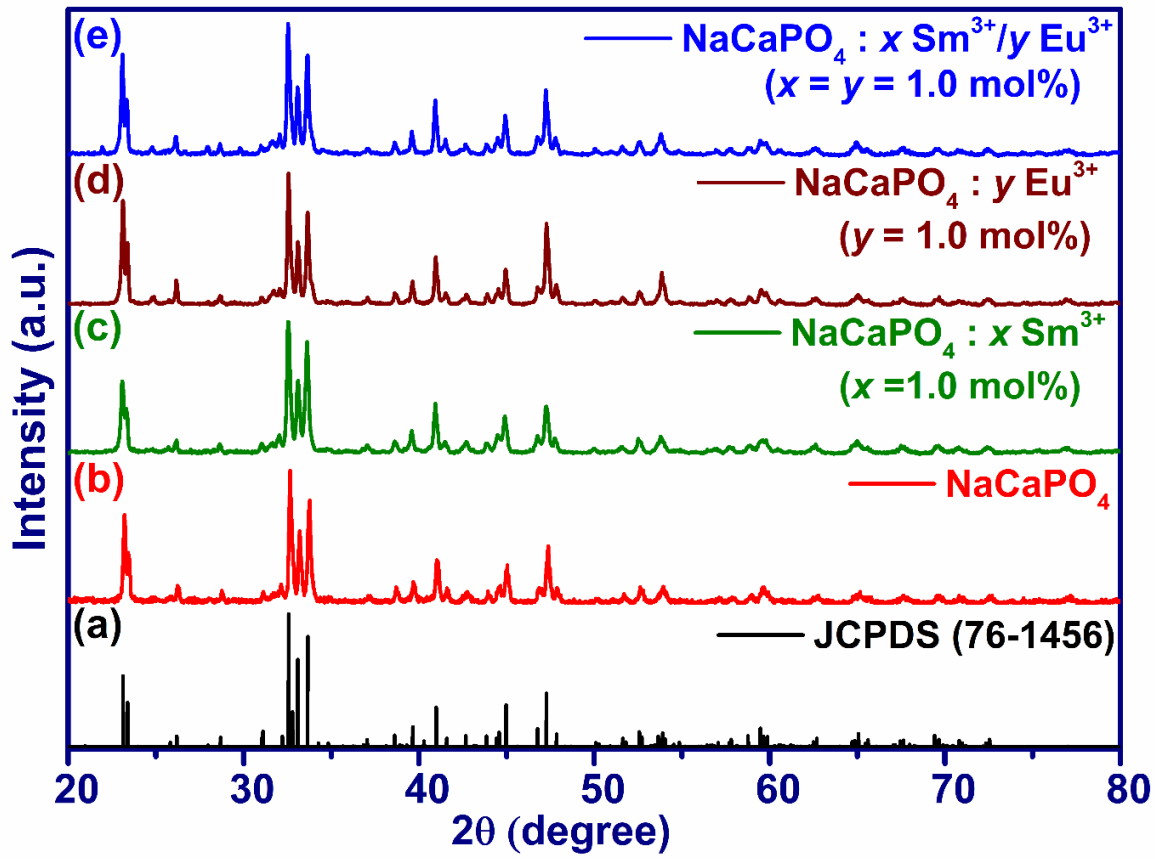


Fig. 1: X-ray diffraction pattern of $NaCaPO_4$ for (a) Standard JCPDS (76-1456), (b) synthesized $NaCaPO_4$ pure (c) $NaCaPO_4$: *x* Sm^{3+} (*x* = 1.0 mol%) (d) $NaCaPO_4$: *y* Eu^{3+} (*y* = 1.0 mol%) doped and (d) $NaCaPO_4$:*x* Sm^{3+}/*y* Eu^{3+} (*x* = *y* = 1.0 mol%) co-doped sample.

Accepted

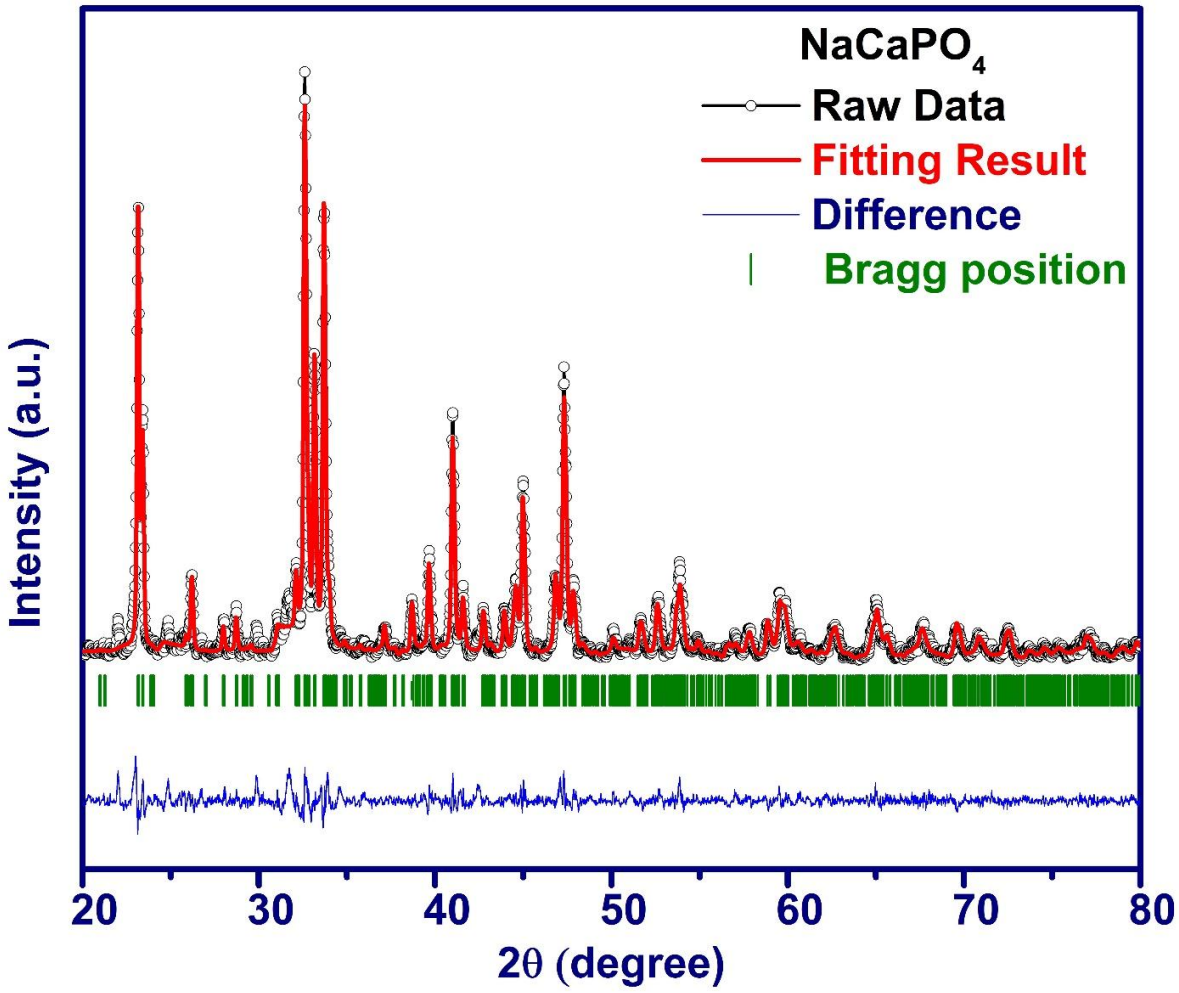


Fig. 2: Rietveld refinement of synthesized $NaCaPO_4$ pure sample.

Accep

ACCEPTED MANUSCRIPT

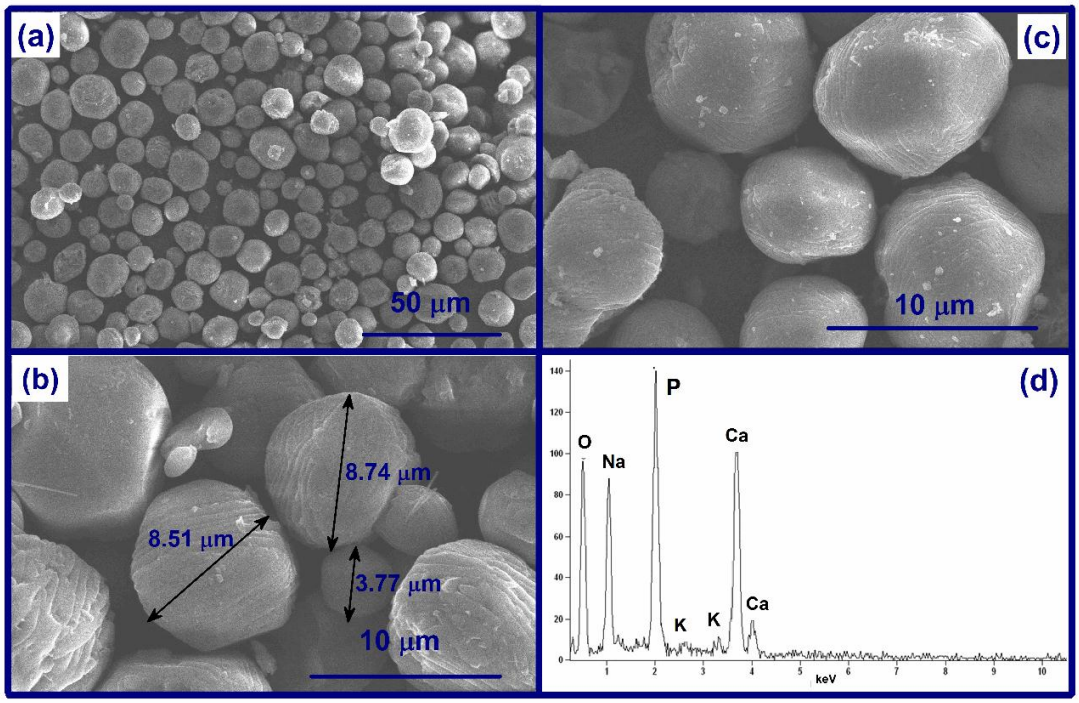


Fig. 3: SEM images of pure synthesized $NaCaPO_4$ sample (a & b), (c) $NaCaPO_4$:*x* Sm^{3+}/*y* Eu^{3+} (*x* = *y* = 1.0 mol%) co-doped sample (d) EDS image of $NaCaPO_4$ pure sample.

Accepted manuscript

ACCEPTED MANUSCRIPT

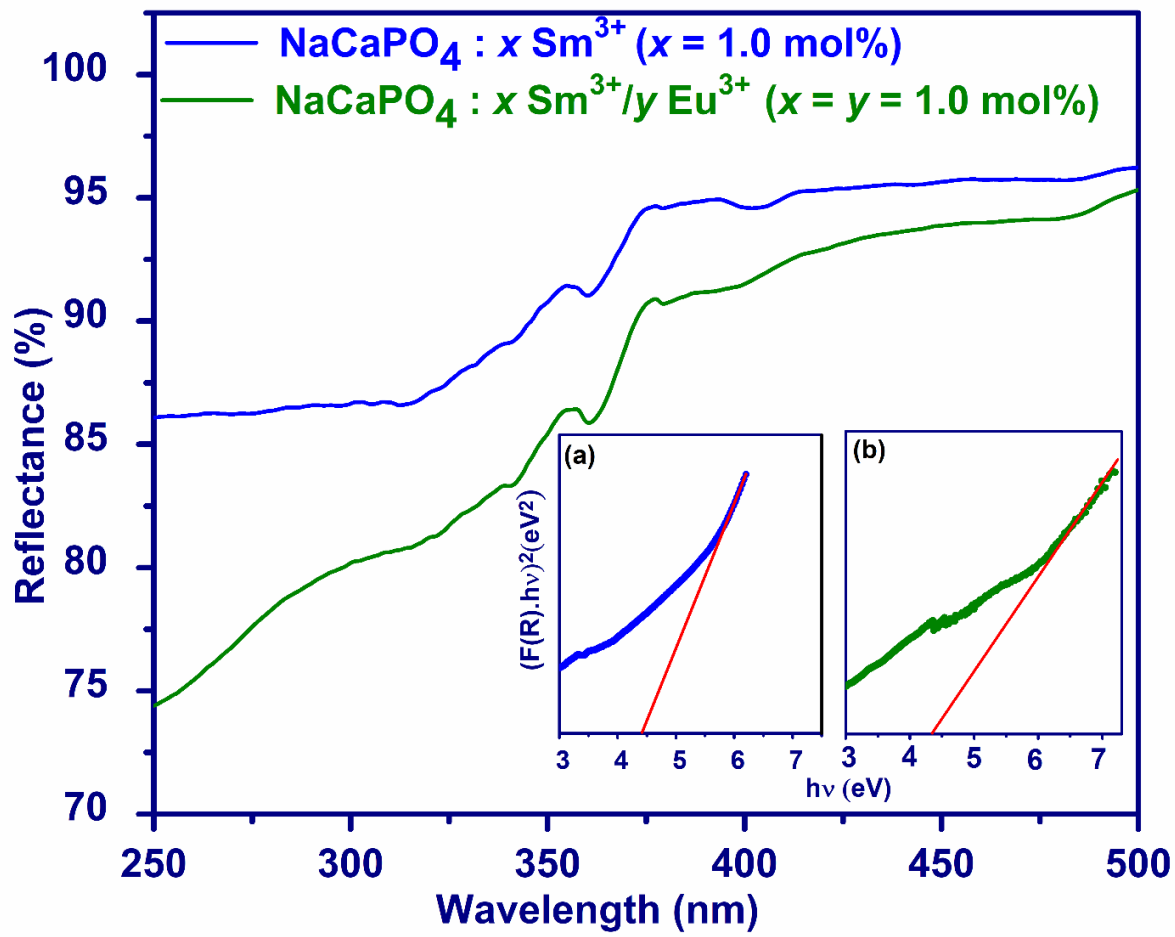


Fig. 4: Diffuse reflectance spectra of 1.0 mol% Sm^{3+} doped $NaCaPO_4$ and *x* Sm^{3+}/*y* Eu^{3+} (*x* = *y* = 1.0 mol%) co-doped $NaCaPO_4$ (Inset: Represent the optical band gap of (a) $NaCaPO_4$: *x* Sm^{3+} (*x* = 1.0 mol%), (b) $NaCaPO_4$: *x* Sm^{3+}/*y* Eu^{3+} (*x* = *y* = 1.0 mol%) co-doped sample.

Accepted

ACCEPTED MANUSCRIPT

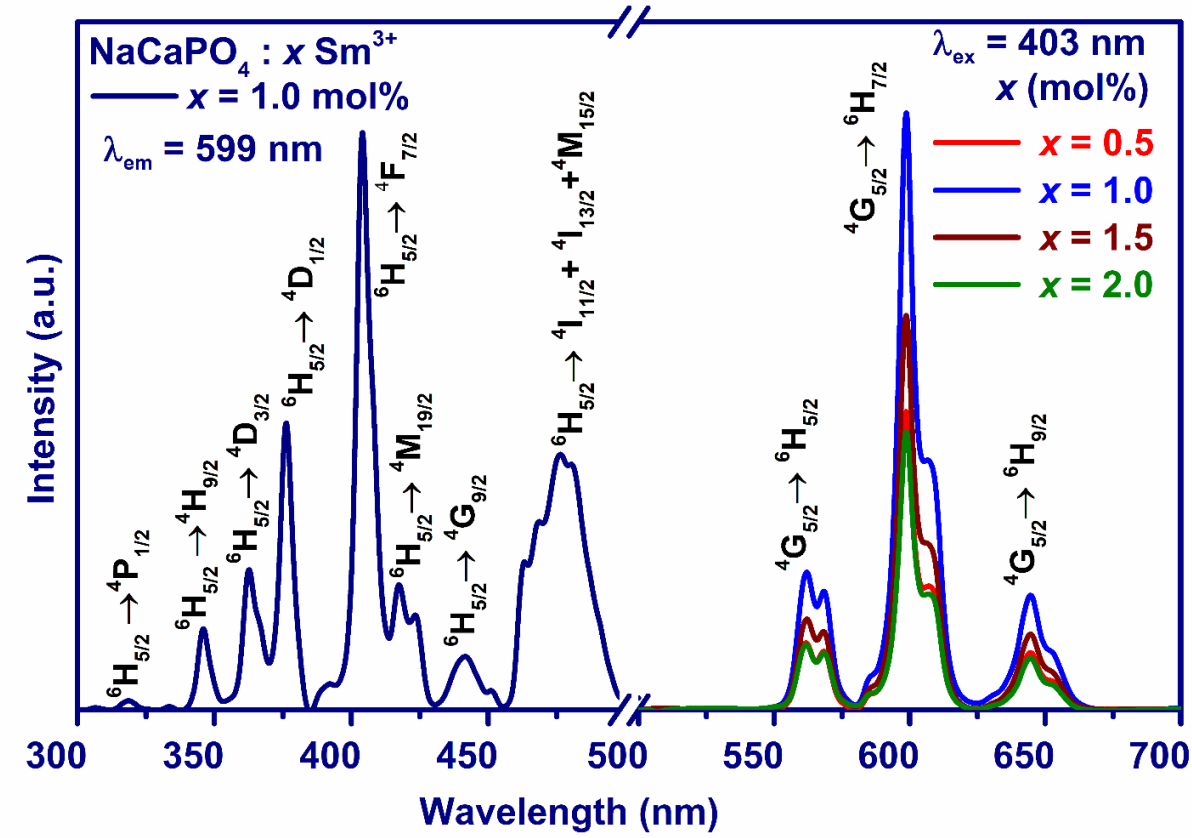


Fig. 5: PLE spectrum of $NaCaPO_4$: *x* Sm^{3+} (*x* = 1.0 mol%) phosphor and emission spectra of $NaCaPO_4$: *x* Sm^{3+} (*x* = 0.5, 1.0, 1.5, 2.0 mol%) phosphors.

Accepted M

ACCEPTED MANUSCRIPT

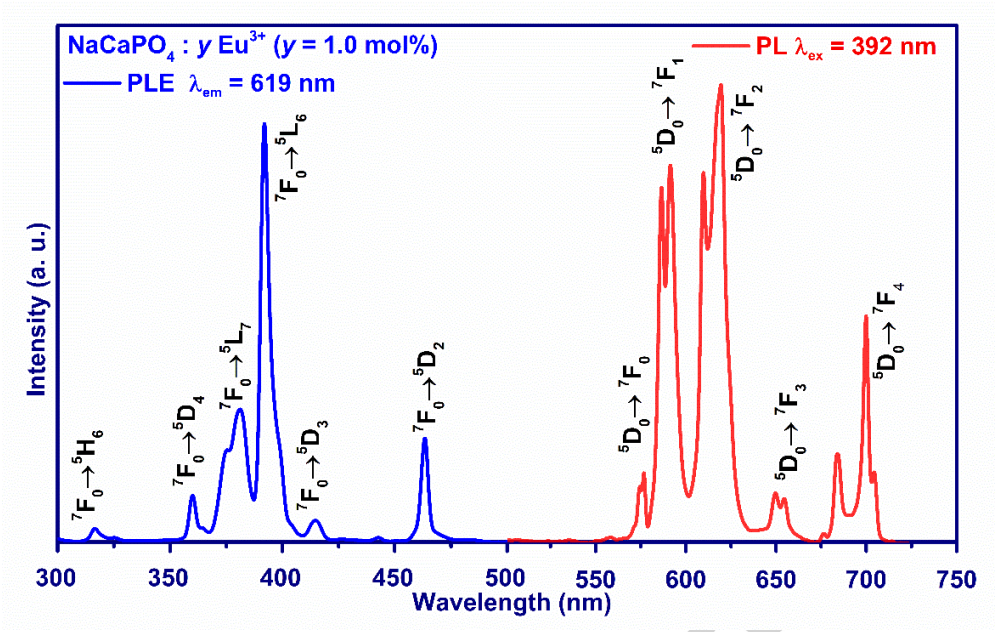


Fig. 6: PLE and emission spectra of $NaCaPO_4$: *y* Eu^{3+} (*y* = 1.0 mol%) phosphors

Accepted manuscript

ACCEPTED MANUSCRIPT

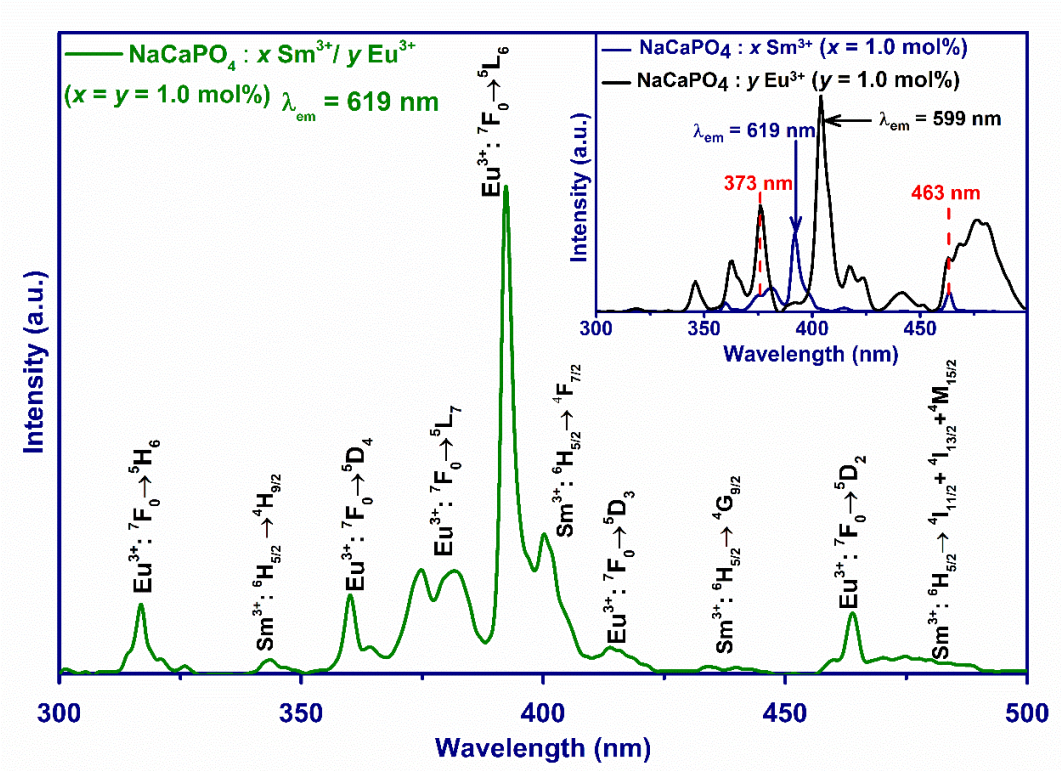


Fig. 7: Excitation spectrum of $NaCaPO_4$: *x* Sm^{3+}/*y* Eu^{3+} (*x* = *y* = 1.0 mol%) co-doped phosphors. (Inset: Represent the excitation spectrum of $NaCaPO_4$: *x* Sm^{3+} (*x* = 1.0 mol%) and $NaCaPO_4$: *y* Eu^{3+} (*y* = 1.0 mol%) phosphors).

Accepted manuscript

ACCEPTED MANUSCRIPT

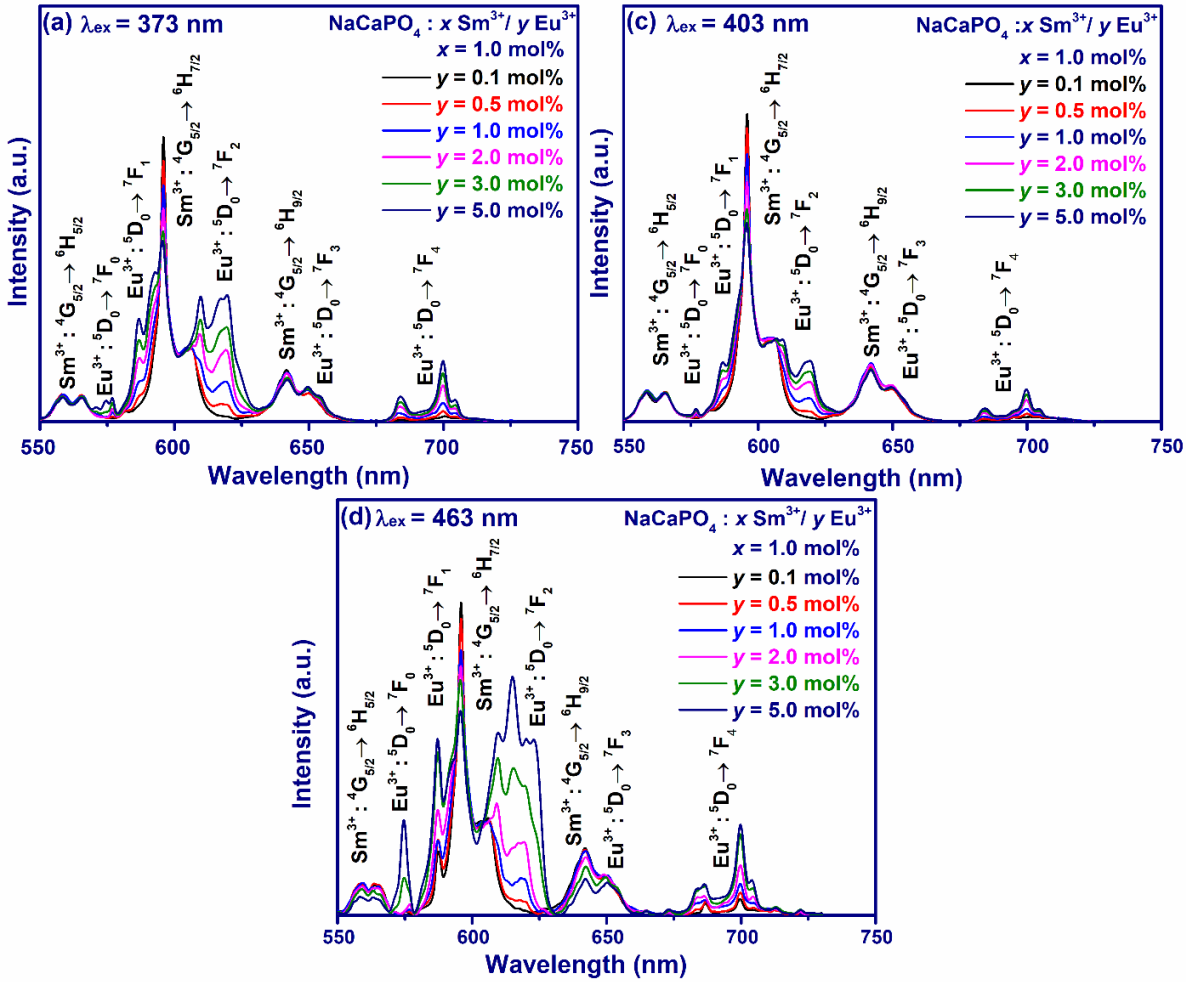


Fig. 8: Emission spectra of $NaCaPO_4$: *x* Sm^{3+}/*y* Eu^{3+} (*x* = 1.0 mol% & *y* = 0.5, 1.0, 2.0, 3.0, and 5.0 mol%) phosphors under different excitations (λ_{ex} = 373, 403 and 463 nm)

Accepted

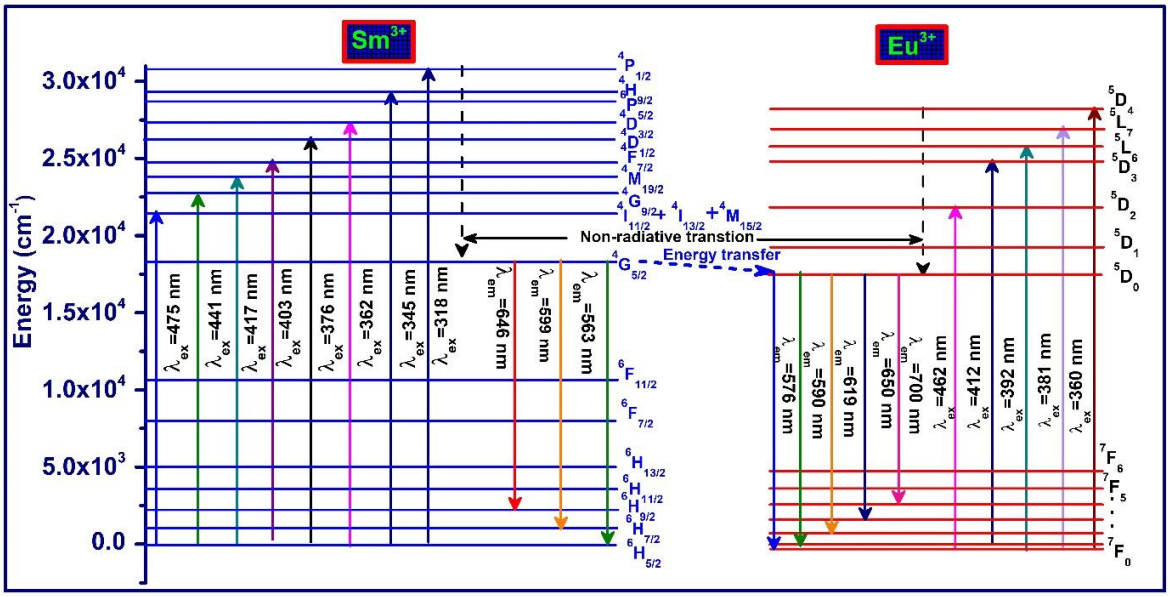


Fig. 9: Energy level diagram showing excitation, emission and energy transfer involved in Sm^{3+} and Eu^{3+}ions co-doped $NaCaPO_4$ phosphors.

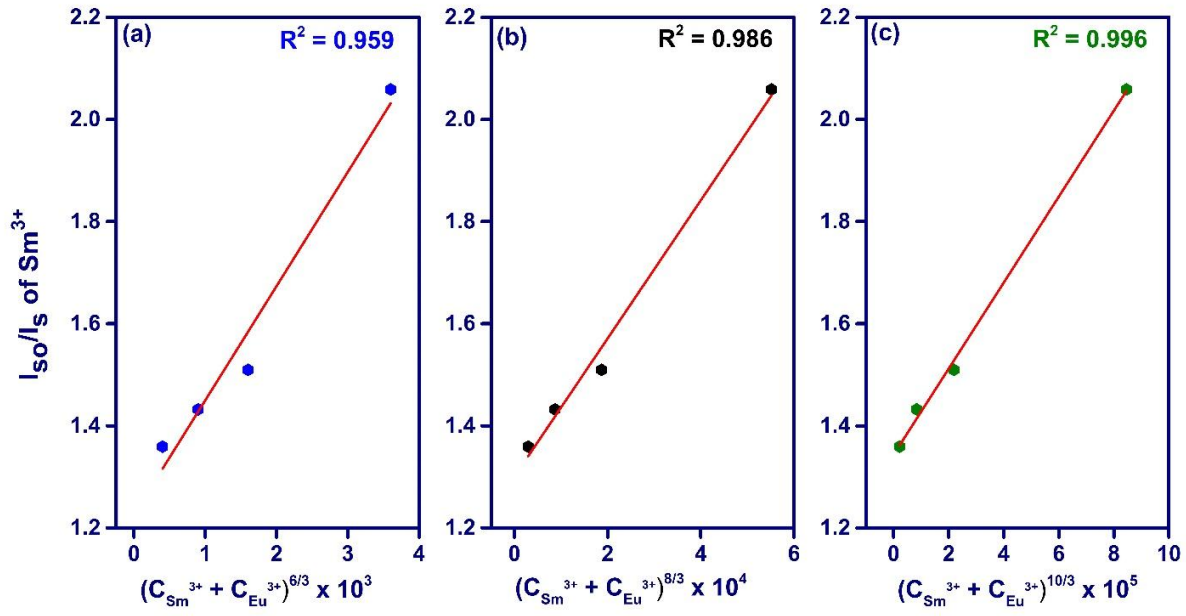


Fig. 10: Dependence of I_{SO}/I_S of Sm^{3+} on (a) $(C_{Sm+Eu})^{6/3}$, (b) $(C_{Sm+Eu})^{8/3}$ and (c) $(C_{Sm+Eu})^{10/3}$ in the $NaCaPO_4$: x Sm^{3+}/y Eu^{3+} (x = 1.0 mol% & y = 0.5, 1.0, 2.0, 3.0, and 5.0 mol%) phosphors for 403 nm excitation.

ACCEPTED MANUSCRIPT

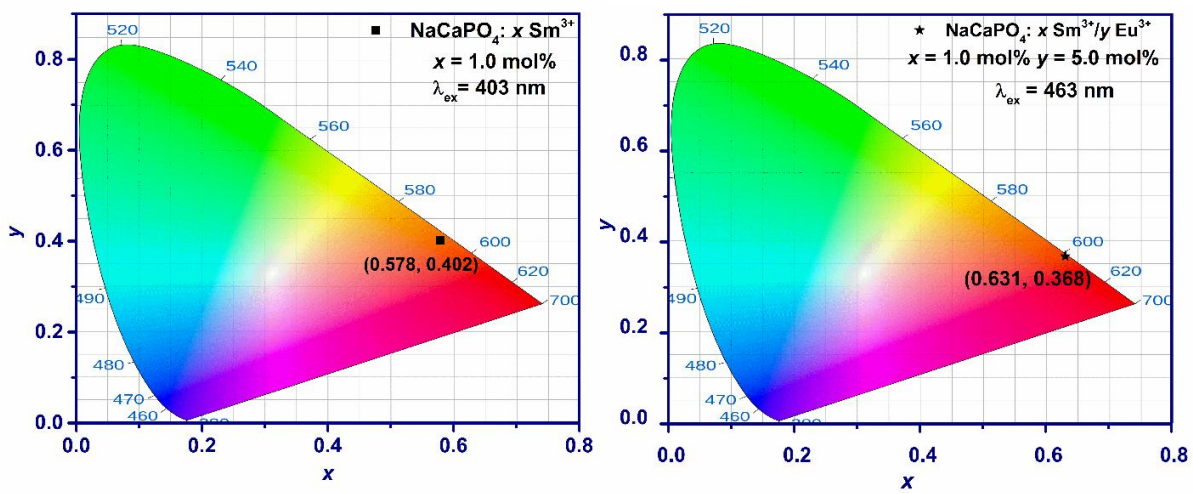


Fig. 11: CIE color coordinates of (a) $NaCaPO_4$: *x* Sm^{3+} (*x* = 1.0 mol%) under excitation wavelength of 403 nm and (b) $NaCaPO_4$: *x* Sm^{3+}/*y* Eu^{3+} (*x* = 1.0 mol% & *y* = 5.0 mol%) under excitation wavelength of 463 nm.

Accepted manuscript

ACCEPTED MANUSCRIPT

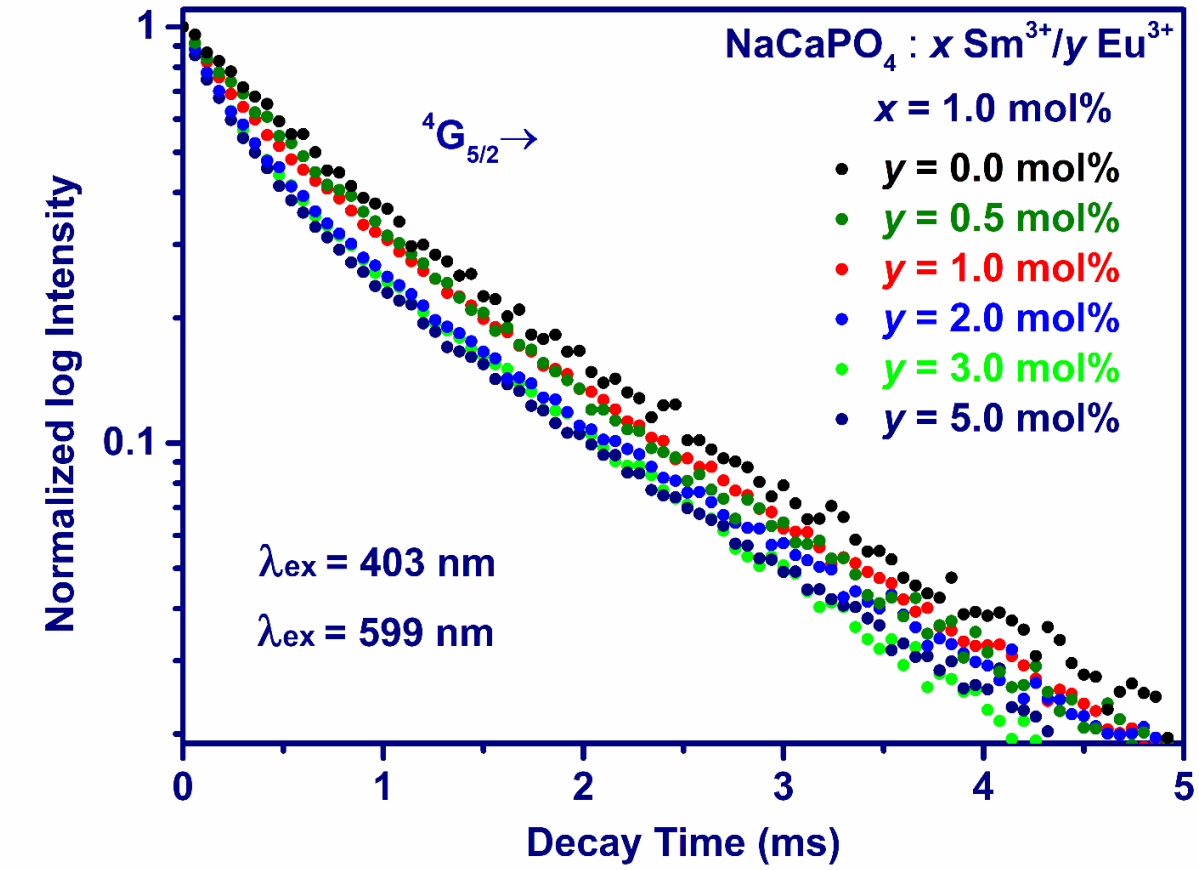


Fig.12: Decay profile of $NaCaPO_4$: *x* Sm^{3+}/*y* Eu^{3+} (*x* = 1.0 mol% & *y* = 0.0, 0.5, 1.0, 2.0, 3.0, and 5.0 mol%) phosphors under excitations and emission of λ_{ex} = 403 nm and λ_{em} = 599 nm.

Accepted

Received: 27 March 2018 | Revised: 14 May 2018 | Accepted: 14 May 2018

DOI: 10.1002/ctpp.201800033

ORIGINAL ARTICLE

Contributions to Plasma Physics

Terahertz radiation emission using plasma-filled dielectric liner with the effects of pre-modulated relativistic electron beam

Jyotsna Panwar | **Suresh C. Sharma**

Department of Applied Physics, Delhi Technological University, Delhi, India

***Correspondence**
Suresh C. Sharma, Department of Applied Physics, Delhi Technological University, Shahbad Daulatpur, Bawana Road, Delhi 110042, India.
Email: suresh321sharma@gmail.com

We propose a theoretical model for the efficient emission of high-power terahertz (THz) radiation. The pre-modulation of the beam is accounted for by the interaction of the two laser beams with the relativistic electron beam (REB). The pre-modulated REB travels through a dielectric liner waveguide, which is filled with a plasma. The REB travels near the dielectric lining boundary and therefore transfers maximum energy to the electromagnetic radiation wave via Cerenkov interaction. The growth rate and efficiency of the radiation wave are examined and found to be altered by the parameters of the REB and the dielectric medium. The growth rate varies as one-third power of the beam density and as two-thirds power of the amplitude of the pump wave field. The proposed scheme seems to be an effective method for the generation of tunable THz radiation.

KEYWORDS

premodulated REB, terahertz radiation

1 | INTRODUCTION

During the past few decades, the emission of terahertz (THz) radiation has attracted the attention of researchers to explore new models to study its potential for various applications in the field of spectroscopy, biomedical imaging, security analysis, telecommunications[1–4] etc. Various schemes that involve the use of relativistic electron beam (REB)[5–7] and laser beams[8,9] have been employed to study the generation of THz radiation.

The emission of THz radiation by beating two Gaussian pulsed laser beams in a rippled plasma with neutral–electron collision has been proposed by Bakhtiari et al.[10] They observed that by optimizing the parameters of the laser beams, the collisional plasma, and the array structure, the efficiency of the radiation is enhanced to a considerable amount.

Namiot et al.[11] studied the generation and amplification of high-frequency THz electromagnetic waves by employing a thin dielectric plate that does not behave as a slow wave structure, but still the interaction was effective.

The use of REBs employed in free-electron lasers results in a radiation with augmented growth and efficiency. The use of relativistic electrons in the emission of THz radiation via non-linear coupling with the plasma beat wave was proposed by Gupta et al.[12] They found that the efficiency of the system improves with increase in the velocity of the beam.

Auger decay helps in the electronic structural analysis of solids, molecules, and atoms. Schütte et al.[13] studied the emission of Auger electrons due to the ionization of Xe and Kr in the strong oscillating field of THz radiation.

Malik et al.[14] proposed that the power and frequency of THz radiation excited resonantly by the mixing of two Gaussian laser pulses in a periodic density rippled plasma in the presence of external magnetic field can be tuned by the magnetic field, periodicity and amplitude of the density ripples.

The emission of THz radiation by the photoelectron current induced by the ionization of a gas due to non-linear mixing of the fundamental and second harmonic of ultra-short laser pulses was studied analytically by Kim et al.[15]

 © 2018 WILEY-VCH Verlag GmbH & Co. KGaA, Weinheim

Recently, the excitation of electromagnetic waves by the interaction of a self-modulated electron beam and an over-dense plasma was studied by Yang et al.[16] by using particle-in-a-cell (PIC) simulation. Because of the resonance between the plasma wakefield and the electron beam, plasma oscillations are amplified to generate THz radiation.

Wang et al.[17] observed that the polarization, frequency, and amplitude of the electromagnetic wave can be altered by the bias applied to the plasma slab and the density of the plasma.

For the generation of THz radiation via Cerenkov interaction, either a slow wave structure or a wiggler is employed. Cerenkov free-electron laser acts as a slow wave structure by employing a dielectric lining in a waveguide and has been proposed for the generation of millimetre and sub-millimetre wavelenghts.[18–20] The use of a pre-bunched electron beam in free-electron lasers leads to coherent emission with reduction in the accumulation time of the radiation.[21,22]

Sharma and Bhasin[23] studied the effect of beam pre-bunching on the Cerenkov free-electron laser and found that significant improvement in gain and efficiency can be achieved if the frequency of the modulated electron beam becomes comparable to that of radiation wave.

Tripathi and Liu[24] observed that for the generation of a particular frequency wave, the dielectric lining on the waveguide should withstand high power densities and also reduces the constraint for the beam voltage.

Kibis et al.[25] studied the emission of THz radiation by applying a potential difference across the ends of a quasi-metallic carbon nanotube. The emission was found to be strongly influenced by the voltage applied in the ballistic regime.

A magnetized plasma medium that acts as non-linear medium permits the propagation of electron beams with high current as it supresses the space charge effects. It also offers the possibility of using moderate-energy electron beams for obtaining high-frequency radiation.[26,27]

Antonsen et al.[28] addressed the propagation of laser pulses in miniature non-uniform plasma channels due to the channel inhomogeneity and manifestation of guided waves, and achieved efficient excitation of the radiation.

Chauhan and Parashar[29] analysed the emission of THz radiation for both homogenous and inhomogeneous plasma densities via the non-linear mixing of lasers that are incident obliquely on the plasma slab.

The generation of THz radiation by the direct conversion of an ultra-short laser pulse due to the excitation of a oscillations of plasma has been suggested by Gildenburg.[30]

Malik[31] observed that an external magnetic field helps in obtaining collimated radiation with improved efficiency and tunability.

The experimental investigations of Chen et al.[32] suggested that the use of multiple air plasmas leads to the efficient generation of THz radiation due to the superposition of the individual fields.

Singh and Malik[33] analysed the contribution of a collisional plasma under the influence of a magnetic field on the efficiency and amplitude of the THz radiation.

To our knowledge, no study has been carried out on THz radiation emission by employing a dielectric liner and pre-modulated REB. In this work, we have designed an analytical formalism to examine the generation of high-frequency THz radiation waves by the interaction of a density-modulated REB with a dielectric-lined waveguide in the presence of an external magnetic field. The mechanism of the scheme is as follows; First, the REB gets velocity-modulated in the modulator region and then, on further travelling through the drift space, the velocity modulation is translated into density modulation. The density-modulated REB travels through the waveguide space in close proximity with the dielectric lining. The Poynting flux is concentrated largely in the dielectric space, and the velocity of the electromagnetic mode is reduced so that it becomes comparable to the beam velocity. At the expense of beam energy, the radiation wave grows. The pre-modulation of REB and its interaction with dielectric-lined waveguide is shown in Section 2. The results are included in Section 3. Section 4 concludes the paper.

2 | PHYSICAL MODEL

In the present model, we examine the emission of a THz radiation wave by taking into account the interaction of a density-modulated REB with a dielectric-lined waveguide. First, for the pre-modulation of the REB, we consider two laser beams with frequencies ω_{l1} and ω_{l2}, respectively, and with electric fields

$\overrightarrow{E_{l\eta}} = \overrightarrow{A_{l\eta}} e^{-i(\omega_{l_\eta} t - k_{l_\eta} z)}$, where $\eta = 1, 2$ for lasers 1 and 2, respectively.

The REB is propagating in the z-direction with initial beam velocity v_{ib} and beam density n_{ib}.

The laser beams interact with the REB in the modulator region, where the beam acquires a transverse velocity component $\overrightarrow{v_{l\eta}} = \frac{e\overrightarrow{E_{l\eta}}}{m_e \gamma_0 i\omega_{l_\eta}}$, where $\gamma_0 = \left(1 - \frac{v_{\mathrm{ib}}^2}{c^2}\right)^{-1/2}$ is the relativistic gamma factor and m_e is the electronic mass. The beam then gets velocity-modulated at the frequency difference of two lasers (i.e.,$\omega_{\mathrm{eb}} = \omega_{l1} - \omega_{l2}$) due to the pondermotive force ($\overrightarrow{F_{\mathrm{bp}}}$) exerted

on the electron beam by the laser beams:

$$\overrightarrow{F_{\rm bp}} = \frac{-e}{2c}[\overrightarrow{v_{l\eta}} \times \overrightarrow{B^{*}_{l\eta}} + \overrightarrow{v^{*}_{l\eta}} \times \overrightarrow{B_{l\eta}}] = F_{0b} e^{-i(\omega_{\rm eb} t - k_{\rm eb} z)} \tag{1}$$

where $\overrightarrow{B_{l\eta}} = \frac{c(\overrightarrow{k_{l\eta}} \times \overrightarrow{E_{l\eta}})}{\omega_{l\eta}}$ is the magnetic field due to the laser beams, and $F_{0\rm b} = \frac{eA_{l1}A_{l2}k_{\rm eb}}{2m_{\rm e}\gamma_0\omega_{l1}\omega_{l2}}$, and $(\omega_{\rm eb}, k_{\rm eb})$ is frequency and wave number, respectively, of the REB.

The electron beam responds to the pondermotive force through the relativistic equation of motion $\frac{d(\gamma \overrightarrow{v})}{dt} = \frac{\overrightarrow{F_{\rm b}}}{m_{\rm e}}$, which can be linearized to yield the modulated beam velocity $(v_{\rm b}^{\rm m})$ using $\overrightarrow{v} = v_{\rm ib}\hat{z} + v_{\rm b}^{\rm m}\hat{z}$ and $\gamma = \gamma_0 + \frac{v_{\rm ib}\gamma_0^3 v_{\rm b}^{\rm m}}{c^2}$ as

$$v_{\rm b}^{\rm m} = -\xi_{\rm m} v_{\rm ib} \sin(\omega_{\rm eb} t_{\rm M} + \theta_{\rm m}), \tag{2}$$

where $\xi_{\rm m} = \frac{k_{\rm eb} l_{\rm d}}{2\gamma_0^4} \frac{c^2}{v_{\rm ib}^2} \frac{e^2 A_{l1} A_{l2}^{*}}{m_{\rm e}\omega_{l1}\omega_{l2}c^2} \frac{\sin\theta_{\rm m}}{\theta_{\rm m}}$ with $\theta_{\rm m} = \frac{(\omega_{\rm em} - k_{\rm em} v_{\rm ib}) l_{\rm M}}{2v_{\rm ib}}$ being the phase angle of the modulator, $t_{\rm M}$ is the time when the beam enters the modulator region, and $l_{\rm M}$ is the length of the modulator space.

The velocity-modulated beam then travels through the drift space, where, due to acceleration and deceleration, the velocity modulation translates into density modulation. Further, following the analysis by Kumar and Tripathi,[34] the expression of the modulated beam density $(n_{\rm b}^{\rm m})$ can be written as

$$n_{\rm b}^{\rm m} = -2n_{\rm ib} J_1 \left(\frac{\omega_{\rm eb} l_{\rm D} \xi_{\rm m}}{v_{\rm ib}} \right) \cos(\omega_{\rm eb} t_{\rm D} - \phi_{\rm m}), \tag{3}$$

where t_D is the time at which the beam leaves the drift space and enters the waveguide, $\phi_{\rm m} = \frac{\omega_{\rm eb}(l_{\rm M} + l_{\rm D})}{v_{\rm ib}} - \theta_{\rm m}$, with $l_{\rm D}$ being the length of the drift space, and J_1 is the first-order Bessel's function.

Next, we consider the interaction of the density-modulated REB with the transverse magnetic (TM) mode. A cylindrical waveguide with dielectric lining is considered. The radius of the waveguide is $r_{\rm w}$ with plasma filled in region I $(0 < r < r_{\rm d})$ and the dielectric lining in region II $(r_{\rm d} < r < r_{\rm w})$. The azimuthally symmetric TM mode is supported by the waveguide with $\overrightarrow{E_{\rm t}^{\rm m}} = \overrightarrow{A_{\rm t}^{\rm m}} e^{-i(\omega_{\rm t} t - k_{\rm t} z)}$, where $(\omega_{\rm t}, k_{\rm t})$ is the frequency and wave number of the TM waveguide mode, respectively. The permittivity of the plasma medium is $\varepsilon_{\rm p} = [1 - \frac{\omega_{\rm p}^2}{\omega_{\rm t}^2}$, where $\omega_{\rm p}\left(= \frac{4\pi n_{\rm ep} e^2}{m_{\rm e}}\right)^{1/2}$ is the electron plasma frequency and $n_{\rm ep}$ is the plasma electron density], and that of the dielectric medium is $\varepsilon_{\rm d}$.

The current density of the pre-modulated electron beam leads to the excitation of the TM mode in the plasma-filled waveguide. The density profile of the electron beam is considered as $n_{\rm ib} = N\delta(r - r_{\rm b})$, where $N = \frac{n_0}{2\pi r_{\rm b}}$ and $r_{\rm b}$ is the radius of the electron beam. The pre-modulated beam travels in close proximity with the dielectric lining. A magnetostatic wiggler magnetic field, $\overrightarrow{B_{\rm h}} = B_{0\rm h} e^{-ik_{\rm h} z}\hat{x}$ is introduced into the waveguide, which acts as a pump field, and a strong guide magnetic field $B_{\rm s}$ is externally applied such that it guides the beam in the axial direction in the waveguide. The oscillatory velocity acquired by the electron beam due to the pump wave in the frame of electrons moving with velocity $v_{\rm ib}$ is obtained as $\overrightarrow{v'_{\rm ob}} = \frac{e\overrightarrow{E'_{\rm h}}}{im_{\rm e}(\omega'_{\rm h} - \omega'_{\rm ce})}$, where the prime denotes the quantities in the moving electron frame, $E'_{\rm h} = \frac{\gamma_0}{c}(\overrightarrow{v_{\rm ib}} \times \overrightarrow{B_{\rm h}})$, $\omega'_{\rm h} = \gamma_0 k_{\rm h} v_{\rm ib,}$ and $\omega'_{\rm ce}\left(= \frac{eB'_{\rm s}}{m_{\rm e}c}\right)$ is the electron cyclotron frequency.

The equilibrium is perturbed by an electromagnetic perturbation due to the TM mode, and the response of the mode to the electron beam in terms of the perturbed beam velocity $(\overrightarrow{v'_{\rm 1b}})$ is

$$\overrightarrow{v'_{\rm 1b}} = \frac{e\overrightarrow{E_{\rm t}^{\rm m'}}}{m_{\rm e} i(\omega'_{\rm t} - \omega'_{\rm ce})}.$$

The pump wave and the electromagnetic perturbation exerts a pondermotive force $(F_{\rm 1p})$ on the beam of electrons, given as

$$F'_{\rm 1p} = eik'_{\rm eb}\phi'_{\rm 1p}\hat{z},$$

where

$$\phi'_{\rm 1p} = -\frac{m_{\rm e}}{2e} v'^{*}_{\rm ib} \cdot v'_{\rm 1b} = \frac{eE'^{*}_{\rm hr} E^{\rm m*}_{\rm tr}}{2m_{\rm e}(\omega'_{\rm h} - \omega'_{\rm ce})(\omega'_{\rm t} - \omega'_{\rm ce})}, \tag{4}$$

$\phi'_{\rm 1p}$ is the pondermotive potential. The phase matching condition demands $\omega'_{\rm t} = \omega'_{\rm eb} + \omega'_{\rm h}$ and $k'_{\rm t} = k'_{\rm eb} + k'_{\rm h}$.

The response of beam of electrons to the pondermotive potential in terms of the perturbed beam velocity $(v'_{\rm bp})$ and density $(n'_{\rm bp})$ can be obtained as

$$v'_{\rm bp} = -\frac{e\nabla'\phi'_{\rm 1p}}{m_{\rm e} i\omega'_{\rm eb}}$$

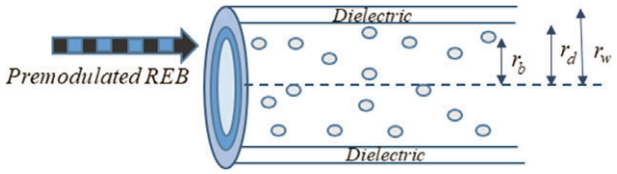


FIGURE 1 Schematic of the interaction of density-modulated relativistic electron beam (REB) with a plasma filled dielectric-lined waveguide

$$n'_{\mathrm{bp}} = \frac{\nabla' \cdot ((n'_{\mathrm{ib}} + n_{\mathrm{b}}^{\mathrm{m}'})v'_{bp})}{i\omega'_{\mathrm{eb}}} = \frac{en'_{\mathrm{ib}}\nabla'^2\phi'_{1\mathrm{p}}}{m_{\mathrm{e}}\omega'^2_{\mathrm{eb}}}, \tag{5}$$

where $n'_{\mathrm{ib}} = \frac{n_{\mathrm{ib}}}{\gamma_0}$, $\phi'_{1\mathrm{p}} = \frac{\phi_{1\mathrm{p}}k_{\mathrm{eb}}}{k'_{\mathrm{eb}}}$, $k'_{\mathrm{eb}} = \gamma_0\left(k_{\mathrm{eb}} - \frac{\omega_{\mathrm{eb}}v_{\mathrm{ib}}}{c^2}\right)$, and $\omega'_{\mathrm{eb}} = \gamma_0(\omega_{\mathrm{eb}} - \kappa_{\mathrm{eb}}v_{\mathrm{ib}})$ are the Lorentz-transformed quantities from the electron frame to the lab frame. The density of particles at $(\omega'_{\mathrm{t}}, k'_{\mathrm{t}})$ can be written as $n^{1\prime}_{\mathrm{bp}} = \frac{\nabla'.(n'_{\mathrm{bp}}\overrightarrow{v'_{\mathrm{ob}}})}{2i(\omega'_{\mathrm{t}} - \omega'_{\mathrm{ce}})}$.

On using the Lorentz-transformed quantities, the expression for nonlinear current density ($J_{1\mathrm{b}}$) in the axial direction can be simplified as

$$J_{1\mathrm{bz}} = -n^1_{\mathrm{bp}}ev_{\mathrm{ib}} = \frac{e^3(n_{\mathrm{ib}} + n_{\mathrm{b}}^{\mathrm{m}})v_{\mathrm{ib}}^2B_{\mathrm{h}}\nabla \cdot (\nabla^2\phi'_{1\mathrm{p}})}{2m_{\mathrm{e}}^2\gamma_0^2(k_{\mathrm{h}}v_{\mathrm{ib}} - \omega_{\mathrm{ce}})(\omega_{\mathrm{t}} - \omega_{\mathrm{ce}})(\omega_{\mathrm{eb}} - k_{\mathrm{eb}}v_{\mathrm{ib}})^2}. \tag{6}$$

To analyse the TM mode, the wave equation is employed as

$$\frac{\partial^2\overrightarrow{E_{\mathrm{tz}}}}{\partial r^2} + \frac{1}{r}\frac{\partial\overrightarrow{E_{\mathrm{tz}}}}{\partial r} - \left(\frac{\omega_{\mathrm{t}}^2}{c^2}\varepsilon - k_{\mathrm{t}}^2\right)\overrightarrow{E_{\mathrm{tz}}} = \frac{-4\pi i\omega_{\mathrm{t}}}{c^2}\overrightarrow{J_{1\mathrm{bz}}}. \tag{7}$$

The RHS of the above wave equation can be simplified to

$$\frac{e^4\pi\omega_{\mathrm{t}}(n_{\mathrm{ib}} + n_{\mathrm{b}}^{\mathrm{m}})k_tv_{ib}^2B_h^2\left(1 - \frac{v_{\mathrm{ib}}}{\sqrt{\varepsilon}c}\right)\frac{\partial}{\partial r}\left(\frac{\partial^2E_{\mathrm{tr}}}{\partial r^2} + \frac{1}{r}\frac{\partial E_{\mathrm{tr}}}{\partial r} - k_{\mathrm{t}}^2E_{\mathrm{tr}}\right)}{m_{\mathrm{e}}^3\gamma_0^3c\alpha^2(k_{\mathrm{h}}v_{\mathrm{ib}} - \omega_{\mathrm{ce}})^2(\omega_{\mathrm{t}} - \omega_{\mathrm{ce}})^2(\omega_{\mathrm{eb}} - k_{\mathrm{eb}}v_{\mathrm{ib}})^2}. \tag{8}$$

Here $E_{\mathrm{tr}} = -i\left(\frac{k_{\mathrm{t}}}{\alpha^2}\right)\frac{\partial E_{\mathrm{tz}}}{\partial r}$.

The above expression drops to zero for region I, and the solution is same as mentioned in Equation 8 i.e., $E_{\mathrm{tz}} = \varphi(r)$, where $\varphi(r) = A_{t1}I_0(\alpha r)$ for region I $(0 < r < r_{\mathrm{d}})$, and $\varphi(r) = A_{t2}\left[J_0(\beta r) - \frac{J_0(\beta r_{\mathrm{w}})Y_0(\beta r)}{Y_0(\beta r_{\mathrm{w}})}\right]$ for region II $(r_{\mathrm{d}} < r < r_{\mathrm{w}})$.

On considering the RHS expression (cf. Equation 8), it is assumed that the eigenvalues are altered, whereas the eigen vector remains unchanged. For region II, the RHS (cf. Figure 1) tends to zero as there is no beam propagation. Equation 7 is multiplied by $\varphi(r)rdr$, and on integrating it from $r = 0$ to r_{w}, we get

$$P\int_0^{r_d} I_0^2(\alpha r)rdr + Q\frac{A_{t2}^2}{A_{t1}^2}\int_{r_{\mathrm{d}}}^{r_{\mathrm{w}}}\left[J_0(\beta r) - \frac{J_0(\beta r_w)Y_0(\beta r)}{Y_0(\beta r_w)}\right]^2 rdr = \frac{R}{(\omega_{\mathrm{eb}} - k_{\mathrm{eb}}v_{\mathrm{ib}})^2}, \tag{9}$$

where $P = \left(\alpha^2 + \frac{\omega_{\mathrm{t}}^2}{c^2}\varepsilon_{\mathrm{p}} - k_{\mathrm{t}}^2\right)$, $Q = \left(\beta^2 - \frac{\omega_{\mathrm{t}}^2}{c^2}\varepsilon_{\mathrm{d}} + k_{\mathrm{t}}^2\right)$ and

$$R = \frac{e^4\pi\omega_{\mathrm{t}}(n_{\mathrm{ib}} + n_{\mathrm{b}}^{\mathrm{m}})v_{\mathrm{ib}}^2B_{\mathrm{h}}^2\left(1 - \frac{v_{\mathrm{ib}}}{\sqrt{\varepsilon}c}\right)\int_0^{r_d}\frac{\partial}{\partial r}\left(\frac{\partial^3}{\partial r^3} + \frac{1}{r}\frac{\partial^2}{\partial r^2} - k_{\mathrm{t}}^2\frac{\partial}{\partial r}\right)I_0^2(\alpha r)rdr}{m_{\mathrm{e}}^3\gamma_0^3c^3(k_{\mathrm{h}}v_{\mathrm{ib}} - \omega_{\mathrm{ce}})^2(\omega_{\mathrm{t}} - \omega_{\mathrm{ce}})^2}.$$

On taking k_{t} to be a constant and varying the TM mode frequency around$\omega_{\mathrm{t}} = \omega_{\mathrm{tm}}$, we obtain

$$(\omega_{\mathrm{t}} - \omega_{\mathrm{tm}})\left(\frac{\partial\alpha^2}{\partial\omega_{\mathrm{t}}} + \frac{2\omega_{\mathrm{t}}}{c^2}\varepsilon_{\mathrm{p}}\right)\int_0^{r_d} I_0^2(\alpha r)rdr + \left(\frac{\partial\beta^2}{\partial\omega_{\mathrm{t}}} - \frac{2\omega_{\mathrm{t}}}{c^2}\varepsilon_{\mathrm{d}}\right)\frac{A_{t2}^2}{A_{\mathrm{t1}}^2}\int_{r_{\mathrm{d}}}^{r_{\mathrm{w}}}\left[J_0(\beta r) - \frac{J_0(\beta r_{\mathrm{w}})Y_0(\beta r)}{Y_0(\beta r_{\mathrm{w}})}\right]^2 rdr = \frac{R}{(\omega_{\mathrm{eb}} - k_{\mathrm{eb}}v_{\mathrm{ib}})^2}. \tag{10}$$

The Equation 10 can be further simplified into

$$(\omega_{\mathrm{t}} - \omega_{\mathrm{tm}})(\omega_{\mathrm{t}} - (k_{\mathrm{t}} - k_{\mathrm{h}})v_{\mathrm{ib}})^2 = \frac{R}{T\left(\frac{\partial\beta^2}{\partial\omega_{\mathrm{t}}} - \frac{2\omega_{\mathrm{t}}}{c^2}\varepsilon_{\mathrm{d}}\right)}, \tag{11}$$

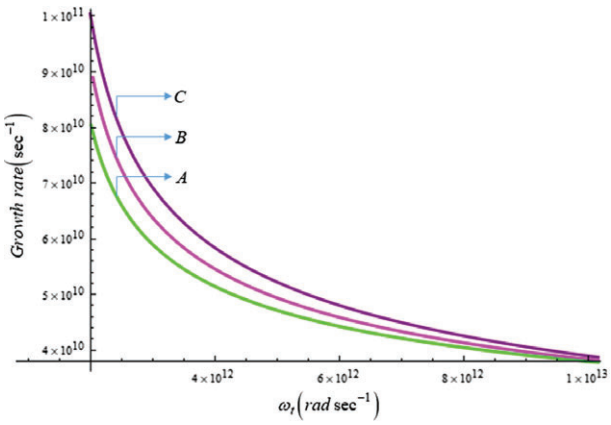


FIGURE 2 Growth rate variation with radiation frequency for different beam densities for (A) $n_{ib} = 8 \times 10^{14}$ cm^{-3}, (B) $n_{ib} = 10 \times 10^{14}$ cm^{-3}, (C) $n_{ib} = 12 \times 10^{14}$ cm^{-3}

where

$$T = \int_0^{r_d} I_0^2(\alpha r) r dr + \left[\frac{\frac{\varepsilon_d}{\varepsilon_p} I_0(\alpha r_d) Y_0(\beta r_w)}{J_0(\beta r_d) Y_0(\beta r_w) - J_0(\beta r_w) Y_0(\alpha r_d)} \right]^2 \int_{r_d}^{r_w} \left[J_0(\beta r) - \frac{J_0(\beta r_w) Y_0(\beta r)}{Y_0(\beta r_w)} \right]^2 r dr.$$

The growth rate (Γ_{tm}) of the radiation wave can be defined by using $\omega_t = \omega_{tm} + \delta_t = (k_t - k_h) v_{ib} + \delta_t$ and taking the imaginary part of δ_t:

$$\Gamma_{tm} = \frac{\sqrt{3}}{2} \left(\frac{Rc^2}{2T\omega_t} \right)^{1/3}, \tag{12}$$

where δ_t is the small frequency mismatch.

For a completely plasma-filled waveguide ($0 < r < r_d$), the dispersion relation for the TM mode is given by

$$\omega_t^2 = \omega_c^2 + \frac{k_t^2 c^2}{\varepsilon_p}, \tag{13}$$

where ω_c is the mode cut-off frequency of waveguide.

From the relation $\varepsilon_p = \left(1 - \frac{\omega_p^2}{\omega_t^2} \right)$, we can inferr that an increase in the plasma density leads to a decrease in plasma permittivity, and from Equation 13, it can be seen that this will lead to an increase in radiation frequency. Thus, the growth rate of the radiation wave falls off with the increase in plasma density.

The efficiency (η_{tm})of the radiation wave can be expressed as

$$\eta_{tm} = \frac{\Gamma_{tm}}{\omega_t} \frac{\gamma_0^3}{\sqrt{3}(\gamma_0 - 1)} = \frac{1}{2} \left(\frac{Rc^2 \gamma_0^9}{T\omega_t^4 (\gamma_0 - 1)^3} \right)^{1/3}. \tag{14}$$

3 | RESULT AND DISCUSSIONS

The present study was carried out to analyse the growth rate and efficiency of the radiation wave by considering an analytical model in which a density-modulated REB interacts with the slow wave structure. The effect of the beam and the dielectric medium was studied on the output THz radiation, for which the following typical parameters were considered; REB velocity $v_{ib} = 0.94c$, relativistic gamma factor $\gamma_0 = 2.94$, density of the beam $n_{ib} = 9 \times 10^{14}$ cm^{-3}, length of the modulator space $l_M = 0.55$ cm, drift space length $l_D = 1.2$ cm, electron beam radius $r_b = 0.02$ cm, radius of the waveguide $r_w = 0.04$ cm, and width of dielectric lining $(r_w - r_d) = 0.01$ cm.

The influence of different beam densities on the growth rate of the output radiation with radiation frequency is shown in Figure 2. The figure shows that the growth rate of the wave increases with the increase in the density of the electron beam. This is because, with the increase in the beam density, more number of electrons are available to transfer their energy to the radiation wave, allowing the wave to grow. Further, the growth rate declines with the increase of the radiation frequency.

Figure 3 illustrates the effect of beam velocity on the growth rate of the radiation wave for different values of the dielectric constant. As the dielectric constant increases, the phase velocity of the electromagnetic mode reduces in order to have substantial interaction with the electron beam and hence the growth rate increases. Further with the increase of the beam energy, the frequency of the wave increases and hence the growth rate decrease with the beam velocity.

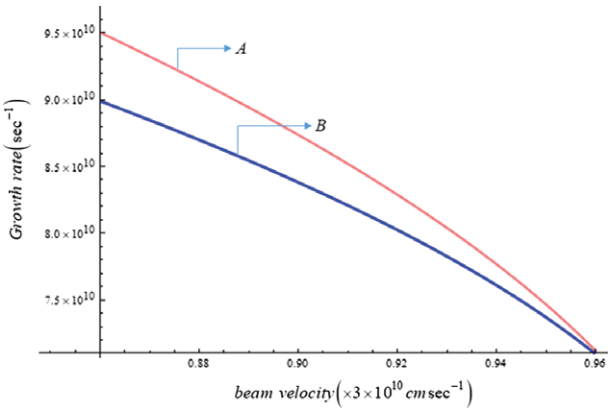


FIGURE 3 Variation of growth rate with beam velocities for different dielectric constant for (A) $\varepsilon_d = 2.1$, and (B) $\varepsilon_d = 1.7$

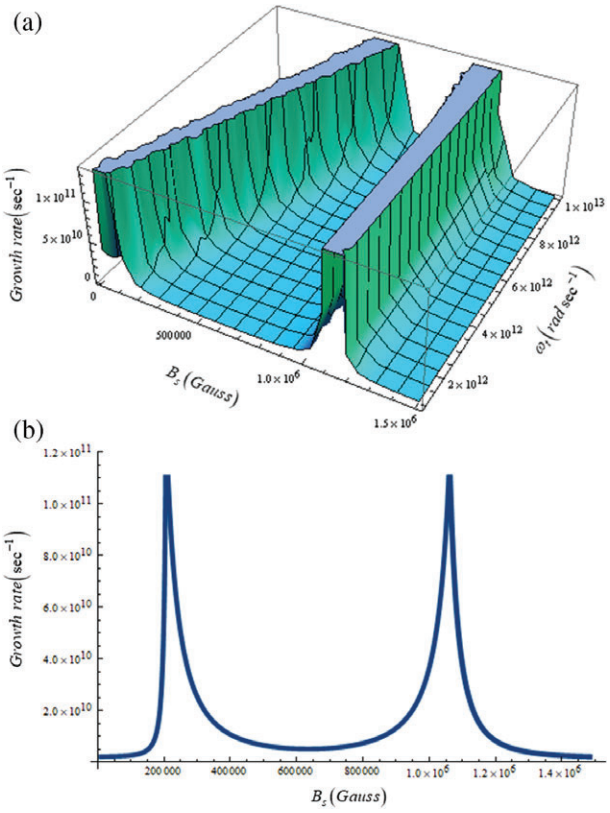


FIGURE 4 (a) Influence of the external magnetic field and radiation frequency on the growth rate of the output radiation. (b) Two-dimensional profile of the plot

The influence of the applied external magnetic field on the THz radiation is shown in Figure 4. The growth rate initially increases as the magnetic field is increased, but at particular value of the magnetic field the frequency of the pump field becomes comparable to the electron cyclotron frequency, at which a peak with maximum growth rate is achieved. The other peak corresponds to the resonance between the electron beam and the cyclotron frequency. The maximum emission of the electromagnetic wave at resonance has been observed by Krafft et al.[35] With further increase of the field, the growth rate drops down. This behaviour agrees with the theoretical observations of Bhasin and Sharma.[36]

Figure 5 shows the variation of the growth rate with the magnitude of the field of the pump wave and the radiation frequency. With the increase of the field of the pump wave, the pondermotive force is exerted more strongly on the beam of electrons, which leads to efficient interaction and hence the growth rate increases.

Figure 6 shows the variation of the efficiency of the system with the radiation frequency for modulated and unmodulated electron beams. The efficiency falls off with the frequency of the radiation wave, and for the density-modulated beam nearly 21% higher efficiency is achieved.

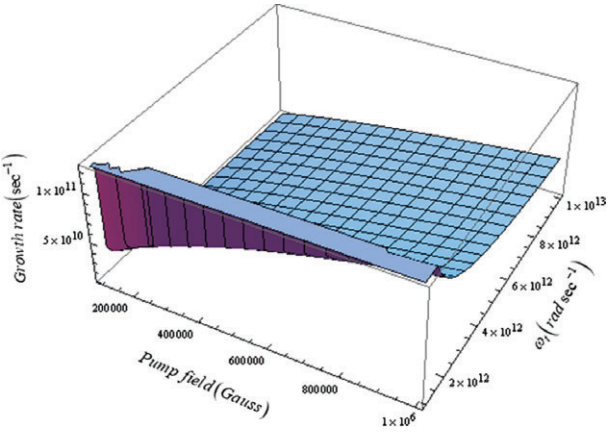


FIGURE 5 Variation of growth rate with the field of the pump wave and the radiation frequency

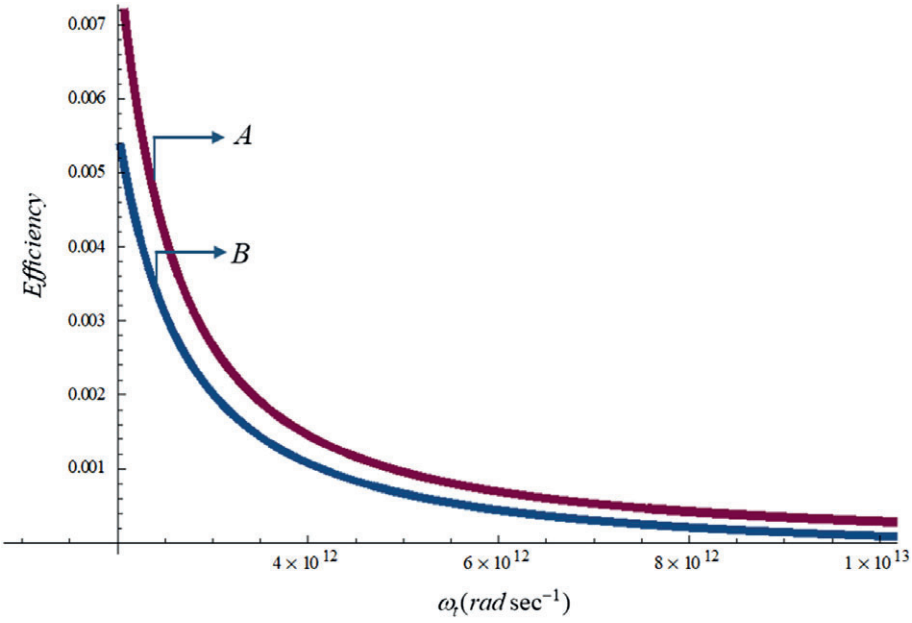


FIGURE 6 Variation of efficiency with radiation frequency for (A) a modulated beam and (B) an unmodulated beam

4 | CONCLUSION

For the efficient generation of the THz radiation wave, a pre-modulated REB is taken into consideration. A dielectric-lined waveguide acts as a slow wave structure, which slows down the phase velocity of the pondermotive wave and thus leads to more effective interaction between the beam and the electromagnetic mode at lower beam energies. The growth rate and efficiency of the radiation wave falls off monotonically with the radiation frequency. The tunability of the radiation wave is determined by the beam parameters and the dielectric constant of the waveguide. The increase in beam density and the dielectric constant of the waveguide leads to the increase in the growth rate. For the applied magnetic field, the growth rate reaches a maximum value when the wiggler wave frequency is comparable to the electron cyclotron frequency. The model seems to be an effective way for the generation of tunable THz radiation which can be particularized for practical applications.

REFERENCES

[1] M. Hangyo, T. Nagashima, S. Nashima, *Meas. Sci. Technol.* **2002**, *13*, 1727.
[2] A. R. Orlando, G. P. Gallerano, *J. Infrared Millim. Terahertz Waves* **2009**, *30*, 1308.
[3] J. F. Federici, B. Schulkin, F. Huang, D. Gary, R. Barat, F. Oliveira, D. Zimdars, *Semicond. Sci. Technol.* **2005**, *20*, S266.
[4] B. Zhu, Y. Chen, K. Deng, W. Hu, Z. S. Yao, in *PIERS Proceed.*, **2009**; 1166–1170.
[5] P. Malik, S. C. Sharma, R. Sharma, *Phys. Plasmas* **2017**, *24*, 073101.
[6] A. Gover, *Phys. Rev. Spec. Top. Accel. Beams* **2005**, *8*, 030701.
[7] J. Panwar, S. C. Sharma, *Phys. Plasmas* **2017**, *24*, 083101.
[8] A. K. Malik, H. K. Malik, S. Kawata, *J. Appl. Phys.* **2010**, *107*, 113105.
[9] M. Singh, S. Kumar, R. P. Sharma, *Phys. Plasmas* **2011**, *18*, 022304.
[10] F. Bakhtiari, S. Golmohammady, M. Yousefi, B. Ghafary, *Phys. Plasmas* **2016**, *23*, 123105.
[11] V. A. Namiot, L. Y. Shchurova, *Phys. Lett. A* **2011**, *375*, 2759.
[12] D. N. Gupta, V. V. Kulagin, H. Suk, *Opt. Commun.* **2017**, *401*, 71.

[13] B. Schütte, S. Bauch, U. Frühling, M. Wieland, M. Gensch, E. Plönjes, T. Gaumnitz, A. Azima, M. Bonitz, M. Drescher, *Phys. Rev. Lett.* **2012**, *108*, 253003.
[14] A. K. Malik, H. K. Malik, U. Stroth, *Phys. Rev. E* **2012**, *85*, 016401.
[15] K.-Y. Kim, *Phys. Plasmas* **2009**, *16*, 056706.
[16] S. Yang, Q. Zhou, C. Tang, S. Chen, *Phys. Plasmas* **2017**, *24*, 123107.
[17] W.-M. Wang, Z.-M. Sheng, X.-G. Dong, H.-W. Du, Y.-T. Li, J. Zhang, *J. Appl. Phys.* **2010**, *107*, 023113.
[18] A. M. Cook, R. Tikhoplav, S. Y. Tochitsky, G. Travish, O. B. Williams, J. B. Rosenzweig, *Phys. Rev. Lett.* **2009**, *103*, 095003.
[19] G. Andonian, O. Williams, X. Wei, P. Niknejadi, E. Hemsing, J. B. Rosenzweig, P. Muggli, M. Babzien, M. Fedurin, K. Kusche, R. Malone, V. Yakimenko, *Appl. Phys. Lett.* **2011**, *98*, 202901.
[20] H. P. Freund, A. K. Ganguly, *Nucl. Instrum. Methods Phys. Res. A* **1990**, *296*, 462.
[21] M. Cohen, A. Kugel, D. Chairman, M. Arbel, H. Kleinman, D. Ben-Haim, A. Eichenbaum, M. Draznin, Y. Pinhasi, I. Yakover, A. Gover, *Nucl. Instrum. Methods Phys. Res. A* **1995**, *358*, 82.
[22] M. Cohen, A. Eichenbaum, M. Arbel, D. Ben-Haim, H. Kleinman, M. Draznin, A. Kugel, I. M. Yacover, A. Gover, *Phys. Rev. Lett.* **1995**, *74*, 3812.
[23] S. C. Sharma, A. Bhasin, *Phys. Plasmas* **2007**, *14*, 053101.
[24] V. K. Tripathi, C. S. Liu, *IEEE Trans. Plasma Sci.* **1989**, *17*, 583.
[25] O. V. Kibis, M. R. da Costa, M. E. Portnoi, *Nano Lett.* **2007**, *7*, 3414.
[26] R. Hedayati, S. Jafari, S. Batebi, *Plasma Phys. Control. Fusion* **2015**, *57*, 085007.
[27] V. K. Tripathi, C. S. Liu, *IEEE Trans. Plasma Sci.* **1990**, *18*, 466.
[28] T. M. Antonsen, J. Palastro, H. M. Milchberg, *Phys. Plasmas* **2007**, *14*, 033107.
[29] S. Chauhan, J. Parashar, *Phys. Plasmas* **2014**, *21*, 103113.
[30] V. B. Gildenburg, N. V. Vvedenskii, *Phys. Rev. Lett.* **2007**, *98*, 245002.
[31] H. K. Malik, *Phys. Lett. A* **2015**, *379*, 2826.
[32] M.-K. Chen, J. H. Kim, C.-E. Yang, S. S. Yin, R. Hui, P. Ruffin, *Appl. Phys. Lett.* **2008**, *93*, 231102.
[33] D. Singh, H. K. Malik, *Phys. Plasmas* **2014**, *21*, 083105.
[34] M. Kumar, V. K. Tripathi, *Phys. Plasmas* **2012**, *19*, 073109.
[35] C. Krafft, G. Matthieussent, P. Thevenet, S. Bresson, *Phys. Plasmas* **1994**, *1*, 2163.
[36] A. Bhasin, S. C. Sharma, *IEEE J. Quantum Electron.* **2009**, *45*, 1129.

How to cite this article: Panwar J, Sharma SC. Terahertz radiation emission using plasma-filled dielectric liner with the effects of pre-modulated relativistic electron beam. *Contributions to Plasma Physics* 2018;1–8. https://doi.org/10.1002/ctpp.201800033

Available online at www.ijapie.org

INTERNATIONAL JOURNAL OF ADVANCED PRODUCTION AND INDUSTRIAL ENGINEERING

IJAPIE-2018-04-228, Vol 3 (2), 41-46

IJAPIE
Connecting Science & Technology with Management.
A Journal for all Products & Processes.

Wind Energy in India: Current Status and Potential

Prem Prakash
(Delhi Technological University, Delhi, India)
Email: ppyadav1974@gmail.com

Abstract : Wind energy sources and technologies have potential to provide solutions to the long-standing energy problems being faced by the developing countries. The renewable energy sources like wind energy can be used to overcome energy shortage in India. To meet the energy requirement for such a fast growing economy, India will require an assured supply of 3–4 times more energy than the total energy consumed today. The renewable energy is one of the options to meet this requirement. In this paper, efforts have been made to summarize the availability, current status of wind energy, wind power potential, wind power growth, repowering wind farms in India and future potentials of renewable energy options in India. This paper also discusses the wind real contribution to electricity demand of India and aspects for improvement of wind technology. This paper also assesses specific policy interventions for overcoming the barriers and enhancing deployment of renewable for the future.

Keywords: Wind energy; repowering wind farms; wind technology; wind potential.

I. INTRODUCTION

Wind energy is the fastest growing sources of energy in the world. Developing countries have witnessed huge gap between demand and supply of the electricity. The socio-economic development of the nation depends on availability of electricity infrastructure, as electricity is the key in development of industrial and commercial establishments. Renewable energy sources such as wind, hydro, solar, biomass are interesting attractive to meet the challenges of growing electricity demand in India. With recent development in wind energy technologies for power generation, wind energy has emerged as a viable and cost effective option for electricity. India is the fifth largest energy producer globally after China, USA, Germany and Spain. But due to lack adequate planning resource crunch the country has only 17.35 GW of installed wind energy.

However during past few decades the Ministry of New and Renewable Energy (MNRE) has taken important steps to accelerate the growth of wind energy installed in India. Wind energy programme have been launched for comprehensive wind resources assessment, R&D works and implemented of new wind energy technologies. The MNRE has announced several fiscal and promotional incentives at the Central Government and State Government levels to encourage private wind energy developers to take-up large commercial projects on wind mills.

II. WORLDWIDE STATUS OF WIND ENERGY

Wind is the key of the energy economy. It is redundant, low cost, and widely distributed; it scales up easily and can be developed quickly. Oil wells go dry and coal seams run out, but the earth's wind resources cannot be depleted. China overtook U.S. as the world leader in wind power in 2011 and 2010 according to a new annual report by the Global Wind Energy Council. Table 1 shows the cumulative installed capacity of top ten countries [1] in the world. Cumulative capacity of U.S.A. is 46.919 GW, Germany having 29.06 GW, Spain have a cumulative capacity of 21.674 GW. India in the world is at fifth position with capacity of 16.084 GW in 2011.

III. INDIA WIND POWER GROWTH

Wind energy in India has emerged sources available in the country. The large numbers of wind energy projects have been started during past few decades. With recent development of the wind turbine technology and continuous improvement in the reliability and conversion efficiency of the wind energy conversion system, the wind energy installation is growing at faster rate than other alternatives. Presently, India [9] has the fifth largest installed capacity of 14158 MW till the end of March 2011. Starting from about 1350 MW in 2001, this figure has been achieved at a CAGR (Compound Annual Growth Rate) of 26 percent for the period 2001-2011.

The estimated wind energy potential in India by wind energy technology (C-WET) and world Institute for the sustainable energy (WISE) are 48.5GW and 100 GW respectively. Recently, the Energy Alternatives India (EAI) has estimated total offshore wind energy in the country to 120 GW, which is about 68 percent of the presently total installed capacity of the country. Therefore such a huge potential if truly exploited through indigenous technology may help in reducing the existing demand and supply gap of the nation.

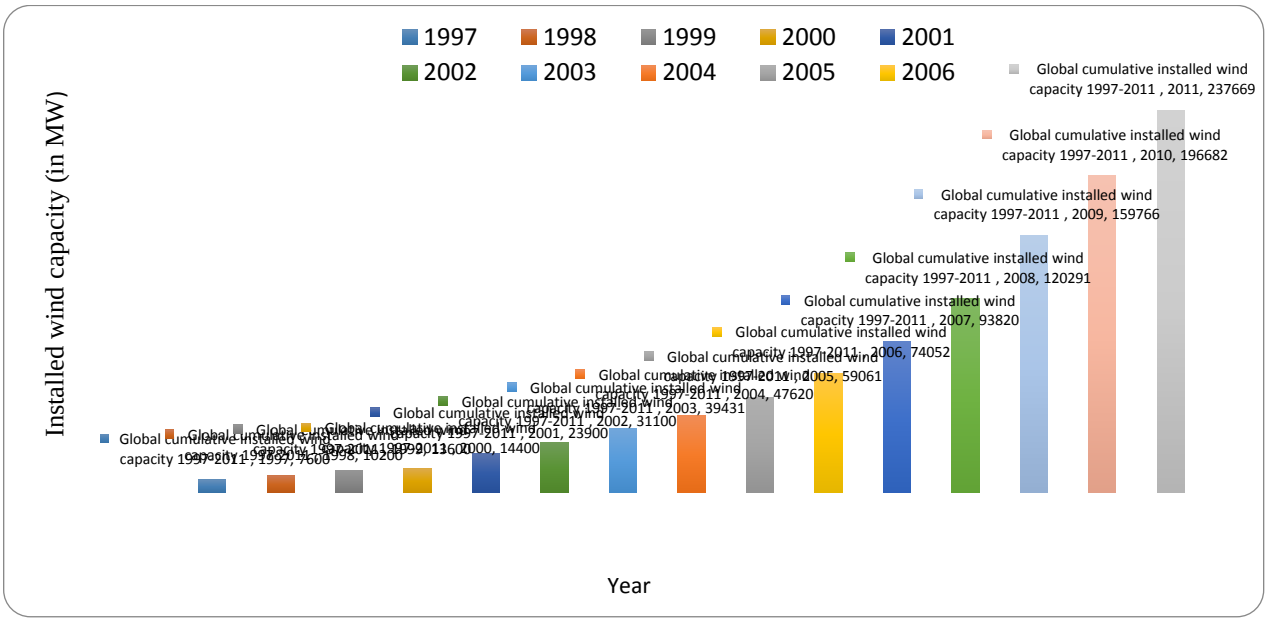


Fig.1 Global cumulative installed wind capacity 1997-2011 [1]

Table 1 Top 10 cumulative installed capacity up to December 2011 [1, 2]

Position	Country	Total Capacity 2011 [GW]	Total Capacity 2010 [GW]	Total Capacity 2009 [GW]
1	**China**	62.364	44.733	25.81
2	**USA**	46.919	40.18	35.159
3	**Germany**	29.06	27.215	25.777
4	**Spain**	21.674	20.676	19.149
5	**India**	16.084	13.065	11.807
6	**Italy**	6.8	5.797	4.85
7	**France**	6.737	5.66	4.754
8	**United Kingdom**	6.54	5.203	4.092
9	**Canada**	5.265	4.008	3.319
10	**Portugal**	4.083	3.702	3.357
12	**Rest of the World**	32.143	26.441	21.872
	Total	**237.669**	**196.682**	**159.766**

IV. REPOWERING WIND FARMS IN INDIA

Replacing old, underperforming wind turbines with modern ones that could offer better returns and more power than before opens up a lucrative opportunity in wind power-that of Repowering. For close to 2 decades the sector has witnessed a number of challenges, opportunities and changes. Over this time, the industry has made path breaking enhancement in turbine efficiency and reliability. Today we have turbines that offer a viable investment in low wind sites while also ensuring improved reliability. This advancement in technology also offers another lucrative opportunity. Repowering wind turbines that are over 15 years old cover a landscape that could easily be called the "Gulf of Wind Energy in India." These turbines hardly do justice to the potential that this region houses. The performance has been below par, and it has been found that most of the turbines that are underperforming are in wind sites which have much lower speeds. It is therefore natural to explore the option of replacing these with modern turbines that could offer better returns and more power than before. In Tamil Nadu, about 60 percent of small wind turbines (<400kW) installed before the year 2000 are operating with plant load factor (PLF) ranging from 10 to 15

percent, where as the new technology wind turbines can operate at a PLF range of 27 to 32 percent in the same sites.

It is also important to plan the project well in advance to ensure that access roads, platforms, storage area and removal /rerouting of the existing lines the wind farms is smooth and does not affect any wind turbines in vicinity.

The challenges include securing necessary approvals and licenses from authorities as well as ensuring a favorable policy and maintaining regulatory transparency and support. It would benefit the industry to replace the inflexible, arbitrary and bureaucratic spacing requirements with a more flexible, fact based regulations. The Government should also encourage Re Powering through various forms of incentives for capacity addition, increase in tariff, etc.

Installation of suitable turbines for a specific site , replacing obsolete technology with technologically advanced variable drive, thereby increasing the average PLF to 27 percent. This will Improve overall performance and hence power generation from 12.5 million units to 30.0 million units, for the same capacity and with existing evacuation infrastructure.

Super Sales India, a part of the Lakshmi Machine Works (LMW) Group joined hands with Gamesa in implementing the first Re-powering project in India named "Project Avatar". At the selected site, the existing wind farm consisted of 29 units of 300 kW turbines and 2 units of 500kW turbines at Kethanur village in Tirupur district, Tamil Nadu. Gamesa undertook a detailed study of the site and surrounding area and recommended that the 11x300 kW turbines could be replaced with 4 units of Gamesa. Wind power generation is multiplied without the need for additional land, efficient use of potential land and more capacity addition per unit of land area .A typical example comparing existing scenario and Re-powering proposal for a wind farm in Coimbatore is given in Table 2.

Table 2 Comparison of existing scenario and Re-Powering proposal [10]

Parameter	**Wind Farm**	
Capacity	8.1 MW	8.5MW
Annual estimated generation	104 Lakh kW	220 Lakh kW
PLF	14.70 percent	29.50 percent

V. WIND POWER POTENTIAL IN INDIA

Wind availability in India is influenced by the monsoon circulations. The Southwest summer monsoon in India starts usually in May-June month when cool and humid air starts moving towards the land also the weaker Northeast monsoon when cool air moves towards the ocean. The wind potential in India is mainly available in the coastal areas of Gujarat, Karnataka and Maharashtra. In addition to these the states of Andhra Pradesh, Tamil Nadu and Madhya Pradesh, Telangana and Kerala have also significant potential of wind energy. Table 3 shows the state wise wind power potential in India. Gujarat having highest wind potential with 84431 MW, Karnataka is on second with 55857 MW, Maharashtra is on third position with a potential of 45394 MW power potential and Andhra Pradesh having wind power potential 44229 MW.

Table 3. State wise % of Wind Potential Utilized (As on 31.03.2016)

S.No	**State**	**Cumulative Wind Power Installed Capacity operational at the end of FY 2016 (MW)**	**Total Wind power potential at 100 meter above ground level (MW)**	**Percentage of Wind Power potential utilized**
1.	Andhra Pradesh	1431.45	44229	3.24%
2.	Gujarat	3948.61	84431	4.68%
3.	Karnataka	2869.15	55857	5.14%
4.	Kerala	43.5	1700	2.56%
5.	Madhya Pradesh	2141.1	10484	20.42%
6.	Maharashtra	4653.83	45394	10.25%
7.	Rajasthan	3993.95	18770	21.28%
8.	Tamil Nadu	7613.86	33800	22.53%
9.	Telangana	77.7	4244	1.83%
10.	Others	4.3	3342	0.13%
Total		**26777.45**	**302251**	**8.86%**

VI. ROLE OF WIND ENERGY IN INDIA

Currently, wind power accounts for about 8 percent of India total installed power capacity, but actual wind energy is about 2 percent of the total generation. This is mainly due to lower capacity utilization factors (CUFs) than do fossil fuel power plants. It is a matter of great concern, that in spite of huge potential of wind energy available in the country, due to unavailability of efficient and reliable energy conversion of systems, the utilisation of wind energy is poor. Table 4

provides insights on possible contributions by wind energy to the total electricity produced in India by 2020.

A. Challenges in Global Positioning

India is finding difficulty in global positioning mainly due to its conservative approach with wind energy density estimation. The ministry of New and Renewable Energy (MNRE) is addressing these issues in the upcoming 12th five year plan by revaluating wind energy potential at higher hub heights and by proposing local content requirements.

Also, the use of indigenous technology in WECs are still not aggressive enough since most of the manufacturing bases in India are merely assembly units which import most the components /subcomponents. It has become essentials to develop indigenous technology in WEC through R&D works and implementation of pilot projects.

Table 4 Summary of wind energy outlook scenario for 2020- India [5]

Growth Scenario	Cumulative Wind Power Capacity (MW)	Electricity Output (GWh)	Share of electricity demand (%)	Output (GWh)
Reference	20332	40665	2.6-2.8	610
Moderate	63230	126459	8.1-8.7	8247
Advanced	134828	269656	17.3-18.6	9438

B. Challenges in Transmission

The intermittent nature of wind has an adverse impact on the grid stability. The wind energy sites are mainly located in coastal area of the country, when the grid stability is not very good. The interconnection of wind farms/mills to the causes the voltage fluctuation and also increases the stress on existing transmission infrastructure. Since the transmission networks maintenance is the responsibility of the state transmission utilities, which are not upgraded during recent past due to lack of resources in the state utilities. Wind energy utilization need upgraded transmission infrastructure in especially coastal areas for effective power evacuation. Presently, the India has no grid codes that include standard for wind integrates and specific the tolerable limit of grid parameters due variable elements products for grid. It is worth to mention that existing grid codes also needed necessary modifications to ensure system operational stability and reliability.

C. Regulatory Challenges

The existing regulation on renewable energy generation, grid connected and transmission changes are not uniform. A national policy on generation, grid connection and transmission of energy produced through Renewable source should be framed to achieve the mission of wind and solar energy set by the Government. Also effort should be made to enhance proactive co-operation between state transmission utilities, and power producers and power purchasers.

D. Technological Challenges

Development of high capacity turbines in recent past has given significant important to the wind energy conversion system. The continuous improvement in the turbine technology has developed confidence among the manufacturers and they are willing to give a guarantee on performance.

The power of wind turbine has a cubic relation with wind speed and hence the interconnection of turbine to grid affects the grid parameters such as power outrages primary fluctuations and voltage fluctuation etc. seems to be an interesting alternative. Utilization of wind energy in low wind speed region is another grey area, where no effects have been made so far. Development of low speed turbine to meant this challenge.

Table 5 Potential areas for generating wind energy (in MW)

S.No.	**States**	**Power generated (in MW)**
1.	Tamil Nadu	6987.60
2.	Maharashtra	2733.30
3.	Gujarat	2966.30
4.	Karnataka	1933.50
5.	Rajasthan	2070.70
6.	Madhya Pradesh	376.40
7.	Andhra Pradesh	245.50
8.	Kerala	35.10
9.	West Bengal	1.1

VII. WIND ENERGY STATUS IN INDIA

India's rapidly growing economy and population leads to relentlessly increasing electricity demand. The IEA predicts that by 2020, 327 GW of power generation capacity will be needed, which would imply an addition of 16 GW per year. This urgent need is reflected in the target the Indian government has set in its 11th Five Year Plan (2007-2012), which envisages an addition of 78.7 GW in this period, 50.5 GW of which is coal. The potential areas for generating power through wind mills are in the states of Tamil Nadu, Karnataka, Kerala, Gujarat, Andhra Pradesh, Maharashtra, Rajasthan and Madhya Pradesh. As of 31st March 2012 the installed capacity of wind power in India was 17.351 GW mainly spread across Tamil Nadu (6987.60 MW), Maharashtra (2733.30 MW), Gujarat (2966.30 MW), Karnataka (1933.50 MW), Rajasthan (2070.70 MW), Madhya Pradesh (376.40MW), Andhra Pradesh (245.50 MW), Kerala (35.10 MW), West Bengal (1.1 MW) as shown in Table 5.

VIII. TRENDS IN WIND TECHNOLOGY

A major trend in wind turbine technologies, observed consistently since early eighties, is to build larger and larger wind turbines. The wind turbine ratings have changed from 25-40 kW to 7 MW and now 10 MW wind turbines are under development. One can make out the immense technological transition that has taken place in wind turbines and engineering of wind turbines in the installation in India. Trends in India mirror international trends except for the fact that there been a lag of about 2 years. This is due to technology transfer issues often related to individual wind turbine suppliers.

Profiles of blades used in earlier turbines are based on National Advisory Committee for Aeronautics (NACA) profiles that result in maximum coefficient of performance of 0.3 to 0.4. Efforts are on to develop blade aerodynamic profiles that are better at harnessing wind energy. Lightness and strength of the materials is important for blades of large wind turbines with a rating of 5 MW, 7MW or 10 MW. A blade is composite material, therefore the properties and interaction between materials during processing need to be well understood to produce high quality components. Materials used while manufacturing blades are birch plywood sticks, core material fiber rods, and fiberglass and epoxy resin. In some designs, carbon epoxy is also used. Traditionally, the wind turbines used to be fixed speed, running at fixed revolutions per

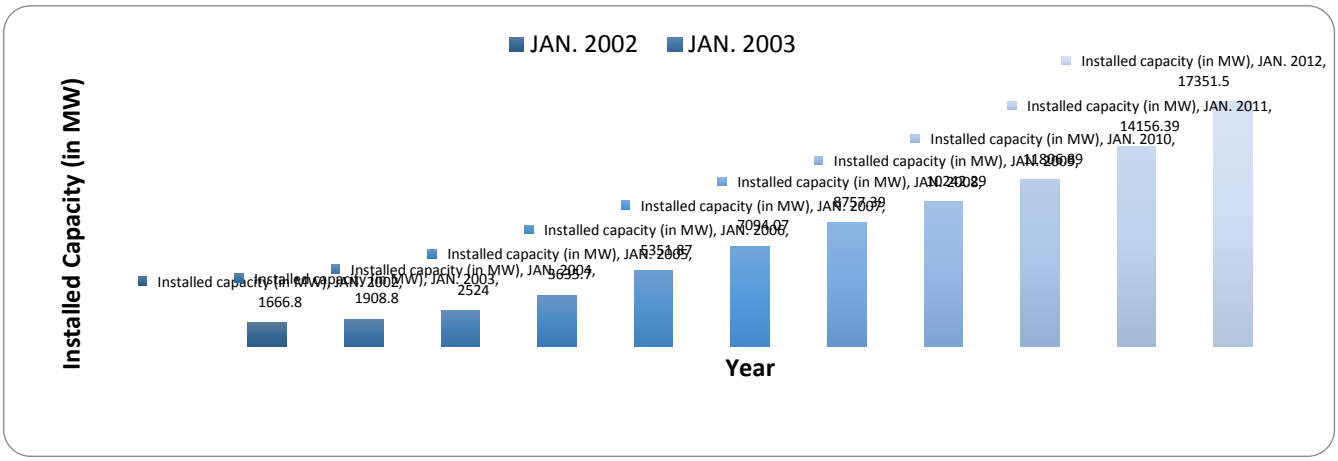


Fig.2 Wind power growth in India (MW) [7,8]

Table 5 Year wise installed capacity in India up to 31.03.2012 [6].

State	Andhra Pradesh	Gujarat	Karnataka	Kerala	Madhya Pradesh	Maharashtra	Rajasthan	Tamil Nadu	West Bengal	Others	Total
Up to March'2002	93.2	181.4	69.3	2.0	23.2	400.3	16.1	877.0	1.1	3.2	1666.8
2002-03	0.0	6.2	55.6	0.0	0.0	2.0	44.6	133.6	0.0	0.0	242.0
2003-04	6.2	28.9	84.9	0.0	0.0	6.2	117.8	371.2	0.0	0.0	615.2
2004-05	21.8	51.5	201.5	0.0	6.3	48.8	106.3	675.5	0.0	0.0	1111.7
2005-06	0.45	84.60	143.80	0.0	11.40	545.10	73.27	857.55	0.0	0.0	1716.17
2006-07	0.80	283.95	265.95	0.0	16.40	485.30	111.90	577.90	0.0	0.0	1742.05
2007-08	0.0	616.36	190.30	8.50	130.39	268.15	68.95	380.67	0.0	0.0	1663.32
2008-09	0.0	313.6	316.0	16.5	25.1	183.0	199.6	431.1	0.0	0.0	1484.9
2009-10	13.6	197.1	145.4	0.8	16.6	138.9	350.0	602.2	0.0	0.0	1564.6

2010-11	55.4	312.8	254.1	7.4	46.5	239.1	436.7	997.4	0.0	0.0	2349.2
2011-12	54.1	789.9	206.7	0.0	100.5	416.5	545.7	1083.5	0.0	0.0	3196.7
Total	**245.50**	**2966.30**	**1933.50**	**35.1**	**376.40**	**2733.30**	**2070.70**	**6987.60**	**1.10**	**3.20**	**17351.5**

per minute (RPM). However, a variable speed concept is considered more suitable because of the flexibility it offers in changing the rotor RPM. A variable speed wind turbine enables greater efficiency at wind speeds between cut-in and related wind speeds of the wind turbine (3-12 m per sec.). A variable speed turbine, due to the power electronics involved can also be grid friendly and minimize the reactive power requirements. Within the variable speed wind turbine category also we have geared and non-geared wind turbines and within the gearless category we can have wind turbines with permanent magnets and electromagnets.

Wind turbines with doubly fed induction generator (DFIG) enable operation of wind turbine in a quasi variable state. In about 10 years of implementation experience, wind turbine or wind power generation in grid connected mode as well as off grid mode has been firmly established as a resource and technology option. We have only harnessed 0.3 percent of the total potential and perhaps 2-3 percent of the electricity demand. From the power system view point there are many challenges associated with wind power that need to be addressed.

IX. CONCLUSION

This paper describes the wind energy potential and installed wind energy in India. The growth of wind energy technologies during last few decades has been summarised through various tables, and illustration in the form of bar charts. The Renewable energy scenario of the country the & also global trends are discussion in detail. The government of India very actively involved in promoting renewable energy. It has been observed that the size of wind turbine has increased and the cost of production has decreased. The future challenge is to bring down the cost further and make it more competitive. The wind turbine cost constitutes 68-84% cost of wind power. India has huge potential for producing wind energy too, but there are still some lacunas. Indian government has laid the foundation for a broad-based renewable energy program to fulfil energy shortage. Despite all its efforts, India is unsettled by China and has now slipped to the fifth rank in its contribution to global wind energy production. Analysis shows that the main factor behind China's lead is presence of a countywide renewable energy law. It may be concluded that India will have to improve in terms of incentives and regulations on renewable energy order to compete with other countries and become the leader in wind energy generation.

REFERENCES

[1]. Global wind report- annual market update 2012, http://www.gwec_net/fileadmin/images/publications/GWEC_annualreport
[2]. http://www.gwec_net/fileadmin/documents/publications/GWEC_PRstats
[3]. MNRE wind power potential in India, http://mnre.gov.in/wpp.htm; [accessed 18.09.2016]
[4]. http://www.cwet_tn.nic.in/html/information_yw.html; [accessed 21.09.2012]
[5]. Ministry of new and renewable energy, http://www.mnre.gov.in/
[6]. http://www.mnre.gov.in/achievements.htm; [accessed 21.09.2016]
[7]. http://gwec_net/index; [accessed 18.09.2012]
[8]. http://www.mnre.gov.in/annualreport [accessed 21.09.2016]
[9]. A. Sharma, J. Srivastava, S.K. Kar and A. Kumar, "Wind energy status in India: Ashort review," Renewable and Sustainable Eenrgy Reviews ,16 (2012) pp.1157-1164
[10]. Akshay Urja, Ministry of New and Renewable Energy, Government of India, vol.5, issue 2, 2011.